

OPTICAL SCIENCES

Mohammed N. Islam
(Ed.)

Raman Amplifiers for Telecommunications 1

Physical Principles



Springer


XTERA™

Founded by H.K.V. Lotsch

Editor-in-Chief: W. T. Rhodes, Atlanta

Editorial Board: T. Asakura, Sapporo
K.-H. Brenner, Mannheim
T. W. Hänsch, Garching
T. Kamiya, Tokyo
F. Krausz, Vienna and Garching
B. Monemar, Linköping
H. Venghaus, Berlin
H. Weber, Berlin
H. Weinfurter, Munich

Springer

New York

Berlin

Heidelberg

Hong Kong

London

Milan

Paris

Tokyo

Physics and Astronomy



ONLINE LIBRARY

<http://www.springer.de>

Springer Series in OPTICAL SCIENCES

The Springer Series in Optical Sciences, under the leadership of Editor-in-Chief *William T. Rhodes*, Georgia Institute of Technology, USA, and Georgia Tech Lorraine, France, provides an expanding selection of research monographs in all major areas of optics: lasers and quantum optics, ultrafast phenomena, optical spectroscopy techniques, optoelectronics, quantum information, information optics, applied laser technology, industrial applications, and other topics of contemporary interest.

With this broad coverage of topics, the series is of use to all research scientists and engineers who need up-to-date reference books.

The editors encourage prospective authors to correspond with them in advance of submitting a manuscript. Submission of manuscripts should be made to the Editor-in-Chief or one of the Editors. See also http://www.springer.de/phys/books/optical_science/

Editor-in-Chief

William T. Rhodes
Georgia Institute of Technology
School of Electrical and Computer Engineering
Atlanta, GA 30332-0250, USA
E-mail: bill.rhodes@ece.gatech.edu

Ferenc Krausz
Vienna University of Technology
Photonics Institute
Gusshausstrasse 27/387
1040 Wien, Austria
E-mail: ferenc.krausz@tuwien.ac.at
and
Max-Planck-Institut für Quantenoptik
Hans-Kopfermann-Strasse 1
85748 Garching, Germany

Editorial Board

Toshimitsu Asakura
Hokkai-Gakuen University
Faculty of Engineering
1-1, Minami-26, Nishi 11, Chuo-ku
Sapporo, Hokkaido 064-0926, Japan
E-mail: asakura@eli.hokkai-s-u.ac.jp

Bo Monemar
Department of Physics
and Measurement Technology
Materials Science Division
Linköping University
58183 Linköping, Sweden
E-mail: bom@ifm.liu.se

Karl-Heinz Brenner
Chair of Optoelectronics
University of Mannheim
Institute of Computer Engineering
B6, 26
68131 Mannheim, Germany
E-mail: brenner@uni-mannheim.de

Herbert Venghaus
Heinrich-Hertz-Institut
für Nachrichtentechnik Berlin GmbH
Einsteinufer 37
10587 Berlin, Germany
E-mail: venghaus@hhi.de

Theodor W. Hänsch
Max-Planck-Institut für Quantenoptik
Hans-Kopfermann-Strasse 1
85748 Garching, Germany
E-mail: t.w.haensch@physik.uni-muenchen.de

Horst Weber
Technische Universität Berlin
Optisches Institut
Strasse des 17. Juni 135
10623 Berlin, Germany
E-mail: weber@physik.tu-berlin.de

Takeshi Kamiya
Ministry of Education, Culture, Sports
Science and Technology
National Institution for Academic Degrees
3-29-1 Otsuka, Bunkyo-ku
Tokyo 112-0012, Japan
E-mail: kamiyatk@niad.ac.jp

Harald Weinfurter
Ludwig-Maximilians-Universität München
Sektion Physik
Schellingstrasse 4/III
80799 München, Germany
E-mail: harald.weinfurter@physik.uni-muenchen.de

Mohammed N. Islam (Ed.)

Raman Amplifiers for Telecommunications 1

Physical Principles

Foreword by Robert W. Lucky

With 222 Figures



Springer

Mohammed N. Islam
Department of Electrical Engineering and Computer Science
University of Michigan at Ann Arbor
1110 EECS Building
1301 Beal Avenue
Ann Arbor, MI 48109-2122
mni@eecs.umich.edu
and
Xtera Communications, Inc.
500 West Bethany Drive, Suite 100
Allen, TX 75013
USA
mislam@xtera.com

Library of Congress Cataloging-in-Publication Data
Raman amplifiers for telecommunications 1: physical principles / editor, Mohammed N. Islam.
p. cm. – (Springer series in optical sciences ; v. 90/1)
Includes bibliographical references and index.
ISBN 0-387-00751-2 (hc. : alk. paper)
1. Fiber optics. 2. Optical communications. 3. Raman effect. 4. Optical amplifiers.
I. Islam, Mohammed N. II. Series.
TL5103.592.F52R35 2003
621.382'75–dc21 2003044945

ISBN 0-387-00751-2 ISSN 0342-4111 Printed on acid-free paper.

© 2004 Springer-Verlag New York, Inc.

All rights reserved. This work may not be translated or copied in whole or in part without the written permission of the publisher (Springer-Verlag New York, Inc., 175 Fifth Avenue, New York, NY 10010, USA), except for brief excerpts in connection with reviews or scholarly analysis. Use in connection with any form of information storage and retrieval, electronic adaptation, computer software, or by similar or dissimilar methodology now known or hereafter developed is forbidden.

The use in this publication of trade names, trademarks, service marks, and similar terms, even if they are not identified as such, is not to be taken as an expression of opinion as to whether or not they are subject to proprietary rights.

Printed in the United States of America.

9 8 7 6 5 4 3 2 1 SPIN 10919521 90/1

www.springer-ny.com

Springer-Verlag New York Berlin Heidelberg
A member of BertelsmannSpringer Science+Business Media GmbH

*To my loving wife,
Nasreen*

Foreword

I remember vividly the first time that I heard about the fiber amplifier. At that time, of course, it was the erbium-doped fiber amplifier, the predecessor of the Raman amplifier that is the subject of this book.

It was an early morning in a forgotten year in Murray Hill, New Jersey at one of our Bell Labs monthly research staff meetings. About twenty directors and executive directors of research organizations clustered around a long table in the imposing executive conference room. Arno Penzias, the vice president of research, presided at the foot of the table.

Everyone who participated in those research staff meetings will long remember their culture and atmosphere. Arno would pick an arbitrary starting point somewhere around the table, and the designated person would head to the front of the table to give a short talk on “something new” in his or her research area. This first speaker would invariably fiddle helplessly with the controls embedded in the podium that controlled the viewgraph projector, but eventually we would hear machinery grinding in the back room as a large hidden mirror moved into place. We would all wait quietly, arranging and choosing our own viewgraphs from the piles that lay on the table in front of every participant.

The rules for the staff meeting were that each speaker was allowed seven minutes and three viewgraphs. However, in spite of Arno’s best efforts to enforce this regimen, everyone took too long and used too many viewgraphs. Various attempts at using loud timers and other incentives all failed. No one could give a respectable talk on a research topic for which they had passionate feelings in seven minutes.

Another rule was that anyone could forfeit his talk by simply saying, “I pass.” This forfeiture was always accepted without comment, but new directors always asked their friends about whether this would constitute a black mark against their performance. No one knew for sure, but rumor had it that it was unwise to pass unless you were truly destitute of material. After all, the implication would be that there was nothing new in your research organization for the last month—not a good indication of your management skills.

With no one passing, and everyone speaking too long, these staff meetings sometimes seemed endless. Computer scientists would talk about new constructs in soft-

ware, systems people would talk about new techniques for speech recognition, physicists would talk about some new laser, chemists would show diagrams of new organic materials, and so forth. It didn't take long for each talk to exceed the understanding of most listeners of whatever specialty was being discussed. I always left with a profound sense of the limitations of my own knowledge, but with an exhilarating inkling into the unfolding of science. It was, perhaps, the best of the old research model in Bell Labs, and in retrospect I can say that in this new competitive world I miss those old scientific-style management meetings.

It was in such a meeting that I first heard about the fiber amplifier. I don't know whether I had been paying attention, but I was immediately galvanized by the implications of this new discovery. One word came to me and blazed across my mind: that word was "transparency."

Surprisingly, in my experience I am not always immediately enthusiastic about a new technology upon initial exposure. One might think that the potentials of great breakthroughs are self-evident, but that does not seem to be the case. When I first heard about the invention of the laser, I had no premonition that lasers would become the primary instrument of the world's telecommunications traffic. When one of the inventors of public key cryptography told me his idea for having two keys, I scoffed at the naiveté of his concept. I remember thinking on first hearing about what is now the principal algorithm for data compression that I thought it was only a theoretical exercise. So my track record for such insights is not altogether good.

However, with the fiber amplifier I went to the other extreme. I foresaw a dramatic revolution in communications. I spoke up at the staff meeting that morning to say that this invention would transform the architecture of communications networks. This would lead to transparent networks, I said, and that this would not necessarily be good for AT&T. I got carried away with this vision, and went on to say that private networks could have their own wavelengths traveling transparently through the network, untouched by the common carrier in the middle. One private network might have "blue" light (figuratively speaking, of course, because we're not talking about visible wavelengths) whereas another would have "green." I foresaw a plug on the wall that passed only the chosen wavelength, which would be owned exclusively by that particular customer's network. AT&T would thus be deprived of the opportunity to process signals for value-added services. AT&T, in fact, wouldn't have any idea what was packed into those wavelengths.

Well, that hasn't exactly happened, but today's optical networks are moving towards increased transparency, and Raman amplifiers will accelerate this trend. The advantages of transparency are compelling. A great many constituent signals can be amplified cheaply in one fell swoop. More importantly, this amplification is independent of the bit rates, protocols, waveforms, multiplexing, or any other particulars of the transmission format. The design isn't "locked in" to any specific format, and as these details change, the amplification remains as effective as ever. In the case of the Raman amplifier, the bandwidth is so enormous that adjectives seem inadequate to describe its potential for bulk amplification.

Transparency in the network is so attractive that probably the only reason it isn't done is that it is so difficult to achieve. One reason is, of course, the necessity for periodically unbundling the signal to add or drop subcomponents. In the digital world

this has usually meant a complete demultiplexing and remultiplexing of the overall signal, an expensive operation. The optical world opens up the possibility of selective transparency for certain wavelengths whereas others are unpacked to do add-drop multiplexing.

So network topology sets limits on transparency. But the other reason transparency is hard to achieve is the implicit accumulation of impairments as a signal incurs successive amplifications. It is ironic that the telephone network was essentially transparent for the first half-century of its existence. Until 1960 the long-haul transmission systems used analogue amplification to boost levels as the signal traversed the nation. The invention of the triode vacuum tube enabled the first transcontinental transmission system to be deployed in the 1920s. It was a marvelous feat to be able to send a band of signals 3000 miles across the country, passing through many amplifiers, accumulating noise and distortion along the way, but still providing intelligible speech at the other end. Some older readers will remember when long distance phone calls sounded crackly and “distant.” Now, of course, it is impossible to tell how far away a connection is. They all sound local, because of digital transmission.

Digital transmission was the triumph of the 1960s. Though now it seems obvious, engineers found the philosophy of digitization hard to grasp for several decades after the invention of pulse code modulation by Reeves in 1939. There is a trade-off here: bandwidth against perfectibility. A 3 kHz voice signal, for example, is transformed by an analogue-to-digital converter into a 64,000 kbps stream of bits, greatly expanding the necessary transmission bandwidth. However, this digital signal can be regenerated perfectly, removing noise and distortion periodically as necessary. A miracle is achieved as the bits arrive across the country in the same pristine form as when they left.

So it was that all long distance transmission was converted to digital format. The introduction of the first lightwave transmission systems hurried this change, inasmuch as lightwave systems were deemed to be “intrinsically digital” because of their nonlinearities and the lack of amplifiers. No one cared much at the time—the early 1980s—but the entire design of the network was predicated on the transmission of 64 kbps voice channels. The multiplexing hierarchy, the electronic switching, the synchronization and timing, and the transmission format assumed that everything was packaged into neat little voice channels. That, of course, was before the rise of the Internet.

Now optical amplification has reversed this trend of the last half-century towards digitization based upon a hierarchy of voice signals. It isn’t just that optical amplifiers have an enormous bandwidth. They do something those old triode vacuum tubes could never do: they amplify without substantially increasing the noise and distortion of the signal. Raman amplifiers are particularly good in this way. Moreover, because Raman amplification is distributed across the whole span of the fiber, the signal level never drops as low as it does when discrete amplifiers are employed. In a system using discrete amplifiers the signal level is at its lowest and most vulnerable right before the point of amplification.

Back at that research staff meeting I was concerned about the implications of transparency to the architecture of the network. A transparent network is, by definition, a “dumb” network. It doesn’t do anything to the signal; it can’t, because it doesn’t

know what the signal is. As an AT&T employee, that sounded threatening. As an Internet user, that sounded empowering. The Internet, after all, was designed around the so-called end-to-end principle. In the architecture of the Internet, intelligence is at the periphery of the network, and the network is as minimally intrusive as is necessary to achieve interconnection. It is an extremely important philosophical principle that was just beginning to be understood in the 1980s. Since then the argument has raged, and the concept of a “stupid” network has been put forward by a number of Internet designers as the ultimate desired objective. If that is so, then the optical amplifier has made possible the ultimate stupid network.

I can’t leave this foreword without mentioning another observation on perhaps a more personal level. Raman amplifiers epitomize for me the transformation of communications from a world of electrical circuits to one of quantum mechanical phenomena. Of course you could argue that transistors themselves depend on quantum mechanical principles, and surely the laser does, and so forth. But for many practical and design purposes these devices could be modeled with traditional circuit equivalents. Since then, however, photonics has increasingly become a showpiece of modern physics. The erbium-doped fiber amplifier had to be understood as a quantum interaction of light with the erbium atom. Raman amplifiers, by contrast, involve the interaction of light with a material structure. We descend ever more into the realm of quantum phenomena, into a world of small and impressive miracles.

A number of my friends and associates at Bell Labs have contributed to this technology and even to this particular book. I’m very proud of the work that they and their peers in academia and other industries have done in the creation of photonics technology. I’ve seen it grow around me and have taken vicarious pride in their accomplishments. Sometimes I tell people that, yes, I know the inventors of this or that great technology, even though I may not have realized at the time the significance of the invention. In the case of Raman amplifiers I remember learning about Raman effects as one of the impairments to be overcome in optical transmission. Researchers in my organization were even then experimenting with Raman amplification, and although there was a glimmer of potential, I can’t say that I was aware of what their future might bring. Perhaps now its day has come, and that’s what this book is all about.

Robert W. Lucky
Fair Haven, New Jersey
March 2003

Preface

Technologies for fiber-optic telecommunications went through a major growth period—some might even say a revolution—roughly during the years 1994 to 2000. This growth came about due to the convergence of several market drivers and technologies. First were data traffic and the Internet, the key drivers of the demand for bandwidth. Prior to the explosion of data traffic and the Internet, voice traffic only grew at an average of 4% a year. The Internet, on the other hand, grew 100% a year or more starting in 1992 and sustained this phenomenal growth rate at least through about 2001. The second was the advent of the optical amplifier, which served the role in optical networks that the transistor had played in the electronics revolution. The optical amplifier was key because it allowed the simultaneous amplification of a number of channels, as opposed to electronic regenerators that operated channel by channel. The third technology was wavelength-division-multiplexing (WDM), which made a single strand of fiber act as many virtual fibers. WDM has allowed the capacity of fibers to be increased by more than two orders of magnitude over the past few years, providing plenty of bandwidth to fuel the growth of data traffic and the Internet. WDM served the role in optical networks that integrated circuits had played in the electronics revolution. Just as the transistor permitted the revolution associated with integrated circuits in electronics, the optical amplifier permitted the revolution associated with WDM in optical networks. Because a number of channels could be simultaneously amplified, the cost of deploying more wavelengths in WDM was gated by the terminal end costs rather than the regenerator costs. Hence far more cost-effective networks became available with the combination of optical amplifiers and WDM.

Raman amplification has been one of the optical amplifier technologies that had a slow start, but then experienced a wide deployment with increasing performance needs of optical networks. It would be reasonable to assume that almost every new or upgraded long-haul (~300 to 600 km between regenerators) and ultra-long-haul (>600 km between regenerators) will eventually deploy some form of Raman amplification technology. Any deployment concerns about discrete or distributed Raman amplification have been outweighed by the performance improvements permitted with Raman amplification. For example, distributed Raman amplification improves

noise performance and decreases nonlinear penalties in WDM networks, thereby alleviating the two main constraints in dispersion-compensated, optically amplified systems. The improved noise performance can be used to travel longer distances between repeaters or to introduce lossy switching elements such as optical add/drop multiplexers or optical cross-connects. Discrete and distributed Raman amplifiers are wavelength agnostic, with the gainband being determined by the pump distribution. Also, discrete Raman amplification can efficiently be integrated with dispersion compensation. Hence, Raman amplification permits wide bandwidth and long reach simultaneously. For instance, commercial systems in 2002 provide 240 channels at 10 Gb/s over 100 nm bandwidth (capacity of 2.4 Tb/s) over 1500 km with static optical add/drop multiplexers at every inline amplifier site (roughly every 80 km). Of course, if less bandwidth is required, then the unrepeatable distance can be even longer.

Although stimulated Raman scattering (SRS) dates back to 1928 [7], it was first studied in optical fibers by Roger Stolen and coworkers in 1972 [10, 9]. Much of the physics of Raman amplification was explored through the 1970s and early 1980s. Then, in 1984 Linn Mollenauer, Jim Gordon, and I suggested the use of Raman amplification in WDM soliton systems [5, 6]. We demonstrated the concept using color center lasers as the pump lasers, and there was a flurry of research on Raman amplification in fiber systems from about 1984 to 1988. However, by 1988 it became clear that erbium-doped fiber amplifiers (EDFAs) were closer to practical deployment, and the Raman work was mostly dropped in favor of rare earth-doped amplifiers. Admittedly, it was a bit difficult to imagine how to put large tabletop lasers such as color center lasers in a central office, in a hut, or under the sea.

Although it seemed that EDFAs would never be displaced as optical amplifiers in fiber-optic systems, by 1997 the scene began to change. Work particularly at Lucent Technologies by Steve Grubb, Per Hansen, Andy Stentz, and others began to show the promise of Raman oscillators pumped by cladding-pumped fiber lasers [1, 2, 4, 3, 8]. I realized the big payoff would be not in oscillators but in Raman amplifiers, and I spunoff from the University of Michigan a startup company called Xtera Communications. Xtera began by trying to develop S-band subsystems (Chapter 10), and later we redirected the business plan to a wideband, long-reach, all-Raman system (Chapter 14).

The key thing to understand is that stimulated Raman amplification had not changed. It was the technology required to make Raman amplifiers that had changed. The most fundamental change was the development and commercialization of practical, high-powered, laser diodes. Although we believed that commercial Raman amplifiers would require cladding-pumped fiber lasers, by 1999 it became clear that laser diodes with sufficient power would be available. This was an extremely important development because it would reduce the cost and size of Raman amplifiers while increasing their reliability. Second, dispersion-compensating fibers (DCF) were being commercialized for use with 10 Gb/s systems. It turns out that the DCF is an excellent gain medium for discrete Raman amplifiers, permitting the integration of dispersion compensation with optical amplification. Finally, all of the required passive components became available at least with fiber pigtails and with the ability to handle high pump powers.

By 2000, Raman amplified systems were becoming commercially available. Several startup companies (e.g., Corvis, Qtera, Xtera) were using Raman amplification as their differentiator. Even the stalwarts of the industry had to take notice of this important technological development. For example, Nortel Networks acquired Qtera, and Lucent Technologies began to develop their all-Raman system, which became commercially available in 2002. It finally looked as if Raman amplification had made inroads in long-haul and ultra-long-haul systems. The noise figure improvement of up to 7 dB was simply too large a system margin to ignore!

With heavy research and development of Raman amplified systems between 1997 and 2002, it would be fair to say that the physics and applications of Raman amplifiers were pretty well understood, at least in the arena of telecommunications. The Raman “buzz” was out there, and telecommunications engineers were constantly asking for a “good reference” that they could read to understand Raman amplification. Raman amplifiers were about to leave the eclectic world of research laboratories and PhDs and perhaps enter the commercial Main Street, and a book that summarized the key physical principles and applications was needed. After all, it would be difficult to deploy and maintain that which was unknown. Therefore, at OFC 2002 I finally agreed to put together this volume, *Raman Amplifiers for Telecommunications*.

For me the assembling of this book is another important step on a long journey. As a graduate student and when I first joined AT&T Bell Labs between 1983 and 1987, we were convinced that Raman amplification was going to be important. At MIT I worked with Linn Mollenauer and Jim Gordon on WDM soliton systems using Raman amplification, and then when I first joined Bell Labs I worked on Raman oscillators and amplifiers. Almost a decade later, I spent five years from 1997 to 2002 transferring to commercialization an all-optical, all-Raman amplified system through Xtera Communications. Now that Raman amplification is finally prime-time for systems, it is necessary to organize, articulate, and share the know-how so that telecommunications and systems engineers can deploy and exploit the technology.

Acknowledgments

This book was written and assembled while I was at Xtera Communications, on a leave of absence from the University of Michigan in Ann Arbor, as well as the first year after I returned to the University. Thanks are due to Professors Richard Brown and Duncan Steel at the University for permitting me to complete this book. Also, I am particularly indebted to Dr. Jon Bayless and Carl DeWilde for encouraging me to put this book together and having the foresight to understand the broader impact that a startup could have by allowing this endeavor.

Many at Xtera Communications worked on Raman amplification and helped in composing this volume. In particular, Amos Kuditcher helped significantly on Chapters 10 and 14. Special thanks are due to Monica Villalobos, without whose help this book could never have been written. Monica kept the process moving forward throughout the year with her usual methodical and professional style. She kept contact with all of the authors, collected all of the chapters, and helped in the hand-off to the

publishers. I think that all of my coauthors would agree that Monica was a pleasure to work with throughout the process.

Finally, I am deeply appreciative of the love, support, and encouragement from my wife, Nasreen, and sons, Sabir and Shawn. The only regret I have in putting this book together is the time it took away from my family.

Mohammed N. Islam
Ann Arbor, Michigan
January 2003

References

- [1] S. Grubb, T. Erdogan, V. Mizrahi, T. Strasser, W.Y. Cheung, W.A. Reed, P.J. Lemaire, A.E. Miller, S.G. Kosinski, G. Nykolak, and P.C. Becker, 1.3 μm cascaded Raman amplifier in germanosilicate fibers. In *Proceedings of Optical Amplifiers and Their Applications*, PD3-1, 187, 1994.
- [2] S.G. Grubb, T. Strasser, W.Y. Cheung, W.A. Reed, V. Mizrahi, T. Erdogan, P.J. Lemaire, A.M. Vengsarkar, D.J. DiGiovanni, D.W. Peckham, and B.H. Rockney, High-power 1.48 μm cascaded Raman laser in germanosilicate fibers, In *Proceedings of Optical Amplifiers and Their Applications*, SA4, 197–199, 1995.
- [3] P.B. Hansen, L. Eskildsen, S.G. Grubb, A.J. Stentz, T.A. Strasser, J. Judkins, J.J. DeMarco, R. Pedrazzani, D.J. DiGiovanni, Capacity upgrades of transmission systems by Raman amplification, *IEEE Photon. Technol. Lett.*, 9:2 (Feb.), 1997.
- [4] P.B. Hansen, L. Eskildsen, S.G. Grubb, A.M. Vengsarkar, S.K. Korotky, T.A. Strasser, J.E.J. Alphonse, J.J. Veselka, D.J. DiGiovanni, D.W. Peckham, D. Truxal, W.Y. Cheung, S.G. Kosinski, and P.F. Wysocki, 10 Gb/s, 411 km repeaterless transmission experiment employing dispersion compensation and remote post- and pre-amplifiers. In *Proceedings of the 21st European Conference on Optical Communications* (Gent, Belgium), 1995.
- [5] L.F. Mollenauer, J.P. Gordon, and M.N. Islam, Soliton propagation in long fibers with periodically compensated loss, *IEEE J. Quantum Electron.* QE-22:157–173, 1986.
- [6] L.F. Mollenauer, R.H. Stolen, and M.N. Islam, Experimental demonstration of soliton propagation in long fibers: Loss compensated by Raman gain, *Opt. Lett.* 10:229–231, 1985.
- [7] C.V. Raman and K.S. Krishnan, A new type of secondary radiation, *Nature* 121:3048, 501, 1928.
- [8] A.J. Stentz, S.G. Grubb, C.E. Headley III, J. R. Simpson, T. Strasser, and N. Park, Raman amplifier with improved system performance, *OFC '96 Technical Digest*, TuD3, 1996.
- [9] R.H. Stolen and E.P. Ippen, Raman gain in glass optical waveguides, *Appl. Phys. Lett.*, 22:276, 1973.
- [10] R.H. Stolen, E.P. Ippen, and A.R. Tynes, Raman oscillation in glass optical waveguide, *Appl. Phys. Lett.*, 20:62, 1972.

Quick Summary of Book

The book is organized into two volumes with three sections. Volume 1 begins with a chapter entitled “Overview of Raman Technologies for Telecommunications.” The first major section (Volume 1, Section A), Raman Physics, contains eight chapters (Chapters 2–9). The second section (Volume 2, Section B) on Subsystems and Modules contains five chapters (Chapters 10–14). Finally, the third section (Volume 2, Section C), Systems Design and Experiments, contains an additional five chapters (Chapters 15–19). Almost half of the book is dedicated to Raman physics, because these are the principles that will remain time invariant. This is covered completely in Volume 1. The second section, Subsystems and Modules, describes applications of Raman technology that will be fairly time invariant, although the details and data of the applications will continuously evolve. Finally, the last section, Systems Design and Experiments, represents a snapshot of the state-of-the-art system demonstrations as of early 2003. This is the section that must necessarily change with time, but at least it can provide a good basis for comparison or updating from 2003. It is important to go all the way from basic physics to systems because they are intimately linked. The basic physics determines what can or cannot be done, and it points to the differential advantages that Raman amplification provides. On the other hand, the systems design and experiments ultimately define what is worth doing and where performance should be optimized. Fortunately, Raman amplification is very rich with physical principles as well as being one of the key enabling technologies for long-haul and ultra-long-haul submarine, terrestrial, soliton, and high-speed systems.

In selecting the topics to be covered in this book as well as the authors to invite, a broad, diverse, and insightful view was sought. As an example, the authors were chosen from industrial labs as well as universities. The industrial laboratories represented include Corning, Furukawa, Lucent Technologies, Nippon Telephone and Telegraph, Nortel Networks, OFS Fitel, Siemens, Tyco Telecommunications, and Xtera Communications. Also, the authors represent the international nature of Raman technology, with contributions from the United States, Europe, Japan, and Russia. Furthermore, young rising stars were invited to contribute chapters as well as the “giants in the field,” starting with Roger Stolen, Linn Mollenauer, and Evgeny Dianov.

It is an honor that so many key researchers in Raman technology accepted the invitation to contribute to this book. The invitation was extended to researchers who have made significant contributions to the technology and whose work has consistently represented the highest quality and deepest insight. Obviously there are many other excellent researchers in the field, but the intent was to cover the main issues in Raman physics, subsystems and modules and systems design and experiments within the limited space of two volumes.

The book begins with “Overview of Raman Technologies for Telecommunications,” which I authored (Chapter 1). Then, the physics section opens with a chapter by Stolen, “Fundamentals of Raman Amplification in Fibers” (Chapter 2), which is fitting since he did much of the original groundbreaking work on Raman amplification in fibers. Noise is a very important aspect of any optical amplifier, and Fludger contributes two chapters on the topic: “Linear Noise Characteristics” (Chapter 4) and “Noise due to Fast Gain Dynamics” (Chapter 8). The most significant technological development for commercial Raman amplifiers is the increase in laser diode power, and Namiki et al., in Chapter 5 describe “Pump Laser Diodes and WDM Pumping.” The other major technological development is the availability of new fibers with efficient Raman gain, and two chapters are dedicated to this topic: in Chapter 6 Grüner-Nielsen and Qian describe dispersion compensating fibers for Raman applications, and in Chapter 7 Dianov describes more forward-looking work on new Raman fibers. The simplest Raman amplifier uses CW pumps and a counterpropagating geometry (i.e., where the pump and signal propagate in opposite directions). However, the performance of this basic Raman amplifier can be improved by a number of emerging techniques. In Chapter 3, Grant and Mollenauer describe the use of time-division multiplexing of pump wavelengths. Then, in Chapter 9 Radic discusses and compares forward, bidirectional, and higher-order Raman amplification.

In the second section, “Subsystems and Modules,” four types of Raman devices are covered: discrete (or lumped) amplifiers, distributed amplifiers, lasers, and a combination of discrete and distributed amplifiers. In Chapter 10 I review work on discrete or lumped Raman amplifiers to open up new wavelength windows, particularly in the short wavelength S-band. Then, Headley et al. review in Chapter 11 work on Raman fiber lasers or oscillators. Next, in Chapter 12, Evans et al. discuss distributed Raman transmission, applications, and fiber issues. One of the most important applications of combined discrete and distributed amplifiers is to broadband transmission systems. One way to achieve the broadband amplifier is to combine erbium-doped fiber amplifiers with Raman amplifiers, and in Chapter 13 Masuda describes hybrid EDFA/Raman amplifiers. Another route to a broadband system is to use all-Raman discrete and distributed amplifiers, and in Chapter 14 on wideband Raman amplifiers I along with coworkers at Xtera illustrate this approach.

The third section of the book focuses on system design and experiments. Some of the challenges of the Raman effect are covered in the first two chapters, and system deployments of Raman amplifiers are discussed in the following three chapters. In Chapter 15 Bromage et al. detail multiple path interference and its impact on system design. Then, in Chapter 16 Krummrich discusses Raman impairments in WDM systems. As examples of areas where Raman amplifiers are a key enabling technology, three system experiments are included. First, in Chapter 17 Kidorf et al. describe

the use of Raman amplifiers in ultra-long-haul submarine and terrestrial applications. Then, in Chapter 18 Mollenauer discusses ultra-long-haul, dense WDM using dispersion-managed solitons in an all-Raman system. Finally, in Chapter 19 Nelson and Zhu illustrate 40 Gb/s Raman-amplified transmission.

Survey of Chapters

VOLUME 90/1

Overview of Raman Amplification in Telecommunications (Chapter 1)

As an overview for the book, this chapter surveys Raman amplification for telecommunications. It starts with a brief review of the physics of Raman amplification in optical fibers, along with the advantages and challenges of Raman amplifiers. It also discusses some of the recent technological advances that have caused a revived interest in Raman amplifiers. Then, distributed and discrete Raman amplifiers are described. Distributed Raman amplifiers improve the noise figure and reduce the nonlinear penalty of the amplifier, allowing for longer amplifier spans, higher bit rates, closer channel spacings, and operation near the zero dispersion wavelength. Discrete Raman amplifiers are primarily used to increase the capacity of fiber-optic networks. Examples of discrete amplifiers are provided in the 1310 nm band, the 1400 nm band, and the short-wavelength S-band.

Section A. Raman Physics

Fundamentals of Raman Amplification in Fibers (Chapter 2)

Raman scattering was first published by C.V. Raman in 1928, and he was awarded the 1930 Nobel Prize for the discovery. In 1972 stimulated Raman scattering was first observed in single-mode fibers, and the Raman gain coefficient was also measured that same year. The chapter focuses on various treatments of the Raman interaction, which can appear to be quite different. The quantum approach treats the problem as a transition rate involving photon number. In the classical approach, the Raman effect is a parametric amplifier with an interaction between signal, pump, and vibrational wave. Finally, the Raman interaction itself can be traced to a small time delay in the nonlinear refractive index. This chapter compares and contrasts these various treatments of the Raman effect in optical fibers. Also, a fundamental treatment of noise in fiber Raman amplifiers is included.

Time-Division Multiplexing of Pump Wavelengths (Chapter 3)

This chapter describes an approach to Raman pumping that uses time-division multiplexing of the pump wavelengths. TDM pumping has several advantages over CW

pumping such as efficient gain leveling with a “smart” pump, the elimination of four-wave mixing between pumps, and the reduction of pump-to-pump Raman interactions. This technique only works with backward Raman pumping, where the pump and signal are counterpropagating. The rate of TDM pumping needs only to exceed 1 MHz, so electronic components for these speeds are widely available and very inexpensive. However, TDM Raman pumping does introduce a new set of problems. The higher gain for signal propagating in the backward direction leads to a larger backward spontaneous Raman noise level. Consequently, Rayleigh scattering of the backward propagating noise can significantly increase the forward noise level under high gain conditions.

Linear Noise Characteristics (Chapter 4)

Spontaneous emission is the inevitable consequence of gain in an optical amplifier. In this chapter, the definition of noise figure is shown to be useful only in characterizing shot noise and signal-spontaneous beat noise. The noise characteristics of both discrete and distributed Raman amplifiers are presented. Also, a general model that accurately predicts both signal propagation and the buildup of amplified spontaneous emission is discussed and compared to measurements. Further measurements and analysis of broadband Raman amplifiers show a clear dependence on temperature, which places a fundamental limit on their performance. Interactions between the pump wavelengths are also shown to play an important role, giving better system performance to longer signal wavelengths at the expense of the shorter wavelengths. Finally, an analysis of the relative linear noise performance of different transmission fibers is presented.

Pump Laser Diodes and WDM Pumping (Chapter 5)

This chapter discusses issues surrounding the pump laser diodes for broadband Raman amplifiers, which range from fundamentals to industry practices of Raman pump sources based on so-called 14XX nm pump laser diodes. The chapter also describes the design and issues of wavelength-division-multiplexed pumping for realizing a broad and flat Raman gain spectrum over the signal band. In addition, practical Raman pump units are illustrated, and the chapter also provides insights into ongoing issues on copumped Raman amplifiers and their pumping sources. The pump laser diodes discussed are InGaAsP/InP GRIN-SCH strained layer MQW structure with BH structure, which are the most widely used in the industry.

Dispersion-Compensating Fibers for Raman Applications (Chapter 6)

Dispersion-compensating fibers are the most widely used technology for dispersion compensation. Also, DCF is a good Raman gain medium, due to a relatively high germanium doping level and a small effective area. Dispersion-compensating Raman amplifiers integrate two key functions, dispersion compensation and discrete Raman amplification, into a single component. Use of DCF for broadband Raman amplifiers

raises new requirements for the properties of the DCF including requirements for gain, double Rayleigh scattering, and broadband dispersion compensation. Dispersion slope compensation is now possible for all types of transmission fibers, and the next challenge for broadband dispersion compensation is dispersion curvature. Dispersion-compensating Raman amplifiers have been realized with high-gain, low-noise figure and low multipath interference arising from double Rayleigh back scattering.

New Raman Fibers (Chapter 7)

Standard transmission fibers with silica core doped with a small concentration of GeO_2 have a low value of the Raman gain and a peak Raman gain at a frequency shift of about 440 cm^{-1} . However, for a number of applications such as discrete Raman amplifiers and Raman fiber lasers, special fibers with much higher Raman gain and/or various Raman frequency shifts are often required. Early experiments show that low-loss, high GeO_2 - and P_2O_5 -doped silica fibers could be promising fiber gain Raman fibers. For example, phosphor-silicate glass has two Raman scattering bands shifted by 650 cm^{-1} and 1300 cm^{-1} , and the cross-section for these bands is 5.7 and 3.5 times higher compared to silica. However, these fibers have met with serious challenges during fabrication by well-developed techniques. Nonetheless, at present germano-silicate and phosphor-silicate Raman fibers are being widely used for constructing CW Raman fiber lasers, which can cover the whole spectral range of 1.2 to 1.75 microns. These CW medium power (1 to 10 W) lasers are a convenient laser source for pumping optical fiber amplifiers and some lasers.

Noise due to Fast Gain Dynamics (Chapter 8)

The time response of the Raman effect is associated with the vibrations of the molecules in the gain medium and is on the order of several hundred femtoseconds. Compared to current data rates, this energy transfer is practically instantaneous, resulting in very fast gain dynamics. In a copumped Raman amplifier, the gain dynamics are averaged due to chromatic dispersion between pump and signal wavelengths. This lessens the impact of the fast physical process and results in a more improved system performance than would otherwise be expected. In a counterpumped Raman amplifier, the different propagation directions of pump and signals average the gain over the cavity length. This much stronger averaging greatly reduces system penalties in counterpumped amplifiers. In this chapter models are developed for co- and counter-pumped Raman amplifiers that quantify both the transfer of relative intensity noise from the pump to the signal and also the signal-to-signal crosstalk, mediated by the pump (crossgain modulation). In addition, the system impact in terms of Q penalty is determined, as well as determining the actual energy transfer from pumps to signals and from crossgain modulation.

Forward, Bidirectional, and Higher-Order Raman Amplification (Chapter 9)

Distributed Raman amplification can be achieved by optical pumping at either end of the fiber. In a unidirectional transmission line, all signals travel in the same direction.

In contrast, bidirectional transmission can be used to realize two-way traffic within a single fiber line: counterpropagating signal traffic is launched and received at the opposite ends of the optical link. A bidirectionally pumped fiber span can support both uni- and bidirectional signal transmission. A unidirectionally pumped span, however, almost exclusively supports unidirectional signal traffic. This chapter explores and compares forward, bidirectional, and higher-order Raman amplification. Higher-order pumping refers to the introduction of shorter-wavelength pumps that are used to pump the pump; that is, the higher-order pump amplifies the first-order pump, which in turn pumps the signal band. Different pumping schemes provide different levels of performance, but each scheme has a trade-off of performance versus pump laser restrictions.

VOLUME 90/2

Section B. Subsystems and Modules

S-Band Raman Amplifiers (Chapter 10)

The design, implementation, and issues associated with S-band amplification are discussed in this chapter, with a special emphasis on lumped Raman amplifiers (LRAs). LRAs can be used in a split-band augmentation strategy with new or already deployed C- and/or L-band systems, which are usually amplified with EDFAs. To open up the S-band, the key enabling technology is the appropriate optical amplifier. Raman amplifiers appear to be a practical solution to the S-band amplifier, and they are a mature technology ready for deployment. Utilizing silica fiber as the gain medium, Raman amplifiers can be readily fusion spliced with the fiber used in the transport infrastructure. LRAs have also been demonstrated with performance on a par with commercial C-band EDFAs in terms of gain, noise figure, and bandwidth. In addition, LRAs can be implemented efficiently using DCF, which means that the lumped amplifier can be integrated with the dispersion compensation. The major challenge of Raman amplifiers has been their lower efficiency than EDFAs, but this discrepancy is narrowing through better gain fibers, higher laser diode pump powers, and the inherent better slope efficiency for Raman amplifiers at higher channel count. The bulk of this chapter focuses on the issues and experimental demonstration of S-band LRAs in fiber-optic transmission systems.

Raman Fiber Lasers (Chapter 11)

This chapter focuses on cascaded Raman fiber lasers (RFL), which use the stimulated Raman scattering in optical fibers to shift the wavelength of light from an input pump laser to another desired wavelength. Devices at almost any wavelength can be made by proper choice of a pump wavelength, and by cascading the pump through several Raman shifts. Although RFL had been demonstrated since the 1970s, the advent of

fiber Bragg gratings made the devices practical. A broadband flat Raman gain profile can be obtained using multiple pump wavelengths, and it is advantageous to have all the required wavelengths emitted from one source. This motivated the development of a multiple wavelength RFL. Single cavities simultaneously lasing from two to six wavelengths have been demonstrated. Finally, distributed Raman amplification techniques have become more sophisticated with the proposed use of higher-order pumping schemes. The use of a RFL is especially suited to this application, inasmuch as large amounts of powers are required at the shortest pump wavelength.

Distributed Raman Transmission: Applications and Fiber Issues (Chapter 12)

The persistent demand for higher performance (capacity, system reach, data rate, etc.) has turned system designers to distributed Raman for its lower noise figure. Today's data-dominated traffic patterns require reach beyond 1000 km, and Raman amplification is one vital tool in pushing out the system reach. This chapter reviews the two most important properties of an optical amplifier—pump efficiency and noise figure—and compares Raman to erbium amplification. The concept of effective noise figure is covered, which leads to a generic system scaling relationship that aids in the prediction of Raman-assisted, system performance improvements. Raman transmission experiments at 10 Gb/s and 40 Gb/s are summarized, and design issues specific to these systems are covered. In addition, dispersion-managed fiber consisting of optical fiber spans that can be optimized for Raman transmission is introduced.

Hybrid EDFA/Raman Amplifiers (Chapter 13)

This chapter describes the technologies needed for cascading an EDFA and a fiber Raman amplifier to create a hybrid amplifier, the EDFA/Raman hybrid amplifier. Two kinds of hybrid amplifiers are defined in this chapter: the “narrowband hybrid amplifier,” and the “seamless and wideband hybrid amplifier.” The narrowband amplifier employs distributed Raman amplification in the transmission fiber together with an EDFA; this provides low-noise transmission in the C- or L-band. The noise figure of the transmission line is lower than it would be if only an EDFA were used. The wideband amplifier, on the other hand, employs distributed or discrete Raman amplification together with an EDFA. The wideband amplifier provides a low-noise and wideband transmission line or a low-noise and wideband discrete amplifier for the C- and L-bands. The typical gain bandwidth of the narrowband amplifier is ~ 30 to 40 nm, whereas that of the wideband amplifier is ~ 70 to 80 nm.

Wideband Raman Amplifiers (Chapter 14)

This chapter describes the design and implementation of wideband Raman amplifiers. All-Raman amplification enables the lowest cost and smallest footprint system, and Raman amplification provides a simple single platform for long-haul and ultra-long-haul fiber-optic transmission systems. Despite a significant list of advantages, a

number of challenges exist for Raman amplification, including: pump–pump interactions, interband and intraband Raman gain tilt, noise arising from thermally induced phonons near the pump wavelengths, multipath interference from double Rayleigh scattering, coupling of pump fluctuations to the signal, and pump-mediated signal crosstalk. Fortunately, design techniques exist for overcoming all of these physical limitations, thus allowing for the relatively simple implementation of 100 nm Raman amplifiers. Although commercially available wideband Raman amplifiers have been limited to a bandwidth of 100 nm to date, laboratory experiments have shown amplifiers with much larger bandwidths. Bandwidths greater than 100 nm are usually achieved with such special techniques as new glass compositions or wavelength guard bands around the pump wavelengths. Finally, the application of wideband Raman amplification in high-performance transmission systems is reviewed. For example, an all-Raman amplifier structure with discrete and distributed amplification can give significant advantages of reach and capacity. Such a design has been implemented, and the transmission feasibility of 240 OC-192 channels over 1565 km standard single-mode fiber has been demonstrated

Section C. Systems Design and Experiments

Multiple Path Interference and Its Impact on System Design (Chapter 15)

Up to the end of the 1990s, the main causes of signal degradation in transmission were fiber nonlinearity and amplified spontaneous emission from optical amplifiers. With the advent of Raman amplification in fiber-optic communications systems, another source of signal degradation has become increasingly relevant: so-called multiple path interference or MPI. This chapter focuses on MPI and its impact on receiver and system design. Optical amplification can exacerbate MPI by providing gain for paths that would otherwise have too much attenuation to be significant. Sources of MPI include discrete reflections within or surrounding optical amplifiers, double Rayleigh scattering in optical amplifiers or in the transmission span, and unwanted transverse mode mixing in higher-order mode dispersion compensators. The properties of MPI and Rayleigh scattering are reviewed, and the techniques for measuring MPI level are then described. The impact of MPI on beat-noise limited receivers is discussed, along with techniques for system design optimization.

Raman Impairments in WDM Systems (Chapter 16)

In most chapters of this book, stimulated Raman scattering is invoked intentionally. Pump radiation is coupled into the fiber carrying the signal radiation to generate Raman gain. However, SRS also occurs unintentionally in WDM transmission systems. Due to the large number of channels inside the Raman gain bandwidth, total power can add up to levels where considerable amounts of SRS are generated, with the signal channels acting as pumps. In contrast to the beneficial effects of intentional Raman pumping, the unintended generation of SRS usually degrades system performance. This chapter addresses effects resulting from the unintended invocation of SRS and

their impact on WDM signal transmission. A number of system impairments result from the interaction between signal channels due to SRS. Effects with time scales well below the bit period affect the mean values of the individual channel powers. On the other hand, fast interactions between individual bits change the variances of the respective channel powers and can be considered as noise. In addition, some selection criteria for transmission fibers with respect to Raman efficiency are provided.

Ultra-Long-Haul Submarine and Terrestrial Applications (Chapter 17)

Ultra-long-haul (ULH) optically amplified transmission systems (defined in this chapter as those spanning from 1500 to 12,000 km) are some of the most technically challenging systems designed today. Undersea cable systems require ULH, inasmuch as the distance across the Atlantic Ocean is approximately 6000 km and the distance across the Pacific Ocean is approximately 9000 km. For terrestrial networks, the ULH networks are needed because of the change in the nature of the traffic. Until a few years ago, voice traffic dominated the network, and a span distance of 600 km satisfied more than 60% of the connections for voice traffic. However, with the Internet dominating the traffic now, a span distance of 3000 km is required to satisfy 60% of the connections for Internet traffic. In terrestrial systems, the marriage of Raman amplification technology and EDFAs has demonstrated great benefit by expanding the bandwidth of amplifiers, extending the distance between amplifiers, and allowing longer distances to be spanned. For submarine systems where the systems are designed to achieve a desired capacity over often the longest transmission distances, shorter span length (than for terrestrial systems) often has to be chosen. For such shorter spans (~50 km), the benefits of Raman amplification are not nearly as substantial. Presently, the most promising candidate use of Raman amplification in submarine systems is the wideband hybrid Raman–EDFA. For systems that require a very wide bandwidth this seems like an attractive way to more than double the transmission bandwidth without doubling the component count.

Ultra-Long-Haul, Dense WDM Using Dispersion-Managed Solitons in an All-Raman System (Chapter 18)

In an all-Raman-amplified system, dispersion-managed solitons can provide for dense WDM, uniquely compatible with all-optical terrestrial networking, robust and error-free over many thousands of kilometers. This chapter discusses various aspects of system design, including optimal dispersion maps, nonlinear and noise penalties, and typical dense WDM system performance. For example, dispersion-managed solitons are described as well as their special, periodic pulse behavior, their advantages over other transmission modes, and the conditions required to create and to maintain them. Also studied is one serious nonlinear penalty they suffer, viz. the timing jitter from collisions with solitons of neighboring channels. Dispersion-managed solitons, in an all-Raman, dense WDM system at 10 Gb/s per channel, makes a natural and comfortable fit with existing terrestrial fiber spans and can provide for transmission that is robust and error-free out to distances of 7000 km or more. In addition, such transmission is uniquely suited to provide the backbone of an all-optical network.

40 Gb/s Raman-Amplified Transmission (Chapter 19)

High-capacity 40 Gb/s transmission systems offer scalable solutions for future traffic growth in the core network. The challenges of 40 Gb/s systems include optical signal-to-noise ratio, fine-tuned dispersion compensation, and polarization mode dispersion. Raman amplification is likely to be a key driver to ease the noise performance and increase the available bandwidth for 40 Gb/s DWDM systems. New fiber technologies provide high system performance and enable a simple and cost-effective dispersion-compensation scheme. More system margin can also be expected from high-coding-gain forward error correction. Optimized modulation formats and high-speed optoelectronics will make practical deployment of 40 Gb/s DWDM systems possible, facilitating multiple terabit transmission over Mm distance at low cost-per-bit-per-kilometer. The challenges of DWDM transmission at 40 Gb/s are addressed in this chapter, along with the technologies enabling 40 Gb/s terrestrial transmission. Also described are advanced experiments and demonstrations at 40 Gb/s using Raman amplification.

Contents

Foreword	vii
Preface	xi
Quick Summary of Book	xv
Contributors	xxvii

VOLUME 90/1

1. Overview of Raman Amplification in Telecommunications <i>Mohammed N. Islam</i>	1
Section A. Raman Physics	35
2. Fundamentals of Raman Amplification in Fibers <i>R.H. Stolen</i>	35
3. Time-Division-Multiplexing of Pump Wavelengths <i>A.R. Grant and L.F. Mollenauer</i>	61
4. Linear Noise Characteristics <i>C.R.S. Fludger</i>	91
5. Pump Laser Diodes and WDM Pumping <i>Shu Namiki, Naoki Tsukiji, and Yoshihiro Emori</i>	121
6. Dispersion-Compensating Fibers for Raman Applications <i>L. Grüner-Nielsen and Y. Qian</i>	161
7. New Raman Fibers <i>Evgeny M. Dianov</i>	191

8. Noise due to Fast-Gain Dynamics
C.R.S. Fludger 213

9. Forward, Bidirectional, and Higher-Order Raman Amplification
Stojan Radic 253

Index 291

VOLUME 90/2

Section B. Subsystems and Modules 301

10. S-Band Raman Amplifiers
Mohammed N. Islam 301

11. Raman Fiber Lasers
C. Headley, M. Mermelstein, and J.C. Bouteiller 353

12. Distributed Raman Transmission: Applications and Fiber Issues
Alan Evan, Andrey Kobayakov, and Michael Vasilyev 383

13. Hybrid EDFA/Raman Amplifiers
Hiroji Masuda 413

14. Wideband Raman Amplifiers
Mohammed N. Islam, Carl DeWilde, and Amos Kuditcher 445

Section C. Systems Design and Experiments 491

15. Multiple Path Interference and Its Impact on System Design
J. Bromage, P.J. Winzer, and R.-J. Essiambre 491

16. Raman Impairments in WDM Systems
P. M. Krummrich 569

17. Ultra-Long-Haul Submarine and Terrestrial Applications
Howard Kidorf, Morten Nissov, and Dmitri Foursa 595

18. Ultra-Long-Haul, Dense WDM Using Dispersion-Managed Solitons in an All-Raman System
Linn F. Mollenauer 627

19. 40 Gb/s Raman-Amplified Transmission
L. Nelson and B. Zhu 673

Index 723

Contributors

Jean-Christophe Bouteiller

OFS Laboratories
25 Schoolhouse Road
Somerset, NJ 08873
USA
Email: jcbouteiller@ofsoptics.com

Jake Bromage

OFS
Crawford Hill Laboratories
791 Holmdel-Keyport Road
Holmdel, NJ 07733
USA
Email: bromage@ofsoptics.com

Carl DeWilde

Xtera Communications, Inc.
500 West Bethany Drive
Suite 100
Allen, TX 75013
USA
Email: cdewilde@xtera.com

Evgeny M. Dianov

A.M. Prokhorov General
Physics Institute
Russian Academy of Sciences
38 Vavilov Str.
119991 Moscow
Russia
Email: dianov@fo.gpi.ru

Yoshihito Emori

Fitel Photonica Laboratory
Optical Subsystem Department
6 Yawata Kaigan Dori
Ichihara 290-8555
Japan
Email: yemori@ch.furukawa.co.jp

René-Jean Essiambre

Lucent Technologies
Bell Laboratories
Crawford Hill Laboratory
Room HOH L-129
791 Holmdel-Keyport Road
Holmdel, NJ 07733
USA
Email: rjessiam@lucent.com

Alan F. Evans

Optical Physics
Science and Technology
Corning Incorporated
SP-AR-02-4
Corning, NY 14831
USA
Email: evansaf@corning.com

Chris R.S. Fludger

Nortel Networks, UK
London Road
Harlow, Essex CM17 9NA
UK
Email : cfludger@nortelnetworks.com

Dmitri Foursa

Tyco Telecommunications
250 Industrial Way West
Eatontown, NJ 07724
USA
Email: dfoursa@tycotelecom.com

Andrew R. Grant

Lightwave Systems Research
Bell Laboratories
101 Crawfords Corner Road
Room 4C-316
Holmdel, NJ 07733-3030
USA
Email: ARGrant@lucent.com

Lars Grüner-Nielsen

Specialty Photonics Division
OFS Denmark
Priorparken 680
DK-2605 Brøndby
Denmark
Email: lgruner@ofsoptics.com

Clifford E. Headley

OFS Laboratories
25 Schoolhouse Road, Room A-16
Somerset, NJ 08873
USA
Email: cheadley@ofsoptics.com

Mohammed N. Islam

Department of Electrical Engineering
and Computer Science
University of Michigan at Ann Arbor
1110 EECS Bldg., 1301 Beal Ave.
Ann Arbor, MI 48109-2122
USA
Email: mni@eecs.umich.edu
and
Xtera Communications, Inc.
500 West Bethany Drive
Suite 100
Allen, TX 75013
USA
Email: mislam@xtera.com

Howard Kidorf

82 Tower Hill Drive
Red Bank, NJ 07701
USA
Email: kidorf@kidorf.com

Andrey Kobyakov

Science and Technology
Corning Incorporated
SP-DV-02-08
Corning, NY 14831
USA
Email: KobyakovA@corning.com

Peter Krummrich

Siemens AG, Information and
Communication Networks
Hofmannstrasse 51
81359 Munich
Germany
Email: peter.krummrich@siemens.com

Amos Kuditcher

Xtera Communications, Inc.
500 West Bethany Drive
Suite 100
Allen, TX 75013
USA
Email: akuditcher@xtera.com

Hiroji Masuda

NTT Network Innovation Laboratories
1-1 Hikarino-oka, Yokosuka
Kanagawa 239-0847
Japan
E-mail: masuda@exa.onlab.ntt.co.jp

Marc Mermelstein

OFS Laboratories
25 Schoolhouse Road, Room A-05
Somerset, NJ 08873
USA
Email: mermelstein@ofsoptics.com

Linn F. Mollenauer
 Lucent Technologies
 Bell Laboratories
 101 Crawford's Corner Road
 Room 4C-306
 Holmdel, NJ 07733
 USA

Shu Namiki
 Manager
 Furukawa Electric Company, Ltd.
 Fitel Photonics Lab, Optical
 Subsystems Department
 6 Yawata Kaigan Dori
 Ichihara 290-8555
 Japan
 E-mail: snamiki@ch.furukawa.co.jp

Lynn E. Nelson
 OFS
 791 Holmdel-Keyport Road
 Room L-137
 Holmdel, NJ 07733
 USA
 Email: lenelson@ofsoptics.com

Morten Nissov
 Transmission Research
 Tyco Telecommunications
 250 Industrial Way West
 Room 1A225
 Eatontown, NJ 07724
 USA
 Email: MNissov@tycotelecom.com

Yujun Qian
 Specialty Photonics Division
 OFS Fitel Denmark I/S
 Priorparken 680
 DK-2605 Brøndby
 Denmark
 Email: yujunqian@ofsoptics.com

Stojan Radic
 Bell Laboratories
 Lightwave Systems Research
 Crawford Hill Laboratory R-231
 791 Holmdel Keyport Road
 Holmdel, NJ 07733-0400
 USA
 Email: radic@lucent.com

Roger H. Stolen
 Department of Electrical
 and Computer Engineering
 Virginia Polytechnic Institute
 and State University
 Blacksburg, VA 24061
 USA
 Email: stolen@vt.edu

Naoki Tsukiji
 Furukawa Electric Company, Ltd.
 Optical Components Department
 2-4-3 Okano, Nishi-ku
 Yokohama 220-6374
 Japan
 Email: tsukiji@yokoken.furukawa.co.jp

Michael Vasilyev
 Corning Incorporated
 Photonic Research and Test Center
 2200 Cottontail Lane
 Somerset, NJ 08873
 USA

Pete J. Winzer
 Lucent Technologies
 Thurn & Taxis Str. 10
 Nuremberg 90411
 Germany
 Email: winzer@lucent.com

Benyuan Zhu
 OFS
 791 Holmdel-Keyport Road
 Room L-111
 Holmdel, NJ 07733
 USA
 Email: byzhu@ofsoptics.com

Chapter 1

Overview of Raman Amplification in Telecommunications

Mohammed N. Islam

1.1. Introduction

In the early 1970s, Stolen and Ippen [1] demonstrated Raman amplification in optical fibers. However, throughout the 1970s and the first half of the 1980s, Raman amplifiers remained primarily laboratory curiosities. In the mid-1980s, many research papers elucidated the promise of Raman amplifiers, but much of that work was overtaken by erbium-doped fiber amplifiers (EDFAs) by the late 1980s. However, in the mid to late 1990s, there was a resurgence of interest in Raman amplification. By the early part of the 2000s, almost every long-haul (typically between 300 and 800 km) or ultra-long-haul (typically longer than 800 km) fiber-optic transmission system uses Raman amplification. There are some fundamental and technological reasons for the interest in Raman amplifiers that this book explores.

As an overview for the book, this chapter surveys Raman amplification for telecommunications. The outline of the chapter is as follows. First we review the physics of Raman amplification in optical fibers, starting with a brief review of Raman gain. Then we discuss the advantages and challenges of Raman amplifiers. We also discuss some of the recent technological advances that have caused revived interest in Raman amplifiers. A comparison is also made between Raman amplifiers and erbium-doped fiber amplifiers.

To describe recent developments in Raman amplifiers, we categorize amplifiers into two categories: distributed and discrete or lumped. There are, of course, also hybrid amplifiers that can be a combination of the two. The second section of the chapter focuses on distributed Raman amplifiers, or so-called DRAs. We show that a DRA can improve the signal-to-noise ratio and nonlinear penalty of amplifiers. We also describe systems using DRAs. Finally, we discuss some of the issues and challenges in using DRAs.

The third section discusses discrete or lumped Raman amplifiers. We show that discrete Raman amplifiers are often used to open up new wavelength bands in fiber systems. For example, discrete Raman amplifiers are used in the 1310 and 1400 nm wavelength bands. The fiber capacity can be almost doubled by opening up the so-called S-band, which covers the wavelength range between 1430 and 1530 nm. Finally,

we describe all Raman transmission system experiments in the short-wavelength S-band to illustrate some of the performance achieved in lumped or discrete Raman amplifiers. In the last section we summarize the chapter.

1.2. Raman Amplification in Optical Fibers

Raman gain arises from the transfer of power from one optical beam to another that is downshifted in frequency by the energy of an optical phonon (a vibrational mode of the medium), as shown in Fig. 1.1. Figure 1.2 shows that Raman amplifiers utilize pumps to impart a transfer of energy from the pumps to the transmission signals through the Raman effect mechanisms. In particular, counterpropagating pump geometry is illustrated. As discussed below, this is commonly used to avoid coupling of pump fluctuations to the signal. Also shown are isolators that can be used around the amplifiers to avoid the amplification of spurious reflections and control of double Rayleigh scattering.

The Raman gain spectrum in fused silica fibers is illustrated in Fig. 1.1 [1, 2]. The gain bandwidth is over 40 THz wide, with the dominant peak near 13.2 THz. The gain band shifts with the pump spectrum, and the peak value of the gain coefficient is inversely proportional to the pump wavelength. In the telecommunications bands around 1500 nm, 13.2 THz corresponds to approximately 100 nm. For example, if the pump is near 1450 nm, then the gain band will be around 1550 nm.

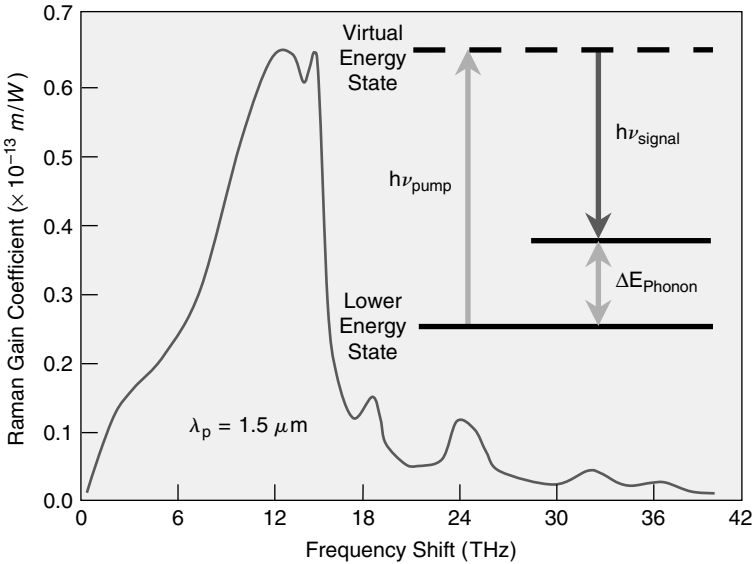


Fig. 1.1. Raman gain curve in fused silica fiber for copolarized pump and signal beams [1, 2]. Inset shows an energy level diagram representative of the Raman process, which takes a higher-energy pump photon and splits it into a lower-energy signal photon and a phonon.

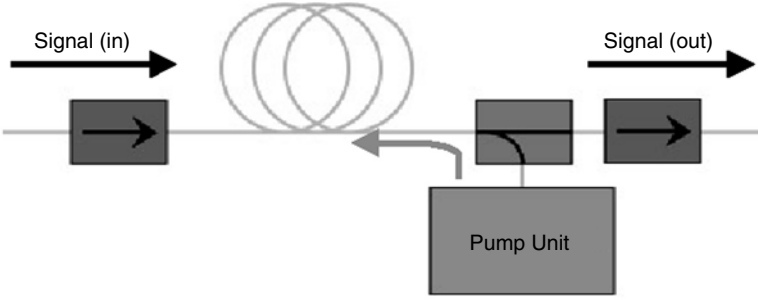


Fig. 1.2. Raman amplifiers transfer energy from the pump beam to the signal beam. The configuration shown has a counterpropagating pump and signal beam.

For the continuous wave case, the interaction between the pump and signal is governed by the following set of coupled equations [2],

$$\begin{aligned}\frac{\partial P_s}{\partial z} &= \frac{g_R}{A_{eff}} P_p P_s - \alpha_s P_s \\ \frac{\partial P_p}{\partial z} &= -\frac{\omega_p}{\omega_s} \cdot \frac{g_R}{A_{eff}} P_p P_s - \alpha_p P_p,\end{aligned}$$

where the absorption coefficients α_s and α_p account for the fiber loss at the signal and pump wavelengths. These equations assume that the pump and signal are copolarized. To simplify the solution, we neglect the first term on the right-hand side of the second equation, which is responsible for pump depletion. Then the signal power can be solved for as follows,

$$P_S(z) = P_S(0)e^{((g_R/A_{eff})P_P z_{eff} - \alpha_S z)},$$

where

$z_{eff} = (1 - e^{-\alpha_p z})/\alpha_p$ is the effective fiber length,
 $\frac{g_R}{A_{eff}}$ is the Raman gain efficiency, with g_R the Raman gain coefficient,
 A_{eff} is the effective core area of the pump,
 $P_P(z)$ is the power of the pump, and
 $P_S(0)$ is the power of the signal.

Because a long fiber length with small core size is required for Raman amplifiers, it is possible to combine the amplification process with the required chromatic dispersion compensation. To achieve the most efficient gain due to Raman, gain fiber with the smallest effective area A_{eff} is best utilized. Of the various fiber types commercially available, dispersion-compensating fiber, or DCF, exhibits the smallest A_{eff} , resulting in the highest Raman gain efficiency (see Table 1.1). The resulting, chromatic dispersion compensation can be achieved simultaneously within the discrete Raman amplifier portion of an “all-Raman” system. External, per band, DCF units,

Table 1.1. Effective Area Ranges for Different Fiber Types

Fiber Type	Effective Area (μm^2) (@ $\sim 1550\text{ nm}$)
SMF	72–80
NZDSF	55–72
DSF	45–50
DCF	20–35

along with their associated attenuation of the signal wavelengths, need not be engineered into the total system span budget. In current systems such as those based on EDFAs, the loss of the DCF is minimized by placing the DCF in the midstage of a two- or more stage amplifier. Even so, some amount of margin must be allocated for the DCF loss, or alternately the additional gain and associated noise required to compensate this loss. With Raman, the DCF provides gain, not loss.

Some of the Raman fundamental properties would appear to be drawbacks for telecommunications applications. However, many of these drawbacks can be overcome by proper design of the amplifier architecture. For example, Fig. 1.3 illustrates the polarization dependence of Raman gain [1]. The copolarized gain is almost an

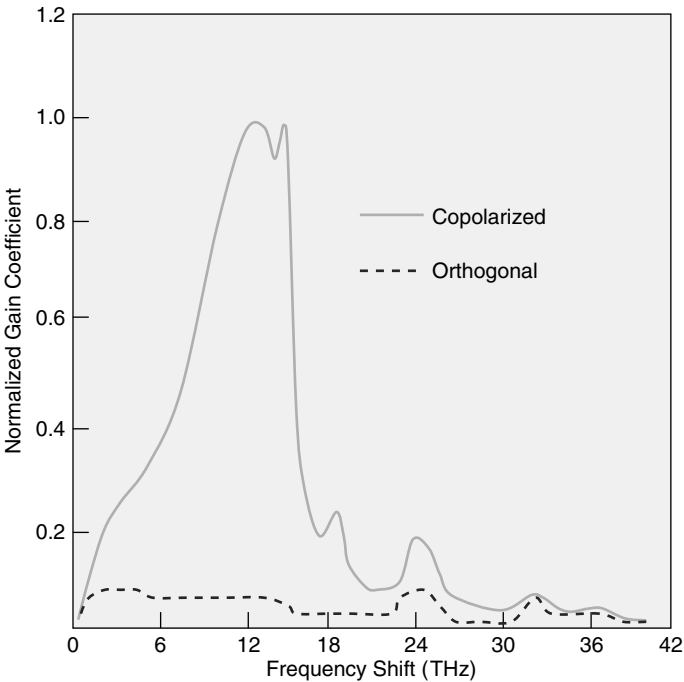


Fig. 1.3. Normalized Raman gain coefficient for copolarized and orthogonally polarized pump and signal beams [1]. Source: R.H. Stolen and E.P. Ippen “Raman Gain in Glass Optical Waveguides” Applied Physics Letters Vol 22 (©1973 AIP)

order of magnitude larger than the orthogonal polarization gain near the peak of the Raman curve. Nonetheless, a polarization-independent Raman amplifier can be made by using polarization diversity pumping to avoid polarization-dependent loss. Furthermore, the mixture of modes in a nonpolarization-maintaining fiber helps to scramble the polarization dependence.

1.2.1. Advantages and Challenges of Raman Amplifiers

Based on the above physics, some of the advantages of Raman amplifiers become clear. First, Raman gain exists in every fiber: this means, for example, that existing links can be upgraded even though they are already installed. This provides a cost-effective means of upgrading, inasmuch as the upgrade can be done from the terminal ends. Second, the gain is nonresonant, which means that gain is available over the entire transparency region of the fiber ranging from approximately 0.3 microns to 2 microns. To illustrate, Fig. 1.4 shows the attenuation versus wavelength for a typical fused silica fiber [4]. For wavelengths below 1310 nm, loss rises from Rayleigh scattering. For wavelengths above about 1620 nm, the loss rises from bend-induced losses as well as infrared absorption. This still provides a window from about 1250 to 1650 nm, or a window of about 50 THz optical bandwidth. Most systems today use erbium-doped fiber amplifiers and operate in the C-band, which stretches between about 1530 and 1565 nm. Extended band amplifiers are beginning to open up the long-wavelength L-band, which is between approximately 1570 and 1610 nm. Therefore, less than half of the low-loss window in the optical fiber is used with current amplifier technology based on EDFAs.

A third advantage of Raman amplifiers is that the gain spectrum can be tailored by adjusting the pump wavelengths. For instance, multiple pump lines can be used to increase the optical bandwidth, and the pump distribution determines the gain flatness. As an example of tailoring of the Raman gain spectrum, Fig. 1.5 shows the gain

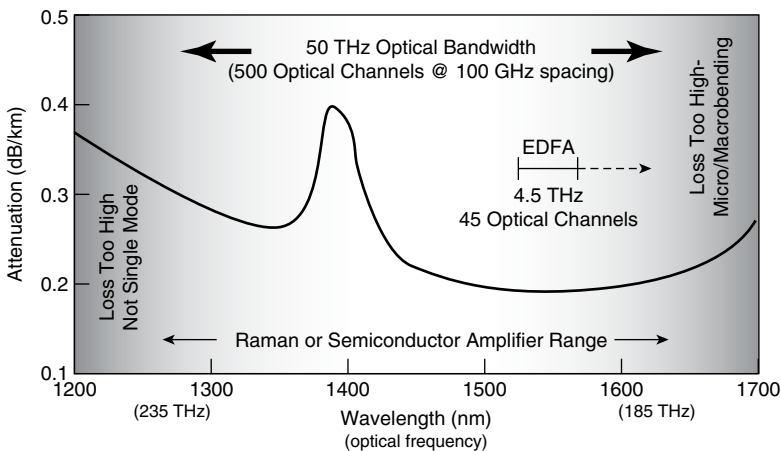


Fig. 1.4. Attenuation versus wavelength for a typical fused silica fiber [4]. Source: R.B. Kummer "Fiber Issues for Nontraditional Wavelength Bands" OFC Technical Digest, pg ThR1-1 (©2000 OSA)

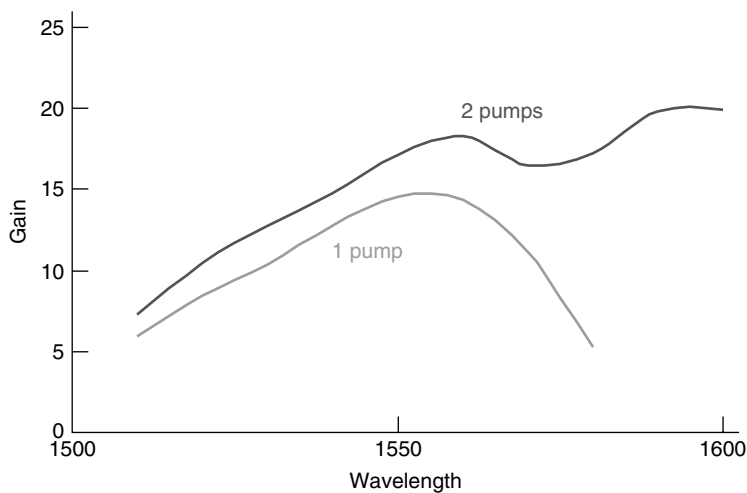


Fig. 1.5. Raman gain spectrum using one or two pump wavelengths [5, 6].

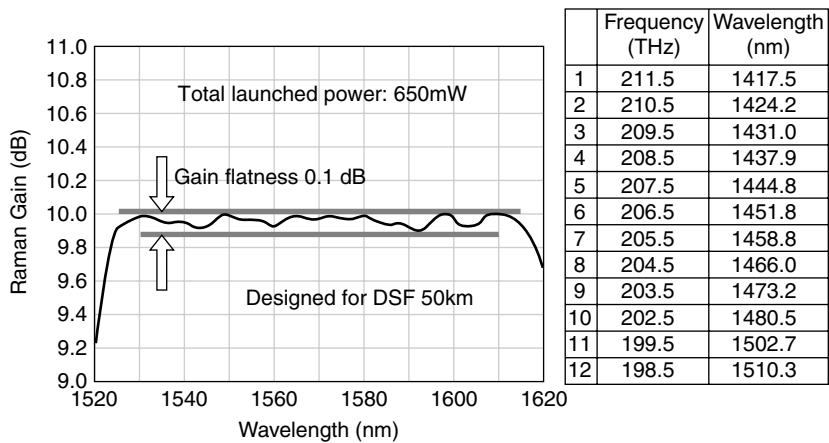


Fig. 1.6. An almost flat Raman gain spectrum stretching from 1530 to 1610 nm. To achieve the flatness, 12 pump wavelengths are used between 1417 and 1510 nm [7]. Source: S. Namiki and Y. Emori “Broadband Raman Amplifiers: Design and Practice” OFC Technical Digest, pg OMB2 (©2000 OSA)

spectrum using one or two pump wavelengths [5, 6]. By placing pump wavelengths approximately 15 to 20 nm apart, the gain band can be almost doubled from 25 to 35 nm. As an extreme example, Fig. 1.6 shows a flat gain spectrum stretching from 1530 to 1610 nm. To achieve a gain flatness of 0.1 decibels, 12 pump wavelengths are used between 1417 and 1510 nm [7].

Another advantage of Raman amplification is that it is a relatively broadband amplifier with a bandwidth >5 THz. In addition, the gain is reasonably flat over a wide wavelength range, thus making it easier to gain flatten. As a comparison,

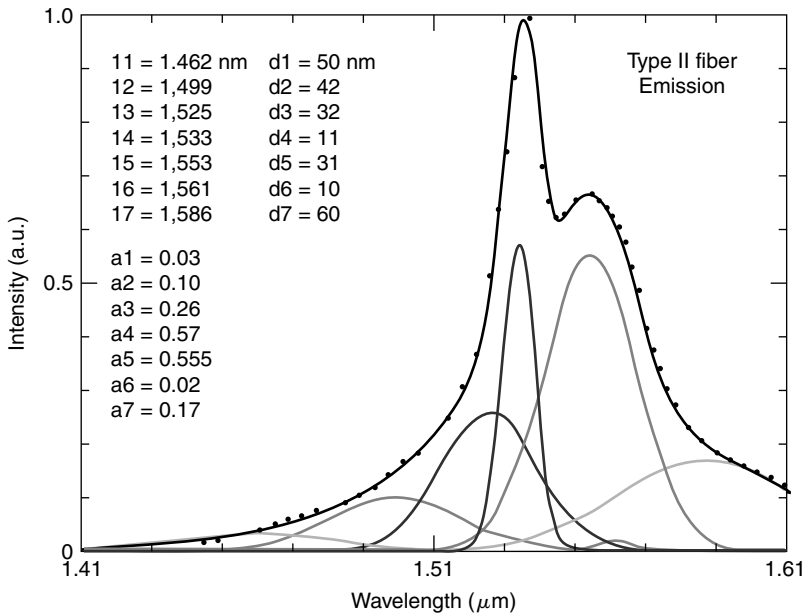


Fig. 1.7. Gain spectrum of an erbium-doped fiber amplifier [8]. Source: E. Desurvire “Erbium-Doped Fiber Amplifiers: Principles and Applications”, Copyright ©1994, John Wiley & Sons, Inc; This material is used by permission of John Wiley & Sons, Inc.

Fig 1.7 shows the gain spectrum of an erbium-doped fiber amplifier. The complexity of the required gain-flattening filter function can be characterized by the number of Gaussian or Fourier terms needed to fit the gain spectrum. The erbium band, in particular, requires five Gaussian terms to fit the usable band [8]. On the other hand, Fig. 1.8 shows a typical spectrum of the Raman amplifier, which typically requires only two Gaussian terms to fit the gain [9].

Despite these advantages, Raman amplifiers were not deployed until the late 1990s. The problem was a relatively poor efficiency of Raman amplifiers at lower signal powers. To illustrate, Fig. 1.9 shows a 1994 curve of fiber amplifiers' gain versus input pump power [8]. Erbium-doped fiber amplifiers required powers in the range of 1 to 10 mW, whereas Raman amplifiers required powers in the range of 1 to 5 W. Therefore, to achieve a gain of 20 dB or more required almost three orders of magnitude more pump power in Raman amplifiers. As discussed below, technological advances have substantially narrowed this difference.

The challenges for Raman amplifiers can be summarized as follows. First, compared to the EDFAs, Raman amplifiers have relatively poor pumping efficiency. Although a disadvantage, this lack of pump efficiency also makes gain clamping easier in Raman amplifiers. Second, Raman amplifiers require a longer gain fiber. However, this disadvantage can be mitigated by combining gain and the dispersion compensation in a single fiber. A third disadvantage of Raman amplifiers is a fast response time, which gives rise to new sources of noise, as further discussed below. Finally, there are concerns of nonlinear penalty in the amplifier for the WDM signal channels.

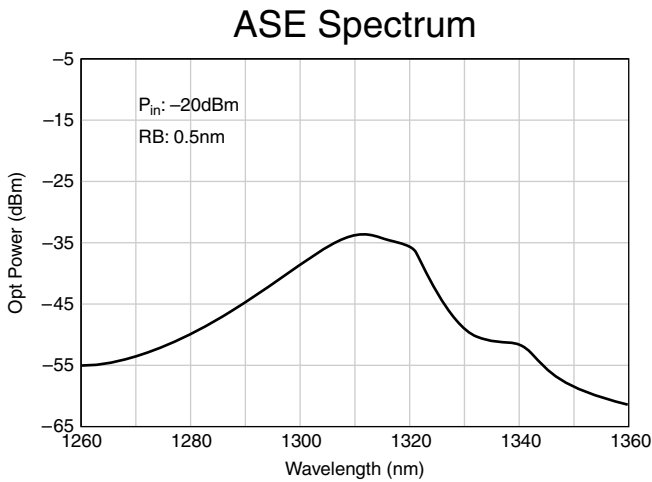


Fig. 1.8. Typical spectrum of a Raman amplifier pumped by one pump wavelength [9]. Source: A.J. Stentz, T. Nielsen, S.G. Grubb, T.A. Strasser and J.R. Pedrazzani “Raman Ring Amplifier at 1.3 μm with Analog-Grade Performance and an Output Power of 23 dBm” OFC Technical Digest, Postconference Edition, pg PD-16 (©1996 OSA)

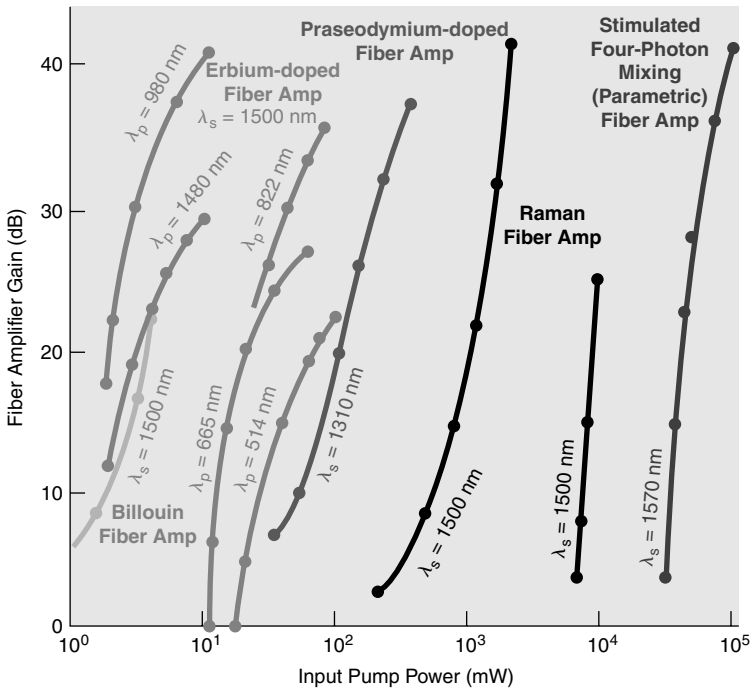


Fig. 1.9. Fiber amplifier gain versus input pump power for a variety of amplifiers, including rare earth-doped amplifiers and Raman amplifiers [8]. Source: E. Desurvire “Erbium-Doped Fiber Amplifiers: Principles and Applications”, Copyright ©1994, John Wiley & Sons, Inc; This material is used by permission of John Wiley & Sons, Inc.

1.2.2. Revived Interest in Raman Amplifiers

Despite these challenges, there has been revived interest in Raman amplifiers. Several technological advances over the last few years have made Raman amplifiers feasible and practical. It is interesting to note that the physics of Raman has not changed, but rather it is new technologies that have enabled Raman amplifiers to come of age. The first key development has been the availability of higher Raman gain fibers with relatively low loss. As an example, there is more than a tenfold increase in gain efficiency in commercial dispersion-compensating fiber compared to standard single-mode fiber. Figure 1.10 illustrates the Raman gain efficiency for different fibers, including standard single-mode fiber (SMF), dispersion-shifted fiber (DSF), and dispersion-compensating fiber (DCF) [7]. Moreover, new Raman gain fibers continue to be introduced commercially with different dispersion profiles and dispersion slopes.

A second key [6] development for Raman amplifiers has been the availability of high pump power laser diodes or cladding-pump fiber lasers. Cladding-pump fiber lasers are now available with output powers in excess of 10 W in a single-mode fiber. Commercial laser diodes are available with more than 300 mW output powers, and they will soon be upgraded to 400 mW [10]. In addition, research on high-power laser diodes shows the availability of output powers in excess of one watt in single-mode fibers in the near future; see, for example, Fig. 1.11 [11].

A third technological development important for Raman amplifiers has been the availability of all fiber components to replace bulk optics. For example, gratings,

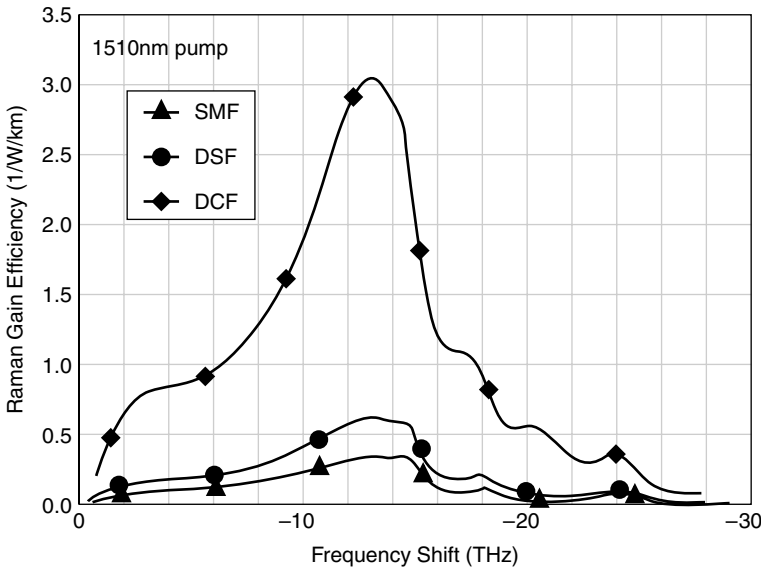


Fig. 1.10. Raman gain efficiency for different fibers, including standard single-mode fiber (SMF), dispersion-shifted fiber (DSF), and dispersion-compensating fiber (DCF) [7]. Source: S. Namiki and Y. Emori “Broadband Raman Amplifiers: Design and Practice” OFC Technical Digest, pg OMB2 (©2000 OSA)

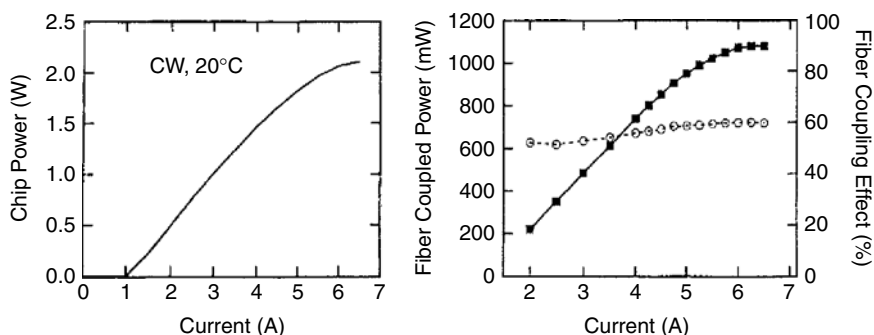


Fig. 1.11. Research on high-power laser diodes shows the availability of output powers in excess of 1 W in single-mode fibers [11]. Source: A. Mathur, M. Ziari, V. Domenic “Record 1 Watt Fiber-Coupled–Power 480 nm Diode Laser Pump for Raman and Erbium Doped Fiber Amplification” OFC Technical Digest, Postconference Edition, pg PD-15 (©2000 OSA)

specialty couplers, WDMs, and the like, are now available for splicing easily into all fiber configurations. In addition, fiber-pigtailed bulk-optic couplers are also now commercially available with full high-power reliability qualifications mainly based on epoxy-free technologies. A spliced-together fiber amplifier configuration is much more resistant to mechanical and environmental disturbances than its bulk-optical counterpart. Thus an up to 100-fold increase in pump power combined with up to a 10-fold increase in Raman gain coefficient leads to renewed interest in Raman amplification in an all-fiber configuration.

1.2.3. Sources of Noise in Raman Amplifiers

There are several primary sources of noise in Raman amplifiers. The first is double Rayleigh scattering (DRS), which corresponds to two scattering events (one backward and the other forward) due to the microscopic glass composition nonuniformity. Amplified spontaneous emission (ASE) traveling in the backward direction will be reflected in the forward direction by DRS and experience gain due to stimulated Raman scattering. This in addition to ASE experiencing multiple reflections will degrade the signal-to-noise ratio. Furthermore, multipath interference of the signal from DRS will also lower the signal-to-noise ratio. DRS is proportional to the length of the fiber and the gain in the fiber, so it is particularly important in Raman amplifiers due to the long length of fiber, where lengths of several kilometers are typically required. From a practical viewpoint, DRS limits the gain per stage to approximately 10 to 15 dB. Higher-gain amplifiers can be obtained through the use of isolators between the multiple stages of amplification. For example, a 30 dB discrete Raman amplifier has been demonstrated commercially with two stages of amplification and a noise figure less than 5.5 dB [12].

The second source of noise arises from the short upper-state lifetime of Raman amplification, as short as 3 to 6 fsec. This virtually instantaneous gain can lead to a coupling of pump fluctuations to the signal. The usual way of avoiding this deleterious

coupling is to make the pump and signal counterpropagating, which has the effect of introducing an effective upper-state lifetime equal to the transit time through the fiber. If copropagating pumps and signals are to be used, then the pump lasers must be very quiet. That is, they must have a very low so-called relative intensity noise or RIN. For example, copropagating pumps use Fabry–Perot laser diodes instead of grating-stabilized laser diodes [13].

A third primary source of noise in Raman amplifiers is the usual ASE. As is typical for reasonable signal power levels, signal-ASE beating noise dominates over ASE–ASE beating noise. Fortunately, Raman amplifiers have inherently low noise from signal-ASE beating because a Raman system always acts as a fully inverted system. For example, the ASE power spectral density can be written as

$$S_{ase}(\nu) = (G - 1)h\nu(N_2/N_2 - N_1)$$

and the noise figure as

$$NF = \frac{1}{G}(2S_{ase}(\nu)/h\nu + 1),$$

where N_2 is the upper state population and N_1 is the lower state population. For Raman amplifiers the $N_2/(N_2 - N_1)$ term is always equal to one, whereas in EDFAs it is usually greater than one [8]. In an EDFA this term is only equal to one for an amplifier fully inverted through the entire length of the gain fiber. On the other hand, since Raman amplifiers use long fiber lengths, the small fraction of passive loss of the gain fiber needs to be added to the noise figure. Nonetheless, discrete Raman amplifiers with noise figures as low as 4.2 dB have been reported [9].

Finally, a fourth source of noise arises from the phonon-stimulated optical noise created when wavelength signals being amplified reside spectrally close to pump the wavelengths used for amplification. In other words, at room or elevated temperatures there is a population of thermally induced phonons in the glass fiber that can spontaneously experience gain from the pumps, thereby creating additional noise for signals close to the pump wavelengths. It has been shown that this effect can lead to an increase in the noise figure of up to 3 dB for signals near the pump wavelength.

A number of papers have shown that there is a fundamental design compromise between bandwidth and low-noise operation in Raman amplifiers [14–16]. As an example, Fludger and coworkers calculate and measure the increased spontaneous emission arising from the thermal distribution of phonons in the ground state. They calculate that in the limit of high gain and lossless fiber, the noise figure NF for the Raman amplifier is given by

$$F = 2 \frac{\sum_i E_i \ln(g_i)}{\sum_i \ln(g_i)}.$$

The denominator is the net gain of the amplifier (the i th term corresponding to the i th pump), and the numerator is the sum over the spontaneous emission factor times the gain contribution for each of the pumps. The spontaneous emission factor E_i is

a Bose–Einstein distribution and takes into account the thermal population of optical phonons in the ground state

$$E(\Delta\nu) = 1 + \frac{1}{\exp\left(\frac{h\Delta\nu}{kT}\right) - 1},$$

where

h = Planck's constant,

k = Boltzman's constant,

T = temperature in Kelvin,

$\Delta\nu_i$ = frequency difference between the i th pump and signal.

The above equations show that the noise figure is dependent on both the spontaneous emission factor and the relative amount of gain provided by each pump wavelength. The increased spontaneous emission is particularly crucial when the signal wavelength is close to the pump wavelength. For example, Fig. 1.12 illustrates the number of spontaneous photons per mode versus frequency, which has a significant increase for small frequency shifts and realistic temperatures.

Figure 1.13 shows the influence of the noise factor for a broadband discrete Raman amplifier [14]. In particular, Fig. 1.13(a) shows the simulated gain spectrum for a five-wavelength pumped, discrete Raman amplifier. The relative gains from each pump were chosen to give the broadest and flattest spectrum with the highest pump wavelength at 1495 nm and the lowest signal near 1500 nm. There is a significant gain contribution from the 1495 nm pump to lower wavelength signals. Fig. 1.13(b) shows the best achievable internal noise figure for the lossless fiber case. Because a substantial amount of the total gain at shorter signal wavelengths is given by the 1495 nm pump, there is increased spontaneous emission as the signals approach the pump.

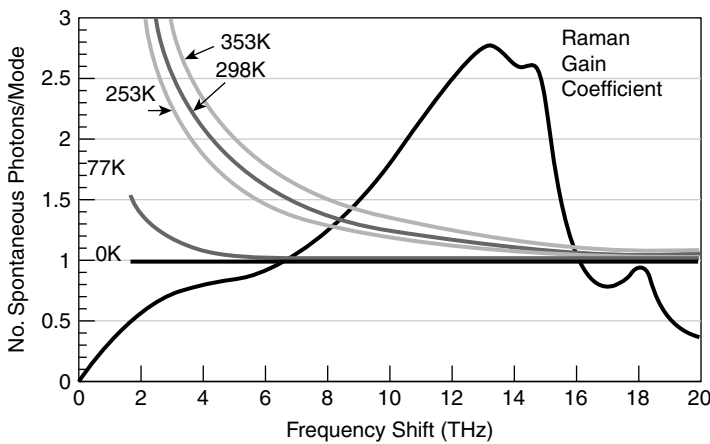


Fig. 1.12. Number of spontaneous photons per mode versus frequency for different temperatures [14]. Source: C.R.S. Fludger and V. Henderek “Fundamental Noise Limits in Broadband Raman Amplifiers” OFC Technical Digest, Postconference Edition, pg MA5 (© 2001 OSA)

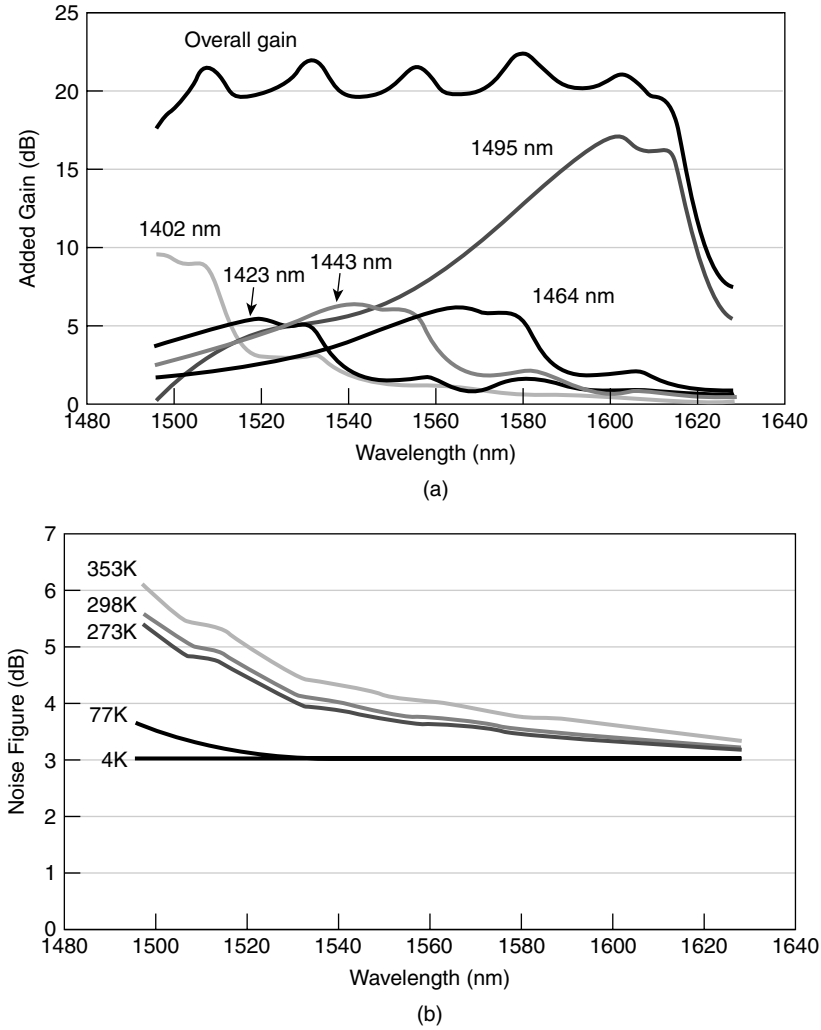


Fig. 1.13. Influence of the noise factor for a broadband discrete Raman amplifier [14]: (a) simulated gain spectrum for a five-wavelength pumped, discrete Raman amplifier; (b) best achievable internal noise figure for the lossless fiber case. Source: C.R.S. Fludger and V. Henderek "Fundamental Noise Limits in Broadband Raman Amplifiers" OFC Technical Digest, Postconference Edition, pg MA5 (© 2001 OSA)

Fludger and coworkers have also experimentally verified the influence of the thermal dependence of the spontaneous noise factor in the noise performance of a DRA. For the measurements, an 80 km length of nonzero dispersion-shifted fiber was placed in a temperature controlled chamber, and the transmission fiber was counter-pumped using a pump assembly designed to give 95 nm flat gain across the C- and L-bands. Figure 1.14 shows the fiber loss with and without a DRA and the effective noise figure at various temperatures. The points indicate measurements, and the solid lines are

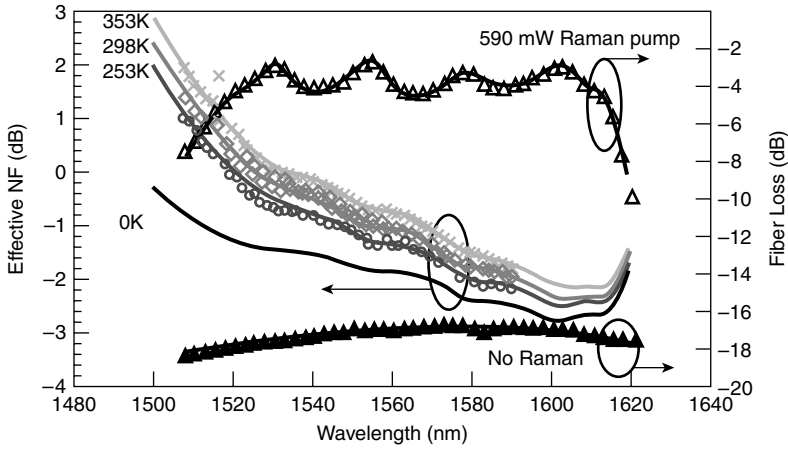


Fig. 1.14. Effective noise figure at various temperatures with and without a Raman pump [14]. Source: C.R.S. Fludger and V. Henderek “Fundamental Noise Limits in Broadband Raman Amplifiers” OFC Technical Digest, Postconference Edition, pg MA5 (© 2001 OSA)

numerical simulations. It can be seen that a temperature variation of between -20°C to 80°C causes approximately 1 dB change in the effective noise figure at shorter wavelengths. Also, despite an almost flat gain, the noise figure can be several dB higher on the short side of the band compared to the long wavelength side of the band.

1.2.4. Raman for DWDM Long-Haul Systems

Raman amplifiers provide a simple single platform for long-haul and ultra-long-haul amplifier needs. Raman amplifiers are broadband and wavelength agnostic. For example, gain bandwidths of up 100 nm have been demonstrated [16, 7, 17, 18, 5, 30, 20], and the 100 nm can fall anywhere in the transparency window between roughly the 1300 and 1650 nm typically used in fiber-optic communications. More recently, a broadband Raman amplifier with a bandwidth of 136 nm has been demonstrated using a pump-and-signal wavelength-interleaved scheme, where stop bands surround the pump wavelengths that are within the signal band [21]. Raman amplifiers can be distributed, lumped or discrete, or hybrid [20, 22–28]. Thus, either Raman amplifiers can serve only as low-noise preamplifiers for rare earth-doped fiber amplifiers, or they can meet the full amplifier needs in all-Raman systems. Also, in Raman amplifiers the amplification and dispersion compensation can be combined in the same fiber length [15, 29, 18, 30, 31]. The dispersion-compensating fiber ends up having net gain rather than loss, which leads to a wider system margin and the ability to insert other elements such as optical add/drop multiplexers into the system.

In the dense WDM long-haul and ultra-long-haul fiber-optic system markets, Raman amplifiers should win out as the dominant form of amplifier due to their simplicity and flexibility. As an example, suppose that a 100 nm wideband system, which overlaps the S-, C-, and L-bands, is to be developed. If the system were to mimic today’s systems, then band combiners and band splitters would be used around

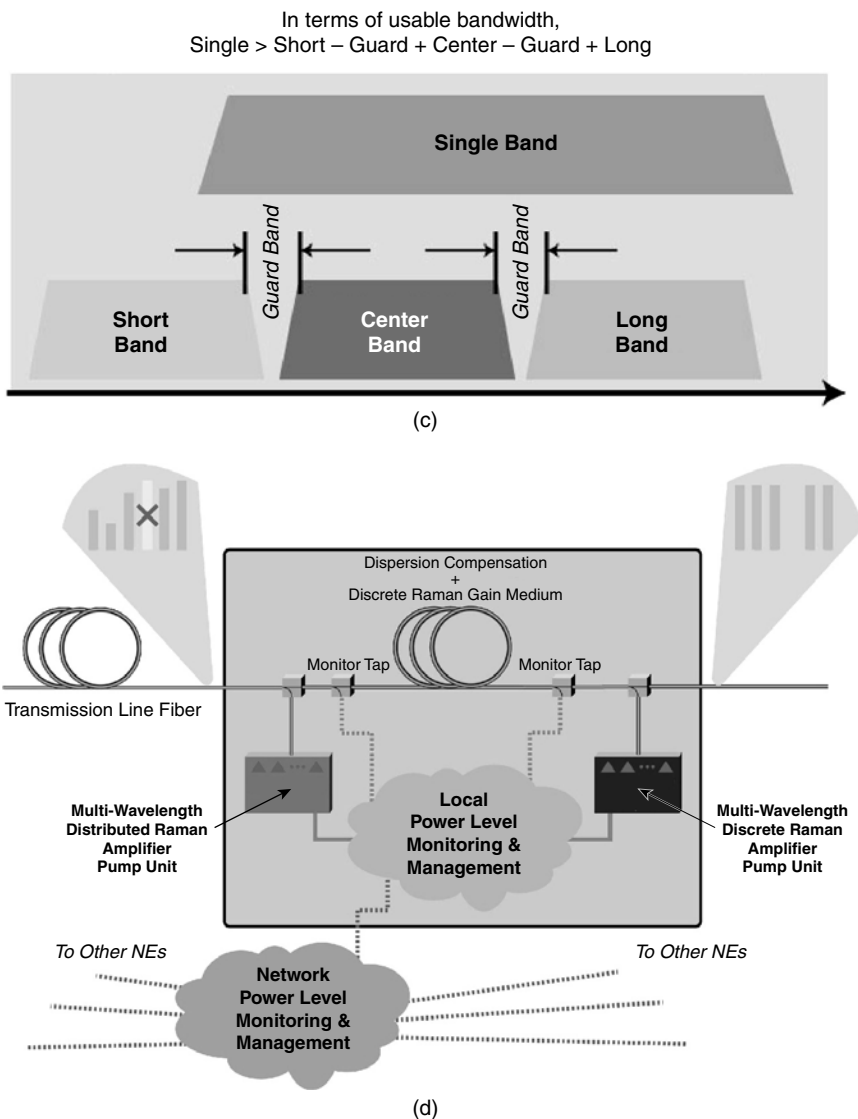


Fig. 1.15. *continued* (c) The systems are not “equivalent” as an all-Raman system offers more bandwidth through a single band without penalties from the obligatory “Guard Bands”; (d) tilt management in an all-Raman amplifier that uses monitoring at two points in the amplifier stage.

but the discrete amplifier is considerably simpler. Fewer pumps are required than for the three-amplifier case, only one monitoring system is required, and the single dispersion-compensating fiber can be combined with the gain fiber in the discrete Raman amplifier. More significantly, the band splitter and combiner are not required, which removes the requirement for guard bands and allocation of 3 dB or more

system margin for the coupler losses. The price to be paid for the simplification in Fig. 1.15(b) is that 100 nm, wideband gain equalization and dispersion compensating fibers are required, as opposed to the typically 35 nm wide devices in use today. For example, this means that dispersion slope compensation as well as dispersion magnitude compensation are required. However, the technologies for these wideband devices are already becoming available commercially.

Management of Raman gain tilt is required in either configuration. Although present in any DWDM system, Raman gain tilt is most problematic in systems spanning near or above 100 nm of gain bandwidth, near the peak of the Raman gain spectrum. This tilt management will be less complicated with an all-Raman system as monitoring of the signal wavelengths can occur across the entire band at just two positions: immediately before amplification and directly after amplification (Fig. 1.15(d)). Dynamic adjustment of any measured tilt (or other gain-affecting event, such as channel drops or additions) can be made through the straightforward adjustment of the Raman pump power levels. The very nature of Raman amplification permits this ability to “shape” the gain spectrum. Monitoring and adjustment of the banded system is more intricate, as a number of monitoring points need to be used together with the different gain adjustments for the discrete amplifiers. This is further complicated by the fact that the greatest amount of Raman gain tilt will be most prevalent between the bands (intradband) and careful coordination of all adjustments, regardless of band, needs to take place.

Additional reliability without added costs is made possible with the all-Raman system. This again is due to the nature of the Raman phenomena. Through the careful selection of the wavelengths utilized in the pumping scheme of the amplifier, a design can be realized that can withstand the failure of one, or even more, of the pump sources themselves. Besides transferring power from the pumps to the signal wavelengths, power transfers due to the Raman effect occur among the signal wavelengths (as in the case of Raman gain tilt) and the pump wavelengths. Thus, a failure to a pump source can be compensated for dynamically through the power level manipulation of the remaining pumps. Other currently available discrete technologies must make use of redundant pumps, thereby increasing costs, or risk going “opaque” when a pump source fails.

1.2.5. Higher Efficiency for Future Systems

The biggest argument made against Raman amplifiers has been the perception of their poor efficiency compared to EDFAs, the industry’s workhorse. However, as the total signal power within the transmission fiber increases as the number of channels and the bit-rate of the channels increase, Raman amplifiers become more and more attractive. In fact, the gain obtained from Raman is greater at the higher input pump powers necessitated by the power levels of future systems (Fig. 1.16(a)). Even the scheme found in most deployed EDFAs, where a 980 nm first-stage pump is used in conjunction with a 1480 nm second-stage pump, are beginning to exhibit the “leveling off” of their gain profile as they reach saturation and fail to provide the same additional gain for similar increases in pump power. Early WDM systems had

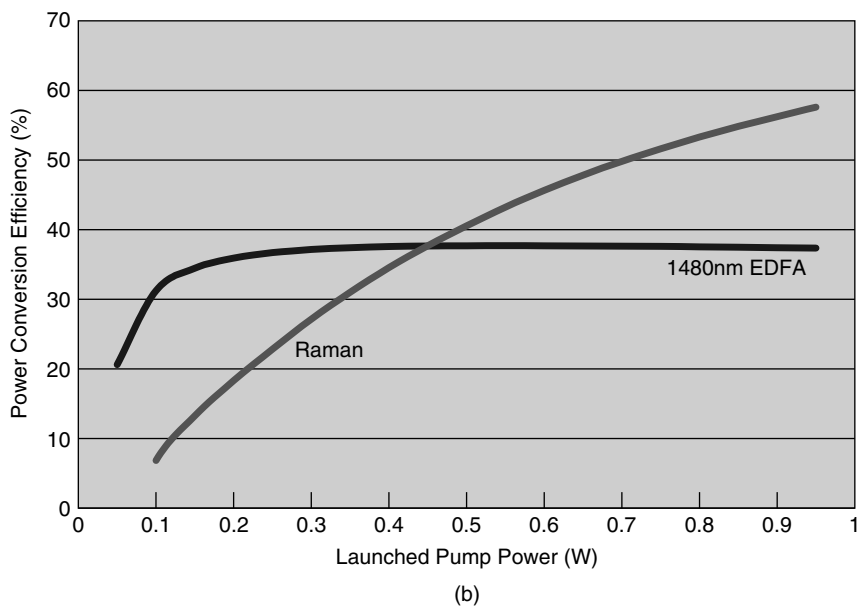
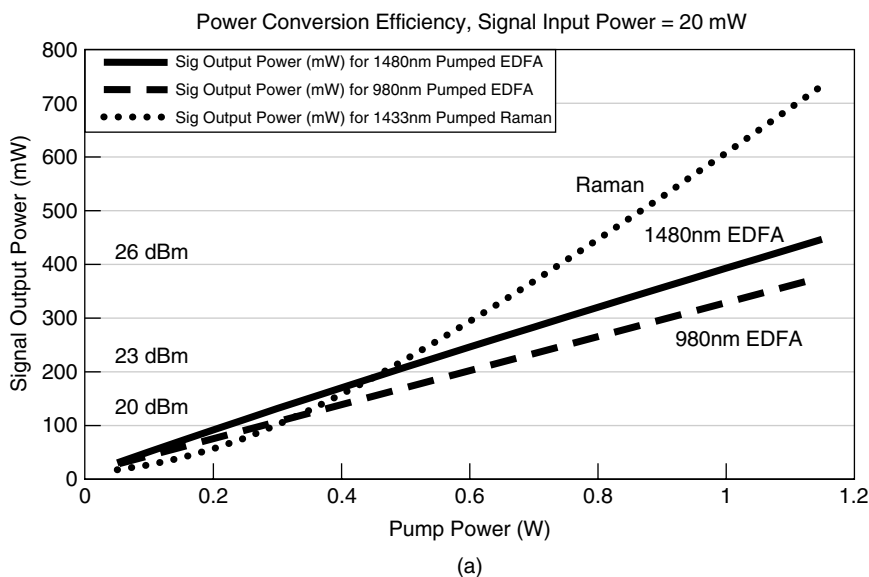


Fig. 1.16. Raman amplifiers surpass the power conversion efficiency of EDFAs at the higher power levels brought about by future high capacity, long-reach systems. A Raman amplifier is compared with a 1480 nm pumped EDFA and a 980 nm pumped EDFA. The signal input power is assumed to be 20 mW: (a) Signal output power versus launched pump power; (b) power conversion efficiency versus launched pump power.

less than 32 channels, or power levels under 100 mW, a region where Raman is much less efficient than EDFAs. In the 1999 to 2001 time frame, systems ranged from 64 to as many as 160 channels, with powers below about 200 mW; the high end of the range is where Raman begins to become competitive with EDFAs. Starting in 2002, systems have been available with 240 channels and more, with signal output powers in the range well above 200 mW. In this new generation of systems, Raman amplifiers are superior in terms of pump power efficiency compared even to 1480 nm pumped EDFAs.

Plotting along alternate axes, Fig. 1.16(b) is a comparison of the power conversion efficiency, or PCE, between a 1480 nm pump EDFA and a Raman amplifier assuming a signal input power of 20 mW. The PCE is defined as $100 \times (\text{output signal power} - \text{input signal power}) / (\text{pump power})$. Here it can be seen that at lower power levels, EDFAs exhibit a PCE of over 30%, whereas Raman remains below 20%. This was to be expected and is in agreement with the efficiency figure found in Fig. 1.9. However, as the power levels required by network capacity increases cause pump power levels into the higher region, Raman becomes more efficient. This can be seen as Raman's PCE crosses over that of EDFAs at around 0.45 W (or about 26 dBm), a level already surpassed in current distributed Raman deployments.

A couple of interesting points to note include comparing the highest level PCE where both the Raman and EDFA "level off." At these points, the ~60% Raman PCE versus the ~40% EDFA PCE results in a more (cost) efficient amplification of the higher-capacity systems. Raman's gain can be further enhanced through an optimization of the gain fiber employed and the pumping strategy.

The details of the assumptions in Fig. 1.16 are as follows. The input is one signal at 1529.5 nm with an input signal power of 20 mW. For the Raman amplifier curve, a Raman pump wavelength of 1433 nm is chosen, so that the signal falls on the gain peak at 13.2 THz away from the pump wavelength. The fiber parameters used correspond to Lucent's WBDK dispersion-compensating fiber. The loss of the fiber at the signal wavelength is 0.472 dB/km, the length of the gain fiber is 5.64 km, and the Raman gain coefficient is 13.5 dB/(W × km). For the EDFA curves, it is assumed that the amplifier is forward pumped by either a 980 nm or 1480 nm pump. The passive loss in the EDFA is assumed to be 0.15 dB/m, and the length of the coil (20 m) is optimized to give maximum signal output power when pumped with 750 mW of 1480 nm pump for 20 mW of input power.

1.3. Distributed Raman Amplifiers

A DRA is an amplifier where the pump power extends into the transmission line fiber. As shown in Fig. 1.17, the DRA utilizes the transmission fiber in the network as the Raman gain medium to obtain amplification. Typically, high-powered, counterpropagating, Raman pumps are deployed in conjunction with discrete amplifiers, such as EDFAs.

The power of using a DRA to improve the signal-to-noise ratio and reduce the nonlinear penalty is illustrated in Fig. 1.18 [32, 17]. In this figure, the signal level in dB

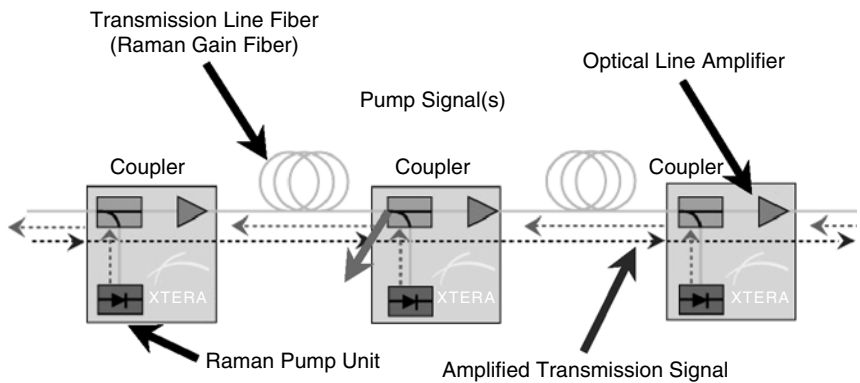


Fig. 1.17. DRAs utilize the transmission fiber in the network as the Raman gain medium to obtain amplification. Typically, high-power, counterpropagating Raman pumps are deployed in conjunction with inline discrete amplifiers such as EDFAs.

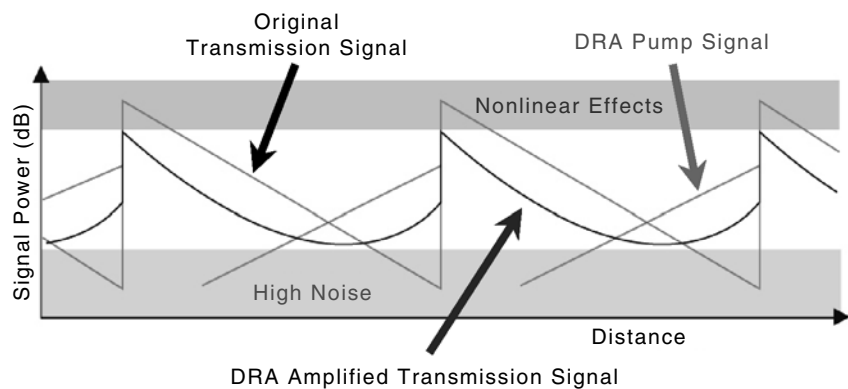


Fig. 1.18. Signal power in a periodically amplified transmission system. Comparison is made between a purely lumped amplified system (“original transmission system”) and a system using DRA to assist in the amplification. Also shown is the pump profile for counterpropagating pump. DRA permits the transmission of the original signal to occur below the level of nonlinear effects because signal amplification along roughly the second half of the span keeps the transmission above the system noise floor.

is plotted versus distance for a periodically amplified system. The sawtoothlike figures correspond to lumped amplification, and the curved figures correspond to the use of a DRA assisting a lumped amplifier. Using a DRA reduces the overall excursion that the signal level experiences. At the top signal level, a DRA does not require as high a signal level. Consequently, nonlinear effects are reduced. At the bottom, the signal does not dip down as low when a DRA is used. Consequently, the signal-to-noise ratio remains higher with the use of the DRA.

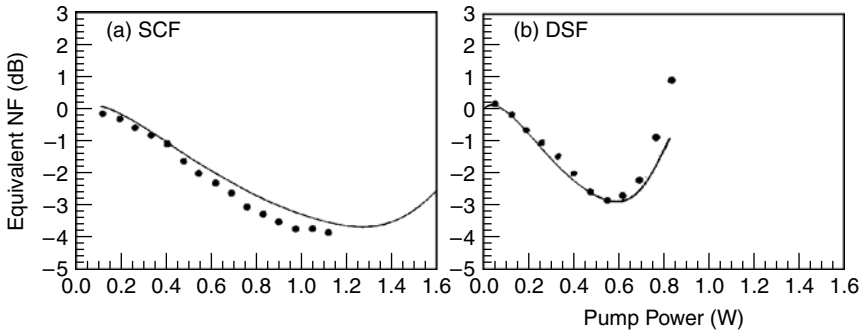


Fig. 1.19. Equivalent noise figure for a distributed Raman amplifier in (a) standard single-mode fiber and in (b) dispersion-shifted fiber [33]. Source: P.B. Hansen, A. Stentz, T.N. Nelson, R. Espindola, L.E. Nelson and A.A. Abramov "Dense Wavelength Division Multiplexed Transmission in 'Zero-Dispersion' DFS by Means of Hybrid Raman/Erbium-Doped Fiber Amplifiers" OFC Technical Digest, Postconference Edition, pg PD8-1 (©1999 OSA)

Calculations by Hansen and coworkers quantify the noise figure improvement when using a DRA for different fiber types [33]. The equivalent noise figure for a DRA is illustrated in Fig. 1.19(a) for a standard single-mode fiber and in Fig. 1.19(b) for a dispersion-shifted fiber. The equivalent noise figure is the noise figure that a discrete amplifier would have if it were placed at the end of the transmission link to obtain the same signal-to-noise ratio. For example, a typical lumped EDFA would have a noise figure of at least 4 dB. Therefore, in a standard single-mode fiber the signal-to-noise ratio (SNR) improvement is about 7.4 dB using a DRA, and in a DSF fiber the SNR improvement is about 6.6 dB.

One way to think about the DRA is to consider it as canceling out the loss for a fraction of the fiber length. Therefore, the SNR improvement can be thought of in terms of an equivalent amplifier spacing. Take, for example, the case of the DSF fiber whereof the SNR improvement is about 6.6 dB at 580 mW of pump power. Figure 1.20 shows the excess noise factor in decibels versus amplifier spacing in kilometers [34]. Assuming that the amplifier sites are spaced by 80 km, using a DRA gives the performance as if the discrete amplifiers were spaced between 35 to 38 km. Thus DRAs give an equivalent performance of much closer spaced amplifiers, giving a very attractive economic incentive for their use.

1.3.1. Demonstrated Benefits of DRAs

There are many examples from the literature that show the advantages of using DRAs in transmission systems. DRAs can be used to achieve longer amplifier spans or higher bit rates. These take advantage of the improvement in SNR. Alternately, DRAs can be used to achieve closer channel spacing or operation near the zero dispersion wavelength. These improvements take advantage of the reduction in nonlinear penalty by using DRAs.

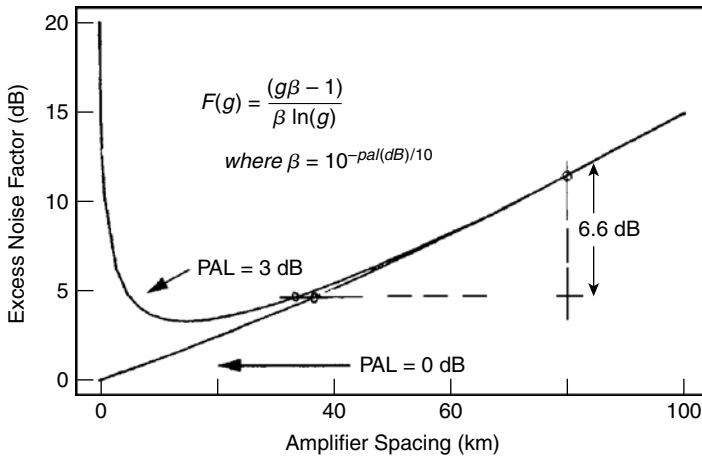


Fig. 1.20. Excess noise factor versus amplifier spacing. A lumped amplifier is assumed with a 0.2 dB/km fiber loss. The top curve is calculated for a postamplifier loss (PAL) of 3 dB, and the bottom curve is calculated for a PAL of 0 dB [34].

Several experiments have shown that longer amplifier spans can be used with the DRA. Elongation of optical repeater spacing is an important issue for terrestrial long-haul optically repeated transmission systems because it leads to a reduction in the number of repeaters and, consequently, a lower total system cost. DRA reduces the equivalent transmission fiber loss and, thus, improves the OSNR. Terahara and coworkers [35] employed a dual-band DRA technique to the C- and L-bands for the first time to long-haul WDM transmission systems. In particular, they transmitted 1.28 Tb/s WDM signals over a 840 km standard single-mode fiber with a 140 km repeater spacing. In comparison, the typical amplifier spacing in a link is about 80 km. The dual-band DRA effectively improves the OSNR by 3.7 dB in the C-band and by 4.3 dB in the L-band.

Garrett et al. [36] also did a field demonstration of DRA with 3.8 dB Q-improvement for 5×120 km transmission compared with just using discrete EDFAs. They demonstrated a DRA in an 8×10 Gb/s WDM experiment with five 120 km spans incorporating 40 km of installed older-vintage fibers. At the optimum pump power level of 650 mW, the average channel Q-value was increased by 3.8 dB for a 5×120 km system, and the number of 120 km spans with an error rate of 10^{-9} was increased from 3 spans to 7 spans.

As an example of higher bit rates achieved using DRAs, Nielsen et al. [37] experimentally show a 3.28 Tb/s (82×40 Gb/s NRZ) record aggregate capacity transmitted over 3×100 km of nonzero dispersion-shifted fiber. The system incorporates for the first time dual C- and L-band transmission and DRA in addition to the 40 Gb/s NRZ line rate. The 3.28 Tb/s capacity is comprised of forty 100 GHz spaced WDM channels in the C-band and forty-two 100 GHz spaced WDM channels in the L-band. Bit error rates of less than 10^{-10} were obtained without the use of forward-error-correction (FEC) for all channels after transmission. The dispersion compensation

corresponds to precompensation and channel decorrelation at the transmitter side as well as postcompensation at the receiver side. The results demonstrate that multi-terabit transmission using 40 Gb/s channels is practical over the repeater spacings present in today's networks.

Several papers have also demonstrated the reduction in nonlinear penalty because of the lower signal levels required with DRAs. As an example of a hero experiment, Suzuki et al. [38] demonstrated 25 GHz spaced, 1 Tb/s (100×10 Gb/s), DWDM transmission with the high spectral efficiency of 0.4 bit/s/Hz in the C-band over a 320 km (4×80 km) DSF. By employing DRA and polarization interleave multiplexing, four-wave mixing is suppressed in the C-band over DSF. Because operation is near the zero dispersion wavelength in DSF, no dispersion compensation is required. Thus, the reduction in nonlinear impairments permits super-dense channel spacing along with operation near the zero dispersion wavelength.

1.3.2. Issues in Using DRAs

DRAs typically use pump bands approximately 100 nm shorter in wavelength than the signal bands. For the C- and L-bands, this means that the pumps for DRA lie in the range of about 1430 to 1485 nm. However, pump bands must be at shorter wavelengths than any signal. Otherwise, the pumps will rob all of the energy of any shorter wavelength signals. Consequently, once the bandwidth exceeds approximately 100 to 120 nm, the DRA can be inconsistent with further band expansion. Therefore the DRA should be used, preferably at the shorter wavelength bands in the fiber. Given a better SNR performance, DRAs are particularly useful when the fiber loss increases. For example, if a 200 nm wide window of the fiber is to be used, then discrete amplifiers can be used for the S-, C-, and L-bands, whereas shorter bands might use hybrid amplifiers with DRAs (c.f. Fig. 1.21).

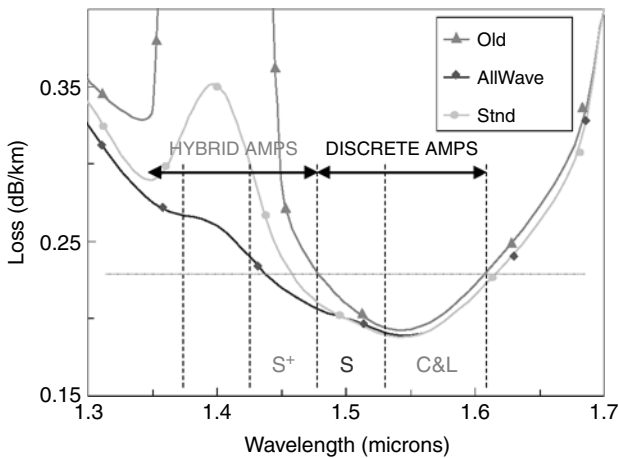


Fig. 1.21. Loss of different fiber types versus wavelength. If a 200 nm wide window of the fiber is to be used, then discrete amplifiers can be used for the S-, C-, and L-bands, whereas shorter bands might use hybrid amplifiers with DRAs.

As can be seen from the preceding examples, there are some key advantages of using DRAs. First is the improvement in noise figure over discrete amplifiers. Thus lower signal powers can be used, a higher loss can be tolerated, or a longer transmission distance can be used between regenerators. A second advantage is a more uniform gain along the length of the fiber. This gives rise to better SNR performance and reduced nonlinear penalty. It is also better for higher bit rates and soliton transmission. Finally, when used in conjunction with an EDFA, the complexity of typical inline amplifiers can be placed in the lumped EDFA. In other words, the DRA is just a low-noise preamplifier. The gain equalization, gain level correction, add/drop multiplexers, and dispersion compensation can all be placed at the midstage in the EDFA.

There are also challenges in using DRAs. A first challenge is that the effective length is less than 40 km of fiber in a typical DRA. For any nonlinear effect, the effective length is set by the attenuation of the pump. For pump wavelengths that are around 1450 nm, the penetration of the pump is less than 40 km into the fiber. A second challenge of using DRAs is the high pump powers propagating in the transmission fiber. For example, the optimal noise figure requires about 580 mW for a DSF, or approximately 1.28 W in a standard single-mode fiber [33]. At these power levels, connectors are highly vulnerable to damage.

In addition, there are issues associated with using DRAs in field deployment. For example, there is a higher sensitivity to spurious reflections. Moreover, there can be sensitivity to environmental and mechanical changes under the ground.

Another potential issue in DRAs is the double Rayleigh scattering penalty. As an example, a comparison is made of a DRA and discrete Raman amplifier. If the same fiber is used in both amplifiers, then the DRA will have a higher DRS penalty. However, if the DRA is made in a typical transmission fiber and the discrete Raman amplifier is implemented in a DCF, then the penalty in the DRA may be less. In other words, the comparison of DRS penalty for a DRA versus a discrete Raman amplifier depends on the specific details of the amplifiers. First, a DRA is compared with a discrete Raman amplifier both of which are implemented in the same fiber. For example, Fig. 1.22(a) plots the effective Rayleigh reflection coefficient in dB versus the fiber length in kilometers for a DSF fiber. Different curves are plotted for no Raman pumps, 400 mW pump power, 600 mW pump power, and 800 mW of pump power. A typical discrete Raman amplifier will be less than 15 km in length, and a distributed Raman amplifier will be at least 40 km in length. Therefore, a DRA has a double Rayleigh scattering penalty as much as 25 dB higher than a discrete amplifier that is implemented in the same fiber type for the same pump power.

On the other hand, Fig. 1.22(b) compares the DRS penalty for a DRA in a standard single-mode fiber (SMF-28) and a discrete amplifier in DCF fiber (DK-40 is 6.5 km long, and DK-80 is 13 km long). In particular, the effective Rayleigh reflection coefficient in dB is plotted versus pump-on/pump-off gain in dB. Because of the higher double Rayleigh scattering coefficient in the DCF, the DRS penalty is higher for a given gain level even though the fiber length is shorter. The simulations assume a pump at 1451 nm, where the loss is 0.29 dB/km for the standard single-mode fiber and 0.63 dB/km for the DCF. The signal is assumed to be at 1550 nm, where the fiber loss is 0.25 dB/km in the standard fiber and 0.49 dB/km in the DCF. The Raman gain coefficient between the simulated wavelengths is 1.62 dB/(W × km) for the standard

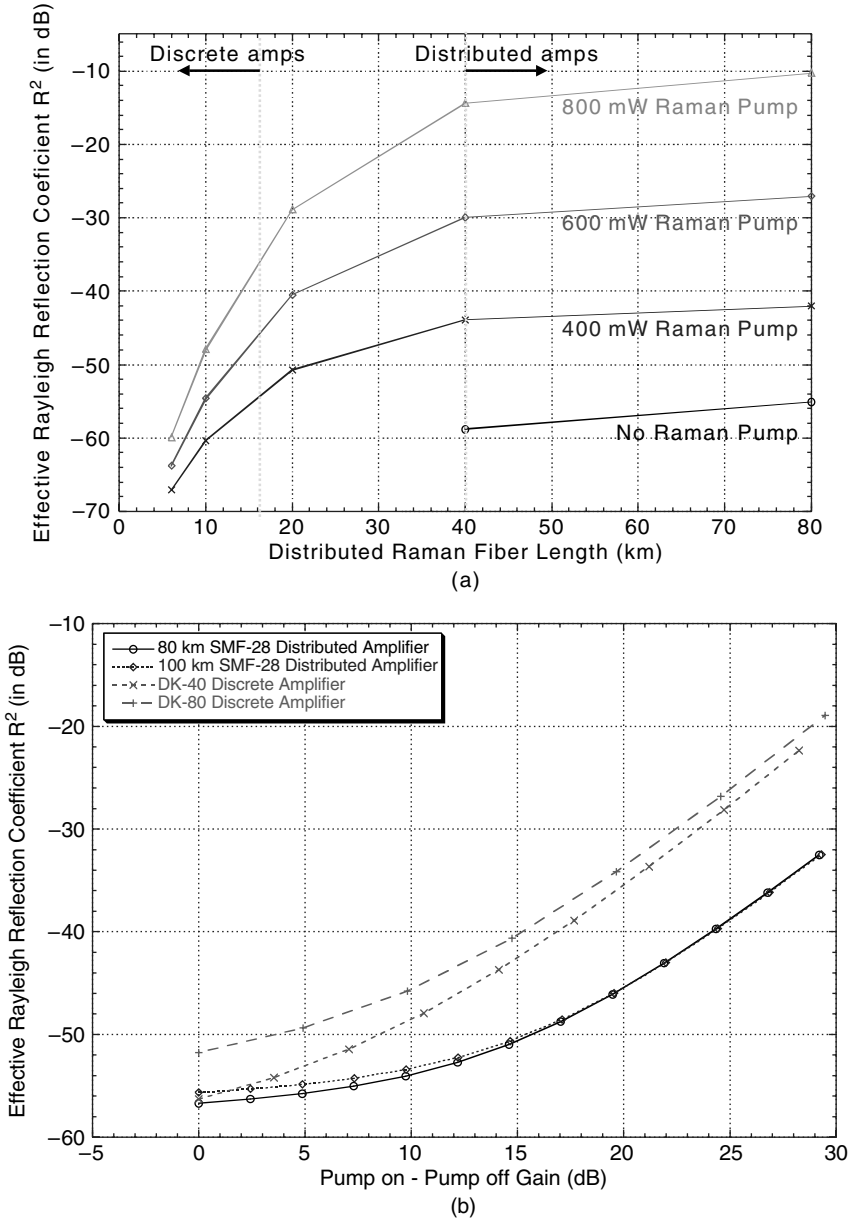


Fig. 1.22. (a) Effective Rayleigh reflection coefficient versus distributed Raman fiber length as calculated for a dispersion-shifted fiber. A discrete Raman amplifier is typically under 15 km, whereas a DRA is at least 40 km long. Curves are shown for no pump power (lowest curve), 400, 600, and 800 mW (highest curve) of pump power; (b) Effective Rayleigh reflection coefficient versus pump-on/pump-off gain for a DRA implemented in standard single-mode fiber (SMF-28) and a discrete amplifier implemented in dispersion-compensating fiber (DK fiber). The length of the DK-40 is 6.5 km, and the length of the DK-80 is 13 km.

fiber and 13.5 dB/(W × km) in the DCF. The Rayleigh scattering coefficient at 1550 nm is −42.3 dB/km for the standard fiber and −33.8 dB/km for the DCF.

In summary, the power and double Rayleigh scattering limits may set some fundamental limits on system applications of DRAs. There are indeed many practical issues related to having an amplifier “stretched across the country.” Despite all of these challenges, DRAs are being used in almost every long-haul and ultra-long-haul transmission system because of the signal-to-noise ratio and nonlinear benefits.

1.4. Discrete Raman Amplifiers

Discrete Raman amplifiers refer to a lumped element that is inserted into the transmission line to provide gain. Unlike a DRA, all of the pump power is confined to the lumped element. For example, Fig. 1.23 shows the typical setup for a lumped Raman amplifier. In this particular case, counterpropagating pump power is confined within the unit by the use of isolators surrounding the amplifier. Compared with Fig. 1.14, no pump power enters the transmission line. Of course, a hybrid amplifier could be made that combines the lumped Raman amplifier with a DRA.

The primary use for discrete Raman amplifiers is to open new wavelength bands in fused silica fibers. For example, different wavelength bands are illustrated in Fig. 1.24 [4]. EDFAs operate in the C-band, which stretches from 1530 to 1565 nm, and the L-band, which stretches from about 1565 to 1625 nm. There is also the S-band, which stretches from roughly 1430 to 1530 nm, which has at least as low a loss as the EDFA bands. Earlier transmission systems were deployed in the 1310 nm band, which can stretch between from 1280 and 1340 nm. There is also a 1400 nm band, which is only useful in new fibers that use special drying techniques to reduce the water peak absorption around 1390 nm. Thus Raman amplifiers can be used to

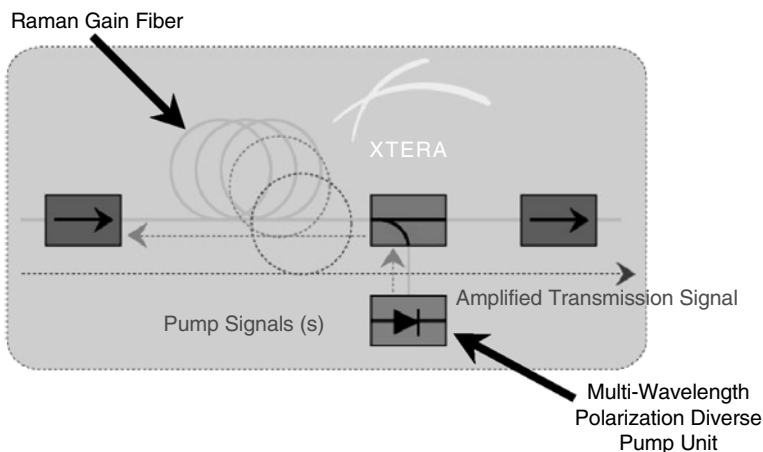


Fig. 1.23. Lumped or discrete Raman amplifiers have the pump power confined to the gain fiber in the amplifier box. Counterpropagating pump power is confined within the unit via isolators.

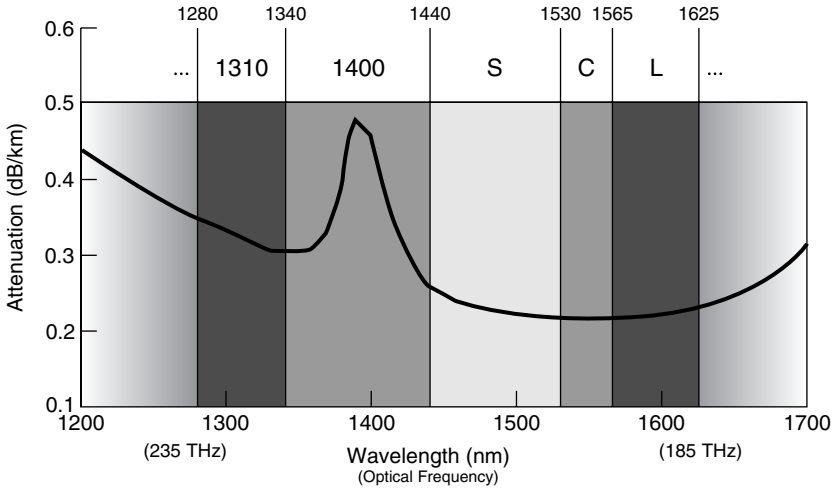


Fig. 1.24. Several windows exist within the low-loss valley of typical fused silica fibers. EDFAs provide gain in the C-band, and extended-band EDFAs can provide gain in the L-band. Raman amplifiers are the only fused-silica-based technology for opening up the S-band [4]. Source: R.B. Kummer “Fiber Issues for Nontraditional Wavelength Bands” OFC Technical Digest, pg ThR1-1 (©2000 OSA)

open up wavelengths between about 1280 and 1530 nm, a wavelength range that is inaccessible by EDFAs.

1.4.1. Amplifiers for 1310 nm and 1400 nm Bands

Some of the earliest work on discrete Raman amplifiers was done for the 1310 nm band and cable television applications. Such an amplifier could take advantage of high-power, directly modulated DFB lasers at 1310 nm as well as the low dispersion of the vast majority of installed fiber at that wavelength. A schematic illustration of the Raman ring amplifier design for analogue applications is depicted in Fig. 1.25 [9]. Light from a neodymium cladding-pumped fiber laser at 1060 nm is injected into the upper half of the amplifier to pump two cascaded Raman lasers that lase between gratings at 1115 and 1175 nm. The interstage isolator is used to reduce the effects of multipath interference due to DRS within the amplifier. The use of strictly counterpropagating pump geometry prevents pump fluctuations from coupling to the signals. Output powers in excess of +23 dBm are generated while maintaining very good analogue signal performance (carrier-to-noise ratio $\text{CNR} > 49$ dB, composite second-order CSO < -60 dBc, and a composite triple beat CTB < -68 dBc).

As an example of the use of this amplifier, a repeaterless, WDM transmission system operating in the 1310 nm wavelength window was demonstrated by means of discrete Raman fiber amplifiers [39]. The Raman post- and preamplifiers both employ a two-stage ring topology, as described above. The power budget is 45.1 dB, leaving a margin of 1.6 dB for a transmission distance of 141 km. The eight channels, ranging in wavelength between 1305.8 to 1311.6 nm, carry data at a rate of 10 Gb/s each.

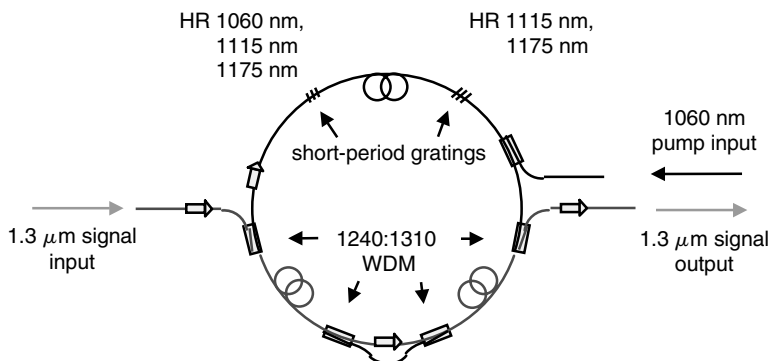


Fig. 1.25. Ring cavity, analogue Raman amplifier for gain in the 1310 nm band. The counter-propagating amplifier corresponds to the lower part of the ring, and the upper part of the ring corresponds to a Raman oscillator and wavelength shifter [9]. Source: A.J. Stentz, T. Nielsen, S.G. Grubb, T.A. Strasser and J.R. Pedrazzani “Raman Ring Amplifier at 1.3 μm with Analog-Grade Performance and an Output Power of 23 dBm” OFC Technical Digest, Postconference Edition, pg PD-16 (©1996 OSA)

This was the first WDM transmission experiment in the 1310 nm window utilizing Raman amplifiers.

Despite this early work on amplifiers for the 1310 nm band, not much commercial activity has transpired since. There are a number of fundamental reasons that keep the 1310 nm from being interesting for long-haul applications. First, the loss is too high. For example, the typical loss in the 1310 nm window is ~ 0.35 dB instead of ~ 0.2 dB in the 1550 nm window. The higher loss translates into shorter distance between regenerators. Second, the 1310 nm is of primary interest for standard single-mode fiber, but it is very difficult to use WDM near the zero dispersion wavelength of fibers. Hence, not too many channels can be opened up in the 1310 nm window. Third, the 1310 nm window is relatively narrow compared to the wide 1550 nm valley. At best an additional 20 nm of bandwidth can be used in the 1310 nm window, and the loss rises very rapidly on the short wavelength side.

Another window where research has been done on discrete Raman amplifiers is the 1400 nm band. Srivastava and coworkers [40] have demonstrated transmission of four 10 Gb/s channels at 1400 nm and sixteen 2.5 Gb/s channels in the 1550 nm window in so-called AllWave fiber, which has low loss and moderate chromatic dispersion in the 1400 nm region. The experimental setup, shown in Fig. 1.26, transmits the two wavelength bands over 80 km of AllWave fiber. Before this experiment, lightwave transmission had been demonstrated in four wavelength windows, 800 nm, 1310 nm, the C-band, and the L-band. With the new fiber type, this experiment opened up a fifth wavelength window, namely, the 1400 nm range. The AllWave fiber has a zero dispersion wavelength around 1310 nm, but special drying techniques are used in the preform to substantially reduce the water absorption peak at 1400 nm. Consequently, the loss of AllWave fiber in the 1400 nm window is about 0.3 dB/km, as compared to over 0.5 dB/km for conventional fiber. In addition, dispersion in the 1400 nm band is about 6–7 ps/nm-km, making AllWave fiber suitable for 10 Gb/s transmission over

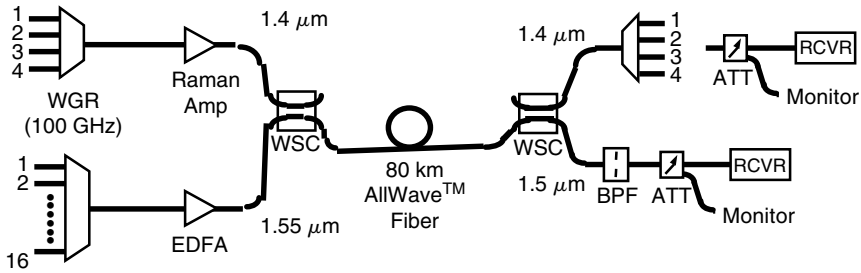


Fig. 1.26. Experimental setup for two-band experiments involving four channels in the 1400 nm band and 16 channels in the C-band [40]. Source: A.K. Srivasta et al “High-Speed WDM Transmission in All Wave Fiber in Both 1.4 μm and 1.5 μm Bands” OFC Technical Digest, pg PD2 (©1998 OSA)

distances of up to 150 km without dispersion compensation. Unfortunately, this amplification window is available for new installations that use the premium-cost fiber.

In many of these early experiments, the Raman amplifiers were pumped by cladding-pumped fiber lasers followed by Raman oscillator wavelength shifters [41]. Cladding-pumped fiber lasers can generate nearly arbitrarily scalable output power in a single-mode fiber. Also, cladding-pumped fibers allow the coupling of light from high-power diode-laser arrays into a single-mode fiber while actually increasing the radiance or brightness of the light by three orders of magnitude because the light is made diffraction-limited.

Efficient conversion of this pump light to wavelengths throughout the IR also requires low-loss cavities for resonant feedback, which are often in the form of cascaded Raman lasers (c.f., Fig. 1.27). Bragg gratings, written into the core of a single-mode fiber by exposure to UV light, can simultaneously provide high reflectivities and low out-of-band losses. The cavity comprises several hundred meters of germano-silicate fiber surrounded by highly reflecting Bragg gratings for each of the intermediate Stokes frequencies. The Raman cascade is then terminated by an output coupler grating, with reflectivity around 20%, which extracts power at the desired wavelength. A high-gain Raman amplifier at any desired wavelength can be constructed by terminating a Raman laser one Stokes order short of where amplification is desired and then pumping a suitable gain fiber.

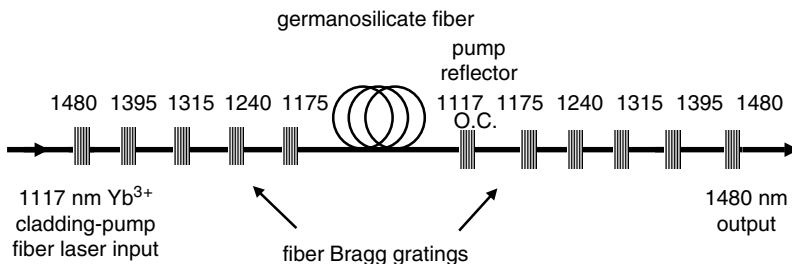


Fig. 1.27. Cascaded Raman oscillator created using low-loss cavities formed using fiber Bragg gratings [41].

1.4.2. Opening Up the S-Band Using Optical Amplifiers

Of the new bands to be opened up, perhaps the most important is the S-band [12, 42]. The S-band has comparable or better attenuation characteristics in standard single-mode fibers than the L-band, and the S-band has far less sensitivity to attenuation caused by bending during cabling and installation than the L-band. In addition, the S-band has better dispersion characteristics in standard single-mode fiber than C- and L-bands. For example, the S-band has approximately 30% less dispersion than the L-band. One cautionary note is that the S-band is not very attractive for fibers that have a zero dispersion wavelength falling within the S-band. This is because near the zero dispersion wavelength four-wave mixing can easily be phase-matched. Figure 1.28 shows, however, that only a few fibers fall into this category.

Three technologies have been studied extensively in hopes of bringing to the lower wavelengths of the S-band the same cost-effective means of optical amplification that EDFAs provide for the C-band. Semiconductor optical amplifiers (SOAs), thulium-doped fiber amplifiers (TDFAs) utilizing either fluoride or multicomponent silicate (MCS) as the dopant host fiber, along with lumped or discrete Raman amplifiers (LRAs) have all been proposed as key enablers for opening up transmission through optical amplification for wavelengths shorter than the traditional 1530 to 1560 nm range of EDFAs. However, the lineages of these three methodologies differ as much as their capabilities.

Various approaches for opening the S-band are detailed in Chapter 10.

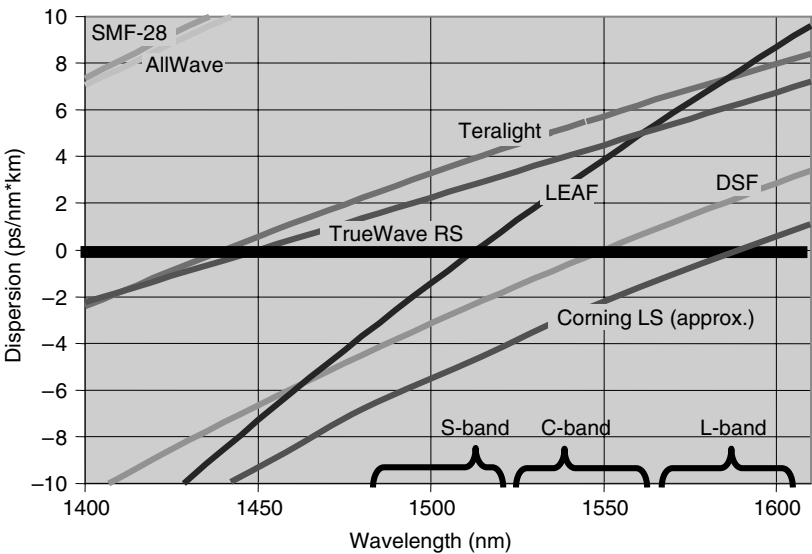


Fig. 1.28. Dispersion versus wavelength for several commercial fiber types. Very few fiber types have a zero dispersion wavelength falling in the S-band, making them less suitable for the S-band due to four-wave mixing penalties.

1.5. Summary

There has been revived interest in Raman amplification due to the availability of high pump powers and improvements in small core size fibers. Two general categories of Raman amplifiers are distributed Raman amplifiers and lumped or discrete Raman amplifiers. DRAs improve the noise figure and reduce the nonlinear penalty of the amplifier, allowing for longer amplifier spans, higher bit rates, closer channel spacings, and operation near the zero dispersion wavelength. DRAs are already becoming commonplace in most long-haul networks.

Discrete Raman amplifiers are primarily used to increase the capacity of fiber-optic networks. Amplifiers have been demonstrated in the 1310 nm band, but this wavelength range suffers from higher loss and more nonlinear penalty in standard single-mode fibers. For fibers with less water absorption, Raman amplifiers can also be used in the 1400 nm band. The capacity of most fibers can almost be doubled by opening up the S-band, which is inaccessible by EDFAs.

Raman amplifiers provide a simple single platform for long-haul and ultra-long-haul amplifier needs. Raman amplifiers are broadband and wavelength agnostic. Raman amplifiers can be distributed, lumped or discrete, or hybrid. Also, in Raman amplifiers the amplification and dispersion compensation can be combined in the same fiber length. For high channel count systems, as will be deployed in the next few years, Raman amplifiers' efficiency actually exceeds even 1480 nm pumped C-band EDFAs. Consequently, Raman amplifiers should see a wide range of deployment in the next few years.

References

- [1] R. H. Stolen and E. P. Ippen, Raman gain in glass optical waveguides. *Appl. Phys. Lett.*, 22:6, 1973.
- [2] G. P. Agrawal, *Nonlinear Fiber Optics*, 2nd ed., New York: Academic, 1995.
- [3] R. H. Stolen, Polarization effects in fiber Raman and Brillouin lasers, *IEEE J. Quantum Electron.*, 15:1157, 1979.
- [4] R. B. Kummer, Fiber issues for nontraditional wavelength bands. In *Proceedings of the Optical Fiber Communication Conference*, Technical Digest, Washington DC: Optical Society of America, ThR1-1, 2000.
- [5] K. Rottwitz and M. Nissov, Detailed analysis of Raman amplifiers for long-haul transmission. In *Proceedings of the Optical Fiber Communication Conference*, Technical Digest, Conference Edition Washington DC: Optical Society of America, TuG1, 1998.
- [6] K. L. Walker, Status and challenges of optical fiber amplifiers and lasers. In *Optical Amplifiers and their Applications 1998*, OSA Technical Digest, Optical Society of America, MB1-1, 1998.
- [7] S. Namiki and Y. Emori, Broadband Raman amplifiers design and practice. In *Optical Amplifiers and Their Applications*, OSA Technical Digest Washington DC: Optical Society of America, OMB2. 2000.
- [8] E. Desurvire, *Erbium-Doped Fiber Amplifiers Principles and Applications*, New York: Wiley, 1994.

- [9] A. J. Stentz, T. Nielsen, S. G. Grubb, T. A. Strasser, and J. R. Pedrazzani, Raman ring amplifier at 1.3 μm with analog-grade performance and an output power of 23 dBm. In *Proceedings of the Optical Fiber Communication Conference*, Technical Digest, Post-conference Edition Washington DC: Optical Society of America, Post-deadline paper 16, 1996.
- [10] J. Yoshida, N. Tsukiji, A. Naki, T. Fukushima, and A. Kasukawa, Highly reliable high power 1480nm pump lasers. In *Testing, Reliability, and Application of Optoelectronic Devices* (Bellingham, WA: SPIE, Society of Photo-Optical Instrumentation Engineers, *Proceedings of SPIE*, Vol. 4285, 146-158, 2001.)
- [11] A. Mathur, M. Ziari, and V. Dominic, Record 1 Watt fiber-coupled-power 1480 nm diode laser pump for Raman and erbium doped fiber amplification. In *Proceedings of the Optical Fiber Communication Conference*, Technical Digest, Postconference Edition Washington DC: Optical Society of America, Post-deadline paper 15, 2000.
- [12] A. B. Puc, M. W. Chbat, J. D. Henrie, N. A. Weaver, H. Kim, A. Kaminski, A. Rahman, and H. A. Fevrier, Long-haul WDM NRZ transmission at 10.7 Gb/s in S-band using cascade of lumped Raman amplifiers. In *Proceedings of the Optical Fiber Communication Conference*, Technical Digest, Postconference Edition Washington DC: Optical Society of America, Post-deadline paper 39.
- [13] V. Dominic, E. Mao, J. Zhang, B. Fidric, S. Sanders, and D. Mehuys, Distributed Raman amplification with co-propagating pump light. In *Optical Amplifiers and Their Applications*, OSA Technical Digest Washington DC: Optical Society of America, OMC5, 2001.
- [14] C. R. S. Fludger and V. Henderek, Fundamental noise limits in broadband Raman amplifiers. In *Proceedings of the Optical Fiber Communication Conference*, Technical Digest, Postconference Edition Washington DC: Optical Society of America, MA5, 2001.
- [15] S. A. Lewis, S. V. Chernikov, and J. R. Taylor, Temperature-dependent gain and noise in fiber Raman amplifiers, *Optics Lett.*, 24:24 (Dec.), 1823–1825, 1999.
- [16] H. Kidorf, K. Rottwitt, M. Nissov, M. Ma, and E. Rabarjaona, Pump interactions in a 100-nm bandwidth Raman amplifier,” *IEEE Photon. Technol. Lett.* 11:5, 1999.
- [17] S. Namiki and Y. Emori, Ultrabroad-band Raman amplifiers pumped and gain-equalized by wavelength-division-multiplexed high-power laser diodes, *IEEE J. Select. Topics Quantum Electron.*, 7:1, 3–16, 2001.
- [18] Y. Emori, Y. Akasaka, and S. Namiki, Less than 4.7 dB noise figure broadband in-line EDFA with a Raman amplified—1300 ps/nm DCF pumped by multi-channel WDM laser diodes. In *Proceedings of Optical Amplifiers and Their Applications*, PD3, 1998.
- [19] Y. Emori and S. Namiki, 100 nm bandwidth flat gain Raman amplifiers pumped and gain-equalized by 12-wavelength-channel WDM high power laser diodes, In *Proceedings of the Optical Fiber Communication Conference*, PD19, 1999. Y. Emori, Y. Akasaka, and S. Namiki, 100 nm bandwidth flat-gain Raman amplifiers pumped and gain-equalized by 12-wavelength-channel WDM laser diode unit, *Electron Lett.*, 35:1355–1356, 1999.
- [20] C. R. S. Fludger, V. Handerek, and R. J. Mears, Ultra-wide bandwidth Raman amplifiers. In *Proceedings of the Optical Fiber Communication Conference*, Technical Digest, 60–62, TuJ3, 2002.
- [21] T. Naito, T. Tanaka, K. Torii, N. Shimojoh, H. Nakamoto, and M. Suyama, A broadband distributed Raman amplifier for bandwidths beyond 100nm. In *Proceedings of the Optical Fiber Communication Conference*, Technical Digest, TuR1, 116–117, 2002.
- [22] H. Masuda, S. Kawai, K. I. Suzuki, and K. Aida, 75-nm 3-dB Gain-band optical amplification with erbium doped fluoride fibre amplifiers and distributed Raman amplifiers in 9×2.5 Gb/s WDM transmission experiment. In *Proceedings of the European Conference on Optical Communications*, vol.5, PDP, 74–74, 1997.

- [23] H. Takara, H. Masuda, K. Mori, K. Sato, Y. Inoue, T. Ohara, A. Mori, M. Mohtuku, Y. Miyamoto, and S. Kawanishi, Ultra-wideband tellurite/silica fiber Raman amplifier and supercontinuum lightwave source for 124-nm seamless bandwidth DWDM transmission. In *Proceedings of the Optical Fiber Communication Conference*, Paper FB1, 2002.
- [24] A. H. Gnauck, G. Raybon, D. Grosz, S. Hunsche, A. Kung, A. Marhelyuk, D. Maywar, M. Movassaghi, X. Liu, C. Xu, X. Wei, and D. M. Gill, 2.5Tb/s (64×42.7 Gb/s) Transmission over 40×100 km NZDSF using RZ-DPSK format and all-Raman-amplified spans. In *Proceedings of the Optical Fiber Communication Conference*, FC2, 2002.
- [25] F. Liu, J. Bennike, S. Dey, C. Rasmussen, B. Mikkelsen, P. Mamyshev, D. Gapontsev, and V. Ivshin, 1.6 Tbit/s (40×42.7 Gbit/s) Transmission over 3600 km UltraWaveTM fiber with all-Raman amplified 100 km terrestrial spans using ETDM transmitter and receiver. In *Proceedings of the Optical Fiber Communication Conference*, FC7, 2002.
- [26] Zhu, L. Leng, L. E. Nelson, L. Grüner-Nielsen, Y. Qian, J. Bromage, S. Stulz, S. Kado, Y. Emori, S. Namiki, P. Gaarde, A. Judy, B. Palsdottir, and R. L. Lingle, Jr., 3.2 Tb/s (80×42.7 Gb/s) Transmission over 20×100 km of non-zero dispersion fiber with simultaneous C+L-band dispersion compensation. In *Proceedings of the Optical Fiber Communication Conference*, Paper FC8, 2002.
- [27] L. Grüner-Nielsen, Y. Qian, B. Pálsdóttir, P. B. Gaarde, S. Dyrbol, and T. Verg, Module for simultaneous C+L-band dispersion compensation and Raman amplification. In *Proceedings of the Optical Fiber Communication Conference*, Technical Digest, TuJ6, 65–66, 2002.
- [28] H. Masuda, S. Kawai, and K.-I. Suzuki, Optical SNR enhanced amplification in long-distance recirculating-loop WDM transmission experiment using 1580nm band hybrid amplifier, *Electron Lett.*, 35:411–412, 1999.
- [29] P. B. Hansen, G. Jacobovitz-Veselka, L. Grüner-Nielsen, and A. J. Stentz, Raman amplification for loss compensation in dispersion compensating fiber modules, *Electron. Lett.*, 34:1136–1137, 1998.
- [30] Y. Emori, Y. Akasaka, and S. Namiki, Broadband losses DCF using Raman amplification pumped by multichannel WDM laser diodes, *Electron Lett.*, 34:2145–2146, 1998.
- [31] S. A. E. Lewis, S. V. Chrenikov, and J. R. Taylor, Broadband high-gain dispersion compensating Raman amplifier, *Electron Lett.*, 36:1355–1356, 2000.
- [32] M. Nissov, C. R. Davidson, K. Rottwitt, R. Menges, P. C. Corbett, D. Innis, and N. S. Bergano, 100 Gb/s (10×10 Gb/s) WDM transmission over 7200 km using distributed Raman amplification. In *Proceedings of the European Conference on Optical Communication 1997*, PD., 9–12, 1997.
- [33] P. B. Hansen, L. Eskildsen, A. J. Stentz, T. A. Strasser, J. Judkins, J.J. DeMarco, R. Pedrazzani, and D. J. DiGiovanni, Rayleigh scattering limitations in distributed Raman pre-amplifiers. *IEEE Photon. Technol. Lett.* 10:159–161, 1998.
- [34] N. S. Bergano, Undersea amplified lightwave system design. In *Optical Fiber Telecommunications IIIA*, ed. S. E. Miller and I. P. Kaminow, Boston: Academic, 302–332, 1997.
- [35] T. Terahara, T. Hoshida, J. Kumasako, and H. Onaka, 128 \times 10.66 Gbit/s Transmission over 840-km standard SMF with 140-km optical repeater spacing (30.4-dB loss) employing dual-band distributed Raman amplification. In *Proceedings of the Optical Fiber Communication Conference*, Postconference Edition, Washington DC: Optical Society of America, Post-deadline paper 28, 2000.
- [36] L. D. Garrett, M. Eiselt, and R. W. Tkach, Field demonstration of distributed Raman amplification with 3.8dB Q-improvement for 5×120 km transmission. In *Proceedings of the Optical Fiber Communication Conference*, Postconference Edition Washington DC: Optical Society of America, Post-deadline paper 42, 2000.

- [37] T. N. Nielsen, A. J. Stents, K. Rottwitt, D. S. Vengsarkar, Z. J. Chen, P. B. Hansen, J. H. Park, K. S. Feder, S. Cabot, S. Stulz, D. W. Peckham, L. Hsu, C. K. Kan, A. F. Judy, S. Y. Park, L. E. Nelson, and L. Grüner-Nielsen, 3.28-Tb/s Transmission over 3×100 km of nonzero-dispersion fiber using dual C- and L-band distributed Raman amplification, *IEEE Photon. Technol. Lett.*, 12:8, 1079–1081, 2000.
- [38] H. Suzuki, J. Kani, H. Masuda, N. Takachio, K. Iwatsuki, Y. Tada, and M. Sumida, 25GHz-Spaced, 1 Tb/s (100×10 Gb/s) super dense-WDM transmission in the C-band over a dispersion-shifted fiber cable employing distributed Raman amplification. In *Proceedings of the European Conference on Optical Communication*, PD 30–31, 1999.
- [39] T. N. Nielsen, P. B. Hansen, A. J. Stebtz, V. M. Aquaro, J. R. Pedrazzani, A. A. Abramov, and R. P. Espindola, 8×10 Gb/s $1.3\text{-}\mu\text{m}$ Unrepeated transmission over a distance of 141 km with Raman post- and pre-amplifiers, *IEEE Photon. Technol. Lett.*, 10:10, 1492–1494, 1998.
- [40] A. K. Srivastava, D. L. Tzeng, A. J. Stentz, J. E. Johnson, M. L. Pearsall, O. Mizuhara, T. A. Strasser, K. F. Dreyer, J. W. Sulhoff, L. Zhang, P. D. Yates, J. R. Pedrazzani, A. M. Sergeant, R. E. Tench, J. M. Freund, T.V. Nguyen, H. Manzar, Y. Sun, C. Wolf, M. M. Choy, R. B. Kummer, D. Kalish and A. R. Chraplyvy, High-speed WDM transmission in all wave fiber in both the $1.4\text{-}\mu\text{m}$ and $1.55\text{-}\mu\text{m}$ Bands, *Optical Amplifiers and Their Applications 1998*, OSA Technical Digest Washington DC: Optical Society of America, PD2, 1998.
- [41] S. G. Grubb and A. J. Stentz, Fiber Raman lasers emit at many wavelengths, *Laser Focus World*, (Feb.), 127–134, 1996.
- [42] J. Bromage, H. J. Thiele, and L. E. Nelson, Raman amplification in the S-band. In *Proceedings of the Optical Fiber Communication Conference*, Technical Digest, ThB3, 383–385, 2002.
- [43] J. L. Gimlett and N. K. Cheung, Effects of phase-to-intensity noise conversion by multiple reflections on gigabit-per-second DFB laser transmission systems, *J. Lightwave Technol.* 7: 888–895, 1989.
- [44] P. B. Hansen, A. Stentz, T. N. Nielsen, R. Espindola, L. E. Nelson, and A. A. Abramov, Dense wavelength-division multiplexed transmission in “zero-dispersion” DSF by means of hybrid Raman/erbium-doped fiber amplifiers. In *Proceedings of the Optical Fiber Communication Conference*, PD8-1, 1999.
- [45] K. Rottwitt and H. D. Kidorf, A 92nm bandwidth Raman amplifier. In *Proceedings of the Optical Fiber Communication Conference*, Paper PD6, 1998.

Chapter 2

Fundamentals of Raman Amplification in Fibers

R.H. Stolen

2.1. Introduction

Raman scattering was discovered independently and almost simultaneously in 1928 by groups in India and Russia [1, 2]. If C.V. Raman had not published first we might know Raman scattering as the Landsberg–Mandelstam Effect. Raman was awarded the 1930 Nobel Prize for the discovery, which was not shared with the Russians. Neither group was actually looking for what we now know as the Raman effect [3]. Landsberg and Mandelstam were looking for a small wavelength shift due to scattering from thermal fluctuations, now called “Brillouin scattering.” Raman was seeking an optical analogue of the Compton effect. It was quickly understood that Raman scattering is a shift in the frequency of scattered light due to interaction of the incident light with high-frequency vibrational modes of a transparent material. It was later pointed out that the correct interpretation had been predicted by A. Smekal in an obscure 1923 theoretical paper [4].

Raman scattering quickly became an analytical tool for the study of vibrational modes of solids, liquids, and gases. Raman scattering is complementary to infrared absorption because modes that are strongly Raman active have weak infrared absorption and vice versa. This point should become clear from the classical picture of Raman scattering presented in Section 2.3.1. Until the development of the argon-ion laser in 1966 most Raman studies used the ultraviolet, blue, or green spectral lines from low-pressure mercury arcs [5]. The use of laser sources led to a resurgence of interest in Raman scattering, which continues unabated [6].

Raman amplification was discovered by accident in 1962 during early experiments with Q -switched Ruby lasers. A Q -switched laser introduces cavity loss to allow the buildup of much higher population inversions and then switches off the loss to produce extremely high output powers. In those experiments, loss was introduced in the cavity using a polarizer and electric field-induced birefringence in a nitrobenzene cell. The surprising result was that an intense output appeared at the Raman-shifted wavelength of nitrobenzene [7].

This Raman-shifted laser output was explained by Hellwarth [8] as stimulated Raman scattering in which the Raman frequency is amplified due to a previously

neglected interaction between the Raman wave and the primary laser wavelength. The stimulated Raman effect was subsequently observed with various samples placed inside and outside the laser cavity [9].

Even in the earliest stages of investigation into fiber-optic communications there was concern about the potential influence of nonlinear interactions such as stimulated Raman scattering. It was realized that because nonlinear interactions depend on interaction length as well as optical intensity, these might occur at extremely low powers in optical fibers [10]. Stimulated Raman scattering was first observed in one of the early Corning single-mode fibers [11]. In the same series of experiments, the Raman gain coefficient of a silica-core fiber was measured. These results were checked with spontaneous Raman cross-section measurements, which were calibrated against the known benzene standard. Out of these measurements came the concept of effective area that applies to almost all nonlinear effects in fibers [12].

In its simplest form, the fiber Raman amplifier is an optically pumped optical amplifier in which an optical signal is amplified by the Raman interaction with a strong optical wave at higher frequency called a “pump.” The signal can be pumped in either direction. As the signal is tuned with respect to the pump frequency the gain is found to be maximum at a frequency separation of 13 THz between pump and signal. If the signal frequency is higher than the pump it will suffer nonlinear absorption rather than amplification. The actual gain curve is broad and closely matches the spontaneous Raman scattering spectrum of the glass. Spontaneous Raman scattering will also occur and is the noise in the Raman amplifier. A comparison of the Raman gain coefficient and spontaneous Raman scattering cross-section at room temperature (300K) is presented in Fig. 2.1.

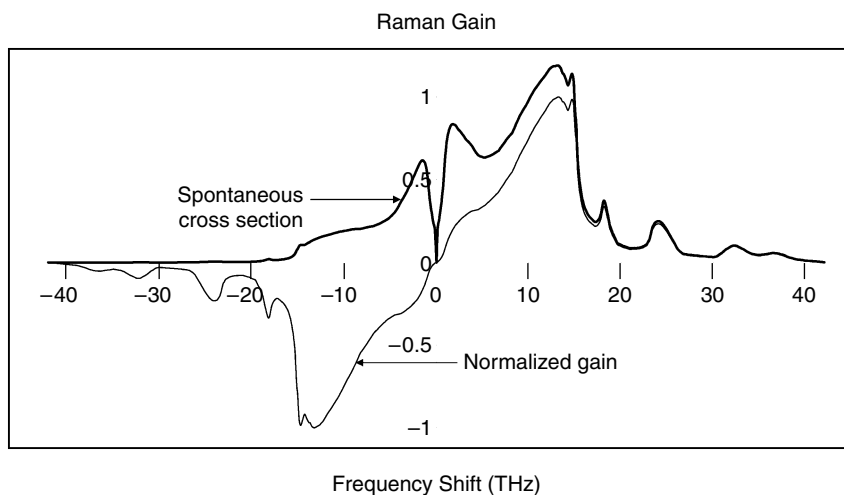


Fig. 2.1. Raman gain coefficient $g(\Omega)$ and spontaneous Raman scattering cross section $\sigma(\Omega)$ at room temperature for fused silica. Ω is the separation between the pump or exciting frequency and the signal or scattered frequency.

The Raman interaction can be treated in various ways, which can appear very different. The quantum approach treats the problem as a transition rate involving photon number. Classically this is a parametric amplifier with an interaction between signal, pump, and vibrational wave. Finally, the Raman interaction itself can be traced to a small time delay in the nonlinear refractive index.

2.2. Quantum Approach to Raman Scattering

2.2.1. Spontaneous Raman Scattering

Despite the fact that the Raman effect was discovered accidentally, the correct interpretation appeared very quickly and is pictured schematically in Fig. 2.2. An incident photon of frequency ν_0 is scattered by a molecule exciting one quantum of vibrational energy Ω and producing a downshifted scattered photon of frequency $\nu_S = \nu_0 - \Omega$. If the molecule already has vibrational energy the incident photon can absorb a quantum of vibrational energy producing an upshifted photon of frequency $\nu_A = \nu_0 + \Omega$. Both downshifted and upshifted frequencies are observed and called Stokes and anti-Stokes spectral lines.

The scattering process is often described in terms of energy levels where a molecule initially in vibrational state “1” is excited to vibrational state “2” by the virtual absorption of a photon of frequency ν_0 and emission of a photon at frequency ν_S . The process is illustrated in Fig. 2.3, where energy levels r are electronic states of the molecule of energy higher than the incident photon energy. The transition rate W_S for excitation of the molecule from the “1” vibrational level to one quantum of excitation is:

$$W_S \propto \left[\sum_r \left(\frac{M_{2r} M_{1r}}{\nu_{r1} - \nu_0} + \frac{M_{2r} M_{1r}}{\nu_{r1} + \nu_S} \right) E_0 \right]^2. \quad (2.1)$$

In (2.1) M_{1r} is a matrix element between the ground state and one of the electronic levels r and M_{2r} is the matrix element between the electronic state and the excited

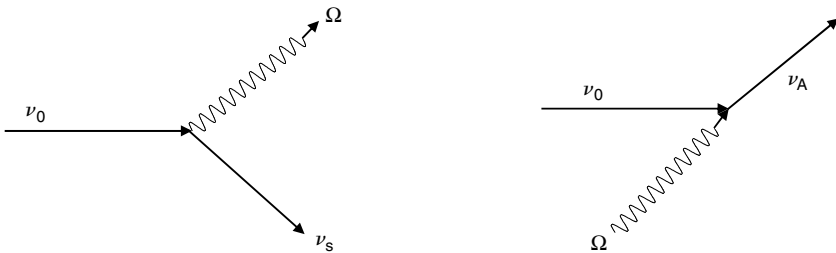


Fig. 2.2. Scattering diagrams for Stokes and anti-Stokes Raman scattering. A Stokes photon is produced by the absorption of an incident photon and the simultaneous creation of one quantum of vibrational energy. An anti-Stokes photon is produced by the absorption of one quantum of vibrational energy.

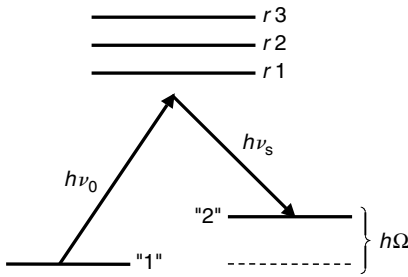


Fig. 2.3. An energy level diagram representing the quantum theory of Raman Stokes scattering. The initial vibrational state is “1” and one quantum of vibrational excitation is “2”. Energy levels “*r*” are a complete set of electronic energy levels.

state “2”. The energy levels of the electronic states are $h\nu_{r1}, h\nu_{r2}, \dots, E_0$ is the amplitude of the incident field at ν_0 , and h is Planck’s constant [13].

Equation (2.1) describes one quantum of excitation of a molecule initially at rest. Usually the molecule is in thermal equilibrium with its surroundings which increases the transition rate by the Bose–Einstein thermal population factor N_Ω . The population factor is given in Eq. (2.2) where k_B is the Boltzmann factor, T is the temperature in degrees Kelvin, and Ω is the vibrational frequency [14].

$$N_\Omega = \frac{1}{e^{h\Omega/k_B T} - 1}. \quad (2.2)$$

Thermal excitation of the vibrations can produce anti-Stokes scattering. Transition rates for Stokes scattering will be proportional to $(1 + N_\Omega)$ and N_Ω for anti-Stokes scattering.

$$W_S \propto N_0(1 + N_\Omega) \text{ Stokes} \quad (2.3a)$$

$$W_A \propto N_0 N_\Omega \text{ anti-Stokes.} \quad (2.3b)$$

N_0 is the incident photon number that is proportional to $|E_0|^2$. The ratio of anti-Stokes to Stokes intensities is $\exp(-h\Omega/k_B T)$. At elevated temperature the anti-Stokes scattered intensity approaches the Stokes intensity. As T approaches zero the anti-Stokes scattering vanishes leaving only the Stokes line.

2.2.2. Stimulated Raman Scattering

To explain stimulated Raman scattering, Hellwarth showed that the transition rate for Stokes scattering also depends on the Stokes photon number as well as the population factor of the vibrational mode [8]. Because the Stokes transition rate is proportional to the change per unit time of the Stokes photon number (2.3a) becomes:

$$\frac{dN_S}{dt} = SN_0(1 + N_\Omega + N_S), \quad (2.4)$$

where S is a rate constant. The inclusion of the factor N_S shows that the Stokes wave will be amplified in the laser cavity. Generation of Stokes photons increases the Stokes photon number, which increases the rate at which Stokes photons are generated.

The amplification part of (2.4) can be converted to gain per unit length G by dividing the rate constant S by the velocity of light at the Stokes frequency c/n_S where n is the refractive index at ν_S .

$$\begin{aligned}\frac{dN_S}{dz} &= GN_S \\ G &= \frac{n_S S N_0}{c}.\end{aligned}\quad (2.5)$$

When the gain per unit length exceeds the cavity losses lasing will occur at the Stokes wavelength.

2.2.3. Raman Amplification and Stimulated Scattering in Fibers

Stimulated Raman scattering is also observed in fibers and in samples placed outside a laser cavity where there are no mirrors to provide feedback. In this single-pass configuration, spontaneous scattered Stokes light is amplified to produce a stimulated Raman output. The procedure first used by R.G. Smith to calculate a stimulated Raman threshold or critical power in a fiber is illustrated in Fig. 2.4 [10]. The fiber is divided into segments of length dz . In each segment the Stokes power increases by spontaneous scattering in the segment and amplification of the Stokes power from all previous segments. There is no input at the Stokes frequency; all the Stokes output is from amplified spontaneous emission.

$$dN_S = dzG(1 + N_S)P_0/A_{eff}. \quad (2.6)$$

N_S is the Stokes photon number in the fiber mode per unit frequency bandwidth; G is the gain coefficient, P_0 the pump power, and A_{eff} the effective area. To bring out the essential features, loss has been neglected. This can be included by replacing the fiber length L with an effective length, which is derived in Appendix A2.3. The thermal occupation number of the vibrational mode is also neglected. This contribution is small at the peak of the Raman gain curve near 13 THz. Integration over the length L gives a net Stokes output of

$$N_S(L) = \left[1 - e^{-GP_0L/A_{eff}}\right] e^{GP_0L/A_{eff}}. \quad (2.7)$$

The quantity in the brackets is an effective input power N_S (noise) which for reasonably large amplifications becomes 1.0. Thus the spontaneous scattering along the fiber has been reduced to an effective input of one photon per mode at the Stokes frequency.

The total Stokes power is then an integral over all frequencies and a threshold or critical power is defined where the Stokes power equals the pump power. The condition for a critical power becomes:

$$\frac{GP_0(crit)L}{A_{eff}} \approx 16. \quad (2.8)$$

Some of the details of Smith's calculation of a critical power are contained in Appendix A2.4.

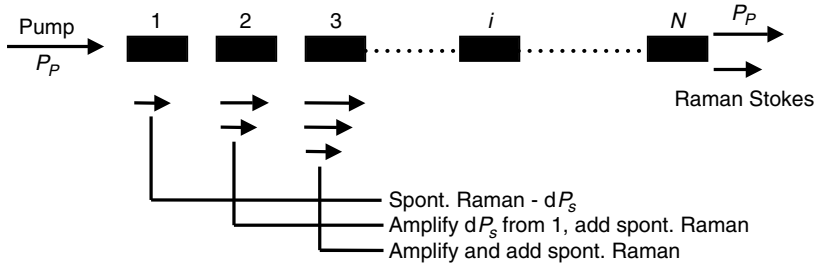


Fig. 2.4. To calculate amplified spontaneous scattering the fiber is divided into short segments. The total noise power at the Raman Stokes frequency is the sum of the amplified spontaneous scattering from each segment.

Here our primary interest is in Raman gain and its associated noise for application in fiber Raman amplifiers. If there is a Stokes signal input $N_S(0)$ the signal amplification and amplified noise will be:

$$N_S(L) = [N_S(0) + N_S(\text{noise})] e^{GP_0L/A_{eff}}. \quad (2.9)$$

The power over frequency bandwidth $\Delta\nu$ is:

$$P_S = h\nu_S \Delta\nu N_S, \quad (2.10)$$

so Eq. (2.9) becomes:

$$P_S(L) = [P_S(0) + h\nu_S \Delta\nu N_S(\text{noise})] e^{GP_0L/A_{eff}}. \quad (2.11)$$

If the loss at the signal and pump wavelengths is included Eq. (2.11) becomes:

$$P_S(L) = [P_S(0) + P_S(\text{noise})] e^{GP_0L_{eff}/A_{eff}} e^{-\alpha_s L}, \quad (2.12)$$

where α_s and α_p are the loss coefficients of the signal and pump wavelengths. The effective length is:

$$L_{eff} = \frac{1 - e^{-\alpha_p L}}{\alpha_p}. \quad (2.13)$$

Note that for large $\alpha_p L$ the effective length becomes the absorption length $1/\alpha_p$. For short fibers L_{eff} is the actual length.

2.3. Classical Picture

2.3.1. Placzek Model of Spontaneous Raman Scattering

The Placzek model treats spontaneous Raman scattering as amplitude modulation, which produces upper and lower sidebands in the scattered light [14, 15]. A Raman active molecule (or mode) vibrates and the electronic polarizability changes at the vibration frequency. The polarizable electronic cloud of the molecule is driven at the optical frequency of the pump. The induced dipole oscillates mostly at the pump frequency but has picked up weak upper and lower sidebands spaced by the molecular vibration frequency (Fig. 2.5).

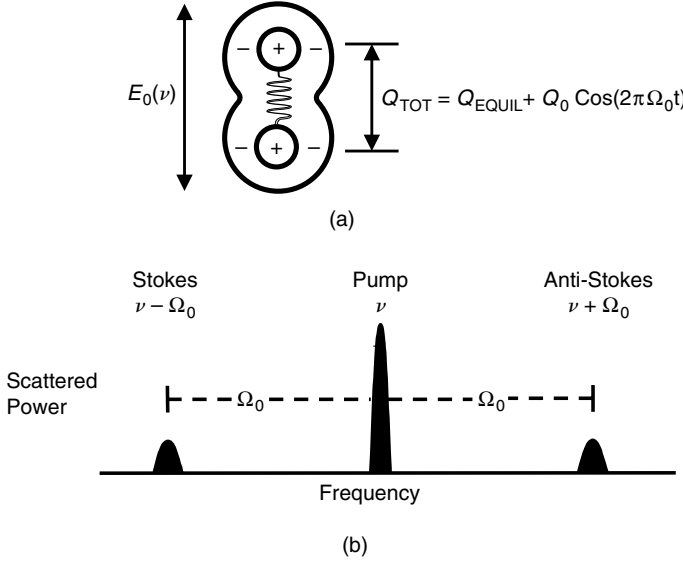


Fig. 2.5. (a) Incident optical field at frequency ν_0 on diatomic molecule of vibrational amplitude Q and frequency Ω_0 ; (b) variation in nuclear separation changes the electronic polarizability which modulates the scattered dipole radiation. Upper and lower sidebands are produced.

The induced dipole moment \mathcal{P} of the molecule becomes:

$$\begin{aligned} \mathcal{P} &= \beta E(2\pi\nu_0 t) = [\beta_0 + (\partial\beta/\partial Q)Q_0 \cos(2\pi\Omega_0 t)] E_0 \cos(2\pi\nu_0 t) \\ \mathcal{P} &= \beta_0 E_0 \cos(2\pi\nu_0 t) + (\partial\beta/\partial Q)E_0 \frac{Q_0}{2} [\cos 2\pi(\nu_0 + \Omega_0) + \cos 2\pi(\nu_0 - \Omega_0)], \end{aligned} \quad (2.14)$$

where β is the molecular polarizability, ν_0 and Ω_0 are the frequencies of the pump and the molecular vibration, and E_0 and Q_0 are the amplitudes of the pump field and molecular vibration as pictured in Fig. 2.5(a). The induced dipole radiates at the pump, Stokes, and anti-Stokes frequencies. Radiation at the pump frequency is Rayleigh scattering. The electric field at the Stokes scattered frequency is proportional to the second derivative of \mathcal{P} so the Stokes-scattered power will be proportional to ν_s^4 . The ν^4 factor also applies to Rayleigh scattering.

The ratio of radiated power at the Stokes frequency to the pump power is called the scattering cross-section and is given by

$$\sigma \propto \frac{P_S}{P_0} \propto \nu_s^4 (n_0/n_s) (\partial\beta/\partial Q)^2 Q_0^2. \quad (2.15)$$

In Eq. (2.15) various constants have been ignored in order to concentrate on the term $\partial\beta/\partial Q$. This factor links the spontaneous Raman scattering cross-section and the Raman gain coefficient. n_0 and n_s are refractive indices at the pump and Stokes wavelengths.

The spontaneous Raman scattering cross-section σ increases with temperature by the factor $1 + N_\Omega$ as given in Eqs. (2.2) and (2.3a). N_Ω is proportional to Q_0^2 where

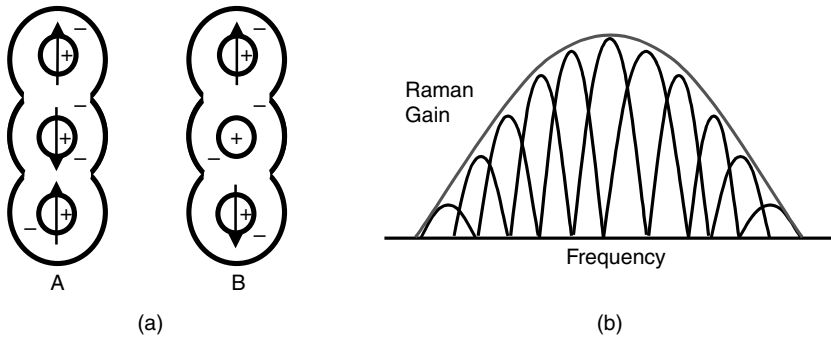


Fig. 2.6. (a) Two vibrational modes of a triatomic molecule. Mode A is infrared active but the polarizability will change at twice the vibrational frequency. Mode B will be Raman active but there will be no dipole moment at the vibrational frequency; (b) the broad Raman bands of glasses are made up of the incoherent addition of many weakly Raman-active localized modes.

Q_0 is the thermal amplitude of the molecular vibration. According to the Placzek model, Stokes and anti-Stokes powers should be equal even if the only molecular motion comes from zero-point fluctuations at $T = 0\text{K}$. Actually there is an asymmetry between the Stokes and anti-Stokes powers and the anti-Stokes scattered power vanishes as the sample temperature approaches $T = 0\text{K}$ whereas the Stokes power does not. This asymmetry can be explained by including the effect of Raman gain as discussed further in Section 2.4.3.

Considerations based on molecular symmetry illustrate why $\partial\beta/\partial Q$ is small for molecular modes with large infrared absorptions. This is illustrated for a triatomic molecule in Fig. 2.6(a). When the incident frequency matches the vibrational frequency of Mode A the induced dipole moment will be large leading to a large IR absorption. There will be no dipole moment produced from the motion of mode B. On the other hand, the symmetry of mode A shows that any change in polarizability from Mode A will occur at twice the vibrational frequency so there will be no first-order Raman scattering. Mode B will have a large Raman cross-section.

The structure of glass is a random network in which the normal modes are fairly localized and act as independent harmonic oscillators spread over a broad frequency range [16]. These modes are weakly Raman active and their incoherent addition produces the broad Raman spectra observed in glasses (Fig. 2.6(b)).

2.3.2. Raman Amplification

The basic features of Raman amplification in a fiber can be seen by considering two copropagating waves separated in frequency by the frequency of a Raman active vibrational mode.

$$\begin{aligned}\frac{dP_1}{dz} &= G_1 \frac{P_2}{A_{eff}} P_1 - \alpha_1 P_1 \\ \frac{dP_2}{dz} &= G_2 \frac{P_1}{A_{eff}} P_2 - \alpha_2 P_2.\end{aligned}\tag{2.16}$$

The Raman interaction transfers power from P_2 to P_1 . P_1 and P_2 are the powers of waves at frequencies ν_1 and ν_2 , where $\nu_2 > \nu_1$. P_1 and P_2 are functions of the propagation distance z ; α_1 and α_2 are absorption coefficients at ν_1 and ν_2 .

In a Raman amplifier P_2 becomes the pump and P_1 is the signal where $P_2 \gg P_1$. We have treated copropagating waves but there will also be Raman gain for counterpropagating waves. The counterpropagating configuration is preferred for system applications because pump fluctuations are averaged out. If the signal is at a higher frequency than the pump it will be absorbed rather than amplified. This is referred to as Raman absorption or the inverse Raman effect [17].

The derivation of Eq. (2.16) is outlined in Appendix A2.1 and is based on the Placzek model. The essential feature is that E_1 and E_2 mix to drive the vibrational mode to an amplitude $Q_0 \sim (\partial\beta/\partial Q)E_1E_2$.

If there are N modes per unit volume the polarization \mathcal{P}_1 at ν_1 will be:

$$\mathcal{P}_1 \propto N(\partial\beta/\partial Q)E_2Q_0 \propto N(\partial\beta/\partial Q)^2E_2^2E_1, \quad (2.17)$$

where the polarization comes from Eq. (2.14) substituting ν_1 and ν_2 for ν_s and ν_0 . The polarization at ν_1 adds to the incoming field E_1 leading to a gain coefficient:

$$G_1 \propto \nu_1(\partial\beta/\partial Q)^2P_2/A_{eff}. \quad (2.18)$$

The polarization in Eq. (2.17) leads to an amplification linear in pump intensity which becomes the power/effective area in a fiber. The gain coefficient in (2.18) brings out several points. The first deals with the frequency factor. The negative gain for E_2 will be proportional to ν_2 . Because $\nu_2 > \nu_1$ the power absorbed from P_2 will be greater than the power gained by P_1 . The difference is power lost to the vibrational mode and dissipated in the glass. The second point is that the gain coefficient is linked to the spontaneous cross-section of (2.15) by the term $(\partial\beta/\partial Q)^2$. This is how the relation between Raman gain and spontaneous Raman cross-section can be derived. That relation is derived in a simpler way in Section 2.3.3. The third point is to note that the gain does not contain the thermal amplitude of the vibrational mode, which appears in the spontaneous cross-section. The spontaneous cross-section is temperature-dependent but the gain coefficient does not depend on temperature. In relating the gain to the spontaneous cross-section it is necessary to divide out the temperature-dependence of the cross-section.

The radial dependence of the electric field in the fiber has been swallowed up in a normalized integral over the mode fields, which has the dimensions of area. The effective area A_{eff} is derived in Appendix A2.2.

$$A_{eff} = \frac{\int \psi_1^2 r dr d\theta \int \psi_2^2 r dr d\theta}{\int \psi_1^2 \psi_2^2 r dr d\theta}. \quad (2.19)$$

2.3.3. Correspondence between Quantum and Classical Treatments of Raman Amplification

Both classical and quantum treatments of Raman amplification in a fiber break the fiber into small segments and add the amplified signal and the amplified spontaneous

scattered light from the entire fiber. Figure 2.4 illustrates a fiber with N sections of length δL with input pump power P_2 and input signal power P_1 . The incremental increase in P_1 in segment i is given in Eqs. (2.20a,b) for the classical and quantum treatments [18].

$$dP_1(i) = G_1 \frac{P_2}{A_{eff}} P_1 \delta L + \eta \sigma_T P_2 \frac{\Delta \nu}{c} \delta L \quad (2.20a)$$

$$dN_1(i) = G_1 \frac{P_2}{A_{eff}} (N_1 + 1 + N_\Omega) \delta L \quad (2.20b)$$

$$P_1(i) = h\nu_1 \Delta \nu N_1(i). \quad (2.20c)$$

In the classical treatment of (2.20a) the second part is the spontaneous scattered power. The total scattered power in a frequency bandwidth $\Delta \nu$ is the total scattering cross-section Ω_T at frequency ν_1 times P_2 at segment i . The capture fraction η is the fraction of scattered power captured by the guide in the forward direction. The first part of (2.20a) is amplification of P_1 which contains amplified input power of P_1 up to segment i plus the sum of the amplified spontaneous emission.

The quantum approach treats the change in photon number at ν_1 in segment i . The power P_1 is related to photon number by (2.20c). In (2.20b) the factor $1 + N_\Omega$ is the spontaneous scattering and corresponds to σ_T of (2.20a). N_Ω is the phonon thermal occupation number that goes to zero at $T = 0K$.

The simplest way to obtain the relation between Raman gain and the spontaneous Raman cross-section is to utilize the requirement that the classical and quantum approaches should produce the same result. In the limit where the input $P_1 = 0$ and the gain is negligible the spontaneous scattered power out of the fiber at frequency ν_1 is the sum of the spontaneous scattered power from all the segments. Here we neglect loss.

$$P_1 L = \eta \sigma_T P_2 L \Delta \nu / c \quad (2.21a)$$

$$P_1(L) = h\nu_1 G_1 P_2 L (1 + N_\Omega) \Delta \nu / A_{eff}, \quad (2.21b)$$

where (2.21a) is the classical result and (2.21b) is the quantum result. The photon number has been converted to power using (2.20c).

The relation between gain and cross-section comes from equating (2.21a) and (b) with two additional considerations. The first is that the cross-section usually used is $\sigma(0)$, the Raman cross section for forward (0°) scattering per unit solid angle per unit frequency in units of cm^{-1} . σ_T and $\sigma(0)$ are related by

$$\sigma_T = 8\pi \sigma(0)/3. \quad (2.22)$$

Polarized Raman scattering follows the same angular dependence as dipole radiation so $\sigma(\theta) = \sigma(0) \cos^2(\theta)$. The Raman spectrum is highly polarized in the high-gain region between 3 and 15 THz. Some of the issues related to the polarization dependence of Raman gain are discussed in Sections 2.6.1 and 2.6.3.

The second consideration is that the capture fraction is related to the effective area. The ratio of capture fraction to effective area can be derived by examining the

fraction of incoherent spontaneous Raman light captured by the fiber [18]. The result is the same for the capture fraction of Rayleigh scattered light [19].

$$\eta A_{eff} = 3\lambda_s^2 / 8\pi n_s^2. \quad (2.23)$$

In (2.23) λ_s is the Stokes scattered wavelength and n_s is the refractive index at λ_s .

The expression for the Raman gain coefficient in terms of the spontaneous Raman scattering cross-section comes from combining (2.21) and (2.23).

$$G(\text{cm/W}) = \frac{\sigma(0)\lambda^3}{c^2 h n^2 (1 + N_\Omega)}. \quad (2.24)$$

The spontaneous cross-section $\sigma(0)$ varies with wavelength as $1/\lambda_s^4$ and with temperature as $1 + N_\Omega$ which was discussed in Section 2.2.1. Thus the Raman gain coefficient is temperature independent and varies with wavelength as $1/\lambda_s$.

2.4. Noise in Fiber Raman Amplifiers

2.4.1. Fundamental 3 dB Noise Limit of a Raman Amplifier

An optical preamplifier increases the signal power so that receiver noise becomes negligible and the dominant noise is that contributed by the amplifier. The resultant signal-to-noise ratio (SNR) is within a few dB of the SNR of an ideal Shott noise limited amplifier [20]. For a discrete ideal optical amplifier the difference between the amplified SNR and the ideal Shott noise limit is 3 dB. For a distributed Raman amplifier the noise factor can even be negative.

The noise in a fiber Raman amplifier is the amplified spontaneous scattering. Although Smith's treatment of Raman gain was designed to calculate a critical power for stimulated Raman scattering it has proved useful for most treatments of Raman amplifier noise [21]. Within the Smith treatment one can find the 3 dB noise limit of the ideal Raman amplifier, the disappearance of the 3 dB excess noise as the amplifier gain goes to zero, and a noise factor greater than 3 dB at elevated temperatures. Rewriting Eq. (2.11), the sum of the amplified signal and noise powers from the Raman amplifier, we obtain:

$$\begin{aligned} P_S(L) &= P_{OPT} = P_S + P_N \\ &= [P_S(0) + P_N(0)]e^{G_S P_P L / A_{eff}}, \end{aligned} \quad (2.25)$$

where P_S and P_N are the signal and noise powers out of the amplifier. $P_S(0)$ is the signal into the amplifier, $P_N(0)$ is a fictitious input power into an ideal noise-free amplifier, and P_P is the pump power.

The 3 dB noise figure of an ideal optical amplifier refers to a decrease by a factor of two in the ratio of electrical signal and noise powers after detection of the amplified optical signal by a noise-free detector [20]. The detected current I is proportional to the total optical power P_{OPT} ,

$$I = R P_{OPT} \propto (E_S + E_N)^2, \quad (2.26)$$

where E_S and E_N are the signal and noise electric fields and R is the detector responsivity. The detected current will contain a signal current $\sim E_S^2$ and two noise terms $\sim 2E_S E_N$ and E_N^2 . The noise terms are called the signal-spontaneous beat noise and the spontaneous-spontaneous beat noise. Usually the signal power is large enough that the signal-spontaneous term is dominant. The spontaneous-spontaneous beat noise is also reduced with an optical filter ahead of the detector.

The electrical signal power is $I_S^2 R_L$ into a load resistor R_L . The noise power is $\langle (I - I_S)^2 \rangle R_L$ and $\langle \rangle$ indicates an average over time. The signal-to-noise ratio is:

$$SNR = \frac{I_S^2}{\langle (I - I_S)^2 \rangle} = \frac{P_S^2}{4P_S P_N}. \quad (2.27)$$

Both the numerator and denominator of (2.27) contain the amplification factor $\exp(2G_S P_P L / A_{eff})$. The expression for the SNR then contains the signal power $P_S(0)$ input to the amplifier and the effective input noise from Eq. (2.11). In the ideal limit where $N_S = 1.0$ the SNR becomes

$$SNR = \frac{P_S(0)}{4h\nu_S \Delta\nu_B}, \quad (2.28)$$

where $\Delta\nu_B$ is the bandwidth of an electrical filter following the detector. This SNR is compared to the SNR of an ideal shot noise limited detector,

$$SNR(\text{shot limit}) = \frac{P_S(0)}{2h\nu_S \Delta\nu_B}. \quad (2.29)$$

The factor of two difference between Eqs. (2.28) and (2.29) is the 3 dB excess noise of the ideal discrete Raman amplifier.

The 3 dB excess noise disappears when the amplifier gain goes to zero as would happen when the pump is turned off. This can be seen from the term in brackets of Eq. (2.7). When the pump power vanishes there is no spontaneous Raman power and no gain.

2.4.2. Noise Figure of a Raman Amplifier

Raman amplifiers are often said to have a negative noise figure. This can happen because of the way noise figure is defined when the transmission fiber is used as the Raman amplifier; a discrete Raman amplifier will have a positive noise figure, which is greater than 3 dB.

A discrete fiber Raman amplifier at the output end of a fiber transmission system is illustrated schematically in Fig. 2.7(a). The noise figure in dB can be defined as minus the log of the ratio of the SNR after the amplifier to the SNR that would be obtained using a fictitious ideal shot noise limited detector.

$$NF = -10 \log \frac{SNR(\text{amp})}{SNR(\text{shot limit})}. \quad (2.30)$$

Using (2.28) and (2.29) the noise figure is $10 \log(2)$ or 3 dB. The excess noise of the discrete Raman amplifier will actually be greater than 3 dB because of the thermal excitation of the vibrational modes. This is the factor N_Ω that was included in

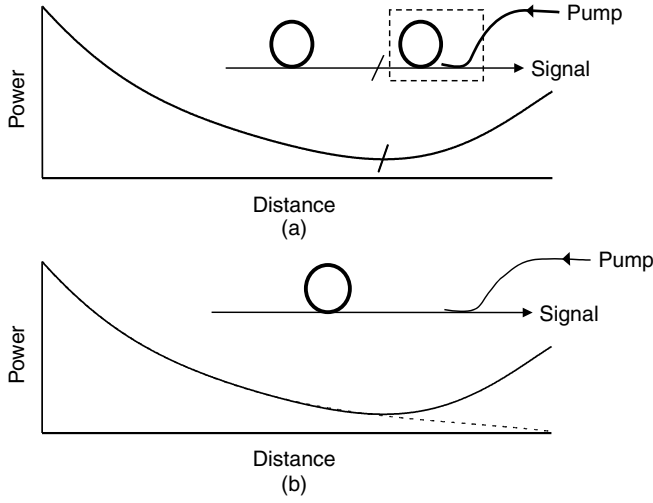


Fig. 2.7. (a) Signal power along the fiber for a discrete fiber Raman amplifier placed at the end of a transmission fiber; (b) signal power along the fiber in which the transmission fiber is a backwards-pumped Raman amplifier.

Eq. (2.20b) but omitted for simplicity in (2.11). Inclusion of the population factor N_Ω (see Eq. (2.2)) modifies the noise factor.

$$NF = 10 \log[2(1 + N_\Omega)]. \quad (2.31)$$

This is a small effect near the Raman gain peak at 13.2 THz. Here N_Ω is 0.138 and the excess noise becomes 3.6 dB. The effect is much larger at smaller frequency shifts. For example, at 3 THz, $N_\Omega = 1.62$ and the excess noise becomes 7.2 dB instead of the ideal 3 dB.

When the transmission fiber is used as a backwards-pumped Raman amplifier the signal will reach a minimum and then rise again because of the amplification as pictured in Fig. 2.7(b). By comparison with the discrete Raman amplifier we identify the signal minimum as the input to the Raman amplifier. The SNR in the limit where $N_\Omega = 0$ is given by Eq (2.28) except the signal power becomes the power at the signal minimum $P_S(-L_A)$.

$$SNR = \frac{P_S(-L_A)}{4h\nu_S\Delta\nu_B}, \quad (2.32)$$

where L_A is the distance from the minimum to the output end. The noise figure for this configuration is obtained from the ratio of (2.32) to the SNR of the detected output signal without amplification using an ideal shot noise limited detector.

$$NF = 10 \log \frac{2P_S(L)}{P_S(-L_A)} = 10 \log(2e^{-\alpha_S L_A}), \quad (2.33)$$

where $P_S(L)$ is the signal output power in the absence of amplification and $P_S(L)$ and $P_S(-L_A)$ are related by the loss at the signal wavelength α_S . The distance from

the output end to the signal minimum is easily found because at this point the gain from Raman amplification equals the fiber loss at the signal wavelength.

$$\alpha_S = G_S \frac{P_P(L)}{A_{eff}} e^{-\alpha_S L_A}, \quad (2.34)$$

where g_S is the Raman gain coefficient, $P_P(L)$ is the pump power introduced at the signal output end, and the losses at the pump and signal wavelengths are assumed to be the same. The noise figure becomes

$$NF = 10 \log \left(\frac{2\alpha_S}{G_S P_P(L)/A_{eff}} \right) = 3.0 - 10 \log \left(\frac{G_S P_P(L)}{\alpha_S A_{eff}} \right). \quad (2.35)$$

This noise figure will be negative for typical Raman gains. For example, a fiber with a loss of 0.22 dB/km at a signal wavelength of 1550 nm and an effective area of $50 \mu\text{m}^2$ is pumped with 500 mW at 1450 nm. The gain coefficient will be approximately 4×10^{-14} m/W so the noise figure from (2.35) becomes -6 dB. Note that the loss in (2.35) is in units of km^{-1} , not dB/km. For this example, the signal minimum will be 40.7 km from the output end of the transmission fiber.

If the loss at the pump and signal wavelengths differ Eq. (2.35) becomes

$$NF = 10 \log[2(1 + N_\Omega)] - \frac{\alpha_S}{\alpha_P} 10 \log \left(\frac{G_S P_P(L)}{\alpha_S A_{eff}} \right). \quad (2.36)$$

In Eq. (2.36) the thermal occupation number N_Ω has also been included. If the pump loss is 0.3 dB/km the noise figure from (2.36) becomes -3 dB. The distance L_A becomes 30.0 km.

The above derivation for the noise figure applies only in the limit where the Raman gain is significantly larger than the fiber loss at the output end. In the limit of large gain, the result of (2.35) does agree with a more complete analysis based on the Smith model for counterpropagating waves [22].

2.4.3. Two-Component Model of Spontaneous Raman Scattering

Spontaneous Raman scattering can be thought of as arising from two sources. The first is the modulation of input light by vibrational modes as described by the Placzek model. The second is Raman amplification of zero-point fluctuations of the electromagnetic field of the vacuum, which provides an effective input field. Inclusion of electromagnetic zero-point fluctuations is known as stochastic electrodynamics [23].

The modulation and amplification contributions to the Stokes scattered power are equal at a temperature of 0K. This two-component model explains the asymmetry between Stokes and anti-Stokes scattering because the upper modulation sideband at $T = 0\text{K}$ is canceled by anti-Stokes absorption as pictured in Fig. 2.8 [24]. Thermal excitation of the vibrational modes produces anti-Stokes scattering and increases the Stokes scattered intensity but the asymmetry remains.

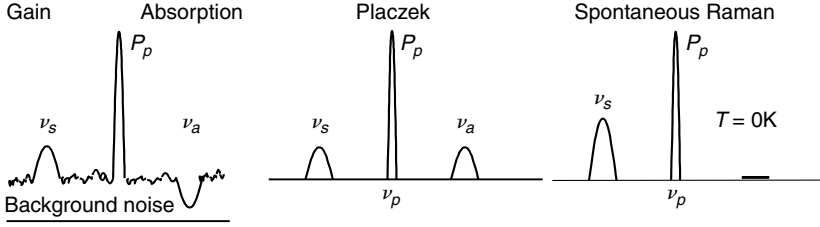


Fig. 2.8. Addition of Raman Stokes gain and “Placzek” Stokes sideband and cancellation of anti-Stokes absorption and anti-Stokes sideband at $T = 0\text{K}$ (From [24]).

The noise power in a fiber Raman amplifier is modeled by adding the spontaneous scattering along the fiber and converting the result to an effective input power amplified by a noise-free amplifier. This effective input power is $h\nu$ per unit frequency interval. In the two-component model half of this effective input power at $T = 0\text{K}$ comes from the zero-point background and half from zero-point fluctuations of the Raman-active medium. In most treatments of spontaneous Raman scattering, amplified zero-point fluctuations are combined with modulation by vibrational modes so all the scattering appears to come directly from the medium.

2.5. Time Domain Picture of Raman Gain

2.5.1. Phenomenological Model

Raman gain is often treated by transforming the wave equation to the frequency domain and introducing a complex frequency-dependent third-order susceptibility $\chi'_3 + i\chi''_3$ [25].

$$\mathcal{P}(\nu_1) = \frac{4\pi}{c^2} (\chi'_3 + i\chi''_3) E_2^2 E_1. \quad (2.37)$$

The imaginary part, χ''_3 is proportional to the Raman gain coefficient and the real part, χ'_3 produces an intensity-dependent phase shift so that χ'_3 is proportional to an intensity-dependent contribution to the refractive index.

$$\frac{dE_1}{dz} = i \frac{\nu_1}{c} \chi'_3 |E_2|^2 E_1 + \frac{\nu_1}{c} \chi''_3 |E_2|^2 E_1. \quad (2.38)$$

The primary contribution to the nonlinear index comes from electronic process but the Raman interaction also contributes about 20% of the nonlinear index.

In the time domain, a high-intensity optical pulse perturbs the electronic structure of a molecule or of a transparent solid and results in an intensity-dependent change in the polarizability. This is the electronic contribution to the nonlinear refractive index which occurs on a time scale shorter than the shortest optical pulses and can be considered to be instantaneous. However, the optically induced perturbation of the

electronic structure also perturbs the field seen by the nuclei. The nuclei then move, which produces a change in the polarizability as discussed in the Placzek model of Section 2.3. The nuclear contribution to the change in polarizability has a time delay related to the oscillation frequency of the vibrational mode. It is this time delay that leads to both a real and an imaginary contribution to the nonlinear index.

2.5.2. Raman Response Function

The Raman contribution to the nonlinear index is described by a convolution of the intensity of an optical pulse with a response function $f(t - t')$ [26].

$$N_2|u(t)|^2 = N_{2\infty}|u(t)|^2 + N_{2R} \int_{-\infty}^t dt' |u(t')|^2 f(t - t'), \quad (2.39)$$

where $|u(t)|^2$ is the intensity of the pulse and $N_{2\infty}$ and N_{2R} are the electronic and Raman contributions to the nonlinear index.

The Raman response function for a silica-core fiber is shown in Fig. 2.9. The response function is basically a decaying sinusoidal oscillation. The oscillation period corresponds to the frequency of the peak of the Raman gain spectrum and the decay rate corresponds to the width of the gain spectrum. The response function is made up of the contributions of many localized modes.

Equation (2.39) shows that the effective nonlinearity will change with optical pulsewidth. Pulses much shorter than the vibrational period see only the electronic

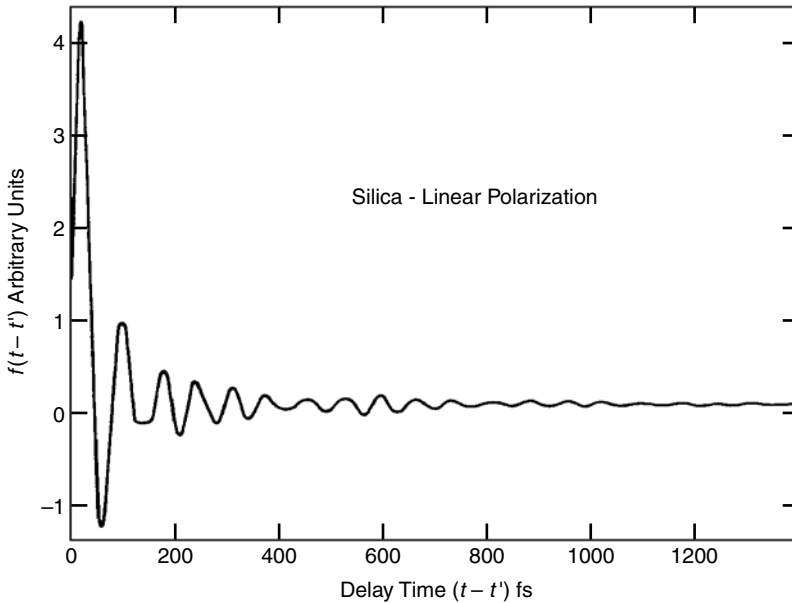


Fig. 2.9. Raman response function of fused silica. This was calculated using only the parallel gain.

nonlinearity. Pulses long on the scale of the response function see the sum of the electronic and Raman contributions to the nonlinear index. For pulses longer than about 100 fs N_2 becomes $N_{2\infty} + N_{2R}$ [27].

The Fourier transform of the Raman response function is a complex susceptibility $N_2(\Omega)$ which is proportional to χ_3 .

$$N_2(\Omega) = N'_2 + iN''_2 = N_{2R} \int_0^\infty f(t-t') \exp[i2\pi\Omega(t-t')] d(t-t'). \quad (2.40)$$

An optical wave made up of a strong ν_2 and a weak ν_1 , where $\nu_2 - \nu_1$ falls within the Raman gain bandwidth, will produce a strong imaginary N_2 . The imaginary part of N_2 is just the Raman gain coefficient for the signal at ν_1 .

2.6. Raman Gain Coefficients

2.6.1. Raman Gain Spectrum

Raman gain measurements in both silica-core and Ge-doped fibers look very much like the fused silica Raman gain spectrum shown in Fig. 2.10. This gain spectrum is a composite of measurements by several different authors of spontaneous Raman scattering in bulk silica samples and silica-core fibers [28]. The two curves are for scattering of light polarized parallel and perpendicular to the polarization of the exciting light. The spontaneous spectrum differs from the gain spectrum by the Bose–Einstein population factor $N_\Omega + 1$ as discussed earlier.

An absolute value of the gain coefficient of silica can be obtained from an early measurement using a pump at 526 nm. A peak gain of 1.86×10^{-11} cm/W was obtained in a fiber short enough to maintain linear polarization; the results agreed with bulk spontaneous scattering measurements in fused silica [12]. Using a linear dependence of the gain coefficient leads to a convenient gain coefficient of approximately

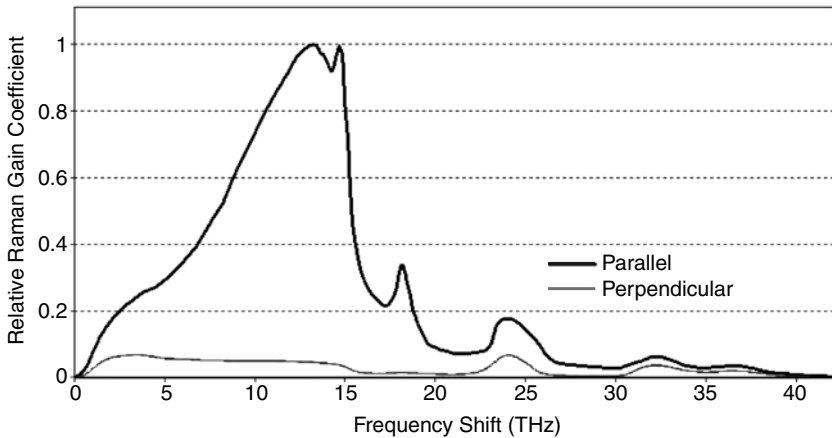


Fig. 2.10. Parallel and perpendicular Raman gain coefficients of fused silica as compiled from several measurements of Raman gain and spontaneous Raman scattering.

1.0×10^{-11} cm/W for a Stokes wavelength of 1.0 micron. It is convenient to approximate the Stokes frequency with the pump frequency but this will exaggerate the gain coefficient by a few percent.

From Eq. (2.24) the Raman gain coefficient is expected to increase linearly with Stokes frequency. The frequency dependence of the gain might be slightly greater than linear because the polarizability of the ions in the glass increases slightly with frequency. This increase in polarizability leads to the frequency dependence of both the linear and nonlinear refractive indices. So far, there is no strong evidence for a frequency dependence greater than linear. However, an argument for an additional factor in the frequency dependence of the gain is included as Appendix A2.5.

2.6.2. Germanium Doping

Germanium doping raises the Raman gain coefficient. The effect is small in standard fibers, which contain about 4 mole % GeO_2 but can raise the gain by about 50% in dispersion-shifted fibers. The gain is more than doubled in dispersion-compensating fibers. A careful series of measurements has been reported for spontaneous Raman scattering versus GeO_2 concentration in a Ge-doped MCVD preform [29]. The maximum increase is at a shift of 430 cm^{-1} where 20 mole % GeO_2 raises the gain by a factor of 2.6 over pure silica glass. For shifts less than 200 cm^{-1} the increase is approximately a factor of 2.

In a fiber the mode field penetrates into the cladding so the effective Raman gain coefficient will be some average over the doping profile, which will be less than the increase in gain from the maximum at the core center. The proper way to include the increase in Raman gain from Ge-doping is to include it in the calculation of the overlap integral. The separation of the gain coefficient and the effective area can be maintained by defining an effective gain coefficient:

$$g_{eff} = \frac{\int \psi_1^2 g(r) \psi_2^2 r dr d\theta}{\int \psi_1^2 \psi_2^2 r dr d\theta}. \quad (2.41)$$

2.6.3. Polarization Dependence of Raman Gain

Raman gain is a maximum if both pump and signal wave have the same polarization state. Over the range of 3 to 15 THz the gain is almost zero for orthogonal polarization states. This applies to orthogonal elliptical polarizations as well as for linear polarizations. In ordinary fibers, the state of polarization varies along the fiber. For some initial distance, both pump and signal waves experience the same variation in polarization state but eventually, because their wavelengths differ, the relative polarization states will be completely random. Thus for short fibers, Raman gain is the same as for parallel linear polarizations and for long fibers the average gain falls to half the maximum gain. The distance over which the gain decreases is not where linear polarization is lost, but rather the distance in which pump and signal polarizations get out of step. This polarization length L_P depends inversely on frequency separation and on fiber birefringence [30].

$$L_P = \frac{1}{\delta n(\nu_0 - \nu_S)}. \quad (2.42)$$

This polarization length may be particularly important in low PMD fibers. For example, the polarization length will be 2 km in a low PMD fiber with effective birefringence of 10^{-8} for a wavelength difference between pump and signal of 100 nm in the 1500 nm wavelength range. At 10 nm pump–signal separation the polarization length is 20 km, which is the nonlinear effective length for typical fibers in this wavelength range. This means that for Raman interaction between dense WDM channels the gain should often be the polarized gain.

For frequency shifts 0 to 3 THz bulk Raman studies show that the gain is depolarized with the perpendicular gain about one third of the parallel gain. This low frequency regime is of concern for Raman interactions of channels in dense WDM systems. The details of Raman gain in this regime are not well understood although a reasonable approximation is to add the parallel and perpendicular gains and divide by two for random polarization states. Note that a measurement of perpendicular and parallel Raman gains in a silica-core polarization-maintaining fiber found a ratio of perpendicular to parallel gains of 45%. The discrepancy between bulk and fiber measurements is not understood [31].

2.6.4. The Search for Other Raman Glasses

There has been investigation of glasses with higher intrinsic Raman gain [32]. Heavy metal oxide glasses have Raman gain coefficients more than 30 times that of silica. It appears, however, that the loss in these glasses will increase faster than the gain [33]. A potential candidate for a high-Raman gain fiber would use a pure GeO_2 core to achieve a gain coefficient about 9 times that of silica [29, 33]. Raman gain has also been seen in liquid-filled hollow-core fibers. The very first observation of a fiber nonlinearity was in a CS_2 -filled fiber Raman laser [34].

Certain dopants incorporated into silica produce large Stokes frequency shifts in fiber Raman lasers. Phosphorus doping leads to a line at 1330 cm^{-1} [35] and H_2 or D_2 in the glass produces lines with extremely large shifts of 4139 and 2975 cm^{-1} [36].

Appendix A2.1. Derivation of Raman Gain

The derivation for Raman gain starts with the wave equation in the plane wave approximation. For simplicity we choose a medium with N independent molecules per unit volume. Because of the Raman interaction there is a contribution to the macroscopic polarization \mathcal{P} that is the sum of the induced dipole moments of the molecules \mathbf{p} .

$$\begin{aligned}\nabla^2 E &= \frac{1}{c^2} \frac{d^2 D}{dt^2} \\ D &= \epsilon E = \epsilon_0 E + 4\pi N p \\ p &= (\partial\beta/\partial Q) Q E,\end{aligned}\tag{A2.1}$$

where $\partial\beta/\partial Q$ is the change in molecular polarizability with mode amplitude Q . Q will depend on the amplitude of optical fields E_1 and E_2 .

The wave equation becomes

$$\frac{d^2 E}{dz^2} - \varepsilon_0 \frac{d^2 E}{dt^2} = \frac{4\pi N}{c^2} (\partial\beta/\partial Q) \frac{d^2(QE)}{dt^2}. \quad (\text{A2.2})$$

The field E contains two waves E_1 and E_2 propagating in the z direction with frequencies ν_1 and ν_2 with $\nu_2 > \nu_1$.

$$\begin{aligned} E_1 &= E_1^+ e^{i(2\pi\nu_1 t - \kappa_1 z)} + E_1^- e^{-i(2\pi\nu_1 t - \kappa_1 z)} \\ E_2 &= E_2^+ e^{i(2\pi\nu_2 t - \kappa_2 z)} + E_2^- e^{-i(2\pi\nu_2 t - \kappa_2 z)}. \end{aligned} \quad (\text{A2.3})$$

The amplitude of the molecular vibration is:

$$Q = Q^+ e^{i2\pi\Omega t} + Q^- e^{-i2\pi\Omega t}. \quad (\text{A2.4})$$

If we concentrate on the term E_1^+ , matching frequencies requires that

$$2i\kappa_1 \frac{dE_1^+}{dz} e^{-i\kappa_1 z} = \frac{4\pi N}{c^2} (\partial\beta/\partial Q) (2\pi\nu_1)^2 Q^- E_2^+ e^{-i\kappa_2 z}. \quad (\text{A2.5})$$

In (A2.5) $\partial^2 E/\partial t^2$ is neglected.

The amplitude Q is driven by mixing E_1 and E_2 . To obtain Q^- as a function of E_1 and E_2 we follow the approach presented by Shen and Bloembergen in an early treatment of stimulated Raman scattering [37]. A single molecule has kinetic energy $T = (\partial Q/\partial t)^2/2$, potential energy $V = 4\pi^2\Omega^2/2$, and an interaction energy $U = \mathbf{p} \cdot \mathbf{E}$. From Eq. (A2.1) $U = (\partial\beta/\partial Q)QE^2$. The Lagrangian L becomes

$$L = T - V + U = \frac{1}{2} \left(\frac{\partial Q}{\partial t} \right)^2 - 2\pi^2\Omega^2 Q^2 + (\partial\beta/\partial Q)QE^2. \quad (\text{A2.6})$$

The addition of a damping term $\Gamma\partial Q/\partial t$ leads to an equation of motion for a driven damped harmonic oscillator.

$$\frac{\partial^2 Q}{\partial t^2} + \Gamma \frac{\partial Q}{\partial t} + (2\pi\Omega_0)^2 Q = (\partial\beta/\partial Q)E^2. \quad (\text{A2.7})$$

The term needed in (A2.5) is Q^- which, at the peak of the response ($\Omega = \Omega_0$) is:

$$Q^- = \frac{i(\partial\beta/\partial Q)E_2^- E_1^+}{2\pi\Gamma\Omega_0} e^{i(\kappa_2 z - \kappa_1 z)}. \quad (\text{A2.8})$$

From Eq. (A2.5) the amplification of E_1^+ from N molecules per unit volume is given by:

$$\begin{aligned} \frac{dE_1^+}{dz} &= \frac{2\pi N(\partial\beta/\partial Q)^2 \nu_1}{n_1 c \Gamma \Omega_0} E_2^+ E_2^- E_1^+ \\ &= g_1 E_2^+ E_2^- E_1^+, \end{aligned} \quad (\text{A2.9})$$

where the gain coefficient g_1 is seen to be proportional to the frequency ν_1 and $(\partial\beta/\partial Q)^2$. In cgs units $E_2^+ E_2^-$ is related to the optical intensity of ν_2 by

$$\text{INTENSITY}(\nu_2) = \frac{n_2 c}{4\pi} E_2^+ E_2^-. \quad (\text{A2.10})$$

Appendix A2.2. The Effective Area

In a fiber the field amplitudes E_1 and E_2 are functions of radial distance as well as z . Instead of dealing directly with this radial variation of electric field it is more convenient to set up the gain in terms of optical powers and an effective area. The radial variation of the electric field in a fiber is given by the fiber mode amplitude. An essential feature of fiber nonlinear optics is that the nonlinear term is so small that the waveguide modes do not change with optical intensity.

$$\begin{aligned} E_1 &= a_1(z)\psi_1(r, \theta) \\ E_2 &= a_2(z)\psi_2(r, \theta). \end{aligned} \quad (\text{A2.11})$$

Equation (A2.9) becomes

$$\frac{da_1^+}{dz}\psi_1 = g|a_2^+a_2^-|\psi_2^2a_1^+\psi_1. \quad (\text{A2.12})$$

To get the equation in terms of optical powers it is useful to define a new field amplitude F that is the square root of the power.

$$\begin{aligned} |F|^2 &\equiv P = \frac{nc}{8\pi}|a|^2\{\psi^2\} \\ \{\psi^2\} &= \int_0^\infty \int_0^{2\pi} \psi^2(r, \theta)rdrd\theta. \end{aligned} \quad (\text{A2.13})$$

Both sides of Eq. (A2.12) are multiplied by ψ_1 and integrated over r and θ . After substitution of P_2 for $|a_2|^2$ using (A2.13) the gain equation becomes

$$\frac{dF_1^+}{dz}\{\psi_1^2\} = \frac{4\pi}{nc}gP_2\{\psi_2^2\psi_1^2\}F_1^+, \quad (\text{A2.14})$$

which can be rewritten in terms of P_2 , G , A_{eff} .

$$\begin{aligned} \frac{dP_1}{dz} &= \frac{4\pi g_1}{nc} \frac{P_2}{A_{eff}} P_1 = G_1 \frac{P_2}{A_{eff}} P_1 \\ A_{eff} &= \frac{\{\psi_1^2\}\{\psi_2^2\}}{\{\psi_1^2\psi_2^2\}}. \end{aligned} \quad (\text{A2.15})$$

An accurate value of A_{eff} requires mode fields at both ν_1 and ν_2 although using the mode field at some intermediate wavelengths is often sufficient. Here ψ_1 and ψ_2 have been assumed to be the fundamental LP_{01} mode although the effective area applies to any pair of fiber modes.

Appendix A2.3. The Effective Length

Loss has not been included in the various equations for Raman amplification in order to bring out some of the essential features. Obviously loss is important in fiber Raman amplifiers and that loss can be different at the pump and signal wavelength. The loss at the pump wavelength is included by replacing the actual fiber length with an effective length as shown in Eq. (2.13).

The differential increase in signal power at some distance z along the fiber will be:

$$dP_S(z) = P_S(z)G_S P_P dz - \alpha_S P_S(z)dz. \quad (\text{A2.16})$$

In (A2.16) we have used only the gain part of Eq. (2.20) and subtracted the differential loss at the signal frequency. The pump power decreases along the fiber because of scattering and absorption loss. In the limit of a strong pump and a weak signal, the fraction of pump power converted to signal is negligible so $P_P(z) = P_P(0) \exp(-\alpha_P z)$, where $P_P(0)$ is the pump power at the fiber input.

$$\frac{dP_S}{P_S} = \left[G_S \frac{P_P(0)e^{-\alpha_P z}}{A_{eff}} - \alpha_S P_S \right] dz. \quad (\text{A2.17})$$

Integrating from 0 to L gives:

$$\ln[P_S(L)/P_S(0)] = \frac{G_S P_P(0)}{A_{eff}} \left[\frac{1 - e^{-\alpha_P L}}{\alpha_P} \right] - \alpha_S L, \quad (\text{A2.18})$$

so that the general expression for the signal output power with loss at the pump and signal is:

$$P_S(L) = P_S(0)e^{G_S P_P(0)/A_{eff} L_{eff} e^{-\alpha_S L}}. \quad (\text{A2.19})$$

If pump and signal are of comparable magnitude it is necessary to use the coupled equations (2.16).

Appendix A2.4. Stimulated Raman Threshold Power

A threshold or critical power can be obtained by using Eq. (2.7) which gives the number of photons in a given Stokes mode [10]. The term in the brackets approaches 1.0 for the large gains required to observe stimulated Raman scattering. The power of one photon per mode per unit frequency is $h\nu$ where ν is the frequency in Hz. The total Stokes power after length L is then the integral over the entire Raman gain curve.

$$P_S(L) = \int_0^\infty h\nu_S d\nu e^{G(v_P - \nu_S)P_P L_{eff}/A_{eff}}. \quad (\text{A2.20})$$

The Raman gain curve is approximated with a Lorentzian function where ν_0 is the frequency of the gain peak γ_0 , and $\Delta\nu$ is the full width half maximum of the gain curve. The exponent will turn out to be large so frequencies near ν_0 make the dominant contribution to the integral and two terms of a series expansion of the Lorentzian function will be sufficient.

$$G(v_P - \nu_S) = \frac{\gamma_0}{1 + \left(\frac{\nu - \nu_0}{\Delta\nu/2} \right)^2} \approx \gamma_0 \left[1 - \left(\frac{\nu - \nu_0}{\Delta\nu/2} \right)^2 + \dots \right]. \quad (\text{A2.21})$$

With these approximations, the Stokes output power becomes

$$P(L) = \frac{\sqrt{\pi}}{2} \frac{\Delta\nu}{\sqrt{G}} e^G$$

$$G = \gamma_0 P_P(0) \frac{L_{eff}}{A_{eff}}. \quad (\text{A2.22})$$

A threshold or critical power is defined as the power for which the Stokes power has grown to equal the pump power. One has to imagine that more pump power is supplied along the fiber to make up for the depletion from Raman conversion. With this definition, the critical power becomes:

$$G_c^{3/2} e^{-G_c} = \frac{\sqrt{\pi}}{2} h\nu_S \gamma_0 \Delta\nu L_{eff} / A_{eff}. \quad (\text{A2.23})$$

G_c varies only slowly with fiber parameters and typically falls in the range 15 to 17. It has been shown that this threshold condition also applies when pump depletion is included except that the Stokes power equals the actual pump power rather than the input power [38].

Appendix A2.5. Additional Wavelength Dependence of Raman Gain

The dominant factor in the wavelength dependence of Raman gain is the linear frequency term in Eq. (2.18). There could also be a small decrease in gain with wavelength because of the frequency dependence of the polarizability β . β increases with frequency because of the electronic transitions in the ultraviolet and is the source of the increase in refractive index with optical frequency. There is also a small increase in nonlinear index with frequency [39].

A rough estimate of the magnitude of this contribution to the wavelength dependence of the Raman gain coefficient can be made by making the assumption that $\partial\beta/\partial Q$ increases linearly with β . The gain coefficient is proportional to $(\partial\beta/\partial Q)^2$ so a linear relationship between $(\partial\beta/\partial Q)$ and β would result in a relation between $(\partial\beta/\partial Q)$ and the refractive index n [40].

$$\varepsilon = n^2 + 1 + 4\pi\mathcal{P} = 1 + 4\pi N\beta$$

$$\frac{\partial\beta}{\partial Q} \sim \beta = \frac{n^2 - 1}{4\pi N}, \quad (\text{A2.24})$$

where ε is the dielectric constant far from electronic transitions, \mathcal{P} is the macroscopic polarizability, and N is the number of molecules. The Raman gain g then would be expected to vary with refractive index n as

$$G \propto \frac{(\partial\beta/\partial Q)^2}{n^2} \propto \frac{(n^2 - 1)^2}{n^2}. \quad (\text{A2.25})$$

This is not a large effect. If we calculate n using standard Sellmeier coefficients [20], it amounts to about 4% between 500 and 1000 nm and 2% between 1000 and 1500 nm. Including this factor will further reduce the gain coefficient from a linear extrapolation of the 526 nm measurement. In Eq. (A2.25) the factor of n^2 from Eq. (2.24) was included and the difference between n_S and n_P was neglected.

References

- [1] C.V. Raman and K.S. Krishnan, "A new type of secondary radiation," *Nature* 121:501–502, 1928; The optical analogue of the Compton effect, 121:711, 1928.
- [2] G.S. Landsberg and L.I. Mandelstam, Eine neue erscheinung bei der lichtzerstreuung in krystallen, *Naturwissenschaften*, 16:557–558, 1928.
- [3] I.L. Fabelinski, Seventy years of combination (Raman) scattering, *Physics-Uspekhi*, 41:1229–1247, 1998.
- [4] A. Smekel, Zur quantentheorie der dispersion, *Naturwissenschaften* 11:873–875, 1923.
- [5] B.P. Stoicheff, Raman effect. in *Methods of Experimental Physics*, vol. 3, ed. D. Williams, New York: Academic, Ch. 2.3, 111–155, 1962.
- [6] J.R. Ferraro and K. Nakamoto, *Introductory Raman Spectroscopy*, San Diego: Academic, 1994.
- [7] E.J. Woodbury and W.K. Ng, Ruby laser operation in the near IR, *Proc IRE*, 50:2367, 1962.
- [8] R.W. Hellwarth, Theory of stimulated Raman scattering, *Phys. Rev.*, 130:1850–1852, 1963.
- [9] R.W. Terhune, Nonlinear optics. *Solid State Des.*, 4:11, (Nov.) 38–46, 1963.
- [10] R.G. Smith, Optical power handling capacity of low loss optical fibers as determined by stimulated Raman and Brillouin scattering, *Appl. Opt.*, 11:2489–2494, 1972.
- [11] R.H. Stolen, E.P. Ippen, and A.R. Tynes, Raman oscillation in glass optical waveguide, *Appl. Phys. Lett.*, 20:62–64, 1972.
- [12] R.H. Stolen and E.P. Ippen, Raman gain in glass optical waveguides, *Appl. Phys. Lett.*, 22: 276–278, 1973.
- [13] W. Heitler, *The Quantum Theory of Radiation*, 3rd ed., London: Oxford University Press, 192, 1954.
- [14] A. Yariv, *Quantum Electronics*, 3d ed., New York: Wiley, 1989.
- [15] G. Placzek, *Handbuch der Radiologie VI* Leipzig: Akademische Verlagsgesellschaft, Teil II 205, 1934.
- [16] R.J. Bell, N.F. Bird, and P. Dean, Vibrational modes of AB₂ glasses, *J. Phys. C (Proc. Phys. Soc.)*, 1:299, 1968.
- [17] W.J. Jones and B.P. Stoicheff, Inverse Raman spectra: Induced absorption at optical frequencies, *Phys. Rev. Lett.*, 13:657–659, 1964.
- [18] R.H. Stolen, Relation between the effective area of a single-mode fiber and the capture fraction of spontaneous Raman scattering, *J. Opt. Soc. Am. B*, 19:498–501, 2002.
- [19] J. Streckert and F. Wilczewski, Relationship between nonlinear effective core area and backscattering capture fraction for single mode optical fibres, *Electron. Lett.*, 32:760–762, 1996.
- [20] G.P. Agrawal, *Fiber-Optic Communication Systems*, New York: Wiley, 1997.
- [21] K. Mochizuki, N. Edagawa, and Y. Iwamoto, Amplified spontaneous Raman scattering in fiber Raman amplifiers, *J. Lightwave Technol.*, LT-4:1328–1333, 1986; Y. Aoki, Properties of fiber Raman amplifiers and their applicability to digital optical communication systems, *J. Lightwave Technol.*, 6:1225–1239, 1988.

- [22] J. Ranka, Unpublished notes.
- [23] P.W. Milonni, *The Quantum Vacuum, An Introduction to Quantum Electrodynamics*, New York: Academic Press, 1994.
- [24] R.H. Stolen, Inverse Raman scattering and the 3 dB noise limit of a fiber Raman amplifier, *Can. J. Phys.*, 78:391–396, 2000.
- [25] Y.R. Shen, *The Principles of Nonlinear Optics*, New York: Wiley, 1984.
- [26] R.H. Stolen, J.P. Gordon, W.J. Tomlinson, and H.A. Haus, Raman response function of silica-core fibers, *J. Opt. Soc. Am. B*, 6:1159–1166, 1989.
- [27] R.H. Stolen and W.J. Tomlinson, Effect of the Raman part of the nonlinear refractive index on propagation of ultrashort optical pulses in fibers, *J. Opt. Soc. Am. B*, 9:565–573, 1992.
- [28] R.H. Stolen, C. Lee, and R.K. Jain, Development of the stimulated Raman spectrum in single-mode fibers, *J. Opt. Soc. Am. B*, 1:652–657, 1984. The low frequency data include subsequent measurements of scattering at small frequency shift and low temperature. The perpendicular spectrum was compiled from several published sources. Both curves are available as data files from the author.
- [29] S.T. Davey, D.L. Williams, B.J. Ainslie, W.J.M. Rothwell, and B. Wakefield, Optical gain spectrum of GeO₂-SiO₂ Raman fibre amplifiers, *IEE Proc. J*, 136:301–306, 1989.
- [30] R.H. Stolen, Polarization effects in fiber Raman and Brillouin Lasers, *IEEE J. Quantum Electron.*, QE-15:1157, 1979.
- [31] D.J. Dougherty, F.X. Kartner, H.A. Haus, and E.P. Ippen, Measurement of the Raman gain spectrum of optical fibers, *Opt. Lett.*, 20:31–33, 1995.
- [32] A.E. Miller, K. Nassau, B. Lyons, and M.E. Lines, The intensity of Raman scattering in glasses containing heavy metal oxides, *J. Non-Cryst. Solids*, 99:289–307, 1988.
- [33] M.E. Lines, Raman gain estimates for high-gain optical fibers, *J. Appl. Phys.*, 62:4363–4370, 1987.
- [34] E.P. Ippen, Low-power quasi-cw Raman oscillator, *Appl. Phys. Lett.*, 16:303–305, 1970.
- [35] V.I. Karpov, E.M. Dianov, A.S. Kurkov, V.M. Paramonov, V.N. Protopopov, M.P. Bachynski, and W.R.L. Clements, LD-pumped 1.48- μ m laser based on Yb-doped double-clad fiber and phosphorosilicate-fiber Raman converter. In *Proceedings of OFC'99* (San Diego, Feb. 21–26), paper WM3, 1999.
- [36] A.R. Chraplyvy and J. Stone, Single-pass mode-locked or Q-switched pump operation of D₂ gas-in-glass fiber Raman lasers operating at 1.56 μ m wavelength, *Opt. Lett.*, 10:344–346, 1985.
- [37] Y.R. Shen and N. Bloembergen, Theory of stimulated Brillouin and Raman scattering, *Phys. Rev.*, 137A:1787–1805, 1965.
- [38] J. AuYeung and A. Yariv, Spontaneous and stimulated Raman scattering in low loss fibers, *IEEE J. Quantum Electron.*, QE-14:347–352, 1978.
- [39] M. Sheik-Bahae, Dispersion of bound electronic nonlinear refraction in solids, *IEEE J. Quantum Electron.* 27:1296–1309, 1991.
- [40] N.L. Boling, A.J. Glass, and A. Owyong, Empirical relationship for predicting nonlinear refractive index changes in optical solids, *IEEE J. Quantum Electron.*, QE-14:601–608, 1978.

Chapter 3

Time-Division-Multiplexing of Pump Wavelengths

A.R. Grant and L.F. Mollenauer

3.1. Introduction

The potential of stimulated Raman scattering to turn transmission fiber spans into their own, *distributed, low-noise* amplifiers has been recognized and generally understood for several decades [1, 2]. Indeed, before the erbium-doped fiber amplifier became available in the late 1980s, the Raman effect provided just about the only practical form of optical gain for fiber transmission, and was used in the first successful long-haul demonstrations [3]. Nevertheless, for early all-optical transmission systems, which tended to involve just one, or at most a handful, of WDM channels, the lumped erbium-doped fiber amplifier became the technology of choice, largely on the issue of the required pump powers. That is, when the total signal power was at most a few mW, there was little incentive to incur the trouble and expense of the hundreds of mW of pump power required for Raman amplification, when a very simple erbium fiber amplifier, pumped with just a few tens of mW, could provide the necessary narrowband gain. Thus the issue of pump power tended to completely overshadow the nearly contemporaneous understanding that distributed Raman amplification could provide for greatly reduced growth of ASE noise, especially in the context of the long (80 to 100 km) amplifier spans typical for terrestrial systems [4]. With the more recent advent of dense WDM and its demands for flat gain over wide bandwidths and greatly increased net signal power, however, the erbium fiber amplifiers rapidly became very complex, and began to require pump powers little different from those required for Raman gain! The consequent commercial development of high-powered, 1480 nm diode lasers (easily generalized to 14XX nm) tended to remove the principal obstacle to the use of Raman gain. Thus Raman amplification is now being rediscovered, not only for its superior noise performance, but equally for the ease with which it enables the establishment and maintenance of flat gain over the wide bands of dense WDM.

The typical broadband Raman amplifier consists of several high-power, CW, diode pump lasers, either grating stabilized or free running, which are then wavelength-division- and/or polarization-multiplexed together [5, 6]. Isolators are typically located within the nest of WDMs to reduce feedback to the pump lasers. Some provision is also made for depolarizing the pump power in order to reduce polarization-

dependent gain. The combined lasers are then coupled with another WDM into the fiber span, where the signal is then amplified.

There are a few drawbacks to that typical arrangement. In the first place, four-wave-mixing between the pumps can generate significant noise components in the signal wavelength band. Second, and equally important, Raman interaction allows the longer wavelength pumps to extract energy from the shorter wavelength pumps. The resultant reduced penetration of the shorter pump wavelengths can then seriously reduce the effective amplifier length and increase the ASE noise growth for the shorter wavelength signal channels. The energy exchange among the pump wavelengths also tends to seriously skew the required relative laser pump powers, especially at high gain levels.

An alternate approach that avoids these problems is to time-division-multiplex the various pump wavelengths, either by sequentially switching on and off a discrete set of pump lasers, or by electronically sweeping the wavelength of a single laser [7]. Such pump TDM eliminates both the four-wave-mixing and the Raman interaction between the different pump wavelengths in an obvious way. The technique works, however, only with backward Raman pumping (i.e., where the pump and signal are counterpropagating); in that case, the net signal gain is determined only by the time-average values of the pump powers, whenever the spatial period of the pump pulse sequence is much less than the effective amplifier length. Because Raman gain extends about 20 km into most transmission fibers, a pump pulse period of ~ 0.2 km, corresponding to a switching rate of ~ 1 MHz, is more than sufficient to thoroughly average the pump power. Electronic components for switching at these speeds are widely available and inexpensive. For forward pumping (pump and signal copropagating), however, the required averaging could be obtained at much higher (and generally impractical) switching speeds, inasmuch as the only walk-off between pump and signal is then just the very small value due to dispersion.

TDM Raman pumping does tend to introduce a new set of problems, however. First, the higher gain for signal propagating in the backward direction leads to a larger backward spontaneous Raman noise level; Rayleigh scattering of that backward propagating noise can then significantly increase the forward noise level under high gain conditions. Second, double-Rayleigh backscattering of the forward propagating signal, a potential source of noise, also increases due to the higher gain in the backward direction. As shown in later sections, however, at typical gain levels, the increased noise from these two effects tends to be small.

3.2. TDM Raman Pumping Schemes

The most basic implementation of pump TDM, shown in Fig. 3.1, is the above-mentioned sequential pulsing of a series of discrete high-power laser diodes, which we hence refer to as DTDM Raman pumping. Each laser is pulsed for an appropriate relative amount of time to achieve the necessary power distribution, once again, at a repetition rate of only ~ 1 MHz, and the pump wavelengths are combined optically just as described earlier for CW pumping [7, 8]. The total time-averaged pump power summed over all lasers has to be approximately the same for TDM and CW pumping, in order

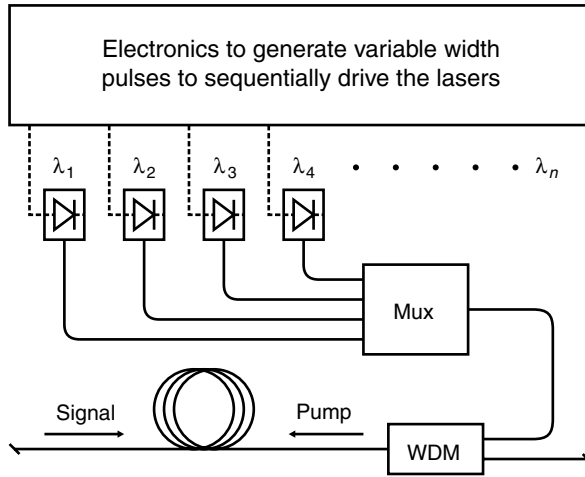


Fig. 3.1. Generalized schematic of a technique for time-division-multiplexing a set of discrete pump lasers.

to achieve the same gain level; note that this is not specific to DTDM Raman pumping but is true of any method of TDM Raman pumping. To achieve broadband gain of 15 dB in a typical transmission fiber span of $55 \mu\text{m}^2$ core area requires about 800 mW into the fiber with CW pumping. Thus the peak power requirement from each laser in a TDM pumping scheme is then also about 800 mW in order to achieve the same (15 dB) of gain. Pump laser modules with this power level are now becoming available.

We have recently performed an experiment using four high-power laser diode modules to demonstrate that useful gain levels can now be achieved with such DTDM. A schematic of the experimental setup is shown in Fig. 3.2 . Each pump module, obtained from Princeton Lightwave Inc., contains two grating-stabilized laser diodes

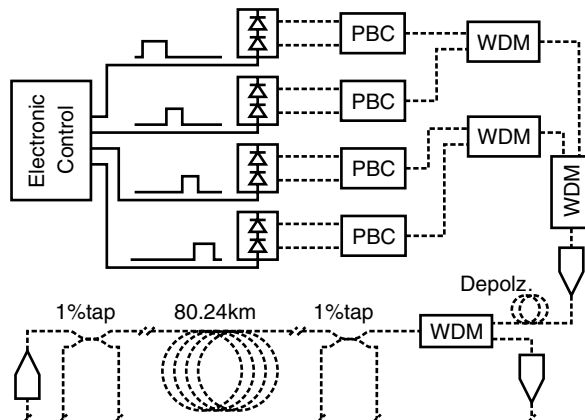


Fig. 3.2. Experimental setup for realizing DTDM Raman pumping.

producing a combined power in excess of 800 mW. The four wavelengths are multiplexed with a combination of polarization beam combiners and WDMs, and an isolator is located after the WDMs to reduce feedback to the laser diodes. A depolarizer made from two pieces of PM fiber, one twice the length of the other and spliced together with optic axes at 45 degrees, is located after the isolator. The two-piece depolarizer is necessary because the WDMs are not polarization maintaining. Isolators are also located at the signal input and output to protect the signal source and reduce backward propagating noise. Taps are used to monitor the pump and signal propagating in both the forward and backward directions. The fiber span is made from two types of nonzero dispersion-shifted fiber, 12.8 km with zero dispersion wavelength $\lambda_0 = 1450$ nm and 67.44 km with $\lambda_0 = 1400$ nm, and the pumps are launched into the fiber piece with $\lambda_0 = 1450$. The dispersion and effective area of both fiber types are 4 ps/nm-km and $55\mu\text{m}^2$, respectively.

The on-off Raman gain over the combined C+L-band is shown in Fig. 3.3; note that an average gain of 13 dB is achieved over a bandwidth of 100 nm. The large gain ripple at short wavelengths results from nonideal wavelengths for the two shortest wavelength pumps.

The time-dependence of the power launched into the fiber from each pump laser is shown in Fig. 3.4. Note that very little ripple is seen in the output power of the lasers. Nevertheless, there is some temporal overlap of wavelengths in adjacent time slots due to a slow electronic drive response time, which is limited mostly by inductance in the wire leads to the pump modules. Keeping the wire leads as short as possible in order to minimize the inductance also helps reduce ringing in the circuit when the laser is switched on and off. Excessive ringing in the drive circuit can reverse-bias the laser diode, causing serious damage to it.

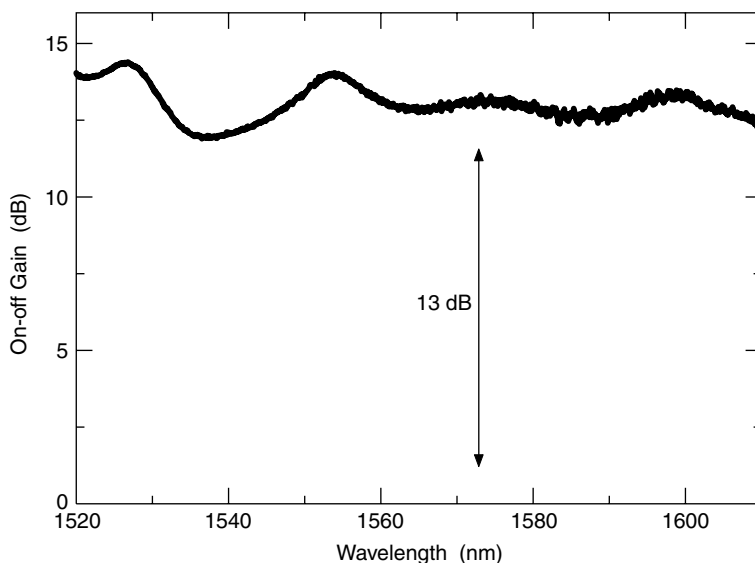


Fig. 3.3. Measured on-off Raman gain of four time-division-multiplexed pump lasers.

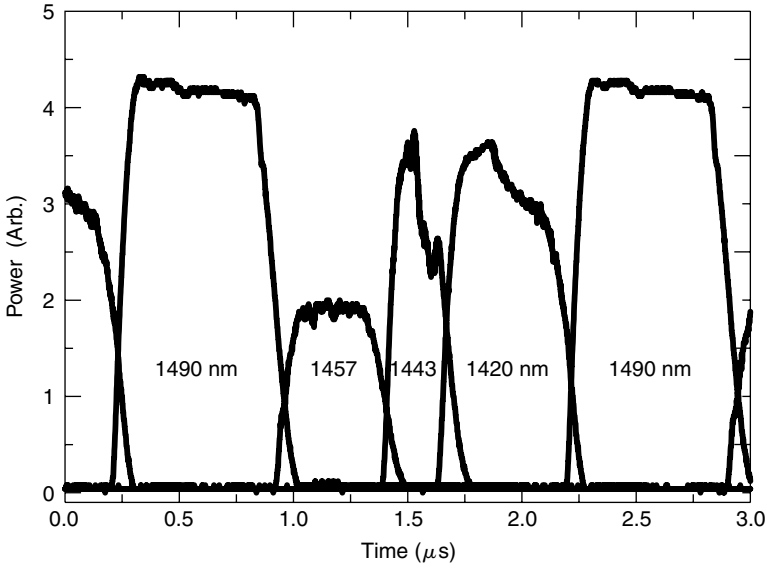


Fig. 3.4. Time-dependence of the power from each pump laser, as measured with a 50 MHz bandwidth detector.

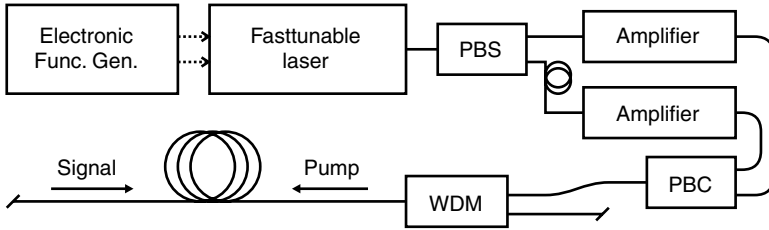


Fig. 3.5. Generalized schematic of TDM Raman pumping using a fast tunable laser followed by a high-power amplifier. The desired pump distribution is obtained by varying the wavelength sweep rate.

A more elegant approach to TDM Raman pumping is shown in Fig. 3.5. This technique [7], which we have named “SMART” Raman pumping, uses a single rapidly and widely tunable source (either a tunable laser alone, or such a laser followed by a broadband high-power amplifier). The tuning speed of the laser wavelength (at many tens of nm/ μ s) is then varied with wavelength in order to obtain the required pump power weighting. As we detail later, the SMART pump allows, at least in principle, for exquisitely precise and dynamically adjustable control of the profile of gain versus wavelength.

As with the DTDM pump, the SMART pump’s output should be depolarized to minimize polarization-dependent gain. This can be achieved by first splitting the

output from the tunable laser between two amplifiers, and then introducing a slight time delay between the outputs from the two amplifiers before recombining them with a polarization beam combiner. Using two amplifiers instead of one also relaxes the power requirement for each amplifier. When only a single pump power amplifier is used with a SMART pump, the output can be effectively depolarized with a length of PM fiber, whose principal axis is spliced at 45 degrees to the initial axis of polarization.

Unfortunately, however, to date the SMART pump remains an essentially hypothetical device, because of the fact that the high-powered source, rapidly tunable over the required wide bandwidth, does not yet exist. On the other hand, the electronics necessary for control of a SMART Raman pump, basically equivalent to an arbitrary waveform generator with a bandwidth greater than 50 MHz, have already been successfully demonstrated in the laboratory, and in reasonably compact form.

One attempt has been made to make a SMART Raman pump using a commercially available fast tunable laser [9, 10]. Unfortunately, however, the bandwidth of the tunable laser was insufficient to make a reasonable test of the gain-flattening potential of such a device. The currently available tunable lasers, designed for use as signal sources, are optimized for extreme wavelength stability, narrow linewidth, and high side-mode suppression. For the SMART pump, however, those characteristics are not particularly important, and could easily be sacrificed in favor of the high bandwidth and facile rapid tuning that it requires.

3.3. Gain Flatness

The first difficulty with any multiwavelength Raman pumping scheme, whether CW, DTDM, or SMART pump, lies in calculating the pump wavelengths and launch powers, or in more generic terms, the launch power distribution, required for a given gain profile. Several groups have presented techniques for calculating the optimum pump wavelengths for a small set of discrete pumps [11–14, 6], and an algorithm has also been created for the continuum limit [15]. In general, any of these techniques will work for both CW and TDM Raman pumping, but a technique that directly calculates the necessary path-average Raman pump power is the most convenient.

The equations describing the Raman interaction between the pumps and signal in fiber are

$$\frac{\partial S(\nu, x)}{\partial x} = [G(\nu, x) - \alpha(\nu)]S(\nu, x) \quad (3.1)$$

$$\frac{\partial F(\nu, x)}{\partial x} = [G(\nu, x) - \alpha(\nu)]F(\nu, x) \quad (3.2)$$

$$\frac{\partial B(\nu, x)}{\partial x} = -[G(\nu, x) - \alpha(\nu)]B(\nu, x), \quad (3.3)$$

where $S(\nu, x)$, $F(\nu, x)$, $B(\nu, x)$ are, respectively, the signal, forward pump, and backward pump powers in both polarization modes, and $\alpha(\nu)$ is the (frequency-dependent) fiber loss coefficient. The noise term, not shown, can be ignored as long as pump

depletion due to the noise is negligible (as is usually the case). Here the pump and signal are in nonoverlapping wavelength bands and have been split into separate equations for simplicity. The function $G(\nu, x)$ represents both gain and depletion due to the Raman interaction and is given by

$$G(\nu, x) = \frac{\nu}{A(\nu)} \int \tilde{R}(\nu - \nu)[S(\nu, x) + B(\nu, x) + F(\nu, x)] d\nu \quad (3.4)$$

with the Raman coefficient \tilde{R} given by

$$\tilde{R}(\Delta > 0) = \frac{R(\Delta)A(\nu_p)}{[\nu_p - \Delta]}, \quad (3.5)$$

where R is the typical Raman coefficient with units /W-km, $\tilde{R}(-\Delta) = -\tilde{R}(\Delta)$, ν_p is the center frequency of the pump, and $A(\nu_p)$ is the fiber effective area at ν_p . An approximation of the fiber effective area has been made where

$$A(\nu) + A(\nu) = A(\nu)[2 + C[\nu - \nu]]. \quad (3.6)$$

The factor C is a constant describing the wavelength-dependence of the effective area. This approximation greatly simplifies the evaluation of $G(\nu, x)$, but it breaks down when the effective area varies by a large amount over the signal and pump bands.

Integrating Eq. (3.1) from 0 to L produces an equation that relates the path-average signal powers to the path-average pump powers.

$$\ln \left[\frac{S(\nu, L)}{S(\nu, 0)} \right] + \alpha(\nu)L = \frac{\nu L}{A(\nu)} \int \tilde{R}(\nu - \nu)[S_{\text{avg}}(\nu) + B_{\text{avg}}(\nu) + F_{\text{avg}}(\nu)] d\nu. \quad (3.7)$$

The net signal gain is given by the first term on the left-hand side of the equation. The net gain is now a function of just the fiber loss α , the fiber length L , and the path-average powers S_{avg} , B_{avg} , F_{avg} . Note that the path-average signal power is a predetermined quantity in a transmission system designed for optimal performance. The most time-consuming part of the calculation, propagation of the variables down the fiber, is now separate from the optimization part.

A further simplification is made by transforming from a continuum of wavelengths to a set of discrete pumps. When needed, a continuum is later approximated with a large set of discrete pumps. Each discrete pump has a center frequency given by ν_i and a path-averaged lineshape given by $\psi(\nu - \nu_i)$. There is no longer any distinction between forward and backward pumps, so instead, these two terms are lumped into a single term called P_{avg} . Incorporating these changes into Eq. (3.7) and defining a new Raman coefficient \bar{R} yields the very useful equation:

$$\frac{A(\nu)}{\nu L} \left[\ln \left[\frac{S(\nu, L)}{S(\nu, 0)} \right] + \alpha L \right] - \int \tilde{R}(\nu - \nu) S_{\text{avg}}(\nu) d\nu = \sum_i P_i \bar{R}(\nu_i - \nu) \quad (3.8)$$

where

$$\bar{R}(\delta) = \int \tilde{R}(\delta) \psi(\delta - \Delta) d\delta. \quad (3.9)$$

The first two terms on the left-hand side of Eq. (3.8) are the net gain and fiber loss. The third term is the gain and depletion due to Raman interactions within the signal band alone. This term can be surprisingly large. Using a typical path-average signal power over the combined C+L-band, a more than 1 dB variation is generated across the signal band from this Raman interaction among the signals.

The final term on the right-hand side of Eq. (3.8) is the on-off Raman gain from the pumps. What remains to be determined are the path-average pump powers and frequencies that minimize the deviation from the desired gain profile. Given a set of pump frequencies, the optimum powers are quickly calculated, because Eq. (3.8) is a linear function of the pump powers [15, 16]. When only a few pumps are to be used, picking the optimum wavelengths is the most difficult part, because the Raman coefficient is a complicated function of wavelength. In the continuum limit, a large number of pumps can be evenly distributed across a band of wavelengths, thus eliminating the need to pick optimum pump wavelengths.

The next step after calculating optimal pump wavelengths and path-average pump powers is to calculate the fiber launch powers. This is done with an iterative loop, where in each loop, the pumps and signals are propagated down the fiber, during which the path-average is calculated. After calculating the path-average for a particular input power, that quantity is compared to the optimum path-average and a new launch power determined. The cycle is repeated until the desired accuracy is achieved. This process can take several hours to accurately integrate the propagation equations and to iterate a sufficient number of times. Nevertheless, for CW pumping, this entire process must be carried out to properly account for the pump-to-pump Raman interaction.

On the other hand, for TDM pumping, the following very good approximation eliminates the need for this lengthy calculation.

$$\frac{P_{\text{avg}}(\nu)}{P_0(\nu)} = \frac{1 - e^{-\alpha_{\text{eff}}(\nu)L}}{\alpha_{\text{eff}}(\nu)L}, \quad (3.10)$$

where P_{avg} is the path average power, P_0 is the launch power, and α_{eff} is an effective fiber loss equal to the actual fiber loss at the pump wavelength plus the average loss due to depletion by the signal.

$$\alpha_{\text{eff}}(\nu) = \alpha(\nu) + \frac{\nu}{A(\nu)} \int \tilde{R}(\nu - \nu') S_{\text{avg}}(\nu') d\nu'. \quad (3.11)$$

The pump depletion needs to be taken into account more carefully through simulation when the depletion is large, although this is not the case for typical values of the gain and signal power.

Using approximate mathematical forms of the Raman coefficient to speed up the calculations does not always capture the important structure necessary for accuracy. Thus all the optimum combinations of pump powers and frequencies reported here were calculated using the experimentally measured values for the Raman gain and fiber loss shown in Figs. 3.6 and 3.7, respectively. The Raman gain coefficient is a complicated function of the frequency shift between pump and signal, although the basic shape of the Raman coefficient is fairly constant from one fiber type to another.

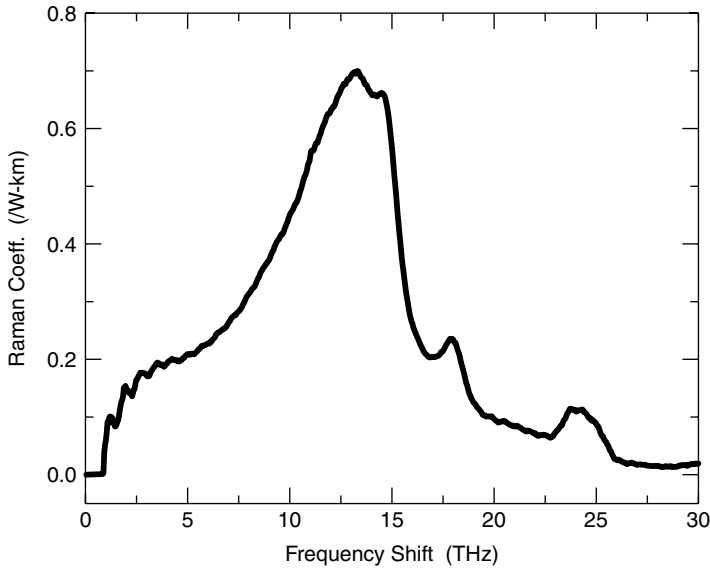


Fig. 3.6. The measured Raman gain coefficient for nonzero dispersion-shifted fiber [17, 15]. The effective core area is $55 \mu\text{m}^2$. The coefficient was not measured for small shifts. (©2002 IEEE).

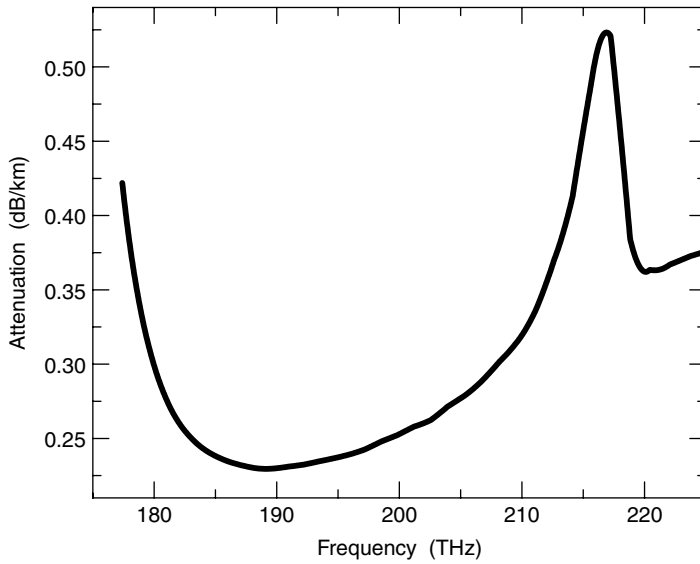


Fig. 3.7. The measured fiber loss rate of nonzero dispersion-shifted fiber [15] (©2002 IEEE).

Thus, when appropriately scaled for effective fiber core area, the above curves tend to be universal.

Any practical system will require some gain feedback to optimize the gain leveling in order to compensate for changes in signal loading and different types of fiber in the initial setup. Gain control and feedback in a transmission system using DTDM Raman pumping or SMART pumping requires less computation than with CW pumping. Using Eq. (3.8), which relates the gain to the path-average pump powers, corrections to the path-average pump powers are quickly calculated from the necessary gain correction. But converting that change in path-average power to a change in launch power requires lengthy computation with CW pumping, whereas with TDM pumping, the change in launch power is simply in direct proportion to the change in path-average power. Also, the CW calculation requires knowledge of the current pump powers, whereas with TDM pumping those numbers are not required, and as such, the final results are less dependent upon the accuracy of the calculation.

We now show several examples of how very well the just-described algorithm works for calculating optimal combinations of pump wavelengths and powers to produce the flattest possible gain. First, Fig. 3.8 shows the computed path-average pump powers and resultant gain for the case of four pumps with a gain bandwidth of 8 THz, corresponding to the combined C+L-band. (Note that the path-average pump powers reported here apply equally well for CW and TDM pumping, whereas the input pump powers are different for those two cases.) Each pump laser in the

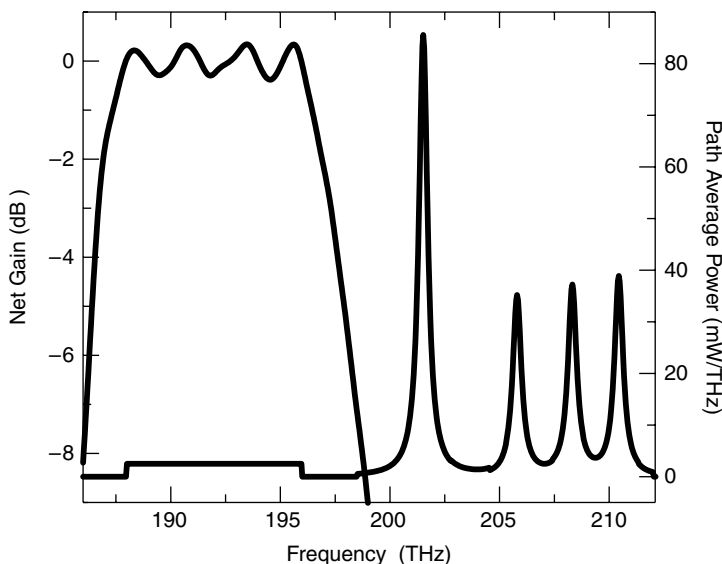


Fig. 3.8. Calculated path-average power and associated Raman gain for a four-wavelength Raman pump configuration. The gain region extends over the combined C+L-band [15] (©2002 IEEE).

calculation has a Lorentzian lineshape with a FWHM of 0.5 THz (~ 3.6 nm). Most of the gain is derived from the longest wavelength laser, because its gain bandwidth extends over the entire signal bandwidth; the remaining lasers just fill in where the gain from the longest wavelength laser falls off. Note also that the gain ripple is uniformly distributed across the signal band and that the number of ripple peaks matches the number of pumps, as might be expected with a small number of pumps. Finally, note that the gain spectrum falls off quickly outside the desired gain region. This fall-off is important in a long-haul system, as it prevents the buildup of ASE which can then deplete the pumps and thereby modify the gain level and profile.

Next we show two examples calculated in the limit of a pump continuum, as would be appropriate for a SMART pump. The continuum is approximated using 50 pumps spaced 0.24 THz apart with linewidths of 0.6 THz. The best results are more or less universally obtained when the pump bandwidth is at least 3 THz wider than the signal bandwidth; below that pump bandwidth, the gain tends to drop off near the edges of the signal band.

Figures 3.9 and 3.10 show, respectively, the path-average pump powers and gain spectra for a 3 THz wide signal bandwidth obtained with a 6 THz pump band and an 8 THz gain bandwidth obtained with a 12 THz pump bandwidth. For a better appreciation of the extremely flat gains obtained, the top of the gain curve of Fig. 3.10 is shown expanded in Fig. 3.11; note that the gain ripple here is less than 0.002 dB! Also note that the path-average pump powers in each case have a similar structure, viz., a large peak at low frequency (long wavelength), followed by a narrow dip and

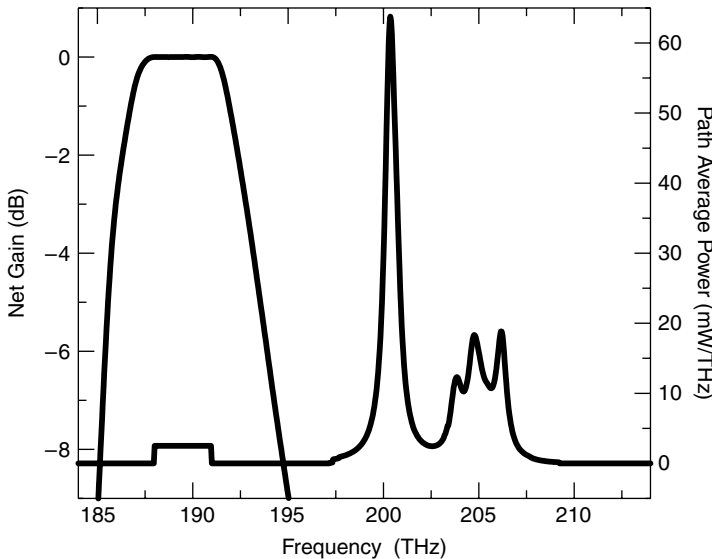


Fig. 3.9. Calculated path-average power and net gain in the limit of a pump continuum [15]. The signal band extends over 3 THz and the pump band over 6 THz (©2002 IEEE).

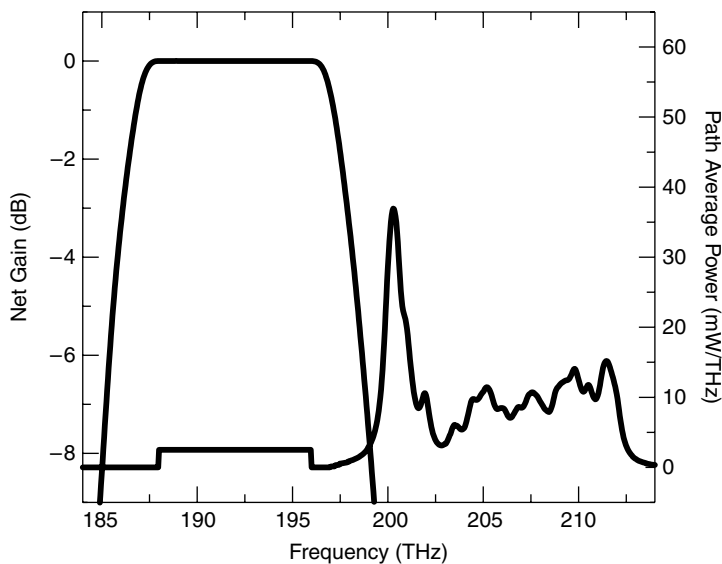


Fig. 3.10. Calculated path-average power and net gain in the limit of a pump continuum [15]. The signal band extends over 8 THz and the pump band over 12 THz (©2002 IEEE).

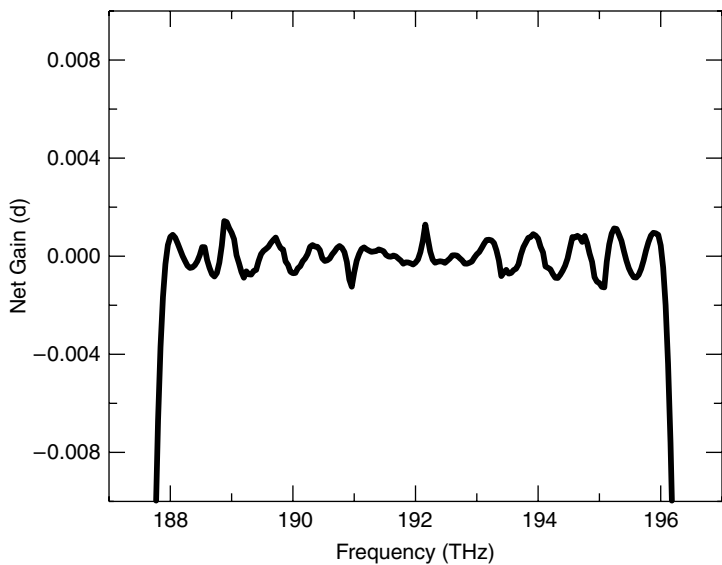


Fig. 3.11. Expanded view of the top of the gain curve shown in Fig. 3.10 [15] (©2002 IEEE).

then an extended region with low power and significant structure. We also note that in other, similar, calculations we have been able to show that just about any reasonably smooth gain curve that may be desired, such as gain with a linear or curved tilt, can also be as easily achieved as the very flat gains shown here. One important aspect that we have not yet fully explored, however, is the minimum characteristic linewidth of a gain peak or other anomaly that can be compensated using a SMART Raman pump.

Calculation of the pump wavelength tuning with time for a SMART Raman pump configuration is possible once the launch power distribution is known. First the line-shape of the pump laser must be deconvolved from the desired launch power spectrum. The time versus wavelength is then calculated using the relation

$$t(\lambda) = \tau \int_{\lambda_{\min}}^{\lambda} \frac{L(\Lambda)}{P_l(\Lambda)} d\Lambda. \quad (3.12)$$

Then switching the dependent and independent variable, $t(\lambda) \Rightarrow \lambda(t)$, a wavelength versus time trace is determined. Here τ is the period in time over which the wavelength is scanned, $P_l(\Lambda)$ is the output power of the laser, and $L(\Lambda)$ is the desired launch power at wavelength Λ . The wavelength versus time shown in Fig. 3.12 is that producing the path-average power shown in Fig. 3.10; here we have assumed a constant output power with wavelength and a pump linewidth much less than the tuning bandwidth. Note that the slope is small where high power is needed and large where only low power is needed. The bandwidth of the electronics and the tuning speed of the laser will limit the ability of an actual device to trace out this curve. As noted earlier,

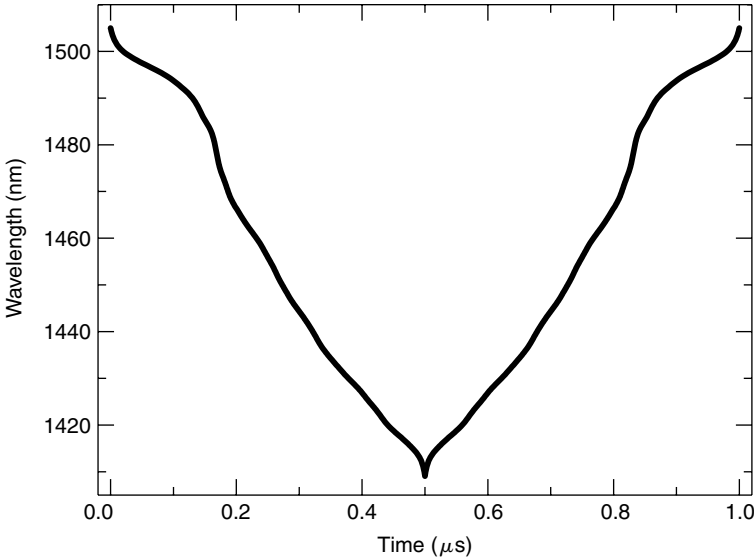


Fig. 3.12. Calculated wavelength variation with time of a SMART pump to achieve flat gain over the combined C+L-band.

however, initial calculations suggest that an electrical bandwidth of 50 MHz should be sufficient.

Another important issue is that of the total pump power required to achieve a given peak gain as the pump and signal bandwidths are increased. Note from Fig. 3.13 that the pump power increases essentially linearly with increasing bandwidth. Because of the large intrinsic bandwidth of the fundamental Raman gain curve, however, that relationship is not a direct proportionality.

As noted earlier, the Raman interaction among the pumps with CW pumping is a significant problem, especially when the gain is greater than 15 dB. Both Figs. 3.14 and 3.15 refer to a 100 km span, pumped to unity gain (23 dB), and show complementary aspects of strong Raman interaction among the pumps. A gain of 23 dB is a bit higher than would typically be used, but does clearly illustrate the point. Note from Fig. 3.14 that the lowest-frequency pump (at 200 THz) experiences very little loss compared to the highest-frequency pump (at 216 THz), due to the Raman interaction between them. Note from Fig. 3.15 that almost all the launch power is concentrated at the short-wavelength side of the spectrum with CW pumping, whereas with TDM the distribution is much more uniform. (There is a large peak at long wavelengths (low frequency) in the TDM pumping trace but the area under this peak isn't large compared to the total area.) It is always thus, for CW pumping, and when high gain is required: almost all the necessary power for the lowest-frequency pump comes from the higher-frequency pumps. As the gain is lowered, the launch power becomes less localized near the short-wavelength side with CW Raman pumping.

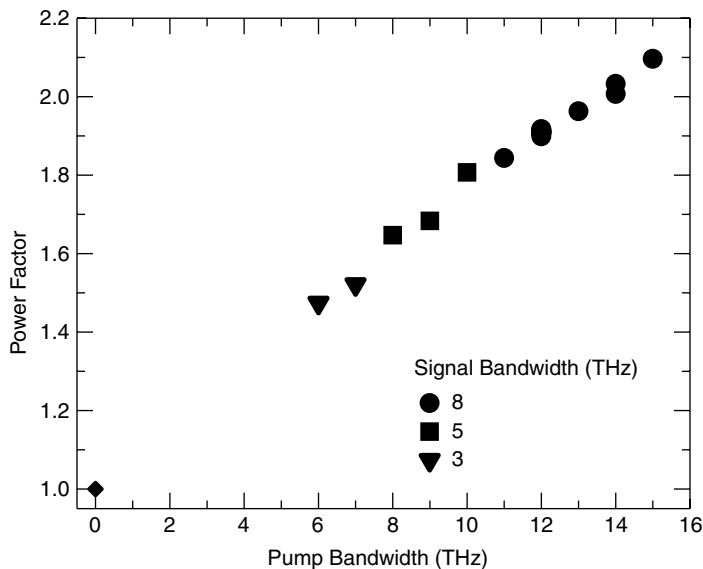


Fig. 3.13. Relative pump power required to achieve a given peak gain as a function of the pump bandwidth [15] (©2002 IEEE).

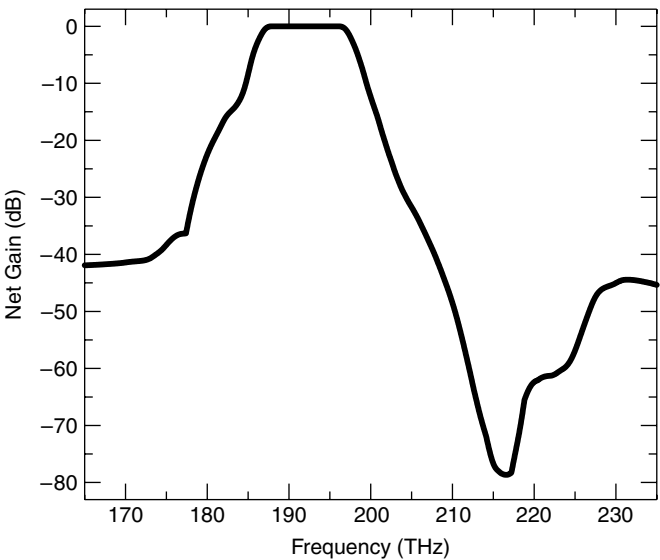


Fig. 3.14. The net gain and loss for 100 km of nonzero dispersion-shifted fiber pumped to unity net gain.

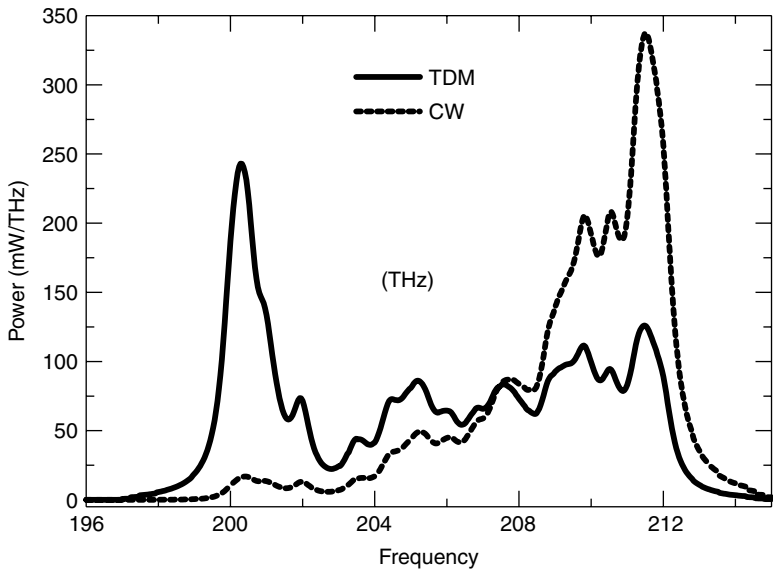


Fig. 3.15. The calculated launch power for CW and TDM Raman pumping required to match the path average power shown in Fig. 3.10.

To confirm this sort of strong Raman pump interaction, we have measured the required pump launch powers of the experimental configuration shown in Fig. 3.2 for both CW and DTDM pumping. These results are shown in Fig. 3.16 for an average gain of 13 dB. Care was taken to match the gain profiles in each case. The expected large difference in launch powers is seen for the 1420 and 1490 nm pump lasers when comparing CW and DTDM pumping.

The pump-to-pump Raman interaction also changes the effective attenuation length of the various pump wavelengths, as can be inferred from Fig. 3.14. As noted above, the long-wavelength pumps quickly drain power from the short-wavelength pumps, thereby greatly increasing the effective rate of attenuation. The degree to which the gain is distributed along the fiber length directly affects the noise figure of the amplifier. Short-wavelength channels that are pumped primarily by the short-wavelength pump have a gain profile which is much less distributed than for channels pumped by the long-wavelength pump. The signal power evolution is shown in Fig. 3.17 for CW pumping of a 100 km span to unity gain. The path-average signal powers are the same for both the CW and TDM cases. Note, however, that the signal power variation is 5 dB greater for the short-wavelength channel compared to the long-wavelength channel. Note also that in order to maintain a constant path-average signal power with wavelength, the signal launch powers must vary by 2 dB across the band. By contrast, with TDM pumping, there is very little variation in the power evolution between the signal channels. The only difference is due to variations in the fiber attenuation across the signal and pump bands, but this is a small effect for most fiber types.

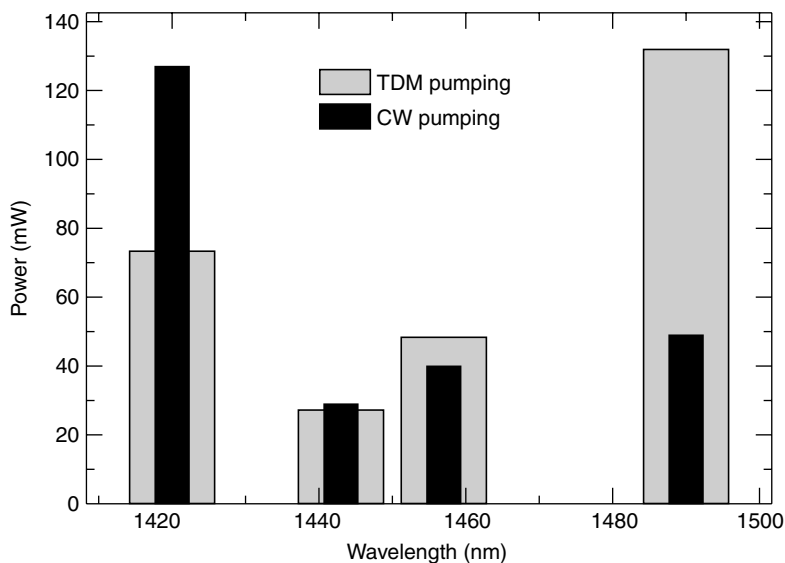


Fig. 3.16. Measured fiber launch powers to achieve broadband gain of 13 dB for both CW and DTDM pumping.

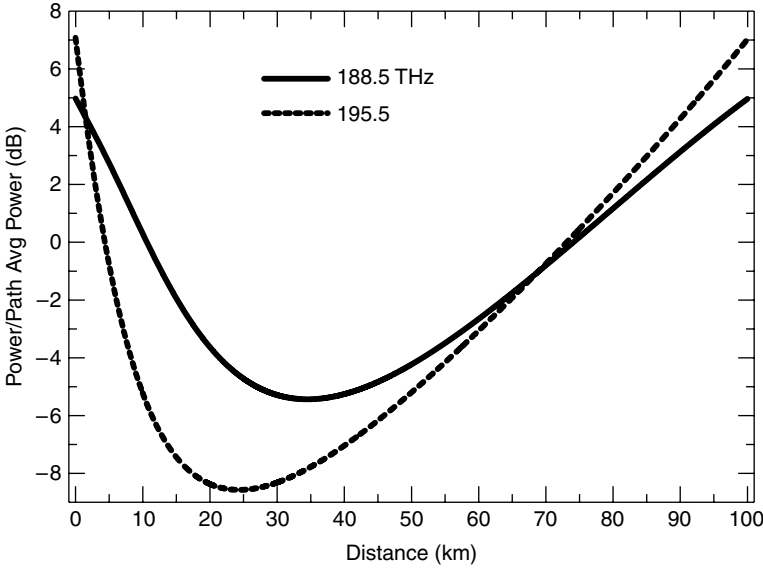


Fig. 3.17. Calculated signal power evolution in a 100 km fiber span pumped to unity net gain. The path-average signal power is the same for both the CW and TDM cases.

3.4. Temporal Gain Ripple

The forward gain that results from backward TDM Raman pumping isn't completely independent of time. Instead, there is a small remnant temporal gain variation at the same rate as the pump pulses. Consider a single pump with an output power that varies in a square wave pattern with period τ and pulse width Δ . Assuming that pump depletion by the signal is negligible, the gain for this configuration is calculated by summing up the gain from each pulse along the fiber. Performing this sum, the maximum and minimum gains can be found. A useful quantity to examine is the ratio of the gain ripple, $\ln(G_{\max}) - \ln(G_{\min})$, to the average gain $[\ln(G_{\max}) + \ln(G_{\min})]/2$.

$$\Gamma \equiv 2 \frac{\ln(G_{\max}) - \ln(G_{\min})}{\ln(G_{\max}) + \ln(G_{\min})} = 2 \frac{1 - e^{-\rho(\tau - \Delta)}}{1 + e^{-\rho(\tau - \Delta)}}, \quad (3.13)$$

where $\rho = \beta V_g/2$, β is the attenuation coefficient at the pump wavelength (/km), and V_g is the group velocity (km/s). The dividend of 2 appears in the expression for ρ because the pump and signal are propagating in opposite directions. The quantity Γ is directly related to values that can readily be measured in an experiment, viz., the average signal value S_{avg} , the peak-to-peak signal ripple $S_{\text{pk-pk}}$, and the average on-off gain $G_{\text{on-off}}$.

$$\Gamma = \frac{S_{\text{pk-pk}}/S_{\text{avg}}}{\ln(G_{\text{on-off}})}. \quad (3.14)$$

Because the fiber loss rate and pulse rate are both much less than one, Eq. (3.13) is accurately approximated as

$$\Gamma \simeq \frac{\beta V_g(\tau - \Delta)}{2}. \quad (3.15)$$

Putting a repetition rate of 500 kHz with a 25% duty cycle and a fiber attenuation of 0.23 dB/km into this equation yields $\Gamma = 0.008$, that is, a peak-to-peak ripple that is just 0.8% of the on-off gain. A ripple of this magnitude is essentially negligible. Note that even with a gain of 25 dB, this fraction would yield a peak-to-peak ripple of only 0.2 dB. Ripple reduction is also achieved by appropriately choosing the relative phases of the pumps in adjacent fiber spans such that the ripples cancel out.

We have tested the above model experimentally. In the experiment a high-power laser diode operating at 1440 nm was electrically pulsed with a 25% duty cycle and launched into the fiber, where it produced an on-off gain of ~ 7 dB, and a signal near the peak of the resultant Raman gain was launched in the forward direction. The signal power was measured with a fast detector on an oscilloscope with the pump on and also with the pump off. The measured waveform, peak-to-peak ripple, and theoretical predictions are shown in Fig. 3.18 for rates from 250 kHz to 1 MHz. The measured peak-peak values agree well with the predictions of Eq. (3.15). Differences between the theory and experiment can be attributed to the nonsquare shape of the optical pulses in the experiment, when square pulses were assumed in the theory. The

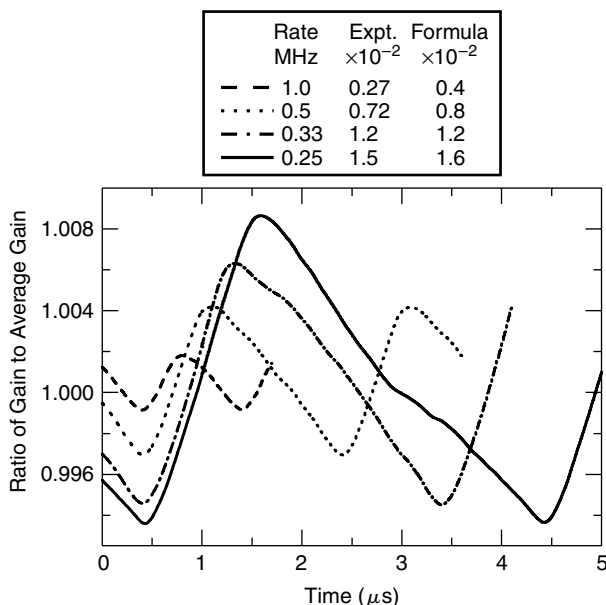


Fig. 3.18. Experimentally measured temporal gain ripple for various pumping rates with an on-off Raman gain of 7 dB and a duty cycle of 25%. The predictions of Eq. (3.15) are shown for comparison.

largest discrepancy is found with the shortest pulses (highest pumping rate), where the deviation from a square pulse shape was greatest.

A TDM Raman amplifier is only employed when several pump wavelengths are needed. The net ripple from such a multiple pump source can be less than that of the single pump sources discussed thus far in this section. With multiple pumps, the ripple introduced by each pump has its own proper phase. The long-wavelength channels are pumped almost exclusively by the long-wavelength pump, therefore they tend to experience a ripple close to that calculated from Eq. (3.15). Short-wavelength channels, on the other hand, receive significant gain from each of the pump wavelengths, and because the phases of the ripples from the various pumps are distributed over 2π , the net ripple will then be much less than that calculated from Eq. (3.15).

3.5. Four-Wave-Mixing

Four-wave-mixing (FWM) is a nonlinear process where two photons with frequencies ν_1 and ν_2 are destroyed while two new photons ν_3 and ν_4 are created. Energy is always conserved in this process; thus $\nu_1 + \nu_2 = \nu_3 + \nu_4$. Phase matching of the wavevectors $\kappa_1 + \kappa_2 = \kappa_3 + \kappa_4$ is necessary for FWM to develop efficiently. In a long dispersive fiber, the phase matching condition is satisfied only around the zero dispersion wavelength λ_0 . Thus the worst case occurs when λ_0 falls within the pump band, especially near the long-wavelength pump. In that case, strong components are generated within the signal band. Although the four-wave-mixing components in this case are copropagating with the pump, the FWM is typically high enough with CW operation such that Rayleigh backscattering of those FWM components can significantly degrade the optical signal-to-noise ratio (OSNR).

TDM Raman pumping tends to eliminate this problem by eliminating temporal overlap of the pump pulses. In practice, however, it is difficult to eliminate all such temporal overlap of the various wavelengths. The intensities in the overlap may be high, so the FWM is efficient, but inasmuch as the overlap is only for a small fraction of time, the time-averaged intensity of the FWM components is weak. (Once again, it is only by way of Rayleigh backscattering, a time-averaging process, that the FWM components can join the signal and threaten the OSNR.) In addition, in most cases, the pulse time ordering can be chosen such that troublesome pump wavelengths are not in adjacent time slots.

We have experimentally observed the power of TDM pumping to suppress FWM by using the setup shown in Fig. 3.2. Measurements of all signals copropagating with the pump were made with a sensitive OSA. The four-wave-mixing components with DTDM pumping for pumps in adjacent time slots are shown in Fig. 3.19 and the spectra for the same pumps operating CW are shown in Fig. 3.20. Also shown in the figures are the spectra with only a single pump operating. Note that although strong FWM components are observed in the CW case, only a very small peak is observed with TDM. In this particular case λ_0 is low enough such that the FWM components don't fall within the signal band.

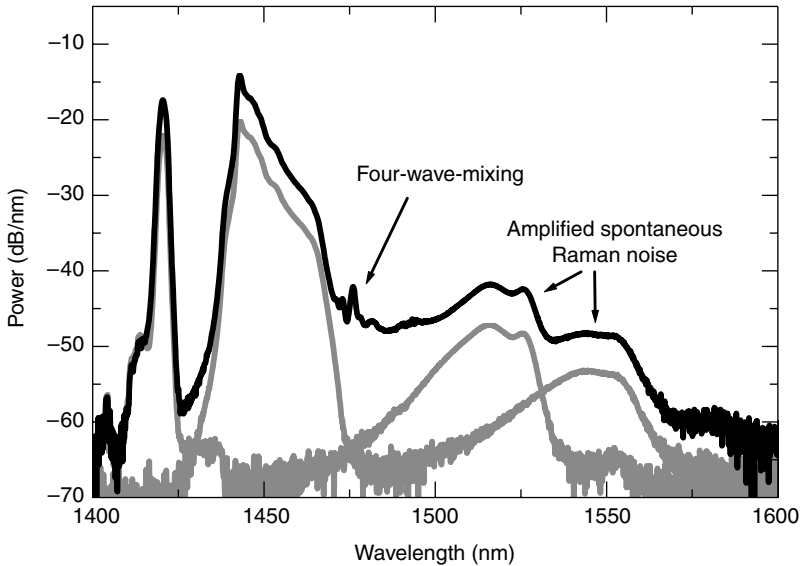


Fig. 3.19. Experimentally measured four-wave-mixing with TDM pumping. For comparison, the spectrum of each pump running alone is also shown; for clarity, these spectra were shifted by -5 dB. A weak four-wave-mixing component is observed because there is some overlap of the pump pulses.

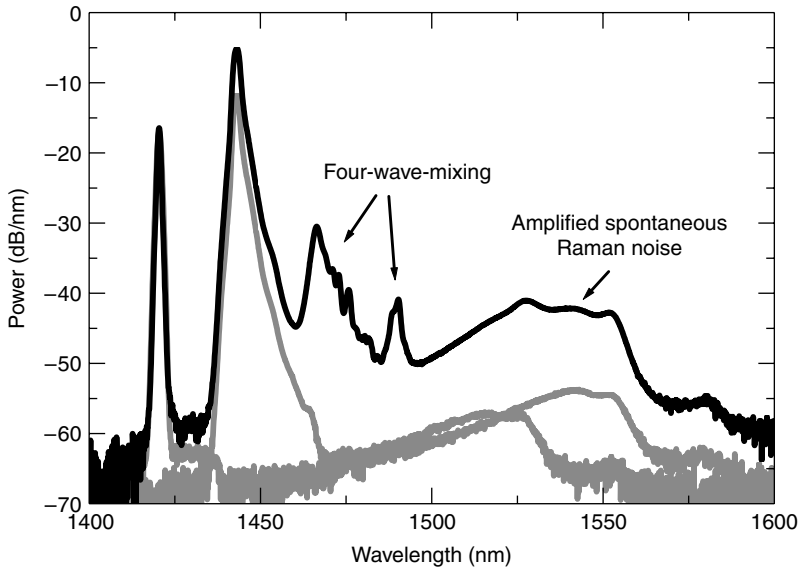


Fig. 3.20. Experimentally measured four-wave-mixing with CW pumping. For comparison, the spectrum of each pump running alone is also shown; for clarity, these spectra were shifted by -5 dB. Strong four-wave-mixing components are observed.

3.6. Spontaneous Raman Noise

The path-average pump power as seen by the signal in the forward direction is the integral along the fiber length of the time-averaged pump power. This is not the case for a signal copropagating with the pump. Here the path-average pump power depends upon whether the signal is in phase or out of phase with the pump pulse. It is only when the pump pulses are shorter than the group velocity dispersion walk-off between the pump and signal (a condition most severe and difficult to satisfy), that the time-averaged power is again appropriate. Neglecting pump depletion and defining α to be the fiber loss rate, P_0 to be the peak pump launch power, and D to be the pump duty cycle, then the forward on-off Raman gain is given by

$$G(v) = \exp\left[\frac{R(v - \nu)P(v)D[1 - \exp[-\alpha L]]}{\alpha}\right]. \quad (3.16)$$

The gain in the backward direction when the pump and signal are in phase is

$$G(v) = \exp\left[\frac{R(v - \nu)P(v)[1 - \exp[-\alpha L]]}{\alpha}\right] \quad (3.17)$$

and when the signal is out of phase with the pump, the gain is given by

$$G(v) = 1. \quad (3.18)$$

The factor of D in the exponential makes the peak gain in the forward direction significantly smaller than in the backward direction. Because the noise grows rapidly with gain, the excess noise generated in the backward direction, even when time-averaged, will be significantly larger than the noise in the forward direction. Rayleigh scattering of that enhanced backward noise can then significantly increase the noise level in the forward direction.

The time-averaged spontaneous Raman noise in the forward direction due to spontaneous Raman scattering is given by

$$N_F = 2h\nu RP_0 D e^{(RP_0 D)/\alpha} \int_0^L \exp\left[-y[\alpha + \beta] - \frac{RP_0 D e^{-\alpha y}}{\alpha}\right] dy. \quad (3.19)$$

The contribution to forward propagating noise from Rayleigh scattering of backward propagating spontaneous Raman noise is given by

$$N_B = 2h\nu RP_0 D e^{(RP_0 D)/\alpha} \sigma \int_0^L \int_0^x \exp\left[[\beta - \alpha]y + \frac{RP_0 e^{-\alpha y}}{\alpha} - 2\beta x - \frac{RP_0[1 + D]e^{-\alpha x}}{\alpha}\right] dy dx, \quad (3.20)$$

where σ is the Rayleigh scattering coefficient, α is the fiber loss at the pump wavelength, β is the fiber loss at the signal wavelength, S_0 is the signal launch power, D is the duty cycle, ν is the signal wavelength, and R is the Raman gain coefficient. In both Eqs. (3.19) and (3.20) it is assumed that pump depletion due to the Raman effect is negligible and that the pulse width is much less than the characteristic attenuation length of the fiber. These equations can be quickly evaluated on a fast computer. The log of the ratio of these two noise contributions gives the additional penalty for using TDM Raman pumping rather than CW Raman pumping. This ratio is plotted versus duty cycle for several gain values in Fig. 3.21. Note that the penalty quickly grows with increasing gain and decreasing duty cycle.

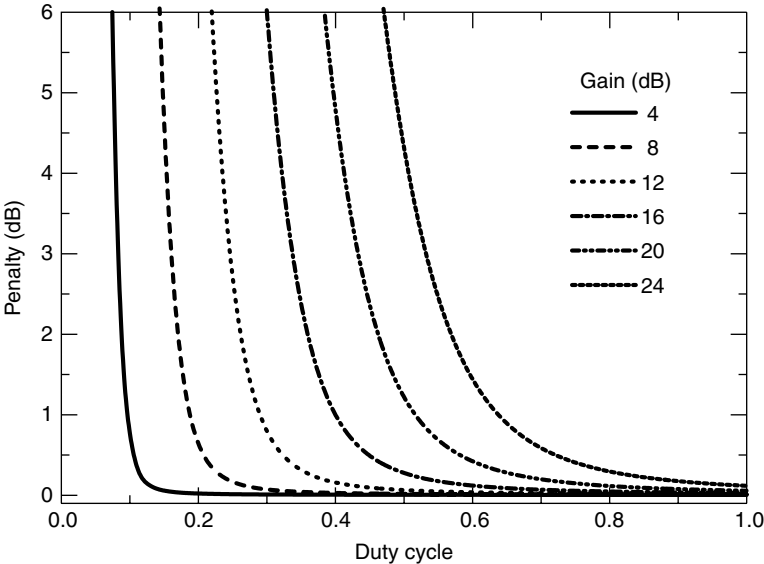


Fig. 3.21. The calculated increase in forward propagating noise due to Rayleigh scattering of backward propagating noise with TDM Raman pumping. The penalty is plotted versus duty cycle for several gain values.

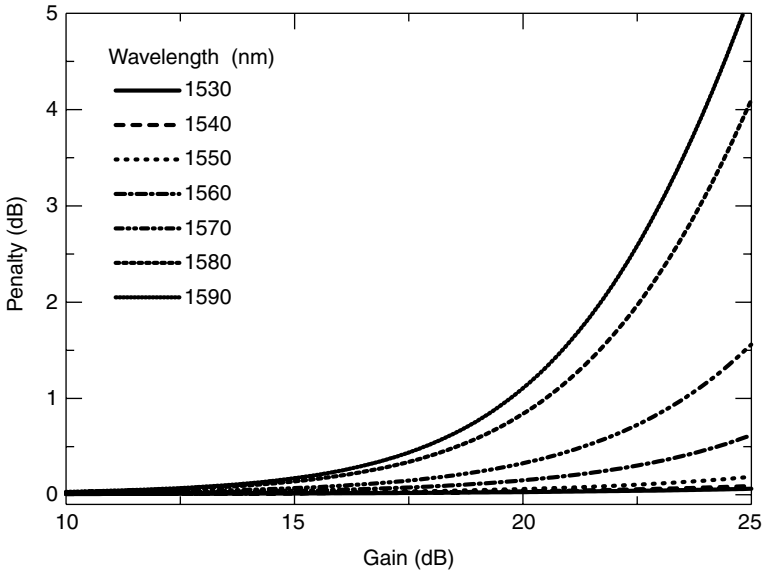


Fig. 3.22. The calculated increase in forward propagating noise due to Rayleigh scattering of backward propagating noise with TDM Raman pumping. The penalty was calculated for broadband Raman gain using four wavelengths. The peak output power at each wavelength was assumed to be equal and the duty cycle then adjusted to level the gain.

The situation becomes more complicated when several pump wavelengths are used. The noise problem is not severe at short signal wavelengths, because each pump contributes to the gain, producing quasiCW pumping. Only at long wavelengths, where the gain is derived entirely from one pump wavelength, is there a problem. Luckily, the longest wavelength pump is also the pump with the highest power. The higher power can be achieved by increasing the duty cycle for this laser which then reduces the noise penalty.

To explore this effect, we have calculated the additional noise penalty for the case where flat broadband gain is obtained over the combined C+L-band from four TDM pump lasers, each with the same peak output power. The penalty is plotted versus on-off gain for several different wavelengths in Fig. 3.22. Note that the penalty can be kept below 0.5 dB for all wavelengths out to a gain of 18 dB.

3.7. Double-Rayleigh Scattering Noise

Double-Rayleigh backscattering of the signal itself, also known as double-Rayleigh scattering (DRS), can be a significant source of noise. The higher gain in the backward direction obtained with Raman gain also increases the DRS noise penalty [18]. Assuming no pump depletion, the equation describing DRS for CW pumping is given by

$$N_{DRS} = S_0 e^{\delta} L^2 \sigma^2 \int_0^1 \int_x^1 \exp \left[2\rho \left[e^{\alpha L y} - e^{\alpha L x} \right] - 2\beta L[y - x] \right] dy dx, \quad (3.21)$$

where

$$\rho = \frac{R P_0 e^{-\alpha L}}{\alpha} \quad (3.22)$$

and where α is the fiber loss at the pump wavelength, β is the fiber loss at the signal wavelength, σ is the Rayleigh scattering coefficient, R is the Raman coefficient, and S_0 is the signal launch power. A more complicated equation can be derived for TDM pumping but is not shown. This equation is quickly solved with a fast computer, and analytic solutions can be found for certain cases, such as those of uniform gain or no gain at all. We have calculated the DRS-to-signal ratio using parameters from the experimental setup shown in Fig. 3.2. The ratio is plotted in Fig. 3.23 versus gain for both TDM and CW pumping. The extra penalty for TDM pumping is the difference between the TDM and CW curves, and grows to approximately 4 dB at a gain of 15 dB. System performance in many cases is not limited by DRS, so a 4 dB increase in the DRS penalty is generally insignificant.

We have measured the DRS noise penalty in an experiment where the DRS decay in time is observed immediately after the signal is turned off. This method is similar in some ways to the methods of [19] and [20], although other methods also exist [21]. The characteristic decay time of the DRS is approximately the transit time through the fiber under test. The only trick is to ensure that when the signal is turned off, the residual leakage is much less than the DRS level itself.

The apparatus we used to measure the DRS is shown in Fig. 3.24. The fiber loop here corresponds to the experimental setup of Fig. 3.2. The signal source is allowed

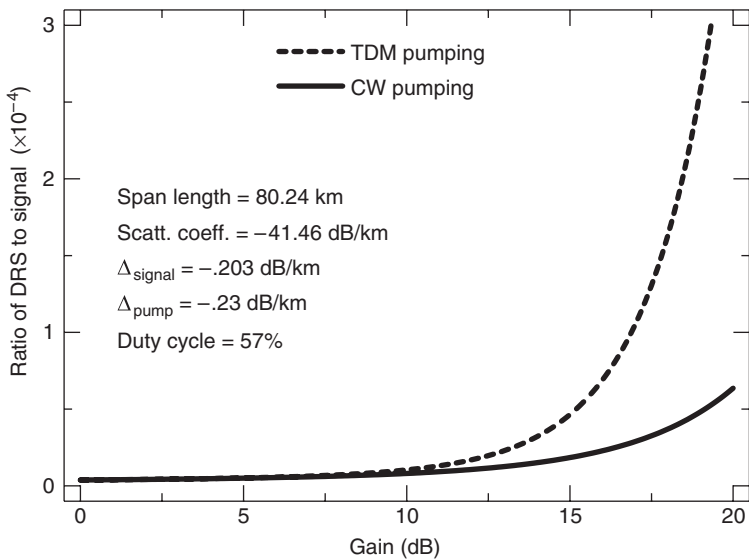


Fig. 3.23. Calculated ratio of DRS noise-to-signal for CW and TDM Raman pumping after transmission through the fiber span versus the on-off Raman gain in the forward direction.

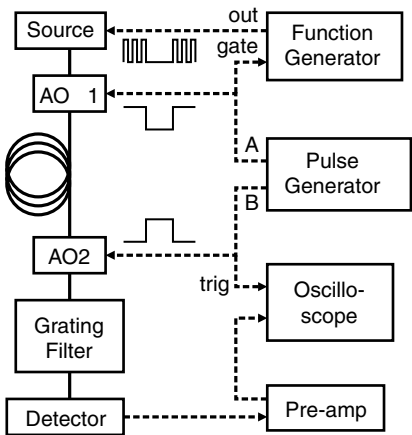


Fig. 3.24. Experimental configuration for measuring double-Rayleigh scattering.

to run for a sufficiently long time to bring the DRS to a steady state. This amount of time is equal to four trips through the fiber span, but if gain depletion is truly negligible, it can be reduced to three trips. When the DRS reaches a steady state, the source is quickly turned off by directly modulating the source laser and also by switching an AO modulator. The source laser is modulated at 500 kHz coherently with the switching of the signal source and the AO modulator. This allows any signal to be clearly distinguished from the DRS. A second AO modulator is used after the loop to block the signal going to the detector while the DRS is building up in the loop.

This prevents the detector and electronic amplifier from being saturated and reduces the waiting time for settling of the detector. The switching on of the second modulator is delayed from the turning off of the first modulator by the transit time of the signal through the fiber span. A narrowband optical filter is used to select either the DRS or the SRS for measurement, by tuning the filter wavelength to just off or on the channel under test. Actually, the “just off” measurements were made both above and below the channel, and the results averaged to eliminate any effect of gain slope. The signal from the detector is amplified and fed into a fast digital oscilloscope. The scope is triggered by the electronic pulse generator that drives the AO modulators. Up to 50 traces were coaveraged on the oscilloscope to reduce the noise.

The time-averaged signal launch power in these measurements was 0.58 mW, a value approximately three to four times larger than that used in a typical system. Increasing the launch power has no effect on the DRS-to-signal ratio, but does decrease the SRS-to-signal ratio. This is because the DRS scales linearly with signal launch power, and the SRS is independent of signal launch power, inasmuch as pump depletion by the signal can be ignored.

We found our technique to be sensitive enough to measure the DRS without any gain, because no evidence of any signal was seen in even that DRS measurement. The DRS with no gain is shown in Fig. 3.25. The Rayleigh scattering coefficient was calculated with this data in order to predict, via simulation, the decaying DRS signal.

The DRS was measured for both CW and TDM pumping with the same on-off Raman gain. A 1490 nm pump laser was used in the experiment and was pulsed at a rate of 825 kHz with a 57% optical duty cycle. The signal channel was at the peak of the

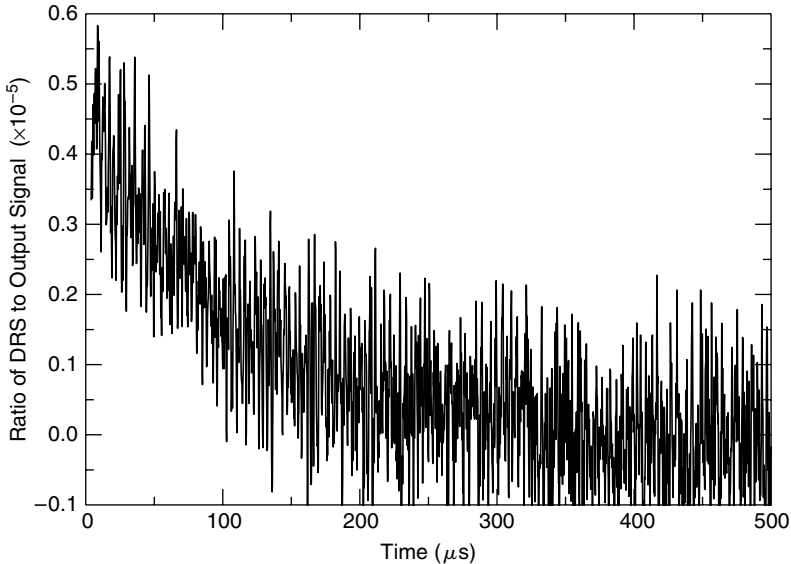


Fig. 3.25. Experimental measurement of the decay of DRS noise with no Raman gain after the signal is turned off.

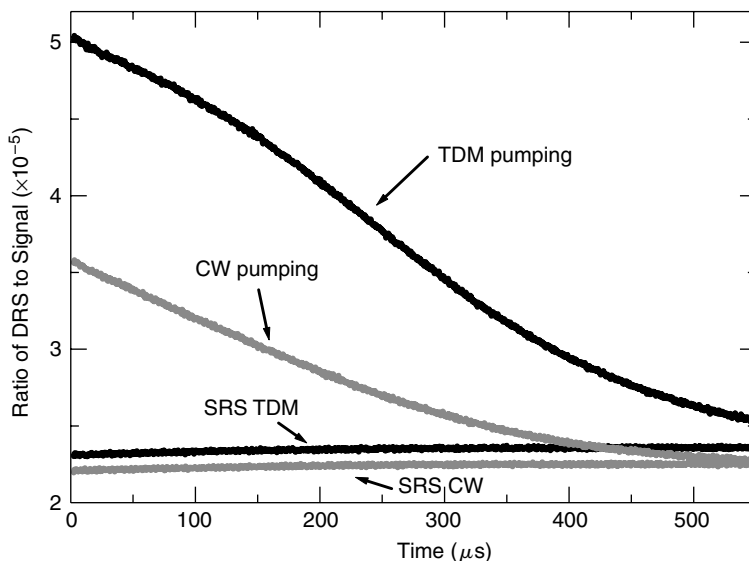


Fig. 3.26. Experimentally measured decay of the DRS noise-to-signal ratio with 13.1 dB of Raman gain after the signal is turned off.

Raman gain (with $\lambda = 1591.1$ nm). The experimental DRS-to-signal ratio is plotted for a gain value of 13.1 dB in Fig. 3.26. The value of the signal power used to calculate that ratio is the steady-state signal power after transmission through the span, but before the signal is turned off, not the signal power launched into the span. Calculations of the DRS decay are shown in Fig. 3.27. Square wave optical pulses are assumed in the calculation, along with zero group velocity dispersion and no pump depletion. The steady-state DRS values are found by extrapolating the data back to when the signal is turned off. The SRS signal increases by 2% over the course of the DRS measurement due to the reduction in pump depletion when the signal is turned off.

The shape of the experimental DRS curve agrees well with the model predictions, suggesting that our simple model is sufficient. The small differences can be attributed to the facts that the shape of the pulse in the model doesn't match that in the experiment, that pump depletion was ignored in the model, that zero group velocity dispersion was assumed, to error in the value of the scattering coefficient, and to uncertainty in some optical connections.

The higher DRS and SRS noise penalties that accrue with TDM Raman pumping can be reduced while keeping most of the benefits. Multiple lasers can be pulsed at the same time in a DTDM scheme or with a SMART pump; multiple lasers could be operated slightly out of phase. The pumps that are pulsed simultaneously should be close in wavelength so as to minimize their Raman interaction and also chosen such that they don't produce any troublesome four-wave-mixing components. This would increase the duty cycle of the longest-wavelength pump and reduce the noise penalties. Consider the DTDM case shown in Fig. 3.8, where the relative pump powers are 100:40:43:45. When all the lasers are pulsed sequentially, the % duty cycles (long

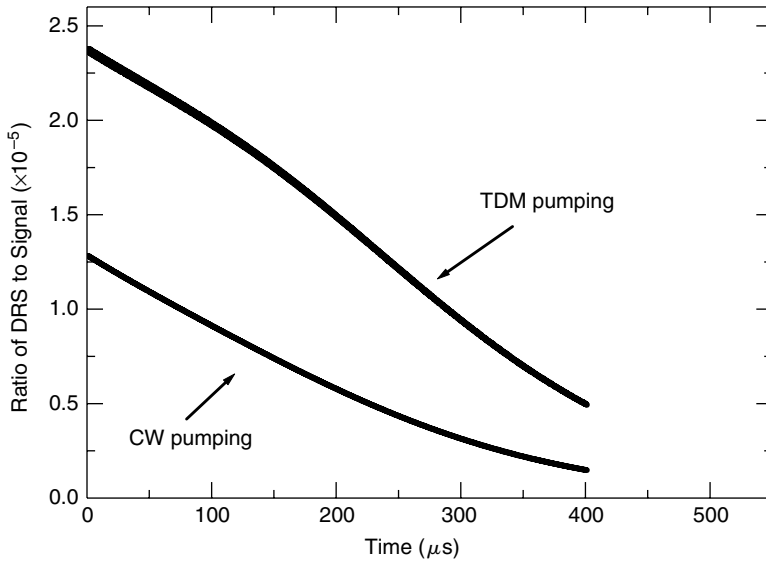


Fig. 3.27. Calculated decay of the DRS noise-to-signal ratio when the signal is turned off. The calculation parameters were chosen to match the experimental configuration as closely as possible.

to short wavelength) are 44:17:19:20, whereas if the two short wavelengths and two long wavelengths are pulsed at the same time, then the duty cycles are 69:28:30:31. Looking back to Figs. 3.23 and 3.22, increasing the duty cycle from 44 to 69% greatly reduces the noise penalty. Note that the durations of pulses need not be equal when the pumps are pulsed simultaneously.

3.8. Conclusions

Raman amplification has many clear advantages, but there is still some debate over the best way to configure a Raman pump for practical applications. TDM Raman pumping has several advantages over CW Raman pumping, but it also has a few disadvantages. The best choice, however, depends upon the specific situation. When the best noise performance is necessary then CW is probably the best choice. If a small noise penalty can be tolerated, then TDM has many additional benefits over CW pumping, such as efficient gain leveling with a SMART pump, the elimination of four-wave-mixing, and the elimination of pump-to-pump Raman interactions.

Another issue that has not been discussed is cost. At this moment CW Raman is more cost effective because the output power of each TDM pump must be the same as the combined output power of all the CW pumps. Currently, lasers are priced in dollars per milliwatt. With this pricing scheme, an N wavelength TDM pump would cost approximately N times as much as the corresponding CW pump. However, the maturation of high-power laser diode technology may change the pricing scheme to

one based more on a per-module cost rather than a per-milliwatt cost. When that happens, the TDM Raman amplifier and the CW Raman amplifier will be approximately equal in price.

References

- [1] A. Hasegawa, Numerical study of optical soliton transmission amplified periodically by the stimulated Raman process, *Appl. Optics*, 23:3302–3305, Oct., 1984.
- [2] L. F. Mollenauer and J. P. Gordon and M. N. Islam, Soliton propagation in long fibers with periodically compensated loss, *IEEE J. Quantum Electron.*, QE-22:157–173, Jan., 1986.
- [3] L. F. Mollenauer and K. Smith, Demonstration of soliton transmission over more than 4000 km in fiber with loss periodically compensated by Raman gain, *Optics Lett.*, 13:675–677, Aug., 1988.
- [4] J. P. Gordon and L. F. Mollenauer, Effects of fiber nonlinearities and amplifier spacing on ultra-long distance transmission, *J. Lightwave Technol.*, 9:170–173, Feb., 1991.
- [5] S. Namiki and Y. Emori, Ultrabroad-band Raman amplifiers pumped and gain-equalized by wavelength-division-multiplexed high-power laser diodes, *IEEE J. Select. Topics Quantum Electron.*, 7:3–16, Jan/Feb., 2001.
- [6] H. Kidorf, K. Rottwitz, M. Nissov, M. Ma, and E. Rabarijaona, Pump interactions in a 100-nm bandwidth Raman amplifier, *IEEE Photon. Technol. Lett.*, 11:530–532, May, 1999.
- [7] L. F. Mollenauer, A. R. Grant, and P. V. Mamyshev, Time-division multiplexing of pump wavelengths to achieve ultrabroadband, flat, backward-pumped Raman gain, *Optics Lett.*, 27:592–594, April, 2002.
- [8] C. R. S. Fludger, V. Handerek, N. Jolley, and R. J. Mears, Novel ultra-broadband high performance distributed Raman amplifier employing pump modulation. In *Technical Digest OFC' 2002*, 183–184, 2002.
- [9] P. J. Winzer, K. Sherman, and M. Zirngibl, Time-division multiplexed Raman pump experiment using a tunable c-band laser, *IEEE Photon. Technol. Lett.*, 14:789–791, June, 2002.
- [10] P. J. Winzer, K. Sherman, and M. Zirngibl, Experimental demonstration of time-division multiplexed Raman pumping. In *Technical Digest OFC' 2002*, 184–185, 2002.
- [11] V. E. Perlin and H. G. Winful, On distributed Raman amplification for ultrabroad-band long-haul WDM systems, *J. Lightwave Technol.*, 20:409–416, March, 2002.
- [12] X. Zhou, C. Lu, P. Shum, and T. H. Cheng, A simplified model and optimal design of a multiwavelength backward-pumped fiber Raman amplifier, *IEEE Photon. Technol. Lett.*, 13:945–947, Sept., 2001.
- [13] M. Yan, J. Chen, W. Jiang, J. Li, J. Chen, and X. Li, Automatic design scheme for optical-fiber Raman amplifiers backward-pumped with multiple laser diode pumps, *IEEE Photon. Technol. Lett.*, 13:948–950, Sept., 2001.
- [14] B. Min, W. J. Lee, and N. Park, Efficient formulation of Raman amplifier propagation equations with average power analysis, *IEEE Photon. Technol. Lett.*, 12:1486–1488, Nov., 2000.
- [15] A. R. Grant, Calculating the Raman pump distribution to achieve minimum gain ripple, *IEEE J. Quantum Electron.*, 38, Nov., 2002.

- [16] W. H. Press, S. A. Teukolsky, W. T. Vetterling, and B. P. Flannery, *Numerical Recipes in C: The Art of Scientific Computing*, 2nd ed. UK: Cambridge University Press, Chap. 10, 1999.
- [17] A. Stentz, K. Rottwitt, E. Pratt, and L. F. Mollenauer, private communication, 1999.
- [18] A. Artamonov, V. Smokovdin, M. Kleshov, S. A. E. Lewis, and S. V. Chernikov, Enhancement of double Rayleigh scattering by pump intensity noise in fiber Raman amplifiers. In *Technical Digest OFC' 2002*, 186, 2002.
- [19] S. A. E. Lewis, S. V. Chernikov, and J. R. Taylor, Characterization of double Rayleigh scatter noise in Raman amplifiers, *IEEE Photon. Technol. Lett.*, 12:528–530, May, 2000.
- [20] S. R. Chin, Temporal observation and diagnostic use of double Rayleigh scattering in distributed Raman amplifiers, *IEEE Photon. Technol. Lett.*, 11:1632–1634, Dec., 1999.
- [21] C. R. S. Fludger and R. J. Mears, Electrical measurements of multipath interference in distributed Raman amplifiers, *J. Lightwave Technol.*, 19:536–545, April, 2001.

Chapter 4

Linear Noise Characteristics

C.R.S. Fludger

4.1. Introduction

Spontaneous emission is the inevitable consequence of gain in an optical amplifier. In this chapter, the definition of noise figure is shown to be useful only in characterizing shot noise and signal–spontaneous beat noise. The noise characteristics of both discrete and distributed Raman amplifiers are then presented. The choice of discrete amplifiers alone, or together with distributed optical amplifiers results as a trade-off between maximizing optical signal-to-noise ratio at the expense of increases in non-linear distortion of the signal due to high signal intensities. Hansen et al. [1] showed that distributed amplification could be used to obtain a significant improvement in system margin that could be used to upgrade the transmission capacity, either in terms of more channels, or a faster line rate.

A general model that accurately predicts both signal propagation and the buildup of ASE is discussed and compared to measurements. Measurements and analysis of linear noise performance for a system enhanced with distributed Raman amplification is presented.

Further measurements and analysis of broadband discrete Raman amplifiers show a clear dependence on temperature which places a fundamental limit on their performance. Even with idealized fiber and high optical gain, a single-stage, counter-pumped, broadband discrete Raman amplifier will have a noise figure that is greater than the quantum limit at room temperature. It is also shown that the noise performance of a distributed Raman amplifier exhibits these temperature characteristics and measurement results are presented from a 95 nm bandwidth amplifier that agree well with the numerical model. Interactions between the pump wavelengths are also shown to play an important role, giving better system performance to longer signal wavelengths at the expense of shorter wavelengths.

Finally, an analysis of the relative linear noise performance of different transmission fibers is presented, showing up to a 2 dB variation in OSNR using 500 mW (Class 3B laser safety limit) pump power depending on fiber type.

4.2. Receiver Noise Sources

Although modern optical fiber transmission systems are predominantly digital systems, the use of optical amplifiers instead of optoelectronic regenerators implies noise builds up along the line in much the same way as for an analogue system. The noise sources present at the optical detector are:

1. Shot noise—related to the time uncertainty of a photon arriving at the photodetector;
2. Beat noise—beating between ASE components (spontaneous–spontaneous beat noise), and beating between ASE components and the signal (signal–spontaneous beat noise);
3. Interference noise—this can be interference between two signals or the transfer of optical phase noise to electrical intensity noise by the photodiode. The phase noise may arise from a signal suffering multiple reflections or scattering events.

In conventional optically amplified systems, where the signal powers are kept relatively high, signal–spontaneous beat noise dominates over spontaneous–spontaneous beat noise, shot noise, and the thermal noise of the photodetector. The use of dense wavelength-division-multiplexing (DWDM), faster data rates, and longer transmission distances is beginning to make nonlinear distortion of the signal a more and more important consideration. This topic is dealt with later in this chapter.

4.3. Noise Figure

The concept of noise figure is already a well-established method of characterizing the buildup of noise in electrical components [2]. The definition of a noise figure that has been used for electrical components is the signal-to-noise (SNR) ratio at the input of a device divided by the signal-to-noise ratio at the output:

$$F = \frac{SNR_{in}}{SNR_{out}}. \quad (4.1)$$

It has been the convention in optical communications to define SNR in terms of electrical powers at an ideal receiver [3] and therefore optical powers and noises must be converted to the electrical currents. The input SNR is given in terms of a Poisson distributed, shot noise limited source. The SNR is therefore given by the square of the mean signal photon number (n_s) divided by the mean square photon number fluctuations:

$$SNR = \frac{\langle I_s \rangle^2}{\langle \Delta I_s^2 \rangle} = \frac{\langle n_s \rangle^2}{\langle \Delta n_s^2 \rangle}. \quad (4.2)$$

Haus [4] has recently suggested that a better definition of SNR would be to maintain the definition in the optical domain. This would give the SNR as the ratio of signal power (energy), to the mean square fluctuations of the signal amplitude, and maintain some consistency with the original IEE definition of a noise figure.

The conventional noise figure is not signal independent unless the signal photon number is large. Only when the signal photon number is high can the standard cascade formula for a noise figure be used. However, this is normally the case in optical communications systems and it is the conventional definition that is adopted here. The SNR at the input of a component is given by that of a shot noise limited source of optical power P_s :

$$SNR_{in} = \frac{\langle I_s \rangle^2}{\langle \Delta I_s^2 \rangle} = \frac{\Re^2 P_s^2}{S_{i_shot_in}}, \quad (4.3)$$

where \Re is the responsivity of the photo detector and $S_{i_shot_in}$ is the electrical power spectral density (PSD) of the shot noise at the input to the device. The PSD of the noise at the output has contributions from signal-spontaneous beat noise, spontaneous-spontaneous beat noise, shot noise, multipath interference, and other noise:

$$S_{i_out}(f) = S_{i_shot_out} + S_{i_sig_spon} + S_{i_spon_spon}(f) + S_{MPI}(f) + S_{i_other}(f). \quad (4.4)$$

The SNR at the output of the device is therefore given by

$$SNR_{out} = \frac{\langle I_s \rangle^2}{\langle \Delta I_s^2 \rangle} = \frac{\Re^2 G^2 P_s^2}{S_{i_out}(f)}. \quad (4.5)$$

The shot noise is assumed to be Poisson distributed such that the noise figure as defined by Eq. (4.1) is:

$$\begin{aligned} F &= \frac{S_{i_shot_out} + S_{i_sig_spon} + S_{i_spon_spon}(f) + S_{i_MPI}(f) + S_{i_other}(f)}{G^2 S_{i_shot_in}} \\ &= \frac{1}{G} + \frac{S_{i_sig_spon} + S_{i_spon_spon}(f) + S_{i_MPI} + S_{i_other}}{2h\nu G^2 \Re^2 P_s}, \end{aligned} \quad (4.6)$$

where h is Planck's constant and ν is the optical frequency of the signal. If we consider the case of an optical receiver with a square optical bandpass filter of bandwidth B_0 , a laser source of linewidth $\Delta\nu$ and power P_s , and an optical amplifier of optical noise power spectral density ρ_{ASE} and gain G , but containing internal reflections R_1 and R_2 at its input and output, the total noise figure is:

$$\begin{aligned} F &= F_{shot} + F_{sig_spon} + F_{spon_spon} + F_{MPI} + F_{other} \\ &= \frac{1}{G} + \frac{1}{h\nu} \left[\frac{2\rho_{ASE}}{G} + \frac{2\rho_{ASE}^2}{G^2 P_s} B_0 \Lambda\left(\frac{f}{B_0}\right) + 2P_s R_1 R_2 \frac{2/\pi \Delta\nu}{1 + (f/\Delta\nu)^2} \right] + F_{other}, \end{aligned} \quad (4.7)$$

where $\Lambda(f)$ is a normalized triangular function with height 1 at $f = 0$, and height 0 at $f = 1$. In a well-controlled amplifier, the MPI term will not be present. However, if this is not the case, it can dominate over other noise terms inasmuch as it is both proportional to the signal power and to the gain of the amplifier (the effective reflection coefficient $R_{1/2}$ can be a function of the amplifier gain for double Rayleigh scatter). It should also be noted that the noise figure is not independent of the signal power even if MPI is ignored. However, the second term in brackets, corresponding to the

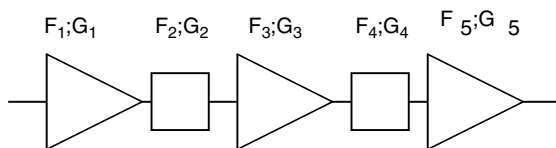


Fig. 4.1. A series of optical components with individual gains and noise figures.

spontaneous–spontaneous beat noise is inversely proportional to both the signal power and square of the gain, and proportional to the square of optical noise PSD (ρ_{ASE}), which is a small number. Therefore, if the signal powers are high, and an optical filter is being used at the photodetector, the signal–spontaneous beat noise will dominate and the noise figure reduces to the more common signal power independent form:

$$F = F_{shot} + F_{sig_spon} = \frac{1}{G} + \frac{2\rho_{ASE}}{h\nu G}. \quad (4.8)$$

In this reduced form, the usual microwave cascade formula can be used to calculate the total noise figure of a series of components [3]. A cascade formula also exists for the power-dependent form of the noise figure although it is more complicated [5].

For a series of components (see Fig. 4.1), which may be optical fibers (with only shot noise figure terms), or optical amplifiers (with shot noise and signal–spontaneous beat noise terms), the total noise figure is given by

$$F_{total} = F_1 + \frac{F_2 - 1}{G_1} + \frac{F_3 - 1}{G_1 G_2} + \cdots + \frac{F_{N-1} - 1}{G_1 G_2 \cdots G_{N-3} G_{N-2}} + \frac{F_N - 1}{G_1 G_2 \cdots G_{N-1}}. \quad (4.9)$$

Therefore, once the noise figure of the individual components has been characterized, the total noise figure for a system can be calculated.

It is fundamental to realize that although the noise figure is often measured in the optical domain, its definition remains in the electrical domain, and in its useful form (Eq. 4.8), only characterizes shot noise and signal–spontaneous beat noise.

If other noise sources such as multipath interference are included, the noise figure becomes frequency- and signal power-dependent, and therefore less useful for system design. Figure 4.2 shows the electrical noise figure measurements for a well-designed EDFA and a single-stage discrete Raman amplifier using 13 km of DSF. In the case of the EDFA, both optical and electrical measurements of the noise figure agree well at around 5 dB with gains of 12 and 26 dB. Some measurement noise is apparent at frequencies below 50 MHz. The Raman amplifier shows a significant discrepancy between optical and electrical measurements of the noise figure. Multipath interference caused by double Rayleigh scattering leads to an increase in the noise at low frequencies. At relatively low gains and frequencies of about 200 MHz, the optical and electrical measurements converge. At high gains, the impact of MPI is large and can be seen to extend up to much higher frequencies. The electrical noise figure for the Raman amplifier will vary with both gain and input signal power. Although this measurement can be used to show the presence of MPI,

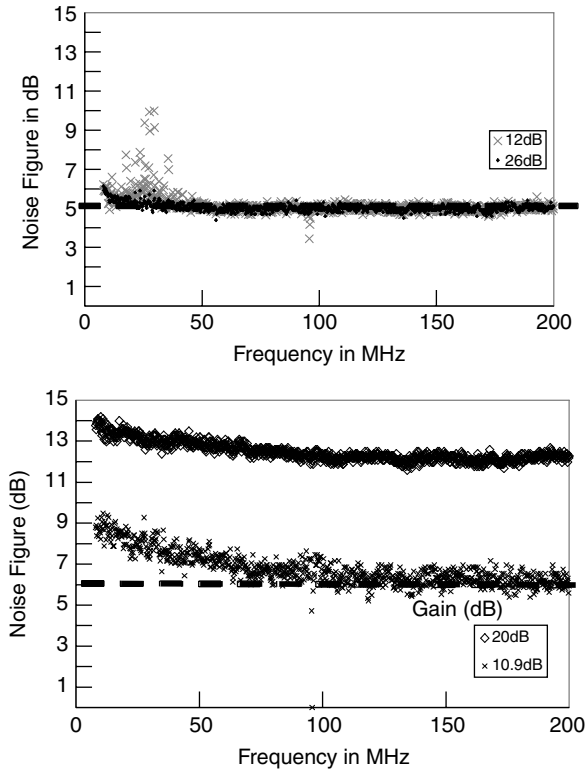


Fig. 4.2. Noise figure measured electrically for EDFA (left) with optical noise figure of 5 dB, and Raman amplifier (right) with optical noise figure of 6 dB. Dashed lines indicate optical measurements and dots indicate electrical measurements.

it is not a particularly helpful measurement for characterizing a system. It is more useful to be able to quantify the amount of MPI and ASE separately because the penalties caused by each noise source are different. ASE can be quantified by an optical measurement of the noise figure whereas MPI can be determined using electrical measurements. Therefore, when discussing the linear noise performance of a Raman amplifier, it is assumed that we are considering only the buildup of spontaneous emission.

4.4. Effective Noise Figure

The concept of an effective noise figure (ENF) can be used to compare *linear* transmission systems with and without distributed amplification [12]. However, in a real transmission fiber, distributed Raman amplification will change the signal powers as they propagate down the fiber. In a nonlinear system this will lead to changes in four-wave mixing, self-phase modulation, cross-phase modulation, and interchannel

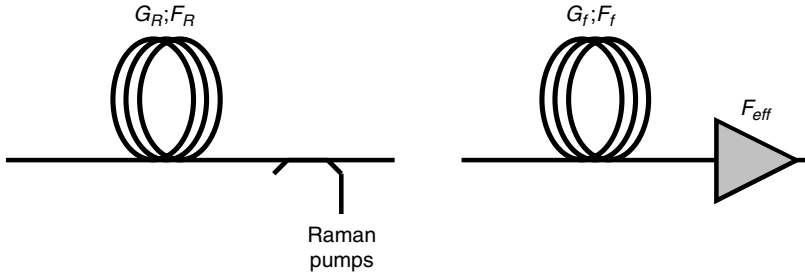


Fig. 4.3. Configuration for defining effective noise figure.

stimulated Raman scattering. The increase in nonlinearities is dealt with later in this book.

The definition of effective noise figure is the noise figure of an imaginary optical amplifier that provides the same noise performance benefit of the Raman pumped transmission fiber (see Fig. 4.3). Here G_R and F_R are the gain and noise figure of the Raman pumped transmission system. G_f and F_f are the gain (1/fiber loss) and noise figure of the unpumped transmission system. Note that G_R and G_f may be less than 1, indicating that there is a net loss in the transmission fiber. F_{eff} is the noise figure of an imaginary optical amplifier placed at the end of the transmission system giving the same noise performance as the Raman pumped system.

Equating the two systems we have:

$$F_R = F_f + \frac{F_{eff} - 1}{G_f}. \quad (4.10)$$

Therefore, the effective noise figure F_{eff} can be found:

$$F_{eff} = F_R G_f. \quad (4.11)$$

The effective noise figure can have a negative value since Eq. (4.11) is the ratio of the noise figures for the pumped and unpumped transmission fiber.

A discrete amplifier such as an EDFA may be included in a composite effective noise figure. This can be found by equating the total noise figure for the system in the case with Raman amplification, and an imaginary system with an EDFA with an effective noise figure (see Fig. 4.4).

$$F_R + \frac{F_{EDFA} - 1}{G_R} = F_f + \frac{F_{eff} - 1}{G_f}. \quad (4.12)$$

Therefore, rearranging the equation above,

$$F_{eff} = F_R G_f + (F_{EDFA} - 1) \frac{G_f}{G_R}. \quad (4.13)$$

The equivalent imaginary discrete amplifier suppresses the noise generated from the real discrete EDFA, by the added gain in the transmission fiber. If there is sufficient

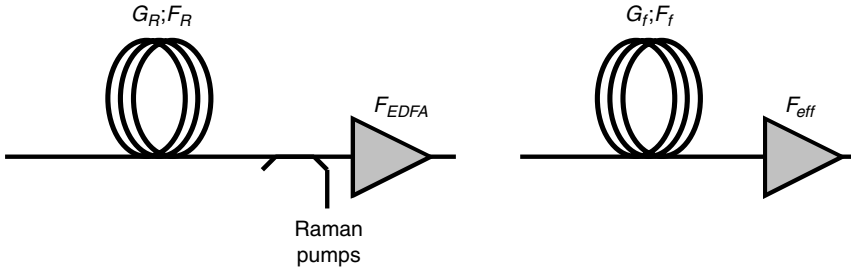


Fig. 4.4. Configuration for defining effective noise figure, including a discrete amplifier.

gain, the effective noise figure may be below the quantum limit of 3 dB for a discrete amplifier, and can be negative. This result does not indicate that the distributed amplifier subtracts noise from the signal. Instead, it shows the noise figure that a discrete amplifier at the end of the fiber span would have to possess to exhibit the same noise performance as the distributed amplifier. In effect, the distributed amplifier can outperform the best theoretical discrete amplifier. The effective noise figure is inversely proportional to the optical signal-to-noise ratio (OSNR), so that if the effective noise figure decreases by 1 dB, the OSNR will improve by 1 dB.

4.5. General Signal Model

This section considers the steady-state propagation of signals and pumps in Raman amplified systems. Compared with current data rates, the energy provided by the Raman pumps is transferred almost instantaneously to the signals, such that the gain experienced by those signals can be calculated from the instantaneous pump power at a given point in the fiber. If there are significant low-frequency data or large numbers of channels are suddenly added or dropped in a DWDM system, large power transients may result [6]. In these cases, the effect of dispersion would be important for copumped amplifiers, and the effective (interaction) fiber length would be important for counter-pumped amplifiers. The fast-gain dynamics of Raman amplifiers is dealt with later in this book. To analyze the steady-state propagation of the signals and pumps, a time-independent set of differential equations may be used. Simple analytical expressions may be derived [7, 8] for the SRS interaction of a single pump and signal beam although all rely on assumptions of an undepleted pump, and may not be extended to multiple pump wavelengths or DWDM systems. Tariq and Palais [9] were probably first to present numerically modeled results of the SRS interactions between copropagating signal channels in standard transmission fibers. Here this model was extended to include the interactions between both copropagating signal channels and counterpropagating pumps. A similar model has also been proposed by Kidorf et al. [10].

First, high signal powers may lead to a depletion of the pump as all the energy is transferred to the signals by the stimulated emission. Second, a numerical model can

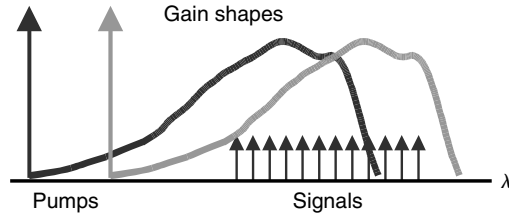


Fig. 4.5. Distribution of pump and signal wavelengths.

also take account of multiple pumps, which can be used to flatten the gain spectrum. Finally, both signals and pumps will transfer energy among themselves and this effect is shown to become much stronger as the pump wavelengths become separated and longer wavelength pumps fall into the gain bandwidth of shorter wavelength pumps (see Fig. 4.5).

In general, the steady-state propagation of the N signals and P pumps in the optical fiber can be described by

$$\frac{1}{P_{si}} \frac{dP_{si}}{dz} = -\alpha_{si} + \sum_{j=1}^P C_{ps_ji} P_{pj} + \sum_{j=1}^{i-1} C_{ss_ji} P_{sj} - \sum_{j=i+1}^N \left(\frac{\nu_{si}}{\nu_{sj}} \right) C_{ss_ij} P_{sj} \quad (4.14)$$

$$\frac{1}{P_{pi}} \frac{dP_{pi}}{dz} = -\alpha_{pi} + \sum_{j=1}^N \left(\frac{\nu_{pi}}{\nu_{sj}} \right) C_{ps_ij} P_{sj} + \sum_{j=1}^{i-1} C_{pp_ij} P_{pj} - \sum_{j=i+1}^P \left(\frac{\nu_{pi}}{\nu_{pj}} \right) C_{pp_ji} P_{pj}, \quad (4.15)$$

where P_{si} and P_{pi} are the instantaneous power of the i th signal at optical frequency ν_s , and i th pump at optical frequency ν_p , respectively, at point z along the fiber. α_s and α_p are the fiber attenuation for the signals and pumps. C_{ps} , C_{ss} , C_{pp} are the Raman gain efficiency coefficient between the pumps and signals, signals and signals, and pumps and pumps, respectively. These equations neglect the buildup of spontaneous emission which may be considered separately.

The first term in Eqs. (4.14) gives the linear fiber loss and the second term is the power gained from the pump wavelengths. The third and fourth terms represent the power gained from shorter wavelength signals and lost to longer wavelength signals, respectively, resulting in SRS gain tilt. The first term in Eq. (4.15) also represents the linear fiber loss and the second term gives the power lost to the signals resulting in saturation of the amplifier. The third and fourth terms give the Raman interactions between the pump wavelengths where the third terms represent the power gained from shorter wavelengths, and the fourth term gives the power lost to longer wavelength pumps. It is assumed that the pumps and signals are arranged in order of increasing wavelength. The $-/+$ sign at the start of Eq. (4.15) allows for the case of a counterpropagating or copropagating pump, respectively.

Accurate modeling of WDM systems pumped with multiple Raman pumps may be performed using fiber loss and Raman gain efficiency data gained from measurements. The counter-pumped case represents a two-point boundary condition problem where

the signal and pump powers are known at the start and end of the fiber, respectively. These types of problems may be solved using “shooting” or “relaxation” techniques, or a deferred correction technique with Newton iteration.

4.5.1. Analytical Signal Model

Although the complete modeling of Raman amplifiers requires the signal and pump propagation equations to be solved numerically, closed-form analytical expressions can be useful in giving some insight into the signal behavior in the gain fiber. For the case of a single pump and signal with negligible depletion of the pump, Eq. (4.15) may be greatly simplified and solved as [7],

$$P_p(z) = P_{p0} \exp(-\alpha_p(L - z)) \quad (4.16)$$

$$P_p(z) = P_{p0} \exp(-\alpha_p z) \quad (4.17)$$

for a counter- or copumped amplifier, respectively, of length L . Because there is only a single signal, there is no SRS interaction and Eq. (4.15) may be easily solved:

$$P_s(z) = P_s(0) \exp \left(-\alpha_s z + C_R P_p(0) \left(\frac{e^{-\alpha_p L} [e^{\alpha_p z} - 1]}{\alpha_p} \right) \right) \quad (4.18)$$

$$P_s(z) = P_s(0) \exp \left(-\alpha_s z + C_R P_p(0) \left(\frac{1 - e^{-\alpha_p z}}{\alpha_p} \right) \right) \quad (4.19)$$

for a counter- or copumped amplifier, respectively, with Raman gain efficiency C_R . The net gain (G) at the end of the fiber of length L for both pump configurations is:

$$G = T \cdot G_a = \exp(-\alpha_s L + C_R P_p(0) L_{eff}), \quad (4.20)$$

where T is the loss of the fiber, G_a is the “added Raman gain” and L_{eff} is the effective length of the fiber that is determined at the pump wavelength:

$$L_{eff} = \frac{1 - e^{-\alpha_p L}}{\alpha_p}. \quad (4.21)$$

In the undepleted pump approximation, the signal profile can be expressed independently of the Raman gain efficiency coefficient or pump power by substituting for the added Raman gain. For the co- and counter-pumped amplifier with added gains G_f and G_b , respectively,

$$P_s(z) = P_{s0} \exp \left[-\alpha_s z + \frac{\ln(G_f)}{L_{eff}} \frac{1 - e^{-\alpha_p z}}{\alpha_p} + \frac{\ln(G_b)}{L_{eff}} \frac{e^{-\alpha_p L} (e^{\alpha_p z} - 1)}{\alpha_p} \right]. \quad (4.22)$$

The Raman gain efficiency (C_R) and attenuation at the pump wavelength determine how much pump power is required to achieve a given gain. However, the power profile of the signal is governed only by the attenuation of the fiber at the pump and signal wavelengths.

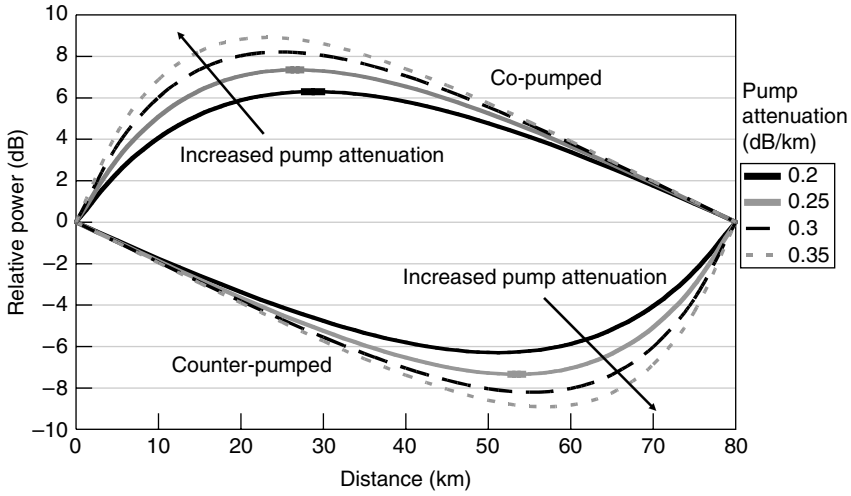


Fig. 4.6. Relative power profile of signal in 80 km fiber compensated using Raman amplification. Top shows copumped fiber, bottom shows counter-pumped fiber. Signal attenuation is 0.2 dB/km.

The effect of the fiber attenuation on 80 km of fiber made transparent using a co- or counterpropagating Raman pump can be seen in Fig. 4.6. When the Raman pump is copropagating with respect to the signal, the pump power will be strongest at the start of the fiber resulting in a large amount of gain (see top set of traces). Fiber attenuation at the pump wavelength will reduce the power of the pump, resulting in a gradual reduction in gain. Eventually the fiber loss will dominate the signal profile. With a counter-pumped configuration, there is little pump power at the start of the fiber and the signal undergoes linear loss from the fiber attenuation. The pump power from the end of the fiber becomes progressively stronger such that the signal experiences gain in the last part of the fiber. The effect of greater attenuation at the pump wavelength can also be seen in Fig. 4.6. As this attenuation is increased, the gain becomes concentrated towards the ends of the fiber and the excursions of the signal profile become wider.

For a fixed level of gain, the pump power is approximately proportional to the attenuation at the pump wavelength ($P_p \propto 1/L_{eff}$). This is important since to obtain gain in the conventional erbium band (1530 to 1565 nm), pumps are required at 1420 to 1460 nm which lies close to the OH^- absorption peak in many fiber types. Some modern transmission fibers have removed this excess fiber loss through better manufacturing methods allowing Raman pumps to be used more efficiently.

4.6. Modeling Noise

The accumulation of spontaneous emission in a Raman amplifier can be modeled using differential equations. Stolen and Bosch showed in 1982 [11] that the spontaneous emission spectrum has a temperature dependence, and Hansen et al. [12] included the

coupling between forward and backward traveling ASE which becomes important at high gains. For multiple pump wavelengths, the propagation and accumulation of ASE for a co- or counter-pumped amplifier can be described by

$$\frac{d\rho_a^+(z)}{dz} = -\alpha_s \rho_a^+(z) + \sum_i C_{Ri} P_{pi}(z) (\rho_a^+(z) + h\nu E_i) + S\alpha_R \rho_a^-(z) \quad (4.23)$$

$$-\frac{d\rho_a^-(z)}{dz} = -\alpha_s \rho_a^-(z) + \sum_i C_{Ri} P_p(z) (\rho_a^-(z) + h\nu E_i) + S\alpha_R \rho_a^+(z), \quad (4.24)$$

where ρ_a is the optical power spectral density in 1 polarization mode and 1 Hz bandwidth of the forward or backward traveling wave, α_s is the fiber attenuation at the signal wavelength, C_R is the Raman gain efficiency coefficient, P_{pi} is the power of the i th Raman pump, h is Planck's constant, ν is the optical frequency of the ASE, S is the Rayleigh backscatter capture coefficient, α_R is the Rayleigh scattering loss, and E is the spontaneous emission factor. This is a Bose–Einstein distribution, and takes into account the thermal population of optical phonons in the ground state [13–15]:

$$E = 1 + \frac{1}{\exp\left(\frac{h\Delta\nu}{kT}\right) - 1}, \quad (4.25)$$

where k is Boltzman's constant, T is the temperature in Kelvin, and ν is the frequency difference between the pump and signal. The first term in Eqs. (4.23) and (4.24) represents the linear loss due to fiber attenuation whereas the second term represents both the generation of spontaneous noise, and the amplification of the noise by the Raman pumps. The final term provides the coupling between forward and backward traveling ASE due to Rayleigh scattering.

The powers of the backward propagating pumps and forward propagating signals are first calculated along the fiber length, assuming that the ASE causes negligible saturation when compared to the signals. Equations (4.23) and (4.24) may then be solved numerically as a two-point boundary value problem where $\rho_a^+ = 0$ at $z = 0$ and $\rho_a^- = 0$ at $z = L$.

4.6.1. Analytical Approximations

If the signal is assumed to be very small compared to the pump such that depletion of the pump is negligible, the propagation of the pump for co- and counter-pumped configurations is given by

$$P_p(z) = P_{p0} \exp(-\alpha_p z) \quad (4.26)$$

$$P_p(z) = P_{p0} \exp(-\alpha_p (L - z)). \quad (4.27)$$

Ignoring Rayleigh scattering of the ASE, Smith [16] derived analytical expressions for the resultant ASE produced by co- and counter-pumped amplifiers. These may be easily modified to include the Bose–Einstein factor (E). These equations have been

extended here, for the case where co- and counter-pumping are used at the same time:

$$\begin{aligned} \rho_a(z) = & h\nu E \int_0^z \left[\frac{\ln(G_f)}{L_{eff}} e^{-\alpha_p \xi} + \frac{\ln(G_b)}{L_{eff}} e^{-\alpha_p (L-\xi)} \right] e^{-\alpha_s (z-\xi)} \\ & \times \exp \left\{ \frac{\ln(G_f)}{L_{eff}} \frac{e^{-\alpha_p \xi} - e^{-\alpha_p z}}{\alpha_p} + \frac{\ln(G_b)}{L_{eff}} \frac{e^{-\alpha_p L} (e^{\alpha_p z} - e^{\alpha_p \xi})}{\alpha_p} \right\} d\xi, \end{aligned} \quad (4.28)$$

where G_f and G_b are the added gains from the copump and counter-pump (i.e., ignoring fiber loss), respectively, and L_{eff} is the effective length at the pump wavelength:

$$L_{eff} = (1 - e^{-\alpha_p L}) / \alpha_p. \quad (4.29)$$

Chinn [17] later simplified the counter-pumped case using Gamma functions (Γ) and incomplete Gamma functions (I). For the counter-pumped amplifier:

$$\begin{aligned} \rho_a(L) = & E h \nu C_R P_{p0} \int_0^L \exp \left(-(\alpha_s + \alpha_p)z + C_R P_{p0} \frac{(1 - e^{-\alpha_p L})}{\alpha_p} \right) dz \\ = & E h \nu \left(\frac{\alpha_p}{C_R P_{p0}} \right)^{\alpha_s / \alpha_p} \exp \left(\frac{C_R P_{p0}}{\alpha_p} \right) \Gamma \left(1 + \frac{\alpha_s}{\alpha_p} \right) \\ & \times \left[I \left(1 + \frac{\alpha_s}{\alpha_p}, \frac{C_R P_{p0}}{\alpha_p} \right) - I \left(1 + \frac{\alpha_s}{\alpha_p}, \frac{C_R P_{p0}}{\alpha_p} e^{-\alpha_p L} \right) \right]. \end{aligned} \quad (4.30)$$

If the attenuation at the pump and signal wavelengths is assumed to be equal, the above expression simplifies greatly:

$$\rho_a(L) = E h \nu \left[\left(1 + \frac{\alpha}{C_R P_{p0}} e^{\alpha L} \right) G - \left(1 + \frac{\alpha}{C_R P_{p0}} \right) \right], \quad (4.31)$$

where the net gain for the span (G) is:

$$G = \exp(-\alpha_s L + C_R P_{p0} L_{eff}). \quad (4.32)$$

4.7. Measurements of ASE Performance of Raman Amplifiers and Comparison with Simulations

Expressions using the undepleted pump approximation are useful for quick estimates of amplifier behavior but are inaccurate for analyzing the performance of real Raman amplifiers. Numerical simulations allow the following factors to be taken into account when determining the noise performance of real Raman amplifiers.

4.7.1. Rayleigh Scattering of ASE

As the gain becomes large within the amplifier, there is a significant contribution to the forward ASE, from Rayleigh scattered ASE that was traveling in the backward direction. As this contribution becomes larger and larger, the amplifier will eventually lase. A single-cavity discrete Raman amplifier was constructed using 12.7 km of dispersion-shifted fiber. The pump at 1455 nm was counterpropagated using optical circulators (see Fig. 4.7(a)). The gain and noise figure were measured

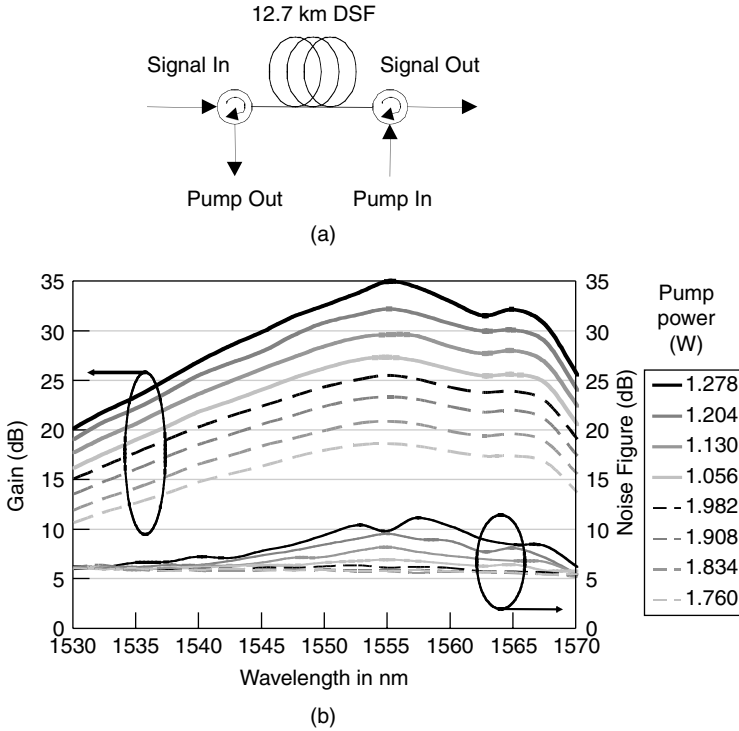


Fig. 4.7. (a) Experimental configuration and (b) measured increase in optical noise figure due to coupling of forward and backward ASE in a 12.7 km discrete Raman amplifier with pump at 1455 nm.

optically using a swept wavelength technique. The noise figure remains at about 6 dB until the gain becomes large enough such that Rayleigh scattered ASE is coupled between backward and forward directions. Between 1 and 1.2 W, the noise figure spectra begin to follow the form of the gain spectra because the ASE coupling will be greatest at wavelengths where the gain is highest. At very high gains of beyond 32 dB, the amplifier begins to lase and the ASE spectrum becomes unstable.

Multiple-stage discrete amplifiers may be constructed where each stage is isolated. Backward traveling ASE from the second-gain stage is prevented from entering the first-gain stage so that the coupling between forward and backward traveling ASE is greatly reduced. In a distributed amplifier where there is little opportunity to place isolators in the transmission path, Rayleigh scattered ASE can place a limit on the maximum gain achievable [12]. Figure 4.8 shows optical measurements and numerical simulations of the fiber loss and effective noise figure for a 88 km length of standard fiber (NDSF) pumped using a 1455 nm fiber laser. The signal and noise measurements were performed on a 1550 nm DFB laser. It can be seen that the fiber loss decreases linearly with increased pump power, eventually becoming transparent at about 700 mW. The effective noise figure (defined using Eq. (4.11)) begins to show

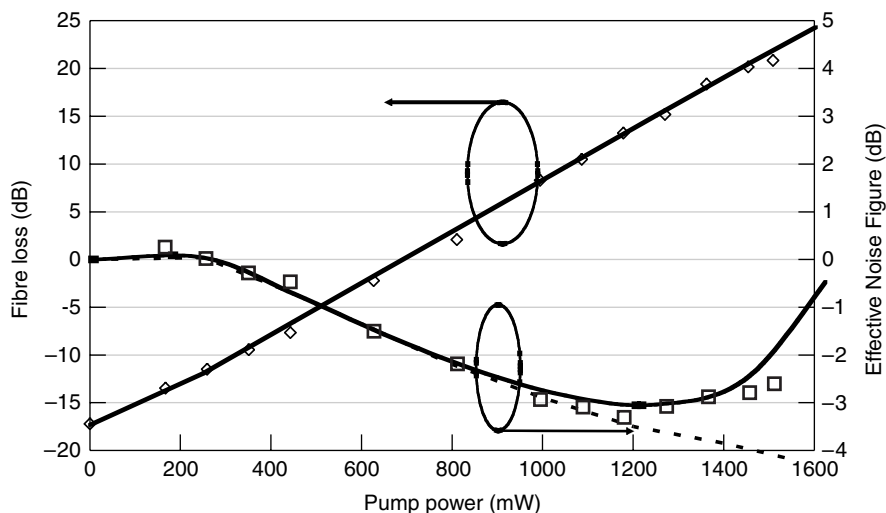


Fig. 4.8. Gain and effective noise figure for 88 km of standard fiber (NDSF), pumped at 1455 nm. Dots show measurements and lines show numerical simulations. Dashed line indicates analytical solution. Backscatter coefficient $S = 0.00125$.

an improvement after a few hundred milliWatts, and then displays an almost linear decrease with pump power. At about 1200 mW, the gain in the fiber becomes large enough to make Rayleigh scattering of the ASE significant, after which increased gain results in a higher effective noise figure and worse performance. The analytical calculations can be used to determine the performance if the Rayleigh scattering were removed. In this case, the effective noise figure (shown as a dotted line) would continue to decrease with more pump power, suggesting a better system performance.

Numerical solutions (shown as solid lines) give very good agreement with the measured data. The backscatter coefficient for NDSF was determined from a separate measurement of the single Rayleigh backscatter from a signal laser that showed the reflected signal was -32 dB weaker than the forward traveling signal. It is clear that the analytical solution will give reasonable agreement when the Raman gain remains low.

4.7.2. Temperature-Dependent ASE

The Raman effect is a very low noise process, and in most single-channel cases amplification will result in the emission of nearly one spontaneous photon per mode. In single-channel experiments where the pump and signal are separated by about 13 THz (the peak for the silica Raman gain spectrum), this is quite a good approximation to make. An ultrabroadband WDM system may have wavelength channels that lie close to Raman pump wavelengths. As the difference between pump and signal frequencies becomes small and therefore the energy difference between the ground and first energy level becomes small (see Fig. 4.9(a)), there is an increased probability of finding the glass molecule at the first energy level rather than the ground state. This results in

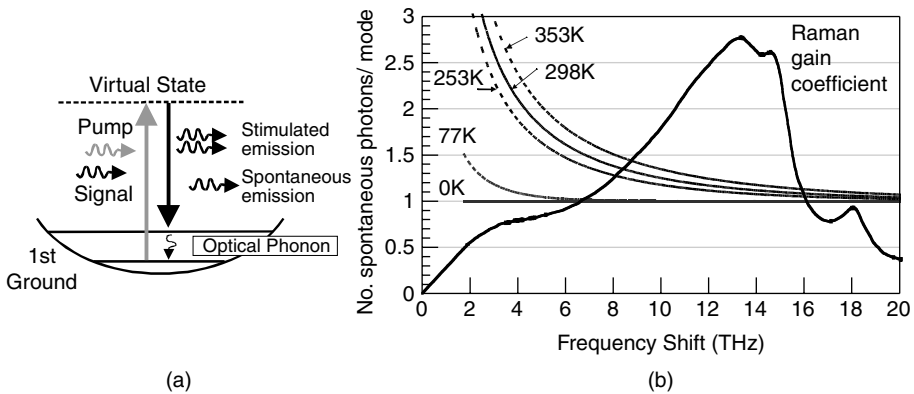


Fig. 4.9. (a) Energy level diagram for stimulated and spontaneous emission; (b) number of spontaneous photons/mode for different frequency shifts and temperatures.

a greater probability of spontaneous emission when the pump photon is incident on the molecule, and therefore a larger amount of spontaneous noise from the amplifier. Figure 4.9(b) shows the number of spontaneous photons per mode that would be emitted at each frequency shift along the silica Raman gain spectrum at various temperatures. It can be seen that at 0K, the optimum of one photon per mode is emitted. As the temperature increases, there is a dramatic increase in the amount of spontaneous emissions at shorter frequency shifts. At room temperatures, a noticeable tilt appears across the gain spectra, even at frequency shifts of between 10 and 14 THz.

Because the gain peak lies at shifts of about 13 THz where the noise emission tends to one photon per mode, it might be expected that this increase in emission at small frequency shifts could be ignored. In order to investigate the temperature dependence of a broadband-distributed Raman amplifier, a pump unit was constructed, giving 95 nm of flat gain across the C- and L-band. A spool of 80 km NZ-DSF was placed in a temperature-controlled chamber and counter-pumped using 1423, 1443, 1464, and 1495 nm polarization and wavelength multiplexed diodes. Splices and connectors were kept outside the chamber since these can also show temperature-dependent loss. Figure 4.10 shows the span loss spectrum for 80 km fiber, both with and without Raman gain. The pump unit is able to provide gain of 13 dB, between 1517 nm and 1612 nm with only 2 dB of ripple, without the use of gain-flattening filters. There was no variation in the gain spectrum when the temperature was varied between -20°C and $+80^{\circ}\text{C}$, whereas below -20°C , microbending caused excess losses in the fiber. The amount of added Raman gain is slightly higher at shorter wavelengths to allow for greater span loss. The effective noise figure for the Raman-pumped fiber can also be seen in Fig. 4.10 and shows a worse performance at shorter wavelengths. This is predominantly due to increased spontaneous emission as the pump and signal wavelengths approach each other, although the effect of increased fiber attenuation pump wavelengths and interpump SRS also contribute. Numerical simulations give excellent agreement and can show the result of reducing the spontaneous noise factor (E) to 1 photon per mode (at 0K). It can also be seen that a temperature variation

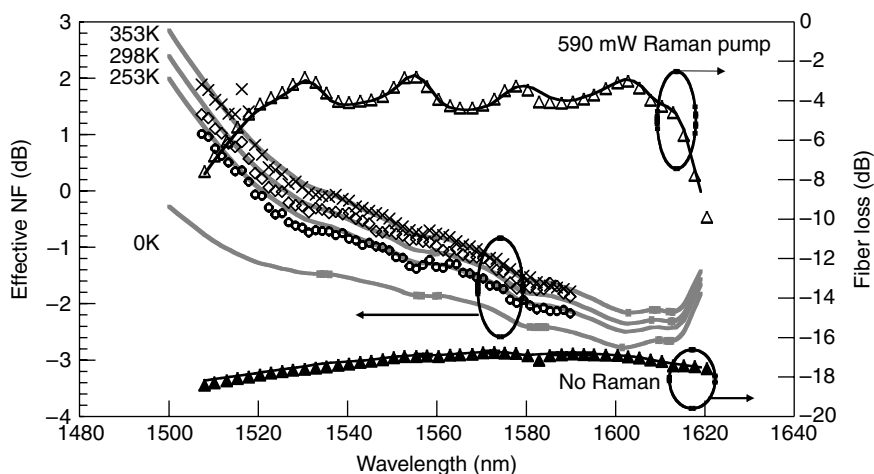


Fig. 4.10. Effective noise figure and span loss for 80 km distributed amplifier at various temperatures.

of between -20°C and 80°C causes approximately 1 dB change in the effective noise figure at short wavelengths. This temperature dependence would need to be taken into account when allocating a system budget where cables suspended along telegraph pylons may experience temperatures of -40°C whereas those traversing deserts may be at $+80^{\circ}\text{C}$.

The reason for the large increase in spontaneous emission at shorter wavelengths can be understood by decomposing the gain spectrum into its constituent components provided by each pump wavelength. Figure 4.11 shows the results using the pump unit above, but providing roughly 10 dB gain. It is noticeable that the longest pump wavelength at 1495 nm provides the largest amount of gain over the entire bandwidth. Even at 1525 nm, this pump supplies 25% of the total gain. This is not always obvious when setting the relative pump powers inasmuch as the Raman interactions between the pumps will transfer energy from the shorter to the longer wavelength pumps. The increase in temperature-dependent noise at signal wavelengths around 1525 nm can be attributed to the significant contribution to the gain of the 1495 nm pump, and increased spontaneous noise factor as signals approach the pump wavelengths.

4.7.3. Multiple Pump Interactions

Another contribution to the tilt in the effective noise figure spectrum can be understood by studying the interaction of the pump wavelengths in the fiber. The pump wavelengths will also act as Raman pumps for each other so that shorter wavelengths will transfer energy to the longer wavelengths. This has some advantages in that to obtain a roughly flat gain spectrum, most of the gain should be provided by the longest wavelength pump. If there were no pump interactions, the longest pump wavelength would need to be launched with the highest energy whereas the pump interactions allow this pump to obtain energy from several lower energy pumps at shorter wavelengths.

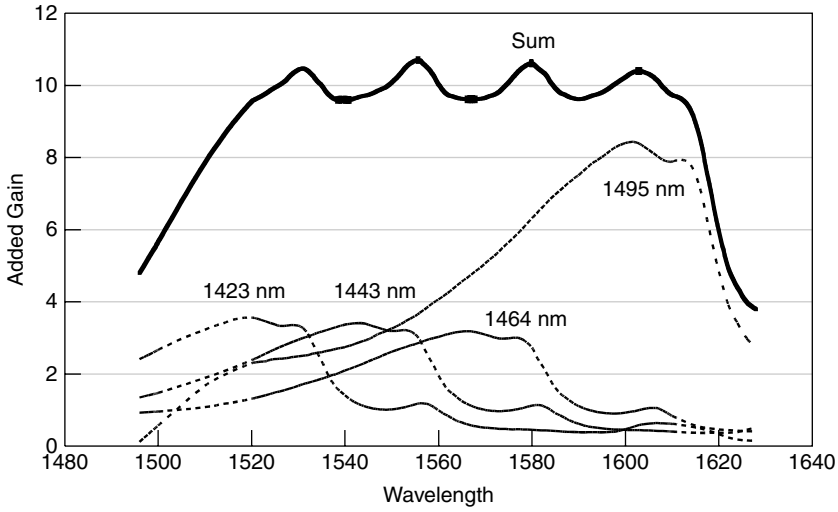


Fig. 4.11. Simulation showing relative contributions to a 10 dB flat gain spectrum from pumps at 1423, 1443, 1464, and 1495 nm.

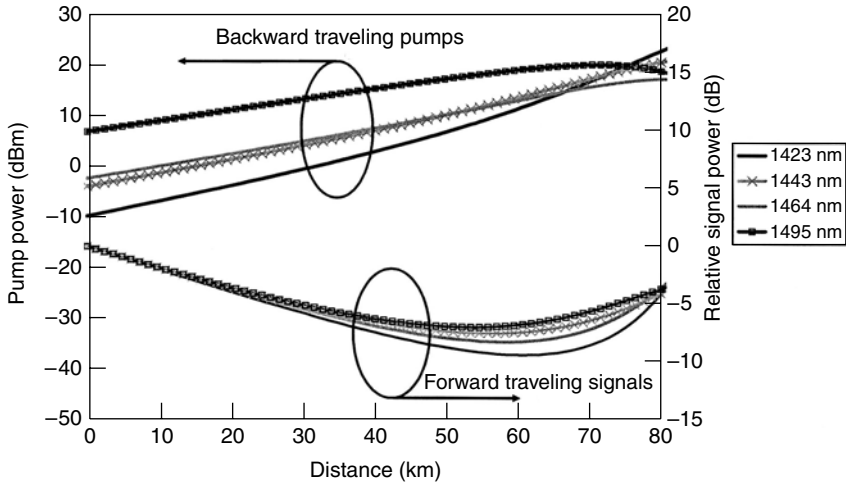


Fig. 4.12. Power evolution of backward traveling pumps (upper lines) and forward traveling signals (lower lines). Pump wavelengths are at 1423, 1443, 1464, and 1495; signal wavelengths are at 1530, 1555, 1577, and 1602 nm.

However, this pump interaction has important implications for the noise performance of different wavelength channels in a WDM system. The evolution of the backward traveling pumps for the four-pump Raman module that was constructed can be seen in Fig. 4.12. It is noticed that although the shortest wavelength pump at 1423 nm is launched with the highest power, it is quickly drained by the other pump wavelengths and has the lowest power after 15 km of fiber. The 1495 nm pump

actually receives gain in the first 10 km and maintains a relatively high power throughout the rest of the fiber at the expense of the other pump wavelengths. This pump will therefore give the largest total gain and provide gain deeper into the transmission fiber.

Four signal channels at 1530, 1555, 1577, and 1602 nm which correspond to the peak gain wavelengths from each individual pump (see Fig. 4.12) initially undergo the linear loss of the fiber. At roughly 40 km into the fiber the forward propagating signals begin to interact with the backward propagating pumps. Since the 1423 nm pump has a higher power at this point in the fiber, the 1602 nm channel receives the greatest gain. On the other hand, the 1525 nm channel receives most of its gain at the far end of the fiber.

In the counter-pumped configuration, the shorter wavelength pumps will therefore provide most gain at the end of the fiber, whereas longer wavelength pumps are able to extend gain further into the transmission fiber. Hence the effective noise figure or OSNR spectrum tends to show longer wavelength channels performing better than shorter wavelength channels.

Figure 4.13 shows measurements and numerical simulations of the fiber loss and effective noise figure for 80 km of fiber using four-pump wavelengths. The pump power at each wavelength is varied in order to achieve an optimum flat gain spectrum and measurements were performed using a low-power swept wavelength source. As the total pump power is increased and the fiber loss is reduced, the effective noise figure decreases. The results indicate that shorter wavelength channels perform worse than longer wavelength channels, and that this difference becomes greater as the total pump power is increased. Numerical simulations can also be used to determine the effective noise figure if pump-to-pump interactions were eliminated (dotted lines), but at the same time, the pump powers are adjusted to give the same gain spectrum. This reduces the performance difference over the 95 nm bandwidth from 3 dB to 1.5 dB. As the gain is increased, the effective noise figure curves remain almost parallel to one another whereas if pump interactions are included, the long wavelength channels receive more benefit.

The remaining performance difference is mainly due to the increase in spontaneous emission as the signal wavelengths approach the pump. The lowest dotted line shows simulations with no pump-to-pump interactions and a temperature of 0K. The effective noise figure is almost flat at -2 dB and shows the same ripple as the gain curve.

4.7.4. Linear Noise Performance Under DWDM Conditions

Raman amplifiers offer great potential because of their ability to provide gain over a large bandwidth. In a distributed Raman amplifier, the power of an individual signal channel is likely to be small in comparison to the pump and will cause very little pump depletion. In a DWDM system the channel count may be as high as 100 channels, with individual signal channel launch powers typically between 0 and +5 dBm. Together, these signals may present powers that are enough to saturate the Raman gain, requiring an increase in pump powers. As well as necessitating higher-power pumps for DWDM systems, complex control algorithms are needed for multiple wavelength Raman amplifiers because saturation will not be homogeneous.

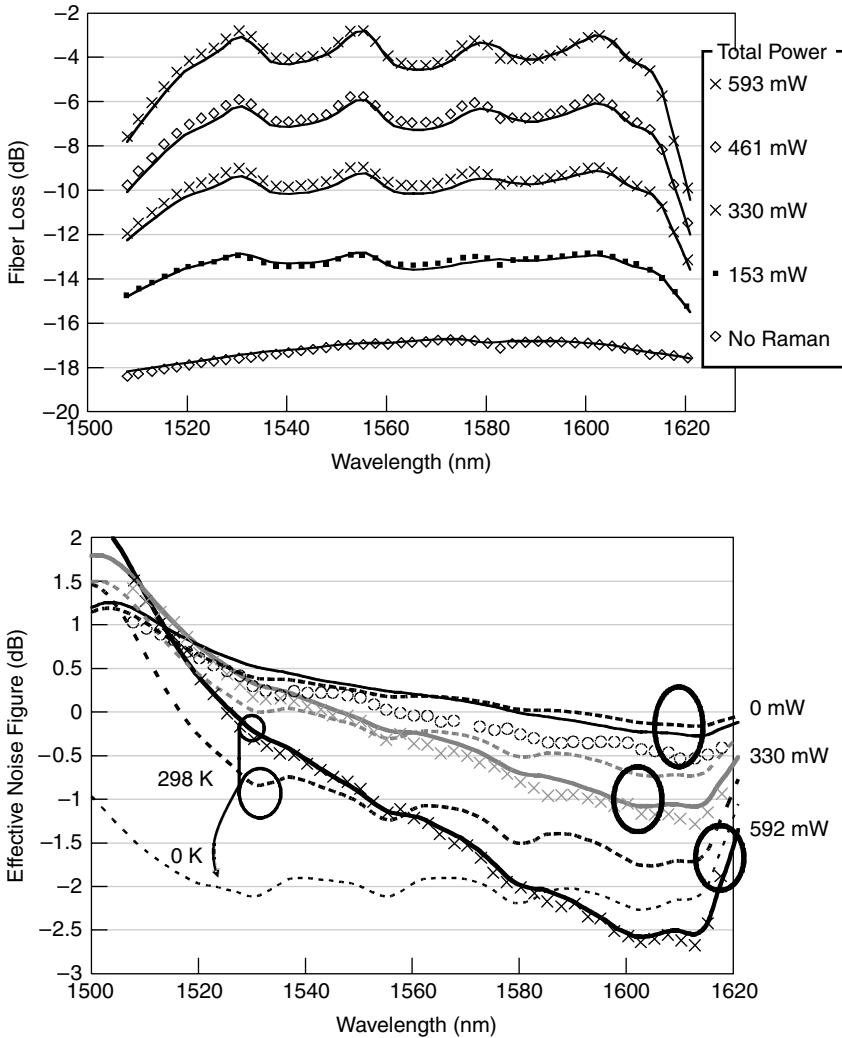


Fig. 4.13. (a) Fiber transmission loss and (b) effective noise figure for 80 km TrueWave® RS counter-pumped at 1423, 1443, 1464, and 1495 nm with various total pump powers. Dots show measurements, solid lines show numerical solutions, and dashed lines indicate numerical solutions without pump-to-pump interactions.

An experiment was performed using 39 signal channels between 1530 and 1560 nm, placed on the ITU grid. These were wavelength multiplexed and launched into 80 km TrueWave® RS (NZ-DSF). The laser drive currents were optimized to maintain the signal powers to within 0.5 dB of one another, and an attenuator allowed all signal powers to be varied between -10 dBm/ch and $+7$ dBm/ch. A polarization scrambler operating at several MHz was used to broaden the signal spectrum to alleviate any Brillouin scattering.

The 80 km fiber was then counter-pumped using 1423, 1443, and 1464 nm FBG semiconductor diode lasers. At low-signal launch powers, the pumps were able to compensate for the entire span loss (see Fig. 4.14(a)). As the signal power is increased to typical operating conditions (0 dBm/ch), pump depletion occurs and the overall gain is reduced. The effective noise figure (Fig. 4.14(b)) increases due to a drop in gain, and the tilt in the gain and effective noise figure becomes greater due to SRS interaction between the channels. Numerically modeled results including pump depletion give good agreement with the measured data.

It might be expected that inasmuch as the gain spectrum is a composite one, produced by three individual pumps, the behavior of the amplifier is heterogeneous. This is indeed the case when the Raman amplifier is saturated by a single wavelength channel [18]. The saturation spectrum can, however, behave almost homogeneously when

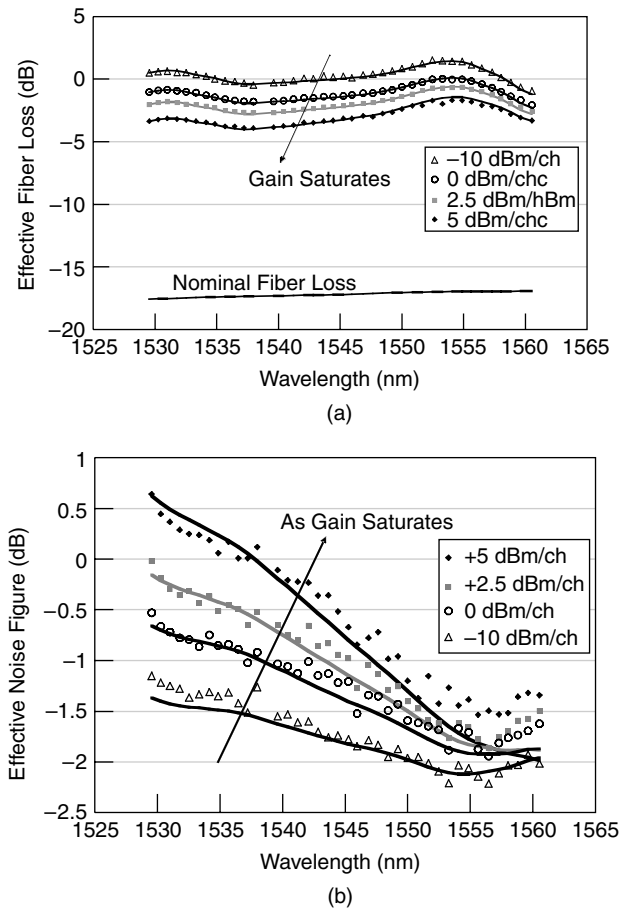


Fig. 4.14. Gain saturation of an 80 km distributed Raman amplifier using TrueWave® RS (NZ-DSF) and (b) effective noise figure. Dots show measured results and solid lines show simulations.

saturated by a DWDM signal, extracting power from many pump wavelengths [19]. A large amount of the total pump power is launched at the shortest wavelength due to pump-to-pump interactions. A DWDM system may significantly deplete this pump wavelength, reducing the gain for short wavelength channels and reducing the amount of power available to be drained by the longer wavelength pumps. Because the long-wavelength pumps have less power, they also provide less gain. The overall result is a gain spectrum that saturates almost homogeneously although SRS interaction between signal channels can produce some tilt.

A control loop may be adopted to modify the pump powers at 1423, 1443, and 1464 nm, in order to maintain the gain at a constant level. An optical spectrum analyzer was used to measure the signal powers, and the pump powers were modified to clamp the gain. The effective fiber loss (shown in Fig. 4.15(a)), was kept constant at about -5 dB although the signal launch power was varied from -10 dB/ch to $+5$ dB/ch. A small discrepancy of about 0.8 dB can be seen at 1555 nm, due to

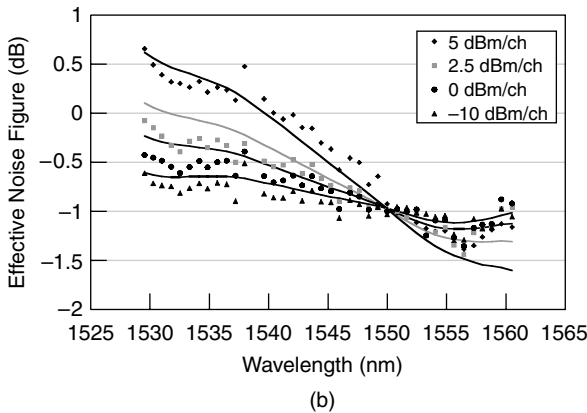
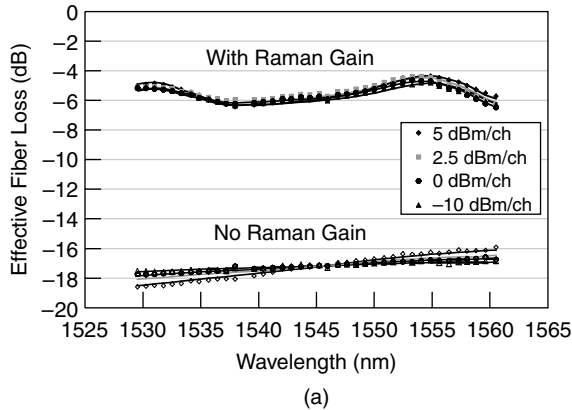


Fig. 4.15. (a) Measured and simulated gain spectra for different signal launch powers using gain control and (b) measured and simulated effective noise figures. Dots indicate measurements and lines show simulated results.

limited precision in adjusting the pump powers. Without Raman pumping, the SRS gain tilt between signal channels is almost 2 dB. When the pump powers are adjusted to maintain a constant Raman gain, the SRS tilt can be compensated. However, the tilt still manifests itself in an OSNR penalty which can be seen from the effective noise figure. An examination of the pump powers needed to maintain the constant gain spectrum reveals that under saturation, the lowest pump wavelength at 1423 nm requires the greatest increase with the other pumps at 1443 and 1464 nm needing only slight power changes. The shortest wavelength pump provides most of its gain at the end of the fiber and this effect is increased by pump saturation by the signals and depletion by the other pumps, resulting in a worse effective noise figure. Pump depletion shortens the effective length over which the gain occurs, resulting in the effective noise figure being raised.

SRS signal-to-signal crosstalk and pump depletion results in both the tilt of the effective noise figure about the center channel, and an increase in effective noise figure. These effects can be modeled by numerical methods.

4.8. Fundamental Limits for Discrete Broadband Amplification

Although analytical solutions are unable to provide us with an accurate model for the behavior of Raman amplifiers, they can be used to give insight into the noise performance limit of a single-cavity discrete Raman amplifier. In a discrete Raman amplifier, the wavelength dependence of the noise figure will be determined by four main factors. These include the gain spectrum and component losses at the amplifier input, SRS interactions between the pump wavelengths, and increased spontaneous emission due to the thermal distribution of phonons in the ground state.

In order to investigate the best performance of a *discrete single cavity, counter-pumped Raman amplifier*, the undepleted pump approximation is used, and later a lossless fiber is assumed. If the pump-to-pump interactions were included, the performance of the shortest wavelength signals would suffer as a result of a reduction of gain at the front of the amplifier. To obtain the optimum performance for a single cavity, the fiber loss is ignored, and at best, no pump interaction occurs. The gain (G) is given by

$$G = \exp \left(-\alpha L + L_{eff} \sum_i C_{Ri} P_{pi} \right) = \exp(-\alpha L) \prod_i g_i, \quad (4.33)$$

where L is the fiber length, α is the fiber attenuation, and L_{eff} is the effective length of the fiber. C_{Ri} is the Raman gain efficiency for a signal interacting with the i th pump at power P_{pi} , and g_i is the gain given by the i th pump. The amplified spontaneous emission $A(L)$ at the end of the amplifier stage is given by

$$A(L) = h\nu \left[\frac{\sum_i E_i \ln(g_i)}{\sum_i \ln(g_i)} \right] \left\{ \left(1 + \frac{\alpha L_{eff} \exp(\alpha L)}{\sum_i \ln(g_i)} \right) G - \left\{ 1 + \frac{\alpha L_{eff}}{\sum_i \ln(g_i)} \right\} \right\}. \quad (4.34)$$

In the limit of a high gain and lossless fiber, the noise figure for the Raman amplifier is given by

$$F = \frac{1}{G} + \frac{2A(L)}{h\nu G} \approx 2 \frac{\sum_i E_i \ln(g_i)}{\sum_i \ln(g_i)}. \quad (4.35)$$

This simple but important equation indicates that the noise figure is dependent on both the spontaneous emission factor E_i , and the relative amount of gain provided by each pump wavelength. This sets a compromise between broadband and low noise operation in a single gain stage. If the pump and signal are widely spaced, the spontaneous emission factor will tend to one. This is usually the case with a single Raman pump at 1455 nm and a signal at the peak gain wavelength of 1550 nm, resulting in a high gain and a low noise figure. When the signal and pump lie close together, the spontaneous emission factor may be large. If the ratio of the gain given by that pump to the overall total gain from all the pumps is small, the noise figure will also tend to 3 dB. However, if a pump provides a large amount of gain to the closely spaced signal, there will be a large increase in the excess spontaneous noise. Figure 4.16(a) shows the simulated gain spectrum for a five-wavelength pumped, single-cavity discrete Raman amplifier. The relative gains from each pump were chosen to give the broadest and flattest spectrum with the highest pump wavelength at 1495 nm and the lowest signal near 1500 nm. It can be seen that the 1495 nm pump provides the largest gain and makes a significant contribution at shorter wavelengths.

Using Eq. (4.35), Fig. 4.16(b) shows the best achievable internal noise figure for this discrete Raman amplifier stage. It can be seen that since a substantial amount of the total gain at shorter wavelengths is given by the 1495 nm pump, there is increased spontaneous emission as the signals approach the pump. At room temperature, the internal noise figure of the amplifier is between 5 and 6 dB below 1520 nm. The total noise figure of the amplifier will be greater than this once fiber loss and the insertion loss of components at the amplifier input are included. As the temperature varies between 253K (-20°C) and 353K ($+80^\circ\text{C}$), the noise figure varies by between 0.5 and 0.75 dB. At much lower temperatures, the phonon distribution is reduced and the spontaneous emission factor tends to one, reducing the noise figure to the quantum limit of 3 dB.

Although this places a limit on the performance of a *single-cavity*, counter-pumped Raman amplifier, schemes may be devised in order to enhance the gain from the shorter wavelength pumps at the front end of the overall amplifier. In particular, the amplifier could be split into several stages where the shortest wavelength pumps were used in the first stage, and the longest wavelength pump only provides gain in the last stage. The enhanced noise contribution from the long wavelength pump would be suppressed by the gain in the first stages. In practice, the fiber and component loss experienced by the long wavelength signals will probably remove any benefit. Alternatively, a copumping scheme could be used for the shortest wavelength pump. Although the ASE performance would be improved, penalties may occur due to the fast-gain dynamics of the amplifier.

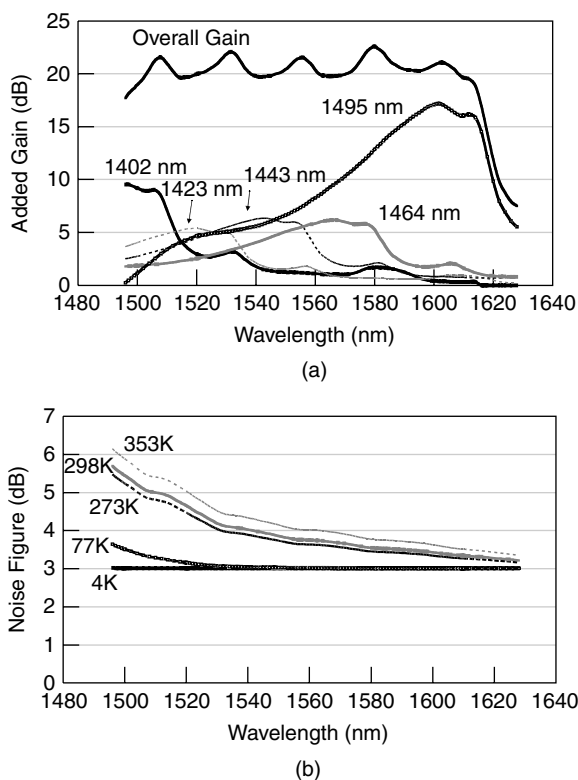


Fig. 4.16. (a) Composite gain spectrum for a discrete Raman amplifier pumped with five wavelengths; (b) best achievable noise figure for a broadband single-cavity, discrete Raman amplifier at various temperatures.

4.9. Measurements of Commercial Transmission Fiber Types [20]

The Raman gain experienced by a signal depends upon both the doping of the fiber and the wavelengths of pump and signal. Many modern fibers use depressed cladding and doping to control the chromatic dispersion and mode field of the signal. To predict the performance of an optical communications system, it is more useful to define a coefficient that is specific to a given fiber type. This is the Raman gain efficiency coefficient (C_R) and can take into account the mode overlap of pump and signal fields, and may be easily measured [21]. The experimental setup is shown in Fig. 4.17. The tunable laser is swept from 1460 nm to 1600 nm and the power spectra recorded using an optical spectrum analyzer (OSA). The fiber under test is reverse-pumped using a pair of optical circulators and a high-power 1455 nm fiber laser.

The reverse-pump power of the 1455 nm laser in the fiber under test was measured using a high-power detector. By recording the optical spectrum with and without the Raman pump (G_a), the Raman gain efficiency coefficient can be determined from the undepleted pump approximation:

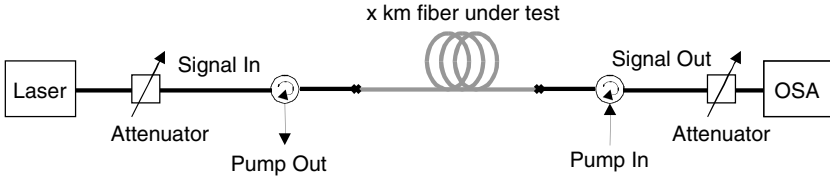


Fig. 4.17. Experimental setup for measuring Raman gain efficiency.

$$C_R(\lambda, 1455\text{nm}) = \frac{g_R(\lambda)}{A_{eff(s,p)} \cdot K} = \frac{\ln(G_a(\lambda))}{P_p \cdot L_{eff}}, \quad (4.36)$$

where $C_R(\lambda)$ is the Raman gain efficiency ($\text{W}^{-1} \cdot \text{km}^{-1}$) using a depolarized 1455 nm pump of power P_p (W). L_{eff} is the effective fiber length (km) defined at the pump wavelength with fiber attenuation α_p :

$$L_{eff} = (1 - e^{-\alpha_p L}) / \alpha_p. \quad (4.37)$$

Because this equation is only valid for small signal gain, in the case of negligible pump depletion, measurements of the output pump power were taken for various input signal powers to ensure that the pump was not being depleted. At low pump powers the gain is small, which makes errors in measuring the gain appear more significant. At high pump powers and for long fiber lengths, there is a significant amount of amplified spontaneous emission generated which can give erroneous measurements of the output signal power. For very high gains and pump powers, the amplifier may lase and the signal power becomes unstable.

Measurements were performed on a range of modern transmission fibers: conventional NDSF, Corning LEAF, Corning DSF, Corning NZ-DSF, Lucent Allwave (similar to NDSF but with low water loss), Lucent TrueWave® RS, pure-silica core as shown in Table 4.1.

From the Raman gain efficiency spectra (Fig. 4.18) it can be seen that the smaller core, dispersion-shifted fibers show a larger amount of gain and that the conventional NDSF, the new Allwave and pure-silica core fibers have the least. The shape of the curves is also similar although the peak at 430 cm^{-1} is more pronounced for the dispersion-shifted fibers which tend to have a greater amount of germania. A comparison with the pure-silica core fiber shows a reduction in the peak at 430 cm^{-1} and a larger peak at 490 cm^{-1} as highlighted by Davey et al. [22]. The fiber loss (shown in

Table 4.1. Transmission Fiber Data

Fiber	Allwave	Corning NZ-DSF	LEAF	NDSF	TrueWave® RS	Pure Silica Core	Corning DSF
Length (km)	40.1	19	15.1	13.2	40.6	40	24.3
Eff. Area at 1550 nm (μm^2)	80	50	75	80	55	110	55

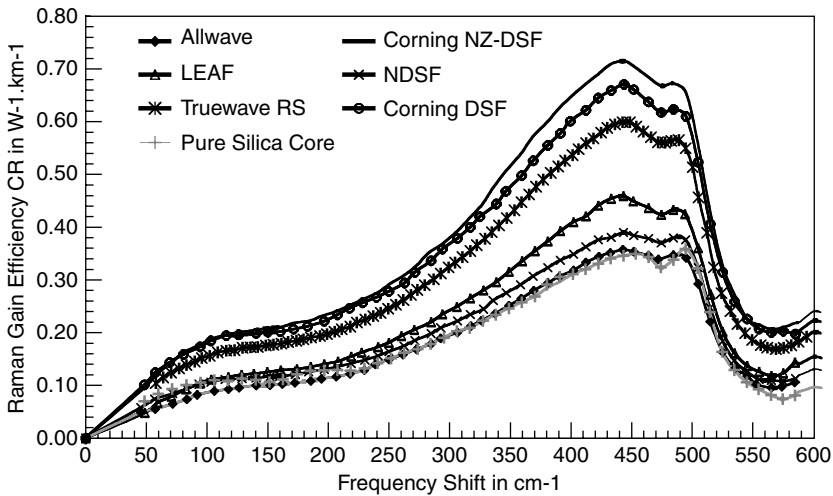


Fig. 4.18. Raman gain efficiency spectra for various modern transmission fibers.

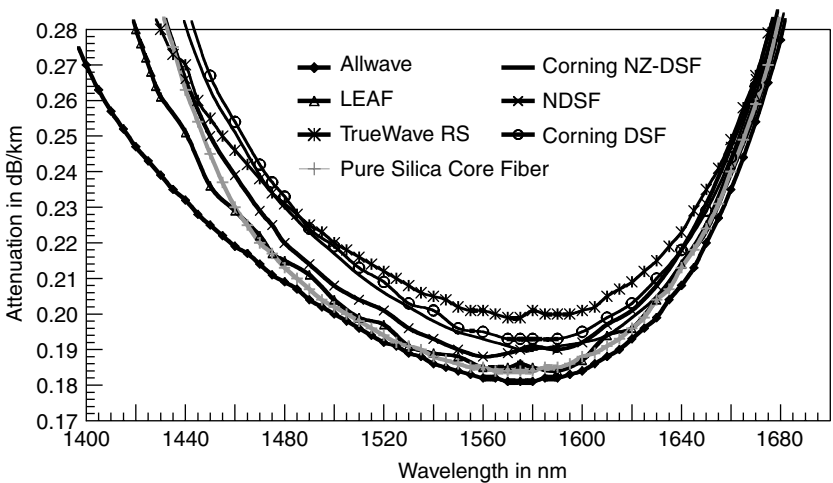


Fig. 4.19. Attenuation curves for various modern transmission fibers.

Fig. 4.19) is also important for efficient Raman amplification and good signal transmission. For gain in the low-loss window used by modern optical communications systems (1520 to 1620 nm), a Raman pump is needed between 1400 and 1500 nm. This lies close to the water absorption peak in many optical fibers. Fiber types such as Allwave have eliminated this excess loss, which allows the pump to propagate farther into the transmission fiber. Other fiber types such as LEAF or TrueWave® RS, have a greater signal and pump attenuation but also give a higher Raman gain efficiency, and require less dispersion compensation. In many cases, optical communications

systems are designed for an existing fiber infrastructure. Accurate measurements of Raman gain will be an essential fiber parameter when upgrading or installing new systems.

4.10. Analysis of Relative Linear Noise Performance of Different Transmission Fibers [20]

The Raman gain spectra and fiber attenuation data may be used to predict the improvement in system performance by using distributed Raman preamplification in the system fiber. The numerical model can be used to predict the effective fiber loss and noise figure of a Raman-pumped transmission fiber. In order to compare the effects of Raman gain on the optical signal-to-noise performance of a future system, 25 dB spans of each fiber were compared, each with 0.5 dB connector loss. 40 channels were simulated at 100 GHz spacing, centered in the conventional EDFA band (1530 to 1565 nm), each launched at +5 dBm. The signal fiber attenuation was set at that of the 1530 nm channel so that the variation of fiber attenuation with wavelength did not affect the OSNR.

The total noise figure of the system was calculated by cascading the noise figures and gain for the Raman transmission fiber and the EDFA amplifiers (6 dB noise figure). The arrangement for the components can be seen in Fig. 4.20. The gain of the EDFA is matched to the effective loss of the fiber so that the total system is transparent. It is assumed that the noise figure of the EDFA remains constant, even though the effective gain of the amplifier has dropped. For this analysis, the noise was calculated in a bandwidth of 0.5 nm and five spans were used. The noise figure (F_T) for k stages is given by

$$\begin{aligned}
 F_T &= F_{R1} + \frac{F_{EDFA1} - 1}{G_{R1}} + \frac{F_{R2} - 1}{G_{R1}G_{EDFA1}} + \cdots \\
 &\quad + \frac{F_{Rk} - 1}{G_{R1}G_{EDFA1} \cdots G_{R(k-1)}G_{EDFA(k-1)}} + \frac{F_{EDFAk} - 1}{G_{R1}G_{EDFA1} \cdots G_{Rk}} \\
 &= k \left(F_R + \frac{F_{EDFA} - 1}{G_R} - 1 \right) + 1,
 \end{aligned} \tag{4.38}$$

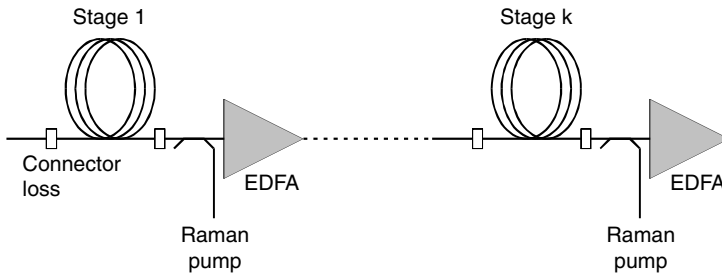


Fig. 4.20. System configuration for analysis.

where k is the number of stages, F_{EDFA} and G_{EDFA} are the noise figure and the gain of the EDFA, respectively, and F_R and G_R are the noise figure and gain (transmission coefficient) for the Raman-pumped fiber. The optical signal-to-noise ratio can be calculated according to:

$$F_T = \frac{P_{ase}}{h\nu\Delta\nu G_T} + \frac{1}{G_T} \quad (4.39)$$

$$OSNR = \frac{S}{P_{ase}} = \frac{S}{h\nu\Delta\nu k \left(F_R + \frac{F_{EDFA}-1}{G_R} - 1 \right)}, \quad (4.40)$$

where h is Planck's constant, ν is the signal frequency, and $\Delta\nu$ is the optical bandwidth. Two pump wavelengths at 1427 and 1455 nm were simulated to produce a relatively flat gain spectrum, and the OSNR from the 1530 nm channel (worst case) was compared for each transmission fiber.

Figure 4.21 shows the variation of system OSNR (in 0.5 nm bandwidth) and individual-stage pumped fiber loss for the 1530 nm channel. It can be seen that an improvement in OSNR of 5 to 6.5 dB can be expected for pump powers of 500 mW, which is the current Class 3B laser safety limit. In Raman pumping the system fiber's effective loss decreases by between 10 and 16 dB. The most effective fiber for distributed Raman gain is the Corning NZ-DSF fiber which gives slightly better performance over a standard dispersion-shifted fiber. The NDSF and Allwave fibers gave the least amount of improvement although the simulations indicate that although there is a large variation in the distributed gain between the fibers, the change in OSNR is not so dramatic. However, the pump requirement to achieve a given OSNR improvement can vary by 200 mW. It should also be remembered that only the linear

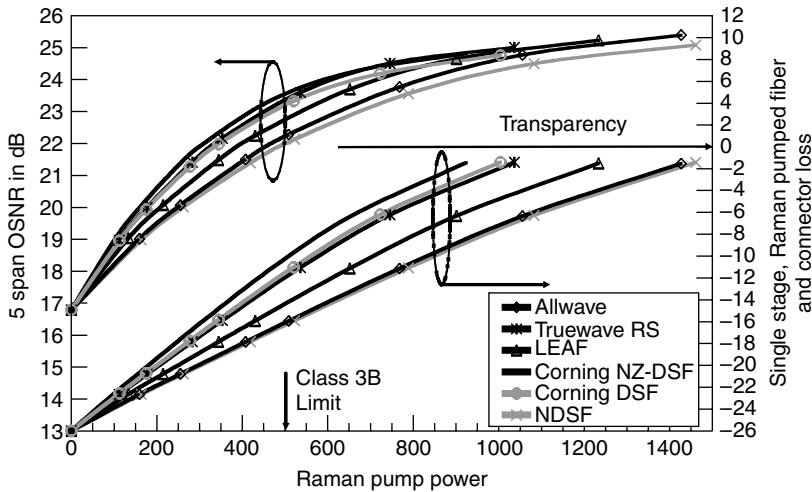


Fig. 4.21. Effective fiber loss and OSNR improvement for various Raman pump powers and fiber types.

noise performance has been considered here, and the presence of nonlinearities in the fiber will also limit the benefit seen when adding gain to the transmission fiber.

4.11. Summary

This chapter has focused on the linear noise performance of Raman amplifiers and the use of the noise figure to characterize this performance. The noise figure has been shown to be a useful parameter in specifying the noise produced by signal-spontaneous beat noise and shot noise in optically amplified systems. Although these noise sources are signal-power independent and can be easily quantified using an optical measurement, multipath interference is best characterized separately inasmuch as the system penalties are different. Effective noise figure has also been defined and can be used to show the performance benefits of distributed Raman amplification.

A model has been presented that can fully describe the propagation of signals and the buildup of ASE in a Raman amplifier. Coupling between forward and backward traveling ASE is an important factor at high gains. Furthermore, pump interactions and the thermal distribution of phonons in the ground state have been shown to give better system performance to longer wavelength channels at the expense of short wavelength channels. Also, high-power DWDM signals will saturate the gain of distributed Raman amplifiers. Pump power control can be used to maintain a constant gain spectrum although the effective noise figure is still increased due to a shortening of the effective fiber length whereas any SRS crosstalk among the signal channels now manifests itself as a tilt in the effective noise figure. Measurements on several Raman amplified systems show excellent agreement with the numerical calculations. A theoretical model has been presented that shows that a single-stage, discrete Raman amplifier based on silica-germania will have a noise figure significantly greater than the 3 dB quantum limit.

Finally, the numerical model has been used in conjunction with measurements of Raman gain efficiencies and loss for a variety of system fibers, in order to predict the linear system enhancement from distributed Raman amplification. These show a 4.5 to 6.5 dB improvement in OSNR when using a 500 mW pump, a variation of up to 2 dB depending on fiber type.

References

- [1] P.B. Hansen, L. Eskildsen, S.G. Grubb, A.J. Stentz, T.A. Strasser, J. Judkins, J.J. De-Marco, R. Pedrazzani, and D.J. DiGiovanni, Capacity upgrades of transmission systems by Raman amplification, *IEEE Photon. Technol. Lett.*, 9:2 (Feb.), 262–264, 1997.
- [2] H.T. Friis, Noise figure of radio receivers, *Proc IRE*, 32:419–422, 1944.
- [3] E. Desurvire, *Erbium Doped Fiber Amplifiers*, New York: Wiley, 98, 1994.
- [4] H.A. Haus, The noise figure of optical amplifiers, *IEEE Photon. Technol. Lett.*, 10:11 (Nov.), 1998.
- [5] E. Desurvire, Comments on “The noise figure of optical amplifiers”, *IEEE Photon. Technol. Lett.*, 11:5, (May), 620 and 621, 1999.

- [6] C. Chen and W.S. Wong, Transient effects in Raman optical amplifiers, OAA2001, Paper OMC2, 2000.
- [7] R.G. Smith, Optical power handling capacity of low loss optical fiber as determined by stimulated Raman and Brillouin scattering, *Appl. Optics*, 11:11 (Nov.), 2489–2494, 1972.
- [8] J. Auyeung and A. Yariv, Spontaneous and stimulated Raman scattering in long low loss fibers, *IEEE J. Quantum Electron.*, QE-14:5, (May), 347–352, 1978.
- [9] S. Tariq and J.C. Palais, A computer model of non-dispersion-limited stimulated Raman scattering in optical fiber multiple-channel communications, *J. Lightwave Technol.*, 11:12 (Dec.), 1914–1924, 1993.
- [10] H. Kidorf, K. Rottwitz, M. Nissov, M. Ma and E. Rabarjaona, Pump interactions in a 100-nm bandwidth Raman amplifier, *IEEE Photon. Technol. Lett.*, 11:5, (May), 530–532, 1999.
- [11] R.H. Stolen and M.A. Bosch, Low-frequency and low temperature Raman scattering in silica fibers, *Phys. Rev. Lett.*, 48:805–808, 1982.
- [12] P.B. Hansen, L. Eskildsen, A.J. Stentz, T.A. Strasser, J. Judkins, J.J. DeMarco, R. Pedrazzi, and D.J. DioGiovanni, Rayleigh scattering limitations in distributed Raman pre-amplifiers, *IEEE Photon. Technol. Lett.*, 10: (Jan.), 159–161, 1998.
- [13] S.T. Davey, D.L. Williams, B.J. Ainslie, W.J.M. Rothwell, and B. Wakefield, Optical gain spectrum of GeO₂-SiO₂ Raman fibre amplifiers, *IEE Proceedings*, 136: Pt J, 301–306, (1989).
- [14] K. Rottwitz, M. Nissov, and F. Kerfoot, Detailed analysis of Raman amplifiers for long-haul transmission, OFC 1998, 30, TuG1, 1998.
- [15] M.A. Farahani and T. Gogolla, Spontaneous Raman scattering in optical fibers with modulated probe light for distributed temperature Raman remote sensing, *J. Lightwave Technol.*, 17:8 (August), 1379–1391, 1999.
- [16] R.G. Smith, Optical power handling capacity of low loss optical fibers as determined by stimulated Raman and Brillouin scattering, *Appl. Optics*, 11:11, (Nov.), 2489–2494, 1972.
- [17] S.R. Chinn, Analysis of counter-pumped small-signal fibre Raman amplifiers, *Electron. Lett.*, 33:7, (March 27), 2489–2494, 1997.
- [18] S.A.E Lewis, S.V. Chernikov and J.R. Taylor, Gain and saturation characteristics of dual wavelength-pumped silica-fibre Raman amplifiers, *Electron. Lett.*, 35:14, (July 8), 1178–1179, 1999.
- [19] C.R.S. Fludger, Dynamic gain tilt of a gain flattened distributed Raman amplifier under saturation in a DWDM system, OAA 2000, Quebec City, July, 2000.
- [20] C.R.S. Fludger, A. Maroney, N. Jolley, and R.J. Mears, An analysis of the improvements in OSNR from distributed Raman amplifiers using modern transmission fibres, OFC 2000, FF2-1, 2000.
- [21] R. Billington, Measurement methods for stimulated Raman and Brillouin scattering in optical fibres, NPL Report, COEM 31, June, 1999.
- [22] S.T. Davey, D.L. Williams, D.M. Spirit, and B.J. Ainslie, The fabrication of low loss high NA silica fibres for Raman amplification, *SPIE 1171: Fiber Laser Sources and Amplifiers*, 1989.

Chapter 5

Pump Laser Diodes and WDM Pumping

Shu Namiki, Naoki Tsukiji, and Yoshihiro Emori

This chapter discusses issues surrounding the pump laser diodes for broadband Raman amplifiers, which range from fundamentals to industry practices of Raman pump sources based on the so-called 14XX nm pump laser diodes. It also refers to design issues of wavelength-division-multiplexed (WDM) pumping for realizing a broad and flat Raman gain spectrum over the signal band. Section 5.1 introduces fundamentals of pump laser diodes. Section 5.2 refers to the principle and design issues of WDM pumping technique. Section 5.3 discusses details of pump laser diodes and their efficiently combining and depolarizing technologies. Section 5.4 describes practical Raman pump units. And Section 5.5 briefly touches upon ongoing issues on copumped Raman amplifiers and their pumping sources.

This chapter is mainly devoted to a particular type of pump laser diodes called InGaAsP/InP GRIN-SCH strained layer MQW structure with BH structure, which is most widely used in the market.

5.1. Fundamentals of Pump Laser Diodes

Although an origin of high-power 14XX nm laser diodes derives from the motivation toward commercialization of Raman amplifiers for telecommunications [1], such lasers were extensively developed as a 1480 nm pump laser for EDFA (erbium-doped fiber amplifier) [2–5]. The increase of channel counts in WDM systems has been a driving force for the development of high-power pump lasers. And also, high-power 14XX nm pump lasers triggered the actual applications of Raman amplifiers to commercial WDM systems [6, 7].

Since over-200 mW output 14XX nm laser modules [8, 9] appeared in commercial use in 1998, the development of the high-power 14XX nm laser has been accelerated drastically. Up to now, 400 mW fiber-coupled power was practical [10].

The performance of a high-power pump laser with high reliability is limited by the following two factors, maximum fiber coupled power and maximum operating ambient temperature.

In order to achieve higher maximum fiber coupled power, it is necessary to maximize the facet power from the laser chip and coupling efficiency between the laser chip and optical fiber. The simple way to obtain higher optical output is to operate the laser chip at a large injection current. This causes, however, the larger power consumption and higher junction temperature of the laser chip to worsen reliability.

The maximum operating ambient temperature is determined by the power consumption of the laser chip, the thermal impedance throughout the heat dissipation path inside the laser module, and the heat absorption performance of the thermoelectric cooler (TEC). The power consumption of the laser chip becomes larger with increasing operating current of the laser chip. This increases the TEC heat load, and then the power consumption of the TEC increases drastically, making high ambient temperature operation difficult. Thus, it is critically important to reduce the power consumption of the pump laser module. The solutions are to reduce the series resistance and thermal impedance of the laser chip [10, 11]. And the TEC should be optimized according to the laser operating power [10, 11].

In this section, fundamentals are described for a high-power pump laser with high reliability.

5.1.1. Laser Diode Technologies for High-Power Operation

The principal part of 14XX nm laser chips is made of GaInAsP/InP compound semiconductor grown by epitaxial growth techniques such as MOCVD (metal organic chemical vapor deposition) and MBE (molecular beam epitaxy). To enhance the stimulated emission for laser operation we need population inversion in the semiconductor laser by current injection. To achieve population inversion efficiently, a double-heterostructure (DH) laser [12], in which the thin semiconductor active layer is sandwiched between layers of different semiconductor compounds, has been widely used as a basic structure for highly efficient laser diodes. Figure 5.1 shows the schematic representations of the band diagram under a forward-bias condition, the refractive index profile, and the optical-field distribution of light generated at the junction of a DH laser. As can be seen in Fig. 5.1, because the bandgap energy of the active layer is lower than other layers, the carriers are confined inside the active region—where radiative recombination occurs—by the heterojunction barriers, preventing the carriers from moving out of the active region without recombination.

Because the refractive index of the active layer is larger than the index of its surrounding layers, a three-layer optical waveguide is formed in parallel to the layer interfaces. To achieve more efficient confinement of both the carriers and radiated lightwave, widely applied for high-power 14XX nm pump lasers is the so-called GRIN-SCH strained layer MQW structure with BH structure, which stands for graded index, separate confinement heterostructure strained layer multiple quantum well structure with buried heterostructure [13, 14]. The details are discussed in the subsequent sections.

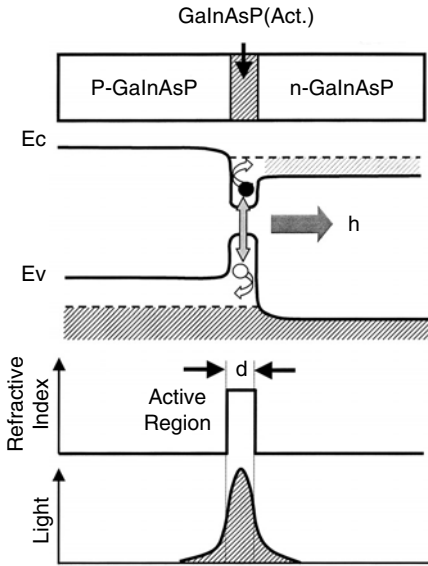


Fig. 5.1. Schematic representations of, from the top to the bottom, the layer structure of material, the band diagram under a forward-bias condition, refractive index profile, and optical-field distribution of light generated at the junction of a DH laser.

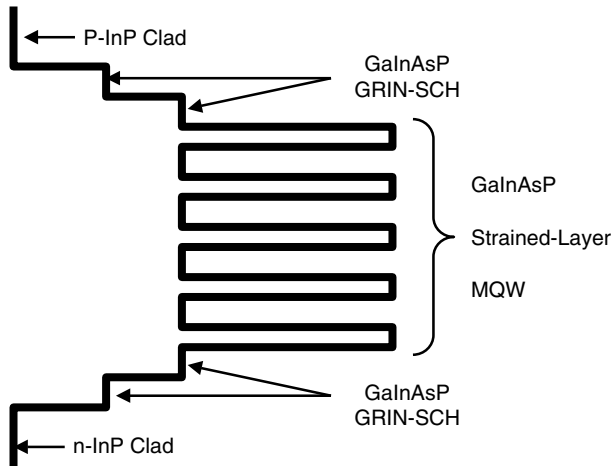


Fig. 5.2. Schematic band diagram of GRIN-SCH-strained MQW.

5.1.2. Laser Diode Structure

The active layer of most pump lasers consists of a compressive strained MQW with GRIN-SCH layers. Figure 5.2 shows a typical band diagram of the active region of pump laser [13].

Compared to a lattice-matched MQW active layer or a bulk type active layer, a compressive strained MQW has the advantage of obtaining a larger optical gain at the

same injection current. In the case of a laser with a compressive strained MQW active layer, sufficient laser oscillation could be achieved with a small optical confinement factor because of large optical gain. Here the optical confinement factor represents the ratio of the optical intensity distributed in the active layer to the total optical intensity. We note that the small optical confinement factor decreases the internal loss of the laser cavity. Thus we are able to lengthen the laser cavity, which reduces both series resistance and thermal impedance of the laser chip, keeping the slope efficiency (W/A) sufficiently high. Here the slope efficiency is defined as the ratio of the optical output change to the change of injected current.

In addition, the small optical confinement factor allows adoption of a lower equivalent refractive index difference between the active region and the InP cladding layers. This small refractive index difference widens the cut-off width of the active optical waveguide. Here, the cut-off width is defined as the maximum width in which only one fundamental transverse mode is excited. Thus it is desirable to adopt the compressively strained MQW active region, because we can widen the active region stripe as well as lengthen the laser chip cavity. As a result, we can reduce both series resistance and thermal impedance, and hence achieve high-power operation of the laser.

GRIN-SCH structure has an advantage of higher carrier injection efficiency into the active region in comparison to a single-step SCH structure. This enables both low-threshold and high-power operation. Thus compressive strained MQW with GRIN-SCH structure is suitable for realizing high-power semiconductor lasers.

Figure 5.3 shows the so-called BH-structure of the laser chip [10, 11]. The p-n-p-InP current blocking layers are formed around the active region, which minimize the leakage current and stable fundamental transverse mode operation. BH-structure can be so designed as to realize a nearly round shape beam pattern, leading to a high coupling efficiency between the laser chip and a single-mode fiber. To obtain higher output power from the front facet, both AR (antireflection) film and HR (high-reflection) film are coated on both the front and rear facets, respectively.

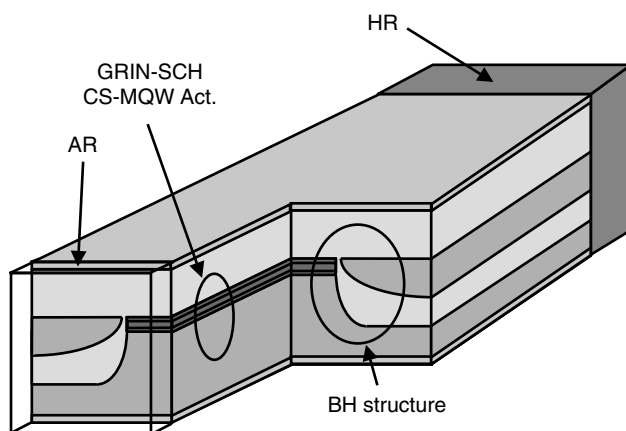


Fig. 5.3. Laser chip the structure.

5.1.3. Laser Module Structure

Figure 5.4 shows the appearance of the 14-pin butterfly laser module [10, 11]. Here the optical fiber is fixed to the package via sleeve by YAG laser spot-welding.

Figure 5.5 shows a cross-sectional view of the laser module [10, 11]. A pump laser module consists of the laser chip, an optical coupling system so as to couple the laser beam launched from the laser chip to the optical fiber, and a TEC. The temperature of the laser chip is measured by a thermistor sensor mounted near the laser chip and stabilized by the TEC. The laser chip is mounted on the TEC via the submount (heat sink).

Generally, the laser chip launches a light beam in a cone angle of approximately 20 degrees. The optical beam is collimated by the first lens, and then is focused by

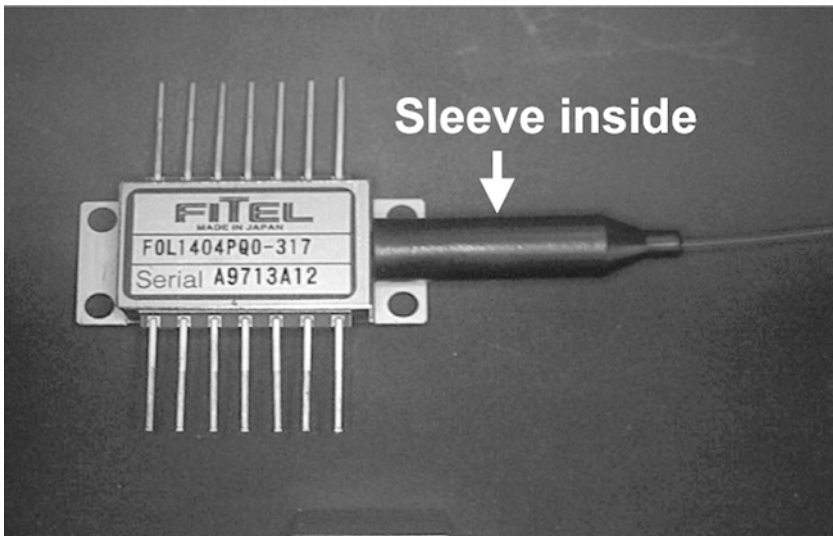


Fig. 5.4. Pump laser module.

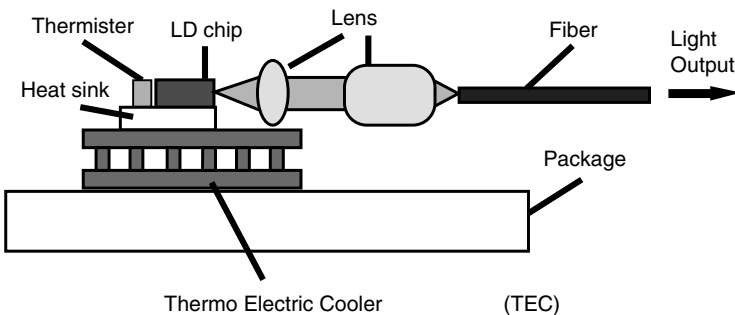


Fig. 5.5. Cross-sectional view of pump laser module.

the second lens on the core facet of the optical fiber. The position accuracy of these optical components should be within 1 to 10 μm . In particular, the core position of the optical fiber should be fixed with submicron accuracy. The laser chip is spatially coupled to the optical fiber through these two lenses; therefore it is easy to insert optical “bulk” components such as an optical isolator between the first and second lenses.

5.1.4. Performances

Figure 5.6 shows typical L - I (light output, L versus current, I) characteristics of the high-power 14XX nm pump laser. The laser has 1.5 mm long cavity and is operated at a laser chip temperature of 25°C. Fiber-coupled power of 400 mW was obtained at an operation current of 1270 mA. The maximum output power reached a half watt, which was limited by thermal roll-off.

Figure 5.7 shows the relation between the fiber-coupled power and laser-driving power of this device. Figure 5.8 shows the cooling capacity of the TEC of this pump laser module. It is noteworthy that this pump laser module can be operated up to 75°C of case temperature. Figure 5.7 shows that the electrical power of 2.8 W is consumed when fiber-coupled power of 400 mW is required. In addition, as Fig. 5.8 demonstrates, TEC draws an electric power of 7.2 W when case temperature should sustain at high temperature of 75°C under the same fiber-coupled power as the above.

5.1.5. Reliability

Figure 5.9 shows the life test result which plots the change in operating current of the 18-laser chips with 1.5 mm cavity length at 80% of maximum output power for over

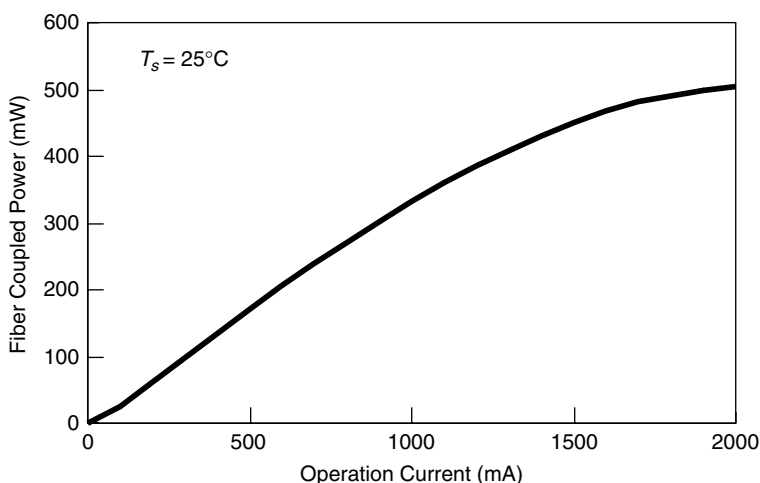


Fig. 5.6. L - I characteristics of a typical Fabry-Perot 1480 nm pump laser.

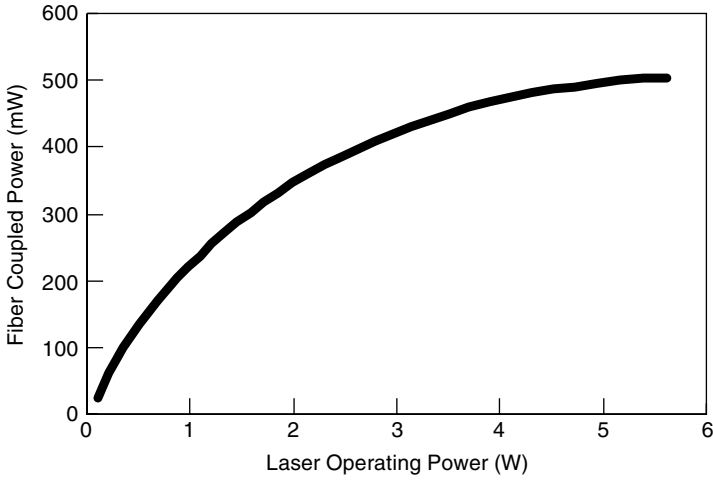


Fig. 5.7. L - W characteristics of a typical Fabry-Perot 1480 nm pump laser.

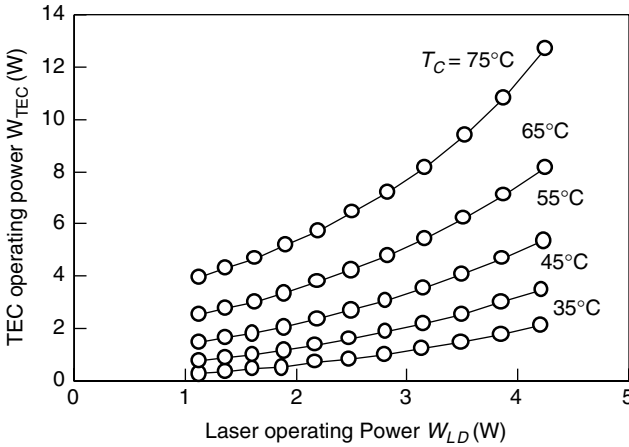


Fig. 5.8. TEC operating power versus laser operating power of a typical Fabry-Perot 1480 nm pump laser.

5000 hours at 60°C [10]. They exhibited a stable operation, and any random sudden failures have never been observed.

Through accelerated aging tests for various conditions, median lifetimes could be obtained for the four types of lasers with different cavity lengths of 0.8, 1, 1.3, and 1.5 mm, respectively; those were plotted in the Arrhenius relationship, as shown in Fig. 5.10 [10]. The activation energies of the median lifetime were almost the same value of 0.62 eV for all four types of lasers. The 1.5 mm cavity chips were operated in a higher-power condition at the same junction temperature, compared

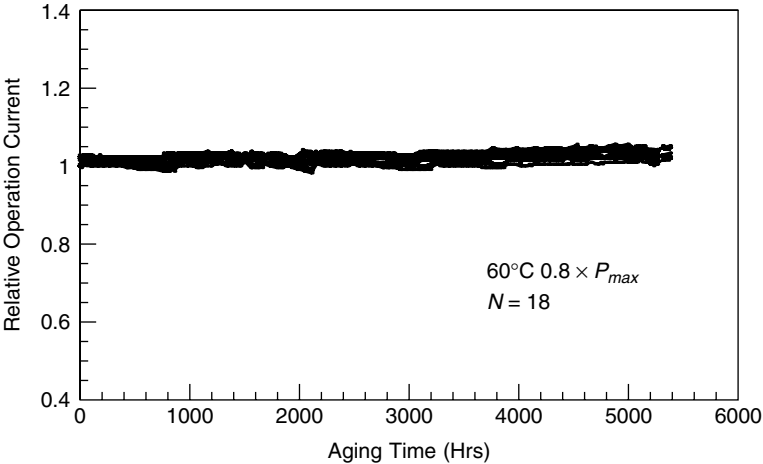


Fig. 5.9. Life test drift plots.

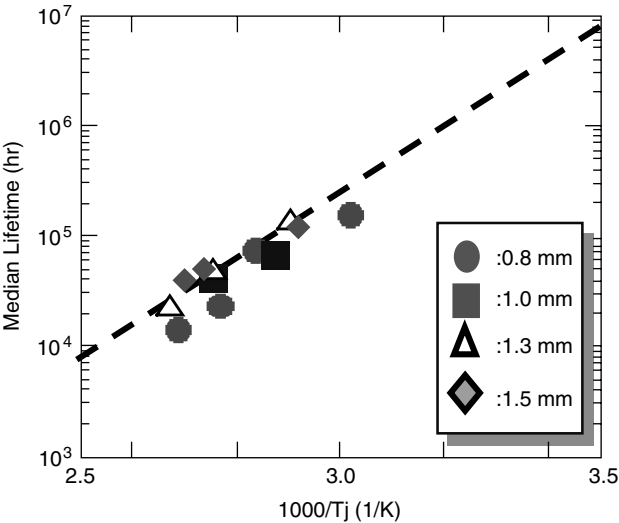


Fig. 5.10. Arrhenius relationship plots. The numbers in mm represent the cavity length of the samples.

with shorter cavity laser chips. However, the laser chip with 1.5 mm cavity has a longer median lifetime than the others. This indicates that the laser chip does not degrade due to the optical power itself within the present optical power range. Using this activation energy and thermal impedance of 11 K/W in the butterfly package as shown in Fig. 5.4, the median lifetime was estimated to be around one million hours for 275 mW fiber-coupled power in a 1.5 mm cavity laser chip at 25°C.

The reliability of laser modules is closely related to the following considerations:

- (i) The displacements should be minimized at any mechanical joints by avoiding the creep in solder or the cracks at spots of YAG laser spot-welding.
- (ii) Metal parts should be carefully designed with respect to mechanical structure accounting for thermal expansion in order to avoid deformation of piece parts and members.
- (iii) Contamination should be minimum in package sealing by keeping clean facets on the laser chip, package window, fiber edge, and lenses, in order to suppress package-induced failure.

In addition, according to the recent increase in output power of the laser chip, endurance against high optical power exposure to optics such as the lens, isolator, coupler, and fiber has to be guaranteed.

5.2. WDM Pumping for Broadband Raman Amplifiers

5.2.1. Principle

If we denote the frequencies of pump light, optical phonon, and signal light as ν_p , ν_{ph} , and ν_s , respectively, the stimulated Raman scattering can occur when

$$\nu_s = \nu_p - \nu_{ph}. \quad (5.1)$$

Suppose that multiple pump frequencies are incident to the Raman medium; then we will have each individual stimulated Raman scattering corresponding to each pump frequency simultaneously. Namely, for the i th pump frequency, the above process will become

$$\begin{array}{c} \vdots \\ \nu_{s,i} = \nu_{p,i} - \nu_{ph} \\ \vdots \end{array} \quad (5.2)$$

This means that different frequencies of signal light can receive gain individually from different frequencies of pump light in one Raman medium at the same time. This feature is important for broadband amplification used in WDM transmission, because we can realize a broad and flat spectral shape of Raman gain in the optical fiber by using multiple pump frequencies. In this chapter, we call this pumping scheme “WDM pumping,” as pump lasers are wavelength-division-multiplexed in such schemes.

In optical fiber, the optical phonon shows a broad continuum spectrum. Therefore, the Raman gain spectrum generated by one frequency of pump light is already broad over 10–20 nm in the 1550 nm signal wavelength range. As a result, in WDM pumping, each Raman gain caused by each frequency of pump light typically overlaps the other. Therefore, in contrast to Eq. (5.2), one signal frequency will receive a sum of the overlapped gains from the different pump frequencies.

Let us consider the evolution of signal light power along distance and define the Raman gain coefficient. If we account for attenuation of the optical fiber and Raman gain by the single-pump frequency only, then the evolution of signal light power is written as [15]

$$\frac{dI_s(z)}{dz} = g_R(v_p, v_s) I_p(z) I_s(z) - \alpha I_s, \quad (5.3)$$

where I_s and I_p are powers of the signal and pump light, respectively, z is the propagation distance, g_R is the Raman gain coefficient as a function of the pump and signal frequencies, and α is the fiber attenuation coefficient. In the case of WDM pumping, the above equation is modified to

$$\frac{dI_s(z)}{dz} = \sum_i g_R(v_{p,i}, v_s) I_{p,i}(z) I_s(z) - \alpha I_s, \quad (5.4)$$

where subscript i denotes the i th pump frequency. The on-off Raman gain at the fiber output at distance L is then expressed in linear scale as

$$G_{lin.} = e^{\sum_i g_R(v_{p,i}, v_s) \overline{I_{p,i}(z)} L}, \quad (5.5)$$

where $\overline{I_{p,i}(z)}$ denote the path average power of $I_{p,i}$ over distance L . If we express the above equation in terms of dB units, we have

$$\begin{aligned} G_{dB} &\propto \sum_i g_R(v_{p,i}, v_s) \overline{I_{p,i}(z)} L \\ &\equiv \sum_i C_i g_R(v_{p,i}, v_s), \end{aligned} \quad (5.6)$$

where C_i is defined as a weighting factor for the i th pump frequency. This indicates that the composite Raman gain spectrum is expressed as the logarithmic sum of individual Raman gain spectra generated by different pump frequencies differently weighted by the path average pump powers, and laterally shifted by the pump frequency difference with respect to each other. It is convenient to exploit this “superposition rule” for designing composite Raman gain spectra obtained with various sets of pump frequencies.

5.2.2. Design Issues

For WDM transmission, Raman amplifiers are usually so designed as to provide broad and flat gain spectra under different constraints in terms of number of pumps, range of signal band, type of fiber used, amount of target gain and gain flatness, and so on. One convenient way to design a broadband Raman amplifier is: determination of pump wavelengths, followed by estimation of how much pump power is necessary for each pump wavelength, and finally configuration of passive combiners [16].

Using the superposition rule discussed in the previous section, we can iteratively but easily determine an optimum set of pump wavelengths. As we determine which fiber we use, the Raman gain coefficient spectrum is given. Then, in the frequency domain, setting the pump frequency fixes the lateral position of the Raman gain spectrum. As we learned in the previous section, the spectral profile of the Raman gain coefficient appears as logarithmic Raman gain. The magnitude of logarithmic Raman gain is given through the path average pump power that is yet unknown at this stage. The important purpose of this stage is to test whether the given set of pump wavelengths is sufficient for the required target gain shape. In this respect, we can use arbitrary weighting factors to adjust the magnitude of the Raman gain, regardless of discussing how much pump power we need.

Once we choose a set of pump wavelengths, a composite logarithmic Raman gain is thus easily obtained through simply summing each logarithmic Raman gain in accordance with Eq. (5.6). Adjusting the weighting factors, we can see possible composite gain spectra for the given set of pump wavelengths to find the desired shape.

Figure 5.11 shows an example of how the superposition rule agrees well with the measurement. In this example, 11 pump wavelengths are used. The plots compare the composite gain with adequate weighting factors with that actually obtained from experiment with adequately adjusted pump powers.

One simple question may naturally arise: How should we pick up a set of wavelengths in the very first place? It is not so simple to answer this question in general,

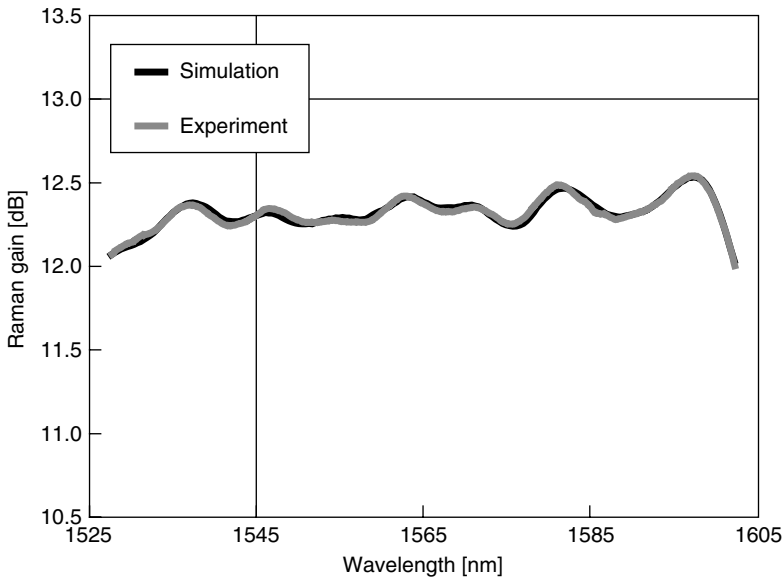


Fig. 5.11. Experimental verification of superposition rule.

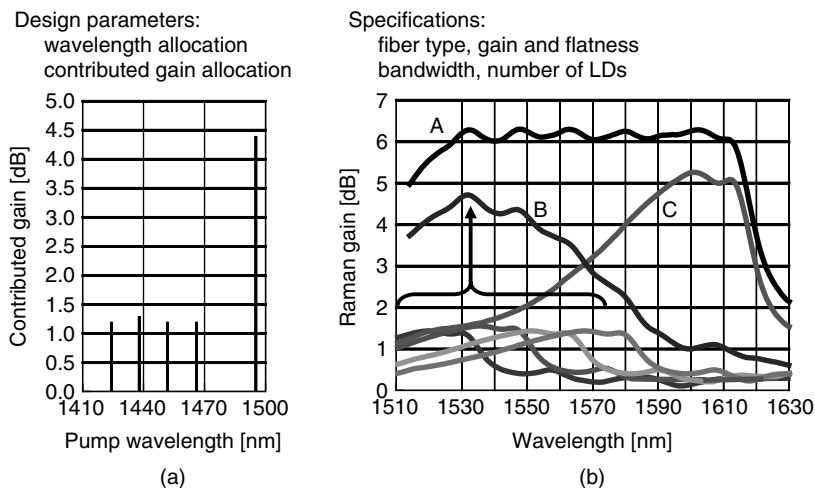


Fig. 5.12. Design of broadband Raman amplifier; (a) pump wavelength allocation with weighting factors (contributed gain); (b) the corresponding composite gain spectra.

but here is a hint from which we may understand how a composite Raman gain spectrum is formed. The Raman gain spectrum in optical fiber usually has an asymmetric shape around the peak: namely, it has a steeper slope on the high frequency side of the peak. If we try to realize a flat-top spectral shape using WDM pumping and the superposition rule, we should compose the equal-degree but opposite slopes to be added to each other. Because of its asymmetric shape, we need to prepare a number of tiny Raman gain curves slightly shifted from each other to make up a smooth slope opposite to the slope that appears on the low-frequency side of the peak in a gain curve caused by a single pump frequency. Figure 5.12 shows an example of how we construct such opposite slopes. In this case, we use five pump wavelengths, and the four shorter pump wavelengths are exploited for constructing the smooth slope, labeled B, opposite the slope by the longest pump wavelength labeled C. The interval between the curves B and C is so adjusted as to best achieve the flat and broad composite gain shape labeled A in Fig. 5.12. The ordinate of the graph Fig. 5.12(a) is labeled “contributed gain,” by which we mean the weighting factor C_i in Eq. (5.6).

Once we fix the wavelength of each pump to be used in the system, we then need to estimate how much pump power is required for each pump. For this purpose we have to calculate the path average power of each pump. Calculating the path average pump power is not straightforward as each pump is subject to pump-to-pump energy transfer caused by stimulated Raman scattering among pumps. Due to pump-to-pump energy transfer, pump light at shorter wavelengths suffers from extra loss whereas pump light at longer wavelengths receives gain from pump light at shorter wavelengths. Therefore, pump light at different wavelengths experiences different evolutions. Figure 5.13 shows the simulated evolutions of five pump wavelengths with 100 mW incident powers launched into a dispersion-shifted single-mode fiber

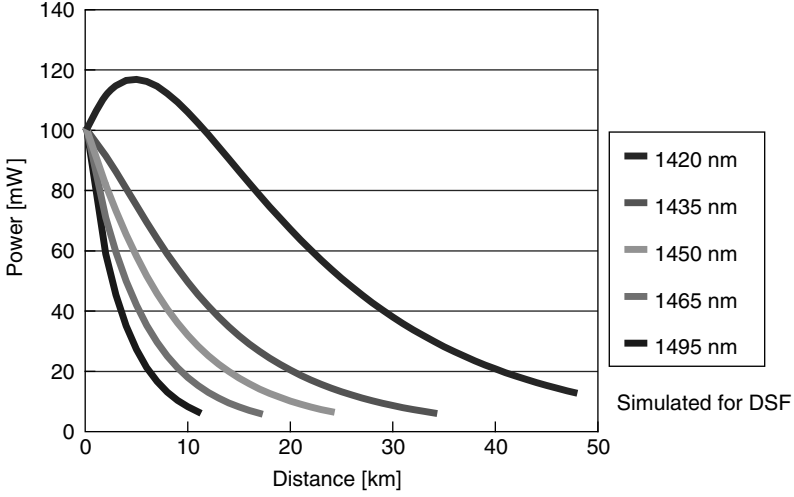


Fig. 5.13. Different power excursions of different pump wavelengths due to pump-to-pump Raman interactions.

(DSF). As shown in the figure, we can see that the shortest pump wavelength suffers from the largest attenuation and the longest pump wavelength experiences a gain.

A general numerical model for stimulated Raman scattering in the case of WDM pumping is written [16–19]:

$$\begin{aligned}
 \frac{dP_v^\pm}{dz} = & -\alpha_v P_v^\pm + \varepsilon_v P_v^\mp \\
 & + P_v^\pm \sum_{\mu > v} \frac{g_{\mu v}}{A_\mu} (P_\mu^+ + P_\mu^-) \\
 & + 2h\nu \sum_{\mu > v} \frac{g_{\mu v}}{A_\mu} (P_\mu^+ + P_\mu^-) [1 + \Theta(\mu - \nu, T)] \Delta\mu \\
 & - P_v^\pm \sum_{\mu < v} \frac{\nu}{\mu} \frac{g_{v\mu}}{A_v} (P_\mu^+ + P_\mu^-) \\
 & - 4h\nu P_v^\pm \sum_{\mu < v} \frac{g_{v\mu}}{A_v} [1 + \Theta(\nu - \mu, T)] \Delta\mu,
 \end{aligned} \tag{5.7}$$

where subscripts μ and ν denote optical frequencies, superscripts $+$ and $-$ denote forward- and backward-propagating waves, respectively, P_v is optical power within infinitesimal bandwidth $\Delta\nu$ around ν , α_v is the attenuation coefficient, ε_v is the Rayleigh backscattering coefficient, A_v is the effective area of optical fiber at frequency ν , $g_{\mu\nu}$ is the Raman gain parameter at frequency ν due to pump at frequency μ , h is Planck's constant, T is temperature, and $\Delta\mu$ is the bandwidth of each frequency component around frequency μ . $\Theta(\nu_p - \nu_s, T)$ is the mean number

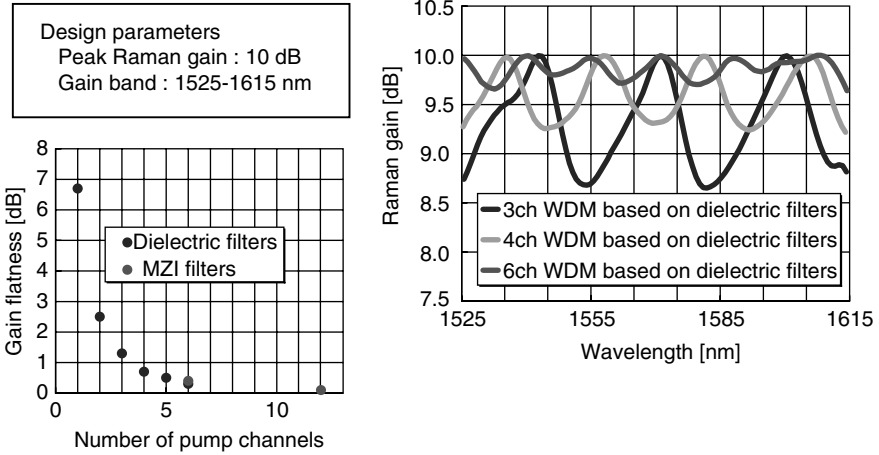


Fig. 5.14. Flatness and the number of pump channels. Inset shows examples of flat composite gain spectra of optimally allocated 3, 4, and 6 pump wavelengths. MZI filters are plotted only for 6 and 12 pump channels.

of phonons in thermal equilibrium at temperature T , or the Bose–Einstein factor:

$$\Theta(\nu_p - \nu_s, T) = \frac{1}{\exp\left[\frac{h(\nu_p - \nu_s)}{kT}\right] - 1}. \quad (5.8)$$

In this model, we include pump-to-pump, pump-to-signal, and signal-to-signal Raman interactions, pump depletions due to Raman energy transfer, Rayleigh backscattering, fiber loss, spontaneous Raman emission noise, and thermal noise. For calculation of Fig. 5.13 or the path average power only, we may ignore the Rayleigh scattering term and noise terms.

Let us now discuss how many pump wavelengths should be used. The answer, of course, depends upon details of the system of interest. It may be straightforward that a larger number of pump wavelengths for a given bandwidth can realize a smoother and flatter gain shape. Figure 5.14 plots the relation between the gain ripple and the number of pump wavelengths for C- and L-band operation. Using more than 10 pump wavelengths, less than 0.1 dB of gain flatness can be achieved. In Fig. 5.14, arbitrary pump frequencies were used for dielectric filters, and regular frequency intervals were used for Mach–Zehnder interferometer (MZI) filters.

5.2.3. Requirements for Pump Sources

The key device for Raman amplifiers is undoubtedly the pump laser. Broadband Raman amplifiers became commercially practical once high-power pump laser diodes for WDM pumping were developed. For C- and L-band Raman amplifiers, pump wavelengths should range roughly from 1400 to 1500 nm. This is why we sometimes

call the pump lasers for WDM pumped Raman amplifier “14XX nm pumps.” In this section, we briefly discuss the requirements for 14XX nm pump laser diodes.

There are three pumping schemes for Raman amplifiers. The most common is called “counter-pumping,” in which the pump and signal propagate in opposite directions. Another scheme is called “copumping,” in which the pump and signal propagate in the same direction. The third scheme is “bidirectional pumping.” Copumping gives rise to noise transfer from pump to signal. It also suffers from larger effects of polarization-dependent gain and nonlinear signal phase shifts.

Some important characteristics of pump lasers for WDM pumping are high power, high efficiency, wavelength stability, high reliability, low relative intensity noise (RIN), low degree of polarization (DOP), high threshold of stimulated Brillouin scattering (SBS), and so on.

WDM pumping is advantageous because the use of more pump wavelengths can improve gain flatness and reduce the pump power per pump laser at the same time. A 14XX nm pump laser for WDM pumping is typically required to have 100 to 300 mW. These output power values are now commercially available. The use of a polarization beam combiner (PBC) can further reduce the necessary output power per laser, or increase the combined pump power at one pump wavelength.

A relatively narrow spectral width and wavelength stability are particularly important for WDM pumping. This is mainly for two reasons: because the gain spectral shape is susceptible against the wavelength shift, and because pump lasers with different wavelengths must be efficiently combined through WDM couplers in WDM pumping. In order to maintain a stable composite Raman gain spectra with high efficiency, the pump lasers must have relatively narrow and stable lasing spectra. Figure 5.15 shows gain error versus pump wavelength stability. In order to narrow and stabilize the output spectra of pump lasers, fiber Bragg grating (FBG) is typically used as an external cavity to the pump laser diode.

RIN and DOP values of pump lasers are not as important for the counter-pumping scheme. Raman amplifiers usually employ counter-pumping because they tend to become immune to pump RIN and DOP as well as they better suppress fiber nonlinearities as compared with the copumping scheme. On the other hand, the use of

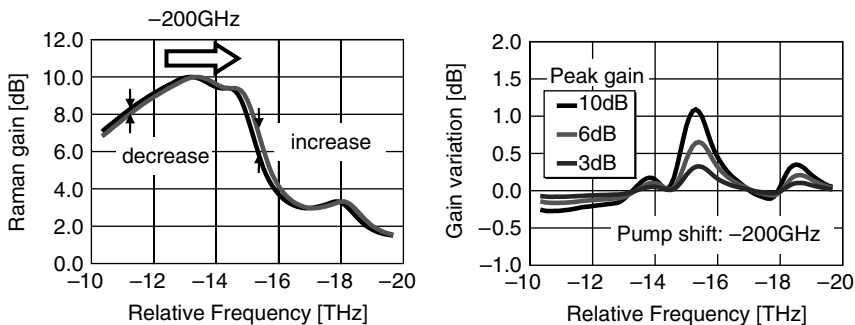


Fig. 5.15. Raman gain variation due to -200 GHz pump wavelength shift.

copumping, although RIN and DOP values of pump lasers become critical, can better suppress multiple path interference (MPI) noise and further reduce output power per laser diode in the bidirectional pumping scheme.

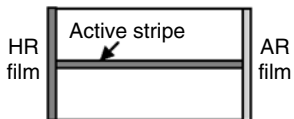
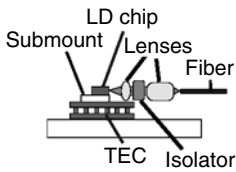
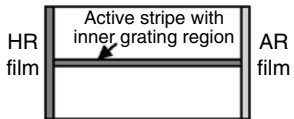
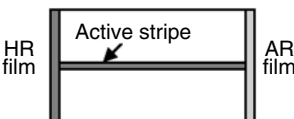
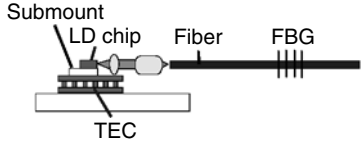
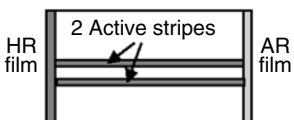
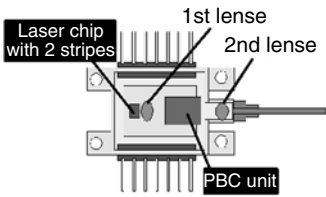
A good copumping laser source has yet to be developed. One fundamental trade-off is that better RIN characteristics usually entail a narrow linewidth of longitudinal modes resulting in a relatively low threshold of SBS. The final section of this chapter discusses details of such issues.

5.3. Pump Laser Sources for Broadband Raman Amplifiers

5.3.1. Types of Pump Lasers

In this section, structures and performances are introduced for Raman pump lasers. In the Raman amplifier system, an appropriate choice of the pump lasers is necessary in accordance with performance requirements of the system. Table 5.1 shows comparison of the chip structures and package structures of various pump lasers used for broadband Raman amplifiers. Also, Figs. 5.16 through 5.19 show comparison of characteristics among various pump lasers [20, 21].

Table 5.1. Laser Chip and Package Structures of Pump Lasers

Types	Laser chip structure	Package structure
FP laser		
IGM laser		
FBG laser		
Hybrid pump		

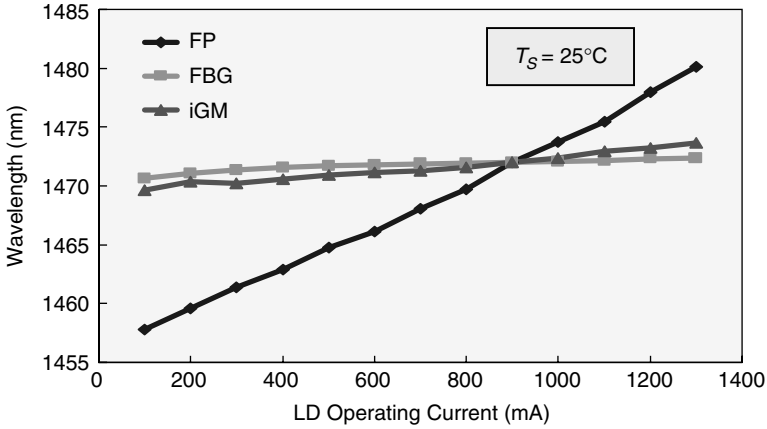


Fig. 5.16. Operating current dependencies of oscillation wavelength of laser modules at 25°C of T_{LD} .

5.3.1.1. FBG (Fiber Bragg Grating) Laser

The FBG laser [8] is a wavelength-stabilized laser using a Fabry–Perot (FP) laser and an external FBG that is fabricated in the fiber pigtail as shown in Table 5.1. It has the features of “excellent wavelength stability,” “sufficiently narrow lasing spectral width,” “very high SBS threshold power,” and “comparatively large RIN,” as respectively shown in Figs. 5.16 through 5.19. Because of these features, it is currently the most widely used pump laser for backward pumping Raman amplifiers. A resonator of FBG laser is formed between FBG and FP laser chips that has AR (antireflectance) film on the front facet to reduce the influence of laser’s FP mode gain (see Table 5.1). And the narrow oscillation spectrum according to the bandwidth of FBG is obtained. Figure 5.17 shows the spectrum of the FBG laser, which contains FP modes, the modes resulting from the resonance due to the external cavity by the FBG, and the envelope dictated by the reflection spectrum of the FBG. RIN spectra are shown in Fig. 5.18. The periodic noise peaks in the RIN spectrum of the FBG laser originate from resonance between the FBG and the laser chip, and appear about every 100 MHz, which corresponds to the distance of a laser chip and FBG of 1 m.

However, such a long resonator gives an excellent benefit in terms of suppressing SBS. The FBG laser is operated in the state of so-called “coherence collapse” [22, 23]. In other words, the distance between the FBG and laser chip is sufficiently longer than the coherent length of FP laser beam. This condition makes the phase of optical feedback from the FBG to the laser chip random and, consequently, the linewidth in each longitudinal mode becomes very wide because the phase in the laser beam is “washed out” by the random phases. Thus, the FBG laser has wider linewidths compared to other types of lasers and this feature gives very high SBS threshold power. In fact, the SBS characteristic has the relation of a trade-off in general with RIN performance, as can be inferred by comparing Figs. 5.18 and 5.19.

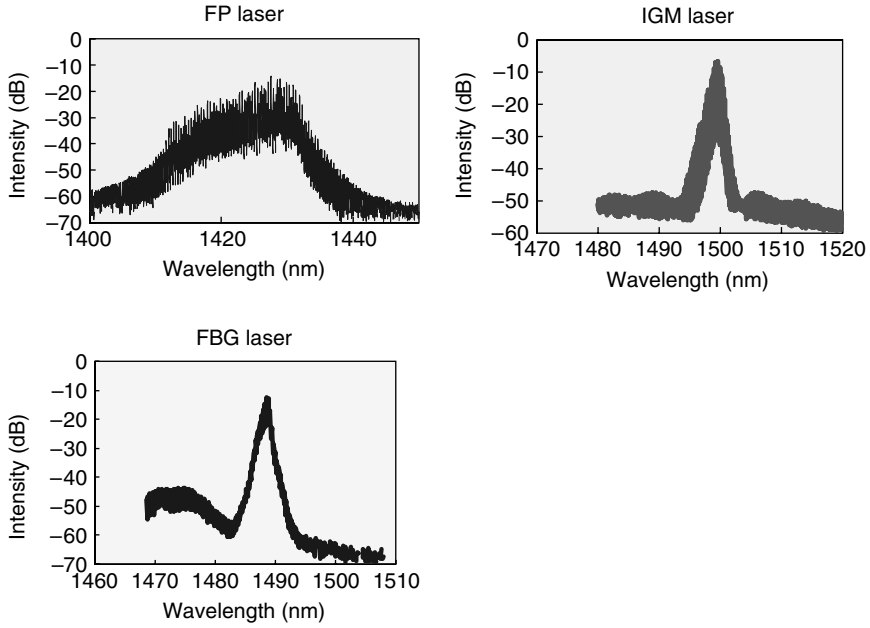


Fig. 5.17. Optical output spectra of different types of pump lasers.

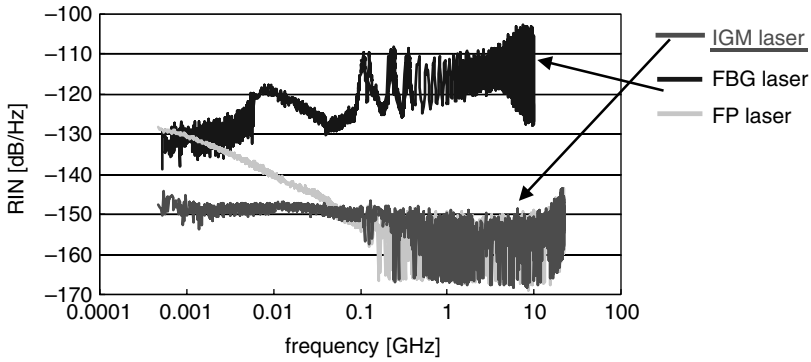


Fig. 5.18. RIN characteristics.

Note: The threshold power of SBS is approximated by the following simple expression [24],

$$P_{th} = 21 \frac{A_{eff}}{G_b L_{eff}} \left\{ 1 (F_l < F_b), \quad \frac{F_l}{F_b} (F_l > F_b) \right\}, \quad (5.9)$$

where, F_l is the spectral line width of the laser, F_b is the Brillouin linewidth, A_{eff} is the effective area of the fiber, L_{eff} is the effective length of the fiber, and G_b is

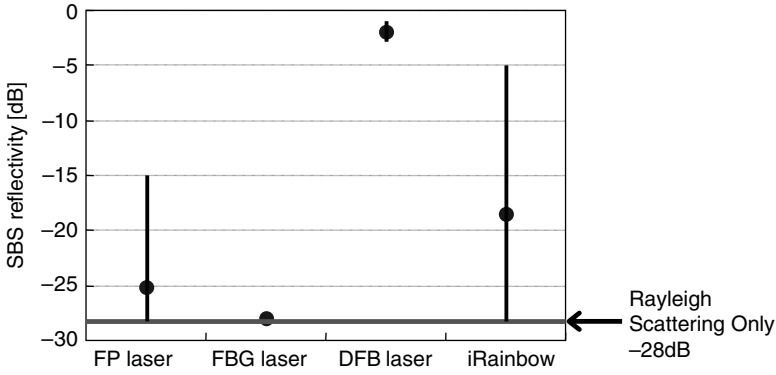


Fig. 5.19. Comparison of SBS performances for a 55 km DSF for transmission line with the transmission loss of 0.21 dB/km at 1550 nm, the dispersion of -0.07 ps/km/nm at 1550 nm, the A_{eff} of $47 \mu\text{m}^2$ at 1550 nm, and the zero dispersion wavelength of 1551 nm.

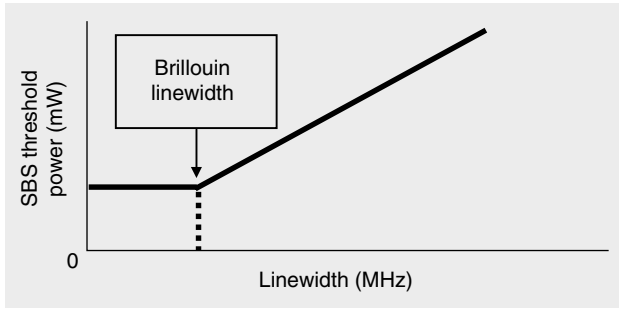


Fig. 5.20. Theoretical relationship between the linewidth of laser and SBS threshold power.

the material parameter. As shown in Fig. 5.20, when the linewidth is narrower than the Brillouin linewidth, SBS threshold power is constant. And when the linewidth is wider than the Brillouin linewidth, the SBS threshold power increases proportionally to the linewidth of the lasing mode.

5.3.1.2. FP (Fabry–Perot) Laser

The detailed structure of the FP laser is described in Sections 5.1.1 and 5.1.2. The FP laser has a relatively good RIN as shown in Fig. 5.18, so it may be used as a pump light for copumped Raman amplifiers. The mean oscillating wavelength of this laser strongly depends on operating current. The dependency is several times larger than that of FBG lasers as shown in Fig. 5.16. Wavelength variation of the FP laser is due to the increase in junction temperature of the active region with increased current, and is dominated by temperature dependency of the band gap of the active region. Therefore, for application to Raman amplifiers, wavelength variation is often

compensated for by way of decreasing laser temperature according to the increase of the operating current.

5.3.1.3. IGM (Inner Grating Multimode) laser

The IGM laser [20, 21, 25, 26] is characterized by a grating layer built in the laser cavity. And the oscillating wavelength is stabilized by this internal grating structure optimized for selecting more than three longitudinal modes. By eliminating external FBG, a low RIN characteristic could be obtained, because the low-frequency resonance between the laser chip and the FBG is also eliminated. An optical isolator could be integrated inside the package, because the laser chip does not need optical feedback from an external resonator as does the FBG laser. The dependence of the oscillation wavelength on the operating current in the IGM laser is dictated by the thermal expansion and temperature dependence of the refractive index in the internal grating layer. The dependence is about four times smaller than that of the FP laser. This laser is expected as a low-noise wavelength-stabilized pump source, particularly for copumped Raman amplifiers. Detailed characteristics and technical issues of the IGM laser are described in Section 5.2.

Another, but similar approach to the IGM laser is multimode operation of the DFB laser, called the multimode DFB laser [27].

5.3.1.4. Hybrid Pump

The hybrid pump [28] is a pump laser with very high fiber-coupled power of over 1 W and low DOP by means of integration of a two-stripe laser chip and PBC (polarization beam combiner).

The structure of the hybrid pump is shown in Table 5.1. The PBC-block is located between the first and second lenses. The two laser beams are combined by an integrated PBC, and coupled into a common SMF fiber-pigtail through the second lens. Two laser stripes are electrically connected in parallel. The integrated PBC includes a half-wave plate at one input path in order to make the two input beams orthogonally polarized.

The coupling efficiency for single-mode fiber is about 80%. This value is almost equal to the product of the insertion loss of the PBC and the coupling efficiency of a conventional laser module. The width of the active layer in a hybrid pump is substantially twice as wide as that of a single stripe laser due to the two-stripe structure. And the active areas of both types have almost the same series resistance and thermal impedance per unit active area. Therefore, the hybrid pump has better series resistance and thermal impedance. In fact, the power consumption can be smaller than conventional single-stripe laser modules for the same optical output power. The power consumptions of the single-stripe laser module that has 2 mm of cavity length and the hybrid pump of 1.5 mm of cavity length are compared in Fig. 5.21. By using the hybrid pump, about 20% reduction in power consumption is achieved at the fiber output power of 500 mW. Moreover, as shown in Fig. 5.22, DOP was reduced to 5% or less, which is generally suitable for Raman amplifiers.

This technology could be combined with either the IGM or FBG laser.

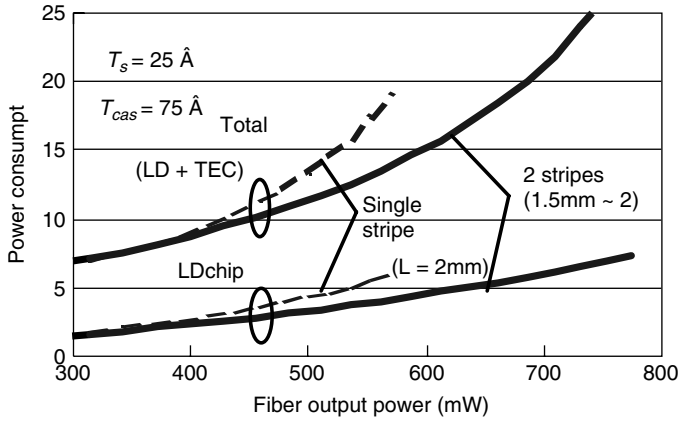


Fig. 5.21. Power consumption of the hybrid pump compared with a conventional single-stripe laser module.

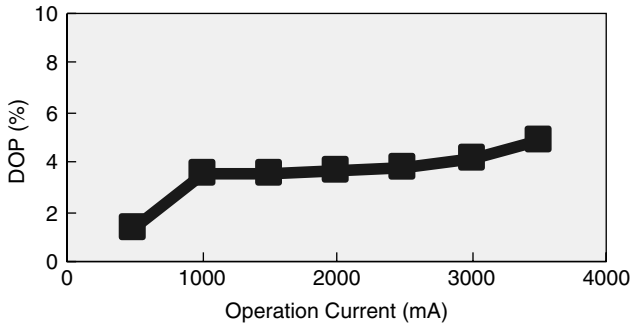


Fig. 5.22. Operating current dependency of DOP in hybrid pump.

5.3.1.5. Other Types of Pump Lasers

Besides the GRIN-SCH strained layer MQW structure with BH structure based on InGaAsP/InP material, there have also been proposed several laser structures suitable for achieving high-power output operation in the 14XX nm range.

One approach would be widening the active stripe of the laser in order to achieve both low thermal impedance and low series resistance, by using laser structures such as the ridge-waveguide laser [29], flared laser [30], and active MMI (multi-mode-interference) laser [31].

By using the ridge-waveguide structure with a very long cavity length of 3 mm and a wide ridge width, maximum fiber-coupled power of 710 mW was achieved [29].

The cavity of the flared laser consists of a single-mode section and a flared amplifier section as shown in Fig. 5.23 [30]. The flared amplifier section has a wider area than the single-mode section. Over 525 mW of fiber-coupled power was reported by using this structure [30].

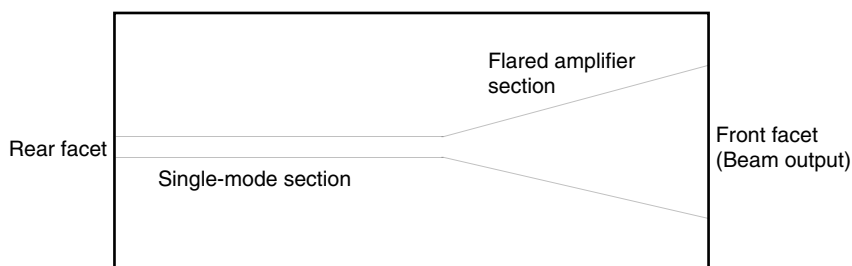


Fig. 5.23. Schematic of flared laser.

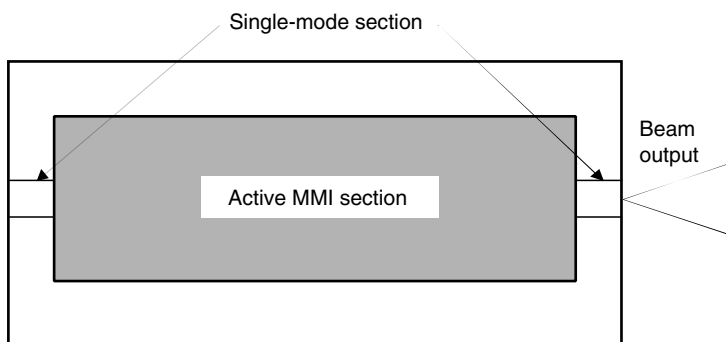


Fig. 5.24. Schematic of active MMI laser.

The active MMI laser has a laser cavity comprising a single-mode section and a multimode section as shown in Fig. 5.24 [31]. The optical mode field of the multimode section is coupled into the single-mode section with very small coupling loss by the MMI effect. And also, the active multimode section is much wider than the single-mode section, resulting in a small power consumption of the laser. By this structure, it is reported that the electric power consumption was reduced by 50% compared to a conventional structure [31].

The other approach would be changing basic materials. By using AlGaInAs/InP-based ridge-waveguide structure, over 500 mW fiber-coupled power was reported [32]. This high-power operation was achieved by improvement in temperature dependency of lasing performances. AlGaInAs/InP materials have a larger conduction band offset compare to that in InGaAsP/InP, providing strong carrier confinement that leads to lower carrier leakage at a high operating junction temperature.

5.3.2. Wavelength-Division-Multiplexing of Pump

5.3.2.1. WDM Couplers for WDM Pumping

WDM couplers are used to efficiently combine different pump wavelengths into a single fiber. There are a number of technologies to realize efficient WDM couplers.

There may be three typical types of WDM couplers for WDM pumping of Raman amplifiers: based on dielectric thin film interference filters, another is based on imbalanced Mach–Zehnder interferometers, and the fused-fiber coupler. The first type is also called a “bulk” type WDM coupler, as the thin film filters are so-called bulk optics. And in bulk type WDM couplers, light through fiber has to travel in a free space and pass through the bulk optics. The second type can be realized with a planar lightwave circuit (PLC). The third one, the fused-fiber coupler, is based on modal interferences in the fused fiber section.

The frequency spacing between pumps for WDM pumping is typically from 1 to 4 THz, because a Raman gain spectrum has approximately a few THz width. The spacing also depends upon the system requirements especially in terms of flatness. As was previously discussed with respect to Fig. 5.14, the number of pump wavelengths, or pump frequency spacing, determines the degree of flatness.

The frequency, or wavelength, spacing determines in principle the passband width of the WDM coupler. The spectral width of pump lasers has to be narrower than the passband width of the WDM coupler for efficient combining. The combination efficiency of WDM couplers depends on the shape of the transmission spectrum of WDM couplers and the shape of the lasing spectrum of pump lasers. The typical transmission spectra of thin film filters and the other two types, Mach–Zehnder interferometers and fused-fiber couplers, are different. Figure 5.25 compares such difference.

A merit of thin film filters is the flat-top shape of the transmission spectrum. This feature results in relatively stable transmission characteristics against fluctuations in pump wavelength. Another merit of these filters is that uneven pump wavelength spacing can be designed without loss of efficiency. On the other hand, both Mach–Zehnder interferometers and fused-fiber couplers have sinusoidal transmission spectra so that the pump frequency spacing tends to be periodical for relatively high efficiency.

A merit of Mach–Zehnder interferometers and fused-fiber couplers is low excess loss. Both fused-fiber couplers and PLC have very low excess loss because they can consist of very low loss waveguides. On the other hand, bulk couplers must use free-space coupling optics that usually entail a coupling loss of typically 0.2 dB. But for

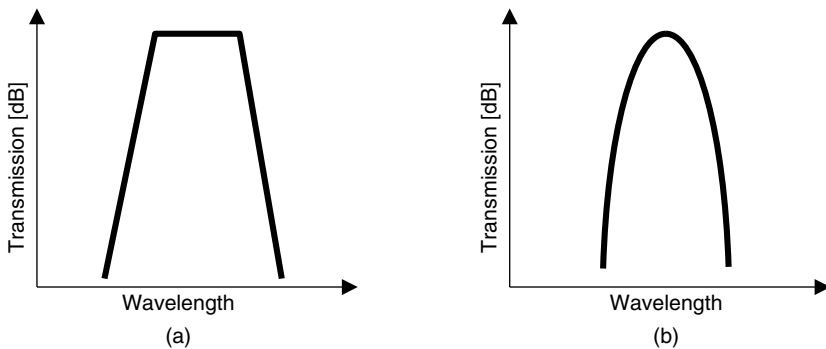


Fig. 5.25. Transmission spectra of (a) dielectric thin film filter and (b) Mach–Zehnder interferometer.



Fig. 5.26. WDM coupler comprising 16 integrated Mach–Zehnder interferometers on one PLC chip. Courtesy of Fitel Photonics Laboratory, Furukawa Electric Co., Ltd.

Mach–Zehnder interferometers and fused-fiber couplers, because the transmission spectra are sinusoidal, the spectral width of pump lasers has to be narrower than the passband.

The PLC-based Mach–Zehnder interferometer has an advantage in terms of integration. Let us define N as the number of pump wavelengths for WDM pumping. Then the necessary number of WDM couplers is $N - 1$. For a large number of pump wavelengths, say 12, it would be significant whether we need to use 11 discrete WDM couplers or a single all-in-one integrated PLC coupler. Figure 5.26 shows an integrated Mach–Zehnder interferometer coupler based on PLC. It contains 16 Mach–Zehnder interferometers on one PLC chip.

5.3.2.2. PBC

Another efficient means to combine two laser outputs is the use of the polarization beam combiner (PBC). The PBC is a device that efficiently combines two orthogonally polarized light inputs into one common single-mode fiber. Because pump laser diodes have linearly polarized output, two of them can be efficiently combined through a PBC.

A merit of this combiner is that the output spectra of two input lasers may be the same or significantly overlapped. Therefore, in the case where one pump laser is short of its output power, we can add another pump laser by using a PBC to supplement the output power in one pump wavelength. Figure 5.27 shows a photograph of a PBC. Another merit of using this technology is low DOP, which value is important for a pump source to suppress the polarization-dependent gain (PDG) of the Raman amplifiers. Details are discussed in the next section.

One drawback of using this technology is, of course, that it adds components and occupies a larger space. In the previous section, the hybrid pump was introduced. It contains a PBC inside the laser package so that this drawback becomes minimal.

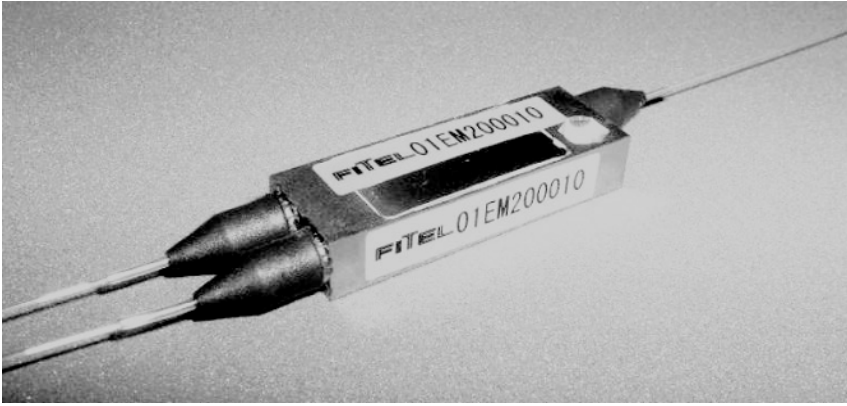


Fig. 5.27. PBC. Courtesy of Fitel Products Division, Furukawa Electric Co., Ltd.

5.3.3. Depolarization of Pump Lasers

Depolarization is important because the polarization-dependent gain of Raman amplifiers is sensitive to the degree of polarization of pump sources. Pump laser diodes usually have very high DOP as the output is TE mode only, or almost completely linearly polarized. This section discusses the relation between PDG and DOP in Raman amplifiers, and a depolarization technique of pump laser diodes.

5.3.3.1. PDG and DOP

Figure 5.28 plots the relation between PDG and DOP [33]. Because PDG is presumed to be proportional to the magnitude of Raman gain, the PDG value along the ordinate of the plot is normalized by the Raman gain and expressed in units of dB/dB. This means that for the Raman gain of 10 dB, the ordinate should be multiplied by 10 for the absolute PDG value. It is shown in the figure that one should reduce DOP values as much as the PDG value becomes sufficiently low.

Figure 5.28 contains two plots: one is for counter-pumping and the other is for copumping. Raman gain occurs almost only when the states of polarization (SOP) of pump and signal are aligned. However, because the relative orientation between SOPs of the pump and signal changes during propagation through the transmission fiber that has slight random birefringence, the dependence of PDG on DOP is not straightforward. In particular, counter-pumping has less PDG for a given DOP value of the pump as compared with copumping. This is because counter-pumping has stronger averaging effects through randomizing the relative SOP orientation between the pump and signal. Thus the slope of the curves in Fig. 5.28 may vary for different types and lengths of fibers, pumping scheme, and other system parameters such as polarization mode dispersion (PMD).

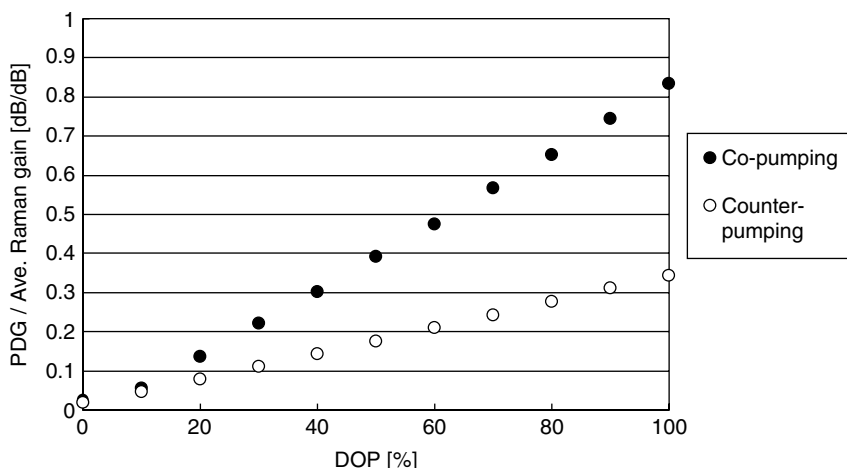


Fig. 5.28. Relation between PDG and DOP. Data were taken for 25 km SMF at the pump wavelength of 1450 nm and the peak Raman gain was 4.2 dB for counter-pumping and 3.8 dB for copumping.

5.3.3.2. Design of Depolarizer

The output from a pump laser diode is linearly polarized. The linear polarization state can be maintained over the fiber pigtail if one uses polarization-maintaining fibers (PMFs). It is relatively easy to realize low-loss depolarizers for stable linear polarization inputs by making use of a PMF fusion-spliced to the pigtail PMF of the laser at 45° from the principal axes [34, 35]. There may be other types of depolarizers that comprise split branches using couplers. However, this section only refers to a depolarizer using a straight configuration of PMFs or high-birefringent components, as this type of depolarizer should be particularly simple and of low loss.

Figure 5.29 shows the principle of a depolarizer. This depolarizer uses a high-birefringence material, which is in this case a PMF, to realize a delay between the

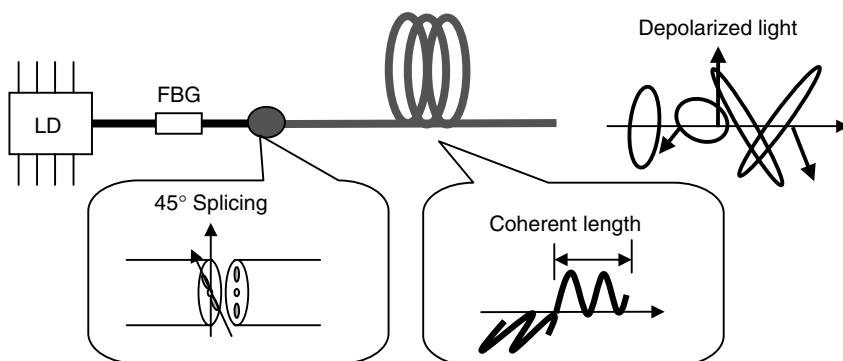


Fig. 5.29. Principle of depolarizer.

two eigenmodes of propagation. In this configuration, the output from the laser diode is split into two propagation modes with the delay, and they are recoupled at the exit of high-birefringence PMF. The DOP at the output of the depolarizer as a function of PMF length is therefore expressed as the Fourier transform of the optical spectrum of the laser. Because pump lasers usually have multiple longitudinal modes, the curve of the DOP versus PMF length will have many peaks. The width of each peak is approximately inversely proportional to the spectral width of the pump laser, and the envelope of the peaks has a width inversely proportional to the linewidth of each longitudinal mode of the laser. The interval between the two adjacent peaks is inversely proportional to the longitudinal mode spacing of the laser. So it would be better to use a pump laser with broad spectral width for better depolarization.

5.3.3.3. Performances

Figure 5.30 shows the comparison between the experiment and simulation of DOP values versus PMF length. A good agreement is obtained and the performance is also good. In practice, however, it is necessary to consider the incompleteness of linear polarization at the output from pump laser diodes.

In a production process of pump lasers, one of the principal axes of the PMF pigtail is aligned with the TE-mode output of the laser chip so as to excite only one propagation mode of the PMF pigtail. This process can never be perfect enough and, consequently, a small portion of the TE-mode output from the laser chip is coupled with the other eigenmode of the PMF pigtail. In this case, the SOP at the output of the PMF pigtail of the pump laser will not be stable, because the amount of the delay between the two eigenmodes inside the PMF pigtail is sensitive to temperature. For the perfect linear polarization case, there is only one eigenmode excited in the PMF pigtail in the first place.

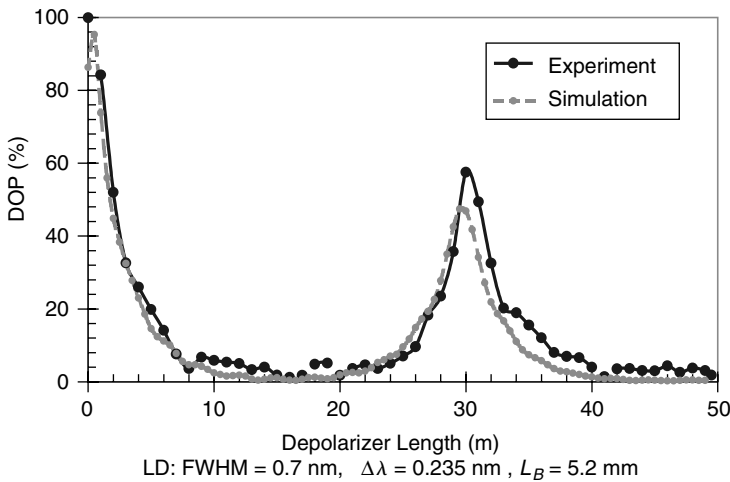


Fig. 5.30. Comparison between simulation and experimental results of DOP versus depolarizer PMF length.

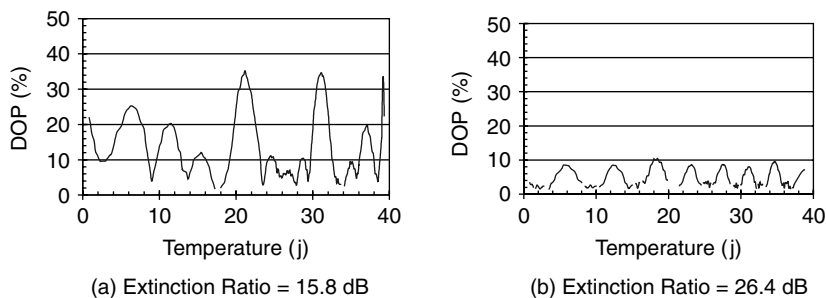


Fig. 5.31. Temperature dependence of the PMF depolarizer.

If the input SOP to the depolarizer PMF is unstable, the DOP value at the output of the depolarizer will also be unstable. This observation can be verified by comparing the temperature dependences of the DOP for pump lasers with PMF pigtailed with high and low extinction ratios. Figure 5.31 compares those. Figure 5.31(a) shows the temperature dependence of the DOP for the laser with the PMF pigtail having an extinction ratio of 15.8 dB, and Fig. 5.31(b) shows that of 26.4 dB. It is important to note that even the extinction ratio of 26.4 dB is not high enough for achieving DOP values less than 5% over the operating temperature range. Practically speaking, an extinction ratio less than 26.4 dB is difficult to guarantee 100% in real production.

In order to improve the temperature stability of the depolarizer, it is necessary to allow arbitrary input SOP to depolarizers. One solution is to optimally increase the length of the PMF pigtail of the pump laser module [35]. Figure 5.32 shows the temperature dependence of DOP obtained with such a depolarizer with an optimally

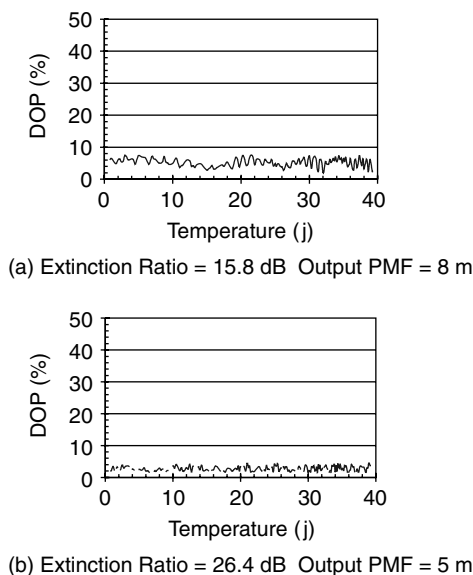


Fig. 5.32. Temperature dependence of the Lyot type depolarizer.

increased length of the pigtail PMFs for the same pump lasers for Fig. 5.31(a) and (b). Comparing Fig. 5.31, Fig. 5.32 clearly shows the effectiveness.

Another alternative is either to achieve much more precise alignment of the PMF pigtail with respect to the TE mode of the laser output, or to use a polarizer at the input to the PMF. A polarizer with enough high extinction ratios would be able to increase the degree of linear polarization launched into the depolarizer PMF.

5.4. Raman Pump Units

This section shows some practical design issues of a Raman pumping unit. We first describe what is typically included in such a unit. Secondly, the thermal design for reducing the package size is discussed. Then design examples of prototypes are presented and finally a concept of an upgradable Raman pumping unit is proposed.

5.4.1. Configurations

When we employ a distributed Raman amplifier for a WDM system, we typically install a Raman pump unit as illustrated in Fig. 5.33. In order to obtain a broadband Raman gain spectrum, it is necessary to use WDM pumping. A depolarizer and/or a polarization combiner are usually attached to the pump lasers so as to reduce the degree of polarization of pump light. A pump power monitor is often required to control and maintain the output power of the unit. Thus it typically includes several pump lasers, PBC, WDM couplers, isolators, tap couplers for monitoring, monitor photodiodes, signal-pump-WDM coupler, drive and monitoring circuits, heat sink, and so on. The allocation of pump wavelengths depends on the system requirements as discussed in Section 5.2.2.

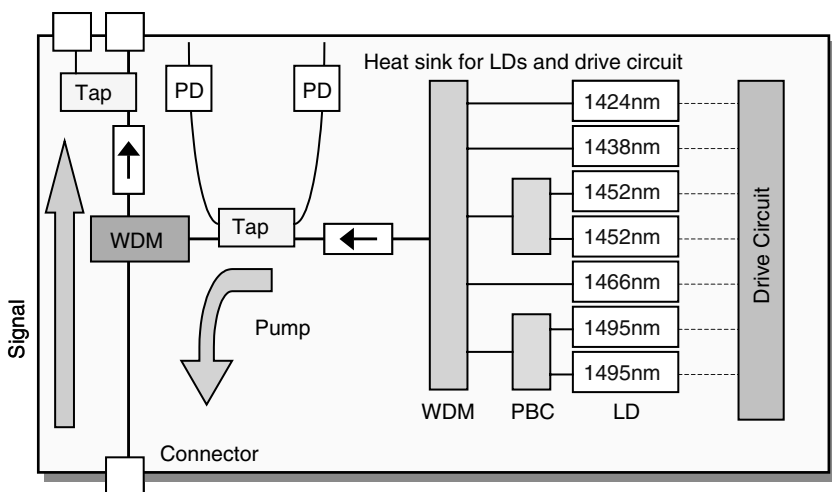


Fig. 5.33. Schematic of typical WDM pumping Raman pump module.

5.4.2. Thermal Management

An important issue for the design of a Raman pump unit is thermal management. Because the pump lasers are driven relatively hard as compared to those built in EDFA, the power consumption as well as thermal dissipation becomes an issue. In order to enhance thermal dissipation, a larger heat sink is inevitable. However, because of the physical constraints of the system, the size of Raman pump units, in particular the height, is usually limited. When enough space for a heat sink is not available, the use of a heat pipe is effective to transport the heat efficiently from one place to another. Heat pipe is a copper-sealed tube in which the pressure is very low, containing a tiny amount of water. The water inside evaporates in operating temperature range to

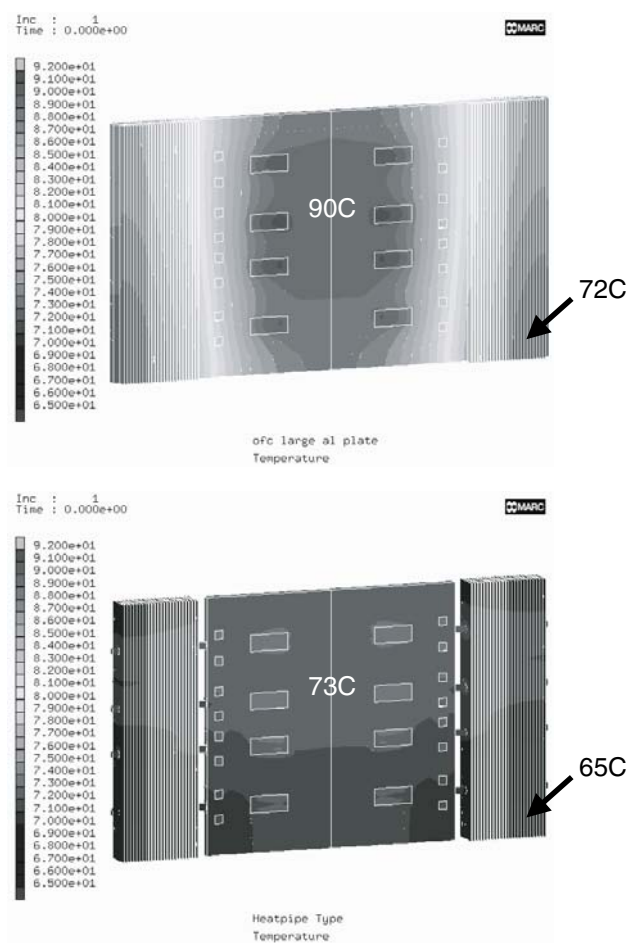


Fig. 5.34. Simulated temperature distribution of heat sinks with and without using heat pipes. The ambient temperature is 50°C. Heat load per laser is 14 W including driving FETs, and air flow is 1 m/s.

create a current of molecules transporting heat from one end to the other. The effective thermal conductivity is 100 times as large as that of diamond. Figure 5.34 compares the temperature increase with and without heat pipes. For the air flow of 1 m/s, the heat dissipation per laser of 14 W including the power consumed by the driving FETs, and the ambient temperature of 50°C, the highest temperature of a heat-pipe heat sink is 17.3 degrees lower than that of a normal aluminum heat sink of the same size.

5.4.3. Examples

5.4.3.1. Five-Wavelength Pump Unit

Figure 5.35 shows a photograph of a Raman pump unit equipped with heat pipes. This unit can carry up to eight pump lasers and is only one inch thick, yet with enough heat

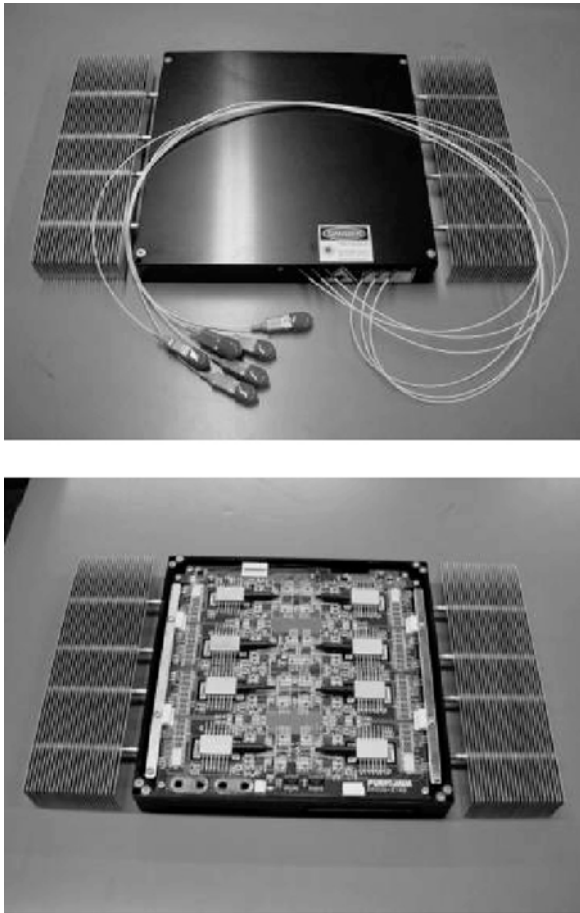


Fig. 5.35. Five-wavelength Raman pump module. Courtesy of Fitel Products Division, Furukawa Electric Co., Ltd.

dissipation. Because this unit is designed to be controlled by an outside computer through an RS-232 interface, operation can be flexible according to the operating software.

5.4.3.2. Thirteen-Wavelength Pump Unit

Figure 5.36 shows a highly integrated Raman pump module for providing broadband gain and small gain ripple. This unit comprises 13 pump lasers having different wavelengths, PLC-MZI type pump combiner, isolator, and optical output monitor tap. This unit does not include any drive electronics circuit. The dimensions of the unit are $215 \times 120 \times 30$ mm, which would be almost the same size as conventional EDFAs.

5.4.3.3. Low-Cost and Compact Dispersion Compensating Raman Amplifier

Figure 5.37 shows a low-cost and compact Raman amplifier, in which a dispersion and dispersion slope compensation fiber module (DSCM) and a Raman pump unit are integrated. DSCM can be so designed as to compensate for any types and length of transmission fiber spans. This Raman pump unit includes two pump lasers, polarization maintaining fiber type depolarizers, two WDM couplers, an isolator, a monitor coupler, two monitor photodiodes, and drive electronics to keep constant output



Fig. 5.36. Thirteen-wavelength Raman pump module. Courtesy of Fitel Photonics Laboratory, Furukawa Electric Co., Ltd.

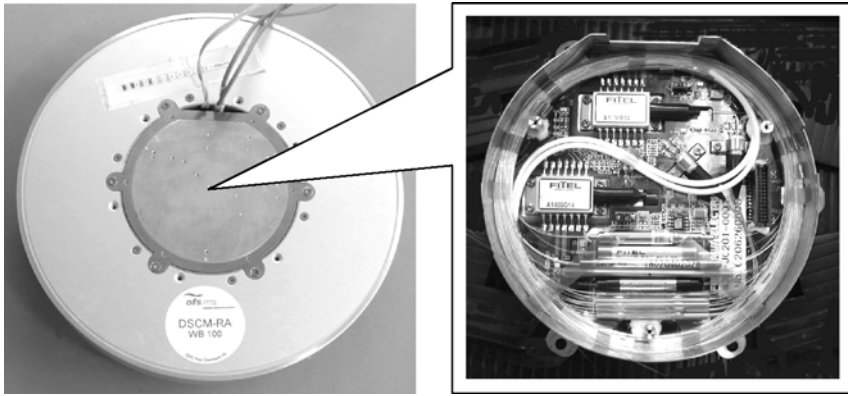


Fig. 5.37. Dispersion compensating Raman amplifier. Courtesy of Fitel Products Division, Furukawa Electric Co., Ltd.

power. The volume of this amplifier is the same as an ordinary DSCM, because the Raman pump unit is embedded in the center room of the DSCM. This type of Raman amplifier is typically operated at a lossless gain level.

5.4.3.4. Upgradeable Raman Amplifier

Figure 5.38 shows gain spectra of an upgradeable Raman amplifier where C-, L-, and C + L-band operation can be realized by selecting appropriate sets of pump channels among only five wavelengths for the respective operation bands. C-band Raman gain is obtained with the set of 1424 and 1452 nm, and L-band gain is obtained with the set of 1466 and 1495 nm. Besides the above four wavelengths, an ad hoc pump channel of 1438 nm is required for the C + L-band. Thus, in order to recycle the use of these

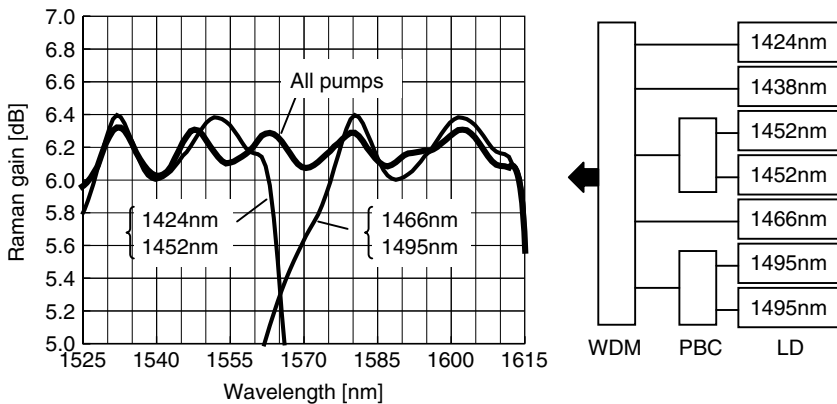


Fig. 5.38. Composite Raman gains upgradeable from either C- or L- to C + L-band operation with recycling use of pump lasers. Source: S. Namiki and Y. Emori "Ultrabroad-Band Raman Amplifiers Pumped and Gain-Equalized by Wavelength-Division-Multiplexing High-Power Laser Diodes" IEEE Journal of Quantum Electronics Vol. 7 (©2001 IEEE)

pump wavelengths, this scheme can provide an upgradable solution with a reasonable flatness maintained for all cases. The ad hoc channel is not used in individual band operations, but only turned on for C + L-band operation.

The reason why the ad hoc channel is necessary derives from the asymmetric profile of the Raman gain spectrum. As discussed in Section 5.2, for flattening the gain we need a set of small Raman gain spectra laterally shifted from each other to compose a smooth gain slope opposite the smooth gain slope on the lower frequency side of the Raman gain peak by a single pump frequency. When operating only in either the C- or L-band, we use just two pump wavelengths in the present case. On the other hand, in the case of C + L-band operation, we need four wavelengths for the set on the shorter wavelength side to maintain the same degree of flatness and recycle the use of the pump lasers used for either C- or L-band operation.

5.5. Copumping Laser Diodes

Raman amplifiers employed for practical use are mostly counter-pumped, because counter-pumping better maintains the quality of the amplified signal than copumping, particularly with regard to the factors: RIN transfer noise from pump lasers, polarization dependence of gain, and nonlinear effects in the amplifier fiber. On the other hand, in most cases, a copumped Raman amplifier entails smaller amplified spontaneous emission noise than a counter-pumped one. Therefore, it is still worth investigating the possible applications of copumping. This chapter discusses some applications of copumping and a new type of pump laser, or IGM lasers, suitable for WDM copumping.

5.5.1. Copumping of Raman Amplifiers

It is well known that shorter wavelength signals tend to have larger noise figures in a WDM counter-pumping scheme due to pump-to-pump and signal-to-signal stimulated Raman scatterings in addition to thermal noise and wavelength dependence of fiber attenuation coefficients [36].

Because a copumped Raman amplifier can have lower ASE noise than a counter-pumped one, a wavelength-dependent gain caused by an additional copump source produces a wavelength-dependent improvement of the noise figure. Figure 5.39 shows the schematic drawing of a proposed method to reduce the wavelength dependence of the optical noise figure. The counter-pumping source includes five wavelengths, which can produce broadband Raman gain having flatness better than 1 dB. On the other hand, the copumping source includes the only shorter three wavelengths among those in the counter-pumping source. The reason for the selection is to obtain the wavelength-dependent copumped Raman gain suitable for flattening the optical noise figure [25, 37].

Figure 5.40 shows the measured Raman gain and optical noise figure of broadband Raman amplifiers with and without using the copumping source. In this experiment, 76 km of standard single-mode fiber is used as the gain medium, and the gain and

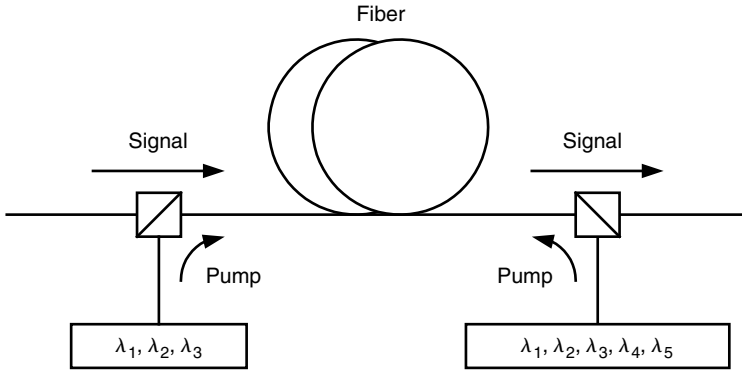


Fig. 5.39. NF tilt scheme using copumping.

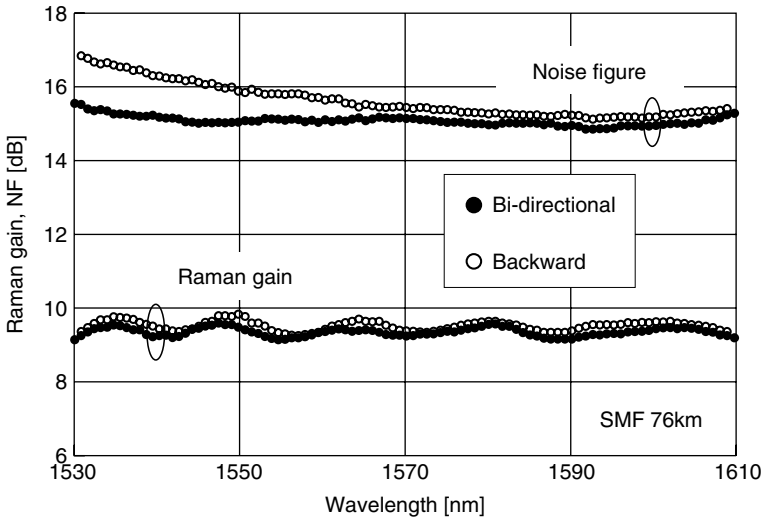


Fig. 5.40. NF tilts for counter- and bidirectional pumpings.

noise figure are measured by using a tunable laser source. The signal power launched into the fiber is less than 0 dBm. The noise figure accounts for the fiber and passive component loss. Less than 0.5 dB of gain flatness and 0.7 dB of noise flatness over 80 nm of signal bandwidth are demonstrated by adjusting the balance between co- and counter-pumping sources. As shown in Fig. 5.40, counter-pumping causes large wavelength dependence of the noise figure, and the optimized bidirectional pumping reduces the dependence by virtue of the copumps having the shorter wavelengths.

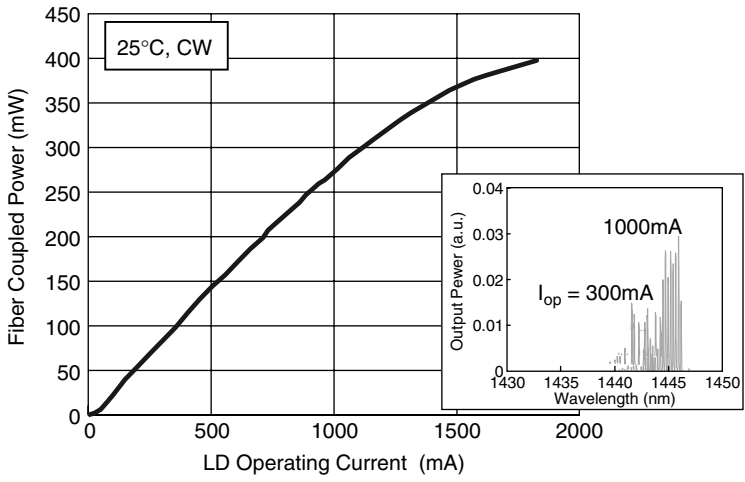
Note that the use of copumping raises the path-averaged power of the signal or nonlinear effects, although it may improve the ASE noise figure and multipath interference noise due to double Rayleigh scattering. Therefore, we have to optimize

the balance between co- and counter-pump power so as to obtain the best quality of the signals in the overall performance.

5.5.2. Recent Progress of Copumping Laser Diodes

As a recent progress of copumping laser diodes, this section describes detailed characteristics of the IGM laser. As introduced in Section 5.3.1, the IGM laser is a wavelength-stabilized low-noise laser with an internal grating layer optimized for selecting multiple longitudinal modes. So it could be an ideal copumping laser. Figure 5.41 shows L - I characteristics and oscillation spectra in linear scale of the IGM laser. The maximum fiber output power was 400 mW. It is important to note that it is so designed as to assure multiple-longitudinal-mode oscillations for reducing SBS. The SBS light strongly aggravates the noise performance of Raman amplifiers and can cause crucial problems.

The SBS threshold power of the IGM laser is smaller than that of the FBG laser, because the spectral linewidth of each mode in the IGM laser is much narrower than that of the FBG laser (see Section 5.3.1.1). Figure 5.42 shows the relation between SBS reflectivity and the number of longitudinal modes in the IGM laser [26]. In this experiment, a 55 km long DSF with the transmission loss of 0.21 dB/km at 1550 nm, the dispersion of -0.07 ps/km/nm at 1550 nm, the A_{eff} of $47 \mu\text{m}^2$ at 1550 nm, and the zero dispersion wavelength at 1551 nm was used for the transmission line. Here the number of longitudinal modes is defined as the number of modes in the spectral width at 10 dB down from the peak. The SBS reflectivity tends to decrease with increasing number of longitudinal modes in the IGM laser, as shown in Fig. 5.42. IGM lasers, especially those having more than 18 longitudinal modes, exhibited sufficiently



Characteristics

Fig. 5.41. L - I characteristics and spectra of IGM laser.

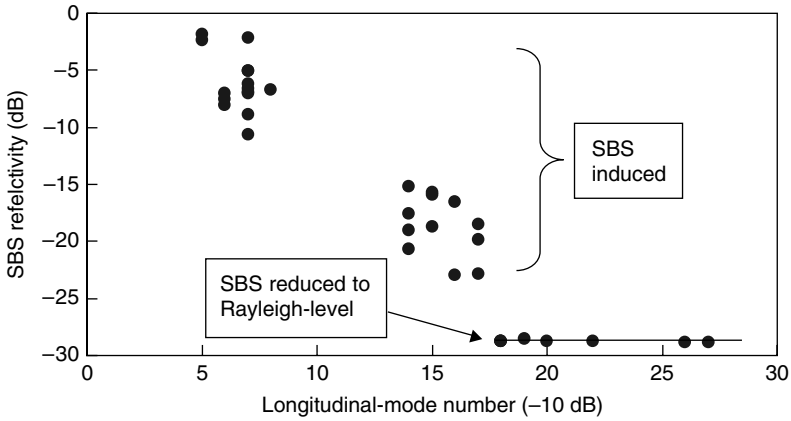


Fig. 5.42. Dependency of SBS reflectivity on the number of longitudinal modes.

suppressed SBS reflectivity below -29 dB, which corresponds to Rayleigh scattering. It is confirmed that SBS-free operation up to 270 mW fiber input power could be obtained by using an IGM laser having over 18 longitudinal modes.

By detailed investigations, it was shown that an increase in the number of modes results in wider linewidths per longitudinal mode. So, SBS could be reduced mainly by the following two factors: lower power per longitudinal mode, and increase of SBS threshold power per longitudinal mode [26].

It was shown that applying frequency modulation (dithering) to the IGM laser was effective for suppressing SBS [21, 38]. By applying a frequency modulation, the spectral linewidth of the laser is broadened because the optical cavity length of a laser chip fluctuates as a result of thermal variation due to the injected current fluctuation. This is a well-known technique for suppressing SBS in the case of a DFB laser [39]. Figure 5.43 shows an example of experimental results for SBS suppression by frequency dithering. Here modulation index is defined as the ratio of the modulation amplitude of optical power to the average output power. When the dithering at a 1% modulation index was applied, the SBS was successfully suppressed down to Rayleigh scattering level over the dithering frequency range of 10 kHz to 100 kHz. Further suppression could be achieved at a 10% modulation index for a wider range over 3 kHz.

It is known that RIN of multiple-longitudinal-mode lasers increases during transmission along a dispersive fiber line due to the so-called mode partitioning noise (MPN) [40]. Figure 5.44 shows comparison of the RIN characteristics after transmission through a TrueWave[®] RS fiber [21]. The increase in RIN after fiber transmission for the IGM laser is smaller than that for the FP laser, which is attributable to the smaller number of longitudinal modes in the IGM laser than in the FP laser. However, we should note that it is not clear yet how these results influence the transmission characteristics of signal light in Raman amplification systems. The performance of copumped Raman amplifiers should significantly depend upon the characteristics of pumping light sources. We note that further studies are necessary in this area.

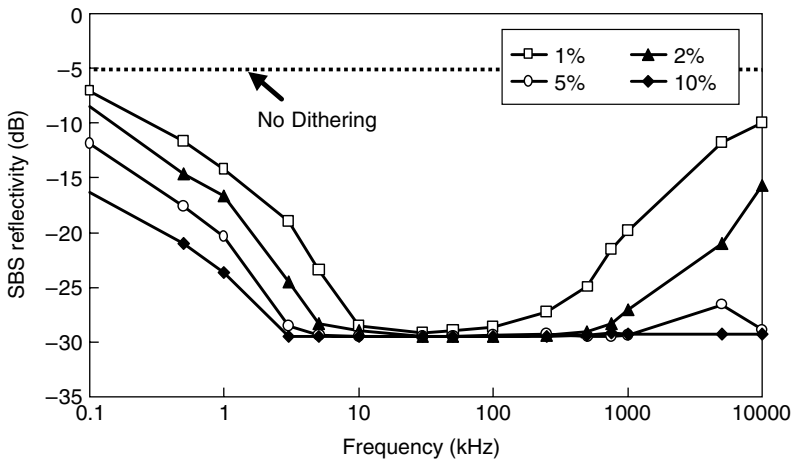


Fig. 5.43. SBS suppression versus dithering frequency in the IGM laser.

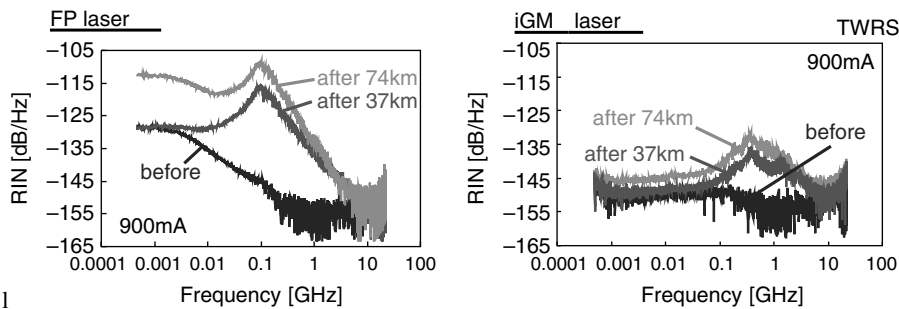


Fig. 5.44. RIN spectra before and after transmission of TrueWave® RS fiber.

Acknowledgments

The authors wish to thank Drs. Junji Yoshida and Toru Fukushima for useful technical discussions and thorough proofreading. They are also indebted to Dr. H. Yanagawa and Mr. M. Shibata for their encouragement.

References

[1] M. Nakazawa, Y. Kimura, and K. Suzuki, *Appl. Phys. Lett.*, 54:295, 1989.
[2] I. Mito, H. Yamazaki, H. Yamada, T. Sasaki, S. Takano, Y. Aoki, and M. Kitamura, 170 mW high power CW operation in 1.48–1.51 μm InGaAs MQW-DC-PBH LD. In *Proceedings of the Seventh International Conference on Integrated Optics and Optical Fiber Communication* (Kobe, Japan), 20 PDB-12, 1989.
[3] H. Asano, S. Takano, M. Kawaradani, M. Kitamura, and I. Mito, 1.48- μm high power InGaAs/InGaAsP MQW LD's for Er-doped fiber amplifiers, *Photon. Technol. Lett.*, 3:5, 415–417, 1991.

- [4] K. Yamada, S. Oshiba, T. Kunii, Y. Ogawa, T. Kamijoh, T. Nonaka, and Y. Kawai, More than 3000 hours stable CW operation of 1.48 μm LD for EDFA pumping source. In *Proceedings of OAA* (Monterey, CA), WA-3, 1990.
- [5] H. Kamei, N. Katoh, J. Shinkai, H. Hayashi, and M. Yoshimura, Technical digest of OFC (San Jose, CA), 45, 1992.
- [6] Y. Emori, Y. Akasaka, and S. Namiki, Broadband lossless DCF using Raman amplification pumped by multichannel WDM laser diodes, *Electron. Lett.*, 34:2145–2146, 1998.
- [7] Y. Emori, K. Tanaka, and S. Namiki, 100 nm bandwidth flat-gain Raman amplifiers pumped and gain-equalised by 12-wavelength-channel WDM laser diode unit, *Electron. Lett.* 35:1355, 1999.
- [8] S. Koyanagi, A. Mugino, T. Aikiyo, and Y. Ikegami, The ultra high-power 1480 nm pump laser diode module with fiber Bragg grating. In *Proceedings Optical Amplifiers and Their Applications*, MC2, 1998.
- [9] T. Kimura, N. Tsukiji, A. Iketani, N. Kimura, H. Murata, and Y. Ikegami, High temperature operation quarter watt 1480 nm pump LD module. In *Proceedings of Optical Amplifiers and Their Applications*, Thd12, 1999.
- [10] N. Tsukiji, J. Yoshida, T. Kimura, S. Koyanagi, and T. Fukushima, Recent progress of high power 14XXnm pump lasers, In *Proceedings of ITcom '01 on Active and Passive Optical Components for WDM Communication* (Denver) vol. 4532:349–360, 2001.
- [11] J. Yoshida, N. Tsukiji, A. Nakai, T. Fukushima, and A. Kasukawa, Highly reliable high power 1480 nm pump lasers for EDFAs and Raman amplifiers. In *Proceedings of Photonics West '01 on Testing, Reliability, and Applications of Optoelectric Devices* (San Jose), vol. 4285:146–158.
- [12] Y. Suematsu and A.R. Adams, *Hand Book of Semiconductor Lasers and Photonic Integrated Circuit*, 28, London: Chapman & Hall.
- [13] A. Kasukawa, T. Namegaya, N. Iwai, N. Nakayama, Y. Ikegami, and N. Tsukiji, Extremely high power 1.48 μm GaInAsP/InP GRIN-SCH strained MQW lasers, *IEEE Photon. Tech. Lett.*, 66:1, 4, 1994.
- [14] T. Hosoda, Y. Sasaki, H. Yamazaki, and K. Komatsu, Over 300mW-output power 1.48-um wavelength EDFA pumping ASM LDs. In *Proceedings of Optical Amplifiers and Their Applications*, Thd11, 1999.
- [15] G.P. Agrawal, *Nonlinear Fiberoptics*, 3d ed., San Diego: Academic, 2001.
- [16] S. Namiki, and Y. Emori, Ultrabroad-band Raman amplifiers pumped and gain-equalized by wavelength-division-multiplexed high-power laser diodes, *IEEE J. Select Topics Quantum Electron.*, 7:3, 2001.
- [17] H. Kidorf, K. Rottwitt, M. Nissov, M. Ma, and E. Rabarjaona, Pump interactions in a 100-nm bandwidth Raman amplifier, *IEEE Photon. Technol. Lett.*, 11:530, 1999.
- [18] B. Min, W.J. Lee, and N. Park, Efficient formulation of Raman amplifier propagation equations with average power analysis, *IEEE Photon. Technol. Lett.*, 12:1486, 2000.
- [19] M. Achtenhagen, T.G. Chang, B. Nyman, and A. Hardy, Analysis of multiple-pump Raman amplifier, *Appl. Phys. Lett.*, 78:1322, 2001.
- [20] N. Tsukiji, J. Yoshida, S. Irino, T. Kimura, Y. Ohki, and M. Funabashi. High power, high reliable, wavelength-stabilized low noise 14XX nm pumps for Raman amplifiers, In *Proceedings of OECC'02* (Yokohama), 10C3-7, 2002.
- [21] Y. Ohki, N. Hayamizu, H. Shimizu, S. Irino, J. Yoshida, N. Tsukiji, and S. Namiki, Increase of relative intensity noise after fiber transmission in co-propagating Raman pump lasers. In *Proceedings of OAA'02* (Vancouver, Canada), PD7, 2002.
- [22] R.W. Tkach and A.R. Chraplyvy, Regimes of feedback effects in 1.5-pm distributed feedback lasers, *J. Lightwave Technol.*, LT-4:11, 1655–1661, 1986.
- [23] C.R. Giles, T. Erdogan, and V. Mizrahi, Simultaneous wavelength-stabilization of 980-nm pump lasers, In *Proceedings of OAA*, Technical Digest Series, vol. 14, PD11, 1993.
- [24] R.G. Smith, Optical power handling capacity of low loss optical fibers as determined by stimulated Raman and Brillouin scattering, *Appl. Opt.* 11:2489–2494, 1972.

- [25] S. Kado, Y. Emori, S. Namiki, N. Tsukiji, J. Yoshida, and T. Kimura, Broadband flat-noise Raman amplifier using low-noise bi-directionally pumping sources. In *Proceedings of ECOC'01*, (Amsterdam), PD.F.1.8, 2001.
- [26] N. Tsukiji, N. Hayamizu, H. Shimizu, Y. Ohki, T. Kimura, S. Irino, J. Yoshida, T. Fukushima, and S. Namiki, Advantage of inner-grating-multi-mode laser (iGM-laser) for SBS reduction in co-propagating Raman amplifier. In *Proceedings of OAA'02* (Vancouver, Canada), OMB4, 2002.
- [27] R.P. Espindola, K.L. Bacher, K. Kojima, N. Chand, S. Srinivasan, G.C. Cho, F. Jin, C. Fuchs, V. Milner, and W.C. Dautremont-Smith, High power, low RIN, spectrally broadened 14xx DFB pump for application in co-pumped Raman amplification. In *Proceedings of ECOC '01* (Amsterdam), PD. F.1.7, 2001.
- [28] T. Kimura, M. Nakae, J. Yoshida, S. Iizuka, A. Sato, H. Matsuura, and T. Shimizu, 14XX nm over 1W pump laser module with integrated PBC. In *Proceedings of OFC'02* (Anaheim, CA) ThN5, 2002.
- [29] D. Garbuzov, R. Menna, A. Komissarov, M. Maiorov, V. Khalfin, A. Tsekoun, S. Todorov, and J. Connolly, 1400–1480nm ridge-waveguide pump lasers with 1 watt CW output power for EDFA and Raman amplification. In *Proceedings of OFC '01* (Anaheim, CA), PD18, 2001.
- [30] A. Mathur, M. Ziari, and M. Hagberg, High power grating stabilized 1480nm flared semiconductor pump laser. In *OSA Trends in Optics and Photonics Series*, vol. 30, OAA '99:187–190, 1999.
- [31] K. Hamamoto, M. Ohya, and K. Naniwae, High power and low driving voltage 14XXnm active Multi-Mode-Interferometer (MMI) laser diode for fiber amplifier. In *Proceedings of OECC '02*, (Yokohama), 10C3-7, 2002.
- [32] A. Hohl-AbiChedid, A. Rice, J. Li, X. Chen, R. Salvatore, Y. Qian, R. Bhat, M. Hu, and C. Zah, High power and high efficiency single mode AlGaInAs/InP 14xx laser with high temperature operation. In *Proceedings of OAA'02* (Vancouver), OMB2, 2002.
- [33] Y. Emori and S. Namiki, State of the art in diode pumped Raman amplifiers. In *Proceedings of OAA2001* (Stresa, Italy), OMC1, 2001.
- [34] Y. Emori, S. Matsushita, and S. Namiki, Cost-effective depolarized diode pump unit designed for C-band flat-gain Raman amplifiers to control EDFA gain profile. In *Proceedings of the Optical Fiber Communication Conference*, OSA Technical Digest Series (Optical Society of America, Washington DC) FF4, 2000.
- [35] S. Matsushita, J. Shinozaki, Y. Emori, and S. Namiki, Design of temperature insensitive depolarizer for Rama pump laser diode. In *Proceedings of the Optical Fiber Communication Conference*, OSA Technical Digest Series (Optical Society of America, Washington DC) WB3, 2002.
- [36] C.R.S. Fludger, V. Handerek, and R.J. Mears, Fundamental noise limits in broadband Raman amplifiers. In *Proceedings of the Optical Fiber Communication Conference*, OSA Technical Digest Series (Optical Society of America, Washington DC) Paper MA5, 2001.
- [37] S. Kado, Y. Emori, and S. Namiki, Gain and noise tilt control in multi-wavelength bi-directionally pumped Raman amplifier. In *Proceedings of the Optical Fiber Communication Conference*, OSA Technical Digest Series (Optical Society of America, Washington DC) TuJ4, 2002.
- [38] J. Yoshida, N. Tsukiji, T. Kimura, M. Funabashi, and T. Fukushima, Novel concepts in 14xx nm pump lasers for Raman amplifiers. In *Proceedings of ITcom '02 on Active and Passive Optical Components for WDM Communication II* (Boston), vol. 4870:169–182, 2002.
- [39] Y.-K. Park, D.A. Fishman, and J.A. Nagel, US patent. No. 5329396, 1994.
- [40] R.H. Wentworth, G.E. Bodeep, and T.E. Darcie, Laser mode partition noise in lightwave systems using dispersive optical fiber, *J. Lightwave Technol.*, 10:1 (Jan.), 84–89, 1992.

Chapter 6

Dispersion-Compensating Fibers for Raman Applications

L. Grüner-Nielsen and Y. Qian

6.1. Introduction

Dispersion-compensating fibers (DCF) are the most widely used technology for dispersion compensation. The idea to additionally use the DCF as a Raman gain medium was originally proposed by Hansen et al. in 1998 [1]. This was quickly followed by Emori et al., [2], who demonstrated a broadband lossless DCF using multiple-wavelength Raman pumping. DCF is a good Raman gain medium, due to a relatively high germanium doping level and a small effective area. Normally, a discrete Raman amplifier will contain several kilometers of fiber, adding extra dispersion to the system that must be handled in the overall dispersion management. Dispersion-compensating Raman amplifiers integrate two key functions, dispersion compensation and discrete Raman amplification, into a single component.

Recently all-Raman systems have been demonstrated using a combination of Raman amplification in the transmission fiber and dispersion-compensating Raman amplifiers (DCRA) [3, 4]. Such all-Raman systems offer many intriguing advantages. Compared to EDFA systems, amplification in any wavelength band is possible, and very broad, seamless transmission bands can be amplified. Such broadband all-Raman systems can be realized with only a few components and are therefore expected to be cost effective.

Use of DCF for DCRA raises new requirements for the properties of the DCF including requirements for gain, double Rayleigh scattering, and broadband dispersion compensation.

Section 6.2 of this chapter reviews the basics of dispersion compensation including dispersion slope compensation and how to cope with dispersion curvature. Section 6.3 reviews properties of DCF including broadband dispersion compensation, Raman gain efficiency, and double Rayleigh back scattering (DRB). Section 6.4 is the central section on DCRA, reviewing typical amplifier properties and how to cope with impairments such as multipath interference due to DRB and nonlinearities. The final section deals with optimization of DCF for use in DCRA.

6.2. Basic Principles of Dispersion-Compensating Fibers

6.2.1. Dispersion

The dispersion (D) of a single-mode fiber is defined as

$$D = \frac{1}{L} \frac{d\tau}{d\lambda}, \quad (6.1)$$

where τ is the group delay time, L the length, and λ the wavelength. The dispersion is closely related to the second derivative of the propagation constant β ,

$$D = -\frac{2\pi c}{\lambda^2} \frac{d^2\beta}{d\omega^2}, \quad (6.2)$$

where c is the speed of light in vacuum and ω the angular frequency. Theoretical textbooks often define the second derivative of β as the dispersion, but in practical use the definition in Eq. (6.1) is utilized.

The dispersion in single-mode fibers can be divided into three terms [5]:

Material dispersion,
Waveguide dispersion, and
Profile dispersion.

The material dispersion is the dominant dispersion factor in standard nonshifted telecommunication fibers. In dispersion-shifted fibers the material and waveguide dispersion are equal in magnitude, whereas the waveguide dispersion is dominant in dispersion-compensating fibers. The profile dispersion, which is due to the different material dispersion of the different dopants, is very small in normal fibers and can therefore be neglected.

Because of the nonzero spectral width of an optical signal, the dispersion leads to pulse broadening due to different group delays of the different spectral components of the signal. For narrowband externally modulated lasers the spectral width of the signal is governed by the modulation. Increased modulation speed leads to increased spectral width. The tolerable pulse broadening, on the other hand, decreases with the modulation frequency. Therefore the dispersion tolerance decreases with the square of the bit rate (B) and linearly with the transmitted length [6]. The maximum transmission length for dispersion-limited transmission is therefore given as

$$L_{\max} = \frac{K}{B^2 D}, \quad (6.3)$$

where K is a constant depending on details of the transmitter and receiver, the modulation format, and the allowed penalty. Maximum transmission distances for bit rates of 2.5, 10, and 40 Gbit/s are shown in Table 6.1 for a conventional standard single-mode fiber (SSMF) with a dispersion of 16.5 ps/(nm · km) as well as a nonzero dispersion fiber (NZDF) with a dispersion of 4.5 ps/(nm · km). Nonreturn to zero (NRZ) modulation is assumed and a 1 dB eye-closure penalty.

It is clear from Table 6.1 that for bit rates of 10 Gbit/s and above, dispersion is a limiting factor and requires compensation.

Table 6.1. Transmission Distances of NRZ Signal for 1 dB Eye Closure Penalty due to Dispersion

Bit Rate Gbit/s	SSMF km	NZDF km
2.5	927	3400
10	58	213
40	3.6	13

6.2.2. Use of Dispersion-Compensating Fiber

The basic principle for use of dispersion-compensating fiber is shown in Fig. 6.1. By inserting a DCF with negative dispersion into the link, the positive dispersion of the transmission fiber can be compensated.

Figure 6.1 illustrates the lumped application of DCF, where the DCF is an integrated part of the repeater. The DCF can also be deployed as a part of the transmission span itself. This is especially attractive for long distance submarine applications [7, 8], but is considered for terrestrial applications as well [9, 10]. In this chapter, only lumped applications are considered. The amplifiers in Fig. 6.1 could either be erbium-doped fiber amplifiers (EDFA) or, more relevant to this chapter, Raman pumps for pumping of the transmission fiber and the DCF.

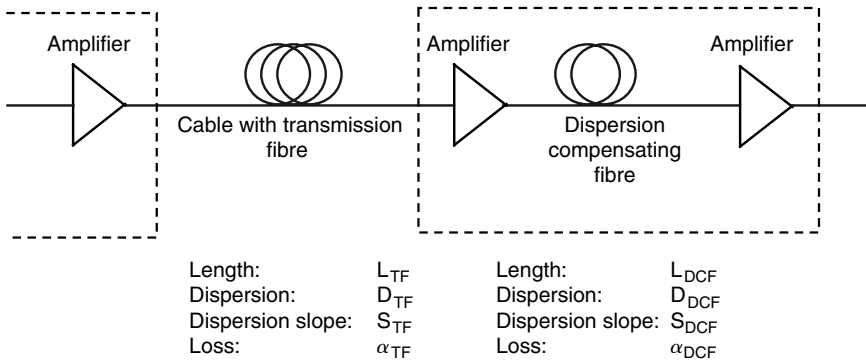
The total dispersion and attenuation of the link are given by

$$D_T = D_{TF}L_{TF} + D_{DCF}L_{DCF}. \quad (6.4)$$

$$\alpha_T = \alpha_{TF}L_{TF} + \alpha_{DCF}L_{DCF}. \quad (6.5)$$

If total compensation of the dispersion is required, the length of the DCF (L_{DCF}) is chosen so $D_T = 0$. However, due to nonlinear effects and possible chirp in the transmitter, 100% compensation is not always the optimum [11].

One of the drawbacks of DCF is, as illustrated by Eq. (6.5), that it adds loss. For non-Raman pumped DCF the added loss must be compensated with additional gain

**Fig. 6.1.** The basic principle of dispersion compensation.

in the amplifiers, degrading the signal-to-noise ratio and increasing the cost of the system. To overcome this problem the DCF should have as high a negative dispersion (D_{DCF}) as possible and as low an attenuation (α_{DCF}) as possible. Therefore, a figure of merit (FOM) for non-Raman pumped dispersion-compensating fibers can be defined as

$$FOM = -\frac{D_{DCF}}{\alpha_{DCF}}. \quad (6.6)$$

It should be emphasized that this FOM is not suited for optimizing DCF for Raman pumped applications, as discussed in Section 6.5.

If L_{DCF} is chosen so $D_T = 0$, the total loss is calculated from Eqs. (6.4) to (6.6),

$$\alpha_T = \left(\alpha_{TF} + \frac{D_{TF}}{FOM} \right) L_{TF}. \quad (6.7)$$

It can be observed from (6.7) that the only DCF parameter determining the added loss is the FOM.

6.2.3. Dispersion Slope Compensation

For systems using only a single or a few WDM channels at 10 Gbit/s for distances up to ~ 500 km, it will normally be sufficient to have the right amount of dispersion compensation at a single wavelength. However, as broadband DWDM systems have been developed, it has become necessary to consider the precision of the dispersion compensation over a broad wavelength range. The requirements are further tightening as systems operating at 40 Gbit/s line rates are now becoming commercially available, as well as ultra-long-haul, 10 Gbit/s systems over 2000 to 4000 km. To have the right amount of dispersion compensation over a broad wavelength range, the dispersion slope should be compensated as well.

The total dispersion slope of the system in Fig. 6.1 is:

$$S_T = L_{TF} S_{TF} + L_{DCF} S_{DCF}. \quad (6.8)$$

As seen from Eq. (6.8), a negative dispersion slope of the DCF is necessary in order to achieve slope compensation ($S_T = 0$). If the length of the DCF is chosen to give full dispersion compensation ($D_T = 0$), then the condition for full slope compensation is that the relative dispersion slope of the DCF shall be equal to the relative dispersion slope of the transmission fiber,

$$RDS_{DCF} = RDS_{TF}. \quad (6.9)$$

The relative dispersion slope is defined as the ratio of dispersion slope to dispersion

$$RDS = \frac{S}{D}. \quad (6.10)$$

Typical dispersion properties of different commercially available transmission fibers are summarized in Table 6.2.

Table 6.2. Typical Properties of Some Commercially Available Transmission Fibers at 1550 nm

Fiber Type	Dispersion [ps/nm·km]	Dispersion Slope [ps/nm ² ·km]	RDS [nm ⁻¹]	Effective Area [μm ²]
Conventional SSMF	16.5	0.058	0.0036	82
TrueWave [®] REACH fibre	7.1	0.042	0.0058	55
TeraLight ^a fibre	8	0.058	0.0073	63
TrueWave [®] RS fibre	4.5	0.045	0.010	52
ELEAF ^a fibre	4.2	0.085	0.020	72

^aTeraLight is a registered trademark of Alcatel; LEAF is a registered trademark of Corning.

In a system with full dispersion compensation, but only partial slope compensation, the total slope of the system can be calculated as

$$S_T = L_{TF} S_{TF} (1 - DSCR), \quad (6.11)$$

where DSCR is the dispersion slope compensation ratio, defined as

$$DSCR = \frac{RDS_{DCF}}{RDS_{TF}} = \frac{\frac{S_{DCF}}{D_{DCF}}}{\frac{S_{TF}}{D_{TF}}}. \quad (6.12)$$

6.2.4. Dispersion curvature

For the most critical applications, it is not sufficient to match the dispersion slope. Even the dispersion curvature has to be considered. The dispersion curvature (C) can be defined as

$$C = \frac{dS}{d\lambda} = \frac{d^2 D}{d\lambda^2}. \quad (6.13)$$

In the most commonly used wavelength range, the C + L band (1530 to 1610 nm), the dispersion curvature of most transmission fibers is very low. This is not necessarily the case for the DCF.

A useful term to describe the problem is the relative dispersion curvature (RDC), which can be defined as

$$RDC = \frac{C}{D}. \quad (6.14)$$

To illustrate the usefulness of RDC, consider a link of N fibers. The resulting dispersion curvature of the link C_L can be calculated as

$$C_L = \frac{1}{L} \sum_{i=1}^{i=N} RDC_i \cdot D_{tot,i}, \quad (6.15)$$

where RDC_i is the RDC of fiber i , $D_{tot,i}$ is the total dispersion (in ps/nm) of fiber i , and L is the total link length.

Dispersion-compensating fibers generally have dispersion versus wavelength behavior as shown in Fig. 6.2.

The generic curve has an inflection point where the curvature changes from negative to positive. The smallest curvature occurs when the inflection point is located within the operating wavelength range. This is further illustrated in Fig. 6.3 [12].

Link 1 is composed of a NZDF with $RDS = 0.0097 \text{ nm}^{-1}$ at 1550 nm. Link 2 is composed of a NZDF with $RDS = 0.018 \text{ nm}^{-1}$ at 1550 nm. The DCF for link 1 operates around the inflection point and has a RDC of $-2 \cdot 10^{-6} \text{ nm}^{-2}$ at 1550 nm.

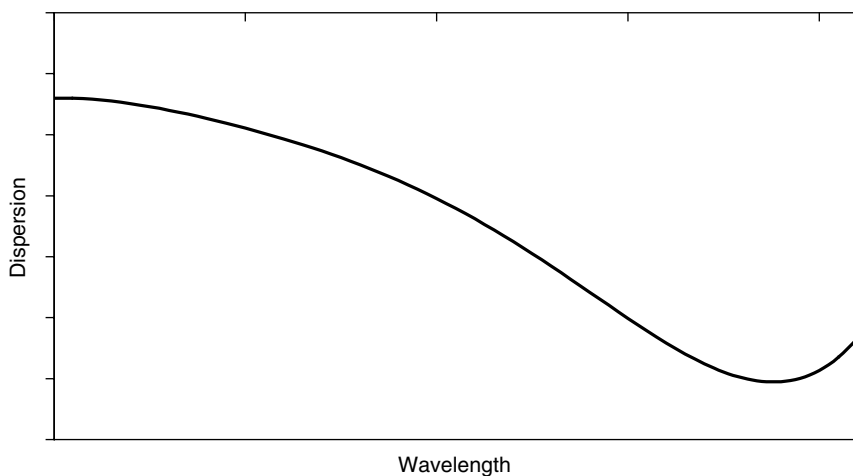


Fig. 6.2. General shape of dispersion versus wavelength for DCF.

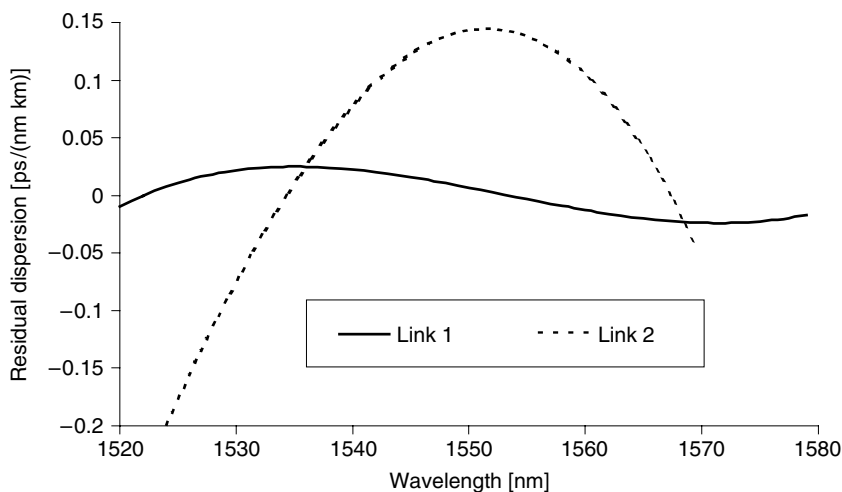


Fig. 6.3. Residual dispersion for two links. Link 1 uses DCF operating around the inflection point. Link 2 uses DCF operating at wavelengths below the inflection point [12].

The DCF for link 2 operates at wavelength below the inflection point and has a RDC of $440 \cdot 10^{-6} \text{ nm}^{-1}$ at 1550 nm.

6.3. Properties of Dispersion-Compensating Fibers

Dispersion-compensating fibers have seen considerable progress over the last several years, and DCFs with RDS matching all common transmission fibers have been demonstrated [12–17] as well as DCFs with improved FOM [18]. DCFs are commercially available from several companies. As an example, Table 6.3 shows typical DCF properties for fibers from OFS (formerly Lucent Technologies Optical Fiber Solutions).

A special type of DCF that has received some recent interest is a DCF supporting more than one mode. The device uses a higher-order mode of the DCF and has mode converters at both ends to convert from the fundamental mode to the higher-order mode at the input and vice versa at the output end [19–21]. The advantage is that the higher-order mode has quite a large effective area on the order 50 to $70 \mu\text{m}^2$. Unfortunately, such fibers have a very low Raman gain efficiency due to the high effective area and because the mode converters have a limited bandwidth. The bandwidth limitation of the mode converters means that normally they will work only for the signal and not for the pump. For that reason this technology is not considered further here.

6.3.1. Broadband Dispersion Compensation

An exciting potential of Raman amplifiers is the possibility for very broadband amplification. This raises the need for DCF that can provide very broadband dispersion compensation. Such DCF can actually only be fully utilized in all-Raman systems, as illustrated in Fig. 6.4.

In the traditional system using EDFAs, the bands have to be split and one DCF is usually required for each band. In an all-Raman system, the same DCF is used to cover the entire system bandwidth for both dispersion compensation and as gain medium [22, 23]. A much simpler configuration is obtained and no channels are lost between the bands.

Table 6.3. Typical Properties at 1550 nm for DCF from OFS (December 2002)

Fiber Type	Dispersion [ps/nm·km]	Dispersion Slope [ps/nm ² ·km]	RDS [nm ⁻¹]	Effective Area [μm ²]
St.-DCF	−100	−0.23	0.0023	20
EWB-DCF	−120	−0.44	0.0037	21
HS-DCF	− 95	−0.65	0.0065	15
EHS-DCF	−120	−1.2	0.010	14
UHS-DCF	−130	−2.1	0.016	14

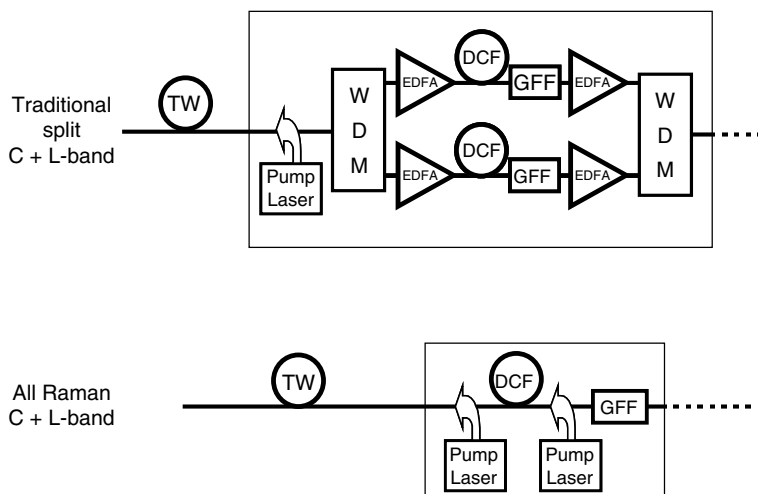


Fig. 6.4. Advantage of all-Raman C + L-band transmission.

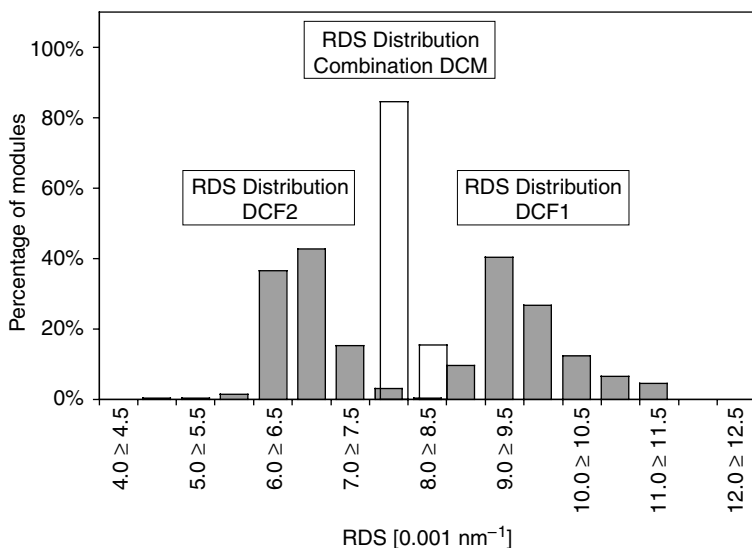


Fig. 6.5. RDS distributions for two DCFs and a combination DCF module made from the two fibers.

One potential problem is that DCF is quite sensitive to small perturbations of its index profile [24]. This implies that in a DCF population there will be some variation in both dispersion and RDS. Trimming the length of the DCF easily adjusts for the variation in dispersion but the variation in RDS can be a problem especially for broadband dispersion compensation. A solution is to use DCF modules that are a combination of two DCFs. This is illustrated in Fig. 6.5. At 1580 nm the average

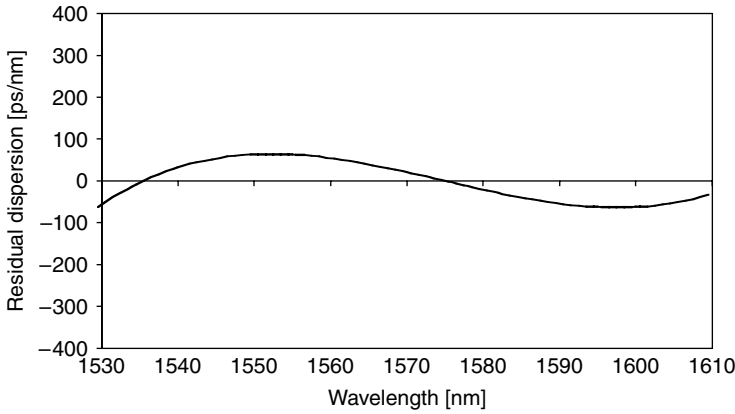


Fig. 6.6. Residual dispersion of 1500 km link of TrueWave® REACH fiber compensated by a combination DCF module.

RDS of DCF1 is 0.00965, and that for DCF2 is 0.00666 nm^{-1} . The target RDS for the combination DCF module is 0.00795 nm^{-1} , matching the RDS of TrueWave® RS at 1580 nm. It can be seen that the accuracy of the RDS is improved by roughly a factor of 10 for the combination module.

As an example of achievable performance, the residual dispersion of a link of 1500 km TrueWave® REACH fiber compensated by a combination of two DCFs is shown in Fig. 6.6. Both DCFs were optimized to work around the inflection point.

DCF modules can also be made by combining DCF with conventional standard single-mode fiber. This technique can be used to increase the RDS, as required for some applications involving nonzero dispersion fibers with high RDS. An example is shown in Fig. 6.7, where a transmission fiber with a RDS of 0.020 nm^{-1} is compensated with a DCF with RDS of 0.016 nm^{-1} . By adding SSMF (and increasing the length of the DCF), full slope compensation can be achieved. The drawback is that the extra fiber gives higher loss.

6.3.2. Raman Gain Efficiency

For unsaturated Raman amplification (when pump depletion can be ignored) the Raman gain efficiency C_R can be calculated from the linear Raman on-off gain, G_{on-off} (ratio of output signal power with pump “on” to that with pump “off”), and fiber effective length L_{eff} as

$$C_R = \frac{\ln(G_{on-off})}{P_p \cdot L_{eff}}; \quad L_{eff} = \frac{1}{\alpha_p} \cdot (1 - e^{-\alpha_p \cdot L}), \quad (6.16)$$

where P_p is the pump power, and α_p is the fiber attenuation at pump wavelength.

DCFs usually have high germanium doping levels and small effective areas, so the Raman gain efficiencies are quite high. This makes DCF attractive for DCRA [1, 25].

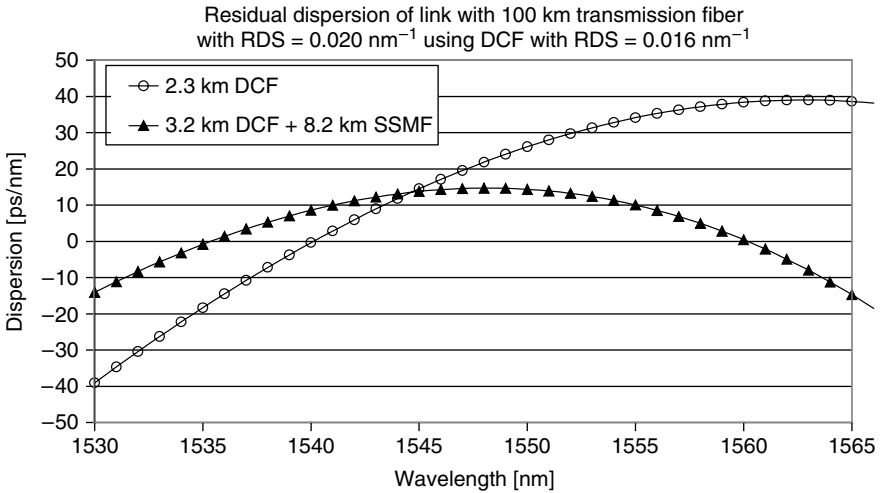


Fig. 6.7. DCF combined with SSMF to increase RDS.

The Raman gain efficiency can be measured using the small-signal fiber Raman amplification as shown by Eq. (6.16). The measured Raman gain efficiency spectra for different kinds of fibers, EHS-DCF, EWB-DCF, Truewave[®] RS, and SSMF (Tables 6.2 and 6.3), are illustrated in Fig. 6.8(a). The peaks are approximately scaled to the germanium doping levels and inversely proportional to effective area and the pump wavelength. It can also be noted that at low germanium doping levels as for SSMF, the Raman gain spectrum reveals two peaks around its maximum. This is due to the Raman nature of silica. Fibers with higher germanium doping concentration show the single peak around a frequency shift of 13 THz due to the germanium dominating the Raman gain [26].

6.3.3. Double Rayleigh Backscattering

Unlike EDFAs with lengths on the order of meters, fibers used for Raman amplification are much longer. Discrete Raman amplifiers have lengths of several to tens of kilometers, and distributed Raman amplifiers have lengths of tens to hundreds of kilometers. The double Rayleigh backscattering [27] is thus more pronounced during Raman amplification than for EDFAs. DRB causes a delayed replica of the signal with the same propagation direction as the signal that interferes with the signal and generates noise. This is referred to as multipath interference (MPI). DRB-induced MPI crosstalk is detrimental to the system performance and is one of the limiting penalties in Raman amplification [28–31].

To evaluate the DRB-induced MPI, the fiber Rayleigh backscattering coefficient is the key parameter. One can measure the fiber Rayleigh scattering coefficient by using optical time domain reflectometry (OTDR) [32]. A more accurate way that

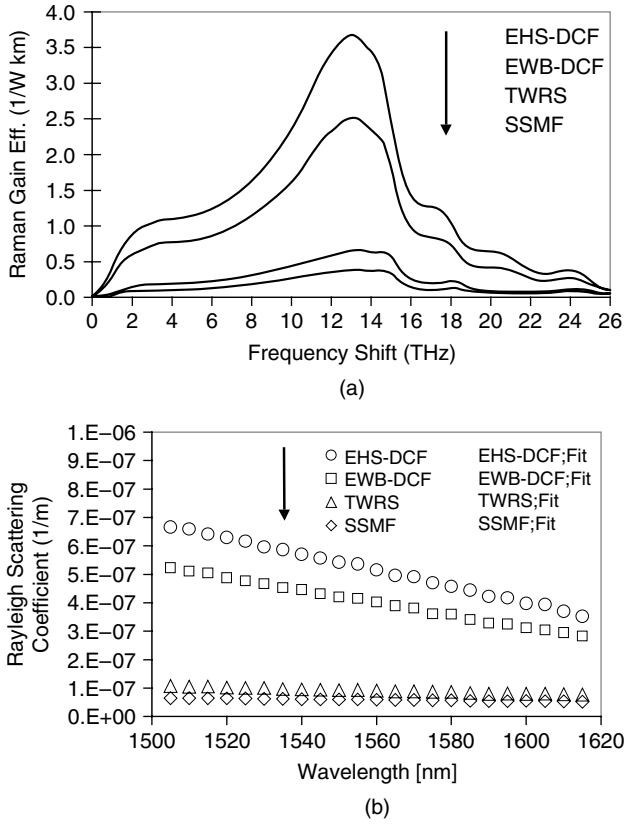


Fig. 6.8. Measured typical spectral dependence for (a) Raman gain efficiency pumped at 1453 nm; and (b) Rayleigh scattering coefficient κ .

additionally allows for easy wavelength scanning is to use a return loss module [33]. The fiber Rayleigh scattering coefficient κ can be calculated from the measured return loss R of the fiber under test:

$$\kappa = \frac{2\alpha R}{\alpha_1^2 (1 - e^{-2\alpha L})}. \quad (6.17)$$

Here, α is the loss of the fiber, α_1 is the loss from the other discrete points including splicing, connector, and the like, and L is the length of the fiber.

Measurements of typical Rayleigh scattering coefficients from this technique are shown in Fig. 6.8(b) for EHS-DCF, EWB-DCF, TWRS, and SSMF. The wavelength range is 1500 to 1620 nm, covering the S + C + L-band, where most of the fiber Raman amplifiers operate presently.

The theoretical analysis shows that the DRB coefficient is inversely proportional to the fiber effective area and the square of wavelength [25, 33]. Therefore, the wave-

length dependence of the DRB coefficient κ can be expressed from the measured DRB coefficient at the center wavelength 1560 nm in the form of

$$\kappa(\lambda) = \frac{A_{eff}(1560 \text{ nm}) \cdot 1560^2}{A_{eff}(\lambda) \cdot \lambda^2} \cdot \kappa(1560 \text{ nm}), \quad (6.18)$$

where λ is the wavelength in nm and A_{eff} is the fiber effective area. The fitting lines using this formula including the variation in effective area with wavelength are in reasonably good agreement with the measured data as shown in Fig. 6.8(b).

The measured fiber Raman gain efficiency, attenuation, effective area, and DRB can now be used in Raman amplification simulations using the conventional steady-state model [6], including signal, pump, ASE, and DRB noise, and so on. [25, 27]. Such simulations show good agreement with measurements, as demonstrated later in this chapter.

6.4. Dispersion-Compensating Raman Amplifiers

6.4.1. Applications

A DCF without Raman amplification introduces extra loss into the system, thus increasing the need for gain in the discrete amplifiers and degrading the noise performance. A discrete Raman amplifier will contain several kilometers of fiber, adding further dispersion to the system that must be handled by the dispersion compensation on top of the dispersion of the transmission fiber. Dispersion-compensating Raman amplifiers integrate these two key functions, dispersion compensation and Raman amplification, into a single component. Compared to an EDFA-based system, DCRA can be easily adjusted and extended to any seamless transmission band, for example, E-, S-, C-, L-, and/or U-band [34, 23, 22, 35–37], without extra passive components. This is cost effective and especially attractive in all-Raman, ultra-broadband, high-capacity systems [3, 4, 10, 9, 38, 34]. In addition, the Raman gain can be simply adjusted by WDM pumps [2, 37] or TDM pumps [39, 40] to achieve a flat gain spectrum without a high-loss gain-equalizer.

A high-gain DCRA can contribute gain to an all-Raman system and reduce the Raman gain in the transmission fibers [3, 4]. A transparent DCRA is beneficial for improving the noise performance in repeaters [41].

6.4.2. Amplifier Properties

6.4.2.1. Raman Characterization Setup

Raman amplification can be characterized by using the setup shown in Fig. 6.9(a) [42]. The device under test can, for example, be a bidirectionally pumped DCRA consisting of a DCF as the gain medium, depolarized multichannel pump source with controlling electronics, and other optical passive components such as a coupler, isolator, and the

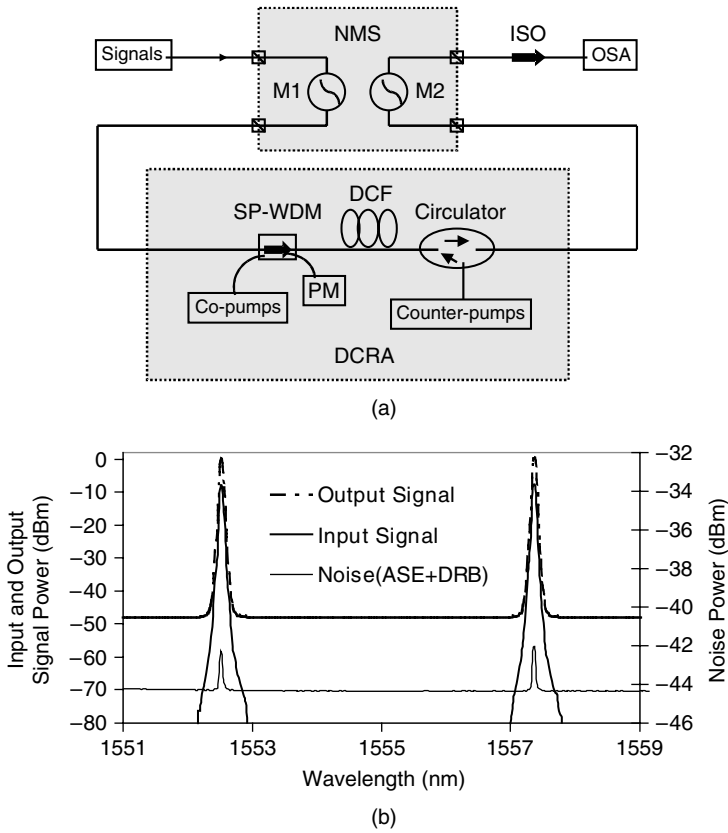


Fig. 6.9. (a) Schematic of a bidirectionally pumped DCRA in a Raman characterization setup; (b) typical measured signal and noise (ASE + DRB) spectra. SP-WSM: signal-pump wavelength division multiplexer including a built-in isolator; OSA: optical spectrum analyzer; ISO: isolator; PM: power monitor; NMS: noise measurement system; M1/M2: signal input/output modulator.

like. The input and output signals can be modulated independently by AO modulators at a suitable frequency and duty cycle. One can then measure the input and amplified signals using an optical spectrum analyzer when the two modulators are in phase. The noises, including ASE and DRB, can be recorded when the two modulators are out of phase. This is referred to as the modified optical time domain extinction method in analogue to EDFA measurement [43].

Typical measured signal and noise spectra can be seen in Fig. 6.9(b). The Raman net gain is calculated from the measured input and output signal powers. The interpolated ASE power at the signal wavelength, together with the Raman gain, is used to calculate the noise figure, and the DRB power subtracted from the total noise can be used to calculate the OSNR due to DRB. The DRB-induced MPI is just the inverse (linear) OSNR due to DRB.

The MPI due to DRB can also be measured electrically by measuring the laser relative intensity noise (RIN) with an electrical spectrum analyzer [44]. It is worth noting that the optical measurement of MPI gives the worst-case result because all polarizations of both the DRB noise and the signal are included. In the electrical measurement, the MPI is dependent on the degree of polarization of the DRB noise [45]. For unpolarized DRB noise, the electrically measured MPI will be around 3 dB lower than the optical measurements [46].

6.4.2.2. Raman Net Gain, NF and MPI due to DRB

As an example, measured and simulated net gain, noise figure, MPI, and output power as functions of input signal power are shown in Fig. 6.10 [37]. Good agreement between measurement and simulations is observed.

A 3.9 km EHS-DCF for dispersion compensation of 90.8 km TWRS is used in this C-band DCRA. The link residual dispersion is within ± 0.1 ps/km · nm from 1528.8 to 1567.2 nm. The average loss of this DCRA in the C-band is around 5 dB without Raman pumping. The saturation effect can be seen from the curves for high signal amplification and the saturation power can be estimated to be 23 dBm in Fig. 6.5(d), with maximum 589 mW pumping. The NF is independent of the signal level for unsaturated Raman amplification, but will be much higher in the saturation region due to the rapid increase of double Rayleigh backscattered ASE [25]. The deviations of measurements from simulations at high signal level are mainly due to the SBS effect [25, 26]. Note that these measurements are performed with 600 GHz channel spacing, so it can be expected that for a real system using 25 to 100 GHz channel spacing, the signal power per channel will be 6 to 24 times lower for the same amount of total power. In addition, signals are usually coded with a bit rate higher than 1 Gbit/s, so the SBS threshold will be drastically higher. Therefore, the SBS effect will not be a serious limitation for Raman amplification in real systems. Spectral broadening or phase modulation of the signal can also be used to eliminate SBS.

Three-wavelength counter-pumps, as shown in Table 6.4, are chosen to achieve optimized flat gain. The measured gain flatness is within ± 0.13 dB for 8 dB net gain, close to the simulated flatness of ± 0.16 dB, as shown in Fig. 6.11(a). The average noise figure is 5.6 dB with MPI of -46 dB. The noise figure spectrum is tilted due to fiber attenuation and temperature limitation of ASE [47]. The measured average net gain, NF, and MPI versus pump power is displayed in Figure 6.11(b). Raman net gain efficiency can be deduced as 28.5 dB/W. MPI increases about 1 dB for 1 dB gain increase. It should be noted that DRB-induced MPI for this DCRA without Raman pumping is very low, only -59 dB. MPI for 0 dB net gain is below -54 dB. The NF is less than 6 dB and is nearly independent of the pump power for net gain of several dB.

Different transmission fibers require different DCF. For example, the DCF length will be much longer for compensation of SSMF compared to compensation of NZDF. Figure 6.12 displays the simulation results of EWB-DCF and EHS-DCF for compensation of 80 km SSMF and TWRS, respectively. Three counterpropagating pumps with a total pump power of 660 mW are used for amplification in the C-band. The EWB-DCF is about three times as long as the EHS-DCF, due to the much higher

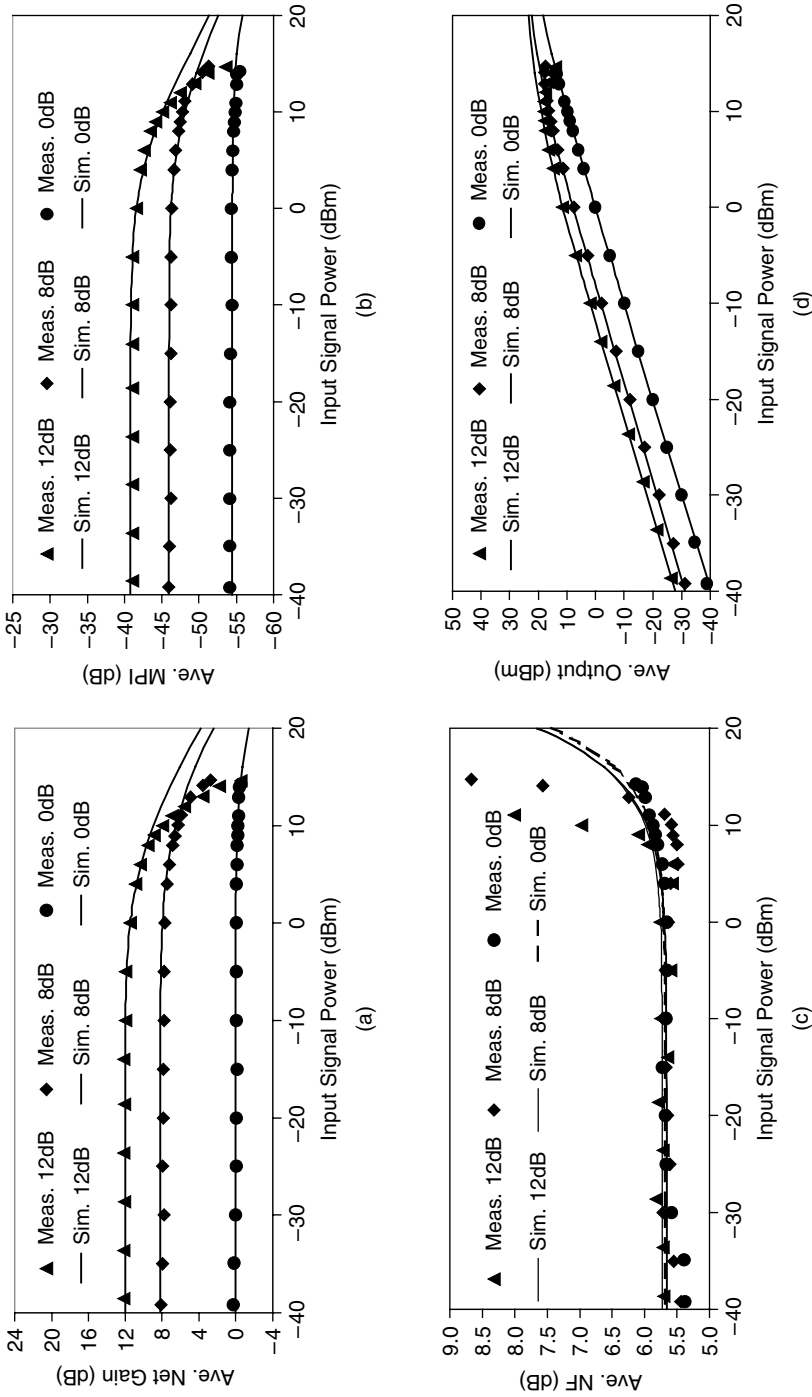


Fig. 6.10. Measured and simulated average: (a) net gain; (b) multipath interference MPI; (c) noise figure NF; and (d) output power versus input signal power for average net gain of 12, 8, or 0 dB. 3.9 km EHS-DCF was used [37].

Table 6.4. Pump Configuration

Pumps	Total (mW)	1426 nm	1438 nm	1466 nm
For 12 dB net gain	589	194	194	201
For 8 dB net gain	451	135	121	195
For 0 dB net gain	160	52	36	72

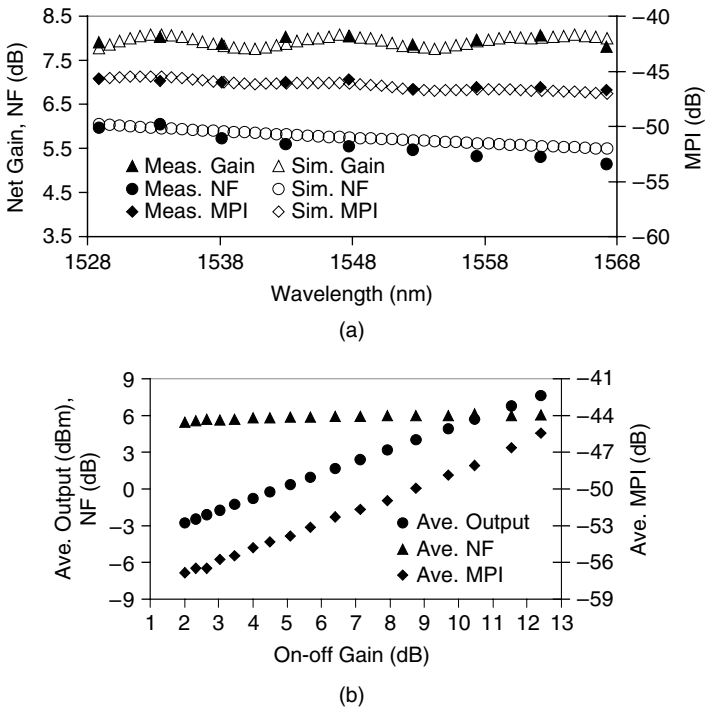


Fig. 6.11. (a) Measured and simulated net gain, NF, and MPI for optimized 38.4 nm spectral range centered at 1548 nm; (b) measured average Raman gain, NF, and MPI dependence on Raman on-off gain with 0 dBm input signal power [37].

dispersion of SSMF compared to TWRS. Due to the longer length of the EWB-DCF, it has a higher gain, but the noise figure is 1 dB higher than EHS-DCF. The MPI for EWB-DCF is around 5 dB higher than EHS-DCF for the same net gain level, again due to the longer length. Thus, from a Raman amplification point of view, EHS-DCF for dispersion compensation of TWRS will have much lower noise impairment on the transmission system compared with EWB-DCF for SSMF.

6.4.3. Amplifier Configurations

Due to the relatively long fiber length of Raman amplifiers compared to EDFAs, DRB-induced MPI [28, 48, 31, 49–51], ASE, and fiber nonlinear effects [52, 53] can be major impairments in real systems.

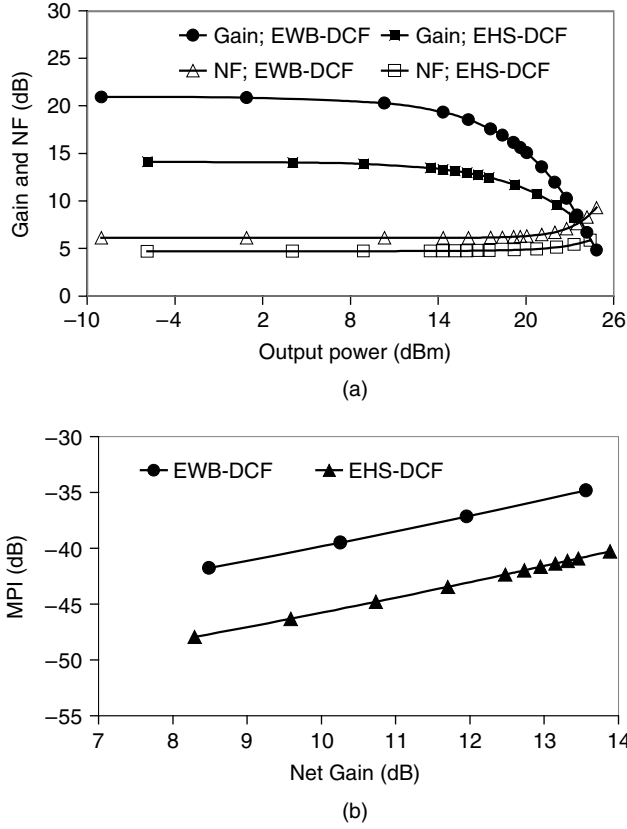


Fig. 6.12. (a) Simulated Raman net gain and noise figure as functions of output signal power for a total pump power of 660 mW; (b) simulated MPI due to DRB versus net gain. Fibers are EWB-DCF and EHS-DCF for 80 km SSMF and TWRS compensation, respectively.

To minimize the noise figure, the signal power excursion should be minimized; thus copumping is a promising technique. To minimize the MPI due to DRB, bidirectional pumping and a multistage DCRA design with interstage isolator [54–56, 53] are preferable. However, to mitigate the nonlinear impairments, the path-averaged signal power should be minimum; so copumping would not be the best solution. A DCRA can be optimally designed with respect to both linear and nonlinear impairments by using the equations described in [52].

6.4.3.1. Linear Impairments

For a DCRA, the inband crosstalk comes from the DRB of signal and discrete reflections, such as connectors. The beating between the ASE and signal will induce interference. Several types of crosstalk result in power penalties in real systems, and these can be formulated for optically preamplified receivers in the form of [31]:

$$\text{Penalty (dB)} = -20 \cdot \text{Log}(1 - N \cdot R_C \cdot Q^2), \quad (6.19)$$

where R_c is the total crosstalk for a single span and N is the number of amplifier spans. $Q = 6$ for $BER = 10^{-9}$.

To maintain the power penalty within 0.5 dB of $Q = 6$ for transmission over 40 amplifier spans, the crosstalk per fiber span should be kept below -44 dB.

To implement Raman amplification, one can use a co-, counter-, or bidirectional pumping configuration. Copumped Raman amplifiers suffer from high relative intensity noise transfer from the pump [57, 58], but give the lowest noise figure of the three pumping configurations due to high path average power. Recently, pump lasers with very low RIN have become available, so co- or bidirectional pumping has become practical. counter-pumped Raman amplifiers average the noise fluctuation from the pump, but the gain excursion in the fiber is the maximum, resulting in the largest noise figure. For bidirectional pumping, a moderate noise figure can be obtained, with the extra advantage of minimum DRB-induced MPI [28, 42, 22, 52] due to minimum gain excursion along the fiber.

The minimum MPI and MPI improvement by using 50% bidirectional pumping can be calculated as illustrated in Fig. 6.13 for SSMF and EWB-DCF. The simulation is performed for small-signal amplification using equations in Nissov et al. [28]. It can be seen that the MPI improvement is strongly dependent on the fiber length and the Raman net gain. A short length (around 10 km) DCRA benefits much less than long transmission fibers (around 100 km) in distributed RA. This is because the MPI improvement level depends on the gain excursion difference among different pumping configurations. For long transmission fibers, the effective length is much shorter than the fiber length, so there will be a higher gain excursion difference between co- (or counter-) and bidirectional pumped amplifiers. The DCRA with shorter length will exhibit less gain excursion difference because the Raman effective length is close to the fiber length.

For 10 dB net gain, the MPI improvement for 17.6 km of EWB-DCF (for dispersion compensation of 120 km of SSMF) would be around 2 dB whereas for 100 km of SSMF it could be as high as 15 dB. A DCRA made of 9.5 km of EWB-DCF (for 60 km SSMF dispersion compensation) exhibits MPI improvement of 0.7 dB with 50% copumping at 8 dB net gain [42].

To improve the NF tilt in broadband DCRA, it is useful to design a bidirectionally pumped DCRA with copumping for the shorter part of the transmission band, but counter-pumping for the longer band [59, 22, 23].

A C + L-band DCRA composed of two DCFs was constructed for compensation of 100 km TW[®] REACH [22, Section 6.3.1, Figure 6.6]. The Raman gain, NF, and MPI using two different pumping schemes are displayed in Fig. 6.14, with pumping configurations shown in Table 6.5.

Six pump wavelengths are used in the counter-pumped DCRA. The average net gain is 10.4 dB with flatness of ± 1.2 dB, whereas the average NF is 6.7 dB with flatness of ± 1.8 dB. The average MPI is -43.4 dB.

For the bidirectional pumping case, the copumped C-band and counter-pumped L-band are designed as shown in Table 6.5. The net gain flatness is improved to ± 0.8 dB, whereas the average NF is decreased to 5 dB with improved flatness of

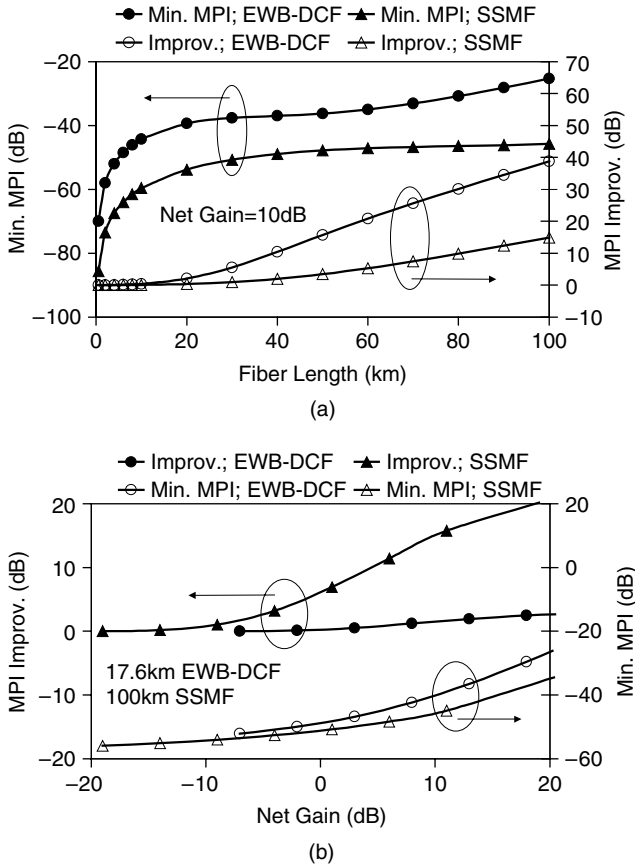


Fig. 6.13. Simulated minimum MPI and MPI improvement by 50% copumping as functions of (a) fiber length with net gain of 10 dB and (b) net gain for small-signal Raman amplification in two different fibers: SSMF and EWB-DCF.

± 0.7 dB. The average MPI is also improved to less than -45 dB. The noise improvement is due to the lower gain excursion along the fiber by using bidirectional pumping.

Another way to improve the MPI performance for DCRAs is to design multistage amplifiers with the same type of fibers but different lengths [54–56], or different types of fibers. The key technique is to use a midstage isolator (or circulator) together with couplers to build a bridge for the pump to reach all the stages, but block the signal back reflections among different stages. The MPI improvement can be as high as 15 dB with an optimized 60% length proportion for a two-stage discrete RA with 5 km of HNLF [56]. The NF degradation due to extra passive components was less than 1 dB in this case.

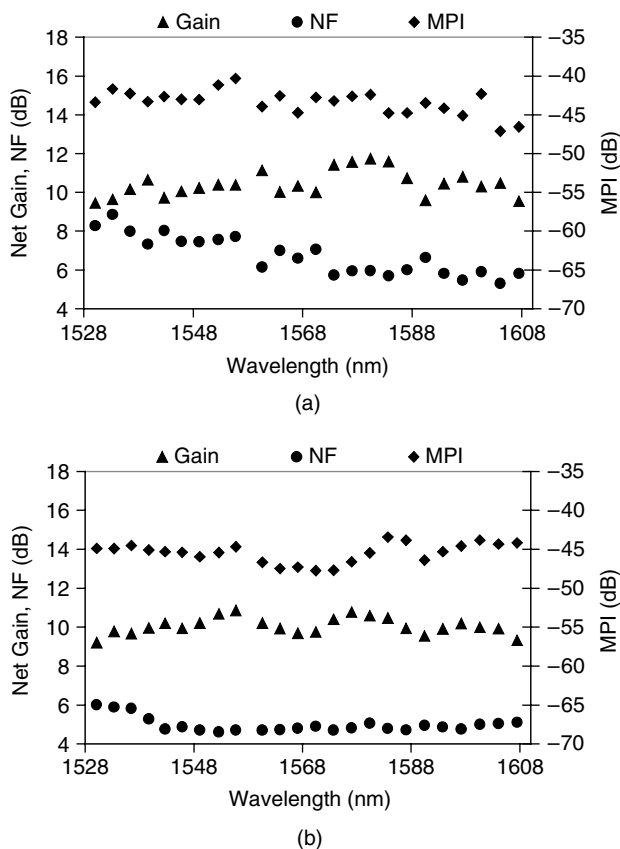


Fig. 6.14. Measured gain, noise figure, and MPI due to DRB using (a) counter-pumping scheme and (b) bidirectional pumping scheme [22]. The pump configuration is shown in Table 6.5.

Table 6.5. Pump Configurations for Counter- and Bidirectionally Pumped C + L-Band DCRA

Config.	1428 nm	1445 nm	1467 nm	1484 nm	1491 nm	1507 nm	Total
Count. P	297 mW	297 mW	162 mW	41 mW	93 mW	78 mW	967 mW
Bidir. P	360 mW,co ^a	360 mW,co ^a	86 mW	0 mW	138 mW	98 mW	1042 mW

^aCopump is noted as “co” whereas others are all counter-pumped.

MPI and NF improvements of 7 and 2 dB, respectively, have been demonstrated by counter-pumping the first-stage fiber and using the residual pump to counter-pump the second stage [53]. The first-stage fiber length is 36% of the total 6 km of HS-DCF.

6.4.3.2. Nonlinear Impairments

The nonlinear impairments [60, 52, 61, 29, 62] in Raman amplification will impose limitations for its application in real systems. These impairments include SBS, in-

trachannel SRS, self-phase modulation (SPM), cross-phase modulation (XPM), and four-wave mixing (FWM). The last two effects can affect both multichannel signals and/or multichannel pumps.

DCF has the general spectral dispersion behavior as shown in Fig. 6.2; that is, it will never reach zero dispersion at either pump or signal wavelength. Therefore, FWM will normally not be a consideration in DCRA's.

SBS can be diminished by broadening the signal spectral width or phase modulating the signal. SRS-induced Raman tilt can be compensated by proper adjustment of pump wavelengths and powers for WDM-pumped DCRA.

A DCRA has a higher fiber nonlinear coefficient than transmission fiber, but the DCRA length is generally significantly shorter than that of distributed RA, so their gross nonlinear impairments are comparable.

The nonlinear phase shift φ due to SPM can be calculated from the fiber nonlinear coefficient γ as

$$\varphi = \int_0^L \gamma(z) \cdot P_s(z) \cdot dz = \gamma \cdot P_s(z=0) \cdot L_{\text{eff}, \text{Raman}}; \quad L_{\text{eff}}(\text{unpumped}) = \frac{1}{\alpha_s} \cdot (1 - e^{-\alpha_s \cdot L}), \quad (6.20)$$

where γ is assumed to be constant along the fiber length, $P_s(z)$ is the signal power in position z , and $L_{\text{eff}, \text{Raman}}$ is the nonlinear effective length for a Raman-pumped fiber. For an unpumped fiber, the nonlinear effective length is solely dependent on the fiber attenuation at signal wavelength α_s and fiber length L , as shown in Eq. (6.20).

Raman amplification will enhance the nonlinear effect by increasing the nonlinear effective length. The nonlinear enhancement ratio R_{NL} is defined as the ratio of the effective length with Raman amplification to the effective length of the unpumped fiber [60, 52, 62]. It has the form of

$$R_{NL} = \frac{\alpha_s}{1 - e^{-\alpha_s \cdot L}} \cdot \int_0^L G_{\text{net}}(z) \cdot dz, \quad (6.21)$$

which is proportional to the path average net gain/signal power along the fiber.

The path-average power is maximum for copumped RA compared to counter- or bidirectional-pumped RA. Thus, the NF is minimum for copumped RA but the nonlinear enhancement is at the maximum as shown in Fig. 6.15. Due to such trade-offs, careful design for DCRA's is needed. For example, a transparent DCRA made of 17.6 km of EWB-DCF will have 1.7 dB NF improvement by copumping compared to counter-pumping. However, the nonlinear enhancement will be 2.2 dB higher than for counter-pumping. If the nonlinear enhancement is fixed as 3 dB, then the counter-pumping scheme supports Raman amplification to a net gain of 3 dB, whereas copumping will only support a net gain of -2 dB. To compensate for the nonlinear enhancement due to Raman amplification, the maximum signal input power should be reduced by the same amount as the nonlinear enhancement. Thus, equivalently, the copumping scheme will reduce the maximum input signal power by 5 dB compared to the counter-pumping scheme for the same nonlinear impairment level. Nonlinear impairments due to Raman amplification will limit the maximum useful signal power in systems.

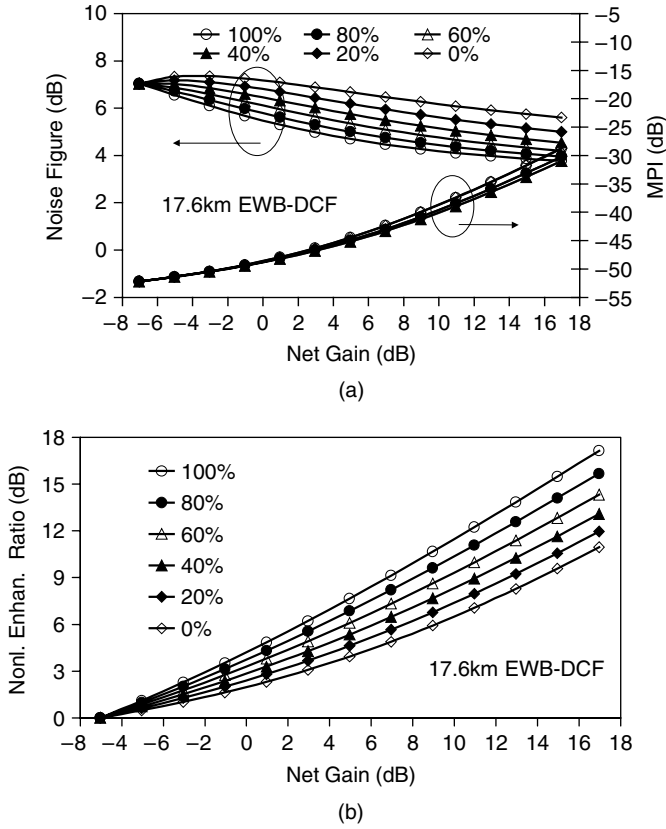


Fig. 6.15. Simulated (a) noise figure and MPI due to DRB and (b) nonlinear enhancement ratio R_{NL} versus net gain for various copump proportions. 17.6 km of EWB-DCF is used, and unsaturated amplification is assumed.

Due to the fundamental limitations of Raman amplification with respect to noise and nonlinearity with a certain level of path-average signal power, the optimum design will focus on the minimization of the signal power excursion, signal-to-signal Raman scattering, and temperature-dependent noise [29]. EDFAs have at least a 3 dB noise figure, so EDFA postamplification will always degrade the noise performance in a Raman-based system.

6.5. Optimizing Dispersion-Compensating Fibers for Use in Discrete Raman Amplifiers

6.5.1. Raman Figure of Merit

The fiber Raman net gain G_{net} is the Raman on-off gain minus the fiber loss and other discrete losses, such as splices, couplers, and the like. Using Eq. (6.16) the net gain

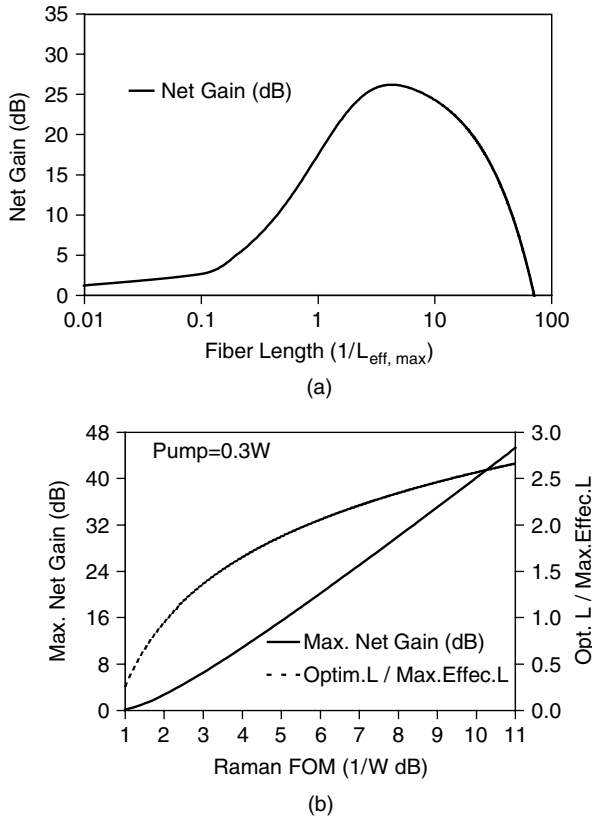


Fig. 6.16. (a) Calculated Raman net gain versus fiber length normalized by maximum effective length; (b) calculated maximum net gain and optical length as functions of Raman figure of merit FOM_R .

can be calculated as:

$$\ln(G_{net}) = C_R P_P L_{eff} - \alpha_S L - \alpha_D; \quad L_{eff} = \frac{1}{\alpha_p} \cdot (1 - e^{-\alpha_p \cdot L}) = L_{eff, \max} \cdot (1 - e^{-\alpha_p \cdot L}), \quad (6.22)$$

where α_s and α_p are the fiber losses at the signal and pump wavelengths, respectively, α_D is the sum of the discrete losses, P_P is the pump power, L the fiber length, and $L_{eff, \max} = 1/\alpha_p$ is the maximum effective length.

The dependence of Raman net gain on fiber length is illustrated in Fig. 6.16(a), using a EWB-DCF as an example. A maximum net gain at an optimum length L_{opt} is observed.

Using the approximation that the fiber attenuation at signal and pump wavelength is the same $\alpha_s = \alpha_p$, the optimum fiber length L_{opt} can be expressed in the form of

$$L_{opt} \approx L_{eff}^{\max} \cdot \ln(FOM_R \cdot P_p); \quad FOM_R = \frac{C_R}{\alpha_p}. \quad (6.23)$$

FOM_R is referred to as the Raman figure of merit [26]. The maximum net gain, which is reached using the optimum fiber length, can thus be obtained as

$$\ln(G_{net}^{max}) \approx FOM_R \cdot P_p - 1 - \ln(FOM_R \cdot P_p) - \alpha_D. \quad (6.24)$$

This is almost linearly dependent on FOM_R as illustrated in Fig. 6.16(b). The highest reported FOM_R is $10.3(\text{W}^{-1} \cdot \text{dB}^{-1})$ [63].

FOM_R is a strong tool for optimizing fibers for discrete Raman amplifiers, if the length can be chosen freely to equal L_{opt} . Unfortunately, that is not the case for a DCRA where the fiber length has to be adjusted to obtain the required amount of dispersion.

6.5.2. Optimizing DCF for DCRA

The optimal DCF for a DCRA should fulfill the following requirements.

1. Dispersion properties:
 - a. RDS matching the transmission fiber;
 - b. Low dispersion curvature;
2. High Raman gain efficiency;
3. Low loss at pump and signal wavelengths;
4. Low Rayleigh backscatter coefficient;
5. Optimum length:
 - a. Long enough to obtain sufficient gain with the available pump power;
 - b. Short enough to minimize MPI due to DRB.

Requirements 2 and 3 can, to some extent, be combined in a requirement of maximizing the Raman FOM_R . Lowering the loss (requirement 3) normally also helps to reduce the Rayleigh backscatter coefficient (requirement 4).

The last requirement can often be the most difficult to fulfill. Using standard DCF, the DCF length tends to be too long when compensating long lengths of SSMF, and it tends to be too short when compensating short lengths of NZDF. In the following, we give an example of how the fiber design can be optimized for compensation of short lengths of NZDF.

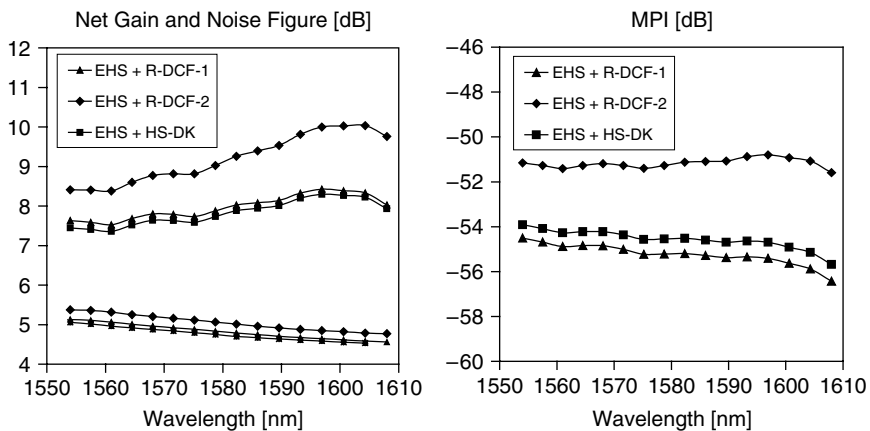
6.5.2.1. Example: Optimized DCF for DCRA for TWRS Fibers

The dispersion-compensating fiber HS-DCF (Table 6.3) is designed to match the dispersion slope of the TWRS transmission fiber in the L-band. Fibers with the same RDS as HS-DCF but with improved Raman gain properties have been produced: R-DCF-1 and R-DCF-2 with the typical values listed in Table 6.6.

The dispersion of the new fibers is lower than that of HS-DCF. Thereby the length of fiber needed for compensating a certain amount of dispersion is increased, resulting in a longer gain medium for Raman amplification. The Rayleigh backscattering, resulting in MPI, is lower and the Raman FOM is higher for both R-DCF fibers making them better suited for Raman amplification, whereas the RDS is almost the same for all three fiber types.

Table 6.6. Measured Fiber Properties

Fiber Type	HS-DCF	R-DCF-1	R-DCF-2
Attenuation @ 1585 nm (dB/km)	0.57	0.34	0.42
Dispersion @ 1585 nm [ps/(nm·km)]	−111	−71	−78
RDS @ 1585 nm (nm ^{−1})	0.0065	0.0060	0.0067
Effective area @ 1580 nm (μm ²)	15.6	21.0	15.5
Raman gain efficiency, pump @ 1453 nm (W ^{−1} km ^{−1})	3.6	2.1	3.2
Raman FOM, pump @ 1453 (W ^{−1} dB ^{−1})	4.4	5.4	5.8
Rayleigh backscattering coefficient (10 ^{−6} m ^{−1})	0.59	0.31	0.49

**Fig. 6.17.** Simulated net gain, noise figure, and DRB MPI in DCRA for compensation of 50 km of TWRS transmission fiber keeping the pump power constant.

Modules for compensating 50 km of TWRS in the L-band have been simulated. They consist of EHS-DCF in combination with HS-DCF or R-DCF-1 or R-DCF-2. Simulations with realistic system parameters have been performed on these modules and are shown in Fig. 6.17. It is seen that with R-DCF-2 an improvement in the gain of up to 1.6 dB can be obtained whereas with R-DCF-1 there is a slight improvement in both gain and MPI.

6.6. Conclusion

Dispersion-compensating fibers are a mature technology for dispersion compensation. Dispersion slope compensation is now possible for all types of transmission fibers. The next challenge for ultra-broadband and precise dispersion compensation is the dispersion curvature. With proper design of the DCF, broadband (e.g., C + L-band) dispersion compensation is possible for certain transmission fibers. DCF capable of

broadband dispersion compensation is especially useful for dispersion-compensating Raman amplifiers where simultaneous dispersion compensation and amplification can be realized with a few components in a cost-efficient manner.

DCF is generally a good Raman gain medium. DCRA has been realized with a high gain for a moderate amount of pump power, low noise figure, and low multipath interference due to double Rayleigh back scattering.

Due to the relatively short length, bidirectional pumping of a DCRA using the same wavelengths for both co- and counter-pumping is not as appealing for reducing MPI and NF as for distributed Raman amplification. For broadband DCRA's, however, it is attractive to have the shorter pump wavelength copropagating and the longer pump wavelength counterpropagating to improve the noise figure and MPI.

Use of DCF for DCRA's leads to new requirements, raising the need for new fiber designs optimized for this application. For example, it can be useful to optimize the DCF, so the required DCF length is not too short in a DCRA compensating a short length of low-dispersion NZDF or, conversely, not too long in a DCRA compensating long lengths of high-dispersion SSMF.

Acknowledgments

The author would like to thank Bera Pálsdóttir and Peter Gaarde from OFS Denmark and Lynn Nelson from OFS Crawford Hill Laboratory for invaluable help in preparing this chapter.

References

- [1] P.B. Hansen, G. Jacobovitz-Veselka, L. Grüner-Nielsen, and A.J. Stentz, Raman amplification for loss compensation in dispersion compensating fibre modules, *Electron. Lett.*, 34:11, 1136–1137, 1998.
- [2] Y. Emori, Y. Akasaka, and S. Namiki, Broadband lossless DCF using Raman amplification pumped by multichannel WDM laser diodes, *Electron. Lett.*, 34:22, 2145–2146, 1998.
- [3] A.H. Gnauck, G. Raybon, S. Chandrasekhar, J. Leuthold, et al., 2.5 Tb/s (64×42.7 Gb/s) Transmission over 40×100 km NZDSF using RZ-DPSK format and all-Raman-amplified spans, In *Proceedings of OFC'02*, FC2, 2002.
- [4] B. Zhu, L. Leng, L.E. Nelson, L. Grüner-Nielsen, Y. Qian, J. Bromage, S. Stulz, S. Kado, Y. Emori, S. Namiki, P. Gaarde, A. Judy, B. Palsdottir, and R. Lingle, 3.2-Tb/s (80×42.7 Gb/s) Transmission over 20×100 km of non-zero dispersion fibre with simultaneous C + L-band dispersion compensation, In *Proceedings of OFC'02*, FC8, 2002.
- [5] K. Petermann, Constraints for fundamental-mode spot size for broadband dispersion-compensated singlemode fibres, *Electron. Lett.*, 19:18, 712–714, 1983.
- [6] G.P. Agrawal, *Nonlinear Fiber Optics*, 3d ed., San Diego: Academic Press, 2001.
- [7] J.-X. Cai, M. Nissov, C.R. Davidson, Y. Cai, A.N. Pilipetskii, H. Li, M.A. Mills, R.-M. Mu, U. Feiste, L. Xu, A. J. Lucero, D.G. Foursa, and N.S. Bergano, Transmission of thirty-eight 40 Gb/s channels (> 1.5 Tb/s) over transoceanic distance. In *Proceedings of OFC 2002*, FC4, 2002.
- [8] G. Vareille, B. Julien, F. Pitel, and J.F. Marcero, 3.65 Tbit/s (365×11.6 Gbit/s) Transmission experiment over 6850 km using 22.2 GHz channel spacing in NRZ format. In *Proceedings of ECOC 2001*, PD.M1.7, 2001.

- [9] C. Rasmussen, S. Dey, F. Liu, J. Bennike, B. Mikkelsen, P. Mamyshev, M. Kimmitt, K. Springer, D. Gapontsev, and V. Ivshin, Transmission of 40×42.7 Gbit/s over 5200 km UltraWave fiber with terrestrial 100 km spans using turn-key ETDM transmitter and receiver. In *Proceedings of ECOC 2002*, PD4.4, 2002.
- [10] B. Zhu, L. Leng, A.H. Gnauck, M.O. Pedersen, D. Peckham, L.E. Nelson, S. Stulz, S. Kado, L. Grüner-Nielsen, R.L. Lingle Jr., S. Knudsen, J.U. Leuholdt, C. Doerr, S. Chandrasekhar, G. Baynham, P. Gaarde, Y. Emori, and S. Namiki, Transmission of 3.2 Tb/s (80×42.7 Gbit/s) over 5200 km of UltraWave fiber with 100 km dispersion-managed spans using RZ_DPSK format. In *Proceedings of ECOC 2001*, PD4.2, 2002.
- [11] R.J. Nuyts, Y.K. Park, and P. Gallion, Dispersion equalization of a 10 Gb/s repeater transmission system using dispersion compensating fibers. *J. Lightwave Technol.*, 15:1, 31–42, 1997.
- [12] M. Wandel, P. Kristensen, T. Veng, Y. Qian, Q. Le, and L. Grüner-Nielsen, Dispersion compensating fibers for non-zero dispersion fibers, *Technical Digest of OFC'2002*, WU1, 2002.
- [13] A.J. Antos and D.K. Smith, Design and characterization of dispersion compensating fiber based on the LP01 mode, *J. Lightwave Technol.*, 12:10, 1739–1745, 1994.
- [14] L. Grüner-Nielsen, S.N. Knudsen, B. Edvold, T. Veng, D. Magnussen, C.C. Larsen, and H. Damsgaard, Dispersion compensating fibers, *Optic. Fiber Technol.*, 6: 164–180, 2000.
- [15] T. Kato, Design optimisation of dispersion compensating fiber for NZ-DSF considering nonlinearity and packaging performance. In *Proceedings of OFC2001*, TuS6, 2001.
- [16] M.J. Li, Recent progress In fiber dispersion compensators. In *Proceedings of ECOC 2001*, Th.M.1.1, 2001.
- [17] L. Grüner-Nielsen and B. Edvold, Status and future promises for dispersion-compensating fibers. In *Proceedings of ECOC'02*, 6.1.1, 2002.
- [18] M. Wandel, T. Veng, Q. Le N.T., and L. Grüner-Nielsen, Dispersion compensating fibre with a high figure of merit. In *Proceedings of ECOC'01*, PD.A.1.4, 2001.
- [19] C.D. Poole, J.M. Wiesenfeld, D.J. DiGiovanni, and A.M. Vengsarkar, Optical fiber-based dispersion compensation using higher order modes near cut-off, *J. Lightwave Technol.*, 12:10, 1746–1758, 1994.
- [20] A.H. Gnauck, L.D. Garrett, Y. Danziger, U. Levy, and M. Tur, Dispersion and dispersion-slope compensation of NZDSF over the entire C band using higher-order-mode fibre, *Electron. Lett.*, 36: 1946, 2000.
- [21] S. Ramachandran, B. Mikkelsen, L.C. Cowsar, M.F. Yan, G. Raybon, L. Boivin, M. Fishteyn, W.A. Reed, P. Wisk, D. Brownlow, and L. Grüner-Nielsen, All-fiber, grating-based, higher-order-mode dispersion compensator for broadband compensation and 1000-km transmission at 40-Gb/s, *Photon. Technol. Lett.*, 13:6, 632–634, 2001.
- [22] L. Grüner-Nielsen, Y. Qian, B. Pálsdóttir, Y. Qian, P.B. Gaarde, S. Dyrbøl, T. Veng, R. Boncek, and R. Lingle, Module for simultaneous C + L-band dispersion compensation and Raman amplification, *OFC'02*, TuJ6, 2002.
- [23] T. Miyamoto, T. Tsuzaki, T. Okuno, M. Kakui, M. Hirano, M. Onishi, and M. Shigematsu, Raman amplification over 100nm-bandwidth with dispersion and dispersion slope compensation for conventional single mode fiber. In *Proceedings of OFC'02*, TuJ7, 2002.
- [24] L. Grüner-Nielsen, B. Edvold, D. Magnussen, D. Peckham, A. Vengsarkar, D. Jacobsen, T. Veng, C.C. Larsen, and H. Damsgaard, Large volume manufacturing of dispersion compensating fibres, *Technical Digest of OFC'98*, 24–25, 1998.
- [25] Y. Qian, J.H. Povlsen, S.N. Knudsen, and L. Grüner-Nielsen, Fiber Raman amplifications with dispersion compensating fibers, *Trends Optics Photon. Series TOPS*, 44: 36–43, 2000.

- [26] Y. Qian, J.H. Povlsen, S.N. Knudsen, and L. Grüner-Nielsen, Fiber Raman amplifications with single-mode fibers, *Trends Optics and Photon. Series TOPS*, 44: 128–134, 2000.
- [27] P.B. Hansen, L. Eskildsen, A.J. Stentz, T.A. Strasser, J. Judkins, J.J. DeMarco, R. Pedrazzani, and D.J. DiGiovanni, Rayleigh scattering limitations in distributed Raman pre-amplifiers, *IEEE Photon. Technol. Lett.*, 10:1, 159–161, 1998.
- [28] M. Nissov, K. Rottwitt, H.D. Kidorf, and M.X. Ma, Rayleigh crosstalk in long cascades of distributed unsaturated Raman amplifiers, *Electron. Lett.*, 35:12, 997–998, 1999.
- [29] V.E. Perlin and H.G. Winful, On trade-off between noise and nonlinearity in WDM systems with distributed Raman amplification. In *Proceedings of OFC'02*, WB1, 2002.
- [30] A. Artamonov, V. Smokovdin, M. Kleshov, S.A.E. Lewis, and S.V. Chernikov, Enhancement of double Rayleigh scattering by pump intensity noise in fiber Raman amplifier. In *Proceedings of OFC'02*, WB6, 2002.
- [31] C.H. Kim, J. Bromage, and R.M. Jopson, Reflection-induced penalty in Raman amplified systems, *IEEE Photon. Technol. Lett.*, 14:4, 2002.
- [32] A.F. Judy, An OTDR based combined end-reflection and backscatter measurement. In *Proceedings of SOFM*, 19–22, 1992.
- [33] P.B. Gaarde, Y. Qian, S.N. Knudsen, and B. Pálsdóttir, Predicting MPI in Raman optical amplifiers by measuring the Rayleigh backscattering coefficient. In *Proceedings of SOFM'02*, 2002.
- [34] T. Tanaka, K. Torii, M. Yuki, H. Nakamoto, T. Naito, and I. Yokota, 200-nm bandwidth WDM transmission around 1.55 μ m using distributed Raman amplifier. In *Proceedings of ECOC'02*, PD4.6, 2002.
- [35] D.A. Chestnut, C.J.S. de Matos, P.C. Reeves-Hall, and J.R. Taylor, Co- and counter-propagating second-order-pumped lumped fiber Raman amplifiers. In *Proceedings of OFC'02*, ThB2, 2002.
- [36] J. Bromage, H.J. Thiele, and L.E. Nelson, Raman amplification in the S-band. In *Proceedings of OFC'02*, ThB3, 2002.
- [37] Y. Qian, C.G. Jørgensen, P.B. Gaarde, B. Pálsdóttir, and B. Edvold, C-band discrete Raman amplification with simultaneous dispersion and dispersion-slope compensation for NZDF. In *Proceedings of OAA'02*, OWB2, 2002.
- [38] D.F. Grosz, A. Agarwal, S. Banerjee, A.P. Kung, D.N. Maywar, A. Gurecich, T.H. Wood, C.R. Lima, B. Faer, J. Black, and C. Hwu, 5.12 Tb/s (128×42.7 Gb/s) Transmission with 0.8bit/s/Hz spectral efficiency over 1280 km of standard single-mode fiber using all-Raman amplification and strong signal filtering. In *Proceedings of ECOC'02*, PD4.3, 2002.
- [39] L.F. Mollenauer, Dispersion managed solitons for ultra long distance, Terabit WDM. In *Proceedings of OFC'00*, Tutorial 5, 2000.
- [40] P.J. Winzer, K. Sherman, and M. Zirngibl, Experimental demonstration of time-division multiplexed Raman pumping. In *Proceedings of OFC'02*, WB5, 2002.
- [41] G. Charlet, W. Idler, R. Dischler, J.-C. Antona, P. Tran, and S. Bigo, 3.2Tbit/s (80'42.7 Gb/s) C-Band transmission over 9'100 km of TeraLightTM fiber with 50 GHz channel spacing. In *Proceedings of OAA'02*, PD1, 2002.
- [42] Y. Qian, S. Dyrbøl, J.S. Andersen, P.B. Gaarde, C.G. Jørgensen, B. Pálsdóttir, and L. Grüner-Nielsen, Bidirectionally pumped discrete Raman amplifier with optimized dispersion compensation for non-shifted transmission fibre. In *Proceedings of ECOC'02*, 6.4.1, 2002.
- [43] S.A.E. Lewis, S.V. Chernikov, and J.R. Taylor, Characterization of double Rayleigh scatter noise in Raman amplifiers, *IEEE Photon. Technol. Lett.*, 12: 528–530, 2000.
- [44] C.R.S. Fludger and R.J. Mears, Electrical measurements of multipath interference in distributed Raman amplifiers; *J. Lightwave Technol.*, 19:4, 536, 2001.

- [45] M.O. van Deventer, Polarization properties of Rayleigh backscattering in single-mode fibers, *J. Lightwave Technol.*, 11: 1895–1899, 1993.
- [46] V. Smokovdin, S.A.E. Lewis, and S.V. Chernikov, Direct comparison of electrical and optical measurements of double Rayleigh scatter noise. In *Proceedings of ECOC'02*, S3.5, 2002.
- [47] S.A.E. Lewis, S.V. Chernikov, and J.R. Taylor, Temperature-dependent gain and noise in fiber Raman amplifiers, *Opt. Lett.*, 24: 24, 1999.
- [48] S. Burtsev, W. Pelouch, and P. Gavrilovic, Multi-path interference noise in multi-span transmission links using lumped Raman amplifiers. In *Proceedings of OFC'02*, TuR4, 2002.
- [49] J. Bromage, L.E. Nelson, C.H. Kim, P.J. Winzner, F-J. Essiambre, and R.M. Jopson, Relative impact of multiple-path interference and amplified spontaneous emission noise on optical receiver performance. In *Proceedings of OFC'02*, TuR3, 2002.
- [50] A. Artamonov, V. Smokovdin, M. Kleshov, S.A.E. Lewis, and S.V. Chernikov, Enhancement of double Rayleigh scattering by pump intensity noise in fiber Raman amplifier. In *Proceedings of OFC'02*, WB6, 2002.
- [51] P. Parolari, L. Marazzi, L. Bernardini, and M. Martinelli, Double Rayleigh backscatter noise measurements in discrete and distributed Raman amplifiers. In *Proceedings of OAA'02*, OWA3, 2002.
- [52] R. Essiambre, P. Winzer, J. Bromage, and C.H. Kim, Design of bidirectionally pumped fiber amplifiers generating double Rayleigh backscattering, *IEEE Photon. Technol. Lett.*, 14:7, 914–916, 2002.
- [53] H.J. Thiele, J. Bromage, and L. Nielsen, Impact of discrete Raman amplifier architecture on nonlinear impairments. In *Proceedings of ECOC'02*, 7.0.2, 2002.
- [54] A.J. Stenz, S.G. Grubb, C.E. Headley, J.R. Simpsonson, T. Strasser, and N. Park, Raman amplifier with improved system performance. In *Proceedings of OFC'96*, TuD3, 1996.
- [55] D. Hamoir, J. Boniort, L. Gasca, and D. Bayart, Optimized, two-stage architecture for Raman amplifiers. In *Proceedings of OAA'00*, OMD8, 2000.
- [56] T. Tsuzaki, T. Miyamoto, T. Okuno, M. Kakui, M. Hirano, M. Onishi, and M. Shigematsu, Impact of double Rayleigh backscattering in discrete fiber Raman amplifiers employing highly nonlinear fiber. In *Proceedings of OAA'02*, OWA2, 2002.
- [57] C.R.S. Fludger, V. Handerek, and R.J. Mears, Pump to signal RIN transfer in Raman fibre amplifiers, *J. Lightwave Technol.*, 19:8, 1140–1148, 2001.
- [58] M.D. Mermelstein, C. Headley, and J.-C. Bouteiller, RIN transfer analysis in pump depletion regime for Raman fibre amplifiers, *Electron. Lett.*, 38:9, 403–405, 2002.
- [59] S. Kado, Y. Emori, and S. Namiki, Gain and noise tilt control in multi-wavelength bidirectionally pumped Raman amplifier. In *Proceedings of OFC'02*, TuJ4, 2002.
- [60] A.F. Evans, J. Grochocinski, A. Rahman, C. Reynolds, and M. Vasilyev, Distributed amplification: How Raman gain impacts other fiber nonlinearities. In *Proceedings of OFC'01*, MA7, 2001.
- [61] J. Bromage, P.J. Winzner, L.E. Nelson, and C.J. McKinstrie, Raman-enhanced pump-signal four-wave mixing in bidirectionally-pumped Raman amplifiers. In *Proceedings of OAA'02*, OWA5, 2002.
- [62] Q.L.N.T., C.G. Jørgensen, L.G. Grüner-Nielsen, and B. Pálsdóttir, Enhancement of nonlinear response of a highly nonlinear fibre due to Raman amplification. In *Proceedings of ECOC'02*, 2002.
- [63] T. Okuno, T. Tsuzaki, H. Hirano, T. Miyamoto, M. Kakui, M. Onishi, Y. Nakai, and M. Nishimura, Nonlinear-fiber-based discrete Raman amplifier with sufficiently suppressed degradation of WDM signal quality. In *Proceedings of OAA'01*, OTuB5, 2001.

Chapter 7

New Raman Fibers

Evgeny M. Dianov

7.1. Introduction

The Raman scattering of light is one of the oldest and most well-studied optical phenomena. It was discovered more than 70 years ago and was named after one of the authors of this discovery. In 1928 C. V. Raman and K. S. Krishnan published the paper in which they described light scattering in liquids, the frequency of the scattering light being less than the frequency of the initial light [1]. The same year Russian physicists G. S. Landsberg and L. I. Mandelstam observed independently a similar light scattering in quartz [2].

It is interesting to note that from the very beginning spontaneous Raman scattering attracted much attention and systematic investigations of it were started in many laboratories. This was connected to a large degree with the possibility of using Raman scattering as an efficient tool for studying the vibronic structure of molecules and crystals.

The advent of lasers allowed the observation of stimulated Raman scattering (SRS). The possibility of effectively transforming the frequency of laser radiation increased interest in this phenomenon even more [3]. SRS, as are other nonlinear optical phenomena, is the most efficient in optical waveguides because these structures maintain high pump power densities over considerable lengths (see, e.g., [4]).

That's why one of the first experiments with newly developed low-loss silica fibers was the experiment on stimulated Raman scattering. In 1971 Stolen et al. [5] observed stimulated Raman emission in a single-mode silica fiber fabricated by Corning Glass Works. On the basis of this experiment the authors were the first to formulate a conclusion about the possibility of constructing wideband optical amplifiers and Raman oscillators tunable over the range of 100 Å.

Already at that time, the fundamental advantages of Raman amplification were clear:

- Amplification at any wavelength, provided the appropriate pump sources are available;
- A fiber itself can be used as an active medium; and
- A pump spectrum determines a gain spectrum.

The main disadvantage was also clear: a low value of the Raman scattering cross-section in glasses, especially in silica glass [6], which is two orders lower than that in some crystals and liquids.

Before proceeding further it is necessary to clarify what a Raman fiber is. Every optical fiber has some Raman gain. Standard transmission fibers with silica core doped by a small concentration of GeO_2 have a low value of Raman gain and a Raman frequency shift of about 440 cm^{-1} . However, for a number of applications such as lumped Raman amplifiers and Raman fiber lasers, special fibers with much higher Raman gain and (or) various Raman frequency shifts are often required. Besides, the shape of the Raman scattering spectrum can be an important feature for some applications. At present such special fibers are named Raman fibers.

The main milestones in the development of Raman fibers are briefly considered in the following.

In 1970 Ippen [7] observed stimulated Raman emission in a liquid core (CS_2) optical fiber. Liquid core fibers are of interest because many liquids have a high value of the Raman scattering cross-section and various Raman frequency shifts. However, they are not compatible with optical fiber communication (OFC) systems and this type of fibers is not considered here.

Pioneer works by Stolen et al. [5, 8] on the observation of stimulated Raman emission and measurement of the Raman gain in a single-mode silica fiber aroused great interest in Raman scattering in various glasses. A large number of glasses were studied in the 1970s and the 1980s, among them single-component glasses, doped-silica glasses, and various multicomponent glasses, including heavy-metal oxides-doped glasses ([9–16] and references therein). The goal of the research was to find glasses with enhanced and (or) new Raman gain features, which could be used as an efficient active medium for Raman fiber lasers and amplifiers.

It was discovered that glasses containing heavy-metal oxides Tl_2O , PbO , Bi_2O_3 , and Sb_2O_3 in combination with GeO_2 , SiO_2 , and As_2O_3 have very high Raman cross-section, 30 and 3 times exceeding that of SiO_2 and GeO_2 , respectively [15]. Two glass systems— $\text{Sb}_2\text{O}_3 \cdot \text{GeO}_2$ and $\text{Sb}_2\text{O}_3 \cdot \text{As}_2\text{O}_3$ —were found to be the most promising materials for high-gain Raman fibers. Unfortunately fabrication technology of low-loss fibers from these glasses has not yet been developed.

The situation was quite the opposite with the technology of doped-silica glasses, the Raman scattering properties of which were investigated in detail. The relative Raman cross-sections of vitreous SiO_2 , GeO_2 , B_2O_3 , and P_2O_5 , widely used in optical fiber technology, were accurately measured by Galeener et al. [11]. It was found that germania glass has the highest cross-section, approximately nine times that of silica.

The frequency shift in germania glass was measured to be about 420 cm^{-1} . Vitreous P_2O_5 is also of great interest because this glass has two Raman scattering bands shifted by 650 and 1300 cm^{-1} . The cross-section for these bands is 5.7 and 3.5 times higher compared to silica. The presence of the Raman scattering band, shifted by 1300 cm^{-1} (i.e., three times that for silica and germania) is the most important feature of P_2O_5 glass. The relative Raman cross-section of B_2O_3 glass is 4.7 with the Raman scattering band maximum at 808 cm^{-1} .

High values of the Raman cross-section of these glasses suggested that binary glasses $\text{SiO}_2\text{--GeO}_2$, $\text{SiO}_2\text{--P}_2\text{O}_5$, and $\text{SiO}_2\text{--B}_2\text{O}_3$ could have high enough Raman gain and new gain bands. The Raman scattering spectra of these glasses and corresponding fibers were investigated in a number of papers [9, 10, 12, 16, 17]. In particular, it was shown that the main bands at 808 cm^{-1} and 650 cm^{-1} in vitreous B_2O_3 and P_2O_5 , respectively, are greatly reduced in binary high-silica glasses, whereas the band at 420 cm^{-1} due to Ge--O--Ge vibration and the band at 1300 cm^{-1} due to P=O vibration remain strong [12]. It was also shown that the Raman cross-section of germanosilicate glass increases linearly with the germania concentration [16].

The obtained results showed that low-loss high GeO_2 - and P_2O_5 -doped silica fibers could be considered as promising high-gain Raman fibers. It was important that these fibers could be fabricated by well-developed techniques (MCVD, VAD, OVD) used for optical fiber production. However, serious problems were met with the fabrication of germanosilicate and phosphosilicate fibers doped by high amounts of P_2O_5 and GeO_2 (more than 17 to 18 and 25 mol%, respectively). These problems were connected with the different melting temperatures and thermal expansion coefficients of SiO_2 , GeO_2 , and P_2O_5 glasses. Besides, it was revealed that optical losses of these fibers grow substantially with increasing GeO_2 and P_2O_5 contents.

So further thorough investigations should be carried out to optimize the composition and parameters of the fibers. Fortunately, a very important achievement, namely, the development and successful demonstration of CW-cascaded Raman fiber lasers and optical amplifiers for a $1.3\text{ }\mu\text{m}$ window [18, 19], strongly stimulated this research. To estimate this achievement note that in the 1980s the technology of optical fiber communication reached the necessary maturity to call for optical amplifiers to proceed further in the creation of advanced OFC systems. Raman fiber amplifiers were considered a main candidate for this purpose. Despite much research that was carried out on Raman fiber amplifiers [20], the absence of appropriate pump sources didn't allow the use of those amplifiers in practice. Because of low Raman gain in glasses the necessary CW pump power at wavelengths of 1.24 and $1.45\text{ }\mu\text{m}$ has to be $\sim 1\text{ W}$ to get high enough amplification at 1.31 and $1.53\text{ }\mu\text{m}$. But such lasers didn't exist at that time. However, independent experiments carried out at the General Physics Institute (Moscow) and at AT&T Bell Labs made it possible to develop practical pumping sources for optical fiber amplifiers, in particular for $1.31\text{ }\mu\text{m}$ Raman fiber amplifiers. As a pump source the CW third Stokes ($1.24\text{ }\mu\text{m}$) obtained by the cascaded stimulated Raman scattering of $1.06\text{ }\mu\text{m}$ laser radiation was used in those experiments. At the General Physics Institute efficient Raman conversion was achieved by using a high GeO_2 -doped low-loss Raman fiber. A cascaded resonant Raman laser cavity utilizing intracavity fiber Bragg gratings was used at AT&T Bell Labs to efficiently convert a CW fiber laser source at $1.06\text{ }\mu\text{m}$ to the third Stokes frequency [19].

Figure 7.1 shows the scheme of a $1.3\text{ }\mu\text{m}$ Raman fiber amplifier, pumped for the first time by CW third Stokes radiation ($1.24\text{ }\mu\text{m}$, 300 mW) [18]. A special high GeO_2 -doped fiber was also used as an active medium of the Raman amplifier. A gain of 10 dB was obtained at the CW pump power of 300 mW using 1.56 km of the

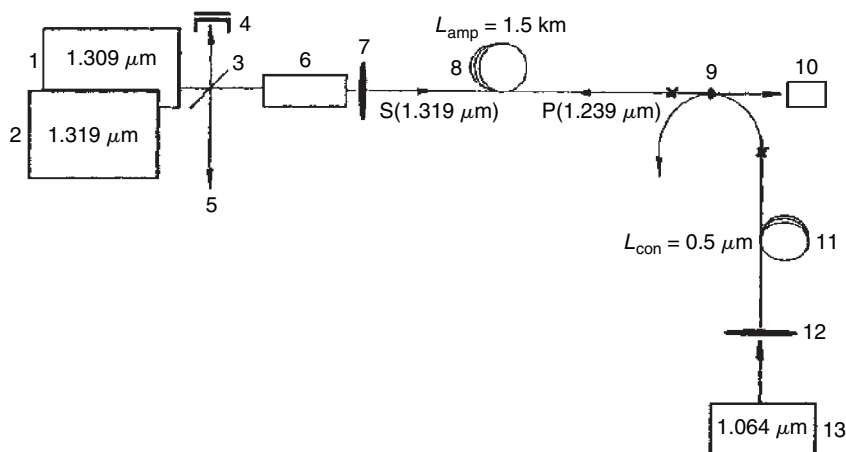


Fig. 7.1. The scheme of the 1.3 μm Raman fiber amplifier: (1) laser diode emitting at $\lambda = 1.309 \mu\text{m}$; (2) CW mode-locking YAG:Nd laser emitting at $\lambda = 1.319 \mu\text{m}$; (3) beam splitter; (4) beam lock; (5) to a spectrum analyzer; (6) acoustooptic modulator; (7,12) microobjectives; (8) amplifying fiber of length $L_{\text{amp}} = 1.5 \text{ km}$; (9) wavelength-division multiplexer; (10) photodiode; (11) fiber converter of radiation to a third Stokes component with length $L_{\text{con}} = 0.5 \text{ km}$; (13) CW YAG:Nd laser emitting at $\lambda = 1.06 \mu\text{m}$; S and P are the signal and pump radiation at the wavelengths of 1.319 (1.309) μm and 1.239 μm , respectively. The crosses identify the splices between the fibers.

fiber with optical losses of 2 and 3 dB/km at wavelengths of 1.31 and 1.24 μm . It is interesting to note that in this paper the following prediction was made. In the case of development of GeO_2 -doped fiber with optical losses $\alpha_{\text{pump}} = 2 \text{ dB/km}$ and $\alpha_{\text{signal}} = 1 \text{ dB/km}$ for 20 mol% of GeO_2 a small signal Raman gain of $\sim 25 \text{ dB}$ could be obtained at pump power of 300 mW. The close figures were obtained in 1998 [21].

The cascaded Raman fiber lasers pumped by laser diodes turned out to be a very efficient source of radiation in the spectral region 1.2 to 1.6 μm which could be used to pump various optical amplifiers. However, to get the radiation in the long-wavelength part of the region, one needs to have more than three Raman cascades (therefore more than three pairs of gratings) if using a germanosilicate fiber [22]. To reduce the number of gratings a high P_2O_5 -doped fiber with a Raman frequency shift of 1300 cm^{-1} was suggested as a Raman medium [23]. This simplified the structure of lasers and increased their efficiency [24].

At present germanosilicate and phosphosilicate Raman fibers are widely used for constructing CW Raman fiber lasers, which can cover the whole spectral region of 1.2 to 1.75 μm [25]. These CW medium-power (1 to 10 W) lasers are a convenient laser source for pumping optical fiber amplifiers and some lasers. These applications ask for some specific requirements on Raman fibers, which are discussed in the next section.

7.2. Most Important Parameters of Raman Fibers

7.2.1. Cross-Section of Spontaneous Raman Scattering (Raman Gain)

The cross-section of spontaneous Raman scattering σ is the most important characteristic of a Raman medium. The definition of σ per molecule follows from an equation for the number of spontaneously scattered quanta N_s per length of material dz per solid angle $d\Omega$ for one polarization [3]:

$$dN_s = N_a N_L \left(\frac{\partial \sigma}{\partial \Omega} \right) d\Omega dz,$$

where N_a is the number of molecules per unit volume in the lower energy state and N_L is the number of incident laser quanta. The stimulated Raman scattering is characterized by exponential amplification of the Stokes wave

$$\frac{dN_s}{dz} = g_R N_s$$

with the Raman gain coefficient

$$g_R [\text{cm}^{-1}] = (N_a - N_b) \left(\frac{\partial \sigma}{\partial \Omega} \right) \frac{c^3 n_L^2 |E_L|^2}{4\pi \nu_s^2 n_s^3 \Gamma_{ab}},$$

where E_L is the amplitude of the laser light wave, N_b is the number of molecules in the upper energy state, n_L and n_s are the indices of refraction at the laser and Stokes frequencies, c is the light velocity, ν_s is the Stokes frequency, and Γ_{ab} is the width of a Stokes line.

The normalized gain

$$C_R \left[\frac{\text{cm}}{\text{W}} \right] = \frac{g_R}{I}$$

is often used. I is the intensity of laser light.

A real Raman gain in a glass optical fiber depends not only on the Raman gain coefficient for a Raman medium, but also on the parameters of the fiber, namely, the effective length and the effective mode area.

In practice the following expression for the fiber Raman gain coefficient is used,

$$C_R \left[\frac{1}{\text{m} \cdot \text{W}} \right] = \frac{\ln G}{L_{eff} P_o},$$

where G is the measured linear small signal gain (on-off) and P_o is the pump power,

$$L_{eff} = \frac{[1 - \exp -\alpha_p L]}{\alpha_p},$$

where α_p are optical losses at the pumping wavelength, L is the fiber length, and L_{eff} is the effective fiber length.

Sometimes it is more convenient to express the fiber Raman gain coefficient by $\text{dB}/(\text{m} \cdot \text{W})$. Then

$$g_0 \left[\frac{\text{dB}}{\text{m} \cdot \text{W}} \right] = \frac{10}{\ln 10} C_R \left[\frac{1}{\text{m} \cdot \text{W}} \right].$$

7.2.2. Spontaneous Raman Scattering Spectrum and Raman Frequency Shift

The spontaneous Raman scattering spectrum determines the gain bandwidth of a fiber and depends on the glass composition.

The Raman frequency shift is usually understood as a frequency difference between pump radiation and the maximum of a Stokes band. The value of the Raman frequency shift determines the wavelength of pumping radiation in Raman amplifiers and the number of cascades in cascaded Raman fiber lasers for the given wavelength of pumping radiation. In the case of multiwavelength pumping of a Raman fiber amplifier the Raman frequency shift determines the maximum gain bandwidth of this amplifier.

7.2.3. Effective Mode Area

The effective mode area is one of the most important characteristics of Raman fibers. It determines the intensity of pumping radiation for the given pump power. In turn the effective mode area is determined by the index profile of a fiber.

7.2.4. Optical Losses

Optical losses of a Raman fiber determine its effective length and are a key parameter of Raman fiber lasers and amplifiers.

7.2.5. Photosensitivity

At present fiber gratings are key elements of Raman fiber lasers and amplifiers. The photosensitivity of Raman fibers allows the writing of gratings directly in Raman fibers and therefore increasing the efficiency of Raman devices.

7.2.6. Threshold of Catastrophic Damage

At present in optical fiber communication systems laser radiation powers in the range of 0.5 to 1 W are widely used for pumping fiber amplifiers. Various Raman fiber lasers generating radiation in the spectral region of 1.2 to 1.7 μm with the output powers of 1 W have been developed. So the threshold of the catastrophic damage of fibers that can take place at the powers of 0.5 to 1 W has become one of the most important characteristics of Raman fibers.

The next section shows that at present both high GeO_2 - and P_2O_5 -doped fibers mostly meet the required characteristics for Raman fibers.

7.3. Recent Advances in Low-Loss High GeO_2 - and P_2O_5 -Doped Optical Fibers

Prospects of wide usage of germanosilicate and phosphosilicate Raman fibers for Raman fiber lasers and discrete Raman amplifiers increased interest in these fibers and led to thorough investigations of stimulated Raman scattering spectra of these fibers [26–35]. The investigations included: measurement methods of SRS spectra [28, 30, 32], dependence of Raman gain coefficient on pump wavelength [35], prediction of

Raman gain spectra for germanosilicate fibers with arbitrary and given index profiles [33, 34], and Raman characteristics of optical fibers for discrete and distributed Raman amplifiers [27, 29, 31, 32]. The Raman gain coefficient has been measured practically for all standard transmission fibers and for a number of experimental ones.

It has been proved that in high GeO_2 -doped fibers the Raman gain coefficient can be six to eight times that of standard transmission fibers. For example, the high GeO_2 -doped Raman fibers developed at the Fiber Optics Research Center (FORC, Moscow) have the Raman gain coefficient of 18,9 (dB/km · W) at 1.5 μm compared to 3.1 and 2.8 (dB/km · W) for NZDSF and LEAF, respectively. The increase of Raman gain in high GeO_2 -doped fibers is due to two reasons: because of the increase of the Raman cross-section and (but more important), because of the decrease of the effective mode area.

The Raman scattering spectrum consists of a single band with the maximum at 440 cm^{-1} .

The Raman scattering spectrum of a P-doped fiber consists of two bands, the narrow one at 1300 cm^{-1} and the broad one with the maximum at $\sim 500\text{ cm}^{-1}$ connected mainly with Si–O–Si vibration. In the case of P_2O_5 -doped fibers with the P_2O_5 concentration of 15 mol% the Raman gain coefficient of 10 (dB/km · W) (for the band at 1300 cm^{-1}) exceeds two to three times that for standard transmission fibers. It is an advantage of a P_2O_5 -doped fiber to have two gain bands because this provides a certain flexibility in constructing a Raman fiber laser for a given wavelength of generation [36].

Figure 7.2 shows spectra of the fiber Raman gain coefficient g_0 for several fibers.

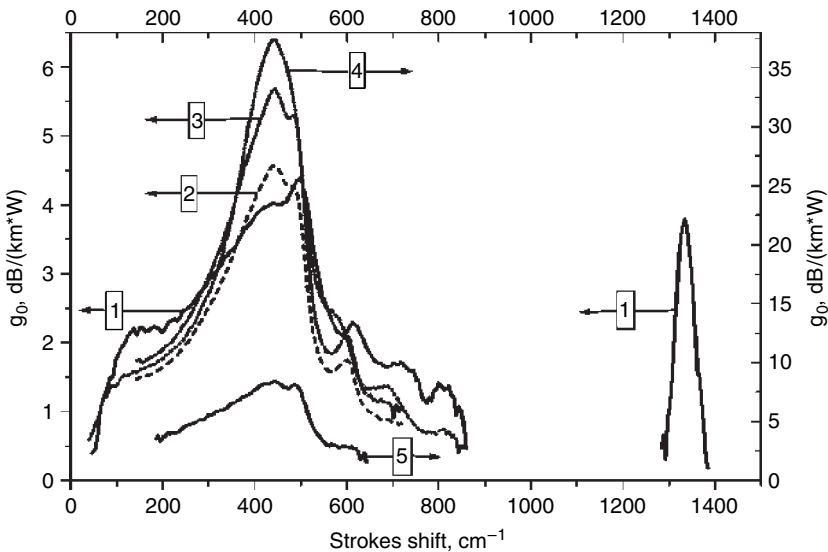


Fig. 7.2. The spectra of a fiber Raman gain coefficient for different fibers: (1) P-doped fiber ($\sim 10\text{ mol}\% \text{ P}_2\text{O}_5$); (2) large effective area fiber; (3) dispersion-shifted fiber; (4) high Ge-doped fiber ($\sim 25\text{ mol}\% \text{ GeO}_2$); (5) nitrogen-doped fiber ($\Delta n \sim 0.01$). Pump wavelength is 1.24 μm .

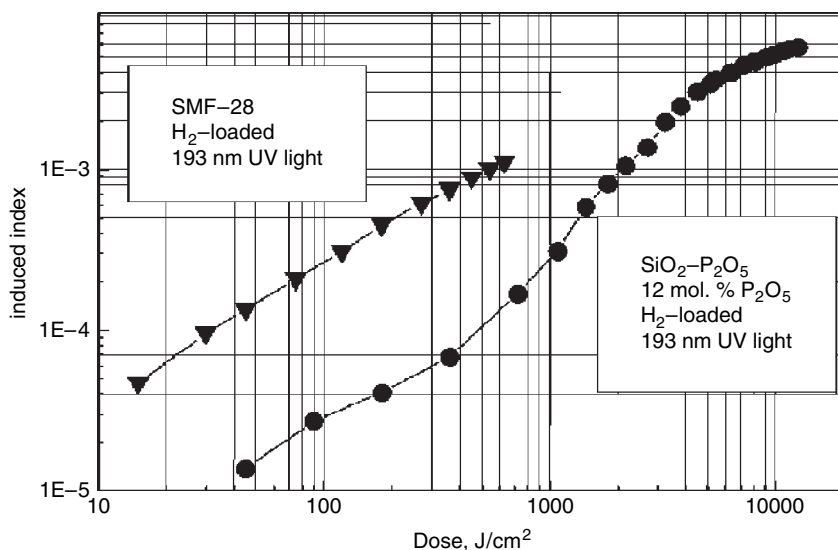


Fig. 7.3. Refractive index change in dependence on 193 nm irradiation dose.

As noted in Section 7.2 the photosensitivity of Raman fibers is of great importance because of wide applications of fiber gratings for Raman lasers and amplifiers. It is well known that germanosilicate fibers possess high photosensitivity which is enhanced with the increase of GeO_2 concentration (see, e.g., [37]). So there are no problems in writing gratings directly in a GeO_2 -doped Raman fiber.

The photosensitivity of P_2O_5 -doped fibers was observed in 1994 (see, e.g., [38, 39]). It was reported that Bragg gratings can be written in a H_2 -sensitized P_2O_5 -doped waveguide by using 193 nm irradiation. The photosensitivity of low-loss high P_2O_5 -doped fibers has been studied at FORC [40]. Figure 7.3 shows the refractive index change dependence on a 193 nm irradiation dose. It is seen that when using 193 nm UV light it is feasible to write strong gratings in H_2 -loaded phosphosilicate fibers.

While considering the most important parameters of Raman fiber optical losses should be regarded as the most serious problem. It has already been mentioned that optical losses of high GeO_2 - and P_2O_5 -doped fibers increase with the content of dopants.

Figure 7.4 shows an experimental dependence of optical losses of a germanosilicate fiber fabricated by a standard MCVD technique on the germania content at the wavelength of $1.55 \mu\text{m}$ (curve 1). Curve 2 shows the Rayleigh scattering. A number of papers devoted to investigations of optical losses in high GeO_2 -doped fibers have been published (see, e.g., [41–48]).

Although the mechanisms of increasing optical losses are not fully understood, some dependencies of optical losses on fiber drawing conditions, the fiber structure, and composition were observed. It has been found that the excess losses decrease with the decrease of drawing temperature [41–43]. Optical losses are sensitive to the difference in softening temperature of core and cladding glasses [42] and are

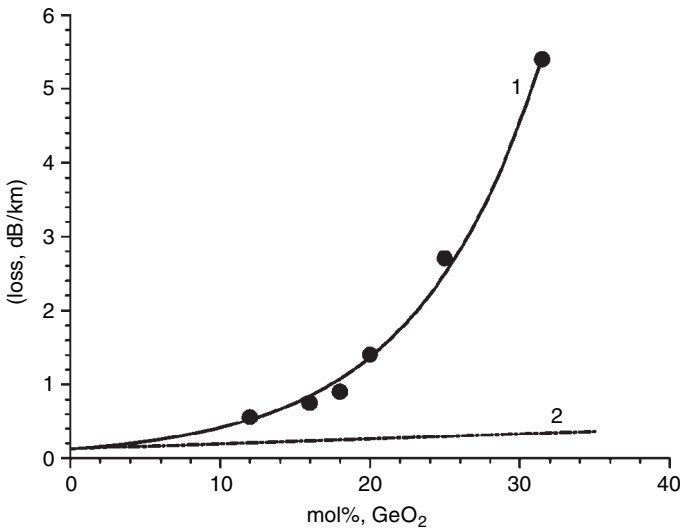


Fig. 7.4. The experimental dependence of optical losses of germanosilicate fibers fabricated by a standard technique on germania content at the wavelength of $1.55 \mu\text{m}$ (curve 1). Curve 2 shows the Rayleigh scattering.

lower in graded index profile fibers [41, 42]. A fluorine-doping core was shown to also decrease optical losses [44, 45]. Taking into account these dependencies high GeO_2 -doped optical fibers with quite low losses have been developed.

Figure 7.5 shows the loss spectra of germanosilicate fibers with 23.5, 26.2, and 29.6 mol% of GeO_2 developed at FORC, using the MCVD technique [49].

The best results for fibers, fabricated by the VAD technique, are 0.35 and 0.51 dB/km at a wavelength of $1.55 \mu\text{m}$ for 25 and 30 mol% GeO_2 , respectively [46].

It should be noted that the VAD method is more advantageous for obtaining lower-loss highly doped fibers because of the absence of an index profile central dip. Besides, it is more flexible in choosing cladding glass, in particular, with lower melting temperature. This allows the drawing of fibers at lower temperature compared to MCVD fibers, where a substrate silica tube is used. Thus, low-loss Raman fibers (1 dB/km) with the concentration of GeO_2 up to 30 mol% have been developed.

Now optical losses in high P_2O_5 -doped silica fibers are considered. Unfortunately, there is the same situation here as for high GeO_2 -doped fiber, that is, the growth of optical losses with the concentration of P_2O_5 . For example, a phosphosilicate fiber doped with 17 mol% P_2O_5 had optical losses of 2.8 and 5.7 dB/km at 1.32 and $1.59 \mu\text{m}$, respectively [50].

The fabrication of high P_2O_5 -doped optical fibers and the investigation of optical losses in these fibers are described in detail in [51, 52]. Some results of this investigation are presented here.

The fibers under study were fabricated by the MCVD technique. The deposited cladding had a $\text{F-P}_2\text{O}_5\text{-SiO}_2$ composition. In order to decrease optical losses, freon ($\text{C}_2\text{F}_3\text{Cl}_3$) was added into the gas mixture during the layer deposition. Figure 7.6

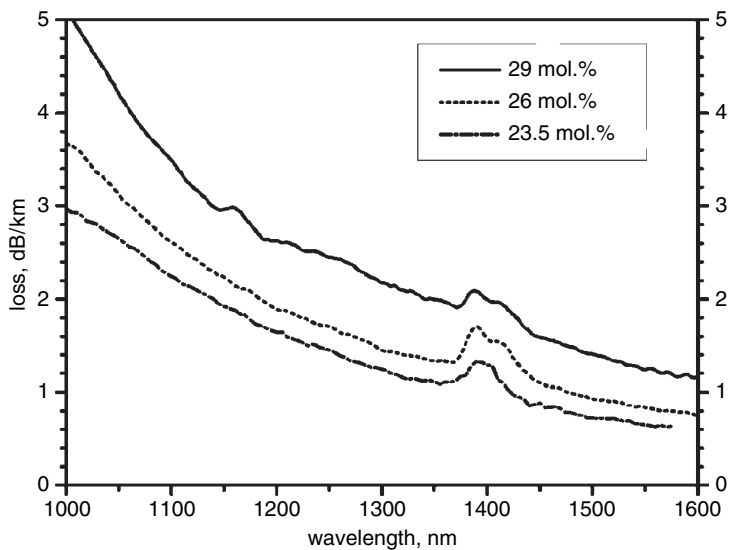


Fig. 7.5. Loss spectra of MCVD germanosilicate fibers.

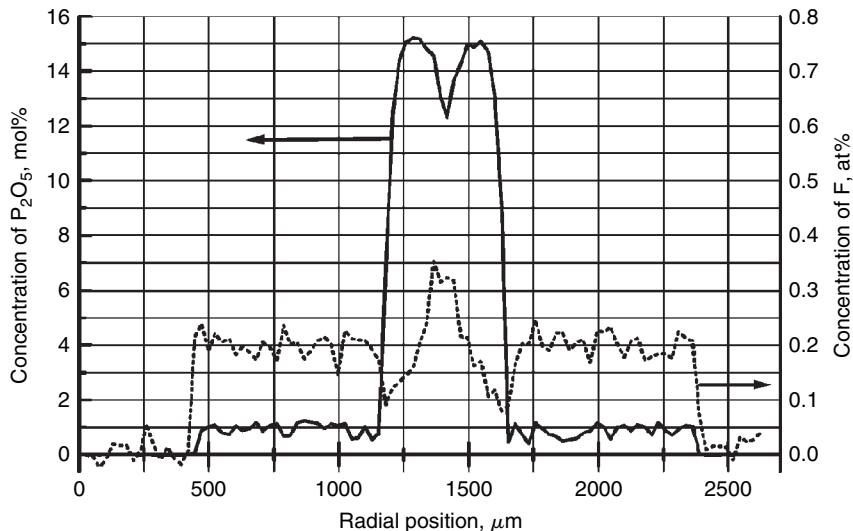


Fig. 7.6. Radial distribution of phosphorus pentoxide and fluorine.

shows the radial distribution of phosphorous pentaoxide and fluorine determined by Xray microanalysis. Figure 7.7 shows the dependence of optical losses at 1.06 and 1.24 μm on the P_2O_5 concentration for different fiber drawing temperatures.

The optical loss spectrum of a phosphosilicate fiber doped with 13 mol% P_2O_5 is shown in Fig. 7.8. It is seen that the optical losses of 1 dB/km in the spectral region of 1.2 to 1.6 μm have been achieved, the optical losses at 1.06 μm being 1.6 dB/km. The

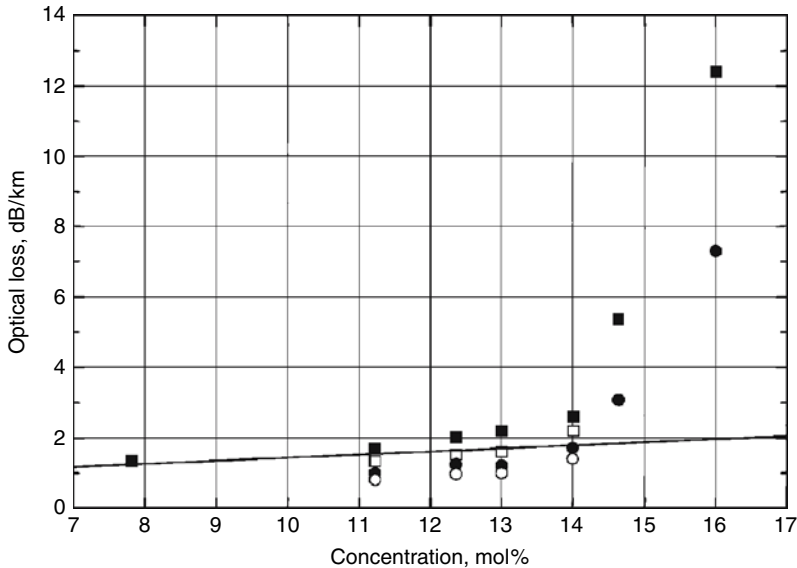


Fig. 7.7. Losses in fibers versus P_2O_5 concentration: ■— at $1.06\ \mu\text{m}$ (fiber drawing temperature 1940°C); □— at $1.06\ \mu\text{m}$ (fiber drawing temperature 1860°C); ●— at $1.24\ \mu\text{m}$ (fiber drawing temperature 1940°C); ○— at $1.24\ \mu\text{m}$ (fiber drawing temperature 1860°C); solid line—evaluation of the minimum Rayleigh losses at $1.06\ \mu\text{m}$ by means of linear approximation of the data for low- P_2O_5 fibers (drawn at 1940°C).

development of low-loss germanosilicate and phosphosilicate Raman fibers allowed the construction of highly efficient Raman fiber lasers and lumped amplifiers (see, e.g., [21, 25, 53]).

The next important issue is a catastrophic damage threshold of Raman fibers. The catastrophic damage of optical fibers (fiber fusion), occurring at relatively low optical powers (less than 1 W CW), was observed for the first time in 1987 [54]. If a fiber is locally heated to the temperature of $\sim 1000^\circ\text{C}$ the laser radiation propagating through the fiber is strongly absorbed by the heated piece of the fiber, increasing the temperature up to 5000 to $10,000^\circ\text{C}$. This high-temperature region will move with the velocity of $\sim 1\ \text{m/s}$ along the fiber towards a source of laser radiation, causing catastrophic damage of the fiber. The damage is manifested by a row of bullet-shaped cavities left in the core of a single-mode fiber (Fig. 7.9). Although a large number of papers have been published since 1987 (see [55, 56] and references therein) one cannot say that the phenomenon is well understood.

At first this phenomenon was considered as a curiosity, but it is now of great importance for optical fiber communication. It is connected with the increase in optical power used in modern optical fiber communication systems. Various laser sources with the output power of $\sim 1\ \text{W}$ have been developed for pumping Er-doped and Raman fiber amplifiers used in the systems.

In the case of propagation of the laser light with this level of power along a fiber any accidents leading to a strong local heating of the fiber can initiate catastrophic

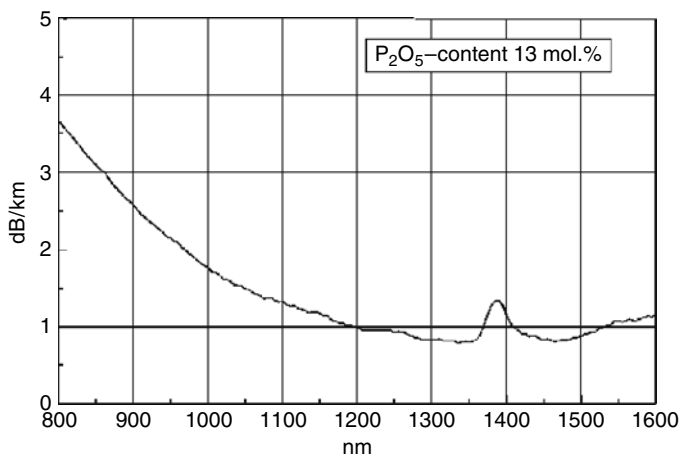


Fig. 7.8. Phosphosilicate fiber loss spectrum.

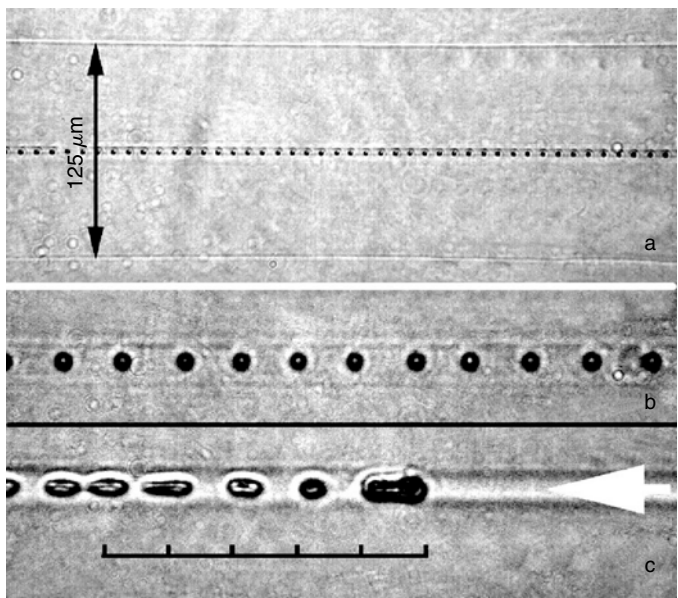


Fig. 7.9. Periodic structure of bubbles in the core of the single-mode fiber, formed under the action of the CW laser radiation of ~ 1 W power; (a) overview, demonstrates the periodicity of bubble formation. The arrow indicates the diameter of the fiber; (b) the same on an enlarged scale; (c) the endpoint of catastrophic damage propagation after the laser power is turned off. Each division of the scale is $10\ \mu\text{m}$ (the scale refers to (b); and (c) white arrow shows the direction of light propagation.

Table 7.1. Parameters of the Fibers

No.	Core Constituents	$\Delta n \times 10^2$	$\lambda_c, \mu\text{m}$	P_{th}, W
1	$\text{SiO}_2\text{--P}_2\text{O}_5$	1.4	1.1	0.85
2	$\text{SiO}_2\text{--GeO}_2$	2.6	1.12	0.45
3	Flexcor (Corning)	0.65	0.9	0.90
4	SMF28 (Corning)	0.41	1.3	1.05
5	$\text{SiO}_2\text{--GeO}_2$	1.0	1.34	0.60
6	$\text{SiO}_2\text{--GeO}_2$	0.15	0.9	1.40
7	$\text{SiO}_2\text{--GeO}_2$	0.15	1.15	1.55
8	$\text{SiO}_2\text{--GeO}_2(+\text{B in cladding})$	0.08	1.0	0.65
9	$\text{SiO}_2\text{--GeO}_2(+\text{F in cladding})$	3.0	0.9	0.35

damage. A sharp fiber bending, a contact of a fiber end with absorbing substances, dust within couplers, or an electrical discharge are the most typical accidents.

There is a threshold value of optical power P_{th} below which the fiber fusion cannot propagate along a fiber. This threshold power for a number of fibers, including germanosilicate and phosphosilicate Raman fibers, has been measured for several wavelengths in the region $1 \div 1.5 \mu\text{m}$ [57]. Table 7.1 shows the parameters of the fibers under investigation and values of the threshold power for the wavelength of $1.24 \mu\text{m}$. Figure 7.10 shows the dependence of the threshold mean light intensity in the core of the fiber I_{th} on the mode field diameter (MFD). The low dispersion of the

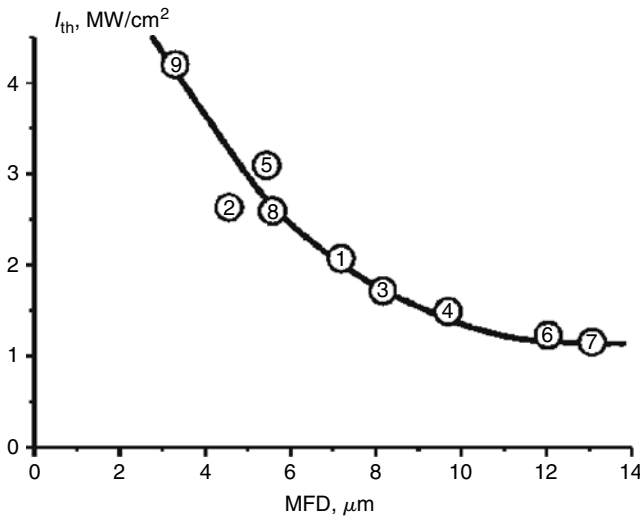


Fig. 7.10. The dependence of the fiber fuse threshold intensity on the mode-field diameter at the wavelength $1.24 \mu\text{m}$ for different fibers. The numbers of the datapoints correspond to the numbers of fibers in Table 7.1.

datapoints around the averaged line indicates that MFD is the principal parameter for the fiber fuse process.

7.4. GeO₂-Based Raman Fibers

GeO₂ glass is a very promising material for Raman fibers. It was already shown that the Raman cross-section of this glass is nine times that of silica, the Raman frequency shift being 420 cm^{-1} [11]. GeO₂-based glasses have been known for many years and various properties of these glasses have been well studied, including viscosity, regions of glass formation in binary germanate systems, the structure of germanate glasses, and melts (see, e.g., [58]). However, technological difficulties in fabricating low-loss GeO₂-based fibers didn't allow widespread applications of the fibers as an active medium for Raman fiber lasers and amplifiers.

It should be noted that in the early 1980s germania fibers were considered as a promising low-loss medium for optical communication and many papers were published devoted to the fabrication of low-loss GeO₂-based fibers, the measurements of main fiber characteristics, and the investigation of nonlinear optical phenomena, primarily, Raman scattering [59–76].

In 1979 Olshansky and Scherer [59] reported on several features of high GeO₂ glasses which make them attractive materials for low-loss, high-bandwidth optical fibers.

According to their estimations, the zero material dispersion wavelength of this glass occurs in the 1.7 to 1.8 μm region and the Rayleigh scattering losses are on the order of 0.15 dB/km at the zero dispersion wavelength. Because the edge of fundamental infrared absorption of GeO₂ glass is shifted to the long wavelengths compared to silica one can expect lower intrinsic losses of germania glass than are found with silica. So the next step should be an experimental confirmation of these estimations.

In 1980 using a high purity GeO₂ glass [60] the zero material dispersion wavelength λ_0 and the Rayleigh scattering losses were measured. It turned out that $\lambda_0 = 1.74$ and $1.733\text{ }\mu\text{m}$ for unannealed and annealed samples, respectively, and the Rayleigh scattering losses are 0.3 dB/km at $\lambda = 1.74\text{ }\mu\text{m}$. Then the absorption spectra of GeO₂ glass samples were measured in the UV and IR regions and the extrapolation of the absorption into the region of small absorption gave the minimum value of 0.1 dB/km at $\lambda \approx 2\text{ }\mu\text{m}$. Total optical losses were found as the sum of Rayleigh scattering and the tails of UV and IR absorption (Fig. 7.11) and amounted to 0.26 and 0.4 dB/km at the wavelengths of 2 and $1.74\text{ }\mu\text{m}$, respectively [61].

Great efforts were directed to the development of low-loss GeO₂-based glass fibers. Various techniques of fiber fabrication were used, including VAD [62–64, 66, 68, 69], MCVD [75], VAD/OVD [72], and rod-in-tube [76]. The following combinations of glasses for the core and the cladding were used: GeO₂ + Sb₂O₃/GeO₂, GeO₂ + Sb₂O₃/silicone resin, GeO₂/GeO₂ + F, and GeO₂/SiO₂. However, the lowest losses obtained amounted to 4 and 15 dB/km at wavelengths of 2 and $2.4\text{ }\mu\text{m}$, respectively [68, 69] and exceeded the estimated intrinsic losses more than 10 times.

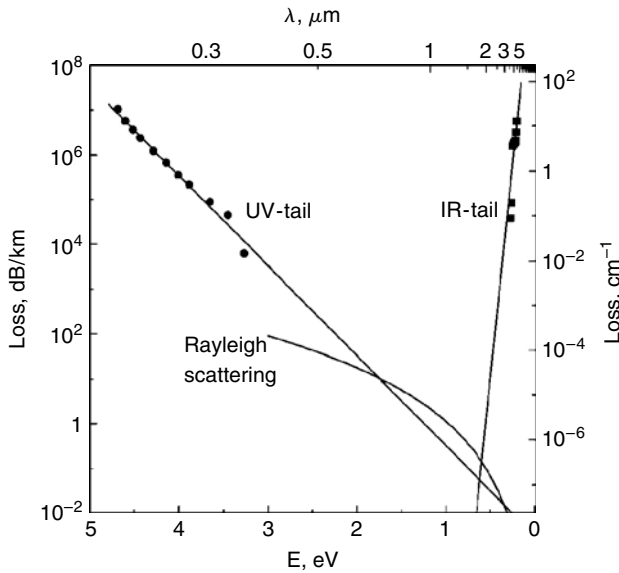


Fig. 7.11. Intrinsic optical losses in GeO_2 glass.

The first observation of single-pass Raman generation in a GeO_2 fiber was made using a multimode fiber with the core diameter of $93 \mu\text{m}$ and the fiber length of 28 m [65]. The authors observed up to six Raman Stokes lines at the pump power of 9 kW from a ML/QS YAG : Nd laser. The value of the critical power was nine times smaller than that for a SiO_2 fiber with the same fiber parameters. These results were consistent with the measurement of relative Raman scattering cross-section of GeO_2 glass [11].

The papers [70–72, 74–76] confirmed a high stimulated Raman scattering efficiency and excellent prospects for GeO_2 -based Raman fibers in various applications. Unfortunately in those early investigations the Raman gain coefficient of GeO_2 glass fibers wasn't measured. Recently the Raman gain coefficient of single-mode GeO_2 fiber ($\Delta n = 0.143$, $\lambda_c = 1.35 \mu\text{m}$) was measured and turned out to be $170(\text{dB}/(\text{km} \cdot \text{W}))$ at $1.3 \mu\text{m}$ [77].

7.5. Tellurite-Based Raman Fibers

Tellurite-based glasses have recently attracted considerable attention as an active material for lasers and optical amplifiers. The advantage of tellurite glasses as a laser material is connected with high-nonlinearity, low phonon energy, high transparency at visible and infrared wavelengths, and good mechanical characteristics.

Tellurite-based glasses have a remarkably high density and refractive index. For example, $d = 5.101 \text{ g/cm}^3$ and $n_d = 2.2$ for TeO_2 glass. The regions of glass formation of many binary tellurite glasses can be found in [78].

Although systematic investigations of tellurite glasses have been undertaken since 1952 [58], the first publication on tellurite-based glass optical fibers appeared in 1980 [79]. Fibers were fabricated with a conventional drawing apparatus at 400°C, using the tellurite-based glass systems: $\text{TeO}_2\text{--WO}_3\text{--Ta}_2\text{O}_5$, $\text{TeO}_2\text{--WO}_3\text{--Bi}_2\text{O}_3$, $\text{TeO}_2\text{--BaO--ZnO}$, and $\text{TeO}_2\text{--BaO--PBO}$. The samples of the glasses were prepared in gold crucibles. The lowest optical losses were 1 dB/m and 20 dB/m at 2 and 4 μm , respectively.

Recently several papers devoted to tellurite-based fiber Raman amplifiers have been published [80–83]. All the papers were published by one group of researchers and contained no information about the composition and fabrication of tellurite-based fibers. It was reported that the maximum gain coefficient of the tellurite-based fiber was 55 $1/\text{W} \cdot \text{km}$, which is more than 10 times that of silica-based fibers. It is known that the Raman gain spectrum of tellurite-based glasses consists of two bands, one at $\sim 400 \text{ cm}^{-1}$ and a stronger band in the spectral region 640 to 740 cm^{-1} [84]. The tellurite-based fiber had Δn of 2.2% and the minimum optical losses of 20.4 dB/km at 1560 nm [80]. Large Raman gain coefficient of the fiber and two-band structure of the gain spectrum make possible wideband gain operation using relatively short lengths of the fiber ($\sim 200 \text{ m}$) and a small number of pump wavelengths.

The 160 nm bandwidth with the gain of over 10 dB and noise figure below 10 dB in the spectral region of 1490 to 1650 nm was achieved using a tellurite-based fiber only 250 m in length and four pump wavelengths [80].

A hybrid tellurite/silica fiber Raman amplifier with seamless gain bandwidth of 135 nm with the minimum gain of 22.8 dB has been reported [83]. These results show a great potential for tellurite-based Raman fibers.

7.6. Conclusion

At present it is clear that Raman fiber lasers and amplifiers are very important devices for optical fiber communication systems (see, e.g., [85]).

Medium-power Raman fiber lasers, pumped by rare earth-doped double-clad fiber lasers, are an efficient light source for the spectral region of 1.2 to 1.75 μm . The main application of these lasers is pumping various fiber amplifiers and lasers. The region of Raman laser generation is limited by a growing intrinsic absorption of silica-based Raman fibers at $\lambda 1.7 \mu\text{m}$.

Using GeO_2 - and TeO_2 -based low-loss Raman fibers it is possible to widen this spectral region up to 4 to 6 μm . Taking into account the tendency in developing CW high-power (up to 1 kW) Yb-doped fiber lasers one can expect some new applications of high-power Raman fiber lasers, such as medical, material processing, and others.

Raman fiber amplifiers are the most universal type of optical amplifiers and they have brilliant prospects for application in future optical communication systems as lumped amplifiers. At present the main shortcoming of Raman amplifiers is their relatively low efficiency. But this could be eliminated by using the above-mentioned germanate or tellurite Raman fibers.

So the most topical research area concerning Raman fibers is the development of technology of low-loss GeO_2 - and TeO_2 -based fibers and also the search for promising new glass compositions. In addition, further improvement of the performance of high CeO_2 - and P_2O_5 -doped silica fibers is also of great importance.

Acknowledgments

I would like to express my sincere gratitude to Drs. M. M. Bubnov and I. A. Bufetov for fruitful discussions and valuable remarks, and to Mrs. S. S. Makarevich for helping me to prepare the manuscript.

References

- [1] C.V. Raman and K.S. Krishnan, A new type of secondary radiation, *Nature*, 121:501–502, 1928.
- [2] G.S. Landsberg and L.I. Mandelstam, Eine neue Erscheinungen bei der Lichtzerstreuung in Kristallen, *Naturwissenschaften*, 16:557, 1928.
- [3] N. Blombergen, The stimulated Raman effect, *Amer. J. Phys.*, 35:989–1023, 1967.
- [4] E.M. Dianov, P.V. Mamyshev, A.M. Prokhorov, and V.N. Serkin, Nonlinear effects in optical fibers. In *Laser Science and Technology-International Handbook*, vol. 6, Harwood Academic Publishers GmbH, Chur, Switzerland, 1989.
- [5] R.H. Stolen, E.P. Ippen, and A.R. Tynes, Raman oscillation in glass optical waveguide, *Appl. Phys. Lett.*, 20:62–63, 1972.
- [6] M.Hass, Raman spectra of vitreous silica, germania and sodium silicate glasses, *J. Phys. Chem. Solids*, 31:415–422, 1970.
- [7] E.P. Ippen, Low-loss quasi-CW Raman oscillator, *Appl. Phys. Lett.*, 16:303–305, 1970.
- [8] R.H. Stolen, E.P. Ippen, and A.R. Tynes, Raman gain in glass optical waveguides, *Appl. Phys. Lett.*, 22:276–278, 1973.
- [9] G.E. Walrafen, and J. Stone, “Raman spectral characterization of pure and doped fused silica optical fibers,” *Appl. Spectro.* 29:337–338, 1975.
- [10] V.V. Grigoryants, B.L. Davydov, M.E. Zhabotinski, V.F. Zolin, G.A. Ivanov, V.I. Smirnov, and Y.K. Chamorovski, Spectra of stimulation Raman scattering in silica fiber waveguides, *Optic. Quantum Electron*, 9:351–352, 1977.
- [11] F.L. Galeener, J.C. Mikkelsen, and R.H. Geils, The relative Raman cross-section of vitreous SiO_2 , GeO_2 , B_2O_3 and P_2O_5 , *Appl. Phys. Lett.*, 32:34–36, 1978.
- [12] N. Shibata, M. Horigudhi, and T. Edahiro, Raman spectra of binary high silica glasses and fibers containing GeO_2 , P_2O_5 and B_2O_3 , *J. Non-Cryst. Solids*, 45:115–126, 1981.
- [13] A.R. Chraplyvy, J. Stone, and C.A. Barrus, Optical gain exceeding 35 dB at $1.56\ \mu\text{m}$ due to stimulated Raman scattering by molecular D_2 in a solid silica optical fiber, *Opt. Lett.*, 8:415–417, 1983.
- [14] K. Nassau, D.L. Chadwick, and A.E. Miller, Arsenic-containing heavy-metal oxide glasses, *J. Non-Cryst. Solids*, 93:115–124, 1987.
- [15] A.E. Miller, K. Nassau, K.B. Lyons, and M.E. Lines, The intensity of Raman scattering in heavy-metal oxides, *J. Non-Cryst. Solids*, 99:289–307, 1988.

- [16] S.T. Davey, D.L. Williams, B.J. Ainslie, W.J.M. Rothwell, and B. Wakefield, Optical gain spectrum of GeO₂-SiO₂ Raman fiber amplifiers, *IEE Proc. Pt.J.*, 136:301–306, 1989.
- [17] K. Suzuki, K. Noguchi, and N. Uesugi, Selective stimulated Raman scattering in highly P₂O₅-doped silica single-mode fibers, *Opt. Lett.*, 11:656–658, 1986.
- [18] *Annual Report of General Physics Institute of the Russian Academy of Sciences for 1993*, section: Optical fiber communication, integrated optics, January, 7, 1994; E.M. Dianov, D.G. Fursa, A.A. Abramov, M.I. Belovolov, M.M. Bubnov, A.V. Shipulin, A.M. Prokhorov, G.G. Devyatykh, A.N. Guryanov, and V.F. Khopin, Low-loss high germania-doped fiber: A promising gain medium for 1.3 μ m Raman amplifier. In *Proceedings of the Twentieth European Conference on Optical Communications*, vol. 1, 427–430, 1994.
- [19] S. Grubb, T. Erdogan, V. Mizrahi, T. Strasser, W.Y. Cheung, W.A. Reed, P.J. Lemaire, A.E. Miller, S.G. Kosinski, G. Nikolak, and P.C. Becker, 1.3 μ m cascaded Raman amplifier in germanosilicate fibers, *Proc. Top. Meet. Opt. Ampl. Appl.*, (Breckenridge), PD3-1, 187–190, 1994.
- [20] E.M. Dianov, Raman fiber amplifiers, *Proc. SPIE*, 4083:90–100, 2000.
- [21] E.M. Dianov, M.V. Grekov, I.A. Bufetov, V.M. Mashinsky, O.D. Sazhin, A.M. Prokhorov, G.G. Devyatykh, A.N. Guryanov, and V.F. Khopin, Highly efficient 1.3 μ m Raman fiber amplifier, *Electron. Lett.*, 34:669–670, 1998.
- [22] S.G. Grubb, T. Strasser, W.Y. Cheung, W.A. Reed, V. Mizrahi, T. Erdogan, P.J. Lemaire, A.M. Vengsarkar, D.J. DiGiovanni, D.W. Peckman, and B.H. Rockney, High-power 1.48 μ m cascaded Raman laser in germanosilicate fibers, *Proc. Top. Meet. Opt. Ampl. Appl.*, (Davos), SaA4, 197–199, 1995.
- [23] E.M. Dianov, M.V. Grekov, I.A. Bufetov, S.A. Vasiliev, O.I. Medvedkov, V.G. Plotnichenko, V.V. Koltashev, A.V. Belov, M.M. Bubnov, S.L. Semjonov, and A.M. Prokhorov, CW high power 1.24 μ m and 1.48 μ m Raman lasers based on low-loss phosphosilicate fibers, *Electron. Lett.*, 33:1542–1544, 1997.
- [24] E.M. Dianov, I.A. Bufetov, M.M. Bubnov, A.V. Shubin, S.A. Vasiliev, O.I. Medvedkov, S.L. Semjonov, M.V. Grekov, V.M. Paramonov, A.N. Guryanov, V.F. Khopin, D. Varelas, A. Iocco, D. Costantini, H.G. Limberger, and R.P. Salathe, CW highly efficient 1.24 μ m Raman laser based on low-loss phosphosilicate fiber. In *Optical Fiber Communications Conference, Technical Digest*, PD-25, San Jose, 1999; V.I. Karpov, E.M. Dianov, V.M. Paramonov, O.I. Medvedkov, M.M. Bubnov, S.L. Semjonov, S.A. Vasiliev, V.N. Protopopov, O.N. Egorova, V.F. Khopin, A.N. Guryanov, M.P. Bachinski, and W.R.L. Clements, Laser-diode pumped phosphosilicate-fiber Raman laser with output power of 1 W at 1.48 μ m, *Opt. Lett.*, 24:887–889, 1999.
- [25] E.M. Dianov, and A.M. Prokhorov, Medium-power CW Raman fiber lasers, *IEEE J. Selected Topics Quantum Electron.*, 6:1022–1028, 2000.
- [26] Ch. Fludger, A. Maroney, N. Jolley, and R. Mears, An analysis of the improvement in OSNR from distributed Raman amplifiers using modern transmission fibers, In *Optical Fiber Communications Conference, Technical Digest* (Baltimore), 100–102, 2000.
- [27] L.E. Nelson, Optical fiber properties for long-haul transmission. In *Proceedings of the 27th European Conference on Optical Communications*, (Amsterdam), 346–349, 2001.
- [28] F. Koch, S.A.E. Lewis, S.V. Chernikov, and J.R. Taylor, Broadband Raman gain characterization in various optical fibers, *Electron. Lett.*, 37:1437–1439, 2001.
- [29] V.L. da Silva, and J.R. Simpson, Comparison of Raman efficiencies in optical fibers, *Optical Fiber Communications Conference. Technical Digest* (San Jose), WK13, 1994.
- [30] D. Mahgerefteh, D.L. Butler, J. Goldhar, B. Rosenberg, and G.L. Burdge, Technique for measurement of the Raman gain coefficient in optical fibers, *Opt. Lett.*, 21:2026–2028, 1996.

- [31] Y. Akasaka, I. Morita, M.-C. Ho, M.E. Marhic, and L.G. Kazjvsky, Characteristics of optical fibers for discrete Raman amplifiers. In *Proceedings of the 25th European Conference on Optical Communication*, vol. I, 288–289, 1999.
- [32] I.A. Bufetov, M.M. Bubnov, V.B. Neustruev, V.M. Mashinsky, A.V. Shubin, M.V. Grekov, A.N. Guryanov, V.F. Khopin, E.M. Dianov, and A.M. Prokhorov, Raman gain properties of optical fibers with a high Ge-doped silica core and standard optical fibers, *Laser Phys.*, 11:130–133, 2001.
- [33] J. Bromage, K. Rottwitt, and M.E. Lines, A method to predict the Raman gain spectra of germanosilicate fibers with arbitrary index profiles, *IEEE Photon. Technol. Lett.*, 14:24–26, 2002.
- [34] I. Flammer, C. Martinelli, and Ph. Guenot, Raman gain prediction in germano-silicate single mode fibers, *Proc. Top. Meet. Opt. Ampl. Appl.* (Vancouver), OMC2, 2002.
- [35] K.J. Cordina, and C.R.S. Fludger, Changes in Raman gain coefficient with pump wavelength in modern transmission fibers, *Proc. Top. Meet. Opt. Ampl. Appl.* (Vancouver), OMC3, 2002.
- [36] E.M. Dianov, I.A. Bufetov, M.M. Bubnov, M.V. Grekov, S.A. Vasiliev, N.S. O.I. Medvedkov, Three-cascaded 1407-nm Raman laser based on phosphorous-doped silica fiber, *Opt. Lett.*, 25:402–404, 2000.
- [37] P.St.J. Russel, J.-L. Archabault, and L. Reekie, Fiber gratings, *Phys. World*, 41–46, (Oct.), 1993.
- [38] B. Malo, J. Albert, F. Bilodeau, D.C. Johnson, and K.O. Hill, Photosensitivity in phosphorus-doped silica glass and optical waveguides, *Appl. Phys. Lett.*, 65:394–396, 1994.
- [39] T. Kitagawa, K.O. Hill, D.C. Johnson, B. Malo, J. Albert, S. Theriault, and F. Bilodeau, Photosensitivity in P_2O_5 - SiO_2 waveguides and its application to Bragg reflectors in single frequency Er^{3+} doped planar waveguide laser, *Optical Fiber Communications Conference, Technical Digest*, San Jose, PD-17, 79–81, San Jose, 1994.
- [40] A.A. Rybaltovskiy, Y.V. Larionov, S.L. Semjonov, V.G. Plotnichenko, E.B. Kryukova, Y.N. Pyrkov, M.M. Bubnov, and E.M. Dianov, Relation between UV-induced refractive index and absorption in phosphosilicate optical fibers. In *Proceedings of Bragg Gratings, Photosensitivity and Poling in Glass Waveguides Topical Meeting*, (Stresa) BThA3, 2001.
- [41] S.T. Davey, D.L. Williams, D.M. Spirit, and B.J. Ainslie, The fabrication of low-loss high NA silica fibers for Raman amplification, *Proc. SPIE*, 1171:181–191, 1989.
- [42] S. Sudo and H. Itoh, Efficient non-linear optical fibers and their applications, *Opt. Quantum Electron.*, 22:187–212, 1990.
- [43] M. Onishi, C. Fukuda, H. Kanamori, and M. Nishimura, High NA double-clad dispersion compensating fiber for WDM systems. In *Proceedings of the Twentieth European Conference on Optical Communications*, 681–684, 1994.
- [44] A.A. Abramov, M.M. Bubnov, E.M. Dianov, S.L. Semjonov, A.G. Shchebunjaev, A.N. Guryanov, and V.F. Khopin, The effect of fluorine co-doping on scattering and absorption properties of highly germanium-doped silica glass. In *Proceedings of the Seventeenth International Congress on Glass*, vol.7, 70–75, 1995.
- [45] E.M. Dianov, V.M. Mashinsky, V.B. Neustruev, O.D. Sazhin, A.N. Guryanov, V.F. Khopin, N.N. Vechkanov, and S.V. Lavrishchev, Origin of excess loss in single-mode optical fibers with high GeO_2 -doped silica core, *Opt. Fiber Technology*, 3:77–86, 1997.
- [46] M. Onishi, T. Okuno, T. Kashiwada, S. Ishikawa, N. Akasaka, and M. Nishimura, Highly nonlinear dispersion shifted fiber and its application to broadband wavelength converter. In *Proceedings of the 23rd European Conference on Optical Communication*, 115–118, 1997.

- [47] M. Onishi, T. Kashiwada, Y. Ishiguro, Y. Koyano, M. Nishimura, and H. Kanamori, High-performance dispersion-compensating fibers, *Fiber Integrated Optics*, 16:277–285, 1997.
- [48] M.M. Bubnov, E.M. Dianov, O.N. Egorova, S.L. Semjonov, A.N. Guryanov, L.A. Ketkova, and V.F. Khopin, Influence of fluorine codoping on optical losses in Ge- and P-doped fibers, *Proc. SPIE*, 4216:164–173, 2001.
- [49] M.M. Bubnov et al., Unpublished results.
- [50] K. Suzuki and M. Nakazawa, Raman amplification in P₂O₅-doped optical fiber, *Opt. Lett.*, 13:666–668, 1988.
- [51] M.M. Bubnov, E.M. Dianov, O.N. Egorova, S.L. Semjonov, A.N. Guryanov, V.F. Khopin, and E.M. DeLiso, Fabrication and investigation of highly phosphorus-doped fibers for Raman lasers, *Proc. SPIE*, 4083:12–22, 2000.
- [52] O.N. Egorova, M.M. Bubnov, I.A. Bufetov, E.M. Dianov, A.N. Guryanov, V.F. Khopin, S.L. Semjonov, and A.V. Shubin, Phosphosilicate-core single-mode fibers intended for use as active medium of Raman lasers and amplifiers, *Proc. SPIE*, 4216:32–39, 2001.
- [53] E.M. Dianov, I.A. Bufetov, M.M. Bubnov, M.V. Grekov, S.A. Vasiliev, O.I. Medvedkov, A.V. Shubin, A.N. Guryanov, V.F. Khopin, M.V. Yashkov, E.M. DeLiso, and D.L. Butler, 1.3 μ m Raman fiber amplifier, *Proc. SPIE*, 4083:101–110, 2000.
- [54] R. Kashyap and K.J. Blow, Observation of catastrophic self-propelled self-focusing in optical fibers, *Electron. Lett.*, 24:47–48, 1988.
- [55] R. Kashyap, A. Sayles, and G.F. Cornwell, Heat flow modeling and visualization of catastrophic self-propagating damage in single-mode optical fibers at low powers, *Proc. SPIE*, 2966:586–591, 1997.
- [56] D.D. Davis, S.C. Mettler, and D.J. DGiovanni, A comparative evaluation of fiber fuse models, *Proc. SPIE*, 2966:592–606, 1997.
- [57] E.M. Dianov, I.A. Bufetov, V.G. Plotnichenko, A.A. Frolov, V.M. Mashinsky, G.E. Snopatin and M.F. Churbanov, Catastrophic destruction of optical fibers of various composition under the laser radiation, *Quantum Electron.*, 32:476–478, 2002.
- [58] H. Rawson, Inorganic glass forming systems, London and New York: Academic, 1967.
- [59] R. Olshansky and G.W. Scherer, High GeO₂ optical waveguides. In *Proceedings of the Fifth European Conference on Optical Communication*, (Amsterdam) 12.5.1–12.5.3, 1979.
- [60] G.G. Devyatykh, E.M. Dianov, N.S. Karpychev, S.M. Mazavin, V.M. Mashinsky, V.B. Neustruev, A.V. Nikolaichik, A.M. Prokhorov, A.I. Ritus, N.I. Sokolov, and A.S. Yushin, Material dispersion and Rayleigh scattering in glassy germanium dioxide, a substance with promising applications in low-loss optical fibre waveguides, *Kvantovaya elektronika*, 7:1563–1566, 1980 (in Russian); *Sov. J. Quant. Electron.*, 10:900–902, 1981 (translation).
- [61] E.M. Dianov, V.M. Mashinsky, and V.B. Neustruev, Estimation of the intrinsic optical losses of germanium-oxide glass, *Kratkie soobsheniya po fizike* (Brief reports on physics), N 3:46–49, 1981 (Lebedev Physics Institute, USSR Academy of Sciences, Moscow).
- [62] K. Sanada, T. Moriyama, T. Shioda, O. Fukuda, K. Inada, K. Chida, Behavior of GeO₂ in dehydration process of VAD method. In *Proceedings of the Seventh European Conference on Optical Communication*, 2.1.1–2.1.4, 1981.
- [63] H. Takahashi, I. Sugimoto, T. Sato, and S. Yoshida, GeO₂–Sb₂O₃ glass optical fibers for 2–3 μ m fabricated by VAD method, In *Proc. SPIE*, 320, Advances in Infrared fibers, II, 88–92, 1982.
- [64] H. Takahashi, I. Sugimoto, and T. Sato, Germanium-oxide glass optical fibre prepared by VAD method, *Electron. Lett.*, 18:398–399, 1982.
- [65] Y. Fujii, H. Takahashi, H. Nakamura, T. Takabayashi, and I. Sugimoto, Efficient single-pass Raman generation in a GeO₂ optical fiber. In *Optical Fiber Communications Conference, Technical Digest*, W12, 92–93, 1983.

- [66] H. Takahashi and I. Sugimoto, Decreased losses in germanium-oxide glass optical fiber prepared by VAD method, *Japan J. Appl. Phys.*, 22:L139–L140, 1983.
- [67] H. Takahashi and I. Sugimoto, Silicone-resin-clad germanium-oxide glass optical fiber, *Japan J. Appl. Phys.*, 22:L313–L314, 1983.
- [68] H. Takahashi, I. Sugimoto, and S. Yoshida, Low-loss germanium-oxide glass optical fiber. In Proceedings of the ninth European Conference on Optical Communication, 61–64, 1983.
- [69] H. Takahashi and I. Sugimoto, A germanium-oxide glass optical fiber prepared by VAD method, *J. Lightwave Technol.*, LT-2:613–616, 1984.
- [70] J. Chang, H. Takahashi, I. Sugimoto, and A. Oyobe, Measurement of chromatic dispersion with a GeO_2 fiber Raman laser. In *Optical Fiber Communication Conference, Technical Digest*, TuD3, 34–35, 1985.
- [71] H. Takahashi, J. Chang, H. Nakamura, I. Sugimoto, T. Takabayashi, and A. Oyobe, Efficient single-pass Raman generation in a GeO_2 optical fiber and its application to measurement of chromatic dispersion, *Opt. Lett.*, 11:383–385, 1986.
- [72] H. Nakamura, S. Shibuya, I. Sugimoto, H. Takahashi, and Y. Mitsuhashi, Fiber Raman laser emission in a pure GeO_2 glass fiber. In Proceedings of the Twelfth European Conference on Optical Communication, 11–14, 1986.
- [73] T. Hosaka, S. Sudo, and K. Okamoto, Dispersion of pure GeO_2 glass core and F-doped GeO_2 glass cladding single-mode optical fibre, *Electron. Lett.*, 23:24–26, 1987.
- [74] A.S. Davison and I.H. White, Highly efficient linearly polarized Raman generation in a germania-core optical fiber, *Electron. Lett.*, 23:1343–1345, 1987.
- [75] A.-M. Peder-Gothi and M. Leppihalme, GeO_2 -core/ SiO_2 -cladding optical fiber made by MCVD process for stimulated Raman applications, *Appl. Phys.*, B42:45–49, 1987.
- [76] T. Hosaka, S. Sudo, H. Itoh, and K. Okamoto, Single-mode fibers with extremely high- Δ and small-dimension pure GeO_2 core for efficient nonlinear optical applications, *Electron. Lett.*, 24:770–771, 1988.
- [77] I.A. Bufetov et al. Unpublished results.
- [78] W. Vogel, H. Bürger, B. Müller, G. Zerge, W. Müller, and K. Forkel, Untersuchungen an Telluritgläsern, *Silikattechnik*, 25:205–209, 1974.
- [79] J.Y. Boniort, C. Brehm, P.H. Dupont, D. Guignot, and C. LeSergent, Infrared glass optical fibers for 4 and 10 micron bands. In Proceedings of the Sixth European Conference on Optical Communication, 61–64, 1980.
- [80] A. Mori, H. Masuda, K. Shikano, K. Oikawa, K. Kato, and M. Shimizu, Ultra-wideband tellurite-based Raman fiber amplifier, *Electron. Lett.*, 37:1442–1443, 2001.
- [81] H. Masuda, A. Mori, K. Shikano, K. Oikawa, K. Kato, and M. Shimizu, Ultra-wide-band hybrid tellurite/silica fiber Raman amplifier. In *Optical Fiber Communication Conference, Technical Digest*, 388–390, 2002.
- [82] H. Masuda, A. Mori, S. Aozasa, and M. Shimizu, TDFA and ultra-wide band amplifiers, *Proc. Top Meet. Opt. Ampl. Appl.*, Vancouver, OTuC1, 2002.
- [83] H. Masuda, A. Mori, K. Shikano, K. Oikawa, K. Kato, and M. Shimizu, Ultra-wide-band Raman amplifier using tellurite and silica fibers, *Electron. Lett.*, 38:867–868, 2002.
- [84] H. Bürger, K. Kneipp, H. Hobert, W. Vogel, V. Kozhukharov, and S. Neov, Glass formation, properties and structure of glasses in the TeO_2 -ZnO system, *J. Non.-Cryst. Solids*, 151:134–142, 1992.
- [85] *Optical Fiber Communication Conference, Technical Digest*, 2002.

Chapter 8

Noise due to Fast-Gain Dynamics

C.R.S. Fludger

8.1. Introduction

The time response of the Raman effect is associated with the vibrations of the molecules in the gain medium and is on the order of several hundred femoseconds [1]. Compared to current data rates, this energy transfer is practically instantaneous resulting in very fast-gain dynamics. Fast-gain dynamics in semiconductor amplifiers results in a large amount of crosstalk between signal channels, even at high frequencies, and poor system performance. However, the Raman effect in optical fibers is quite weak such that the gain cavity needs to be several kilometers long.

In a copumped Raman amplifier, the gain dynamics are averaged due to chromatic dispersion between pump and signal wavelengths. This lessens the impact of the fast physical process and results in improved system performance than would otherwise be expected. In a counter-pumped Raman amplifier, the different propagation directions of pump and signals averages the gain over the cavity length. This much stronger averaging greatly reduces system penalties in counter-pumped amplifiers.

Models developed here quantify both the transfer of relative intensity noise (RIN) from the pump to the signal, and also the signal-to-signal crosstalk, mediated by the pump (crossgain modulation), in co- and counter-pumped Raman amplifiers. Measurements show good agreement with theory for different fibers with various dispersion characteristics and lengths.

As well as determining the actual energy transfer from pumps to signals, and from crossgain modulation, the system impact in terms of Q penalty has also been determined. counter-pumped Raman amplifiers show a good immunity to intensity noise transfer from the pump lasers, and no significant penalty from XGM. Copumped Raman amplifiers show high system impacts if the dispersion zero of the fiber lies between the pump and signal wavelengths, resulting in zero net dispersion and little noise averaging.

8.2. Transfer of Relative Intensity Noise from Pump to Signals

The development of high-power fiber lasers and semiconductor lasers has led to increased interest in using Raman amplification for commercial systems. Fiber lasers, in particular, exhibit large amounts of intensity noise so that counter-pumping has often been used to average this noise over the length of the amplifier [2]. In the first part of this section, the worst-possible case of relative intensity noise transfer is analyzed, where pump and signal copropagate without dispersion. The analysis is then extended to separately consider the cases of propagation of the pump and signal in the presence of dispersion and counterpropagation. The final part of this section draws conclusions based on realistic system scenarios.

The effect of RIN is considered for a strong pump beam traveling in a single-mode optical fiber, either with or against the direction of a coexisting weak signal beam of a different optical wavelength. The fiber is assumed to exhibit wavelength-dependent attenuation and dispersion, but any optical nonlinearity other than Raman scattering is ignored. The signal beam is also assumed to be initially free from RIN, and pump depletion effects are neglected. Numerical techniques can be used to analyze the effect of pump depletion [3]. This has shown a small reduction in the RIN transfer Q -penalty tolerance by 3 to 4 dB/Hz.

Measurement results are then presented on three fiber types selected for their different loss and dispersion in order to confirm the analysis. Finally, predictions are made of the system impairment caused by RIN transfer from the Raman pump.

8.2.1. Maximum RIN Transfer

The maximum amount of relative intensity noise transferred from the Raman pump to the signal channels can be examined by applying a small amount of intensity modulation to the pump power:

$$P_p(\phi) = P_{p0}(1 + m \cos \phi), \quad (8.1)$$

where P_{p0} is the mean launched pump power, m is the modulation index, and ϕ is a phase variable. Assuming there are no averaging effects between the signal and pump, the gain can be calculated from the undepleted pump approximation:

$$G = \exp(-\alpha_s L + C_R L_{eff} P_{p0}(1 + m \cos \phi)), \quad (8.2)$$

where α_s is the attenuation at the signal wavelength, L is the length of the fiber, C_R is the Raman gain efficiency coefficient, and L_{eff} is the effective length.

The instantaneous gain can be expressed in terms of the mean gain $\langle G \rangle$, and may be approximated if the modulation or RIN is assumed to be small:

$$\begin{aligned} G &= \exp(-\alpha_s L + C_R L_{eff} P_{p0}(1 + m \cos \phi)) \\ &= \langle G \rangle \exp(C_R L_{eff} P_{p0} m \cos \phi) \\ &\approx \langle G \rangle (1 + C_R L_{eff} P_{p0} m \cos \phi). \end{aligned} \quad (8.3)$$

The modulation of the pump, mP_{p0} , can be expressed in terms of the mean square fluctuations $\langle \delta P_p^2 \rangle$ and the Raman gain efficiency may be expressed in terms of the amount of Raman gain added to the fiber (G_R in linear units):

$$mP_{p0} = \sqrt{2} \sqrt{\langle \delta P_p^2 \rangle} \quad (8.4)$$

$$\ln(G_R) = C_R P_{p0} L_{eff}. \quad (8.5)$$

The gain expression may be rewritten by substituting Eqs. (8.4) and (8.5) into Eq. (8.3):

$$G = \langle G \rangle \left(1 + \ln(G_R) \sqrt{2} \frac{\sqrt{\langle \delta P_p^2 \rangle}}{P_{p0}} \cos \phi \right). \quad (8.6)$$

If the d.c. gain is ignored, the instantaneous noise on the signal is:

$$\frac{\delta G}{\langle G \rangle} = \ln(G_R) \sqrt{2} \frac{\sqrt{\langle \delta P_p^2 \rangle}}{P_{p0}} \cos \phi. \quad (8.7)$$

The relative intensity noise on the signal r_s is equal to the ratio of the mean square fluctuations in optical power $\langle \delta P_s^2 \rangle$ to the square of the mean optical power $\langle P_s \rangle$. This may be found by integrating the mean square fluctuations of the gain for all phases ϕ :

$$\begin{aligned} r_s &= \frac{\langle \delta P_s^2 \rangle}{\langle P_s \rangle^2} = \frac{1}{2\pi} \int_0^{2\pi} \left(\frac{\delta G}{\langle G \rangle} \right)^2 d\phi \\ &= \frac{\langle \delta P_p^2 \rangle}{P_{p0}^2} \ln(G_R) = r_p \ln(G_R), \end{aligned} \quad (8.8)$$

where r_p is the RIN on the pump laser in linear units:

$$r_p = \frac{\langle \delta P_p^2 \rangle}{P_{p0}^2} \quad (8.9)$$

In decibels, the RIN of the signal R_s can be expressed as the sum of the RIN on the pump R_p and a gain dependent term:

$$R_s = R_p + 20 \log(\ln(G_R)). \quad (8.10)$$

Therefore, in the worst case, the RIN on the signal after the Raman amplifier can be greater than the RIN on the pump.

8.2.2. Copumped Raman Amplifier with Dispersion in the Fiber

In a copumped Raman amplifier, the pump and signal will propagate at slightly different velocities and therefore will “walk-off.” The walk-off is a function of the

dispersion of the fiber, and will average the transfer of the noise from the Raman pump to the signal.

If a small amount of modulation at frequency f is applied to the pump, and assuming the undepleted pump approximation, the pump power at time t and distance z along the fiber is:

$$\begin{aligned} P_p(z, t) &= P_{p0} e^{-\alpha_p z} (1 + m \sin[(2\pi f t - k_p z) + \phi]) \\ &= P_{p0} e^{-\alpha_p z} \left[1 + m \sin \left(2\pi f \left(t - \frac{z}{V_p} \right) + \phi \right) \right], \end{aligned} \quad (8.11)$$

where α_p is the attenuation at the pump wavelength, k_p is the propagation constant, V_p is the group velocity at the pump wavelength, m is the modulation index, and ϕ is the phase of the modulation. If we take a frame of reference, moving at the signal velocity V_s , then $z = V_s t$ and the pump power becomes only a function of time.

$$P_p(t) = P_{p0} e^{-\alpha_p V_s t} \left[1 + m \sin \left(2\pi f t \left(1 - \frac{V_s}{V_p} \right) + \phi \right) \right]. \quad (8.12)$$

The effect of dispersion on the pump modulation seen by the signal is shown in Fig. 8.1. The vertical axis shows the modulation amplitude relative to the mean pump power at the pump input. An increase in dispersion will cause the signal to experience more oscillations in gain in a given length of fiber, within an amplitude envelope governed by the fiber's attenuation.

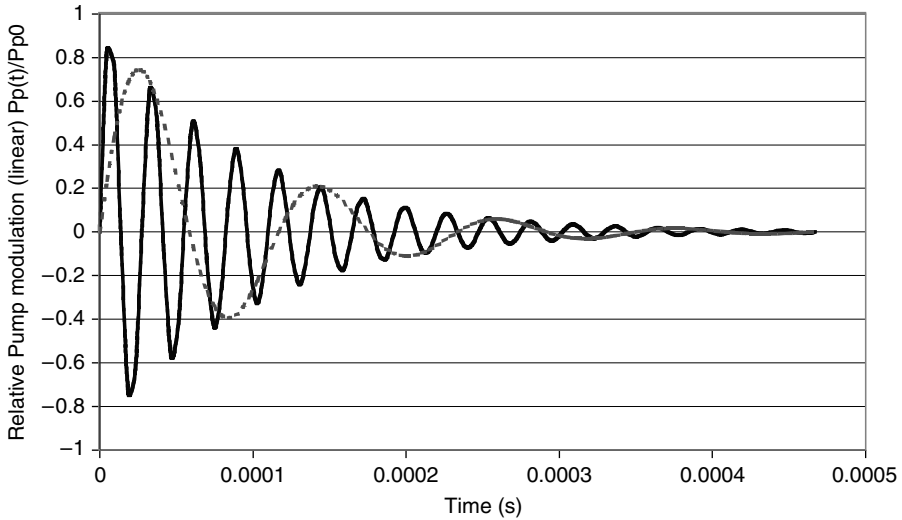


Fig. 8.1. Variation of the pump as seen by the signal in a copumped Raman amplifier. Pump modulation of 100 MHz. Fiber length = 100 km, dispersion = $17 \text{ ps.nm}^{-1}\text{km}^{-1}$ (solid line) and $4 \text{ ps.nm}^{-1}\text{km}^{-1}$ (dotted line), $m = 1$, pump attenuation = 0.22 dB/km, pump at 1455 nm, and signal at 1550 nm.

The propagation of the signal can be determined from a time-dependent differential equation:

$$\begin{aligned} \frac{1}{V_s} \frac{dP_s}{dt} &= -\alpha_s P_s(t) + C_R P_s(t) P_p(t) \\ &= -\alpha_s P_s(t) + C_R P_s(t) P_{p0} e^{-\alpha_p V_s t} \left[1 + m \sin \left(2\pi f t \left(1 - \frac{V_s}{V_p} \right) + \phi \right) \right], \end{aligned} \quad (8.13)$$

where P_s is the signal power and other symbols are defined earlier. For simplicity, a constant b is defined in terms of the difference in group velocity between the pump and signal. This can also be written using the chromatic dispersion D and the wavelength difference $\Delta\lambda$,

$$b = 2\pi \left(1 - \frac{V_s}{V_p} \right) = 2\pi D \Delta\lambda V_s \quad (8.14)$$

Integrating both sides of Eq. (8.13) across the transit time of the fiber (T):

$$\begin{aligned} \int_{P_s(0)}^{P_s(T)} \frac{1}{P_s} dP_s &= \int_0^T -\alpha_s V_s + C_R V_s P_{p0} e^{-\alpha_p V_s t} [1 + m \sin(bft + \phi)] dt \\ &= -\alpha_s V_s T + C_R P_{p0} \frac{(1 - e^{-\alpha_p V_s T})}{\alpha_p} \\ &\quad + C_R V_s m P_{p0} \int_0^T e^{-\alpha_p V_s t} \sin(bft + \phi) dt. \end{aligned} \quad (8.15)$$

The instantaneous gain G can therefore be found and expressed in terms of the mean gain $\langle G \rangle$:

$$\begin{aligned} G &= \exp \left[-\alpha_s V_s T + C_R P_{p0} \frac{(1 - e^{-\alpha_p V_s T})}{\alpha_p} + C_R V_s m P_{p0} \int_0^T e^{-\alpha_p V_s t} \sin(bft + \phi) dt \right] \\ &= \langle G \rangle \exp \left[C_R V_s m P_{p0} \int_0^T e^{-\alpha_p V_s t} \sin(bft + \phi) dt \right]. \end{aligned} \quad (8.16)$$

This can be approximated for small amounts of modulation:

$$G = \langle G \rangle \left[1 + C_R V_s m P_{p0} \int_0^T e^{-\alpha_p V_s t} \sin(bft + \phi) dt \right]. \quad (8.17)$$

The instantaneous fluctuation of the gain, dG , is:

$$\begin{aligned} dG &= \langle G \rangle C_R V_s m P_{p0} \int_0^T e^{-\alpha_p V_s t} \sin(bft + \phi) dt \\ &= \langle G \rangle C_R m P_{p0} \frac{V_s}{(\alpha_p V_s)^2 + (bf)^2} \\ &\quad \times \left[\begin{aligned} &bf \cos(\phi) + \alpha_p V_s \sin(\phi) \\ &-e^{-\alpha_p V_s T} (\alpha_p V_s \sin(bfT + \phi) + bf \cos(bfT + \phi)) \end{aligned} \right]. \end{aligned} \quad (8.18)$$

The modulation of the pump mP_{p0} can be expressed in terms of the mean square fluctuations $\langle \delta P_p^2 \rangle$, and the Raman gain efficiency may be written in terms of the amount of Raman gain added to the fiber (G_R in linear units):

$$\frac{dG}{\langle G \rangle} = \frac{\sqrt{\langle \delta P_p^2 \rangle}}{P_{p0}} \ln(G_R) \frac{V_s/L_{eff}\sqrt{2}}{(\alpha_p V_s)^2 + (bf)^2} \times \left[\begin{aligned} &bf \cos(\phi) + \alpha_p V_s \sin(\phi) \\ &-e^{-\alpha_p V_s T} (\alpha_p V_s \sin(bfT + \phi) + bf \cos(bfT + \phi)) \end{aligned} \right]. \quad (8.19)$$

The relative intensity noise on the signal r_s can once again be found by integrating the mean square fluctuations of the gain for all phases ϕ :

$$\begin{aligned} r_s &= \frac{\langle \delta P_s^2 \rangle}{\langle P_s \rangle^2} = \frac{1}{2\pi} \int_0^{2\pi} \left(\frac{dG}{\langle G \rangle} \right)^2 d\phi \\ &= r_p \ln(G_R)^2 \left(\frac{(V_s/L_{eff})^2}{(\alpha_p V_s)^2 + (bf)^2} \right) (1 - 2e^{-\alpha_p V_s T} \cos(bfT) + e^{-2\alpha_p V_s T}), \end{aligned} \quad (8.20)$$

where r_p is the RIN on the pump laser. Substituting for b , the RIN on the signal expressed in decibels (R_s) is therefore:

$$\begin{aligned} R_s &= R_p + 20 \log(\ln(G_R)) \\ &+ 10 \log \left(\frac{(V_s/L_{eff})^2}{(\alpha_p V_s)^2 + (2\pi D \Delta \lambda V_s f)^2} (1 - 2e^{-\alpha_p L} \cos(2\pi D \Delta \lambda L f) + e^{-2\alpha_p L}) \right), \end{aligned} \quad (8.21)$$

where R_p is the RIN on the Raman pump in decibels. For long lengths of fiber, this simplifies to:

$$R_s \approx R_p + 20 \log(\ln(G_R)) + 10 \log \left(\frac{(V_s/L_{eff})^2}{(\alpha_p V_s)^2 + (2\pi D \Delta \lambda V_s f)^2} \right). \quad (8.22)$$

8.2.3. counter-pumped Raman Amplifier

In a counter-pumped Raman amplifier, the noise on the Raman pump will be averaged over the transit time of the amplifier. Assuming the undepleted pump approximation, the pump power along the fiber may be expressed in terms of time t and distance along the fiber z :

$$\left(\frac{\partial}{\partial z} - \frac{1}{V_p} \frac{\partial}{\partial t} \right) P_p(z, t) = \alpha_p P_p(z, t), \quad (8.23)$$

where V_p is the group velocity at the pump wavelength. If a small amount of modulation is applied to the pump, the power at time t and distance z along the fiber is

as given in Eq. (8.11) with z replaced by $(L - z)$ where L is the fiber length. The propagation of the signal may again be solved using a time-dependent differential equation with the signal moving at group velocity V_s :

$$\left(\frac{\partial}{\partial z} + \frac{1}{V_s} \frac{\partial}{\partial t} \right) P_s(z, t) = -\alpha P_s(z, t) + C_R P_p(z, t) P_s(z, t). \quad (8.24)$$

Assuming a frame of reference moving with the signal, this then reduces to an equation of the form of Eq. (8.13) with z replaced by $(L - z)$ and V_s replaced by $(L - V_s)$. Because the effect of counterpropagation will dominate over that of dispersion, we also assume that the group velocity is the same for the pump and the signal:

$$\frac{1}{V_g} \frac{dP_s}{dt} = -\alpha_s P_s(t) + C_R P_s(t) P_{p0} e^{-\alpha_p(L - V_s t)} \left[1 + m \sin \left(2\pi f \left(2t - \frac{L}{V_s} \right) + \phi \right) \right]. \quad (8.25)$$

The effect of averaging over the transit time of the fiber can be examined by considering the modulation on the pump, as seen by the signal while it propagates down the fiber. Figure 8.2 shows the case for pump modulation frequencies of 1 and 10 kHz. If the pump is modulated at low frequencies, the signal will experience a slowly varying instantaneous gain and a large net change in gain compared to the gain that would be produced by a fixed pump power equal to the mean pump power. High-frequency modulation of the pump will result in the signal experiencing a rapidly oscillating instantaneous gain, and a small net change in gain.

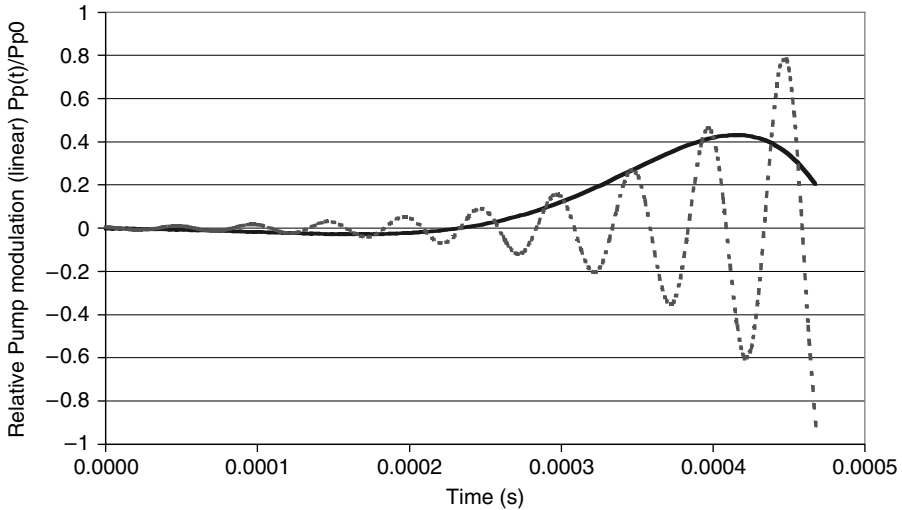


Fig. 8.2. Variation of the pump as seen by the signal in a counter-pumped Raman amplifier for pump modulation of 1 kHz (solid line) and 10 kHz (dotted line). Fiber length = 100 km, $m = 1$; pump attenuation = 0.22 dB/km.

Equation (8.25) can be integrated across the transit time of the fiber (T):

$$\begin{aligned}
 \int_{P_s(0)}^{P_s(T)} \frac{1}{P_s(t)} dP_s &= \int_0^T V_s (-\alpha_s + C_R P_{p0} [1 + m \sin(2\pi f(2t - T) + \phi)]) e^{-\alpha_p(L - V_s t)} dt \\
 &= -\alpha_s L + C_R P_{p0} \frac{(1 - e^{-\alpha_p L})}{\alpha_p} \\
 &\quad + V_s C_R P_{p0} m \int_0^T \sin(2\pi f(2t - T) + \phi) e^{-\alpha_p(L - V_s t)} dt.
 \end{aligned} \tag{8.26}$$

The instantaneous gain G can therefore be expressed in terms of the mean gain $\langle G \rangle$ and a time-averaged modulation:

$$\begin{aligned}
 G &= \exp \left(-\alpha_s L + C_R P_{p0} \frac{(1 - e^{-\alpha_p L})}{\alpha_p} \right. \\
 &\quad \left. + V_s C_R P_{p0} m \int_0^T \sin(2\pi f(2t - T) + \phi) e^{-\alpha_p(L - V_s t)} dt \right) \\
 &= \langle G \rangle \exp \left(V_s C_R P_{p0} m \int_0^T \sin(2\pi f(2t - T) + \phi) e^{-\alpha_p(L - V_s t)} dt \right).
 \end{aligned} \tag{8.27}$$

Because the modulations or noise fluctuations are small, the instantaneous gain can be approximated as

$$G \approx \langle G \rangle \left(1 + V_s C_R P_{p0} m \int_0^T \sin(2\pi f(2t - T) + \phi) e^{-\alpha_p V_s(T-t)} dt \right). \tag{8.28}$$

The instantaneous fluctuation of the gain (dG) is:

$$\begin{aligned}
 dG &= \langle G \rangle V_s C_R P_{p0} m \int_0^T \sin(2\pi f(2t - T) + \phi) e^{-\alpha_p V_s(T-t)} dt \\
 &= \langle G \rangle V_s C_R \frac{P_{p0} m}{(\alpha_p V_s)^2 + (4\pi f)^2} \\
 &\quad \times \left[\alpha_p V_s (\sin(2\pi f T + \phi) + e^{-\alpha_p V_s T} \sin(2\pi f T - \phi)) \right. \\
 &\quad \left. - 4\pi f (\cos(2\pi f T + \phi) - e^{-\alpha_p V_s T} \cos(2\pi f T - \phi)) \right].
 \end{aligned} \tag{8.29}$$

The modulation of the pump ($m P_{p0}$) can be expressed in terms of the mean square fluctuations $\langle \delta P_p^2 \rangle$, and the Raman gain efficiency may be written in terms of the amount of Raman gain added to the fiber (G_R in linear units):

$$\begin{aligned}
 \frac{\delta G}{\langle G \rangle} &= \left(\frac{\sqrt{2} \sqrt{\langle \delta P_p^2 \rangle}}{P_{p0}} \ln(G_R) \frac{V_s / L_{eff}}{(\alpha_p V_s)^2 + (4\pi f)^2} \right) \\
 &\quad \times \left[\alpha_p V_s (\sin(2\pi f T + \phi) + e^{-\alpha_p V_s T} \sin(2\pi f T - \phi)) \right. \\
 &\quad \left. - 4\pi f (\cos(2\pi f T + \phi) - e^{-\alpha_p V_s T} \cos(2\pi f T - \phi)) \right].
 \end{aligned} \tag{8.30}$$

Integrating the mean square fluctuations of the gain for all phases ϕ will give the relative intensity noise on the signal (r_s):

$$\begin{aligned} r_s &= \frac{\langle \delta P_s^2 \rangle}{\langle P_s \rangle^2} = \frac{1}{2\pi} \int_0^{2\pi} \left(\frac{dG}{\langle G \rangle} \right)^2 d\phi \\ &= r_p (\ln(G_R))^2 \frac{(V_s/L_{eff})^2}{(\alpha_p V_s)^2 + (4\pi f)^2} (1 - 2e^{-\alpha_p L} \cos(4\pi f T) + e^{-2\alpha_p L}), \end{aligned} \quad (8.31)$$

where r_p is the RIN on the pump laser. In decibels, the RIN on the signal (R_s) is the sum of the RIN on the pump laser (R_p), a gain-dependent term, and a filtering term:

$$\begin{aligned} R_s &= R_p + 20 \log(\ln(G_R)) \\ &\quad + 10 \log \left(\frac{(V_s/L_{eff})^2}{(\alpha_p V_s)^2 + (4\pi f)^2} (1 - 2e^{-\alpha_p L} \cos(4\pi f T) + e^{-2\alpha_p L}) \right). \end{aligned} \quad (8.32)$$

For long lengths of fiber, this simplifies to

$$R_s \approx R_p + 20 \log(\ln(G_R)) + 10 \log \left(\frac{(V_s/L_{eff})^2}{(\alpha_p V_s)^2 + (4\pi f)^2} \right). \quad (8.33)$$

8.2.4. Discussion of RIN Transfer in Raman Amplifiers

Both Eq. (8.21), for a copumped Raman amplifier, and Eq. (8.32), for a counter-pumped amplifier, show that the relative intensity noise on the signal may be greater than that of the pump, with a maximum given by

$$R_s = R_p + 20 \log(\ln(G_R)). \quad (8.34)$$

Therefore, if the RIN of the signal is to be no greater than the RIN of the pump, at all frequencies, the Raman gain must be limited to 4.3 dB. However, averaging will cause the RIN transfer to be reduced. Counterpropagation averages the noise over the transit length of the fiber, creating a low-pass filter with an extinction of 20 dB per decade. For long lengths of fiber, the -3 dB frequency for counter-pumping is:

$$f_c = \frac{\alpha_p V_s}{4\pi}. \quad (8.35)$$

Typically, this is at a few kiloHertz for most transmission fibers. Copumping will average the noise transfer because the chromatic dispersion in the fiber will cause the signal and pump wavelengths to walk-off. The dispersion also acts as a low-pass filter with an extinction of 20 dB per decade. For copumping in long lengths of fiber, the -3 dB frequency is:

$$f_c = \frac{\alpha_p}{2\pi D \Delta\lambda}. \quad (8.36)$$

For distributed amplifiers, the exponential functions in Eqs. (8.21) and (8.32) become negligible and the -3 dB corner frequencies become independent of the fiber

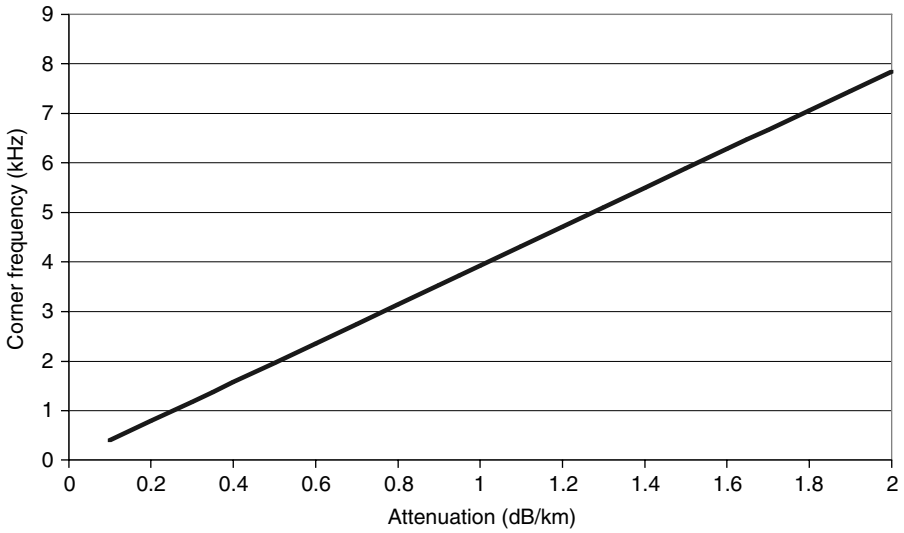


Fig. 8.3. The -3 dB corner frequency as a function of fiber attenuation for a counter-pumped Raman amplifier.

length. Hence fiber span length can be neglected for most distributed amplifiers with 40 km or more of transmission fiber. Fiber attenuation is the dominant factor that defines the corner frequency for a counter-pumped, distributed Raman amplifier. The simple linear relationship between the corner frequency and the fiber attenuation at the pump wavelength is shown in Fig. 8.3. For modern transmission fibers, the filtering effect will occur near 1 kHz, compared to several kHz for dispersion-compensation fiber.

The -3 dB corner frequencies for a distributed, copumped Raman amplifier are also dependent on the relative dispersion in the fiber between the signal and pump wavelengths. For a signal at 1555 nm and a pump at 1455 nm, there will be a linear relationship with attenuation. Due to the large variation when dispersion is included, this is plotted on a logarithmic graph in Fig. 8.4. It can be seen that in low-loss, nondispersion-shifted transmission fibers ($D \approx 15 \text{ ps.km}^{-1}\text{nm}^{-1}$), the corner frequency will occur at about 5 MHz, which could make copumping feasible. Fibers with very low dispersion near 1500 nm will have much higher corner frequencies and therefore the RIN transfer will be much greater.

The dispersion in the fiber may be represented by a dispersion slope (γ) and a dispersion zero wavelength (λ_0):

$$D(\lambda) = \gamma(\lambda - \lambda_0). \quad (8.37)$$

The -3 dB corner frequency for a copumped Raman amplifier will therefore be:

$$f_{3 \text{ dB}} = \frac{\alpha_p}{2\pi\gamma(\lambda_s - \lambda_p) \left| \frac{\lambda_p + \lambda_s}{2} - \lambda_0 \right|}. \quad (8.38)$$

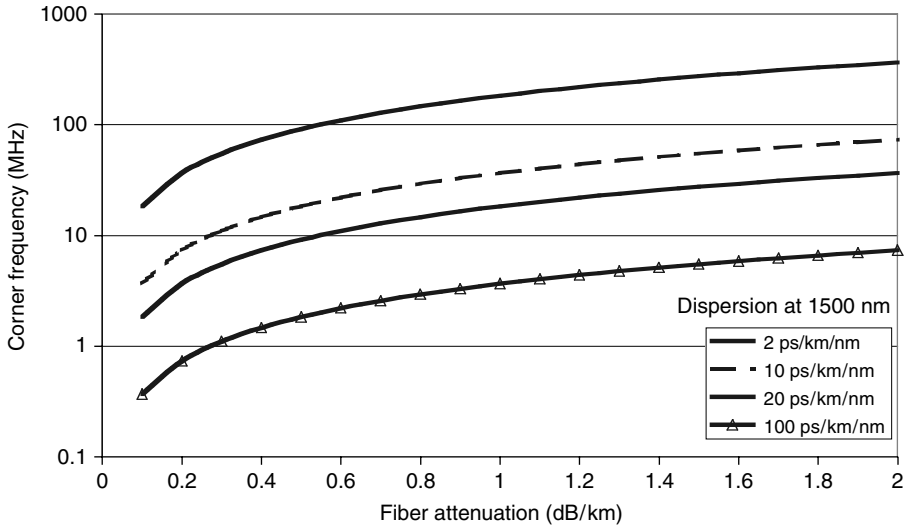


Fig. 8.4. The -3 dB corner frequency as a function of fiber attenuation for a copumped Raman amplifier. Pump and signal wavelengths are spaced at 100 nm.

Figure 8.5 shows a plot of the -3 dB corner frequency for various zero dispersion wavelengths. Equation (8.38) has a root when the dispersion zero is midway between the pump and signal wavelengths. It can be seen from the figure that the corner frequency is greatly increased as the dispersion zero nears 1500 nm. There will therefore be significant RIN transfer at all frequencies if copumping is used in a nonzero dispersion-shifted fiber (NZ-DSF) which has its dispersion zero at 1500 nm. Much better performance could be obtained from standard nondispersion-shifted fiber with a dispersion zero at 1300 nm.

For very short or low-loss lengths of fiber, the corner frequencies will be increased and dips will be superimposed on the RIN transfer function. Examples of this behavior are shown in Fig. 8.6. The depths of these dips will be governed by the total attenuation of the fiber at the pump wavelength, and will tend to zero ($-\infty$ in dB), as the attenuation also tends to zero. For finite attenuation at the pump wavelength, the minima of the dips will coincide with the curve for a long length of fiber. The presence of the dips can be explained by considering a fiber with no loss at the pump wavelength. The gain is therefore evenly distributed along the fiber. If the pump is modulated, the instantaneous gain seen by the signal will vary as the signal propagates. Due to averaging between adjacent half-cycles, frequencies where an exact integer number of modulation cycles are contained in the gain region will result in the net modulation being zero. Conversely, there will always be some residual modulation for frequencies where noninteger numbers of cycles are contained in the gain region. Maximum modulation will appear when an odd number of half-cycles of the modulation are contained in the fiber. As the attenuation in the fiber is increased, perfect gain cancellation cannot be obtained and the dips become less pronounced.

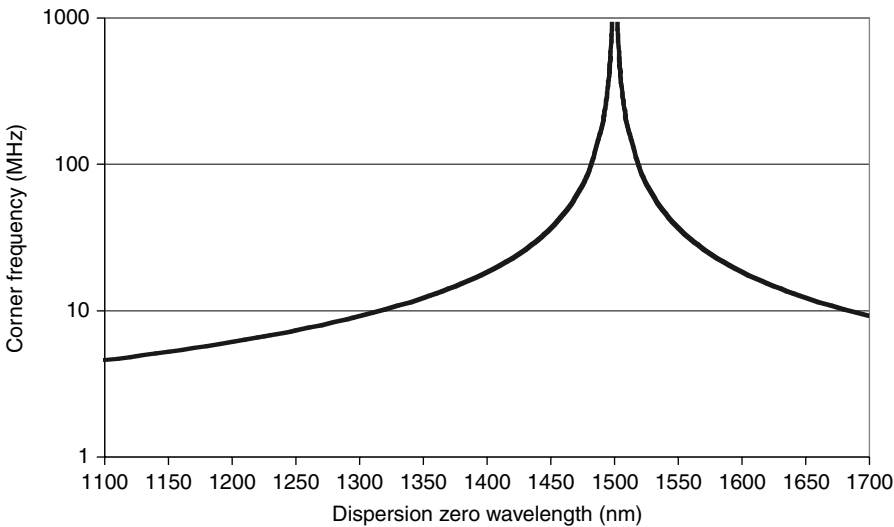


Fig. 8.5. The -3 dB corner frequency for a copumped Raman amplifier as a function of the zero dispersion wavelength in the fiber. Pump attenuation is 0.25 dB/km, dispersion slope is 0.05 ps.nm $^{-2}$.km $^{-1}$, pump wavelength is 1450 nm, and signal wavelength is 1550 nm.

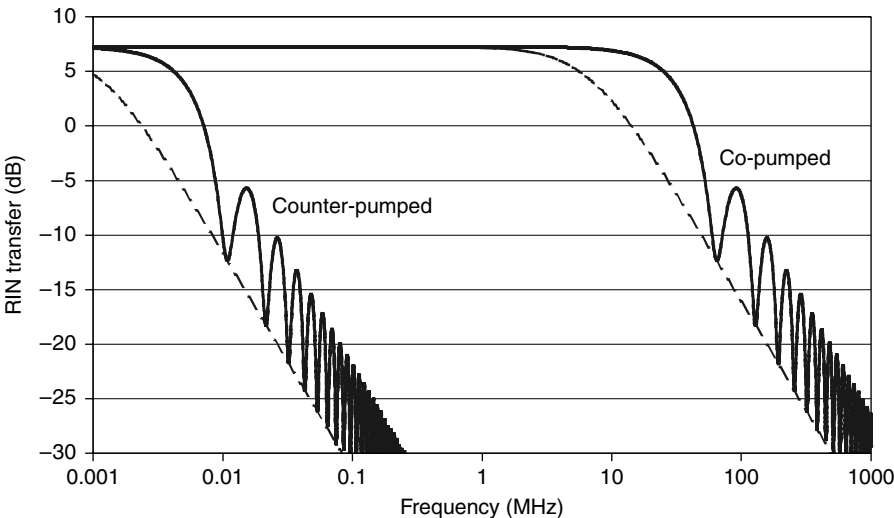


Fig. 8.6. RIN transfer spectrum for co- and counter-pumped Raman amplifiers with 10 dB of gain. Pump attenuation = 0.29 dB/km, length = 10 km (solid line) and 80 km (dotted line), dispersion = 15.6 ps.nm $^{-1}$.km $^{-1}$, pump at 1455 nm, and signal at 1555 nm.

The frequencies of the nulls can be obtained from Eqs. (8.21) and (8.32):

$$\text{For counter-pumping: } f_n = \frac{N}{2T} = \frac{NV_s}{2L} \quad (8.39)$$

$$\text{For copumping: } f_n = \frac{N}{DL\Delta\lambda}, \quad (8.40)$$

where N is an integer value.

8.2.5. Measurements of RIN Transfer

The RIN transfer functions for various fiber types can be determined by applying a known amount of modulation on the Raman pumps and detecting the resulting modulation on the signal channels. A pair of polarization multiplexed semiconductor diodes at a wavelength of 1455 nm were each biased to produce 300 mW output. A small modulation was applied using an electrical network analyzer, and the frequency response of the diodes was measured using a photodiode. An attenuator was used to limit the power into the photodiode to 2.5 dBm.

The Raman pump unit was then used to co- or counter-pump several types of single-mode fiber. Figure 8.7 shows the configurations used for the experiments. In both configurations, an erbium-doped fiber preamplifier (EDFA) was used in conjunction with an attenuator to keep the power at the photodiode at 2.5 dBm. This allowed the launched power of the signal at 1550 nm to be kept low so that the Raman pumps were not depleted in power by the signal, and the propagation of the signal remained in the linear regime. A 2 nm bandpass filter placed at the signal wavelength was used to reduce the spontaneous-spontaneous beat noise at the receiver. Because the power at the photodiode is always kept constant, the ratio of the frequency response of the pump lasers to the response measured on the signal gives the RIN transfer function.

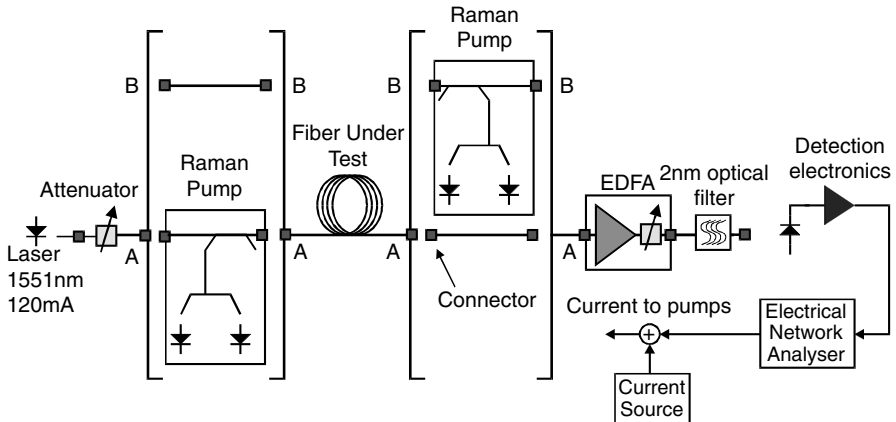


Fig. 8.7. Experimental configurations to measure RIN transfer in a copumped (A) and counter-pumped (B) Raman amplifier.

Table 8.1. Characteristics of Fibers Used for RIN Measurements

Fiber Type	Length (km)	Added gain (dB)	Dispersion @ 1500 nm (ps/km/nm)	Attenuation @ 1455 nm (dB/km)
TrueWave® RS NZ-DSF	81.1	12.6	2.3	0.25
Corning DCM	6.8	7.4	−97.6	1.52
RDF	9.6	7.0	−15.7	0.29

8.2.6. Measurement Results for RIN Transfer

Several fiber types were measured to examine the effect of fiber attenuation, chromatic dispersion characteristics, and fiber lengths. Table 8.1 shows the properties of these single-mode fibers.

Figure 8.8 shows the results for the 81 km of nonzero dispersion-shifted fiber (NZ-DSF). Dispersion-shifted and nonzero dispersion-shifted fibers are attractive for use with distributed Raman amplification because in general they have smaller effective areas than standard nondispersion-shifted fibers and will therefore give greater Raman gain per milliWatt pump power. It can be seen that the measurement data agree very well with theoretical curves. Some measurement errors are apparent at about 1 kHz, 80 kHz, and 2 MHz. At these frequencies the modulation response of the pump lasers and the drive electronics became very small so that the signal-to-noise ratio on the measurements was degraded. The counter-pumped transfer function shows that the RIN from the pump laser is suppressed by more than 50 dB above a frequency of

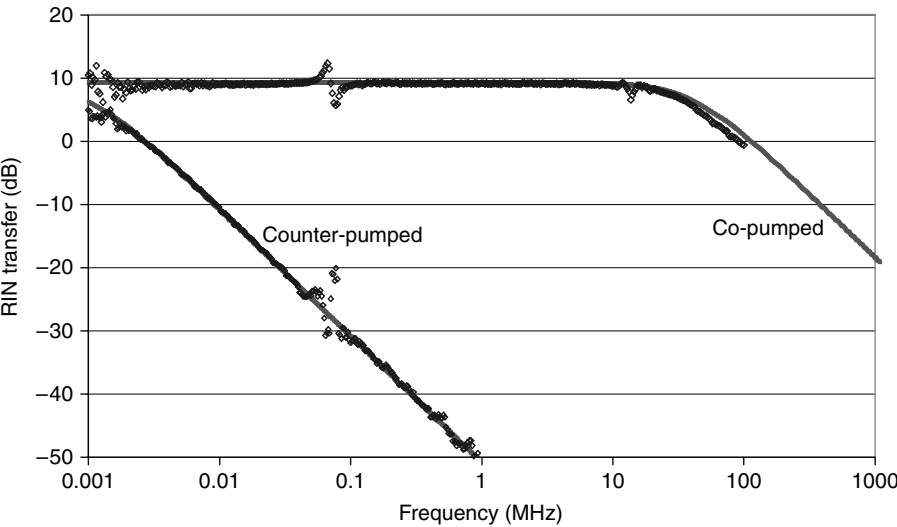


Fig. 8.8. RIN transfer characteristic for 81 km of TrueWave® RS nonzero dispersion-shifted fiber (NZ-DSF). Dots indicate measurements and solid lines are the theoretical calculations.

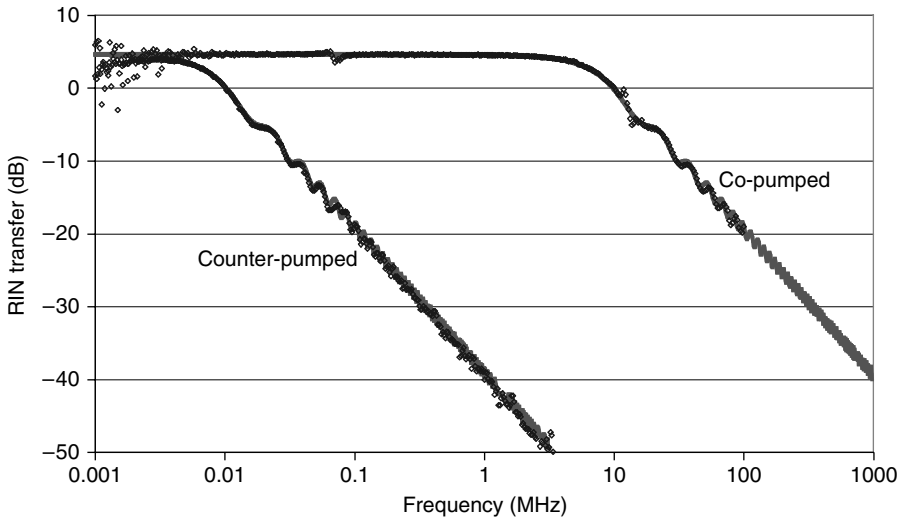


Fig. 8.9. RIN transfer characteristic for a 6.8 km dispersion compensation module (DCM). Dots indicate measurements and solid lines are the theoretical calculations.

1 MHz. The copumped transfer function indicates that the RIN of the signal will be increased by 10 dB relative to the RIN on the pump up to a frequency of 10 MHz. The RIN of the signal relative to that of the pump is only suppressed at frequencies above 100 MHz. This may mean that copumping this NZ-DSF fiber could result in a system penalty due to RIN transfer from the Raman pumps.

The transfer characteristics of a dispersion-compensation module were then measured. This type of fiber has a very small effective area and therefore a high Raman gain efficiency coefficient, although it is difficult to splice to standard fiber resulting in high insertion losses. It can be seen from Fig. 8.9 that since a short length of fiber has been used, ripples have appeared in the transfer function. The high dispersion in the fiber has caused the -3 dB corner frequency for copumping to be less than that for the NZ-DSF. However, the increase in fiber attenuation at the pump wavelength prevents the decrease in corner frequency being dramatic. Ideally, for copumping, the fiber would have a high dispersion and low fiber loss at the pump wavelength.

In order to measure the ripples in the RIN transfer function, a short length of experimental dispersion compensation fiber from Lucent Technologies Denmark (reverse dispersion fiber, RDF) was used. This was dispersion matched to nondispersion-shifted fiber (NDSF) and had a relatively small core so that the Raman gain efficiency was high. The attenuation at the pump wavelength was also relatively low so that any nulls would be quite pronounced. It can be seen from Fig. 8.10 that both the depth and position of the dips agree well with the theoretical predictions. The limited number of measurement points and finite resolution bandwidth on the electrical network analyzer causes only the average RIN transfer function to be measured above 80 kHz on the counter-pumped amplifier. The relatively high chromatic dispersion and low fiber loss results in the -3 dB corner frequency for a copumped Raman amplifier being

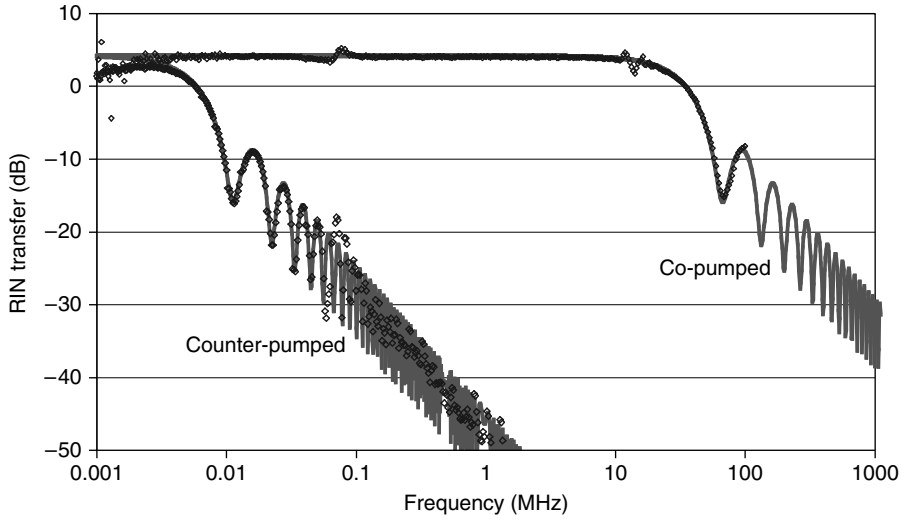


Fig. 8.10. RIN transfer characteristic for 9.6 km of reverse dispersion fiber (RDF). Dots indicate measurements and solid lines are the theoretical calculations.

at 28 MHz. For a long distributed amplifier, this decreases to 6 MHz, making this fiber type much more attractive for copumping than a NZ-DS fiber. NDSF will show similar RIN transfer characteristics although more pump power would be needed to achieve similar values of gain, inasmuch as the effective area is larger.

8.2.7. Q Performance Degradation

The degradation in performance of a transmission system may be estimated by looking at the change in the quality factor (Q):

$$Q = \frac{\langle I_1 \rangle - \langle I_0 \rangle}{\sigma_1 + \sigma_0}, \quad (8.41)$$

where $\langle I_1 \rangle$ is the mean current on “1” bits, $\langle I_0 \rangle$ is the mean current on the “0”s, σ_1 is the standard deviation on the “1”s, and σ_0 is the standard deviation on the 0s. Assuming that the noise on the “0” bits is only due to spontaneous–spontaneous beat noise, and is therefore negligible, the Q in the absence of pump-to-signal RIN is given by

$$Q_s = \frac{\langle I_1 \rangle}{\sigma_1}. \quad (8.42)$$

It is also assumed that the RIN on the signal laser can be treated as a Gaussian random variable and that the Q is therefore degraded to:

$$Q_r = \frac{\langle I_1 \rangle}{\sqrt{\sigma_1^2 + \sigma_r^2}}, \quad (8.43)$$

where σ_r is the standard deviation of the noise from the RIN on the signal. This can be found by integrating the RIN on the signal (r_s) across the receiver bandwidth between frequencies f_1 and f_2 :

$$\sigma_r^2 = \langle I_1 \rangle^2 \int_{f_1}^{f_2} r_s(f) df. \quad (8.44)$$

The Q penalty is therefore given by

$$\begin{aligned} \Delta Q &= \sqrt{1 + \frac{\sigma_r^2}{\sigma_1^2}} \\ &= \sqrt{1 + Q_s^2 \int_{f_1}^{f_2} r_s(f) df}. \end{aligned} \quad (8.45)$$

The penalty, measured in decibels, is therefore:

$$\text{Penalty (dB } Q) = 10 \cdot \log \left(\sqrt{1 + Q_s^2 \int_{f_1}^{f_2} r_s(f) df} \right). \quad (8.46)$$

The penalty due to RIN transfer from co- or counter-pumping may therefore be estimated by integrating the RIN spectra across the receiver bandwidth. In the case of distributed Raman amplification, where the simple expression for RIN may be used, integration across the signal bandwidth gives:

$$\text{For copumping: } \int_{f_1}^{f_2} r_s(f) df = r_p (\ln(G_R))^2 \frac{\tan^{-1} \left(\frac{2\pi D \Delta \lambda}{\alpha_p} f_2 \right) - \tan^{-1} \left(\frac{2\pi D \Delta \lambda}{\alpha_p} f_1 \right)}{2\pi D \Delta \lambda \alpha_p L_{eff}^2} \quad (8.47)$$

$$\text{For counter-pumping: } \int_{f_1}^{f_2} r_s(f) df = r_p (\ln(G_R))^2 \frac{\tan^{-1} \left(\frac{4\pi}{\alpha_p V_s} f_2 \right) - \tan^{-1} \left(\frac{4\pi}{\alpha_p V_s} f_1 \right)}{4\pi \alpha_p L_{eff}^2 / V_s}. \quad (8.48)$$

These may be written in terms of the -3 dB corner frequency (f_c):

$$\begin{aligned} \int_{f_1}^{f_2} r_s(f) df &= r_p (\ln(G_R))^2 \int_{f_1}^{f_2} \frac{df}{1 + f^2/f_c^2} \\ &= r_p (\ln(G_R))^2 f_c \left(\tan^{-1} \left(\frac{f_2}{f_c} \right) - \tan^{-1} \left(\frac{f_1}{f_c} \right) \right). \end{aligned} \quad (8.49)$$

For many operating conditions $f_1 \ll f_c$ and $f_2 \gg f_c$, and this simplifies to:

$$\int_{f_1}^{f_2} r_s(f) df = (\ln(G_R))^2 \frac{\pi f_c r_p}{2}. \quad (8.50)$$

The penalty in Q therefore depends upon the baseline performance (Q_s). Figure 8.11 shows the estimated penalty due to RIN transfer for a co- or counterpropagating

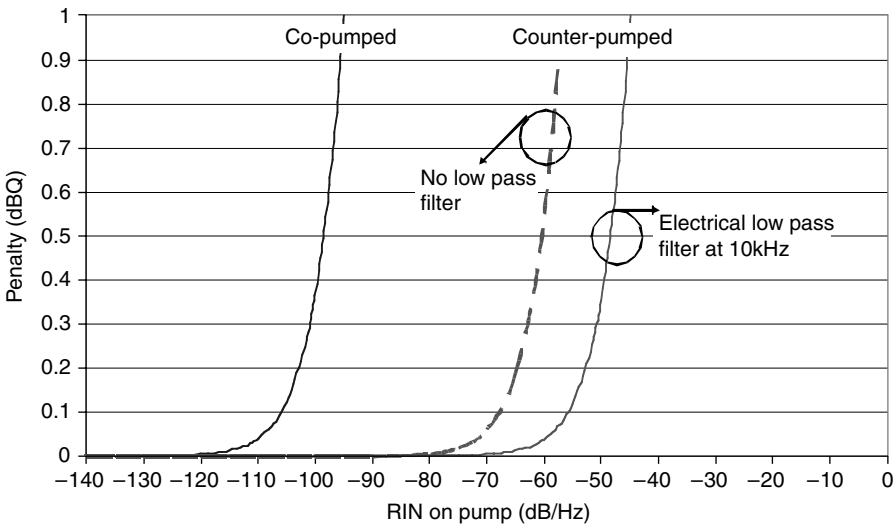


Fig. 8.11. Estimated Q penalty at the receiver for different values of relative intensity noise on the copropagating (left) and counterpropagating (right) pump. Baseline Q_s is 6, fiber type is NDSF with $B_{elec} = 10$ kHz to 20 GHz, dispersion $D = 15$ ps.nm⁻¹.km⁻¹, gain is 10 dB, and attenuation at the pump wavelength is 0.25 dB.km⁻¹. Dashed line shows the penalty with a receiver bandwidth extending to d.c. frequencies.

Raman pump with respect to a Q of 6. It can be seen that the counter-pumped configuration is significantly more tolerant of pump noise than the copumped configuration. Using nondispersion-shifted fiber, a counter-pumped distributed Raman amplifier may have a Raman pump with a RIN of up to -55 dB/Hz without suffering a 0.1 dB $_Q$ penalty whereas a copumped distributed Raman amplifier can tolerate only up to -108 dB/Hz for the same penalty. Also, a counter-pumped distributed amplifier has 50 dB more tolerance to RIN on the Raman pump. The figure uses typical electrical receiver bandwidths for a 40 Gb/s system, with a low-pass roll-off frequency of about 10 kHz. There may be increased penalty and a reduction of RIN tolerance by about 10 dB if the receiver response extends down to d.c. frequencies (see dashed line).

It should be remembered that RIN transfer will accumulate linearly as the number of spans increases. Ten spans of copumped distributed Raman amplifiers with a pump RIN of -110 dB/Hz will show almost 1 dB $_Q$ penalty. RIN values of -160 dB/Hz are typical for DFB lasers, whereas FBG stabilized semiconductor diodes tend to have RIN values of -130 to -140 dB/Hz. Fiber lasers are typically much noisier, with RIN values of between -100 and -90 dB/Hz.

The effect of dispersion on the estimated Q penalties (with respect to a Q of 6) from copropagating RIN transfer is illustrated in Fig. 8.12. The lower set of curves represents the penalties when using a nondispersion-shifted fiber (NDSF) with a dispersion of about 15 ps.nm⁻¹.km⁻¹, whereas the upper set of curves is for a nonzero dispersion-shifted fiber with a dispersion of about 2 ps.nm⁻¹.km⁻¹ at 1500 nm. The NZ-DSF has about 8 dB less tolerance to RIN than the NDSF. If the zero dispersion

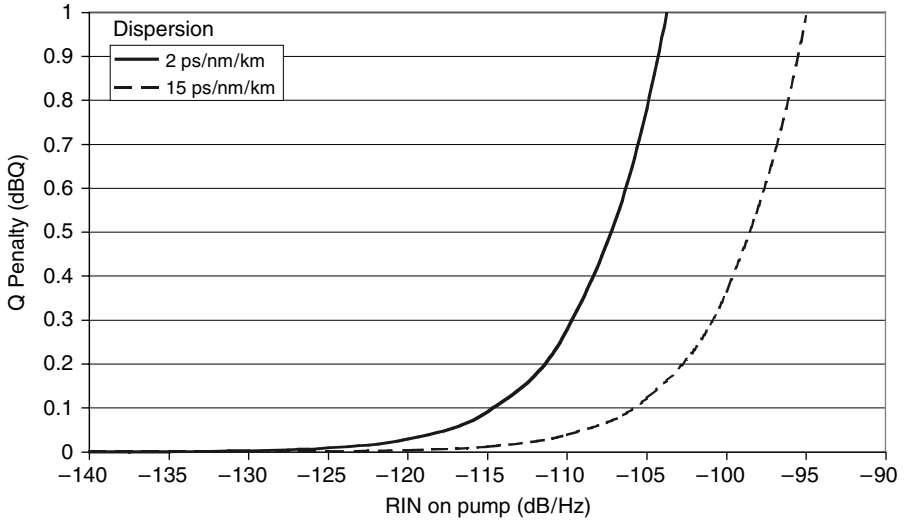


Fig. 8.12. Estimated Q penalty at the receiver for different values of relative intensity noise on the copropagating pump. Baseline Q_s is $6 B_{elec} = 10 \text{ kHz}$ to 20 GHz , dispersion $D = 15 \text{ ps.nm}^{-1}.\text{km}^{-1}$ (dotted line) or $D = 2 \text{ ps.nm}^{-1}.\text{km}^{-1}$ (solid line), gain is 10 dB , and attenuation at the pump wavelength is 0.25 dB.km^{-1} .

wavelength lay at the midpoint of the signal and pump wavelengths, the Q penalty would be significantly greater.

8.3. Pump Induced Crossgain Modulation

Numerical methods have been previously published [4, 5] for the calculation of crosstalk in co- and counter-pumped Raman amplifiers. The analytical theory describing the frequency response of the signal-to-signal crosstalk in Raman amplifiers mediated by the pump (crossgain modulation) is reported here. Approximations are derived in order to explain and clarify the results. An analysis of the degradation in performance of a transmission is also estimated. This work follows and develops upon a method possibly used by Forghieri et al. [5] in a short conference paper, where no details of the mathematical model are shown.

In a similar method to the RIN transfer analysis the effect of a weak signal beam is considered, traveling either with, or against, the direction of a strong pump beam, traveling in a single-mode fiber. This causes small perturbations in the intensity of the strong pump beam which are then transferred to another weak signal beam at a different wavelength, copropagating with the first weak signal beam. Once again, the fiber is assumed to exhibit wavelength-dependent attenuation and dispersion, but any optical nonlinearity other than Raman scattering is ignored. The undepleted pump approximation [6] is assumed, because the effect of crosstalk from a single channel is likely to be small. In the case of a WDM system, each channel will contribute a

small amount of pump-mediated crosstalk which all together may cause a significant system impact.

8.3.1. Crossgain Modulation in Copumped Raman Amplifiers

In the copumped Raman amplifier, dispersion will cause walk-off between the pump and all signal channels due to their propagation at slightly different velocities. The walk-off is a function of the dispersion of the fiber and will average the transfer of energy from both the signal to the pump and from the pump to another signal. Using the undepleted pump approximation, equations may be derived in a similar manner to the RIN transfer analysis. A modulated signal is considered propagating in the same direction as the strong pump beam. This causes small fluctuations in the gain experienced by a second signal, hence contributing towards crosstalk. By taking frames of reference traveling with the pump, and then with the second signal, a transfer function can be derived for the energy transfer (a detailed derivation is included in appendix 8). The variables for first signal have subscript s , the pump has subscript p , and the second signal has subscript c . The transfer function may be written in terms of the added (off-on) Raman gain for both source signal (G_{as}) and the signal receiving the crosstalk (G_{ac}):

$$|H_c(f)|^2 = \left(\sqrt{2} \left(\frac{V_c}{L_{eff}} \right)^2 \frac{v_p}{v_s} \frac{P_{s0}}{P_{p0}} \ln(G_{as}) \ln(G_{ac}) \right)^2 \times \frac{1}{2\pi} \int_0^{2\pi} \left(\int_0^T \left[\exp(-\alpha_p V_c \tau) \int_0^\tau \overline{P_r(\tau_x)} \sin(\varepsilon f \tau_x + \phi) d\tau_x \right] d\tau \right)^2 d\phi, \quad (8.51)$$

where V_c is the speed of light of the second signal in the fiber of transit time T , L_{eff} is the effective length, v_p and v_s are the optical frequencies of the pump and signal light, respectively, of power launch power P_{s0} and P_{p0} , α_p is the attenuation at the pump wavelength, and P_r is a function describing the normalized average power of the first signal with time:

$$\overline{P_r(\tau)} = \exp \left(-\alpha_s V_c \tau + C_{Rs} P_{p0} \frac{(1 - e^{-\alpha_p V_c \tau})}{\alpha_p} \right), \quad (8.52)$$

where α_s is the attenuation at the signal wavelength and ε represents the velocity mismatch between the light beams:

$$\varepsilon = 2\pi \left(1 - \frac{V_p}{V_s} \right) \frac{V_c}{V_p}. \quad (8.53)$$

The form of Eq. (8.51) that describes the crossgain modulation can be explained in terms of the energy transfer from the first signal to the second signal via the pump. The inner integral represents the average energy that the pump has accumulated from the first signal up until time τ . The second integral sums the energy transfer from the pump wavelength to the second wavelength at each point along the fiber.

8.3.2. Crossgain Modulation in counter-pumped Raman Amplifiers

A similar analysis follows for the case where the pump and signals propagate in opposite directions. Here dispersion is considered to be negligible compared to the averaging due to different transit directions so that all signals are assumed to travel at velocity V_g , albeit in different directions. Using the undepleted pump approximation, and considering a small amount of modulation on the first signal (subscript s), the fluctuations on a counterpropagating pump beam (subscript p) may be calculated. This can be used to derive the changes in gain experienced by a second signal (subscript c) copropagating with the first and counterpropagating with respect to the pump. The transfer function may be written in terms of the added (off-on) Raman gain for both source signal (G_{as}) and the signal receiving the crosstalk (G_{ac}):

$$|H_c(f)|^2 = \left(\sqrt{2} \left(\frac{V_g}{L_{eff}} \right)^2 \frac{v_p}{v_s} \frac{P_{s0}}{P_{p0}} \ln(G_{as}) \ln(G_{ac}) \right)^2 \times \frac{1}{2\pi} \int_0^{2\pi} \left[\int_0^T \exp(-\alpha_p V_g (T - \tau)) \int_\tau^T \overline{P_e(\tau_x)} \sin(4\pi f \tau_x + \phi') d\tau_x d\tau \right]^2 d\phi', \quad (8.54)$$

where the variables are the same as the copropagating pump case, and the function P_e describes the normalized power of the first signal at time τ :

$$\overline{P_e(\tau)} = \exp \left(-\alpha_s V_g \tau + \frac{\ln(G_{as})}{L_{eff}} e^{-\alpha_p L} \frac{(e^{\alpha_p V_g \tau} - 1)}{\alpha_p} \right). \quad (8.55)$$

The inner integral in the transfer function represents the transfer of energy from the first signal to the pump at time τ . Because the pump and signal travel in different directions, the integral is now from τ to T rather than 0 to τ , which is the form for the copropagating Raman amplifier. The second integral sums the energy transfer from the pump to the second wavelength at each point along the fiber.

8.3.3. Approximation for Constant Gain per Unit Length

If the fiber loss at the pump wavelength is low, the gain may be considered to be equally distributed along the fiber with gain per unit length κ . If the attenuation at the pump wavelength is considered to be negligible, the modulation transfer function may be simplified.

For the copropagating Raman amplifier, the transfer function is:

$$|H_c(f)|^2 = \left(\left(\frac{V_c}{L_{eff}} \right)^2 \frac{v_p}{v_s} \frac{P_{s0}}{P_{p0}} \ln(G_{as}) \ln(G_{ac}) \right)^2 \frac{1}{[(\kappa V_p)^2 + (\epsilon f)^2]^2} \times \left[(T\epsilon f)^2 + (T\kappa V_p + 1)^2 - 2e^{\kappa V_p T} ((\kappa V_p T + 1) \cos(\epsilon f T) + T\epsilon f \sin(\epsilon f T)) + e^{2\kappa V_p T} \right]. \quad (8.56)$$

This equation represents a low-pass filter, with a roll-off at frequency $\kappa V_p/\varepsilon$ due to dispersion. For the counterpropagating Raman amplifier, the transfer function is:

$$|H_c(f)|^2 = \left(\left(\frac{V_g}{L_{eff}} \right)^2 \frac{v_p}{v_s} \frac{P_{s0}}{P_{p0}} \ln(G_{as}) \ln(G_{ac}) \right)^2 \frac{1}{[(\kappa V_g)^2 + (4\pi f)^2]^2} \\ \times \left[e^{2\kappa V_g T_c} \left[(TV_g\kappa - 1)^2 + (4\pi f T)^2 \right] \right. \\ \left. + 2e^{\kappa V_g T} \left[(TV_g\kappa - 1) \cos(4\pi f T) - 4\pi f T \sin(4\pi f T) \right] + 1 \right]. \quad (8.57)$$

This equation also represents a low-pass filter, with a roll-off at frequency $\kappa V_g/4\pi$ due to the different transit directions.

In both cases, an increase in the gain per unit length κ will cause the roll-off frequency to be raised. However, the slope of the roll-off will vary slightly because of the different boundary conditions used to solve the equations. At low gains, with small values of κ , both transfer functions exhibit roll-offs at 20 dB/decade, due to cancellation of terms in the top and bottom of the equations. As κ increases, the last exponential term in Eq. (8.56) dominates and the roll-off tends towards 40 dB/decade in the copumped Raman amplifier. Here there is both the 20 dB/decade roll-off for the transfer of energy from the signal to the pump, and another 20 dB/decade roll-off for the transfer of energy from the pump to the second signal. In practice, this is difficult to observe because the ideal fiber would be a long fiber with high dispersion and negligible attenuation. Relative intensity noise transfer from the pump also tends to obscure measurements. The presence of attenuation confines the gain to within the effective length of the fiber and limits the averaging due to dispersion.

In the counter-pumped Raman amplifier, the first term in Eq. (8.57) becomes large as κ increases, and the roll-off rate remains at 20 dB/decade. The 40 dB/decade roll-off rate will only be observed in a counter-pumped Raman amplifier if the gain per unit length κ is large and negative (attenuation). This will not be the case for an amplifier, which requires κ to be positive.

The physical difference between the co- and counterpropagating cases may be explained by considering the interactions between the pump and the signals. In the copropagating case, the transfer of energy from the first signal to the pump, and then to the second signal, is averaged along the complete length of the gain medium. Near the end of the fiber, the second signal (probe) will be receiving energy from the pump that has been averaged twice by the dispersion of the fiber. The averaging process is different in the case of the counterpropagating pump. At the start of the fiber the second signal (probe) receives crosstalk energy from the first signal via the pump which has only been averaged once. At the end of the fiber, the pump itself has not interacted with the first signal over a long length, and hence little averaging has taken place. Hence, in a high-gain amplifier with negligible pump attenuation, the roll-off with a copropagating pump will be at a greater rate than for a counterpropagating pump.

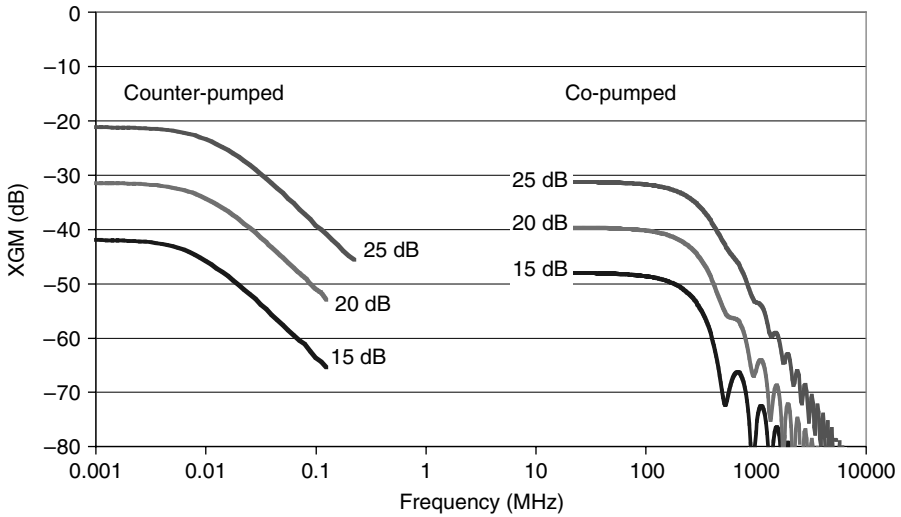


Fig. 8.13. Transfer function for signal spectral density for a discrete Raman amplifier, length 10 km. Attenuation at pump 0.25 dB/km; at signal 0.22 dB/km; peak Raman gain efficiency C_R $0.6 \text{ W}^{-1}\text{km}^{-1}$; input signal power -10 dBm . Dispersion between pump at 1455 nm and signal at 1555 nm is $2.3 \text{ ps.nm}^{-1}.\text{km}^{-1}$.

8.3.4. Simulations of Crossgain Modulation in Discrete Raman Amplifiers

The model (integrating Eqs. (8.51) and (8.54), can be used to predict the noise spectra of high-gain discrete Raman amplifiers. Here we assume the amplifier is a single-stage amplifier with 10 km of NZ-DSF, with a high-power pump at 1455 nm to provide gain at 1555 nm. The crossgain modulation spectra can be seen in Fig. 8.13 for gains of 15, 20, and 25 dB and input signal powers of -10 dBm/ch . The roll-off frequency is about 10 kHz and 200 MHz for the counter- and copumped amplifiers, respectively. An increase in the gain of the amplifier will also slightly raise the roll-off frequency. The rate of roll-off is also higher in the case of the copump, and peaks and nulls are apparent which become less pronounced as the gain increases.

It is apparent that the counter-pumped amplifier gives a larger amount of crosstalk at low frequencies than the copumped case for the same value of gain and signal input power. Although the total amount of energy transferred to the pump is the same for both types of amplifier (if the fiber attenuation is neglected and an undepleted pump is assumed), the place where the transfer occurs is different. In the counter-pumped configuration, the signal power is greatest at the end of the fiber where the pump enters the amplifier. Modulation from the first signal is quickly transferred to the pump. A second probe signal will experience a strong amount of modulation from the front end onwards. In the copumped amplifier, the transfer of energy from the first signal to the pump will build up much more progressively and therefore the second probe signal will not see such a strong amount of modulation throughout the length of the amplifier.

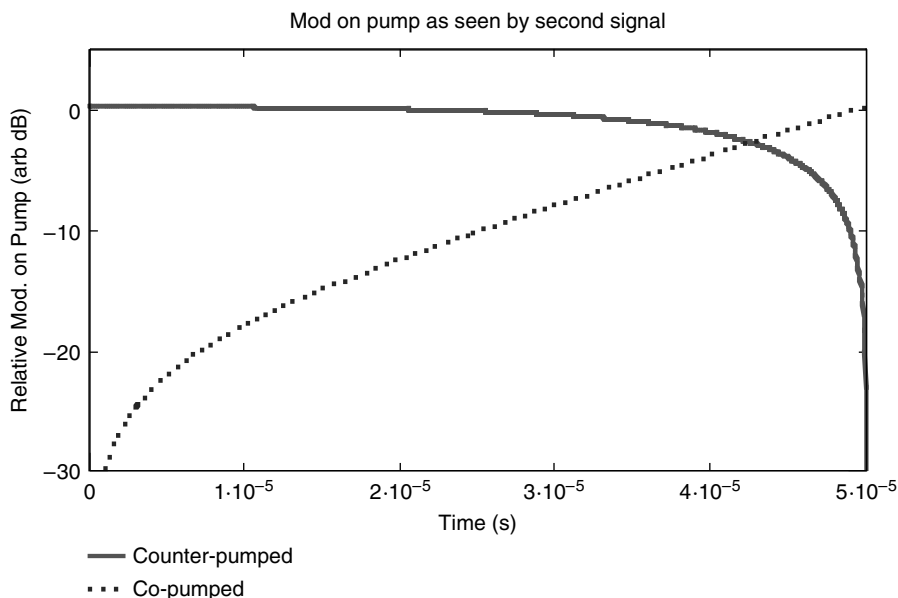


Fig. 8.14. Relative modulation on pump experienced by second probe signal for a co- and counter-pumped Raman amplifier. Length = 10 km; pump and signal attenuations are zero.

Figure 8.14 shows the relative low frequency modulation experienced along the length of the amplifier in the co- and counter-pumped configurations using the pump propagation equations detailed in the appendix, with the d.c. component removed. The case of zero pump and signal attenuation has been considered so that the overall transfer of energy from the first signal to the pump is the same. It can be seen that the amount of modulation accumulated on the pump builds up in proportion to the power of the signal and the pump (here the pump power is constant). For the copropagating pump, the pump modulation is largest at the end of the fiber span and the counter-propagating pump has the largest modulation at the signal input. It is clear from the figure that a second probe signal will experience modulation from the pump over a far greater length in a counter-pumped amplifier than in a copumped amplifier.

8.3.5. Simulations of Crossgain Modulation in Distributed Raman Amplifiers

The model can also be used to predict the crosstalk characteristics for distributed Raman amplifiers (see Fig. 8.15). The transmission fiber is 80 km of NZ-DSF (TrueWave® RS), with a high-power pump at 1455 nm to provide gain at 1555 nm. The signal launch power was 0 dBm/ch.

In a distributed amplifier, the copumped configuration shows a far greater amount of crosstalk than the counter-pumped case at low frequencies. In a copumped distributed amplifier, the pump interacts with a strong signal at the launch end of the fiber and therefore there is a large amount of energy transferred to the pump. In the

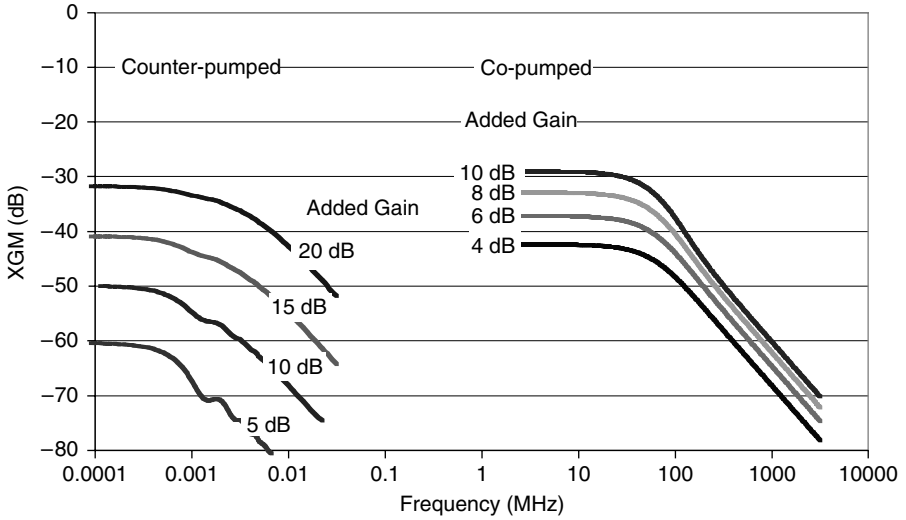


Fig. 8.15. Transfer function for signal spectral density for a co- and counter-pumped distributed Raman amplifier, length 80 km. Attenuation at pump 0.25 dB/km, at signal 0.22 dB/km, peak Raman gain efficiency C_R $0.6 \text{ W}^{-1}\text{km}^{-1}$; input signal power 0 dBm. Dispersion between pump at 1455 nm and signal at 1555 nm is $2.3 \text{ ps.nm}^{-1}.\text{km}^{-1}$.

counter-pumped distributed amplifier, the signal is quite weak when it begins to interact with the pump at the end of the fiber span. Therefore there is less energy transferred to the pump.

In comparison with the discrete amplifier, the distributed amplifier has roll-off frequencies that are about 10 times lower due to the increased fiber length. The crosstalk for the copump is slightly increased because the signal launch power into the fiber span is about 10 dB higher. Both types of amplifier show a slightly greater roll-off frequency for increases in added Raman gain.

8.3.6. Measurements of Crossgain Modulation

The crossgain modulation was measured using a similar method to that which was used to measure the RIN transfer, in order to validate the model. A fiber was either co- or counter-pumped using a pair of polarization multiplexed 1455 nm semiconductor diodes (see Fig. (8.16)). A signal laser at 1554 nm (λ_1) was modulated by an electrical network analyzer and multiplexed with a CW probe laser at 1550 nm (λ_2). The signal and probe lasers were then launched into the test fiber, propagating either with, or against, the direction of the Raman pump. Care was taken to avoid stimulated Brillouin scattering or saturation of the pump laser. A demultiplexer was then used to filter out the modulated signal laser. Any modulation on the probe beam was detected using an optically preamplified photodetector, and displayed on the electrical network analyzer. A 2 nm optical filter was placed after the EDFA preamplifier to reduce spontaneous-spontaneous beat noise. The optical power onto the photodiode was kept constant

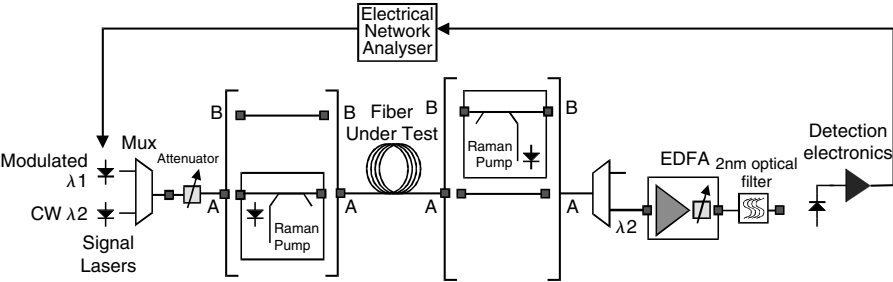


Fig. 8.16. Experimental setup for measuring crossgain modulation in a Raman amplifier.

Table 8.2. Characteristics of Fibers Used for XGM Measurements

Fiber Type	Length (km)	Dispersion @ 1500 nm (ps/km/nm)	Attenuation @ 1455 nm (dB/km)	Attenuation @ 1555 nm (dB/km)	Gain (dB)
TrueWave® RS NZ-DSF	40.4	2.3	0.25	0.20	12
Corning DCM	6.8	−97.6	1.52	0.88	7.5
NDSF	25.5	13	0.25	0.19	6.5

and the crossgain modulation spectrum could be calculated from the ratio of received spectrum from the CW probe after passing through the Raman amplifier (λ_2) and the spectrum from the modulated signal (λ_1), before the Raman amplifier.

The crossgain modulation was measured for three fiber types as shown in Table 8.2.

8.3.7. Results of Crossgain Modulation Measurements

Both the NDSF and NZ-DSF (TrueWave® RS) are relatively low-loss fibers but exhibit different dispersion characteristics. The crossgain modulation characteristics for the NDSF and NZ-DSF are shown in Figs. 8.17 and 8.18 for two different values of signal and probe power. Some measurement noise is visible which is attributed to low crosstalk levels and to the modulation response of the laser diodes under direct current modulation. The laser diodes were designed as CW source lasers. The longer length of the NZ-DSF causes greater averaging such that the roll-off frequency is slightly lower for the counter-pumped NZ-DSF at around 1 kHz. However, inasmuch as there is more dispersion in the NDSF, the roll-off frequency for a copumped amplifier is lower in the NDSF than the NZ-DSF. For a copumped amplifier using NZ-DSF, the crosstalk extends to almost 70 MHz. If the dispersion zero lies precisely between the pump and signal wavelengths, crosstalk will be experienced in the GHz range. Simulations (shown as solid lines) using Eqs. (8.51) and (8.54), agree well with measurements although there is some discrepancy in the roll-off shape. Nevertheless, good predictions of the noise transfer process may be made using the model.

Measurements were also taken for a 6.8 km dispersion compensation module (see Fig. 8.19). Because the fiber length is quite short, the low-frequency roll-off for the

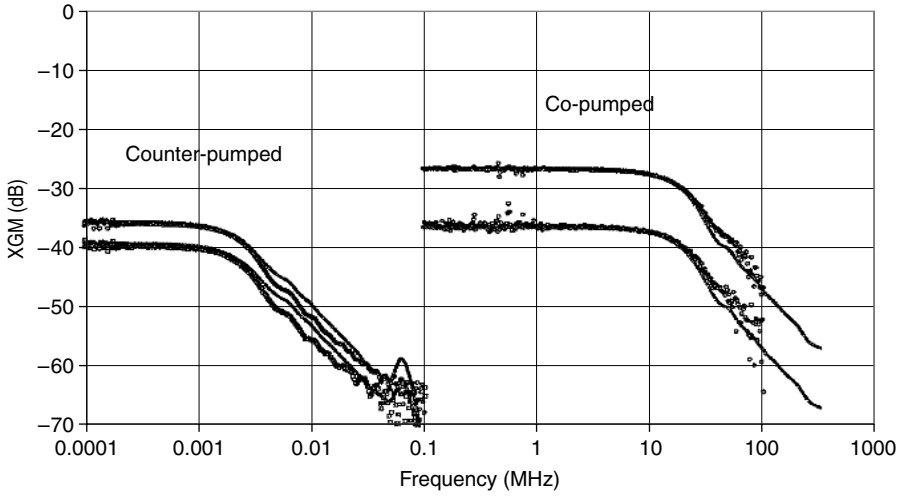


Fig. 8.17. Crossgain modulation for co- and counter-pumped Raman amplifier using 25 km of NDSF for two different values of signal and probe power. Dots indicate measurements and lines are simulations.

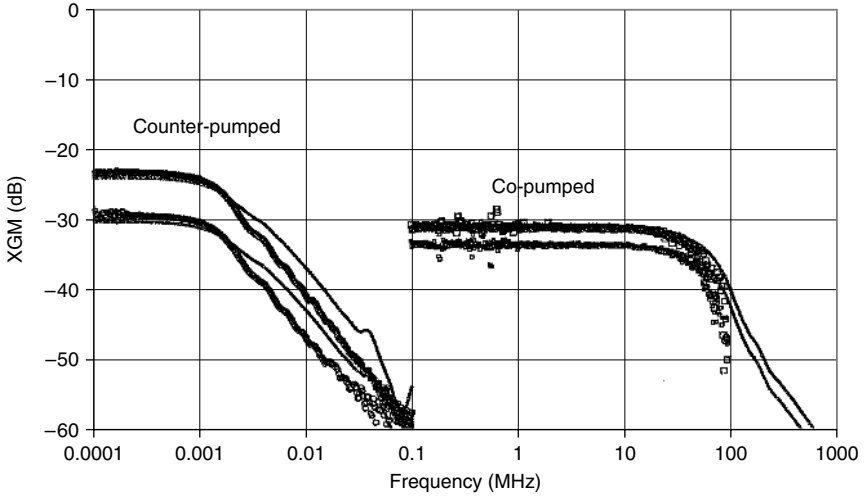


Fig. 8.18. Crossgain modulation for co- and counter-pumped Raman amplifier using 40 km of NZ-DSF for two different values of signal and probe power. Solid lines indicate simulations. Points are measurements.

counter-pumped configuration is at about 10 kHz. counter-pumped discrete Raman amplifiers using short lengths of gain fiber will typically have roll-off frequencies that are 10 times that of a distributed amplifier. The dispersion between pump and signals is quite high for the DCF such that even for only 6.8 km, a counter-pumped amplifier will have a roll-off frequency at around 10 MHz. For the relatively low

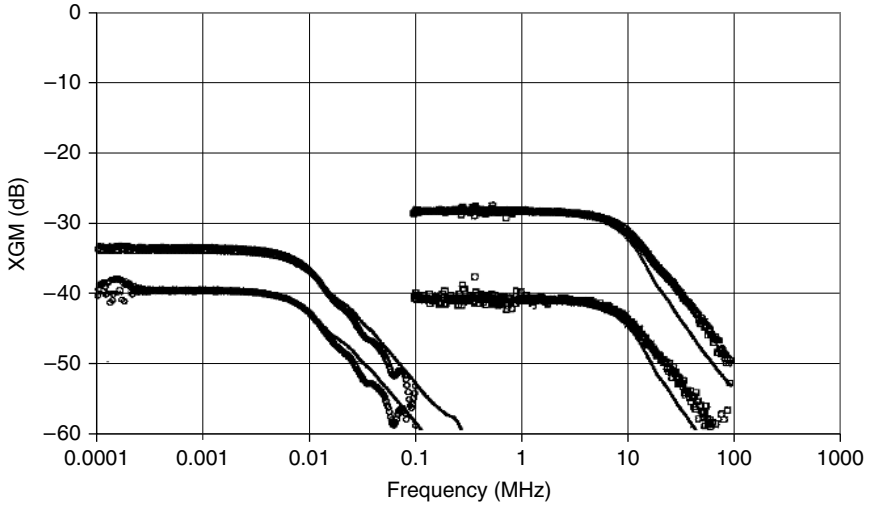


Fig. 8.19. Crossgain modulation for co- and counter-pumped Raman amplifier using 6.8 km of DCF for two different values of signal and probe power. Solid lines indicate simulations. Dots are measurements.

amounts of gain obtained using a semiconductor Raman pump, the trend towards a 40 dB/decade roll-off predicted by theory in the copumped amplifier could not be verified.

8.3.8. Power Penalties due to Pump-Mediated Crosstalk

The previous sections have derived the equations for the power transfer for different frequencies, between signals, via the pump. If the system is assumed to be a Wide Sense Stationary linear stochastic process [7], the power spectral density of the crosstalk on the second signal is given by the product of the power spectral density of the first signal, and the power transfer function $|H_c|^2$:

$$S_c(\Omega) = |H(\Omega)|^2 S_s(\Omega), \quad (8.58)$$

where S_s is the power spectral density (PSD) of the signal. For a rectangular NRZ pseudorandom bit sequence (PRBS) of bit duration T can be calculated, and may be approximated at low frequencies:

$$S_s(\Omega) = \frac{P_1^2 T}{4} \frac{\sin^2(\Omega T/2)}{(\Omega T/2)^2} \left\{ 1 + 2\pi \sum_{m=-\infty}^{\infty} \delta\left(\Omega - \frac{2\pi m}{T}\right) \right\} \approx \frac{P_1^2 T}{4}. \quad (8.59)$$

The noise produced on the signal will be a low-frequency modulation of the gain that the signal experiences. If we assume that this noise represents a zero mean ($\mu = 0$), intensity noise on top of the data signal, the variance of this intensity modulation

can be found by calculating the expectation (E) of the received power. The mean square variation can then be calculated using Parseval's theorem or by using the autocorrelation function [8]:

$$\sigma_c^2 = E[(x - \mu)^2] = E[x^2] - \mu^2 = R_c(0) = \frac{1}{\pi} \int_{0+}^{\infty} |H(\Omega)|^2 S_s(\Omega) d\Omega. \quad (8.60)$$

The degradation in performance of a transmission system may be estimated by looking at the change in the quality factor (Q). The amplitude noise on the signal laser can be treated as a Gaussian random variable and that the Q is therefore degraded to:

$$Q_r = \frac{\langle P_1 \rangle}{\sqrt{\sigma_1^2 + \sigma_c^2}}. \quad (8.61)$$

The Q penalty is therefore given by

$$\Delta Q = \frac{Q_s}{Q_r} = \sqrt{1 + \frac{\sigma_c^2}{\sigma_1^2}} = \sqrt{1 + Q_s^2 \frac{T}{2} \int_{0+}^{\infty} |H(f)|^2 df}. \quad (8.62)$$

The penalty, measured in decibels, is therefore:

$$\text{Penalty (dBQ)} = 10 \cdot \log \left(\sqrt{1 + Q_s^2 \frac{T}{2} \int_{0+}^{\infty} |H(f)|^2 df} \right). \quad (8.63)$$

Although there is no exact analytical solution for the transfer function $H(f)$, the overall result is a low-pass filter. In most cases, a filter shape with a roll-off of 20 dB/decade can be used. This can be fitted to the numerical or measured data using the d.c. value (A) and the 3 dB roll-off frequency $f_{3 \text{ dB}}$:

$$|H(f)|^2 = \frac{A}{1 + \left(\frac{f}{f_{3 \text{ dB}}} \right)^2}, \quad (8.64)$$

where for copumping:

$$A = \left(\frac{1}{L_{eff}^2} \frac{v_p}{v_s} \frac{P_s}{P_p} \ln(G_{as}) \ln(G_{ac}) \right)^2 \times \left(\int_0^L e^{-\alpha_p z} \int_0^z \exp \left(-\alpha_s x + \frac{\ln(G_{as})}{L_{eff}} \frac{1 - e^{-\alpha_p x}}{\alpha_p} \right) dx dz \right)^2 \quad (8.65)$$

$$f_{3 \text{ dB}} \approx \frac{V_p}{\varepsilon L_{eff}} = \frac{V_p}{2\pi L_{eff}} \frac{1 + D_{pc} \Delta \lambda_{pc} V_p}{D_{ps} \Delta \lambda_{ps} V_p}, \quad (8.66)$$

where D_{ps} and D_{pc} are the dispersion between the pump and the first signal at a wavelength difference of $\Delta \lambda_{ps}$, and the pump and the second signal at a wavelength

difference of $\Delta\lambda_{pc}$. This approximation assumes that the 3 dB point is set by the dispersion between the pump and signals over the effective length of the fiber. An equivalent approximation for counter-pumped amplifiers is:

$$A = \left(\frac{1}{L_{eff}^2} \frac{v_p}{v_s} \frac{P_s}{P_p} \ln(G_{as}) \ln(G_{ac}) \right)^2 \times \left(\int_0^L e^{-\alpha_p z} \int_z^L \exp \left(-\alpha_s x + \frac{\ln(G_{as})}{L_{eff}} e^{-\alpha_p L} \frac{e^{\alpha_p x} - 1}{\alpha_p} \right) dx dz \right)^2 \quad (8.67)$$

$$f_{3 \text{ dB}} \approx \frac{V_p}{4\pi L_{eff}}, \quad (8.68)$$

where the 3 dB point is now set by the round-trip transit time over the effective length of the fiber. In general, the crosstalk will accumulate for multiple transmission spans, and for large numbers of signals. Because it can be assumed that the information content of each channel will be uncorrelated, the crossgain modulation will increase linearly with the number of signal channels (S). For long-haul transmission systems where the dispersion is completely or partially compensated per span (of number N), crossgain modulation noise at low frequencies may buildup coherently. For example, if the dispersion “map-height” is 180 ps/nm, the largest walk-off between channels spaced over 20 nm is less than 3.8 ns. Therefore, if the corner frequency is less than 26 MHz, the low-frequency amplitude noise will be the same at each span resulting in the noise being correlated. The penalty would therefore be:

$$\text{Penalty (dBQ)} = 10 \cdot \log \left(\sqrt{1 + N^2(S-1)Q_s^2 \frac{T}{4} A\pi f_{3 \text{ dB}}} \right). \quad (8.69)$$

It is desirable to use multiple pumps to produce a flat gain spectrum. The resulting crosstalk is somewhat complicated by the interaction between copropagating pump wavelengths and the noise transferred by the signals. As an approximation, we might assume that the number of interfering channels will be limited by the number that can be placed upon the gain spectrum from a single Raman pump. From Fig. 8.20, we can estimate that the crosstalk is dominated by about 26 channels on a 100 GHz grid.

Equation (8.69) can be used to estimate the penalties for a NZ-DSF (TrueWave[®] RS) transmission system with 100 km spans, using co- and counter-pumped distributed Raman amplification. Figure 8.21 shows the penalty for the worst-case channel (1530 nm) in a WDM system (26 signals from 1530 to 1556), when amplified using a 1455 nm pump. The bit rate is 40 Gb/s and the Q penalty is based on a linear Q of 6. It is clear that inasmuch as the roll-off frequency for the counter-pumped amplifier is so low, there is negligible impact from crossgain modulation. Copumped amplifiers are likely to be more susceptible to pump-mediated crosstalk because the averaging due to dispersion is less. Significant penalties (greater than 0.1 dB $_Q$), can occur in a single span copumped system with gains greater than 20 dB. Alternatively, similar penalties may result for lower gains of 8 dB when 20 or more spans are used. Other NZ-DSF fiber (such as LEAF) with dispersion zero wavelengths between the pump and signals are likely to show more significant penalties when copumped.

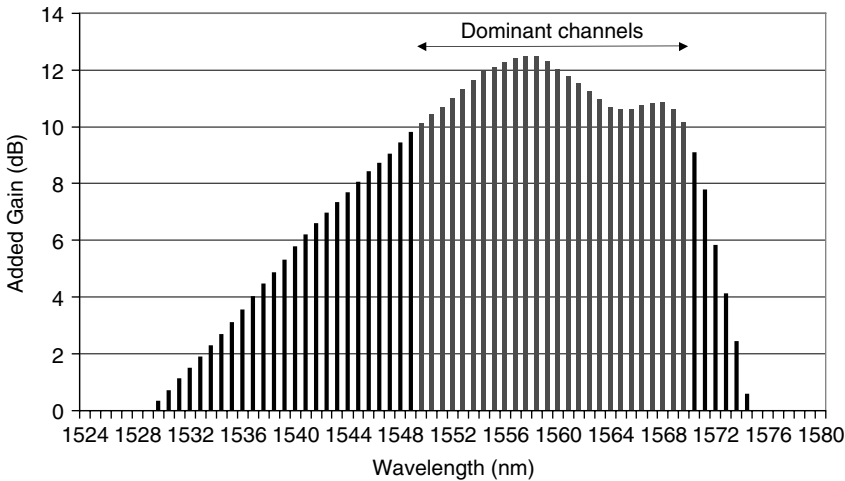


Fig. 8.20. Dominant channels contributing towards signal–signal crosstalk mediated by a single pump wavelength.

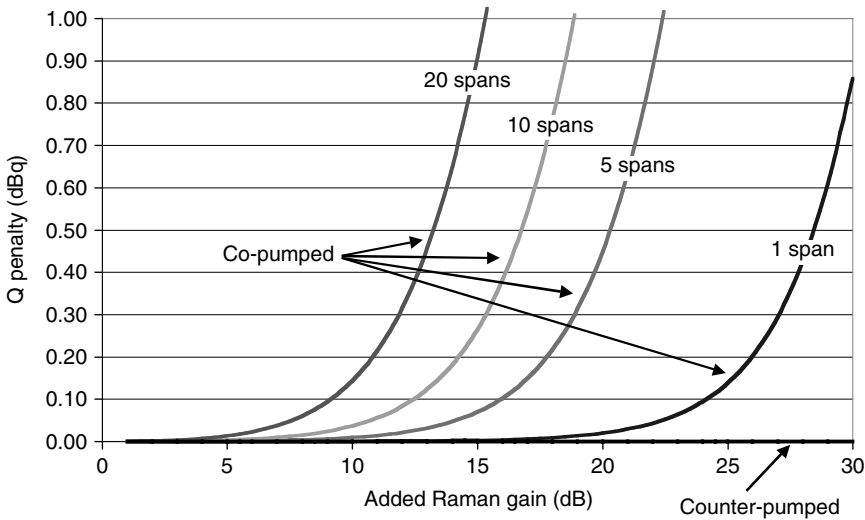


Fig. 8.21. Q penalties for 1 to 20 spans of 100 km TrueWave[®] RS. 26 signals copumped with -5 dBm/ch, and counter-pumped with 0 dBm/ch signal launch power.

8.4. WDM Transients

Although the small-scale effect of signal-to-signal crosstalk via pump modulation has been considered earlier, WDM systems may experience large-scale fluctuations in the input signal powers. This may be due to the adding and dropping of many channels in the course of traffic routing, or due to accidental faults such as a fiber break. In a WDM system, a Raman amplifier will operate in some degree of saturation

such that if the input signal power is reduced, the gain experienced by the remaining channels is increased. The transition between the saturated and unsaturated states can result in both power spikes and power undershoots [9]. Power spikes may result in a higher degree of nonlinearity, error bursts, or damage to optical components. Power undershoots may cause a degradation of signal-to-noise ratio and further burst errors.

Chen and Wong showed that the transients in backward-pumped Raman amplifiers may be modeled using a set of coupled time-varying differential equations that must be solved numerically [9], and Bononi has derived a simplified semianalytical approach [10]. Both methods show the same characteristics, and become more complex as pump-to-pump Raman interactions need to be taken into account [11].

Figure 8.22 shows the signal traces produced when a large step change in signal power enters a counter-pumped Raman amplifier, and saturates the gain [9]. The large overshoot as the signal is added is caused by the unsaturated amplifier gain. The first part of the signal receives a large gain and quickly depletes the pump. Although the leading edge becomes large, there is now less pump power available to the remaining signal. In fact, the trailing signal receives less gain than the steady-state saturated gain of the amplifier and a power undershoot results. For a single pump, the transient lasts approximately three propagation delays of the effective length of the amplifier. In the first propagation delay, the leading edge of the signal causes depletion in the pump. During the second propagation delay, the pump propagates towards the amplifier input. Finally, once the pump fluctuations have subsided, the signal must propagate to the amplifier output.

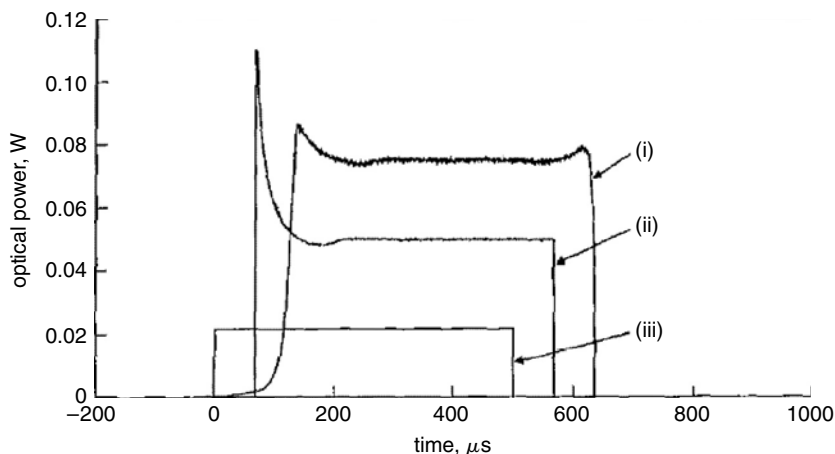


Fig. 8.22. Measured time domain responses of Raman amplifier output and reflection tap: (i) reflected signal $\times 500$; (ii) output; (iii) input signal $\times 10$. Trace printed by permission of Electronics Letters [9]. Source: C-J Chen, W.S. Wong “Transient Effects in Saturated Raman Amplifiers”: IEEE Electronics Letters, Vol. 37, Issue 6 March 2001 (© 2001 IEEE)

8.5. Summary

An analytical model for the transfer of relative intensity noise from the pump to the signal, in co- and counter-pumped Raman amplifiers has been derived. The resulting RIN on the signal channels can be worse than the RIN on the pump lasers. In a counter-pumped Raman amplifier, the different direction of propagation causes both crosstalk and RIN transfer noise to be low-pass filtered. In a copumped Raman amplifier, chromatic dispersion will average the noise transfer. Fibers such as NZ-DSF with their dispersion zero wavelengths between the pump and the signal will exhibit little or no noise averaging at frequencies below 100 MHz. Low-loss, high-dispersion fibers such as NDSF and RDF have -3 dB corner frequencies at about 6 MHz, making these fibers more attractive for copumping distributed Raman amplifiers. Dispersion-compensation fiber may also be appropriate for copumping, although fiber should be selected that has low loss at the pump wavelength to ensure that the gain occurs over a long length of fiber. For short lengths of fiber, such as might be used in a discrete Raman amplifier, dips may appear in the RIN transfer function where averaging over the length of the fiber results in the net transfer tending to zero. Measurements have also been performed on several types of fiber with different loss and dispersion characteristics. These show very good agreement with theory, correctly predicting the depth and frequency position of dips and -3 dB corner frequencies.

A model for the signal-to-signal crosstalk mediated by the pump has also been derived for co- and counter-pumped Raman amplifiers. Data modulation on the signals will result in a small amount of modulation on the Raman pump. This is then transferred to other signals in the gain fiber giving rise to noise. Measurements have been performed on the pump-mediated signal-to-signal crosstalk. The model gives good agreement with measurements, especially at low frequencies.

At low frequencies, distributed Raman amplifiers show a smaller degree of pump-mediated crosstalk in the counter-pumped configuration because the signal power is lower at the point of interaction with the pump at the end of the fiber span. The signal power is quite large at the beginning of the fiber span resulting in more crosstalk for a copumped distributed amplifier.

At low frequencies, discrete Raman amplifiers show a greater degree of pump-mediated crosstalk in the counter-pumped configuration when the gain and signal input power are kept constant. Although the total amount of energy transferred to the pump is the same in both configurations, in a counter-pumped amplifier, energy is more quickly given to the pump as it enters the gain fiber because the signal power is greatest at the output of the amplifier. This results in a second signal experiencing crossgain modulation over a longer length of gain fiber. In most cases random data modulation gives a substantially uniform modulation spectrum at frequencies of interest. The higher corner frequency of copumped amplifiers results in a higher penalty, in spite of the better low-frequency performance compared with counter-pumped amplifiers.

An analysis of system impairment due to RIN transfer shows that for a single span of NDSF, a 0.1 dB $_Q$ penalty, with respect to a noise-only Q of 6 units, is expected for a pump RIN of -108 dB/Hz for copumping and -50 dB/Hz for counter-pumping.

The system is quickly degraded as the RIN on the pump increases beyond these limits. NZ-DSF is expected to be 8 dB less tolerant to pump RIN transfer than NDSF.

An analysis of system impairments due to crossgain modulation shows that there is unlikely to be any impact using counter-pumped amplifiers. Copumped distributed amplifiers using NZ-DSF (TrueWave® RS) are likely to show penalties in a DWDM system with multiple fiber spans. Other NZ-DS fibers may show greater impacts if the dispersion zero lies between the pump and signal wavelengths.

Appendix A8.

A8.1. Pump-Induced Crossgain Modulation in Copumped Raman Amplifiers

In the copumped Raman amplifier, dispersion will cause walk-off between the pump and all signal channels due to their propagation at slightly different velocities. The walk-off is a function of the dispersion of the fiber and will average the transfer of energy from both the signal to the pump and from the pump to another signal.

Using the undepleted pump approximation [1, 2] and considering a small amount of modulation (modulation depth m) at a frequency f applied to the signal, the propagation of the signal at time t and position z , can be described by

$$P_s(z, t) = P_{s0} \exp \left(-\alpha_s z + C_{Rs} P_{p0} \frac{(1 - e^{-\alpha_p z})}{\alpha_p} \right) \left[1 + m \sin \left(2\pi f \left(t - \frac{z}{V_s} \right) + \phi \right) \right], \quad (\text{A8.1})$$

where α_s and α_p are the attenuation at the signal and pump wavelength, respectively (in nepers), V_s is the velocity of the signal wavelength, C_{Rs} is the Raman gain efficiency of the signal wavelength ($\text{W}^{-1} \cdot \text{km}^{-1}$), P_{s0} and P_{p0} are the initial powers (in W) of the signal and pump, respectively, and ϕ is a phase coefficient. Changing the frame of reference to that of the pump, moving at velocity V_p ($z = V_p t$), the signal power at time t is:

$$P_s(t) = \overline{P_s(t)} [1 + m \sin(\eta f t + \phi)], \quad (\text{A8.2})$$

where to simplify notation, two new variables are defined to describe the walk-off (η), and the average optical power:

$$\eta = 2\pi \left(1 - \frac{V_p}{V_s} \right) \quad (\text{A8.3})$$

$$\overline{P_s(t)} = P_{s0} \exp \left(-\alpha_s V_p t + C_{Rs} P_{p0} \frac{(1 - e^{-\alpha_p V_p t})}{\alpha_p} \right). \quad (\text{A8.4})$$

The propagation of the pump can be described by the following differential equation, where the first term represents the linear fiber loss and the second term the loss of energy from the pump at frequency ν_p to the signal at frequency ν_p .

$$\frac{1}{V_p} \frac{dP_p}{dt} = -\alpha_p P_p - \frac{\nu_p}{\nu_s} C_{Rs} P_s P_p. \quad (\text{A8.5})$$

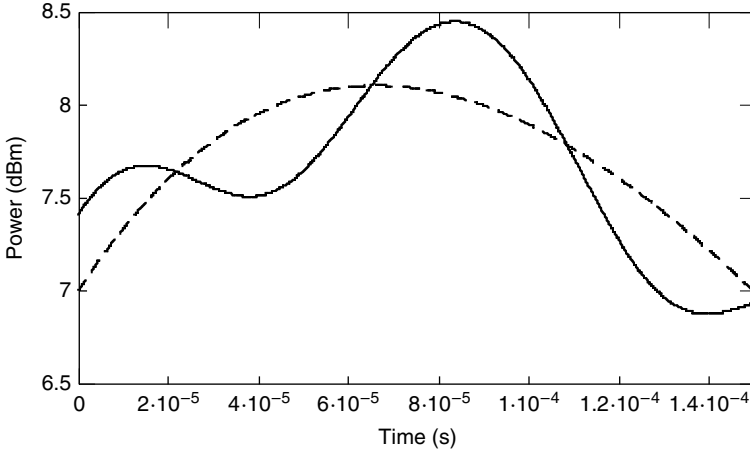


Fig. A8.1. Signal (launch power 5 mW at 1560 nm) as seen by the pump (250 mW at 1440 nm), in a 30 km distributed Raman amplifier (gain 6.3 dB), fiber attenuation 0.21 dB/km. Signal is modulated at 100 MHz and the dispersion zero wavelength is 1560 nm, with $0.08 \text{ ps.nm}^{-2}\text{km}^{-1}\phi = \pi/2$. Dotted line shows mean value.

Integrating both sides, the instantaneous pump power at time t is given by

$$\ln \left(\frac{P_p(t)}{P_{p0}} \right) = -\alpha_p V_p t - \frac{\nu_p}{\nu_s} C_{Rs} V_p \int_0^t \overline{P_s(t)} [1 + m \sin(\eta f t + \phi)] dt. \quad (\text{A8.6})$$

The mean signal power and modulated signal in the reference frame of the pump wave can be seen in Fig. A8.1. It may be noted that in this case, the power profiles at the beginning and end of the fiber are very similar. The resultant modulation on the pump will be the time integral of this function.

The transfer of this pump modulation to a second signal (subscript c) can now be considered, from which the crosstalk will be determined. From Eq. (A8.6), the instantaneous pump power at time t can be approximated because the pump depletion per signal channel is small:

$$\begin{aligned} P_p(t) &\approx P_{p0} \exp \left(-\alpha_p V_p t - \frac{\nu_p}{\nu_s} C_{R1} V_p \int_0^t \overline{P_s(t)} dt \right) \\ &\times \left(1 - \frac{\nu_p}{\nu_s} m C_{R1} V_p \int_0^t \overline{P_s(t)} \sin(\eta f t + \phi) dt \right) \\ &\approx P_{p0} \exp(-\alpha_p V_p t) \left(1 - \frac{\nu_p}{\nu_s} m C_{R1} V_p \int_0^t \overline{P_s(t)} \sin(\eta f t + \phi) dt \right). \end{aligned} \quad (\text{A8.7})$$

The propagation of the second signal at time τ , traveling at velocity V_c and with Raman gain efficiency C_{Rc} , can be described by

$$\frac{1}{V_c} \frac{dP_c}{d\tau} = -\alpha_s P_c + C_{Rc} P_p(\tau) P_c(\tau). \quad (\text{A8.8})$$

Equation (A8.7) can be adjusted to a new frame of reference moving with the second signal ($z = \tau V_c = t V_p$):

$$P_p(\tau) \approx P_{p0} \exp(-\alpha_p V_c \tau) \left(1 - \frac{\nu_p}{\nu_s} m C_{Rs} V_c P_{s0} \int_0^\tau \overline{P_r(\tau)} \sin(\varepsilon f \tau + \phi) d\tau \right), \quad (\text{A8.9})$$

where a new walk-off coefficient ε , and a normalized average power variable $P_r(\tau)$ are defined:

$$\varepsilon = 2\pi \left(1 - \frac{V_p}{V_s} \right) \frac{V_c}{V_p} \quad (\text{A8.10})$$

$$\overline{P_r(\tau)} = \exp \left(-\alpha_s V_c \tau + C_{Rs} P_{p0} \frac{(1 - e^{-\alpha_p V_c \tau})}{\alpha_p} \right) \quad (\text{A8.11})$$

By combining Eqs. (A8.8) and (A8.9), and integrating, the new signal has instantaneous power:

$$\begin{aligned} P_c(\tau) = P_{c0} \exp \left(\int_0^\tau (-\alpha_s V_c + C_{Rc} V_c P_{p0} \exp(-\alpha_p V_c \tau)) d\tau \right) \\ \times \exp \left(- \int_0^\tau \left[C_{Rc} V_c P_{p0} \exp(-\alpha_p V_c \tau) \frac{\nu_p}{\nu_s} m C_{Rs} V_c P_{s0} \right. \right. \\ \left. \left. \times \int_0^\tau \overline{P_r(\tau_x)} \sin(\varepsilon f \tau_x + \phi) d\tau_x \right] d\tau \right). \end{aligned} \quad (\text{A8.12})$$

The first exponential term represents the average signal power at time τ , whereas the second term represents the crosstalk noise from the first signal, mediated by the pump. The ratio of the instantaneous power to the mean power on the second signal can therefore be found and simplified by expanding the exponential for small levels of crosstalk:

$$\begin{aligned} \frac{P_c(T)}{\overline{P_c}(T)} = \exp \left(- \int_0^T \left[C_{Rc} V_c P_{p0} \exp(-\alpha_p V_c \tau) \frac{\nu_p}{\nu_s} m C_{Rs} V_c P_{s0} \right. \right. \\ \left. \left. \times \int_0^\tau \overline{P_r(\tau_x)} \sin(\varepsilon f \tau_x + \phi) d\tau_x \right] d\tau \right) \\ \approx 1 - \int_0^T \left[C_{R2} V_c P_{p0} \exp(-\alpha_p V_c \tau) \frac{\nu_p}{\nu_s} m C_{Rs} V_c P_{s0} \right. \\ \left. \times \int_0^\tau \overline{P_r(\tau_x)} \sin(\varepsilon f \tau_x + \phi) d\tau_x \right] d\tau. \end{aligned} \quad (\text{A8.13})$$

To obtain the modulation transfer, the modulation index (m) can be substituted the ratio of mean square fluctuations to mean power of the first signal (Eq. (A8.14), for and ignoring d.c. terms:

$$m = \sqrt{2} \frac{\sqrt{\langle \delta P_{s0}^2 \rangle}}{P_{s0}}. \quad (\text{A8.14})$$

The modulation transfer function $|H_c(f)|^2$, measured electrically, can be found by squaring and integrating across all phases ϕ :

$$\begin{aligned} |H_c(f)|^2 &= \frac{\langle \delta P_{c0} \rangle^2}{P_c^2(T)} \bigg/ \frac{\langle \delta P_{s0} \rangle^2}{P_{s0}^2} = \left(\frac{v_p}{v_s} \sqrt{2} P_{p0} P_{s0} C_{Rs} C_{Rc} V_c^2 \right)^2 \\ &\times \frac{1}{2\pi} \int_0^{2\pi} \left(\int_0^T \left[\exp(-\alpha_p V_c \tau) \int_0^\tau \overline{P_r(\tau_x)} \sin(\varepsilon f \tau_x + \phi) d\tau_x \right] d\tau \right)^2 d\phi. \end{aligned} \quad (\text{A8.15})$$

This can be rearranged in terms of the added (off-on) Raman gain for both source signal (G_{as}) and the signal receiving the crosstalk (G_{ac}):

$$\begin{aligned} |H_c(f)|^2 &= \left(\sqrt{2} \left(\frac{V_c}{L_{eff}} \right)^2 \frac{v_p}{v_s} \frac{P_{s0}}{P_{p0}} \ln(G_{as}) \ln(G_{ac}) \right)^2 \\ &\times \frac{1}{2\pi} \int_0^{2\pi} \left(\int_0^T \left[\exp(-\alpha_p V_c \tau) \int_0^\tau \overline{P_r(\tau_x)} \sin(\varepsilon f \tau_x + \phi) d\tau_x \right] d\tau \right)^2 d\phi. \end{aligned} \quad (\text{A8.16})$$

Appendix A8.2. Pump-Induced Crossgain Modulation in counter-pumped Configuration

A similar analysis follows for the case where the pump and signals propagate in opposite directions. Here dispersion is considered to be negligible compared to the averaging due to different transit directions. Using the undepleted pump approximation, and considering a small amount of modulation (depth m), at a frequency f applied to the signal, the propagation of the signal at time t and distance z , traveling at velocity V_g is:

$$\begin{aligned} P_s(z, t) &= P_{s0} \exp \left(-\alpha_s z + \frac{C_{Rs} P_{p0}}{\alpha_p} e^{-\alpha_p L} (e^{\alpha_p z} - 1) \right) \\ &\times \left[1 + m \sin \left(2\pi f \left(t - \frac{z}{V_g} \right) + \phi \right) \right]. \end{aligned} \quad (\text{A8.17})$$

Changing our frame of reference to that of the backward traveling pump

($z = L - V_g t$), the signal power at time t is given by

$$P_s(t) = P_{s0} \exp \left(-\alpha_s (L - V_g t) + \frac{C_{Rs} P_{p0}}{\alpha_p} e^{-\alpha_p L} (e^{\alpha_p (L - V_g t)} - 1) \right) \\ \times \left[1 + m \sin \left(2\pi f \left(2t - \frac{L}{V_g} \right) + \phi \right) \right]. \quad (\text{A8.18})$$

The instantaneous pump power $P_p(t)$ can therefore be found by integrating the differential Eq. (A8.5):

$$\ln \left(\frac{P_p(t)}{P_{p0}} \right) = -\alpha_p V_g t - \frac{\nu_p}{\nu_s} C_{Rs} V_g \int_0^t \overline{P_s(t)} [1 + m \sin(2\pi f(2t - T) + \phi)] dt, \quad (\text{A8.19})$$

where the average optical power of the signal is:

$$\overline{P_s(t)} = P_{s0} \exp \left(-\alpha_s V_g (T - t) + \frac{C_{Rs} P_{p0}}{\alpha_p} (e^{-\alpha_p V_g t} - e^{-\alpha_p L}) \right). \quad (\text{A8.20})$$

The instantaneous modulation on the pump wavelength will cause a fluctuation in the gain experienced by a second signal, hence contributing towards crosstalk. In a similar method to the previous analysis for copumped Raman amplifiers, the instantaneous pump power can be referred back to a frame of reference traveling with a second signal, copropagating with the first signal yet counterpropagating with respect to the pump. At time τ , this is:

$$P_p(\tau) = P_{p0} \exp(-\alpha_p V_g (T - \tau)) \left[1 - \frac{\nu_p}{\nu_s} C_{Rs} V_g m P_{s0} \int_\tau^T \overline{P_e(\tau)} \sin(2\pi f 2\tau + \phi') d\tau \right], \quad (\text{A8.21})$$

where $P_e(\tau)$ is the normalized average power:

$$\overline{P_e(\tau)} = \exp \left(-\alpha_s V_g \tau + \frac{C_{Rs} P_{p0}}{\alpha_p} e^{-\alpha_p L} (e^{\alpha_p V_g \tau} - 1) \right). \quad (\text{A8.22})$$

The propagation of the second signal at time τ , copropagating with the first signal will also be described by differential Eq. (A8.8), using the new instantaneous pump power above:

$$P_c(\tau) = P_{c0} \exp \left(\int_0^\tau (-\alpha_s V_c + C_{Rc} V_g P_{p0} \exp(-\alpha_p V_g (T - \tau))) d\tau \right) \\ \times \exp \left(- \int_0^\tau \frac{\nu_p}{\nu_s} C_{Rs} C_{Rc} V_g^2 m P_{p0} P_{s0} \exp(-\alpha_p V_g (T - \tau)) \right. \\ \left. \times \int_\tau^T \overline{P_e(\tau_x)} \sin(2\pi f 2\tau_x + \phi') d\tau_x d\tau \right). \quad (\text{A8.23})$$

The first exponential term represents the average signal power at time τ whereas the second term represents the crosstalk noise from the first signal, mediated by the pump. The ratio of the instantaneous power to the mean power on the second signal

can therefore be found and simplified by expanding the exponential for small levels of crosstalk:

$$\begin{aligned}
 \frac{P_c(T)}{P_c(T)} &= \exp \left(- \int_0^T \frac{v_p}{v_s} C_{Rs} C_{Rc} V_g^2 m P_{p0} P_{s0} \exp(-\alpha_p V_g (T - \tau)) \right. \\
 &\quad \left. \times \int_\tau^T \overline{P_e(\tau_x)} \sin(2\pi f 2\tau_x + \phi') d\tau_x d\tau \right) \\
 &\approx 1 - \frac{v_p}{v_s} C_{Rs} C_{Rc} V_g^2 m P_{p0} P_{s0} \int_0^T \exp(-\alpha_p V_g (T - \tau)) \\
 &\quad \times \int_\tau^T \overline{P_e(\tau_x)} \sin(2\pi f 2\tau_x + \phi') d\tau_x d\tau. \tag{A8.24}
 \end{aligned}$$

As with the copumped analysis, we obtain the modulation transfer function $|H_c(f)|^2$ by substituting the modulation index (m) for the ratio of mean square fluctuations to the mean power of the first signal, ignoring the d.c. terms, squaring and integrating over all phases ϕ :

$$\begin{aligned}
 |H_c(f)|^2 &= \frac{\langle \delta P_{c0} \rangle^2}{P_c^2(T)} \bigg/ \frac{\langle \delta P_{s0} \rangle^2}{P_{s0}^2} = \left(\sqrt{2} C_{Rs} C_{Rc} V_g^2 \frac{v_p}{v_s} P_{p0} P_{s0} \right)^2 \\
 &\quad \times \frac{1}{2\pi} \int_0^{2\pi} \left[\int_0^T \exp(-\alpha_p V_g (T - \tau)) \right. \\
 &\quad \left. \times \int_\tau^T \overline{P_e(\tau_x)} \sin(4\pi f \tau_x + \phi') d\tau_x d\tau \right]^2 d\phi'. \tag{A8.25}
 \end{aligned}$$

This can be rearranged in terms of the added (off-on) Raman gain for both source signal (G_{as}) and the signal receiving the crosstalk (G_{ac}):

$$\begin{aligned}
 |H_c(f)|^2 &= \left(\sqrt{2} \left(\frac{V_g}{L_{eff}} \right)^2 \frac{v_p}{v_s} \frac{P_{s0}}{P_{p0}} \ln(G_{as}) \ln(G_{ac}) \right)^2 \\
 &\quad \times \frac{1}{2\pi} \int_0^{2\pi} \left[\int_0^T \exp(-\alpha_p V_g (T - \tau)) \right. \\
 &\quad \left. \times \int_\tau^T \overline{P_e(\tau_x)} \sin(4\pi f \tau_x + \phi') d\tau_x d\tau \right]^2 d\phi'. \tag{A8.26}
 \end{aligned}$$

References

- [1] R.H. Stolen, J.P. Gordon, W.J. Tomlinson, and H.A. Haus, Raman response function of silica-core fibers, *Optic. Soc. Am. B*, 6; 6 (June), 1989.
- [2] A.J. Stentz, S.G. Grubb, C.E. Headley III, J.R. Simpson, T.Strasser, and N. Park, Raman amplifier with improved system performance, *OFC '96 Technical Digest*, TuD3, 1996.
- [3] M.D. Mermelstein, C. Headley, and J.-C. Bouteiller, RIN transfer analysis in pump depletion regime for Raman fibre amplifiers, *Electron. Lett.*, 38; 9 (25th April), 2002.

- [4] J.S. Wey, D.L. Butler, M. F. Van Leeuwen, L.G. Joneckis, and J. Goldhar, Crosstalk bandwidth in backward pumped fiber Raman amplifiers, *Photon. Technol. Lett.*, 11; 11 (Nov.), 1999.
- [5] F. Forghieri, R.W. Tkach, and A.R. Chraplyvy, Bandwidth of crosstalk in Raman amplifiers, *OFC'94*, FC6, 1994.
- [6] R.G. Smith, Optical power handling capacity of low loss optical fibers as determined by stimulated Raman and Brillouin scattering, *Appl. Optics Lett.*, 11; 11 (Nov.), 1972.
- [7] A. Papoulis, *Probability, Random Variables, and Stochastic Processes*, 3d ed., New York: McGraw-Hill, 298–301.
- [8] A. Papoulis, *Probability, Random Variables, and Stochastic Processes*, 3d ed., New York: McGraw-Hill, 323–324.
- [9] C.-J. Chen, and W.S. Wong, Transient effects in saturated Raman amplifiers, *Electron. Lett.*, 37; 6, 371–373, 2001.
- [10] A. Bononi, Transient gain dynamics in saturated counter-pumped Raman amplifiers, *OFC 2002*, ThR1, March, 2002.
- [11] S. Gray, Transient gain dynamics in wide bandwidth discrete Raman amplifiers, *OFC 2002*, ThR2, March, 2002.
- [12] R.G. Smith, Optical power handling capacity of low loss optical fibers as determined by stimulated Raman and Brillouin scattering, *Appl. Optics Lett.*, 11; 11 (Nov.), 1972.
- [13] G.P. Agrawal, *Non-linear Fiber Optics*, 2nd ed., San Diego: Academic Press, 320.

Chapter 9

Forward, Bidirectional, and Higher-Order Raman Amplification

Stojan Radic

9.1. Raman Amplification in Unidirectional and Bidirectional Optical Transmission

Distributed Raman amplification can be achieved by optical pumping at either end of the fiber. In the copumped Raman configuration, the pump is launched at the front end and copropagates with the optical signal along the transmission span. In the counter-pumped architecture that is widely deployed, the optical pump and signal launch at the opposite ends. Finally, Raman pumping at both ends of the transmission span characterizes the bidirectional scheme. The latter term is also used for optical links that support two-way signal traffic and often leads to confusion. To avoid this ambiguity, we designate optical transmission as unidirectional or bidirectional, independently of any amplification considerations. In unidirectional transmission lines, all signals travel in the same direction. Bidirectional network functionality is supported by a separate fiber that carries signal traffic propagating in the opposite direction. In contrast, bidirectional transmission can be used to realize two-way traffic within a single fiber line: counterpropagating signal traffic is launched and received at the opposite ends of the optical link. A bidirectionally *pumped* fiber span can support both uni- and bidirectional signal transmission. A unidirectionally pumped span, however, almost exclusively supports unidirectional signal traffic.

Historically, unidirectional optical links have been constructed using Raman counterpumping in order to avoid a set of impairments associated with copropagating pumps and signals [1–7]. The preamplifier nature of backward pumping is readily recognized: it increases optical signal power at the end of the span, prior to its reception or another amplification stage. The introduction of a copropagating Raman pump at the beginning of the span allows for considerably more freedom in managing signal power evolution and, consequently, the received optical signal-to-noise ratio (OSNR). Even more importantly, full or partial fiber transparency can be achieved by at least two separate sets of Raman pumps, alleviating the requirements for high pumping power at a single fiber end. The precise gain contributions from Raman co- and counterpumping depend on the signal spectral distribution and the physical characteristics of the fiber.

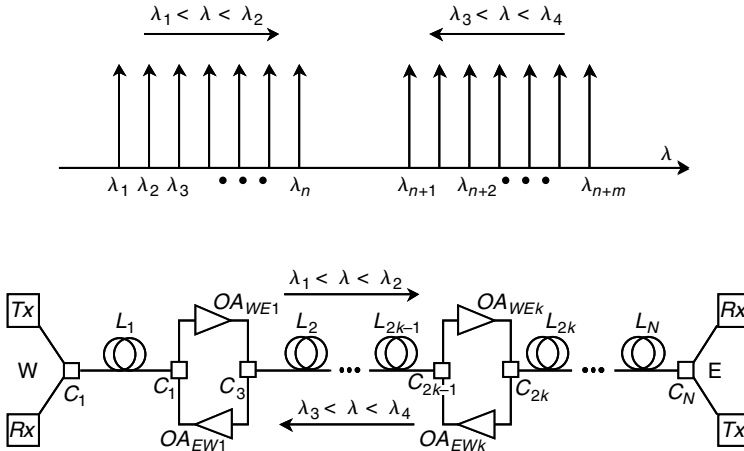


Fig. 9.1. Banded bidirectional optical link. The blue ($\lambda_1 < \lambda < \lambda_2$) band travels from East to West, whereas the red ($\lambda_3 < \lambda < \lambda_4$) band travels in the opposite direction. A dark band ($\lambda_2 < \lambda < \lambda_3$) isolates counterpropagating optical signals. Tx is the optical transmitter, Rx is the optical receiver, OA is the optical amplifier, and C is the routing element (bandsplitter).

Bidirectional pumping, an option in unidirectional transmission, is required in a bidirectional line utilizing distributed amplification. Until recently, bidirectional optical transmission was achieved using lumped amplification exclusively [8–14]. This limitation imposed artificial constraints on the capacity and reach of bidirectional optical links. Bidirectional transmission can be realized in banded, interleaved, or hybrid form, with different distributed amplification implementations. In a banded bidirectional scheme, the available optical spectrum ($\lambda_1 < \lambda < \lambda_4$) is divided into three domains as shown in Fig. 9.1. The short (blue) band ($\lambda_1 < \lambda < \lambda_2$) propagates in the West–East (WE) direction and is amplified at the amplifier nodes OA_{WE} that can be realized in either lumped or distributed form. The long (red) band traffic ($\lambda_3 < \lambda < \lambda_4$) propagates in the opposite direction and, under ideal circumstances, does not interact with any signal from the blue band. The allocation of the dark band ($\lambda_2 < \lambda < \lambda_3$) ensures that optical routing elements (C_k , $k = 1, n$) can be physically realized in order to minimize any crosstalk between counterpropagating traffic [8]. It is important to note that the banded bidirectional scheme differs little from the unidirectional architecture: two separate bands, when isolated properly from each other, are expected to lead to system performance comparable to that associated with unidirectional transmission.

The interleaved bidirectional scheme [14] combines spectrally alternating, counterpropagating optical signals, as illustrated in Fig. 9.2. Channel interleaving in principle eliminates the need for dark band allocation. All signals are allocated within the continuous band ($\lambda_1 < \lambda < \lambda_2$) and require optical amplifiers with identical spectral response for each direction. It can be shown that the interleaved bidirectional channel plan possesses a qualitative advantage in the presence of substantial four-wave mixing (FWM) generation [5, 14]. A predetermined FWM penalty dictates the optical power and frequency separation between two copropagating signals [15]. Spectral

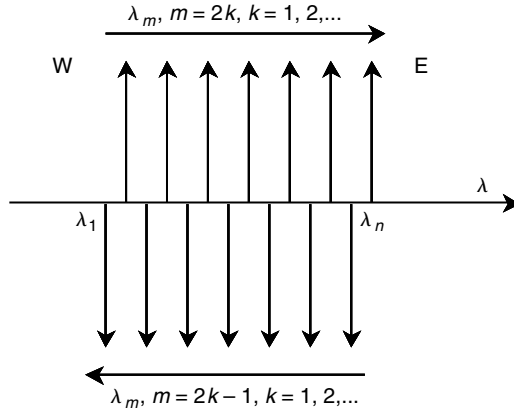


Fig. 9.2. Interleaved bidirectional signal allocation. The even channels ($\lambda_m, m = 2k, k = 1, 2, \dots$) travel in the west–east direction, whereas the odd channels ($\lambda_m, m = 2k - 1, k = 1, 2, \dots$) are transmitted in the opposite direction.

efficiency, defined as an aggregate information capacity carried within the unit of optical spectra, is directly proportional to the channel density. Interleaved bidirectional architecture in principle allows for doubling of spectral efficiency in FWM limited links: although separation between neighboring copropagating channels is preserved, total channel density can be doubled without additional FWM generation. Unfortunately, it can be shown [5, 14, 16] that this advantage comes at a price of increased crosstalk generation that cannot be suppressed by simple path-blocking geometries found in unidirectional and banded bidirectional links.

Finally, a hybrid bidirectional scheme can be constructed by mixing the interleaved and banded schemes, as illustrated in Fig. 9.3. The selection of a particular architecture is typically a complex process that takes into account the quality of the fiber link, the startup and upgrade plans, and the overall system performance in both

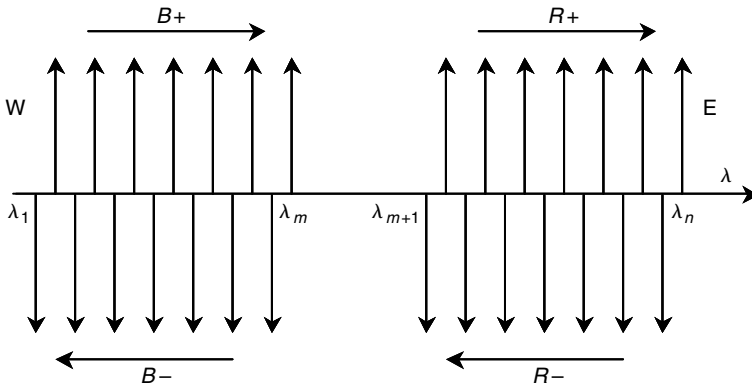


Fig. 9.3. Hybrid bidirectional scheme. Eastward traveling signals are divided into blue ($B+$) and red ($R+$) bands, and interleaved with the eastward traveling signals ($B-$ and $R-$).

partially and fully deployed capacity conditions. Given the requirement that two-way traffic has to be achieved from the start, the initial operation may begin in either the banded or interleaved mode. In a banded startup mode, two counterpropagating bands are first selected ($B + /R-$ or $R + /B-$). The subsequent link upgrade is then performed by introducing the interleaved bands (addition of $R + /B-$ or $B + /R-$). Similarly, an interleaved mode can be used in the startup regime ($B + /B-$ or $R + /R-$), to be followed by a banded upgrade mode.

9.2. Physics of Bidirectional Raman Pumping

9.2.1. Multiple Reflection Model

A rigorous description of bidirectional Raman pumping poses a considerably more difficult problem than that of unidirectional pumping. A complex bidirectional power exchange takes place among the participating signal, pump, and noise waves due to Raman, Rayleigh, and Brillouin interactions [17–25]. Consider the general case of a bidirectionally pumped optical fiber that supports two-way signal traffic, as illustrated in Fig. 9.4. Optical signals S_{\pm} are amplified by co- and counterpropagating

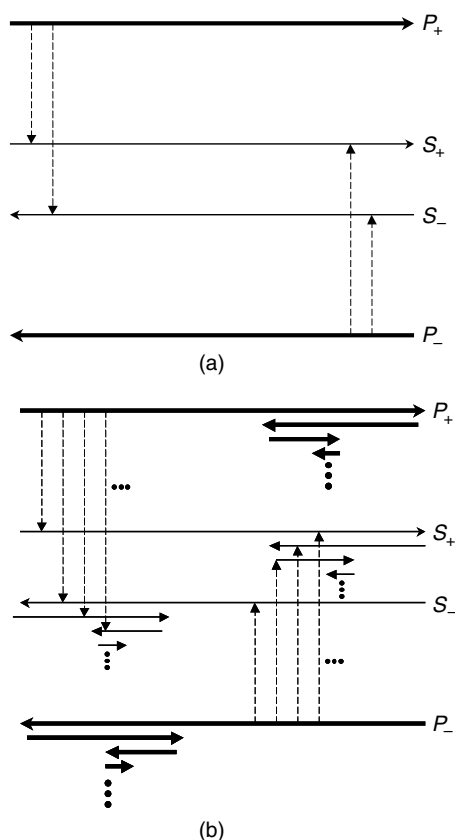


Fig. 9.4. (a) Simplified bidirectional Raman pumping model. Power exchange (dashed arrows) only occurs between the signals and pumps; (b) multiple-reflection model. Power exchange occurs among the pumps, signals, and reflected waves.

Raman pumps P_{\pm} inserted at both fiber ends. In a simplified model (Fig. 9.4(a)), only pump–signal Raman interactions are retained to describe amplification in each direction. A more realistic description of the process includes power transfer via multiple reflections among the signal and pump waves, as illustrated in Fig. 9.4(b). A portion of the signal power is backreflected due to either discrete or Rayleigh backscattering (RB). RB is a fundamental property of the transmission fiber and must be accounted for even in the case of negligible facet (end) reflections. The backscattered signal is amplified by the Raman pumps, and reflected yet again. The process of multiple intrafiber reflections and Raman amplification is repeated indefinitely, and applies not only to the signal, but also to all pump and generated noise waves. Further degrees of complexity are introduced by pump–pump, signal–noise, and pump–noise Raman interactions among multiply reflected optical waves. Finally, Brillouin scattering is yet another interaction channel that can influence the signal power exchange within the bidirectionally pumped fiber span.

A collective of Raman pumps, signals, and inserted and generated noise defines the total optical field propagating in each direction along the transmission line. Spatially evolving power spectral density is associated with each direction, as illustrated in Fig. 9.5. The spectral component $S_{\pm}(z, \omega_j)$ in this notation may represent a pump, a signal, or noise, depending on its frequency. To describe the power evolution along the fiber span, one has to account for Raman- and Rayleigh-mediated interactions among the existing and generated spectral components, in both propagation directions. We start this analysis by considering a forward propagating spectral component $S_{+}(z, \omega_j)$ entering an infinitesimally small section of the fiber $[z; z + \Delta z]$. Depending on its relative frequency position, the spectral component $S_{+}(z, \omega_j)$ can either receive or transfer optical power via the Raman interaction. Co- and counterpropagating components within the $\omega > \omega_j$ spectral domain will act as pumps, transferring elemental powers to $S_{+}(z, \omega_j)$:

$$\Delta_1 S_{+}(z, \omega_j) = g(\omega_k, \omega_j) S_{+}(z, \omega_j) S_{+}(z, \omega_k), \quad (9.1)$$

$$\Delta_2 S_{+}(z, \omega_j) = g(\omega_k, \omega_j) S_{+}(z, \omega_j) S_{-}(z, \omega_k), \quad (9.2)$$

where $g(\omega_k, \omega_j)$ is the normalized Raman gain coefficient [17–20] ($g(\omega_k, \omega_j) = g_R(\omega_k, \omega_j)/A_{eff}$), $\omega_k > \omega_j$, and Δ_1 and Δ_2 correspond to pumping by a co- and counterpropagating wave, respectively. This power transfer takes place regardless of the component nature: $S_{+}(z, \omega_j)$ will be pumped by a signal, pump, or noise wave, as long as the condition $\omega_k > \omega_j$ is satisfied. At the same time, $S_{+}(z, \omega_j)$ acts as a pump with respect to lower frequency waves, leading to the elemental power decrease

$$\Delta_3 S_{+}(z, \omega_j) = -g(\omega_i, \omega_j) S_{+}(z, \omega_j) S_{+}(z, \omega_i) \quad (9.3)$$

$$\Delta_4 S_{+}(z, \omega_j) = -g(\omega_i, \omega_j) S_{+}(z, \omega_j) S_{-}(z, \omega_i), \quad (9.4)$$

where $\omega_i < \omega_j$. Rayleigh backscattering and fiber loss (α) will contribute to the magnitude of $S_{+}(z, \omega_j)$ as follows.

$$\Delta_5 S_{+}(z, \omega_j) = \gamma(\omega_j) S_{-}(z, \omega_j) \quad (9.5)$$

$$\Delta_6 S_{+}(z, \omega_j) = -\alpha(\omega_j) S_{+}(z, \omega_j). \quad (9.6)$$

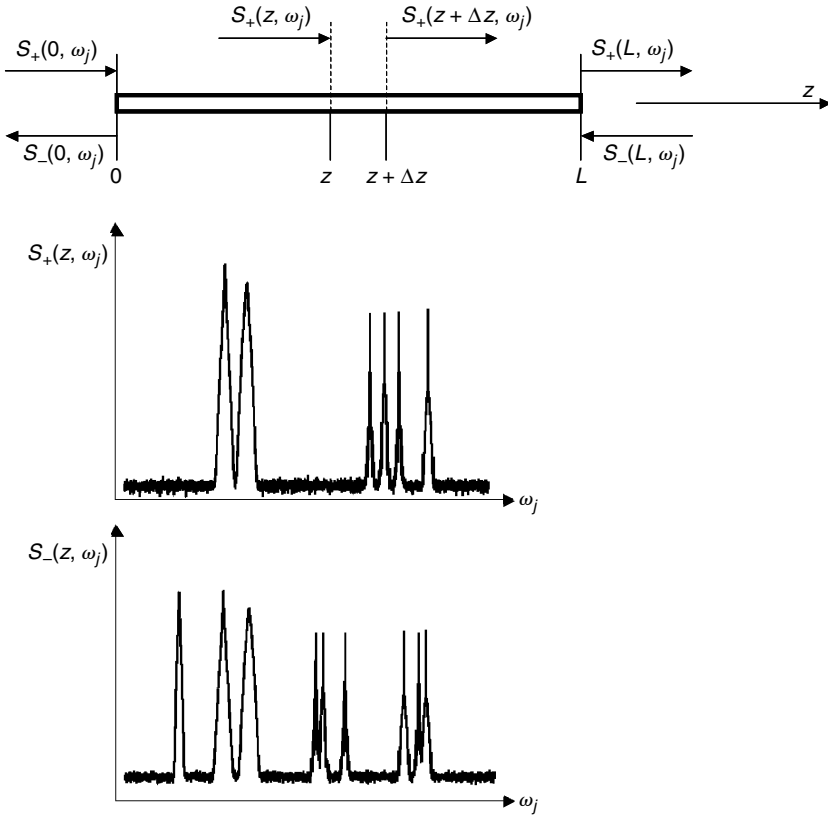


Fig. 9.5. Generalized bidirectional propagation analysis. Spectra of total forward and backward propagating optical fields $S_{\pm}(z, \omega)$ include pumps, signals, and inserted and generated noise.

Spectral summation of the elemental contributions Δ_{1-6} describes the power exchange taking place within the infinitesimal fiber section $[z; z + \Delta z]$. A first-order differential relation can therefore define the spatial evolution of the spectral component $S_+(z, \omega)$:

$$\begin{aligned}
 \frac{dS_+(z, \omega)}{dz} = & -\alpha S_+(z, \omega) + \gamma S_-(z, \omega) \\
 & + \int_{\Omega > \omega} g(\omega, \Omega) [S_+(z, \Omega) + S_-(z, \Omega)] S_+(z, \omega) d\Omega \\
 & - \int_{\Omega < \omega} g(\omega, \Omega) [S_+(z, \Omega) + S_-(z, \Omega)] S_+(z, \omega) d\Omega \\
 & + \frac{h\omega}{\pi} \int_{\Omega > \omega} g(\omega, \Omega) [S_+(z, \Omega) + S_-(z, \Omega)] d\Omega \\
 & - \frac{h\omega}{\pi} \int_{\Omega < \omega} g(\omega, \Omega) [S_+(z, \Omega) + S_-(z, \Omega)] d\Omega.
 \end{aligned} \tag{9.7}$$

In a similar manner, the power of the counterpropagating wave $S_-(z, \omega)$ can be modeled as follows.

$$\begin{aligned}
 \frac{dS_-(z, \omega)}{dz} = & +\alpha S_-(z, \omega) + \gamma S_+(z, \omega) \\
 & + \int_{\Omega > \omega} g(\omega, \Omega) [S_+(z, \Omega) + S_-(z, \Omega)] S_-(z, \omega) d\Omega \\
 & - \int_{\Omega < \omega} g(\omega, \Omega) [S_+(z, \Omega) + S_-(z, \Omega)] S_-(z, \omega) d\Omega \\
 & + \frac{h\omega}{\pi} \int_{\Omega > \omega} g(\omega, \Omega) [S_+(z, \Omega) + S_-(z, \Omega)] d\Omega \\
 & - \frac{h\omega}{\pi} \int_{\Omega < \omega} g(\omega, \Omega) [S_+(z, \Omega) + S_-(z, \Omega)] d\Omega. \tag{9.8}
 \end{aligned}$$

Equations (9.7) and (9.8) represent a rigorous bidirectional model that can be used to accurately predict the behavior of complex optical links incorporating Raman amplification [24–26]. A more sophisticated model [24] would also account for temperature dependence of the transmission fiber. The numerical implementation of this model requires multiple iterations in order to reach the self-consistent solution for counterpropagating optical fields. We illustrate the use of the model by calculating the performance of various pumping architectures over a 200 km nonzero dispersion-shifted (NZDSF) span. In the first example, illustrated in Fig. 9.6(a), a forward propagating signal is amplified by a forward propagating Raman pump. At the maximal pump level (~ 1 W), the transparency condition (on-off gain equal to the span loss) is achieved with low input signal power (-20 dBm). The increase in launched signal power results in considerable pump depletion and eventual loss of transparent link operation. Figure 9.6(b) illustrates the backward Raman pumping of a 200 km NZDSF optical link using the identical signal/pump power budget. The increase in launched signal power in this case results in a more gradual decrease of the total Raman gain. The signal is weakened considerably before being amplified by the counterpropagating Raman pump, resulting in less pump depletion than in the previous example. A bidirectionally pumped unidirectional link is illustrated in Fig. 9.6(c), demonstrating link transparency at identical co- and counterpumping settings of 500 mW. Finally, the performance of bidirectionally pumped bidirectional transmission is calculated and plotted in Fig. 9.6(d) for various launched signal powers.

9.2.2. Single-Pass Analytic Models

The rigorous model described in Section 9.2.1 can be used to accurately design and analyze complex transmission schemes with an arbitrary number of Raman pumps and complex, two-way signal patterns. However, a qualitative understanding of pump–signal interaction might be gained without resorting to the extensive numerical computations required by this model. A simplified, single-pass bidirectional Raman model [19–21] is often used to estimate distributed gain and noise performance. This model assumes that the fiber can be reduced to sections in which either co- or counterpropagating Raman amplification dominates. Polarization effects are not considered in this model.

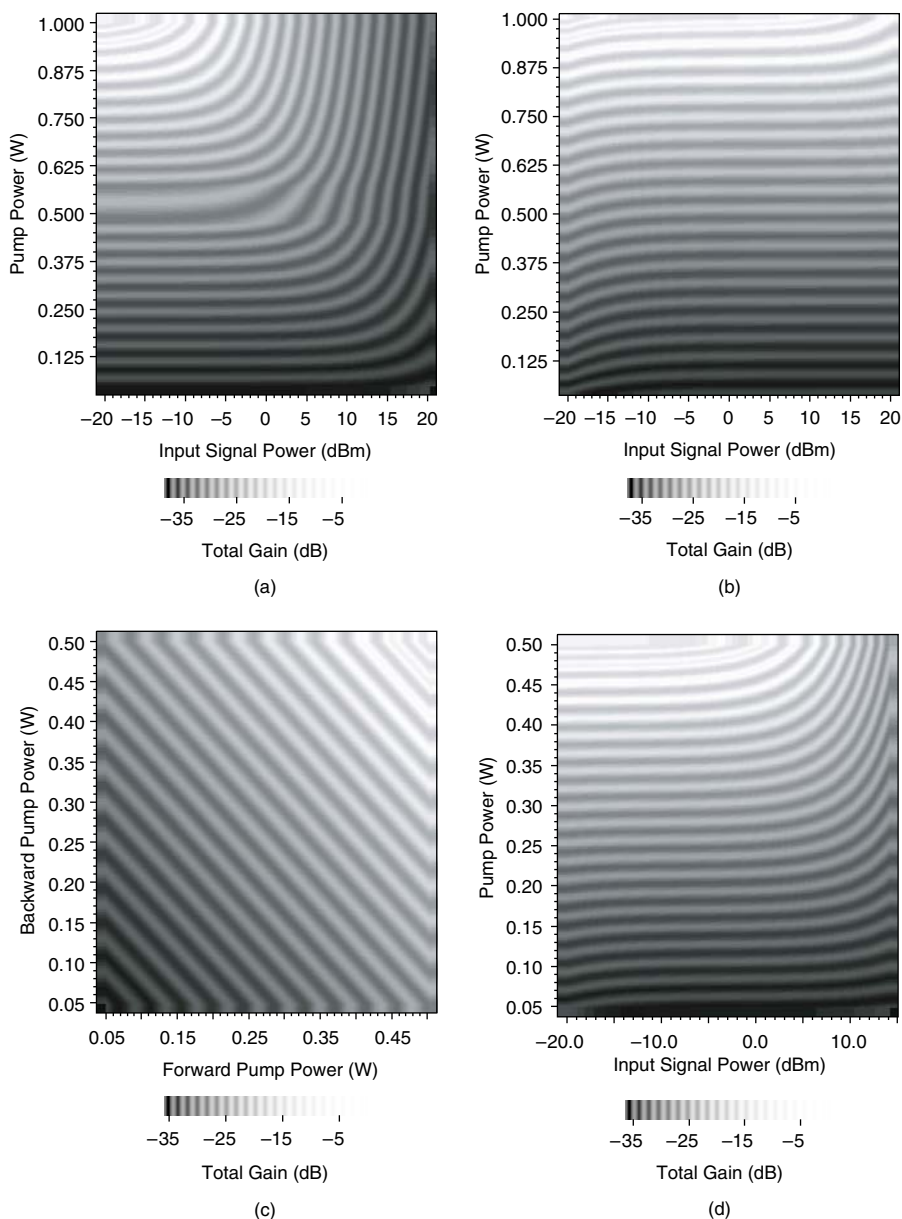


Fig. 9.6. (a) Forward pumped unidirectional optical transmission; (b) backward pumped unidirectional transmission; (c) bidirectionally pumped unidirectional transmission. The input signal power is -20 dBm; and (d) bidirectionally pumped bidirectional transmission with symmetric launch conditions. In each simulation the NZDSF is 200 km long, has a loss of 0.2 dB/km, an effective area of $50 \mu\text{m}^2$ and a Rayleigh scattering coefficient of 0.7 m^{-1} . The pump and signal frequencies are separated by 12 THz. A Raman gain profile with peak ($7 \times 10^{-8} \text{ m/W}$) at 13 THz away from the pump was used in all simulations.

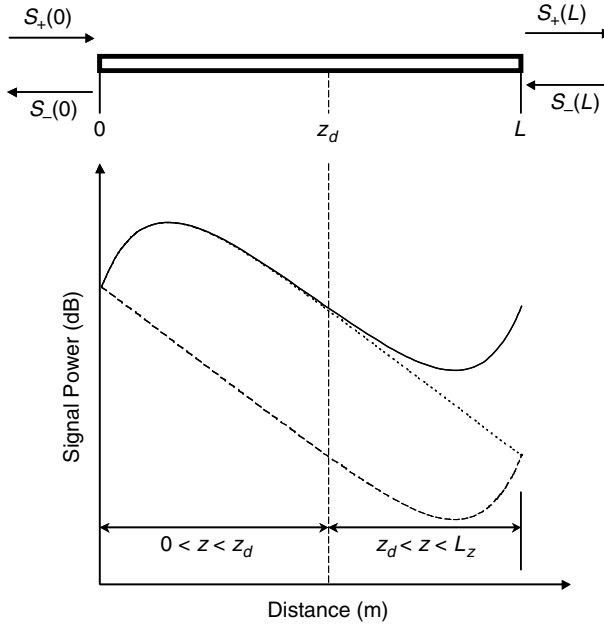


Fig. 9.7. Simplified single-pass model. The fiber is sectioned into segments with a dominant forward and backward propagating Raman pump. Power evolution of forward traveling signal is plotted in presence of forward (dotted line), backward (dashed), and bidirectional Raman pumping (solid line).

Consider a fiber span with signal and pump waves launched at each end, as illustrated in Fig. 9.7. In the absence of backward pumping ($P_- = 0$) and close to the end of a sufficiently long fiber, the power evolution of the forward signal resembles that of unamplified transmission (dotted line). The signal in this region is only influenced weakly by the forward propagating pump. Following this argument [19, 20], one can divide the fiber span into front ($z < z_d$) and rear ($z > z_d$) sections in order to calculate signal power evolution. Similarly, if forward pumping is replaced by backward pumping ($P_+ = 0$), the signal power is altered only weakly by the counterpropagating pump P_- within the $z < z_d$ interval (long dashed line). The evolution of the bidirectionally pumped signal can therefore be calculated by considering the co- and counterpropagating cases separately within two distinct fiber segments (solid line). The partial solutions are required to satisfy a common boundary condition at $z = z_d$. The propagation of the backward signal (S_-) can be described in a similar fashion.

Analytic expressions describing pump and signal propagation can be found if we assume that the launched signal power remains small in comparison to the launched power of the copropagating pumps [19, 20] ($S_+(0) \ll P_+(0)$, $S_-(L) \ll P_-(L)$). Furthermore, we assume that the signal power is insufficient to induce the significant depletion of the counterpropagating pump [20] ($S_+(z)_{z > z_d} \ll P_-(z)_{z > z_d}$, $S_-(z)_{z < z_d} \ll P_+(z)_{z < z_d}$). The pump–signal power exchange within the front ($z < z_d$) fiber section

can be described using a simple set of first-order differential equations [20]:

$$\frac{dS_+}{dz} = gP_+S_+ - \alpha S_+ \quad (9.9)$$

$$\frac{dS_-}{dz} = -gP_+S_- + \alpha S_- \quad (9.10)$$

$$\frac{dP_+}{dz} = -g\frac{\omega_p}{\omega_s}P_+S_+ - \alpha S_+. \quad (9.11)$$

Equations (9.9) to (9.11) were further simplified by assuming a constant Raman gain coefficient within the spectral region of interest ($g(\omega_p, \omega_s) = g = \text{constant}$). A similar set of equations describes signals and pumps within the rear ($z > z_d$) fiber section [30]:

$$\frac{dS_+}{dz} = gP_-S_+ - \alpha S_+ \quad (9.12)$$

$$\frac{dS_-}{dz} = gP_-S_- - \alpha S_- \quad (9.13)$$

$$\frac{dP_-}{dz} = g\frac{\omega_p}{\omega_s}S_-P_- + \alpha P_-. \quad (9.14)$$

Equations (9.8) to (9.14) are solved analytically for the forward propagating signal, resulting in expressions:

$$S_+(z) = S_+(0) \frac{e^{\eta_+(1-e^{-\alpha z})}}{1 + \chi_+ e^{\eta_+(1-e^{-\alpha z})}} e^{-\alpha z}, \quad z < z_d \quad (9.15)$$

$$S_+(z) = S_+(z_d) \frac{e^{\eta_- e^{-\alpha(L-z)}} + \chi_- e^{\eta_-}}{e^{\eta_- e^{-\alpha(L-z_d)}} + \chi_- e^{\eta_-}} e^{-\alpha(z-z_d)}, \quad z > z_d, \quad (9.16)$$

where $\eta_+ = gP_+(0)/\alpha$, $\eta_- = gP_-(L)/\alpha$, $\chi_+ = \omega_p/\omega_s P_+(0)/\alpha$, and $\chi_- = \omega_p/\omega_s P_-(L)/\alpha$. The total signal gain can be calculated simply by concatenating expressions (9.15) and (9.16). The accuracy of the approximation depends critically on the selection of the division point (z_d). The obvious choice is to select the inflection point at which the signal reaches its minimum along the fiber [19] ($z_d = z_{\min}$). However, this choice necessarily neglects the power transfer from the backward pump to the forward propagating signal in the vicinity of z_{\min} . It can be shown that symmetric fiber segmentation [20] ($z_d = L/2$) results in a more accurate approximation of the signal evolution function. This midspan division is substituted in Eqs. (9.15) and (9.16) to calculate the signal power at the end of the fiber span:

$$S_+(L) = S_+(0) \frac{e^{\eta_+(1-e^{-\alpha L/2})}}{1 + \chi_+ e^{\eta_+(1-e^{-\alpha L/2})}} \frac{e^{\eta_- (1 + \chi_-)}}{e^{\eta_- e^{-\alpha L/2}} + \chi_- e^{\eta_-}} e^{-\alpha L}. \quad (9.17)$$

Equation (9.17) allows us to express the signal gain in a bidirectionally pumped transmission span in the relatively simple form:

$$G = \frac{S_+(L)}{S_+(0)e^{-\alpha L}} = \frac{e^{\eta_+(1-e^{-\alpha L/2})}}{1 + \chi_+ e^{\eta_+(1-e^{-\alpha L/2})}} \frac{e^{\eta_- (1 + \chi_-)}}{e^{\eta_- e^{-\alpha L/2}} + \chi_- e^{\eta_-}}. \quad (9.18)$$

In most cases of practical interest, the signal is attenuated substantially after traveling through half of the transmission span, which allows the last relation to be approximated by

$$G = \frac{e^{\eta_+ + \eta_-}}{1 + \chi_+ e^{\eta_+}} \frac{1 + \chi_-}{e^{\eta_-} e^{-\alpha L/2} + \chi_- e^{\eta_-}}. \quad (9.19)$$

The absence of a backward signal allows further simplification of the last relation. The gain associated with bidirectionally pumped, unidirectional signal transmission ($\chi_- = g P_-(L)/\alpha = 0$) is written as

$$G = \frac{e^{\eta_+ + \eta_- (1 - e^{-\alpha L/2})}}{1 + \chi_+ e^{\eta_+}} \xrightarrow{e^{-\alpha L/2} \approx 1} \frac{e^{\eta_+ + \eta_-}}{1 + \chi_+ e^{\eta_+}}. \quad (9.20)$$

On a logarithmic scale, the signal gain is directly proportional to the powers of co- and counterpropagating pumps. The gain compression term ($\chi_+ e^{\eta_+}$) scales linearly with the ratio of the input signal and forward pump powers. Physically, gain compression is caused by forward pump depletion. In most cases of practical interest the pump depletion is negligible ($\chi_+ e^{\eta_+} \ll 1$), leading to a particularly instructive relation for the logarithmic signal gain:

$$G_{\text{dB}} = 4.3(\eta_+ + \eta_- - \chi_+ e^{\eta_+}). \quad (9.21)$$

Consider a practical transmission example that uses the NZDSF fiber characterized by $A_{\text{eff}} = 55 \mu\text{m}^2$, $g \sim 0.4 \times 10^{-13} \text{ m/W}$, $\alpha = 0.23 \text{ dB/km}$ and launched signal power of $S_+(0) = 0.1 \text{ mW}$. Because $\omega_s/\omega_p \sim 1$, the gain compression factor ($4.3\chi_+ e^{\eta_+}$) is approximately $0.43e^{P_+(0)/75}/P_+(0)$, where the launched forward pump power $P_+(0)$ is expressed in milliwatts. Increase in pump power from 100 to 500 mW elevates the gain compression factor from 0.017 to 0.73, which is considered to be small in comparison to the total signal gain in both cases.

Equations (9.15) and (9.16) can be used to estimate the feasible span reach of a bidirectionally pumped optical line [20]. Neglecting the nonlinear signal distortion and any additional crosstalk mechanisms, the span reach is uniquely determined by the minimum acceptable OSNR at the end of the link. The signal is expected to maintain high power and OSNR within the short distance from the launch point. The copropagating Raman pump, playing the role of a distributed signal booster, is typically used to extend this distance farther from the insertion point. In contrast, the backward propagating Raman pump is used to create a distributed preamplifier section on the opposite end of the fiber span. Given the fixed counterpropagating pump power, the OSNR at the end of the span is largely determined by the signal power entering the distributed preamplifier section. A significant loss of signal power before the signal encounters the backward pump will result in a decrease of the overall OSNR. Therefore, a minimal signal power has to be maintained along the entire length of the bidirectionally pumped fiber span. By differentiating Eq. (9.16), the minimal power of the forward propagating signal (S_+^{min}) can be found:

$$S_+^{\text{min}} = S_+(0) \frac{\eta_- e^{\eta_+}}{1 + \chi_+ e^{\eta_+}} e^{1 - \alpha L}, \quad (9.22)$$

where the assumptions of a long span ($\exp(-\alpha L/2) \ll 1$) and the absence of counterpropagating traffic ($\chi_- = 0$) have been made. Given the acceptable minimal signal power, the maximal span reach can be found:

$$L_{\max} = -\frac{1}{\alpha} \ln \left(\frac{S_+^{\min}}{S_+(0)} (e^{-\eta_+} + \chi_+) \right) + \frac{1}{\alpha} \ln \eta_- + \frac{1}{\alpha}. \quad (9.23)$$

To illustrate the practical use of this relation, assume that 300 mW Raman pumps are used at each end of NZDSF fiber ($A_{eff} = 55 \mu\text{m}^2$, $g \sim 0.4 \times 10^{-13} \text{ m/W}$, and $\alpha = 0.23 \text{ dB/km}$). By requiring that the minimal signal power remain within 10 dB of the launched power along the entire span, one finds the feasible span reach to be approximately 190 km.

9.2.3. Noise in Bidirectionally Pumped Fiber Span and Concatenated Links

Smith's analysis [17] of spontaneous noise generation can be adapted to the bidirectionally pumped fiber span. Consider an infinitesimally short section dz located at a distance z from the beginning of the span. The level of amplified spontaneous emission (ASE) generated along this elemental fiber section depends on the local powers of the forward and backward Raman pumps:

$$dN_{ASE}(z) = g P_+(z) + g P_-(z). \quad (9.24)$$

Generated noise travels in both directions, and is amplified by the forward and backward Raman pumps before it reaches the fiber ends. Furthermore, ASE is reflected many times either via distributed (Rayleigh) or discrete scattering mechanisms, making the complete noise evolution difficult to analyze. If one assumes that multiple ASE reflections can be neglected, the total ASE at the end and beginning of the span can be calculated by summing the elemental contributions $dN_{ASE}(z)$ along the entire fiber length. We consider the forward propagating noise first; an equivalent backward analysis can be carried out in a similar fashion. Before reaching the fiber end, the elemental noise contribution $dN_{ASE}(z)$ is both attenuated by the fiber loss (α) and amplified by the forward and the backward Raman pumps:

$$dN_{ASE}(L) = dN_{ASE}(z) e^{-\alpha_s(L-z)} e^{g \int_z^L (P_+(\eta) + P_-(\eta)) d\eta}. \quad (9.25)$$

An achromatic Raman coefficient (g) is assumed for simplicity. The total noise at the end of the fiber is then calculated as a summation along the span:

$$N_{ASE}(L) = \int_0^L dN_{ASE}(z) e^{-\alpha_s(L-z)} e^{g \int_z^L (P_+(\eta) + P_-(\eta)) d\eta} dz. \quad (9.26)$$

Assuming that the signals do not deplete Raman pumps, their power evolution is governed solely by the fiber attenuation:

$$P_+(z) = P_+(0) e^{-\alpha_p z} \quad (9.27)$$

$$P_-(z) = P_-(L) e^{-\alpha_p(L-z)}. \quad (9.28)$$

By substituting expressions (9.24), (9.25), (9.27) and (9.28) into Eq. (9.26), one can calculate the spectral noise density at the end of a bidirectionally pumped fiber span:

$$N_{ASE}(L) = \frac{g}{\alpha_p} \int_0^L [P_+(0)e^{-\alpha_p z} + P_-(L)e^{-\alpha_p(L-z)}] e^{-\alpha_s(L-z)} \times \exp[gP_+(0)(e^{-\alpha_p L} - e^{-\alpha_p z}) + gP_-(0)(1 - e^{-\alpha_p(L-z)})] dz. \quad (9.29)$$

A similar expression can be derived for the backward propagating noise at the beginning of the fiber span $N_{ASE}(0)$. Any noise injected in a fiber in either propagation direction will be amplified and added to the internally generated ASE. Equation (9.29) becomes particularly simple if one assumes symmetric pumping conditions ($P_+(0) = P_-(L) = P$) and comparable fiber attenuation at the pump and signal frequencies ($\alpha_p \sim \alpha_s \sim \alpha$):

$$N_{ASE}(L) = \frac{gP}{\alpha} e^{-\alpha L} \int_0^L [1 + e^{-\alpha(L-2z)}] \exp\{gP[e^{-\alpha L}(1 - e^{\alpha z}) + (1 - e^{-\alpha z})]\} dz. \quad (9.30)$$

Equation (9.29) can be simplified by separating the fiber span into the forward and backward pumped sections. The forward pumping contribution to the total noise at the end of the span can be reduced to [21]

$$N_{ASE}^+(L) = e^{g/\alpha P_+(0)} e^{-\alpha L}, \quad (9.31)$$

where the assumptions of a long fiber span ($\alpha L \gg 1$) and high gain were made ($G \gg 1$). The first factor on the right side of Eq. (9.31) is recognized as the forward on-off Raman gain (G_+), allowing us to write:

$$N_{ASE}^+(L) = G_+ e^{-\alpha L}. \quad (9.32)$$

Using similar assumptions, the backward pumping contribution to the forward propagating noise is calculated as

$$N_{ASE}^-(L) = e^{\frac{gP_-(L)}{A\alpha}} e^{-\ln(\frac{gP_-(L)}{A\alpha})}, \quad (9.33)$$

where $gP_-(L)/A\alpha$ is recognized as the backward Raman gain (G_-). The last equation can be rewritten in a particularly simple form [21]:

$$N_{ASE}^-(L) = G_- e^{-\ln(\ln G_-)} = G_- / \ln(G_-). \quad (9.34)$$

Figure 9.8 illustrates a lumped amplification model constructed by using Eqs. (9.32) and (9.34): forward and backward pumped sections are represented by lumped amplifiers with gains of G_+ and G_- , respectively. The midamplifier loss T accounts for the fiber transmission loss ($e^{-\alpha L}$) incorporated in Eq. (9.33). This simple model is used to estimate noise accumulation in a bidirectionally pumped fiber span supporting unidirectional traffic. It can be easily modified to account for ASE estimation in the opposite transmission direction. Assuming that the noise with power spectral density

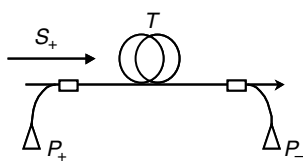
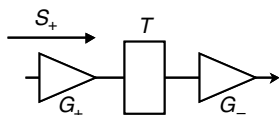


Fig. 9.8. The lumped amplification model. P_{\pm} is the power of the forward/backward propagating Raman pump, T is the span loss, and G_{\pm} is the on-off Raman gain produced by forward/backward pumps.



ρ_{IN} is injected at the beginning of the fiber ($z = 0$), the spectral power density of the total noise at the end of the span is:

$$\rho_{TOT}(L) = \rho_{IN}G_+TG_- + 2h\nu G_+TG_- + 2h\nu G_- / \ln G_-, \quad (9.35)$$

where the factor 2 was added to account for both polarization states. When bidirectional Raman pumping is used to achieve the span transparency ($G_+TG_- = 1$), Eq. (9.35) can be written as

$$\rho_{TOT}(L) = \rho_{IN} + 2h\nu + 2h\nu G_- / \ln G_-. \quad (9.36)$$

The total noise accumulated at the end of N transparently pumped fiber spans is then calculated as

$$\rho_{TOT}^N = \rho_{IN} + 2h\nu N(1 + G_- / \ln G_-), \quad (9.37)$$

where ρ_{IN} represents the noise level launched at the beginning of the first transmission span. Finally, the OSNR of the transparently pumped link constructed of N fiber spans is calculated as

$$\begin{aligned} OSNR_N &= \frac{S_{IN}}{\rho_{TOT}^N} = \frac{S_{IN}}{\rho_{IN} + 2h\nu N(1 + G_- / \ln G_-)} \\ &= \frac{OSNR_{IN}}{1 + 2h\nu N(1 + G_- / \ln G_-) / \rho_{IN}}, \end{aligned} \quad (9.38)$$

where S_{IN} represents the launched signal power and $OSNR_{IN} = S_{IN} / \rho_{IN}$ is the OSNR at the beginning of the optical link.

9.3. Impairments Specific to Forward and Bidirectionally Pumped Optical Links

9.3.1. Forward Pumped Unidirectional Transmission

The use of copropagating Raman pumps introduces impairment mechanisms typically neglected in backward pumped optical links [1–7]. The Raman response allows for near instantaneous signal–pump interactions that invariably lead to transmission penalties, even in the presence of a single optical channel. Impairments due

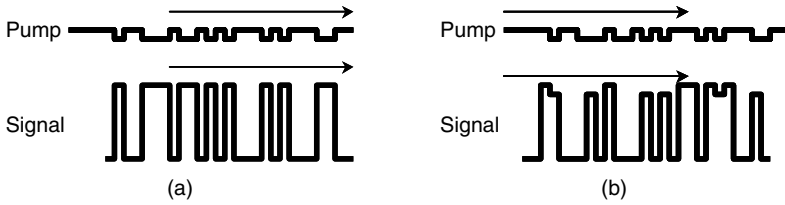


Fig. 9.9. Signal–pump–signal crosstalk: (a) an amplitude modulated signal depletes the co-propagating Raman pump; (b) pump–signal walk-off leads to spatially varying Raman gain and ISI generation.

to multiple-path interference (MPI) and finite pump relative intensity noise (RIN) are discussed in detail in Chapters 9 and 16 and are not revisited here. Figure 9.9 illustrates processes leading to pump-mediated intersymbol interference (ISI) and interchannel crosstalk. Physically, both processes are classified as crossgain modulations: a signal induces pump power depletion that leads to pattern-dependent Raman gain. Consider the case of a single amplitude modulated optical signal copropagating with a Raman pump, as shown in Fig. 9.9(a). The finite dispersion slope of the optical fiber results in different group velocities which leads to pump–signal walk-off. Consequently, the signal wave sees an advancing (or delaying) amplitude-modulated optical pump. The pattern-dependent variation in the pump power is transferred to a delayed portion of the optical signal, thus effectively completing an efficient ISI generation process, as illustrated in Fig. 9.9(b). Interchannel crosstalk requires the presence of at least two optical signals interacting via the Raman process. Similar to the ISI generation mechanism, the pump depletion induced by a signal at one wavelength will be used to modulate the signal at a different wavelength.

Signal–pump–signal crosstalk can be greatly reduced, or at least mitigated by a number of techniques. In the ideal case, the Raman pump is not depleted, thus removing the mediating channel for crosstalk generation. Following this reasoning, it is realistic to expect that a lower degree of pump depletion corresponds to a lower level of induced crosstalk penalty. The increase in channel count, while maintaining total signal power, can also be used to decrease the pump depletion pattern dependence. A large number of statistically independent amplitude-modulated channels results in the averaging of the pump power depletion effects, decreasing the depleting influence of a single optical channel. Finally, the pump-mediated crosstalk generation depends critically on the relative speed of the pump and signal. In the case of counterpropagating pump and signal, the high relative velocity allows for efficient averaging of the pump power fluctuations and significantly lower crosstalk generation. It has been shown [7] that even a moderate increase in the pump–signal walk-off rate can significantly improve ISI and cross-channel crosstalk. Higher data rates lead to the more rapid dispersive spreading of optical pulses and further temporal signal averaging. By quadrupling the data rate from 10 Gb/s to 40 Gb/s, one can maintain a negligible (0.2 dB) eye penalty by reducing [7] the bit walk-off considerably.

The experimental setup shown in Fig. 9.10(a) is used to illustrate the effects of pump depletion in a high-count dense WDM channel amplification. A total of 40

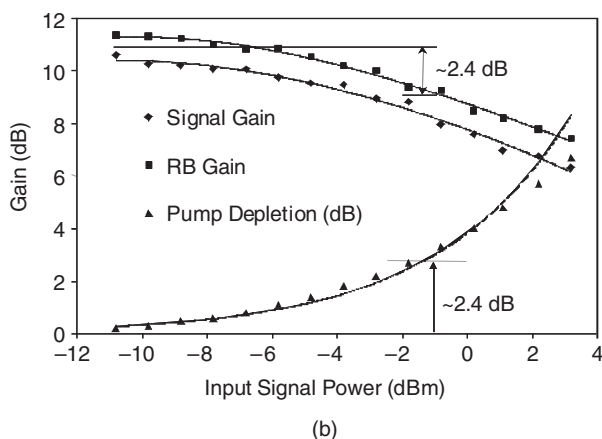
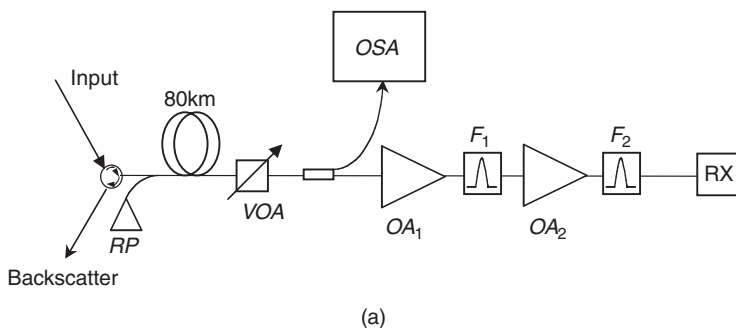


Fig. 9.10. Penalty associated with forward pumped optical transmission: (a) the measurement setup—OSA, optical spectrum analyzer; OA, optical amplifier; F, bandpass filter; RX, receiver; RP, Raman pump; and VOA, variable optical analyzer; (b) measured signal, backscatter gain, and the corresponding pump depletion.

channels is transmitted over 80 km of NZDSF fiber and combined with a forward Raman pump. The channels are modulated using a 10 Gb/s $2^{31} - 1$ pseudorandom bit sequence (PRBS), decorrelated and polarization interleaved to decrease FWM generation in the NZDSF span. Figure 9.10(b) illustrates how the pump depletion increases with the growing input signal power. The output power of the polarization scrambled Raman pump at 1480 nm was maintained and the total input signal power was increased from -12 to 4 dBm. Raman gain compression of 2 dB corresponds to a pump depletion of 2.4 dB, leading to a reasonable expectation of a relatively high transmission penalty. Figure 9.11 illustrates the measured penalty for various total input signal powers. The total penalty measured at -2 dBm of signal power (corresponding to ~ 2.4 dB of pump depletion) is only 0.25 dB. A relatively low penalty corresponding to nearly 40% pump depletion is achieved by the combination of high channel count, signal pattern decorrelation, and polarization interleaving among the signal waves.

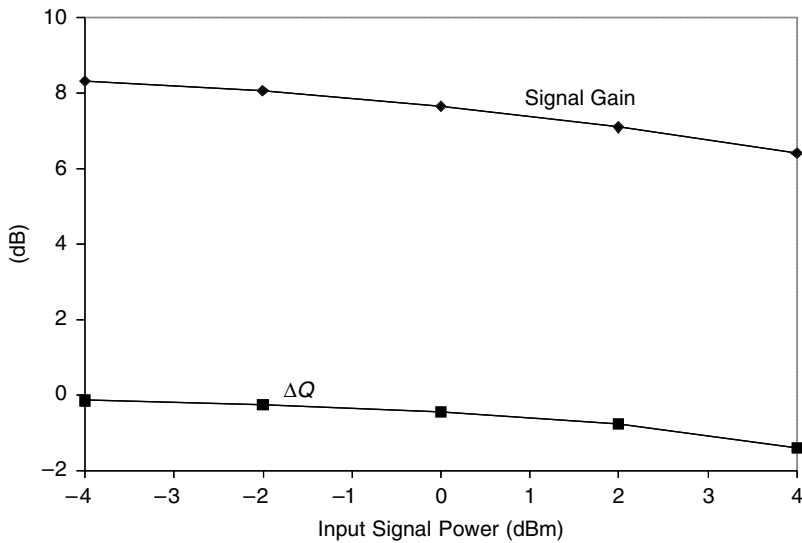


Fig. 9.11. Measured transmission penalty (ΔQ) and corresponding gain depletion. The measurement setup is identical to that described in Fig. 9.10.

Efficient Brillouin scattering from the signal is rarely observed in counterpumped transmission schemes. The signal power reaches its minimum within the backward pumped region, and generally remains far from the Brillouin threshold in all cases of practical interest. In copumped schemes, however, the signal maintains high power close to the front section of the fiber. The launched signal power has to be carefully controlled in order to prevent the onset of Brillouin scattering. Figure 9.12 illustrates the total backscatter received for different signal and pump launch powers. The elevated signal power results in increased Brillouin backscatter. The forward propagating Raman pump will, in turn, amplify the backward scattered wave. Brillouin generation in NZDSF is observed [5] for signal powers exceeding 0 dBm and copropagating

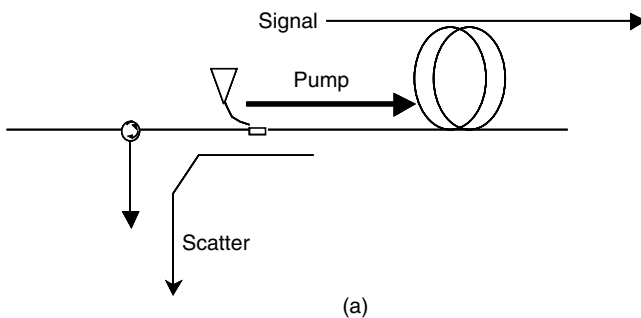


Fig. 9.12. (a) Backscatter measurement setup: a variable Raman pump is colaunches with a signal into 80 km of NZDSF.

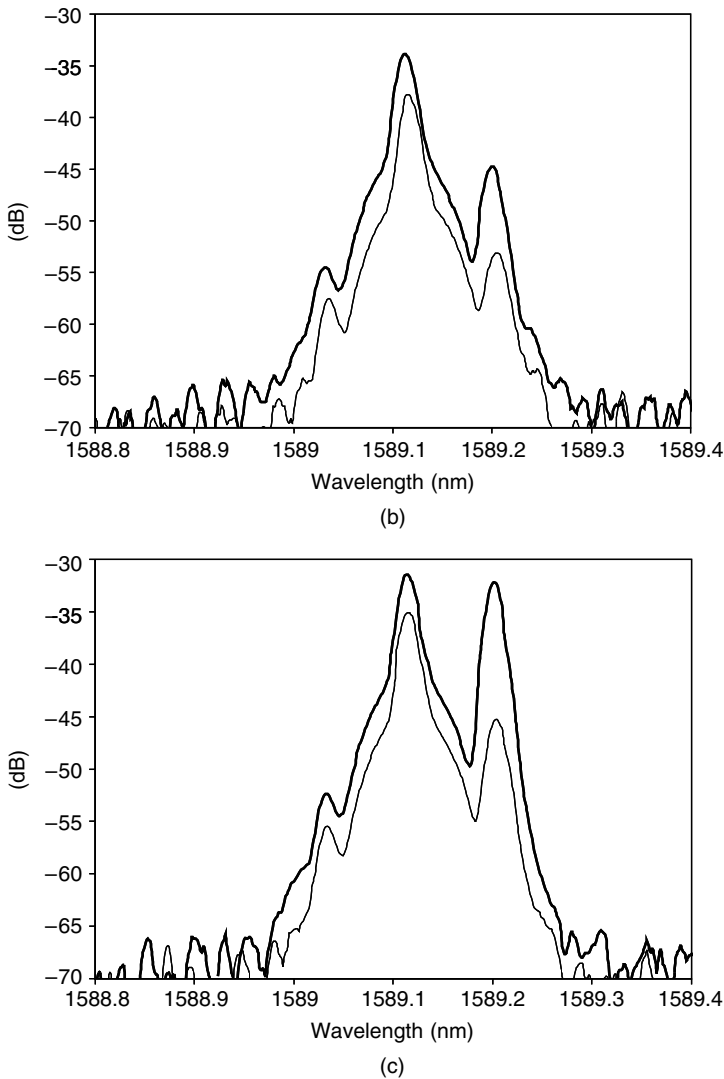


Fig. 9.12. *continued* (b) Backscattered spectrum: the launched signal power is 0 dBm, and the launched pump powers are 0 (thin curve) and 200 mW (heavy curve); and (c) backscattered spectrum: the launched signal power 3.2 dBm, and the launched pump power is 0 (thin curve) and 200 mW (heavy curve).

pump powers of 100 mW. The Brillouin peak is shifted by ~ 11 GHz with the respect to the channel center, and defines the ultimate limit for crosstalk suppression in very dense interleaved channel plans. The combination of signal and pump powers of 3.2 dBm and 240 mW, respectively, results in a downshifted Brillouin peak comparable in power to the total (amplified) Rayleigh backscatter level. Raman-aided Brillouin

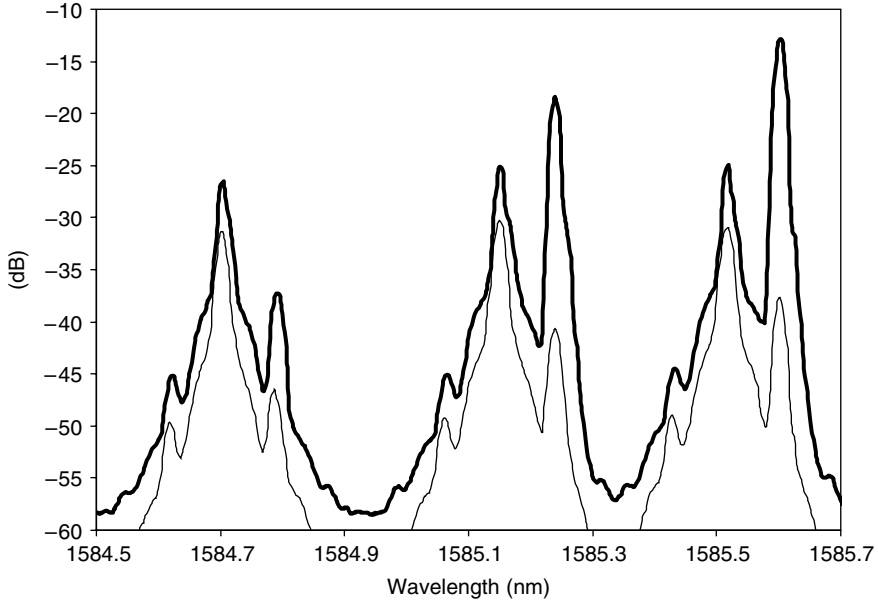


Fig. 9.13. Effects of unequalized channel powers in forward pumped transmission. The spectrum represents a portion of 40-channel traffic launched with a total power of 17 dBm into 140 km of NZDSF. The copropagating Raman pump at 1480 nm has a launch power of 240 mW.

scattering introduces strict requirements on the channel power equalization in WDM transmission. Figure 9.13 illustrates the effect of 2 dB signal variation for various launched powers. However, Brillouin reflection can be suppressed efficiently even in a forward pumped transmission environment, as illustrated in Fig. 9.14.

9.3.2. Bidirectionally Pumped Interleaved Bidirectional Transmission

The presence of the forward Raman pump is expected to amplify the Rayleigh backscatter. If we neglect the effect of multiple reflections, the elevated RB level has a potential to significantly impair the transmission in optical links supporting bidirectional signal traffic. The introduction of forward Raman gain (G_+) raises the RB level considerably, thus enhancing the total crosstalk. Because RB is formed by the optical wave that traverses the Raman pumped region of the fiber at least twice, the upper limit for RB gain can be approximated by G_+^2 . The measured [5] RB increase is significantly lower than G_+^2 , and is more closely approximated by G_+ . This observation can be understood in terms of the distributed nature of RB and Raman gain: the total on-off gain seen by an elemental contribution to the overall RB level competes with transmission loss during its round-trip. Signal scattering occurring closer to the fiber end experiences both higher Raman gain per unit length and lower overall transmission loss.

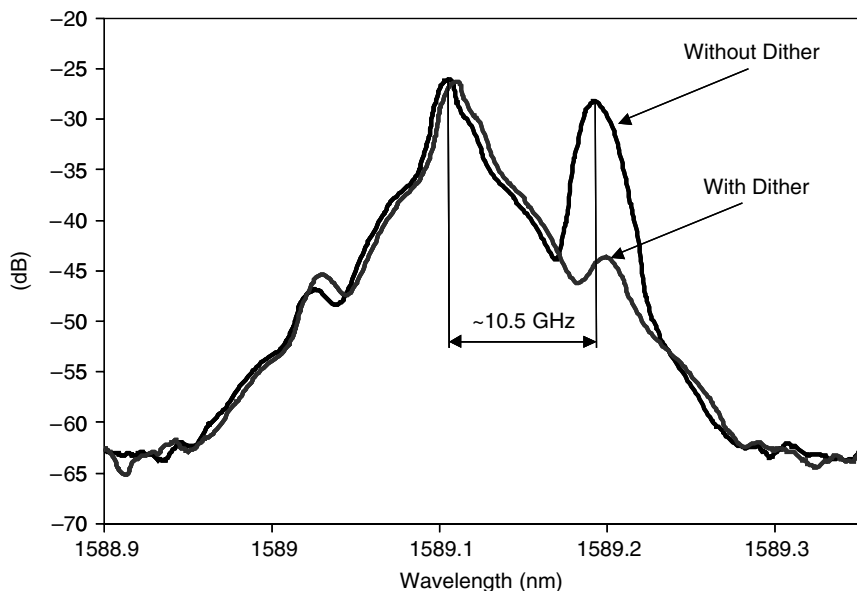


Fig. 9.14. Slow phase dither (~ 100 kHz) can be used to suppress Brillouin backscatter in forward pumped links. The measured spectrum represents the total backscatter from a long NZDSF span for the case of a 3 dBm launched signal amplified by a 200 mW Raman pump.

The transmission setup shown in Fig. 9.15(a) is used to test the limits of hybrid (Raman/EDFA) bidirectional amplification [5]. Two sets of 20 NRZ channels modulated at 10 Gb/s using a $2^{31} - 1$ PRBS word length, are separated by 100 GHz. The channels are orthogonally polarized and combine 50 GHz spaced unidirectional traffic in order to minimize FWM generation in the L-EDFA [6] and NZDSF. The Raman pumps are polarization multiplexed in order to guarantee polarization-invariant amplification of the interleaved channel plan. Figure 9.15(b) illustrates a negligible FWM level resulting from 80 km transmission at 1.2 dBm launched signal power. West–East (WE) traveling optical signals are decorrelated using a -317 ps/nm dispersion compensating module and boosted to 20.5 dBm of total power with a minimum OSNR of 39.7 dB. A variable optical attenuator VOA_{WTX} is used to adjust the signal level amplified by the copropagating Raman pump RP_{WE+} . East–West (EW) traffic is assembled using 40 copolarized signals and is used in an interfering role only. Modulated data are transmitted over the variable loss span comprising NZDSF (L_{1-4}) and $VOA_{W/E}$. The minimum NZDSF coil length is 40 km, in order to guarantee a realistic level of RB and distributed Raman gain. A bidirectional lumped amplifier (BLA) input/output is coupled with a 25 GHz interleaving filter (ILF) providing both routing and suppression functionality with insertion loss varying between 1.8 dB and 2.4 dB. Each filter provides a minimum adjacent channel isolation of 19 dB, with a 3 dB passband of 18 GHz. EDFA–buried ILFs have been demonstrated previously and shown to provide ample crosstalk suppression [2]. Unfortunately, increased span loss

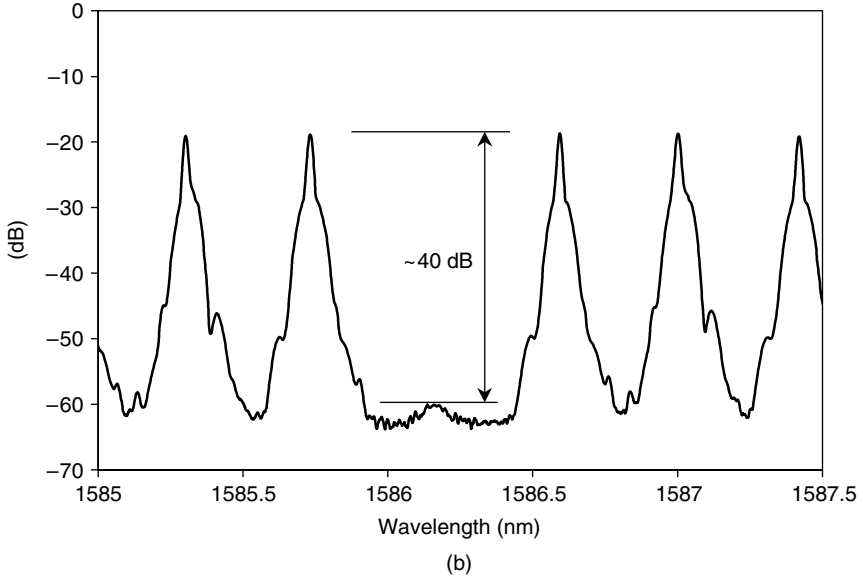
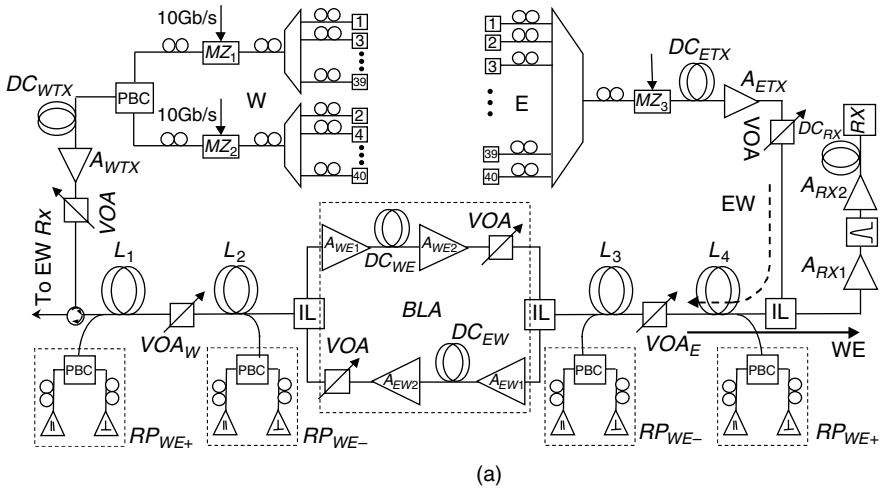


Fig. 9.15. (a) Hybrid transmission experimental setup; (b) intrinsic FWM level associated with the orthogonally polarized channel plan.

requires frontal ILF position, illustrated by Fig. 9.16. The total gain experienced by the WE signal before reaching BLA input is:

$$P_{WE}^{IN} = L_{IL} \times G_{WE+} \times L_F \times G_{WE-} \times L_{IL} \times P_{WE}^L, \quad (9.39)$$

where P_{IN}^{WE} is the signal level at the input of the BLA, G_{WE+} is the codirectional Raman gain, G_{WE-} is the counterdirectional Raman gain, L_F is the span loss, and

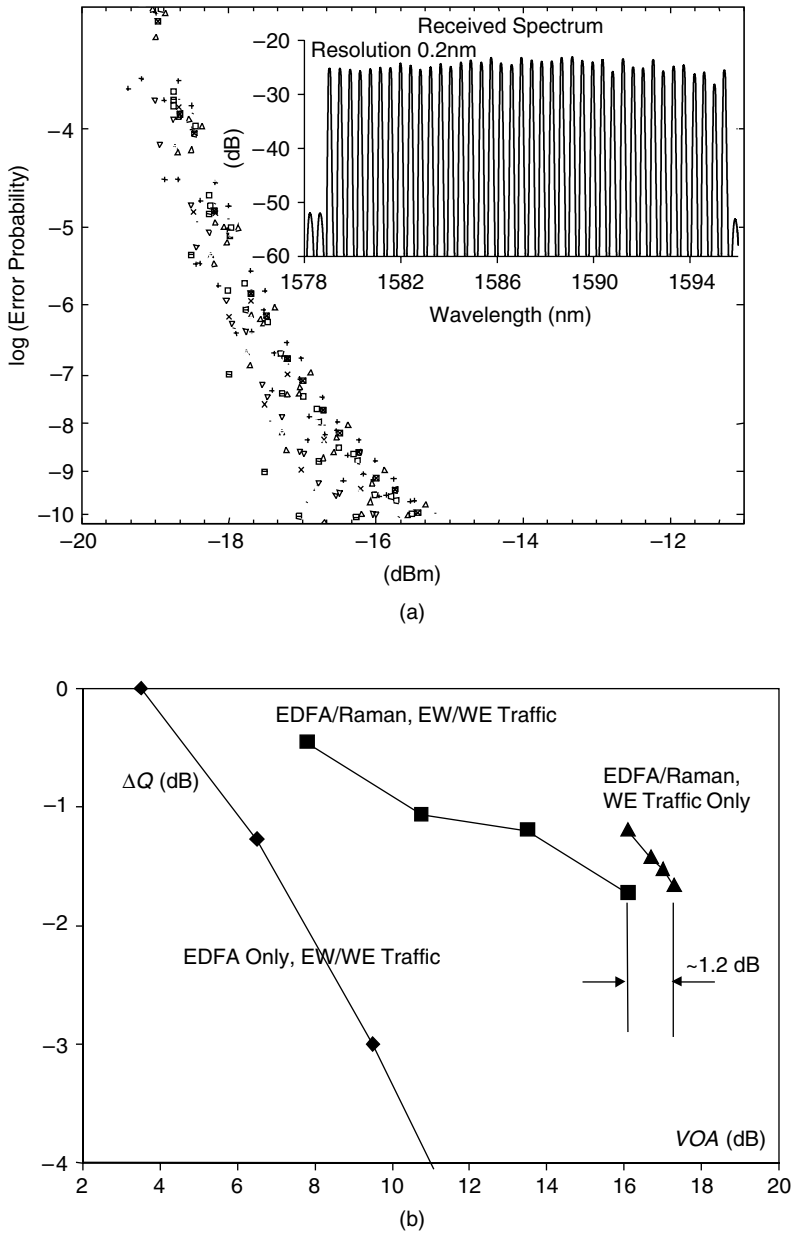


Fig. 9.17. Hybrid amplification performance: (a) error-free transmission over two 140 km NZDSF spans. VOA element (3.5 dB) is placed in the middle of each span, and is surrounded by 60 and 80 km of NZDSF fiber; (b) performance impact of distributed amplification and presence of counterpropagating traffic. $\Delta Q = 0$ corresponds to $Q = 19.4$ dB.

and an additional variable optical attenuator (VOA) are placed in the middle of the fiber span to guarantee a target span loss. This loop construction is considered more rigorous than one using an additional amplifier [14] to cancel the switching loss, because nonlinear signal interaction is negligible within the midspan fiber region. The coil lengths ($L_{1,2}$) are chosen to be 40 km in order to guarantee: (1) a realistic length, as required for RB buildup (> 12 km), (2) sufficient length for distributed gain accumulation (> 30 km), and (3) a combined span loss of 31 dB. In the case when the routing element (V) is a circulator, uninhibited counterpropagation of backward (EW) noise is prevented. This has a potential to change the entire nature of the link in the case of ASE-limited transmission. However, the link under investigation is far from this regime, with performance nearly independent on cascaded (backward) ASE buildup. An amplification node incorporates dispersion compensation ($DC_{WE,EW}$) that, combined with receiver compensator (DC_{Rec}), provides for a 90% compensated link. The presence of distributed Raman amplification requires the peripheral, rather than midstage, placement of interleaving filters used in simultaneous routing and protection roles. A relatively high peak dispersion of 200 ps/nm was measured within the filter transmission band. L-band EDFA was designed and measured to produce maximum of 21 dBm output and an average noise figure of 4.6 dB. Its gain tilt was carefully matched to composite Raman gain shape. EDFA/Raman gain distribution was adjusted in order to provide a total of 32 dB amplification: the EDFA generated 20 dB, whereas 6 dB was obtained from each Raman direction. The output of the EDFA was adjusted in order to generate less than 2 dB of pump depletion in order to minimize signal–pump–signal crosstalk generation and elevated levels of Brillouin backscatter.

Figure 9.19(a) indicates error-free transmission performance after five spans. The minimum received OSNR is 24 dB, as shown in Fig 9.19(b). Figure 9.19(c) illustrates signal degradation with span evolution, indicating a difference of 3.5 dB between the first and the fifth span. The system penalty is attributed to noise buildup and multiple interleaving filter passes. Indeed, by the time that the signal reaches the end of the fifth span, it has already completed 10 filter passes. Figure 9.20(a) illustrates the spectral narrowing induced by filter concatenation after the first, third, and fifth transmission spans. It is apparent that, even in the absence of any noise generation, the useful transmission bandwidth after the sixth span would fall short of the requirements for 10 Gb/s NRZ transmission. In addition, finite filter dispersion further limits the robustness of the link: Fig. 9.20(b) illustrates the detuning margin of a signal received near the sensitivity level. The penalty associated with the presence of the opposite traffic direction was measured to be 0.23 dB at the end of the fifth span.

9.3.3. Bidirectionally Pumped Banded Bidirectional Transmission

The advantages of single-band, bidirectional Raman amplification of interleaved signal traffic need to be contrasted with the fundamental limitations associated with this scheme. The interleaved channel plan used in single-band transmission offers greatly reduced FWM while maintaining high spectral efficiency of the optical link. However, the Raman pumping is required to be strictly symmetrical (identical levels of forward and backward pumping) and does not allow for spectrally separated preamplifier and

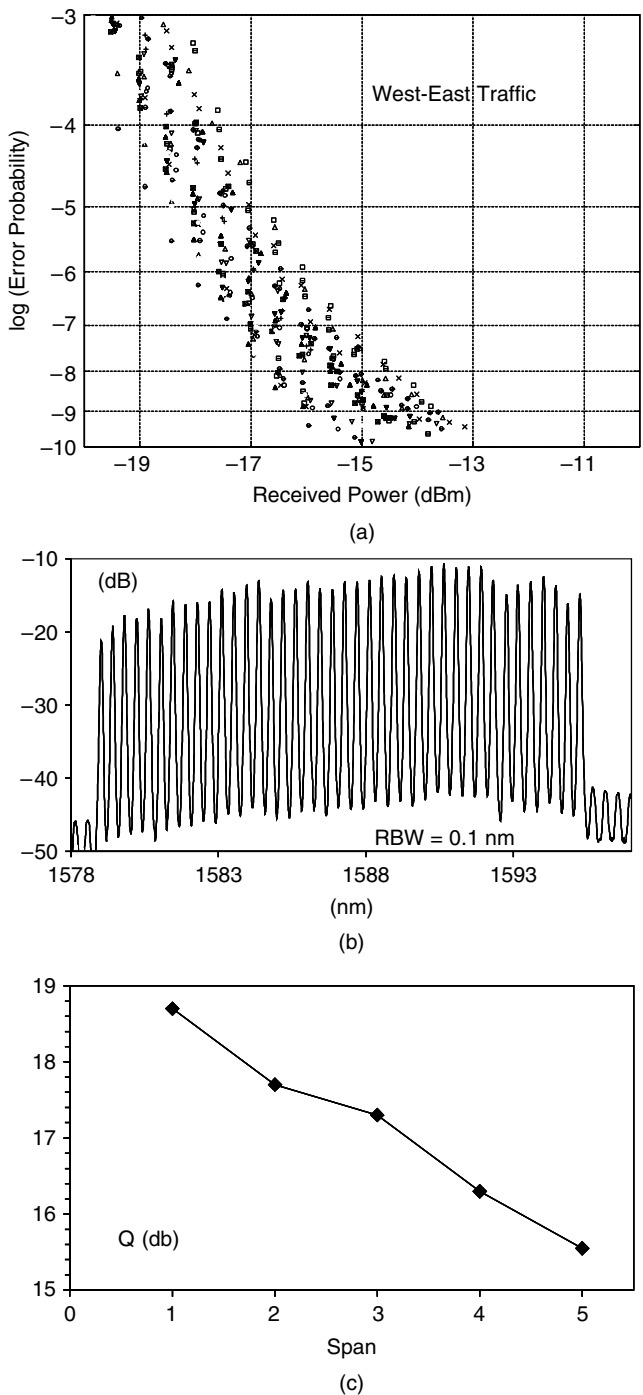


Fig. 9.19. (a) Error-free reception of 40 west-east channels after the fifth span; (b) received spectrum; and (c) Q degradation ($\lambda = 1588$ nm).

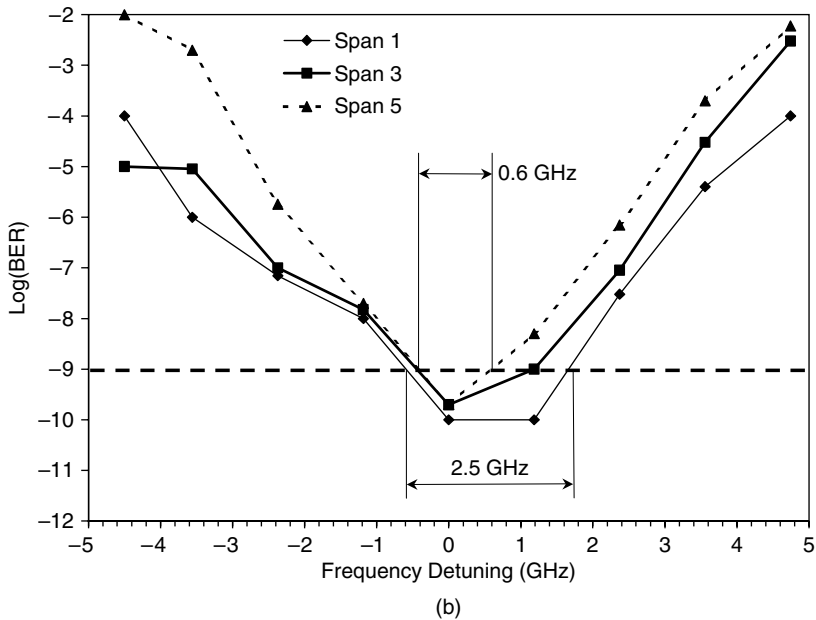
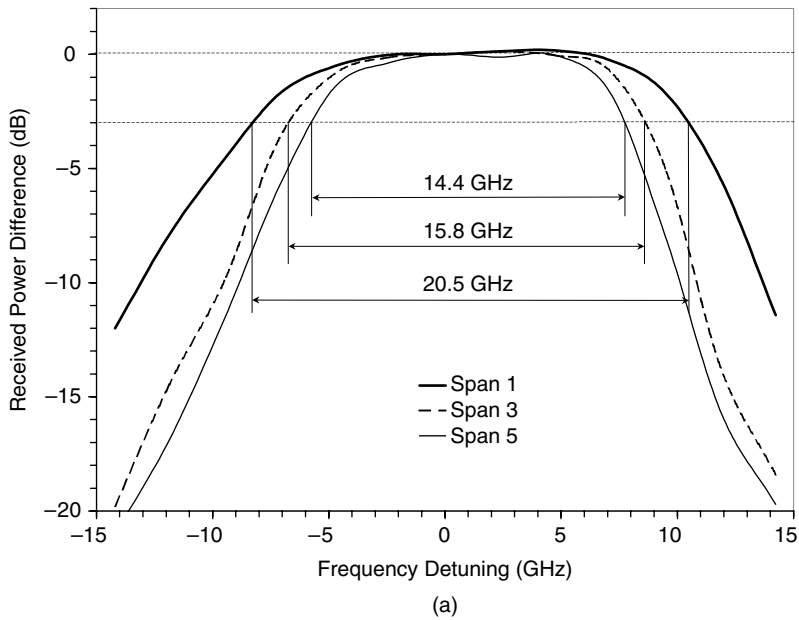


Fig. 9.20. (a) Passband narrowing induced by filter concatenation; (b) channel center frequency detuning tolerance as a function of distance.

booster functions. The forward propagating Raman pump is used to simultaneously boost the forward traveling signal and preamplify the backward traveling channels. The power of the former is considerably higher than that of the counterpropagating signal at the front fiber end. Consequently the forward Raman pump is depleted by the copropagating signal traffic, thus limiting the transfer of optical power from the forward pump to the backward signals. The same problem is encountered at the opposite end of the fiber section: the backward Raman pump is quickly depleted by a strong copropagating signal thus compressing the available gain for the forward channels. In other words, the symmetric pumping scheme inherently requires that each Raman pump play simultaneous booster and preamplification roles. Physically, it can be shown that these requirements are mutually exclusive. High-performance preamplifiers are characterized by a low noise figure and high average inversion levels that require negligible pump depletion. In contrast, relatively low inversion levels that allow considerable pump depletion mark the optimal booster performance.

Banded bidirectional signal traffic [26] allows for the separation of the forward and backward Raman pumping roles. Assume that two distinct spectral windows are allocated for the east–west (EW) and west–east (WE) transmission, as illustrated in Fig. 9.21. The Raman pump wavelengths can be chosen to provide peak gain for EW and WE signal bands separately. Furthermore, both Raman pumps are launched in the direction opposite to that of the signal band they are amplifying. This arrangement ensures that the pumps provide the preamplifier function for the chosen signal bands. The copropagating signal traffic is not expected to deplete either Raman pump significantly because the spectral offset lowers the available copropagating Raman gain significantly. Figures 9.22 and 9.23 compare the pump depletion levels in bidirectional schemes in which Raman pumps are used in (1) simultaneous preamplifier

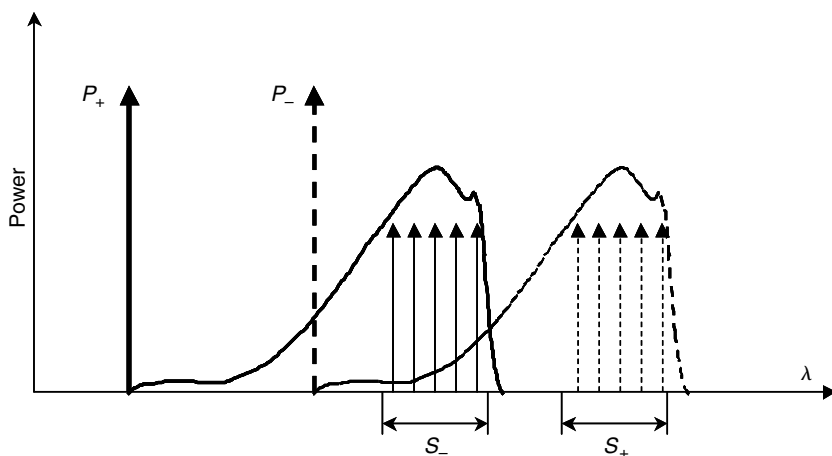


Fig. 9.21. Banded bidirectionally pumped, bidirectional optical transmission. The forward propagating pump (P_+) provides preamplification for the backward traveling signals (S_-); the backward traveling pump (P_-) preamplifies the forward traveling traffic (S_+).

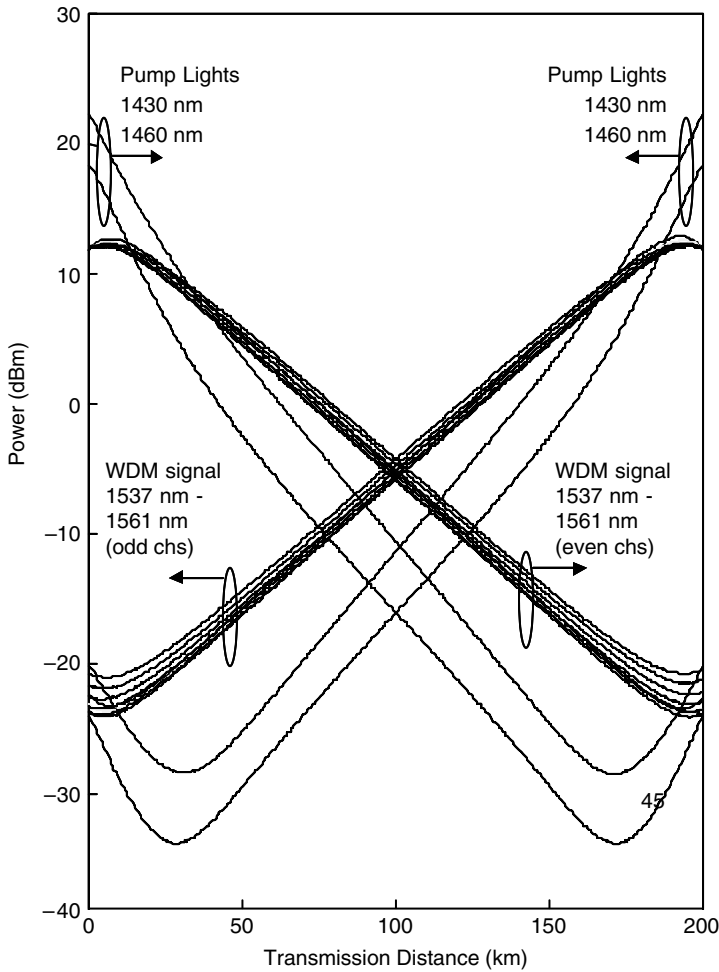


Fig. 9.22. Bidirectionally pumped bidirectional transmission using a single signal band [26]. The power evolution is calculated for 200 km of NZDSF fiber with an effective area of $72 \mu\text{m}^2$, launched signal power of -3 dBm , and 170 mW and 70 mW Raman pumps positioned at 1430 nm and 1460 nm, respectively.

and booster roles, and (2) exclusively in a preamplifier role. The considerable pump depletion that is present in the shared band architecture (Fig. 9.22) is almost absent in the banded transmission scheme (Fig. 9.23). Figure 9.24 illustrates the transmission performance over 200 km of NZDSF fiber. Two sets of 32 channels are modulated at 43 Gb/s and transmitted in each direction. Bidirectional traffic is allocated to the C- and L-bands (1537.4 to 1562.2 nm and 1576.2 to 1602.3 nm) and amplified by dedicated Raman pumps: 1430 and 1460 nm pumps are used to amplify the C-band, whereas 1470 and 1495 nm pumps amplify the L-band.

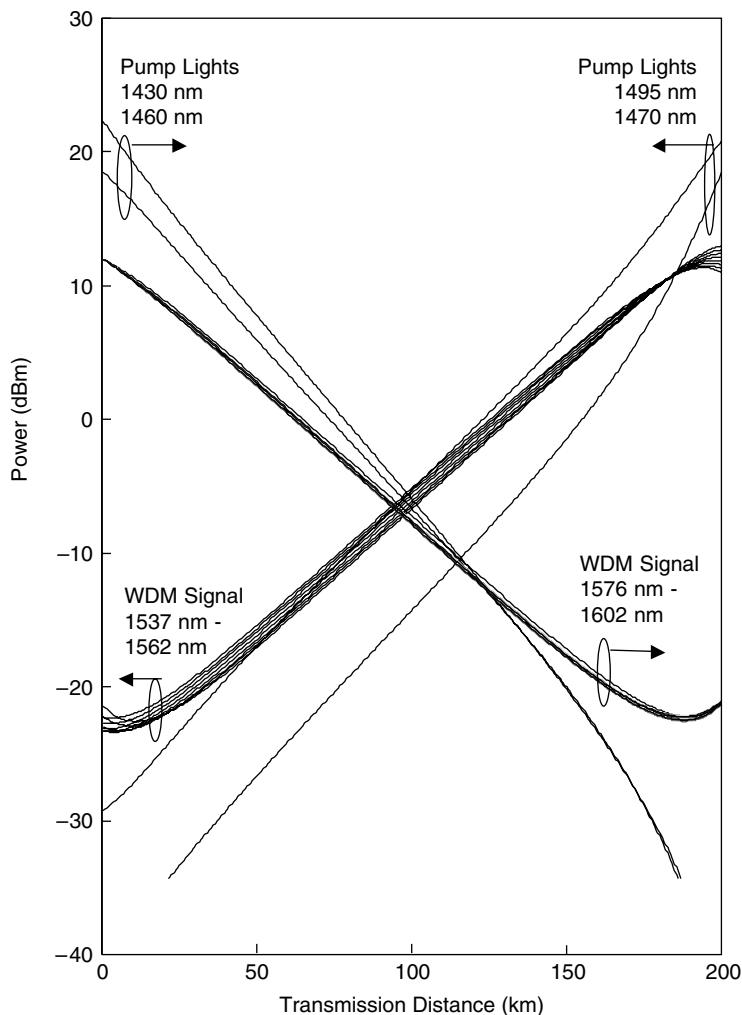


Fig. 9.23. Bidirectionally pumped bidirectional transmission using separate spectral bands [26]. The transmission parameters are the same as in Fig. 9.22.

An increased penalty due to nondegenerate FWM [26, 28] (ND-FWM) was observed at specific channel locations. Elevated ND-FWM is expected for the case in which the zero dispersion wavelength of the transmission fiber is positioned between the Raman pump and signal wavelengths. Figure 9.25 illustrates this effect in the L-band after transmission over 200 km transmission [26]. An effective mitigation technique for ND-FWM, which is similar to those for other FWM impairments, is based on preventing phase matching along the fiber span. The insertion of dissimilar fiber types was shown to reduce ND-FWM to a negligible level.

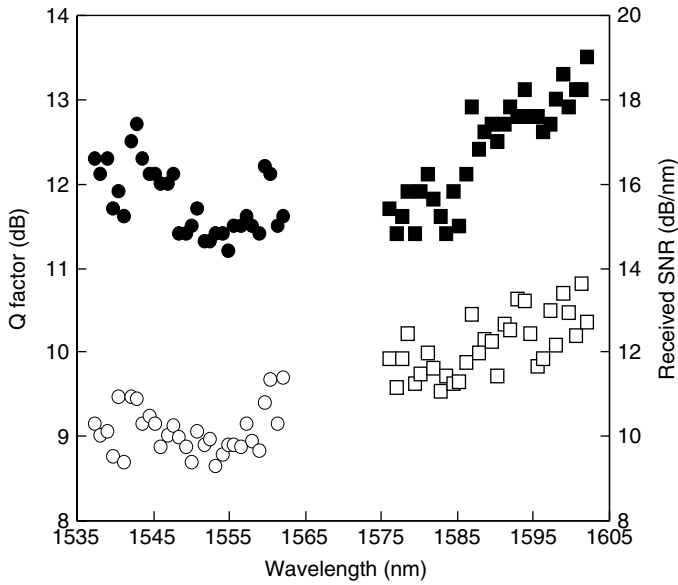


Fig. 9.24. Measured performance of banded bidirectionally pumped optical transmission over 200 km of NZDSF fiber [26].

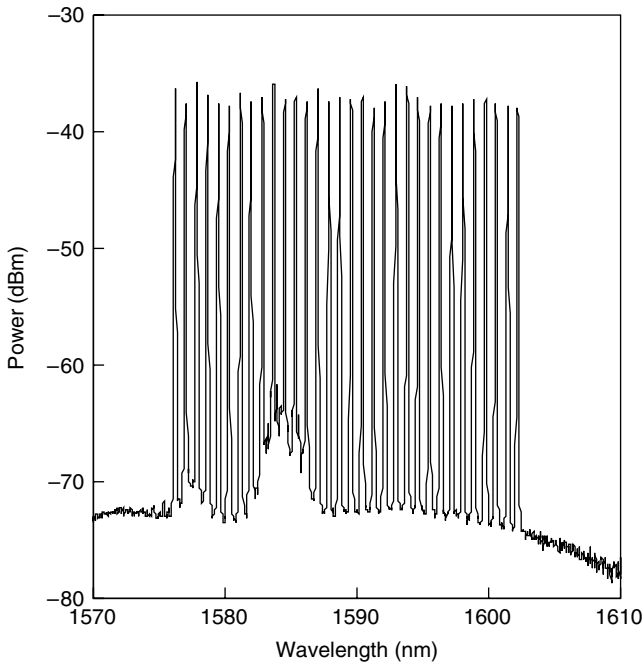


Fig. 9.25. Elevated ND-FWM generation in the L-band [26].

9.4. Higher-Order Raman Pumping

9.4.1. Second-Order Raman Pumping

The distributed amplification analyzed so far is characterized by a Raman pump positioned one Stokes shift away from the signal. This pumping scheme is commonly referred to as first-order amplification, regardless of the relative directions of the pumps and the signals. An alternative scheme that combines first- and second-order amplification was proposed recently for Raman-pumped transmission spans [29–31]. In the first demonstration of this concept [29], the backward propagating (first-order) pump at 1455 nm was used to amplify a forward traveling signal at 1550 nm and combined with a forward (second-order) 1366 nm pump. The second-order pump is used to amplify the counterpropagating first-order pump and provide signal amplification closer to the front section of the fiber. This architecture has a significant advantage compared to an equivalent, bidirectionally pumped span that uses only first-order pumps: although the second-order pump (1366 nm) copropagates with the signal, it does not induce any of the impairments expected in forward amplified transmission spans. The evolution of the backward traveling first-order pump can be tailored precisely by controlling the power of the second-order pump. In turn, this feature allows for almost uniform span transparency to be achieved at the signal wavelength. A combined 1 W of Raman pumping (800 mW and 200 mW at 1366 nm and 1550 nm, respectively) was required to achieve transparency in an 80 km NZDSF transmission span [29]. Second-order bidirectional pumping architecture exhibited a 1 dB improvement in performance relative to the comparable first-order backward pumped configuration.

A bidirectional pumping scheme that combines forward propagating second-order and backward propagating first-order waves requires two pump sources and is limited by noise transfer from the second-order pump to the signal. In addition, the power of the second-order pump is many times higher than that of the first-order pump, making the scheme impractical for long transmission spans. The scheme can be improved by counterpropagating both first- and second-order pumps using multiple-wavelength pump sources. The recent transmission experiment [32], shown in Fig. 9.26, has demonstrated combined first- and second-order amplification using a single pump device [33]. A Yb fiber laser at 1100 nm was used for cascaded generation at 1365 and 1455 nm, providing a stable, depolarized optical power of approximately 1 W. Three first-order Raman pumps are used to contrast the performance of the proposed second-order device. Figure 9.27 illustrates the measured and simulated amplification in 80 km of SMF using both pumping schemes. A three-wavelength device with a

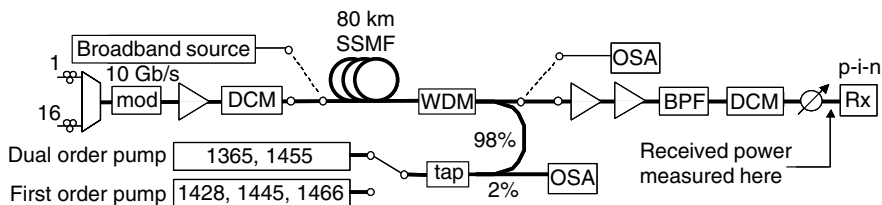


Fig. 9.26. Dual-order transmission setup.

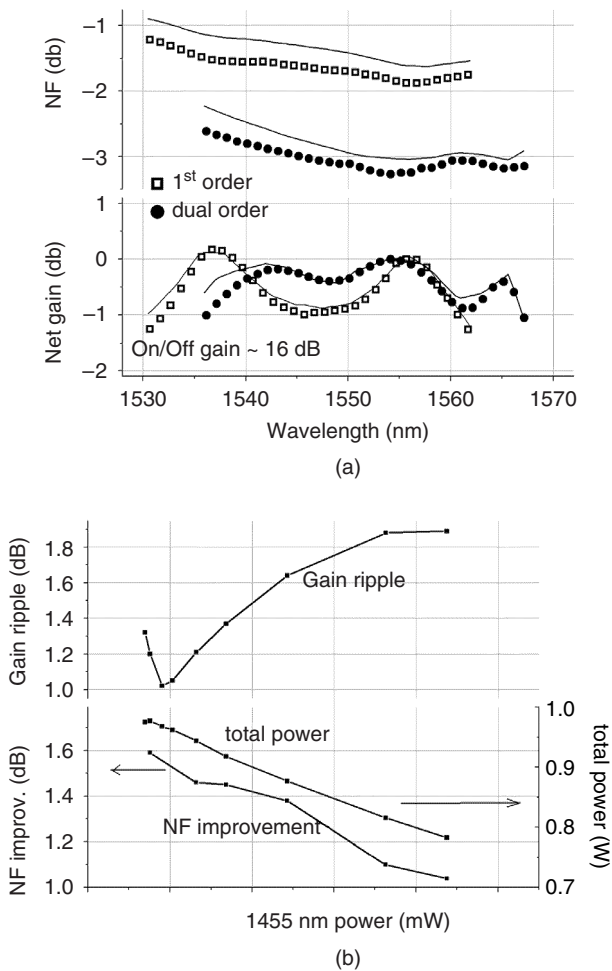


Fig. 9.27. (a) Comparison of NF for first-order (open squares) and dual-order (dots) Raman pumping. Solid lines indicated simulation results; (b) improvement in NF and gain ripple function for second-order pumping scheme.

total power of 580 mW was used in first-order pumping to reach span transparency (on-off gain of 16 dB). The combined first- and second-order pumping was 970 mW. An equivalent noise figure was calculated and measured to be 1.5 dB lower in the latter case. Measured gain ripple and noise generation were found to depend strongly on rational power distribution between 1365 and 1455 nm pumps. Unidirectional signal traffic was propagated under both amplification conditions in order to measure transmission performance. Sixteen optical channels were modulated at 10 Gb/s and transmitted over 80 km of SMF. The BERs for 1550 and 1557 nm channels are plotted in Fig. 9.28, illustrating a consistent 1 dB margin that dual-order pumping has over first-order amplification.

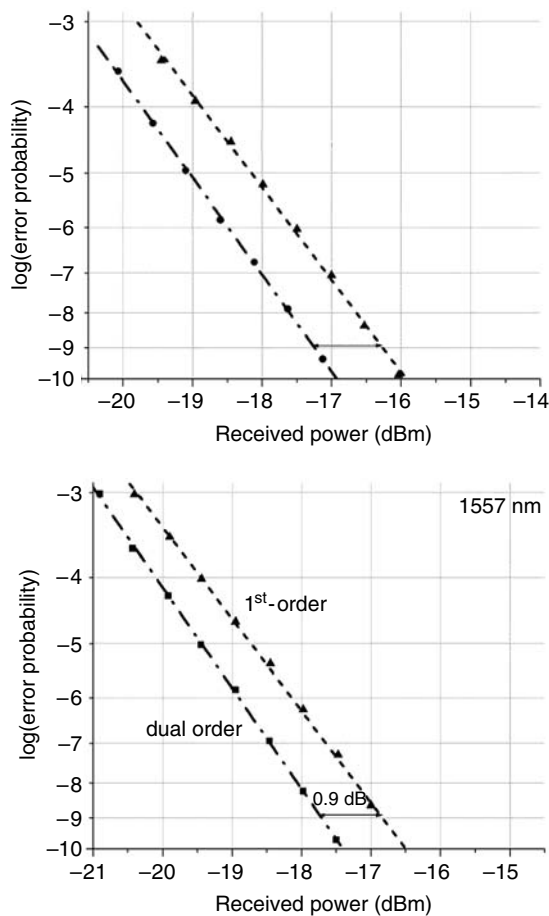


Fig. 9.28. BER measurements for selected (1550 and 1557 nm) channels.

9.4.2. Third-Order Raman Pumping

An additional improvement in transmission performance can be achieved by the introduction of third-order Raman pumping [34]. First- and second-order Raman pumping can be used to control the signal evolution over relatively short spans, because distant first- and second-order gain regions require excessive pump powers. Third-order pumping can be used to extend the distance over which both signal and final (third-order) pump power remains unchanged, as illustrated in Fig. 9.29. Although 1276 and 1356 nm pumps are rapidly depleted (within the first 10 and 30 km of the span, respectively), the final pump cascade (1455 nm) evolves gradually over the entire 120 km span length. As a consequence, signal power evolution is maintained within a remarkably equalized envelope not exceeding 10 dB within the entire length of the transmission fiber. The receiver performance is improved markedly, because the third-order pumping results in a noise level decrease of almost 3 dB relative to the first-order pumping, as illustrated in Fig. 9.30.

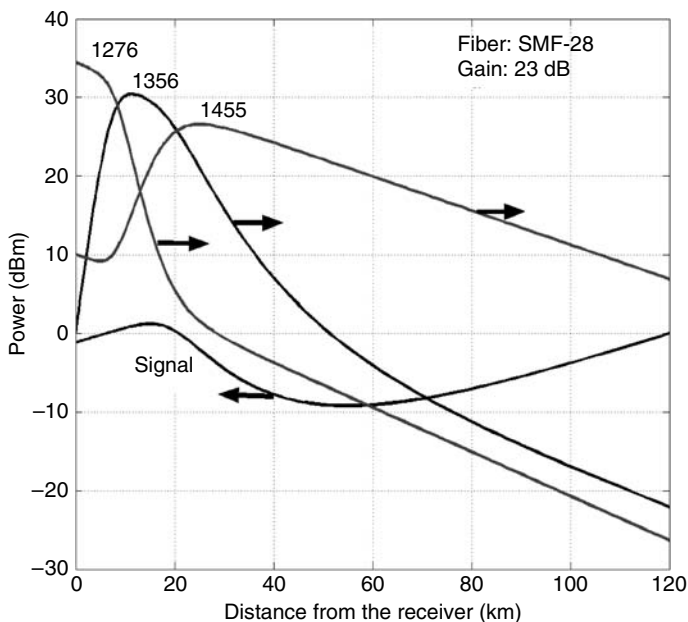


Fig. 9.29. Power evolution with cascaded third-order Raman pumping. Source: S.B. Papernyi, V.I. Karpov and W.R.L. Clements “Third Order Cascaded Raman Amplification” Optical Fiber Conference Proceedings, pg FB4-1 (©2002 OSA)

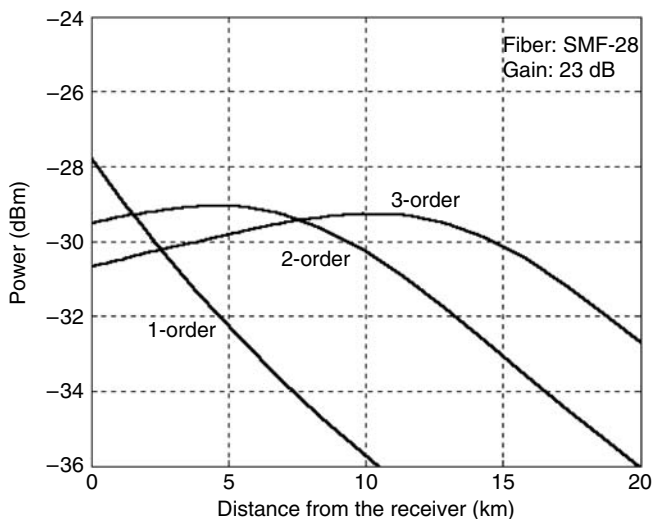


Fig. 9.30. Comparison of received noise power in the case of first-, second-, and third-order Raman pumping. Source: S.B. Papernyi, V.I. Karpov and W.R.L. Clements “Third Order Cascaded Raman Amplification” Optical Fiber Conference Proceedings, pg FB4-1 (©2002 OSA)

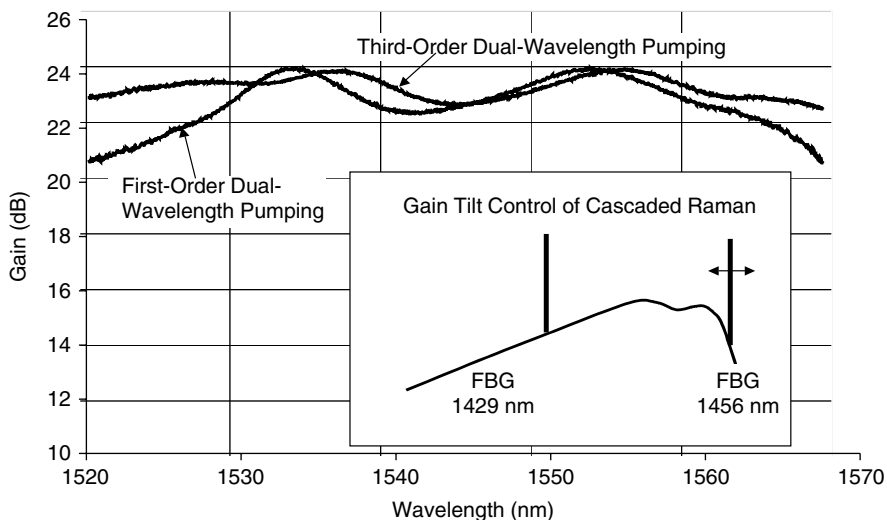


Fig. 9.31. Gain ripple measured in 100 km of NZDSF for different pumping schemes. Source: S.B. Papernyi, V.I. Karpov and W.R.L. Clements “Third Order Cascaded Raman Amplification” Optical Fiber Conference Proceedings, pg FB4-1 (©2002 OSA)

In a transmission experiment over 100 km of SMF, third-order pumping with 1276, 1356, and 1455 nm wavelengths was compared with first-order pumping scheme. In a 2.5 Gb/s link, third-order pumping exhibited a consistent 2.5 dB of receiver sensitivity improvement. The multiwavelength nature of the third-order pumping can be used to achieve gain flatness not attainable by a conventional (first- or second-order) Raman pumping. Figure 9.31 illustrates better than 1.5 dB flatness achieved with a NZDSF link, over the entire C-band. In contrast, a comparable dual-wavelength first-order pumping over the identical span was limited to more than 3 dB of gain ripple.

References

- [1] W. Jiang and P. Ye, Crosstalk in fiber Raman amplification for WDM systems, *J. Lightwave Technol.*, 7: 1407, 1989.
- [2] C.R.S. Fludger, V. Handerek, and R.J. Mears, Pump to signal RIN transfer in Raman fiber amplifiers, *J. Lightwave Technol.*, 19: 1140, 2001.
- [3] V. Dominic, E. M. Mao, J. Zhang, B. Fidric, S. Sanders, and D. Mehuys, Distributed Raman amplification with co-propagating pump light. In *Proceedings of Optical Amplifiers and Their Applications 2001* (Stresa), vol. 60, 63, 2001.
- [4] P. M. Krummrich R. E. Neuhauser, H. Bock, W. Fischler, and C. Glingener, System performance improvements by co-directional Raman pumping of the transmission fiber. In *Proceedings of the 27th European Conference on Optical Communication* (Amsterdam), TuA 1.4, 114, 2001.
- [5] S. Radic, S. Chandrasekhar, P. Bernasconi, J. Centanni, C. Abraham, N. Copner, and K. Tan, Feasibility of hybrid Raman/EDFA amplification in bidirectional optical transmission, *IEEE Photon. Technol. Lett.*, 14: 221, 2002.

- [6] P. M. Krummrich, C.-J. Weiske, A. Schopflin, B. Kessler, and B. Lankl, Reduction of pattern dependent stimulated Raman scattering crosstalk by codirectional Raman pumping. In *Proceedings of Optical Amplifiers and Their Applications 2002* (Vancouver), OtuA3, 2002.
- [7] S. Choudhary and T. Hoshida, Inter-symbol interference and inter-channel crosstalk in Raman amplification with forward pumping. In *Optical Amplifiers and Their Applications 2001*, (Vancouver), OtuA4, 2002.
- [8] C. W. Barnard, J. Chrostowski, and M. Kavehrad, Bidirectional fiber amplifiers, *IEEE Photon. Technol. Lett.*, 14: 911, 1992.
- [9] J. Haugen, J. Freeman, and J. Conradi, Bidirectional transmission at 622 Mb/s utilizing erbium-doped fiber amplifiers, *IEEE Photon. Technol. Lett.*, 4: 913, 1992.
- [10] M. O. van Deventer, *Fundamentals of Bidirectional Transmission over a Single Optical Fibre*, Boston: Kluwer Academic, 1996.
- [11] J.-M. P. Delavaux, C. R. Giles, S. W. Granlund, and C. D. Chen, Repeated bidirectional 10Gb/s-240km fiber transmission experiment, *Opt. Fiber Technol.*, 2: 351, 1996.
- [12] C. H. Kim and Y. C. Chung, 2.5Gb/sx16-Channel bidirectional WDM transmission system using bidirectional EDFA based on SIS etalon filters, *IEEE Photon. Technol. Lett.*, 11: 745-747, 1999.
- [13] J. Kani, M. Jinno, T. Sakamoto, K. Hattori, and K. Oguchi, Bidirectional transmission to suppress interwavelength-band nonlinear interactions in ultrawide-band WDM transmission systems, *IEEE Photon. Technol. Lett.*, 11: 376, 1999.
- [14] S. Radic, S. Chandrasekhar, A. Srivastava, H. Kim, L. Nelson, S. Liang, K. Tai, and N. Copner, Dense interleaved bidirectional transmission over 5×80 km of non-zero dispersion shifted fiber, *IEEE Photon. Technol. Lett.*, 14: 218, 2002.
- [15] S. Radic, G. Pendock, A. Srivastava, P. Wysocki, and A. Chraplyvy, FWM in optical links using quasi-distributed optical amplifiers, *J. Lightwave Technol.*, 19: 636, 2001.
- [16] S. Radic and C. Chandrasekhar, Ultradense bidirectional optical transmission, active and passive optical components for WDM transmission, *Proc. SPIE*, 336, 2001.
- [17] R. G. Smith, Optical power handling capacity of low-loss optical fibers as determined by stimulated Raman and Brillouin scattering, *Appl. Opt.* 11: 2489, 1972.
- [18] M. L. Dakss and P. Melman, Amplified spontaneous Raman scattering and gain in fiber Raman amplifiers, *J. Lightwave Technol.*, LT-3: 806, 1985.
- [19] K. Mochizuki, Optical fiber transmission systems using stimulated Raman scattering: Theory, *J. Lightwave Technol.*, LT-3: 688, 1985.
- [20] S. Chi and M.-S. Kao, Bidirectional optical fiber transmission systems using Raman amplification, *J. Lightwave Technol.*, 6: 312, 1988.
- [21] Y. Aoki, Properties of fiber Raman amplifiers and their applicability to digital optical communication systems, *J. Lightwave Technol.*, 6: 1225, 1988.
- [22] C. Yijiang and A. W. Snyder, Saturation and depletion effects of Raman scattering in optical fibers, *J. Lightwave Technol.*, 7: 1109, 1989.
- [23] B. Foley, M. L. Dakss, R. W. Davies, and P. Melman, Gain saturation in fiber Raman amplifiers due to stimulated Brillouin scattering, *J. Lightwave Technol.*, 7: 2024, 1989.
- [24] H. Kidorf, K. Rottwitt, M. Nissov, M. Ma, and E. Rabarjaona, Pump interactions in a 100nm bandwidth Raman amplifier, *IEEE Photon. Technol. Lett.*, 11: 530, 1999.
- [25] M. Yan, J. Chen, W. Jiang, J. Li, J. C., and X. Li, Automatic design scheme for optical-fiber Raman amplifier backward-pumped with multiple laser diode pumps, *IEEE Photon. Technol. Lett.*, 13: 948, 2001.
- [26] T. Mizuochoi, K. Kinjo, S. Kajiya, T. Tokura, and K. Motoshima, Bidirectional unrepeated 43Gb/s WDM transmission with C/L band-separated Raman amplification, *J. Lightwave Technol.*, 20(12):2079, 2002.

- [27] S. Radic and S. Chandrasekhar, Advances in bidirectional transmission. In *Proceedings of Optical Amplifiers and Their Applications 2002* (Vancouver), Owbl-1, 2002.
- [28] J. Bromage, P. J. Winzer, L. E. Nelson, and C. J. McKinstrie, Raman-enhanced pump-signal four-wave mixing in bidirectionally-pumped Raman amplifiers. In *Proceedings of Optical Amplifiers and Their Applications 2002* (Vancouver), Owa5-1, 2002.
- [29] K. Rottwitt, A. Stentz, T. Nielsen, P. Hansen, K. Feder, and K. Walker, Transparent 80km bi-directionally pumped distributed Raman amplifier with second order pumping. In *Proceedings of the 25th European Conference on Optical Communication* (Nice), II-144, 1999.
- [30] V. Dominic, A. Mathur, and M. Ziari, Second-order distributed Raman amplification with a higher-power 1370nm laser diode. In *Proceedings of Optical Amplifiers and Their Applications 2001* (Stresa), vol. 60, 66, 2001.
- [31] L. Labrunie, F. Boubal, E. Brandon, L. Buet, N. Darbois, D. Doufornet, V. Havard, P. Le Roux, M. Mesic, L. Piriou, A. Tran, and J.-P. Blondel, 1.6 Terabit/s (160×10.66 Gbit/s) unrepeated transmission over 321km using second order pumping distributed Raman amplification. In *Proceedings of Optical Amplifiers and Their Applications 2001* (Stresa), vol. 60, 202, 2001.
- [32] J.-C. Bouteiller, K. Brar, S. Radic, J. Bromage, Z. Wang, and C. Headley, Dual-order Raman pump providing improved noise figure and large gain bandwidth. In *Proceedings of the Optical Fiber Conference 2002* (Anaheim), PD FB-2, 2002.
- [33] M. D. Mermelstein, C. Headley, J.-C. Boutellier, P. Steinvurzel, C. Horn, K. Feder, and B. J. Eggleton, Configurable three-wavelength Raman fiber laser for Raman amplification and dynamic gain flattening, *IEEE Photon. Technol. Lett.*, 13: 1286, 2001.
- [34] S. B. Papernyi, V. I. Karpov, and W. R. L. Clements, Third-order cascaded Raman amplification. In *Proceedings of the Optical Fiber Conference* (Anaheim), FB4, 2002.

Index

- 1310 nm wavelength band, 383
- 14XX nm pump laser diodes, 121
- 14XX nm pumps, 135
- 40 Gb/s Raman-amplified transmission, 673
- 40 Gb/s bit rate systems, 396
- 40 Gb/s terrestrial transmission, 701

- A figure of merit (FOM), 364
- absorption coefficients, 430
- accelerated aging tests, 127
- acoustic phonons, 325
- acousto-optic modulator, 711
- all-optical cross-connects, 596
- all-optical mesh networking, 596
- all-optical terrestrial system, 627
- all-optical transmission, 627
- all-Raman amplifier, 445, 621
- all-Raman system, 17, 627
- AllWave, 681
- amplified spontaneous emission (ASE), 10, 308, 491, 711
- amplitude shift key(-ed) (-ing), 711
- analytical expression, 576
- anti-Stokes scattering, 38
- arrayed waveguide grating (AWG), 334
- arrhenius relationship, 128
- ASE-ASE beat noise, 524
- attenuation, 317

- backward pumping, 458
- backward Raman pumping, 62
- backward spontaneous Raman noise level, 62
- banded bidirectional signal traffic, 280
- banded schemes, 255

- band-limited phase-shaped binary transmission, 711
- bandwidth-limited PSBT (BL-PSBT), 688
- beat noise, 92
- beat noise variances, 522
- beat-noise limited receivers, 522
- BER measurements, 584
- bidirectional pumping, 135
- bidirectional systems, 459
- bidirectional transmission, 253
- bit error rate (BER), 310, 711
- bit error rate test set, 711
- bit rate scaling, 530
- Boltzmann factor, 38
- booster amplifier, 346
- Bose-Einstein distribution, 12, 456
- Bose-Einstein factor, 101
- Bragg grating stabilized laser diodes, 616
- Brightness Theorem, 355
- butterfly laser module, 125

- cable television, 27
- capture fraction, 44
- carrier injection efficiency, 124
- carrier-suppressed return-to-zero (CSRZ), 479, 511, 711
- carrier-suppressed RZ (CSRZ), 686
- cascaded Raman fiber laser (RFL), 194, 353, 385
- cascaded Raman oscillator, 29
- cascaded Raman resonator, 354
- cavity design, 357
- C-band, 5, 301
- channel launch powers, 569

- channel power management, 574
- channel power transients, 581
- chi-squared distribution, 502
- chromatic dispersion, 602, 676
- cladding-pump fiber lasers, 9
- cladding-pumped fiber (CPF), 355
- classical treatments, 43
- closed loop control system, 322
- coherence time, 493
- complex susceptibility, 51
- constant output power mode, 324
- conventional band of EDFA
 - (~1530 to 1565 nm), 711
- copumped Raman amplifier, 213
- copumping, 135, 343
- corner frequency, 222
- Corning DSF, 115
- Corning LEAF, 115
- Corning NZ-DSF, 115
- Corning SMF-28, 373
- cost metric, 445
- cost-per-transmitted-bit, 673
- counter-pumped Raman amplifiers, 213
- counter-pumping, 135
- counterpropagating pump, 2
- counterpropagating pumping, 310
- counterpumping, 343
- coupled mode equations, 454
- critical launch power, 570
- critical power, 39
- crossgain modulation, 231, 235, 267
- cross-phase modulation, 711
- cross-phase modulation
 - (XPM), 304, 315, 589
- crosstalk ratio, 514
- DCF, 3, 681
- decibel/nanometer scale, 575
- degrades system performance, 569
- degree of polarization (DOP), 512
- degrees of birefringence, 512
- dense wavelength-division-
 - multiplex(-ed) (-ing), 711
- dense wavelength-division-
 - multiplexing (DWDM), 673
- dense WDM, 627
- depolarizer, 146
- device-under-test, 517
- dielectric thin film interference filters, 143
- differential group delay (DGD), 678, 711
- differential phase-shift-key(-ed) (-ing), 711
- discrete or lumped Raman am-
 - plifier (LRA), 1, 30, 301
- dispersion, 162, 301
- dispersion compensation, 303
- dispersion curvature, 161
- dispersion map, 628
- dispersion slope, 317
- dispersion slope compensation, 161
- dispersion slope compensation ratio, 165
- dispersion slope-compensation, 447, 449
- dispersion-compensating Ra-
 - man amplifiers, 186
- dispersion-compensating fiber
 - (DCF), 3, 161, 304, 711
- dispersion-compensating
 - module (DCM), 711
- dispersion-compensating mod-
 - ules (DCM), 679
- dispersion-managed fiber, 384
- dispersion-managed solitons, 627
- dispersion-shifted fibers, 463
- distributed feedback laser, 711
- distributed feedback lasers (DFB), 506
- distributed Raman amplification, 338
- distributed Raman amplifier (DRA), 1, 452
- distributed Raman transmission, 383
- DMS, 627
- double Rayleigh backscattering (DRBS), 304
- double Rayleigh scattering (DRS), 2, 10
- double-heterostructure (DH) laser, 122
- double-Rayleigh backscatter (DRBS), 385
- Double-Rayleigh backscattering, 83
- DPSK (differential phase-shift keying), 669
- DRBS crosstalk, 340
- DRS crosstalk, 459
- dual-band hybrid Raman/EDFAs, 694
- dual-order Raman fiber lasers, 377
- duobinary, single/vestigial side-
 - band modulation, 686
- dynamic gain equalizer, 448, 711
- east-west (EW), 280
- EDFA/Raman amplifier combinations, 445
- EDFA/Raman HA, 413
- effective area, 3, 43, 711
- effective length, 24
- effective mode area, 196

- effective noise figure (ENF), 95, 385
- effective Rayleigh reflection coefficient, 25
- effective upper-state lifetime, 348
- elastic scattering, 502
- ELEAF, 681
- electrical beat-noise measurement, 516
- electrical noise figure, 458
- electrical spectrum analyzer, 174, 517
- electrical time-division-
 - multiplex (-ed) (-ing), 711
- electronic regeneration, 627
- electronically sweeping the wavelength, 62
- end-of-life margin, 483
- energy transfer due to SRS, 573
- engineering design rules, 445
- enhanced phase-shaped bi-
 - nary transmission, 711
- Enhanced PSBT (EPSBT), 687
- epoxy pigtailling, 307
- equipartition energy, 643
- equivalent noise figure, 285
- erbium-doped silica fiber: EDSF, 418
- erbium-doped fiber ampli-
 - fier (EDFA), 1, 301, 711
- external-cavity lasers (ECL), 506

- Fabry–Perot laser, 139, 458
- fast interactions, 569
- fast tunable laser, 66
- fast-gain dynamics, 97, 213
- Fiber Bragg Grating laser, 137
- fiber Bragg gratings (FBG), 353
- fiber nonlinearity, 491, 602
- fiber selection, 600
- field autocorrelation, 497
- figure of merit for the Ra-
 - man amplifier fiber, 317
- fine-tuned dispersion, 447
- first-order backward pumped
 - configuration, 284
- first-order PMD, 678
- fluoride, 30, 306
- fluoride EDF (erbium-doped flu-
 - oride fiber: EDFF, 418
- fluoride or multicomponent silicates, 304
- fluoro-zirconate (ZBLAN), 306
- forward error correction (FEC), 310, 688, 711
- forward pumped unidirec-
 - tional transmission, 266
- forward pumping, 458
- Fourier transform, 497
- four-wave mixing (FWM), 303, 314
- four-wave-mixing (FWM), 79, 589, 711
- frequency domain, 494
- frequency modulation (dithering), 157
- frequency-division-multiplexed, 596
- frequency-swept pumping, 468
- full-width at half-maximum, 711
- fundamental 3 dB noise limit, 45
- fused-fiber coupler, 143

- gain compression term, 263
- gain equalizer (GEQ), 417, 448
- gain feedback, 70
- gain flatness, 66
- gain saturation, 317
- gain slope, 324
- gain spectrum, 2
- gain tilt, 324, 576
- gain-flattening filter (GFF),
 - 311, 448, 694, 711
- gain-shifted EDFA, 418
- Gaussian pulse shapes, 531
- Gaussian-like, 502
- GeO₂-based fibers, 204
- germanium doping, 52
- germano–silicate fiber, 29
- germanosilicate, 194
- Gordon–Haus effect, 648
- graded index separate confinement
 - heterostructure strained layer
 - multiple quantum well structure
 - with buried heterostructure, 122
- grating-stabilized lasers, 458
- GRIN-SCH strained layer MQW
 - structure with BH structure, 122
- group-velocity dispersion, 711
- guiding filters, 661

- heavy metal oxide glasses, 53
- high germanium doping, 161
- high P₂O₅-doped optical fibers, 199
- high pump power laser diodes, 9
- high slope dispersion-compensating
 - fiber (HSDK), 363
- higher-order pumping, 468
- higher-order Raman pumping, 284

- high-slope dispersion-
 - compensating fiber, 711
- homogeneous-like, 320
- hybrid amplifier (HA), 1, 413
- hybrid bidirectional amplification, 274
- hybrid bidirectional scheme, 255
- hybrid pump, 140
- Hybrid Raman/EDFA amplifiers, 617
- hybrid TDFA/Raman amplifier, 342, 440
- hybrid tellurite/silica fiber
 - Raman amplifier, 206
- hybrid tellurite/silica Raman amplifiers, 440
- imbalanced Mach–Zehnder
 - interferometers, 143
- inband crosstalk, 492
- incoherent homodyne detection, 334
- indium gallium arsenide, 305
- indium gallium arsenide phosphide, 305
- indium phosphide, 305
- InGaAsP/InP GRIN-SCH strained
 - layer MQW structure, 121
- inhomogeneous gain saturation, 320
- inline amplifier, 329, 413
- Inner Grating Multimode laser, 140
- insertion loss, 274
- integrated circuit, 711
- integrated dispersion compensation, 348
- intensity autocorrelation, 497
- interband stimulated Raman scattering, 328
- interchannel crosstalk, 267
- interchannel interference, 305
- interchannel nonlinear effects, 683
- interference noise, 92
- interferers, 491
- interleaved bidirectional scheme, 254
- International Telecommu-
 - nications Union, 711
- Internet, 595
- intersymbol interference, 305
- intradband stimulated Raman scattering, 453
- intrachannel cross-phase mod-
 - ulation (IXPM), 544
- intrachannel four-wave mixing (IFWM), 544
- inverse dispersion fiber, 711
- isolators, 431
- jitter-killer, 656
- Jones matrix, 506
- Kerr nonlinearity, 538
- Landsberg–Mandelstam effect, 35
- laser module structure, 125
- L-band, 5, 301
- lightwave communication systems, 491
- LiNbO₃ modulator, 313
- linear noise characteristics, 91
- link design value (LDV), 679, 711
- log-linear loss spectrum, 575
- long distance telephony, 596
- long repeater spacing, 622
- long-haul, 1, 445
- long-wavelength band of EDFA
 - (~1570 to 1605 nm), 711
- Lorentzian laser lineshape, 497
- Lorentzian lineshape, 71
- low degree of polarization (DOP), 135
- low-loss splices, 362
- low-noise preamplifier, 616
- LS fiber, 571
- Lucent Allwave, 115
- Lucent TrueWave, 115
- lumped Raman amplifiers, 338
- Mach–Zehnder modulator, 711
- Mach–Zehnder interferometers, 448
- Maple mathematics, 635
- material dispersion, 162
- maximum RIN transfer, 214
- Maxwellian probability density function, 678
- MBE (molecular beam epitaxy), 122
- MCVD technique, 199
- mechanical splicing, 307
- metropolitan optical network, 306
- microelectromechanical sys-
 - tems (MEMS), 448
- midstage loss, 389
- MOCVD (metal organic chemi-
 - cal vapor deposition), 122
- mode partitioning noise (MPN), 157
- modulation technique, 447
- MPI crosstalk, 340
- MPI–MPI beat noise, 502, 524
- Müller matrices, 512
- multicomponent silicate (MCS), 30
- multipath interference (MPI), 119, 304
- multiple interfering fields, 499
- multiple path interference (MPI), 136

- multiple reflections, 602
- multiple Stokes shifts, 356
- multiple wavelength Raman fiber lasers, 365
- multiple-order pump sources, 354
- multiple-order RFLs, 353
- multiple-wavelength RFLs, 353
- multiple-path interference (MPI), 491, 711
- mutually incoherent, 506

- narrowband HA (NB-HA), 413
- ND-FWM, 282
- NDSF, 115
- net effective coding gain, 711
- new wavelength bands, 26
- noise figure, 12, 46, 305
- noise power spectral density, 495
- noise-induced frequency shifts, 648
- nondegenerate FWM, 282
- nondispersion shifted fiber, 711
- nondispersion-shifted fiber (NDSF), 227
- nonlinear distortion, 91
- nonlinear impairments, 180
- nonlinear index of refraction, 603
- nonlinear interactions, 36
- nonlinear penalty, 1
- nonlinear refractive index, 37
- nonlinear Schrödinger (NLS) equation, 629
- nonreturn-to-zero, 686, 711
- non-return-to-zero (NRZ), 310
- nonzero dispersion fiber, 711
- nonzero dispersion-shifted fiber (NZ-DSF), 64, 226

- on-off keyed data transmission, 676
- on-off keying (OOK), 511
- on-off Raman gain, 421
- open-loop operation, 320
- optical add/drop, 306
- optical add-drop multiplexers, 448
- optical confinement factor, 124
- optical cross-connects, 448
- optical interleaver, 711
- optical noise figure, 458
- optical parametric amplifiers, 303
- optical phonon, 2, 325
- optical signal-to-noise ratio (OSNR), 79, 347, 711
- optical spectrum analyzer (OSA), 114, 517
- optical switch, 712

- optical time domain reflectometry (OTDR), 170
- optical time-division-multiplex(-ed) (-ing), 712
- optical time-division-multiplexed (OTDM), 674
- optical time-domain extinction technique, 519
- optical-electrical-optical (O-E-O), 596
- optimized modulation formats, 685
- OSNR budget, 580
- OSNR penalty, 529
- out-of-band crosstalk, 492
- out-of-band forward error correction, 310

- parametric amplifier, 37
- parametric interactions, 303
- path delay, 493
- path-average noise, 644
- path-average power, 605
- path-average pump powers, 71
- path-average signal power, 67, 644
- pattern dependent crosstalk, 585
- pattern-dependent Raman gain, 267
- periodic-group-delay-complemented dispersion compensation, 663
- phase difference, 493
- phase matching, 303
- phase mismatch, 630
- phase-shaped binary transmission, 686, 712
- phase-shift-key(-ed) (-ing), 712
- phonon population factor, 430
- phonon-stimulated optical noise, 11
- phosphorous-doped fiber, 451
- phosphorus doping, 53
- phosphosilicate Raman fibers, 194
- photosensitivity, 196
- Placzek model, 40
- planar lightwave circuit (PLC), 143
- Planck's constant, 38
- PMD coefficient, 678
- Poincaré sphere, 512
- Poisson distributed, 93
- polarization beam combiner (PBC), 144
- polarization controller (PC), 517
- polarization dependence, 4, 52
- polarization evolution, 506
- polarization interleaving, 268
- polarization mode dispersion, 712

- polarization mode dispersion (PMD), 145, 602, 678
- polarization multiplexing, 324
- polarization-dependent gain (PDG), 324
- polarization-dependent loss (PDL), 396, 602, 712
- polarization-division-multiplex(-ed) (-ing), 712
- polarization-interleav(-ed) (-ing), 712
- polarization-mode dispersion, 447
- polarized Raman scattering, 44
- power conversion efficiency, 19
- power partitioning, 367
- power spectral density, 240
- power transients, 583
- preamplifier, 346
- principal state of polarization, 712
- probability density function (PDF), 500
- profile dispersion, 162
- pseudorandom bit sequence (PRBS), 240, 712
- pulse arrival times, 648
- pump depletion, 112, 263, 320
- pump efficiency, 384
- pump laser diodes, 121
- pump–pump interactions, 453
- pump–signal RIN transfer, 459
- pump–signal walk-off, 267
- pumping efficiency, 7
- pump-mediated crosstalk, 240
- pump-mediated intersymbol interference (ISI), 267
- pump-mediated signal crosstalk, 385
- pump-to-pump Raman interaction, 76
- pump-to-signal noise transfer, 385
- pure silica core fiber (PSCF), 571
- pure silica-core fiber (PSCF), 712
- pure-silica core, 115

- Q* scaling relationship, 389
- Q*-factor, 712
- Q*-factor-based MPI tolerance factor, 528
- Q*-spectra, 347
- quality factor (*Q*), 228, 339
- quantum approach, 37

- Raman efficiency, 569
- Raman enhanced fiber (RF), 363
- Raman fiber lasers, 353
- Raman figure of merit, 182
- Raman frequency shift, 196
- Raman gain coefficient, 45, 51, 195
- Raman gain efficiency coefficient (C_R), 114
- Raman gain spectrum, 51
- Raman gain tilt, 17
- Raman oscillator wavelength shifters, 29
- Raman pumping unit, 149
- Raman response function, 50
- Raman scattering, 35
- Raman scattering cross-section, 41
- Raman threshold, 569
- Raman-aided Brillouin scattering, 271
- Raman-assisted repeatered transmission, 384
- rare earth-doped cladding-pumped fiber laser (CPFL), 354
- rare earth-doped fiber amplifiers, 303
- Rayleigh backscatter coefficient, 503
- Rayleigh loss coefficient α_r , 339
- Rayleigh scattering, 502
- Rayleigh scattering loss, 503
- Rayleigh scattering of ASE, 102
- recapture fraction, 503
- receiver noise sources, 92
- receiver sensitivity, 383
- recirculating loop, 480
- recirculating transmission loop, 691
- Reed–Solomon, 712
- Reed–Solomon (RS) code, 688
- Reed–Solomon 255/239, 315
- relative dispersion slope, 164, 449, 712
- relative intensity noise (RIN), 135, 498
- reliability, 126
- repeater spacing, 600
- repeaterless transmission systems, 573
- required OSNR, 525
- resolution bandwidth, 712
- responsivity, 93
- return-to-zero, 686, 712
- return-to-zero (RZ), 511
- return-to-zero differential phase shift keying (RZ-DPSK), 511
- return-to-zero differential-phase-shift-key(-ed) (-ing), 712
- reverse dispersion fiber, RDF, 227
- revived interest, 9
- RFL pump module, 354
- RIN transfer, 221
- ring amplifier, 27
- round-trip gain, 505

- RS (255, 239), 689
- RS (255,223), 689
- rule of thumb, 673
- RZ differential-phase-shift-keying (RZ-DPSK), 686
- S+ bands, 309
- same relative dispersion slope, 683
- S-band, 26, 301
- S-band lumped Raman amplifier (SLRA), 310
- S-band Raman amplifiers, 301
- seamless and wideband HA (SWB-HA), 413
- seamless transmission bands, 161
- second-order Raman pumping, 284
- selecting transmission fibers, 591
- self-phase modulation (SPM), 314, 712
- semiconductor laser diodes, 385
- semiconductor optical amplifier (SOA), 30, 303
- sequential pulsing, 62
- short upper-state lifetime, 10
- shot noise, 91
- Shott noise limited, 45
- signal preemphasis, 462, 465
- signal-ASE beat noise, 524
- signal-MPI beat noise, 502, 524
- Signal-pump-signal crosstalk, 267
- signal-spontaneous beat noise, 46, 340
- signal-to-noise (SNR), 92
- signal-to-noise ratio, 1, 45, 451
- signal-to-signal crosstalk, 112
- signal-to-signal crosstalk mediated by the pump, 245
- silica fiber, 309
- single-mode fiber (SSMF), 571
- single-pass analytic models, 259
- single-sided spectral density, 497
- slope efficiency, 356
- slope-compensating fibers, 449
- slow interactions, 569
- small effective area, 161
- small-scale inhomogeneities, 502
- SMART pump, 65
- soliton propagation, 383
- soliton transmission, 598
- Soliton-Soliton Collisions, 649
- splice loss spectral variation, 317
- splice losses, 363
- split-band augmentation strategy, 348
- splitband configuration, 447
- spontaneous Brillouin scattering, 511
- spontaneous emission factor, 11
- spontaneous noise factor, 13
- spontaneous Raman noise, 81
- spontaneous Raman scattering, 37
- spontaneous-spontaneous beat noise, 46
- spontaneously generated photons, 570
- SRS dynamic crosstalk, 331
- SRS-induced transients, 585
- SSMF, 681
- standard single-mode fiber (SSMF), 310, 712
- states of polarization (PSP), 678
- static gain equalizers, 448
- statistical nature, 590
- stimulated Brillouin scattering, 325
- stimulated Raman scattering, 35, 38, 712
- stimulated Raman threshold, 39
- stochastic electrodynamics, 48
- Stokes scattering, 38
- Stokes vector, 512
- super large area fiber, 712
- superposition rule, 131
- tapered fiber bundle, 355
- TDFA/Raman amplifier, 413
- telecommunications, 1
- telegraph, 596
- tellurite, 449
- tellurite/silica Raman amplifier, 413
- Tellurite-based glasses, 205
- temperature dependence, 100, 430
- temperature-dependent ASE, 104
- temperature-dependence of noise figure, 611
- temperature-dependence of the chromatic dispersion, 677
- temporal fluctuations, 374
- temporal gain ripple, 77
- temporal lens, 656
- Teralight fiber, 698
- terrestrial applications, 595
- terrestrial links, 338
- terrestrial optical transmission systems, 673
- terrestrial systems, 600
- thermal distribution of phonons, 112
- thermal management, 150
- thermal noise, 340
- thermal occupation number, 48
- thermally induced phonon noise, 462

- thermoelectric cooler (TEC), 122
- third-order Raman pumping, 286
- third-order susceptibility, 49
- threshold of catastrophic damage, 196
- thulium-doped fiber amplifier (TDFA), 30, 304
- time delay, 37
- time domain, 494
- time domain picture, 49
- time modulation of the pumps, 461
- time response of the Raman effect, 213
- time-division-multiplex(-ed) (-ing), 712
- time-division-multiplexed (TDM), 305, 674
- time-division-multiplexing, 61, 446
- time-multiplexed pumping, 470
- total launch power, 571
- transit time, 218, 348
- transition rate, 37
- transmission fibers, 569
- transparent photonic networks, 585
- transverse mode mixing, 491
- triangular profile, 574
- TrueWave[®] classic (TW) fiber, 571
- TrueWave[®] REACH, 681
- TrueWave[®] RS, 363, 681
- two-component model, 48
- two-path interference, 495
- two-stage Raman amplifier, 320
- two-way signal traffic, 253
- Type-1 SWB-HA, 434
- Type-2 SWB-HA, 435
- Type-3 discrete SWB-HA, 437
- Type-4 discrete SWB-HA, 437

- ultralonghaul submarine, 595
- ultra-long-haul (ULH), 1, 595
- ultra-long-haul fiber-optic transmission systems, 445
- UltraWaveTM IDF, 681

- UltraWaveTM SLA, 681
- undepleted pump approximation, 99
- unidirectional and bidirectional optical transmission, 253
- unidirectional transmission lines, 253
- unintended generation of SRS, 569

- VAD technique, 199
- variable optical attenuator (VOA), 277
- variance of the depletion, 589
- vestigial sideband (VSB), 474, 712
- vibrational mode, 2, 35, 309
- voice traffic, 595

- walk-off, 215
- waveguide, 306
- waveguide dispersion, 162
- waveguide grating router (WGR), 690, 712
- wavelength add-drop devices, 596
- wavelength agnostic, 14
- wavelength converters, 306
- wavelength-division-multiplex(-ed) (-ing), 712
- wavelength-division-multiplexed (WDM), 301, 447
- wavelength-division-multiplexed (WDM) pumping, 121
- WDM backbone networks, 674
- WDM couplers, 142
- WDM transients, 243
- west-east (WE) transmission, 280
- Wide Sense Stationary linear stochastic process, 240
- wideband amplifiers (WBAs), 445
- Wiener-Khintchine theorem, 497

- Yb-doped, 355

- zero dispersion wavelength, 303
- zero-point fluctuations, 48

Springer Series in OPTICAL SCIENCES

New editions of volumes prior to volume 70

- 1 **Solid-State Laser Engineering**
By W. Koechner, 5th revised and updated ed. 1999, 472 figs., 55 tabs., XII, 746 pages
- 14 **Laser Crystals**
Their Physics and Properties
By A.A. Kaminskii, 2nd ed. 1990, 89 figs., 56 tabs., XVI, 456 pages
- 15 **X-Ray Spectroscopy**
An Introduction
By B.K. Agarwal, 2nd ed. 1991, 239 figs., XV, 419 pages
- 36 **Transmission Electron Microscopy**
Physics of Image Formation and Microanalysis
By L. Reimer, 4th ed. 1997, 273 figs. XVI, 584 pages
- 45 **Scanning Electron Microscopy**
Physics of Image Formation and Microanalysis
By L. Reimer, 2nd completely revised and updated ed. 1998,
260 figs., XIV, 527 pages

Published titles since volume 70

- 70 **Electron Holography**
By A. Tonomura, 2nd, enlarged ed. 1999, 127 figs., XII, 162 pages
- 71 **Energy-Filtering Transmission Electron Microscopy**
By L. Reimer (Ed.), 1995, 199 figs., XIV, 424 pages
- 72 **Nonlinear Optical Effects and Materials**
By P. Günter (Ed.), 2000, 174 figs., 43 tabs., XIV, 540 pages
- 73 **Evanescent Waves**
From Newtonian Optics to Atomic Optics
By F. de Fornel, 2001, 277 figs., XVIII, 268 pages
- 74 **International Trends in Optics and Photonics**
ICO IV
By T. Asakura (Ed.), 1999, 190 figs., 14 tabs., XX, 426 pages
- 75 **Advanced Optical Imaging Theory**
By M. Gu, 2000, 93 figs., XII, 214 pages
- 76 **Holographic Data Storage**
By H.J. Coufal, D. Psaltis, G.T. Sincerbox (Eds.), 2000
228 figs., 64 in color, 12 tabs., XXVI, 486 pages
- 77 **Solid-State Lasers for Materials Processing**
Fundamental Relations and Technical Realizations
By R. Iffländer, 2001, 230 figs., 73 tabs., XVIII, 350 pages
- 78 **Holography**
The First 50 Years
By J.-M. Fournier (Ed.), 2001, 266 figs., XII, 460 pages
- 79 **Mathematical Methods of Quantum Optics**
By R.R. Puri, 2001, 13 figs., XIV, 285 pages
- 80 **Optical Properties of Photonic Crystals**
By K. Sakoda, 2001, 95 figs., 28 tabs., XII, 223 pages
- 81 **Photonic Analog-to-Digital Conversion**
By B.L. Shoop, 2001, 259 figs., 11 tabs., XIV, 330 pages
- 82 **Spatial Solitons**
By S. Trillo, W.E. Torruellas (Eds.), 2001, 194 figs., 7 tabs., XX, 454 pages
- 83 **Nonimaging Fresnel Lenses**
Design and Performance of Solar Concentrators
By R. Leutz, A. Suzuki, 2001, 139 figs., 44 tabs., XII, 272 pages
- 84 **Nano-Optics**
By S. Kawata, M. Ohtsu, M. Irie (Eds.), 2002, 258 figs., 2 tabs., XVI, 321 pages
- 85 **Sensing with Terahertz Radiation**
By D. Mittleman (Ed.), 2003, 207 figs., 14 tabs., XVI, 337 pages

Springer Series in OPTICAL SCIENCES

86 Progress in Nano-Electro-Optics I

Basics and Theory of Near-Field Optics

By M. Ohtsu (Ed.), 2003, 118 figs., XIV, 161 pages

87 Optical Imaging and Microscopy

Techniques and Advanced Systems

By P. Török, F.-J. Kao (Eds.), 2003, 260 figs., XVII, 395 pages

88 Optical Interference Coatings

By N. Kaiser, H.K. Pulker (Eds.), 2003, 203 figs., 50 tabs., XVI, 504 pages

89 Progress in Nano-Electro-Optics II

Novel Devices and Atom Manipulation

By M. Ohtsu (Ed.), 2003, 115 figs., XIII, 188 pages

90 Raman Amplifiers for Telecommunications

By Mohammed N. Islam, 2004, 508 figs., XXX, 740 pages